

LAMINAR CRACKING IN POST-TENSIONED CONCRETE
NUCLEAR CONTAINMENT BUILDINGS

A Dissertation
Presented to
The Academic Faculty

by

Bradley P. Dolphyn

In Partial Fulfillment
of the Requirements for the Degree
Doctor of Philosophy in the
School of Civil & Environmental Engineering

Georgia Institute of Technology
May 2016

Copyright © Bradley P. Dolphyn 2016

LAMINAR CRACKING IN POST-TENSIONED CONCRETE
NUCLEAR CONTAINMENT BUILDINGS

Approved by:

Dr. Kimberly E. Kurtis, Co-Advisor
School of Civil and Environmental
Engineering
Georgia Institute of Technology

Dr. Laurence J. Jacobs
School of Civil and Environmental
Engineering
Georgia Institute of Technology

Dr. James J. Wall
School of Mechanical Engineering,
Adjunct
Georgia Institute of Technology
Electric Power Research Institute

Dr. Lawrence F. Kahn, Co-Advisor
School of Civil and Environmental
Engineering
Georgia Institute of Technology

Dr. T. Russell Gentry
College of Architecture
Georgia Institute of Technology

Date Approved: March 14, 2016

ACKNOWLEDGEMENTS

I would like to express my sincerest gratitude to my advisors, Dr. Lawrence F. Kahn and Dr. Kimberly E. Kurtis. The opportunity to work with the two of them was a major factor in my decision to pursue this research project, and I've learned and grown tremendously through their guidance, teaching, and encouragement. I appreciate Dr. Kahn's presence in the structures lab and his availability to help when issues arose; even when he was helping other students, his input was enlightening to me. I appreciate Dr. Kurtis's intentionality in pushing me to work hard while also looking out for my personal wellbeing. Despite the challenges along the way, I always felt better after talking with her.

I would also like to thank my thesis committee members, Dr. Laurence J. Jacobs, Dr. T. Russell Gentry, and Dr. James J. Wall, for reading this dissertation and providing guidance with various aspects of the research. I'm thankful to Dr. Jacobs for allowing me to use much of his lab equipment for my research and for making me feel like a welcome member of his lab group. I must also thank Dr. Jin-Yeon Kim for helping me learn the principles of ultrasonic testing and data analysis and providing suggestions for effective nondestructive evaluation applications.

I may never have gotten to this point without Dr. Gentry, who played a big role in my transition from architecture to civil engineering and introduced me to research as an undergraduate student. I'm glad that I had the opportunity to work with him on the Georgia Tech Solar Decathlon House and thankful that he's still a part of my learning experience at Georgia Tech.

I would like to thank Dr. Wall, my project manager, for his supportive approach to the work and his willingness to provide resources and involve colleagues to the betterment of the research. This project was funded by the Electric Power Research Institute (EPRI), but their contributions went well beyond that. Maria Guimaraes and Yann Le Pape helped with the early stages of research planning, and Salvador Villalobos helped with nondestructive evaluation towards the end of the project.

This work would not have been possible without the assistance of Daniel Toon at United Forming and the generosity of Ken Bolton and Tom Gilpin at Aluma Systems for allowing us to borrow much of the formwork used in the research. Additionally, I would like to thank Joe Wolfe at W.R. Grace for donating the admixtures used for this project and Andy Chafin at Heidelberg Cement Technology Center for conducting analysis on cement samples. I am also indebted to Jeff Carroll and Philip Snider at the Georgia Department of Transportation (GDOT) for allowing me to use their concrete coefficient of thermal expansion equipment.

I appreciate the years of assistance and friendship that Jeremy Mitchell provided at the structures lab, and I'm grateful for the many undergraduate research assistants that made working at the lab an enjoyable experience: Liz Nolte, Kevin Dascall, Zach Gunter, Jaime Ghitelman, John Jung, Kehinde Alonge, Chiyu Zhang, Mary Shinnars, Vu Nguyen, Tejasvee Prasad, Frank Krech, and James Rowe. I'm also grateful for the regular help at the lab provided by Mitchell McKay, Daniel Schuetz, Lorintz Gleich, Falak Shah, Tim Wright, Sung-Hu Kim, Laura Redmond, Genevieve Pezzola, and Giovanni Loreto.

I've been fortunate to work in a research group with so many great individuals. I thank the following officemate and groupmates for providing such a great atmosphere

each and every day: Robert Moser, Amal Jayapalan, Boyeon Lee, Chris Shearer, Passarin Jongvisuttisun, Nathan Mayercsik, Alvaro Paul, Elizabeth Nadelman, Behnaz Zaribaf, Mehdi Rashidi, Gun Kim, Lisa Burris, La Sasha Walker, and Natalia Cardelino. In addition, I cannot thank Prasanth Alapati enough for allowing me to use his office computer for running simulations and analyses over the past few months.

I am also grateful for my friends and family who have been by my side through this journey and for the support and encouragement that they've always provided. I'm blessed to have lived so close to my grandparents, aunts, uncles, and cousins; I'm always so happy to be able to visit and spend time together.

Most of all, I want to thank my parents, Steve and Pam Dolphyn, and my sister, Melinda Dolphyn, for their endless, unconditional love, support, and encouragement. You've inspired me in countless ways, and I see so much of each of you in who I am today.

TABLE OF CONTENTS

	Page
ACKNOWLEDGEMENTS	iii
LIST OF TABLES	xv
LIST OF FIGURES	xix
LIST OF SYMBOLS	xxix
LIST OF ABBREVIATIONS	xxxii
SUMMARY	xxxiii
 <u>CHAPTER</u>	
1 INTRODUCTION	1
1.1 Purpose and Objectives	1
1.2 Need for Research	2
1.3 Scope	4
1.4 Organization of Dissertation	7
2 LITERATURE REVIEW	9
2.1 Nuclear Reactors and Containments	9
2.1.1 Nuclear Reactor Types	9
2.1.2 Progression of Containment Design	10
2.1.3 Post-Tensioned Concrete Containment Details	10
2.1.4 Crystal River 3 Nuclear Power Plant	14
2.1.4.1 Containment Structure	15
2.1.4.2 Containment Concrete Design	16
2.2 Post-Tensioned Concrete Containment Delaminations	18
2.2.1 Turkey Point 3 Dome Delamination	18

2.2.2 Kaiga 1 Dome Delamination	19
2.2.3 Crystal River 3 Dome Delamination	19
2.2.4 Crystal River 3 Bay 34 Delamination	20
2.2.5 Crystal River 3 Bay 56 and Bay 12 Delaminations	24
2.3 Investigation of Crystal River 3 Bay 34 Delamination	25
2.3.1 Concrete Material Properties	27
2.3.1.1 Compressive Strength	27
2.3.1.2 Tensile Strength	28
2.3.1.3 Modulus of Elasticity and Poisson's Ratio	30
2.3.1.4 Properties Related to Thermal Strains	31
2.3.2 Air Content	31
2.3.3 Discussion on Delaminations	34
2.4 Mechanisms of Degradation of Post-Tensioned Concrete Containments	35
2.4.1 Concrete Drying Shrinkage and Creep	36
2.4.2 Stress Relaxation	37
2.4.3 Thermal Loading	38
2.4.3.1 Elevated Temperatures	38
2.4.3.2 Freeze-Thaw Cycling	41
2.4.4 Carbonation	41
2.4.5 Steel Corrosion	42
2.4.5.1 Corrosion of Conventional Reinforcement	42
2.4.5.2 Corrosion of Prestressed Tendons	43
2.4.5.3 Corrosion of Steel Liner	45
2.4.6 Alkali-Aggregate Reactions	47
2.4.7 Sulfate Attack	49

2.4.8 Mass Concrete Effects	49
2.4.8.1 Criteria and Restrictions for Mass Concrete	50
2.4.8.2 Methods of Limiting Mass Concrete Effects	52
2.4.8.3 Non-Uniform Properties	54
2.4.9 Monitoring Prestressed Concrete Containments for Degradation	54
2.5 Containment Mock-Ups	56
2.5.1 Early Testing	56
2.5.2 1:6-Scale Reinforced Concrete Containment Mock-Up	57
2.5.3 1:4-Scale Prestressed Concrete Containment Mock-Up (Ohi-3)	61
2.5.4 1:10-Scale Prestressed Concrete Containment Mock-Up	63
2.5.5 Non-Uniform 1:3-Scale Mock-Up (MAEVA)	63
2.5.6 Mock-Ups for Seismic Testing	64
2.5.7 Representative Structural Volume Mock-Ups (PACE)	65
2.5.8 Discussion on Containment Mock-Ups	68
2.6 Heat of Hydration of Cementitious Materials	69
2.6.1 Heat of Complete Hydration	70
2.6.2 Degree of Hydration	72
2.6.3 Influence of Temperature on Hydration	72
2.6.4 Nurse-Saul Maturity Function	73
2.6.5 Equivalent Age (Arrhenius) Maturity Function	75
2.6.6 Three-Parameter Model for Degree of Hydration	77
2.6.7 Hydration Parameters	79
2.6.8 Determining Apparent Activation Energy	82
2.6.9 Influence of Activation Energy on Rate of Hydration	86
2.6.10 Literature Values for Apparent Activation Energy	89

2.6.11 Heat Generation and Temperature Change	92
2.7 Thermal Properties of Concrete	93
2.7.1 Specific Heat Capacity	93
2.7.1.1 Typical Values	93
2.7.1.2 Experimental Methods	98
2.7.2 Thermal Conductivity	102
2.7.2.1 Typical Values	103
2.7.2.2 Experimental Methods	106
2.7.3 Thermal Diffusivity	107
2.7.3.1 Literature Values	108
2.7.3.2 Theoretical Solutions for Transient Heat Conduction	110
2.7.3.3 Experimental Methods	120
2.7.3.4 Initial Temperature Differential	124
2.7.3.5 Discussion of Short and Infinite Cylinders	125
2.7.4 Coefficient of Linear Thermal Expansion	129
2.7.4.1 Literature Values	130
2.7.4.2 Experimental Methods	132
3 INFLUENCE OF MASS CONCRETE THERMAL BEHAVIOR ON DEVELOPMENT OF CONCRETE PROPERTIES	139
3.1 Introduction	139
3.1.1 Criteria and Restrictions for Mass Concrete	140
3.1.2 Crystal River 3 Containment Building	141
3.1.2.1 Structure	141
3.1.2.2 Materials	143
3.1.2.3 Properties	146
3.1.2.4 Post-Tensioning	151

3.2 Objective	152
3.3 Experimental Work	152
3.3.1 Mock-Ups	153
3.3.2 Post-Tensioning	159
3.3.3 Materials	165
3.3.3.1 Cement	166
3.3.3.2 Coarse Aggregate	169
3.3.3.3 Fine Aggregate	170
3.3.3.4 Admixtures	171
3.3.4 Property Characterization	171
3.3.4.1 Curing Conditions	171
3.3.4.2 Mechanical Properties	173
3.3.4.3 Coefficient of Linear Thermal Expansion	173
3.3.4.3.1 CRD-C 39-81	174
3.3.4.3.2 AASHTO T 336 and Tex-428-A	175
3.3.4.4 Time of Final Setting	177
3.3.4.5 Density, Percent Absorption, and Percent Voids	178
3.3.4.6 Statistical Analysis	178
3.4 Results and Discussion	179
3.4.1 Density, Percent Absorption, and Percent Voids	179
3.4.2 Naming Convention	179
3.4.3 Mock-Up Temperatures	180
3.4.5 Mechanical Properties	187
3.4.5.1 Compressive Strength	188
3.4.5.2 Splitting Tensile Strength	191

3.4.5.3	Modulus of Elasticity	195
3.4.5.4	Poisson's Ratio	202
3.4.6	Coefficient of Linear Thermal Expansion	206
3.4.6.1	Army Corps CRD-C 39-81	206
3.4.6.2	AASHTO and Texas Method	207
3.4.7	Thermal Stresses	212
3.4.8	Mock-Up Strains	218
3.5	Conclusions	225
4	MODELING CONCRETE PROPERTY DEVELOPMENT	227
4.1	Introduction	227
4.1.1	Objectives	228
4.2	Models for Concrete Properties	229
4.2.1	Hydration Parameters	229
4.2.2	Apparent Activation Energy	231
4.2.3	Development of Concrete Mechanical Properties	232
4.2.3.1	Compressive Strength	232
4.2.3.2	Splitting Tensile Strength	233
4.2.3.3	Modulus of Elasticity	234
4.2.3.4	Poisson's Ratio	235
4.2.4	Concrete Thermal Properties	237
4.3	Experimental Methods	238
4.3.1	Hydration Properties	238
4.3.2	Specific Heat Capacity	239
4.3.3	Thermal Diffusivity	241
4.3.4	Statistical Analysis	242

4.4 Results and Discussion	242
4.4.1 Hydration Kinetics	243
4.4.2 Concrete Maturity	251
4.4.3 Compressive Strength	254
4.4.4 Splitting Tensile Strength	266
4.4.5 Modulus of Elasticity	283
4.4.6 Poisson's Ratio	299
4.4.7 Specific Heat Capacity	300
4.4.8 Thermal Diffusivity	303
4.4.9 Thermal Conductivity	307
4.5 Conclusions	309
5 FINITE ELEMENT ANALYSIS	312
5.1 Introduction	312
5.1.1 Tensile Creep	313
5.1.2 Objectives	314
5.2 ConcreteWorks Modeling	314
5.2.1 Model Inputs	315
5.2.1.1 Mixture Proportion and Material Properties	315
5.2.1.2 Curing, Formwork, and Environmental Conditions	317
5.2.2 ConcreteWorks Results	319
5.2.2.1 General Behavior	319
5.2.2.2 Daily Variation	323
5.2.2.3 Discussion	327
5.3 Replication of ConcreteWorks Results in COMSOL Multiphysics	328
5.3.1 Model Description	328

5.3.2	Results	333
5.3.3	Discussion	335
5.4	Representative Mock-Up Model in COMSOL Multiphysics	335
5.4.1	Determination of Model Symmetry	335
5.4.1.1	Model Description	335
5.4.1.2	Material Properties	338
5.4.1.3	Convective Heat Transfer Coefficient	340
5.4.1.4	Results	342
5.4.2	Final Model	344
5.4.2.1	Model Description	345
5.4.2.2	Functions for Mechanical Properties	347
5.4.3	Results and Discussion	350
5.4.3.1	Temperatures	350
5.4.3.2	Mock-Up Post-Tensioning Stresses	352
5.4.3.3	CR3 PCC Post-Tensioning Stresses	367
5.4.3.4	Discussion of Crack Propagation	371
5.5	Conclusions	373
6	PARAMETER STUDY	375
6.1	Introduction	375
6.1.1	Objectives	375
6.2	Description	375
6.3	Results and Discussion	378
6.3.1	Concrete Material Properties	379
6.3.2	Duct Geometry and Modulus of Elasticity	384
6.3.3	Post-Tensioning Forces	388

6.3.4 Comparison of Parameters	392
6.4 Conclusions	393
7 NONDESTRUCTIVE EVALUATION	395
7.1 Introduction	395
7.1.1 Objectives	396
7.2 Methodology	397
7.3 Results and Discussion	399
7.4 Conclusions	411
8 CONCLUSIONS AND RECOMMENDATIONS	412
8.1 Conclusions	412
8.2 Recommendations	415
8.3 Future Research	416
APPENDIX A: CALCULATIONS AND DERIVATIONS	418
A.1 Volume-to-Surface Area Ratio of Typical CR3 PCC Pour	418
A.2 Datum Temperature for Nurse-Saul Maturity Function	419
A.3 Model for Specific Heat Capacity of Mock-Up Concrete	420
A.4 Balance Line and Depth of Thermal Stress Block	421
APPENDIX B: PROPERTIES OF HARDENED CONCRETE, COMPLETE RESULTS	423
B.1 Percent Absorption, Density, and Percent Permeable Voids	423
B.2 Mechanical Properties	425
B.3 Thermal Properties	457
APPENDIX C: POST-TENSIONING SEQUENCE	459
REFERENCES	463

LIST OF TABLES

	Page
Table 2.1: Prestressed concrete containment types of currently licensed U.S. commercial pressurized water reactors	12
Table 2.2: Primary concrete mix design (saturated-surface dry) used in delaminated region of CR3 PCC	26
Table 2.3: Specific heat capacity values of concrete	94
Table 2.4: Specific heat capacity values of concrete components	95
Table 2.5: Thermal conductivity values of concrete components	104
Table 2.6: Thermal diffusivity trends	110
Table 2.7: Coefficient of linear thermal expansion values for concrete containing limestone coarse aggregate	132
Table 3.1: Primary concrete mix design used in delaminated region of the CR3 PCC	144
Table 3.2: ASTM C150 limits for Type II cement with moderate heat of hydration	144
Table 3.3: Oxide analysis and phase composition of CR3 PCC cement	146
Table 3.4: Compressive strength development of CR3 PCC concrete specimens	149
Table 3.5: Compressive strength development of concrete made with Type II cement	149
Table 3.6: Results of flow test for cementitious grout used for bearing plates	162
Table 3.7: Results of compression tests on cementitious grout specimens	163
Table 3.8: Oxide analysis and phase composition of mock-up cement	166
Table 3.9: Compressive strength of the mock-up concrete	191
Table 3.10: Splitting tensile strength of the mock-up concrete	194
Table 3.11: Modulus of elasticity of mock-up concrete	198
Table 3.12: Poisson's ratio of the mock-up concrete	205

Table 3.13:	CTE results for concrete from the first mock-up tested in accordance with Army Corps CRD-C 39-81	207
Table 3.14:	CTE results for concrete from the first truck of the first mock-up tested in accordance with AASHTO 336 and the Texas Method	211
Table 4.1:	Power law relationship parameters for splitting tensile strength as function of compressive strength	234
Table 4.2:	Mix designs for calorimetry samples	239
Table 4.3:	Experimentally determined apparent activation energy and hydration parameters of mock-up cement paste	251
Table 4.4:	Literature model values for apparent activation energy and hydration parameters of mock-up cement paste with AEA and WRRET	251
Table 4.5:	Parameters for compressive strength development	259
Table 4.6:	Modeled compressive strength of mock-up concrete at 90 days and 36 years	259
Table 4.7:	Parameters for compressive strength development of CR3 PCC concrete and typical concrete made with Type II cement	261
Table 4.8:	Parameters for splitting tensile strength development as a power law function of compressive strength	274
Table 4.9:	Coefficients of determination for regressions of splitting tensile strength with respect to equivalent age	280
Table 4.10:	Power law parameters and coefficients of determination for modulus of elasticity as function of compressive strength	290
Table 4.11:	Exponential function parameters and coefficients of determination for modulus of elasticity as function of equivalent age	293
Table 4.12:	Coefficients of determination for modulus of elasticity as function of equivalent age	296
Table 5.1:	Parameters related to heat generation used in COMSOL	330
Table 5.2:	Values of mechanical properties at 69 days based on fog-cured results	349
Table 6.1:	Values of investigated parameters	376
Table B.1:	Percent absorption, density, and percent permeable voids of hardened concrete for second mock-up	424

Table B.2:	Compressive strength and associated ANOVA results for concrete from the two trucks for the first mock-up	429
Table B.3:	ANOVA results at each age for compressive strength of Ext and Int specimens from first mock-up	432
Table B.4:	Compressive strength and ANOVA results for concrete from the second mock-up	433
Table B.5:	ANOVA results at each age for compressive strength of Ext and Int specimens from second mock-up	434
Table B.6:	ANOVA results for compressive strength of specimens from both mock-ups	434
Table B.7:	Splitting tensile strength and associated ANOVA results for concrete from the two trucks for the first mock-up	436
Table B.8:	ANOVA results at each age for splitting tensile strength of Ext and Int specimens from first mock-up	439
Table B.9:	Splitting tensile strength and ANOVA results for concrete from the second mock-up	440
Table B.10:	ANOVA results at each age for splitting tensile strength of Ext and Int specimens from second mock-up	441
Table B.11:	ANOVA results for splitting tensile strength of specimens from both mock-ups	441
Table B.12:	Modulus of elasticity and associated ANOVA results for concrete from the two trucks for the first mock-up	443
Table B.13:	ANOVA results at each age for modulus of elasticity of Ext and Int specimens from first mock-up	446
Table B.14:	Modulus of elasticity and ANOVA results for concrete from the second mock-up	447
Table B.15:	ANOVA results at each age for modulus of elasticity of Ext and Int specimens from second mock-up	448
Table B.16:	ANOVA results for modulus of elasticity of specimens from both mock-ups	448
Table B.17:	Poisson's ratio and associated ANOVA results for concrete from the two trucks for the first mock-up	450

Table B.18: ANOVA results at each age for Poisson's ratio of Ext and Int specimens from first mock-up	453
Table B.19: Poisson's ratio and ANOVA results for concrete from the second mock-up	454
Table B.20: ANOVA results at each age for Poisson's ratio of Ext and Int specimens from second mock-up	455
Table B.21: ANOVA results for Poisson's ratio of specimens from both mock-ups	455
Table B.22: Thermal diffusivity results	457
Table B.23: Coefficient of linear thermal expansion results as tested in accordance with CRD-C 29-81	458
Table C.1: Dates and ages of mock-up construction and testing	459
Table C.2: Post-tensioning sequence for first mock-up	461
Table C.3: Post-tensioning sequence for second mock-up	462

LIST OF FIGURES

	Page
Figure 2.1: Containment types of currently licensed U.S. commercial nuclear power reactors by year of issuance of initial operating license	12
Figure 2.2: Diagrams of PCC geometry and tendon arrangement	13
Figure 2.3: Typical section of CR3 containment wall	16
Figure 2.4: Diagram of unfolded elevation showing the SGR opening location	21
Figure 2.5: Photograph of delamination after removal of concrete for SGR opening	22
Figure 2.6: Photograph of bay 34 with overlay indicating the extent of the delamination	23
Figure 2.7: Plan diagram showing locations and date of occurrence or identification of CR3 wall delaminations	25
Figure 2.8: Diagram of delaminated region of CR3 PCC with outline of portion of bay in which mix design DM-5-Mod was used	26
Figure 2.9: Remaining prestressing force from lift-off tests normalized by initial prestressing force	40
Figure 2.10: Remaining force from gauges normalized by initial force	40
Figure 2.11: Embedded wood found in containment concrete at Beaver Valley Unit 1 after removal of corroded liner	47
Figure 2.12: Uniaxial specimens for strain concentration and liner tear studies	59
Figure 2.13: Panel mock-ups for investigation of liner behavior at local regions of containment	60
Figure 2.14: Predictions of radial displacement at mid-height of cylinder wall vs. internal pressure	62
Figure 2.15: Rendering of an RSV with tendons and reinforcement shown	68
Figure 2.16: Experimental setup for PACE 1450	68
Figure 2.17: Influence of hydration parameters on the progression of hydration	78
Figure 2.18: Influence of activation energy on age conversion factor	88

Figure 2.19:	Influence of activation energy on reaction rate constant	89
Figure 2.20:	Specific heat capacity of water as a function of temperature	95
Figure 2.21:	Convergence of first-term approximations with theoretical solutions for dimensionless temperature at the axis of an infinite right cylinder and midplane of an infinite plane slab	117
Figure 2.22:	Dimensionless temperature history data	126
Figure 2.23:	Dimensionless temperature history at the center of a cylinder	127
Figure 3.1:	Typical section of CR3 PCC wall	143
Figure 3.2:	Plan drawing of mock-ups as cast and cured	154
Figure 3.3:	Front elevation drawing of mock-ups as cast and cured	155
Figure 3.4:	Section A-A drawing of mock-ups as cast and cured	156
Figure 3.5:	Drawings of gauge location and orientation	158
Figure 3.6:	Detail A (see Figure 3.5) of series of transverse gauges	159
Figure 3.7:	Post-tensioning anchorage system	160
Figure 3.8:	Post-tensioning rod resting on duct embedded in concrete, plywood spacer beneath bearing plate lifting rod to center of duct, and full stack of plates and plywood spacers against the concrete	161
Figure 3.9:	Fresh grout placed on concrete surface beneath bearing plate, bearing plate lowered onto grout, and finished grout after hammering bearing plate and tightening nut	162
Figure 3.10:	Identification of post-tensioning rods and post-tensioning and detensioning sequences	164
Figure 3.11:	Tensile forces in post-tensioning rods	165
Figure 3.12:	C3S and C3S plus C3A contents of cements produced in different years	168
Figure 3.13:	C3A content of cements produced in different years	168
Figure 3.14:	Cumulative 7-day heat of hydration of cements produced in different years	169
Figure 3.15:	Gradation curve of limerock coarse aggregate	170

Figure 3.16: Gradation curve of natural silica sand	171
Figure 3.17: Specimens in match-curing storage tank	172
Figure 3.18: Specimens for CTE testing in accordance with CRD-C 39-81	175
Figure 3.19: Set-up for AASHTO T 336 and Tex-428-A CTE testing	176
Figure 3.20: Concrete specimen curing temperature histories	182
Figure 3.21: Section detail and temperature profile through thickness of second mock-up measured by C gauges at time of maximum temperature differential	183
Figure 3.22: Quadratic regressions of temperature profiles through thickness of second mock-up	185
Figure 3.23: Temperature contours at midheight of second mock-up	187
Figure 3.24: Compressive strength of (a) first and (b) second mock-up concrete	190
Figure 3.25: Splitting tensile strength of (a) first and (b) second mock-up concrete	193
Figure 3.26: Failed I-Int-1 splitting tensile strength specimen tested at 1 day	195
Figure 3.27: Modulus of elasticity of (a) first and (b) second mock-up concrete	197
Figure 3.28: Modulus of elasticity versus compressive strength	201
Figure 3.29: Poisson's ratio of the (a) first and (b) second mock-up concrete	204
Figure 3.30: Cracked specimen from modulus of elasticity and Poisson's ratio testing	205
Figure 3.31: CTE results for concrete from the first mock-up tested in accordance with Army Corps CRD-C 39-81	207
Figure 3.32: Length change and temperature histories for determination of CTE in accordance with AASHTO T 336	208
Figure 3.33: Strain as a function of temperature for determination of CTE in accordance with Tex-428-A	209
Figure 3.34: CTE results for concrete from the first truck of the first mock-up tested in accordance with AASHTO 336 and the Texas Method	210
Figure 3.35: Piecewise-linear regression of AASHTO T 336 results	212

Figure 3.36:	Degree of restraint, maximum temperature difference, modulus of elasticity, and tensile thermal stress of second mock-up normalized by maximum value during first 14 days	214
Figure 3.37:	Thermal stresses and predicted direct tensile strength	217
Figure 3.38:	Rate of temperature change of second mock-up concrete	218
Figure 3.39:	Total strains measured in mock-up during first 12 hours after beginning of concrete placement	219
Figure 3.40:	Total, thermal, and non-thermal strains measured in second mock-up during first 28 days	221
Figure 3.41:	Thermal strain as a percentage of total strain over first 6 days	222
Figure 3.42:	Post-tensioning strains measured in C' gauges of second mock-up	223
Figure 3.43:	Hypothetical stress-strain curve fitting mock-up concrete properties	225
Figure 4.1:	De Schutter and Taerwe (1996) Poisson's ratio model for concrete	236
Figure 4.2:	Coarse aggregate sample preparation for differential scanning calorimetry	240
Figure 4.3:	Full set-up for differential scanning calorimetry	240
Figure 4.4:	Rate of heat evolution and cumulative heat of hydration of representative mock-up cement pastes at 25 °C (77 °F)	244
Figure 4.5:	Peak rates of heat evolution and times to peak rate of heat evolution for tested cement pastes	245
Figure 4.6:	Rate of heat evolution, cumulative heat of hydration, and degree of hydration of representative mock-up cement pastes	246
Figure 4.7:	Variation of the natural logarithm of the hydration time parameter as a function of the reciprocal of the absolute temperature	249
Figure 4.8:	Maturity indices of concrete specimens for first mock-up	253
Figure 4.9:	Equivalent age of concrete specimens for each mock-up	253
Figure 4.10:	Compressive strength of first mock-up concrete	255
Figure 4.11:	Compressive strength of second mock-up concrete	256
Figure 4.12:	Compressive strength as a function of equivalent age of fog- and match-cured specimens	258

Figure 4.13: Compressive strength development of CR3 PCC concrete and typical concrete made with Type II cement	260
Figure 4.14: Compressive strength of match-cured specimens with respect to that of fog-cured specimens	263
Figure 4.15: Compressive strength as a function of equivalent age of match-cured specimens with comparison to 90% relationship	265
Figure 4.16: Splitting tensile strength of first mock-up concrete	267
Figure 4.17: Splitting tensile strength of second mock-up concrete	268
Figure 4.18: Splitting tensile strength with respect to compressive strength of all specimens	272
Figure 4.19: Splitting tensile strength as a function of equivalent age of fog- and match-cured specimens	273
Figure 4.20: Splitting tensile strength with respect to compressive strength of all specimens	275
Figure 4.21: Compressive strength-to-splitting tensile strength (f_c/f_{tsp}) ratio with respect to compressive strength	277
Figure 4.22: Splitting tensile strength with respect to compressive strength with Zain regressions	277
Figure 4.23: Match-cured splitting tensile strengths with respect to equivalent age and corresponding regressions	279
Figure 4.24: Splitting tensile strength of match-cured specimens with respect to that of fog-cured specimens	282
Figure 4.25: Modulus of elasticity of first mock-up concrete	284
Figure 4.26: Modulus of elasticity of second mock-up concrete	285
Figure 4.27: Modulus of elasticity with respect to compressive strength of all specimens with individual power law regressions	288
Figure 4.28: Modulus of elasticity with respect to compressive strength of all specimens with combined power law regressions	289
Figure 4.29: Modulus of elasticity with respect to equivalent age of all specimens with (a) individual and (b) combined exponential regressions	292
Figure 4.30: Modulus of elasticity with respect to equivalent age	294

Figure 4.31: Modulus of elasticity of match-cured specimens with respect to that of fog-cured specimens	298
Figure 4.32: Poisson's ratio of all mock-up concrete specimens	300
Figure 4.33: Specific heat capacities and linear regressions with respect to temperature	301
Figure 4.34: Specific heat capacity of mock-up concrete as function of age	303
Figure 4.35: Dimensionless temperature history at center of specimen during thermal diffusivity testing	304
Figure 4.36: Thermal diffusivity results	305
Figure 4.37: Thermal diffusivity of mock-up concrete	306
Figure 4.38: Temperature history at center of specimen during thermal diffusivity testing	307
Figure 4.39: Calculated thermal conductivity values for mock-up concrete	309
Figure 5.1: Plan view diagram of ConcreteWorks symmetries and results grid	315
Figure 5.2: Ambient temperatures recorded during first 14 days	318
Figure 5.3: Temperature variation modeled by ConcreteWorks along line of symmetry through thickness of mock-up	320
Figure 5.4: Experimental temperatures and corresponding ConcreteWorks results	322
Figure 5.5: Second mock-up Ext temperatures and ConcreteWorks near-surface temperatures during first 14 days	323
Figure 5.6: Comparison of experimental and modeled Ext temperature variation with ambient temperatures	326
Figure 5.7: Concrete surface temperatures modeled in ConcreteWorks for constant ambient temperature of 21 °C (70 °F) and sunny and overcast conditions	327
Figure 5.8: Geometry, mesh, and materials for COMSOL model replicating ConcreteWorks	329
Figure 5.9: Experimental temperatures, corresponding ConcreteWorks results, and COMSOL Multiphysics results for matching ConcreteWorks	334
Figure 5.10: Planes of symmetry utilized in COMSOL model of mock-up	337

Figure 5.11: Preliminary COMSOL model of mock-up	338
Figure 5.12: Preliminary modeled mock-up temperatures	344
Figure 5.13: Preliminary mock-up temperature profiles modeled halfway between the vertical post-tensioning ducts	344
Figure 5.14: Diagrams of final COMSOL model	346
Figure 5.15: Experimental temperatures and temperatures modeled by COMSOL and ConcreteWorks	351
Figure 5.16: Plan view between horizontal ducts of modeled stresses in post-tensioned mock-up concrete	353
Figure 5.17: Plan views of modeled stress-to-splitting tensile strength ratio in post-tensioned mock-up concrete	355
Figure 5.18: Plan details of modeled stress-to-splitting tensile strength ratio in post-tensioned mock-up concrete	356
Figure 5.19: Transverse section view of modeled stresses in post-tensioned mock-up concrete	357
Figure 5.20: Transverse section view of modeled stress-to-splitting tensile strength ratio in post-tensioned mock-up concrete at edge of vertical duct	358
Figure 5.21: Longitudinal section view in plane of horizontal ducts of modeled stresses in post-tensioned mock-up concrete	360
Figure 5.22: Longitudinal section views of modeled stress-to-splitting tensile strength ratio in post-tensioned mock-up concrete	361
Figure 5.23: Longitudinal section details of modeled stress-to-splitting tensile strength ratio in post-tensioned mock-up concrete	364
Figure 5.24: Ratio of modeled stress to splitting tensile strength in plane of horizontal ducts without accounting for curing history	366
Figure 5.25: Longitudinal section details of modeled stress-to-splitting tensile strength ratio in plane of horizontal ducts	367
Figure 5.26: Modeled stresses in plane of horizontal ducts with CR3 PCC post-tensioning loads	368
Figure 5.27: Ratio of modeled stress to splitting tensile strength in plane of horizontal ducts with CR3 PCC post-tensioning loads	369

Figure 5.28:	Detail contours of modeled stress-to-splitting tensile strength ratio in plane of horizontal ducts	370
Figure 5.29:	Ratio of modeled stress to splitting tensile strength in plane of circumferential ducts in CR3 PCC when post-tensioned without accounting for curing history	371
Figure 6.1:	Longitudinal section view of modeled stress-to-splitting tensile strength ratio with points of evaluation identified	377
Figure 6.2:	Influence of concrete spitting tensile strength on the (a) σ_1/f_{tsp} values at each point and (b) relative σ_1/f_{tsp} values at each point	381
Figure 6.3:	Influence of concrete modulus of elasticity on the (a) σ_1/f_{tsp} values at each point and (b) relative σ_1/f_{tsp} values at each point	382
Figure 6.4:	Influence of concrete Poisson's ratio on the (a) σ_1/f_{tsp} values at each point and (b) relative σ_1/f_{tsp} values at each point	383
Figure 6.5:	Influence of duct diameter on the (a) σ_1/f_{tsp} values at each point and (b) relative σ_1/f_{tsp} values at each point	385
Figure 6.6:	Influence of duct wall thickness on the (a) σ_1/f_{tsp} values at each point and (b) relative σ_1/f_{tsp} values at each point	386
Figure 6.7:	Influence of duct modulus of elasticity on the (a) σ_1/f_{tsp} values at each point and (b) relative σ_1/f_{tsp} values at each point	387
Figure 6.8:	Influence of vertical post-tensioning force on the (a) σ_1/f_{tsp} values at each point and (b) relative σ_1/f_{tsp} values at each point	389
Figure 6.9:	Influence of horizontal post-tensioning force on the (a) σ_1/f_{tsp} values at each point and (b) relative σ_1/f_{tsp} values at each point	390
Figure 6.10:	Influence of biaxial tensioning force on the (a) σ_1/f_{tsp} values at each point and (b) relative σ_1/f_{tsp} values at each point	391
Figure 6.11:	Influence of parameters evaluated at point C	393
Figure 7.1:	MIRA antenna	396
Figure 7.2:	Orientation of MIRA scan paths for second mock-up	398
Figure 7.3:	Orientation of B-, C-, and D- scan tomograms relative to MIRA antenna and scan path	399
Figure 7.4:	MIRA tomograms along path between vertical ducts; (a) plan view with B-scan, (b) side elevation with D-scan, and (c) front elevation with C-scan at depth of rebar cage	401

Figure 7.5:	MIRA tomograms along path between vertical ducts; (a) plan view with B-scan, (b) side elevation with D-scan, and (c) front elevation with C-scan at depth of horizontal ducts	402
Figure 7.6:	MIRA tomogram along middle vertical duct; (a) plan view, (b) side elevation, and (c) front elevation with C-scan at depth of horizontal ducts	404
Figure 7.7:	MIRA tomogram along middle vertical duct; (a) plan view, (b) side elevation, and (c) front elevation with C-scan at depth of vertical ducts	405
Figure 7.8:	MIRA tomograms along path between middle horizontal ducts; (a) plan view with D-scan, (b) side elevation, and (c) front elevation with C-scan at depth of vertical ducts	407
Figure 7.9:	MIRA tomograms along horizontal duct; (a) plan view with D-scan, (b) side elevation with B-scan, and (c) front elevation with full-depth C-scan	409
Figure 7.10:	MIRA tomograms along horizontal duct; (a) plan view with D-scan, (b) side elevation with B-scan, and (c) front elevation with C-scan at depth of horizontal ducts	410
Figure B.1:	Compressive strength results for first mock-up sorted by truck and curing condition	435
Figure B.2:	Compressive strength results for second mock-up	435
Figure B.3:	Splitting tensile strength results for first mock-up sorted by truck and curing condition	442
Figure B.4:	Splitting tensile strength results for second mock-up sorted by truck and curing condition	442
Figure B.5:	Modulus of elasticity results for first mock-up sorted by truck and curing condition	449
Figure B.6:	Modulus of elasticity results for second mock-up sorted by truck and curing condition	449
Figure B.7:	Poisson's ratio results for first mock-up sorted by truck and curing condition	456
Figure B.8:	Poisson's ratio results for second mock-up sorted by truck and curing condition	456

Figure C.1: Identification of post-tensioning rods and post-tensioning and detensioning sequences

460

LIST OF SYMBOLS

A	area, m ² (ft ²)
Bi	Biot number
C_f	correction factor
c_p	specific heat capacity at constant pressure, J/kg·K (Btu/lb·°F)
c_v	specific heat capacity at constant volume, J/kg·K (Btu/lb·°F)
D	diameter, m (ft)
D_s	calorimetric differential between test specimen and baseline heat flow rate curves, W (Btu/hr)
D_{st}	calorimetric differential between sapphire standard and baseline heat flow rate curves, mW (Btu/hr)
E	heat input, J (Btu)
E_a	activation energy, J/mol (Btu/lbmol)
E_c	modulus of elasticity of concrete, GPa (ksi)
f_c	compressive strength of concrete, MPa (psi)
f'_c	specified compressive strength, MPa (psi)
f'_{cr}	required average compressive strength, MPa (psi)
f_t	direct tensile strength of concrete, MPa (psi)
f'_t	allowable tensile stress in concrete, MPa (psi)
f_{tsp}	splitting tensile strength of concrete, MPa (psi)
Fo	Fourier number
H_{cem}	total heat of hydration of cement, J/g (Btu/lb)
h	convective heat transfer coefficient, also referred to as film coefficient, W/m ² ·K (Btu/hr·ft ² ·°F)
$J_m(\cdot)$	Bessel function of the first kind for non-negative integer order m

K_r	degree of restraint
k	reaction rate constant
L	length
L_c	characteristic length
L_g	gauge length
M	slope
m	mass, kg (lb)
q	heat flux density, W/m ² (Btu/hr·ft ²)
Q	heat flux, W (Btu/hr)
r	radial coordinate
r^*	dimensionless radial coordinate
R	radius
\bar{R}	universal gas constant, 8.3144 J/mol·K (1.986 Btu/lbmol·°R)
s_s	sample standard deviation
t	time
t_e	equivalent age
T	temperature, °C (°F)
T_i	initial temperature
T_∞	medium temperature
x	coordinate in three-dimensional Cartesian space, m (ft)
x^*	dimensionless spatial coordinate
y	coordinate in three-dimensional Cartesian space, m (ft)
z	coordinate in three-dimensional Cartesian space, m (ft)
α	significance level
α_H	degree of hydration

α_{H_u}	ultimate degree of hydration
α_T	coefficient of linear thermal expansion
β	hydration shape parameter
ΔL	length change
ΔT	temperature difference
θ	time-dependent temperature difference
θ^*	dimensionless temperature
θ_i	initial temperature difference
κ	thermal diffusivity
λ	thermal conductivity, W/m·K (Btu/hr·ft·°F)
ρ	density (unit weight)
τ	hydration time parameter, hr
φ	creep coefficient

LIST OF ABBREVIATIONS

AASHTO	American Association of State Highway and Transportation Officials
ACI	American Concrete Institute
AEA	ASTM C260 air-entraining admixture
ANOVA	one-way analysis of variance
ASTM	American Society for Testing and Materials
CR3	Crystal River Unit 3 Nuclear Generating Plant
CTE	coefficient of linear thermal expansion
GGBFS	ground-granulated blast-furnace slag
PCC	post-tensioning concrete containment building
WRRET	ASTM C494 Type D water-reducing and retarding admixture

SUMMARY

Two full-scale mock-ups of a portion of the post-tensioned concrete containment building (PCC) of the Crystal River 3 Nuclear Generating Plant (CR3) were constructed in order to investigate potential contributing factors to the laminar cracking identified in the plane of the circumferential post-tensioning ducts in 2009. Because the CR3 PCC and the mock-ups met many criteria for consideration as mass concrete, the mock-ups were instrumented with temperature and strain gauges to monitor the thermal behavior of the concrete at early ages. Maximum concrete temperatures of approximately 65 to 70 °C (149 to 158 °F) were reached during the first few days of curing, but the temperature difference between the interior and the surface of the concrete was never sufficient to cause thermal cracking in the mock-ups.

Concrete specimens were prepared from the concrete for each mock-up and were match-cured to the temperature histories at the center and near the front surface of the mock-ups in order to simulate the hottest and coolest curing conditions in the mock-up concrete. These specimens were periodically tested for compressive strength, splitting tensile strength, modulus of elasticity, and Poisson's ratio over a period of 180 days. The mock-ups were biaxially post-tensioned with approximately 50% of the force applied in the CR3 PCC tendons, and the measured longitudinal, vertical, and transverse strains were analyzed using the experimentally determined mechanical properties to confirm the expected general behavior of the mock-ups. Investigation of the transverse strains with respect to the concrete modulus of elasticity and tensile strength indicated that cracking may have occurred locally in the plane of the horizontal post-tensioning ducts, but no

strain gauges recorded discontinuities or distinct transitions in strains that would be indicative of cracking.

The development of the mechanical properties as functions of temperature and time were incorporated in finite element analysis of the mock-ups in order to obtain a better understanding of the response of the mock-ups to thermal stresses and post-tensioning loads. Similar to the findings for the mock-ups, the thermal stresses in the models were determined to be insufficient to cause concrete cracking. However, when biaxial post-tensioning loads representative of the mock-up loads were modeled, stress concentrations in the areas where the horizontal and vertical ducts overlapped greatly exceeded the tensile strength of the concrete, indicating the crack initiation would occur at these locations. When the post-tensioning loads were increased to the level used for the CR3 PCC, the regions of excessive tensile stress increased notably, extending almost continuously along the edges of the ducts. These results suggest that cracking around the ducts in the CR3 PCC was present before the laminar cracking was identified in 2009. Furthermore, radial tensile stresses generated by the circumferential post-tensioning forces in the CR3 PCC would exacerbate the tensile stresses modeled for biaxial compression in the mock-ups.

Ultrasonic shear-wave tomography of the mock-ups was conducted to evaluate the subsurface condition of the mock-ups. No clear indications of extensive cracking in the plane of the ducts was identified, consistent with the strain readings and the finite element analysis. However, the limited resolution of ultrasonic techniques penetrating deep into heterogeneous concrete prevents conclusive determination of the existence or absence of cracks along the ducts, where the greatest tensile stresses were modeled.

Though the results for the experimental mock-ups indicated that extensive laminar cracking did not develop in response to thermal or post-tensioning loads, the observed and modeled response indicates that the cracking risk is far significantly greater for the greater loads and cylindrical geometry of the CR3 PCC.

CHAPTER 1

INTRODUCTION

1.1 Purpose and Objectives

The purpose of this research was to investigate factors potentially contributing to degradations in post-tensioned concrete containments (PCCs), particularly those that could contribute to laminar cracking (delamination) in the plane of the post-tensioning ducts. In consideration of the delamination identified in the plane of the circumferential post-tensioning ducts of the Crystal River Unit 3 Nuclear Generating Plant (CR3) PCC in 2009, this research focused on delaminations in PCCs, but the properties, effects, and evaluation methods that were investigated are relevant to other mass concrete structures with layers of embedded components. The research was based on the following hypotheses:

1. Cracks were present in the plane of the CR3 PCC post-tensioning ducts prior to the 2009 observation of the delamination during the operations related to preparing the steam generator replacement (SGR) opening in the PCC.
2. The mass concrete behavior of the CR3 PCC resulted in thermal cracks in the PCC that contributed to the delamination identified in 2009.
3. High early-age concrete temperatures resulted in reduced late-age mechanical properties that resulted in the CR3 PCC being more susceptible to tensile cracking and delamination in the plane of the circumferential ducts when post-tensioned.

The objective of this research was to identify factors that may have contributed to the delamination in the CR3 PCC via literature review, experimental testing, and finite element analysis. In particular, the research focused on the following six objectives:

1. Identify degradation mechanisms that may have contributed to delaminations in PCCs that have not been previously investigated in the literature.
2. Evaluate the mass concrete behavior of the Crystal River 3 PCC and investigate the potential for early-age thermal cracking.
3. Investigate the influence of high early-age concrete temperatures on the development of the mechanical properties of PCC concrete and on the structural behavior of the PCCs.
4. Determine the influence of material and design parameters on the delamination risk of PCCs.
5. Evaluate the effectiveness of nondestructive evaluation (NDE) techniques for monitoring for and detecting delaminations in PCCs and other mass concrete structures with layers of embedded components.
6. Provide recommendations for analyzing PCCs for evaluation of the risk for delaminations.

1.2 Need for Research

The U.S. currently has 99 commercial nuclear power reactors licensed for operation, generating approximately 19% of the nation's net electricity (U.S. Nuclear Regulatory Commission, 2015). Initially licensed for 40 years of operation, 74 reactors have received renewed licenses for an additional 20 years of operation (U.S. Nuclear Regulatory Commission, 2015), and 17 more reactors are under consideration for license renewal or have letters of intent to apply (U.S. Nuclear Regulatory Commission, 2016), meaning that only 8 of the 99 currently licensed reactors have the original license and are not currently intending to apply for extended licensing.

Considerations are being made for standards for subsequent renewal licenses that would extend operation lives to 80 years (Busby and Carpenter, 2012). However, there is limited experience with reactors beyond 40 years of operation: the world's first and

longest-operating commercial-scale nuclear power reactor, Calder Hall in the United Kingdom, closed in 2003 after nearly 47 years of operation (Brown, 2003). The oldest currently operating reactors in the U.S. are Oyster Creek in New Jersey and Nine Mile Point 1 in New York, both of which began commercial operation 46 years ago in December 1969 (U.S. Nuclear Regulatory Commission, 2015).

The PCC of CR3, which began operation in 1977, belongs to the first generation of fully post-tensioned containment buildings in the U.S. Therefore, PCCs similar to the one at CR3 are likely to be among the first to experience problems related to long-term operation. At these NPPs, the PCC serves as the final barrier to the release of radiation from the enclosed nuclear reactor. As a critical safety-related structure, the long-term integrity of the PCC is necessary for continued operation of the reactor. Existing inspection methods, including visual observation of the concrete surface and monitoring post-tensioning tendon end forces, do not provide an accurate understanding of the subsurface condition of the PCC. The delamination in the CR3 PCC was not identified until it was visually observed after removing approximately 10 inches of concrete from the surface (Performance Improvement International, 2010); other PCCs may have similar cracks that have not been identified due to the size of the structures.

The inability to prevent PCC degradations or to detect them early in development can result in substantial costs. The failed efforts to repair the CR3 PCC cost about \$440 million, and the replacement energy while the reactor was shut down cost as much as \$300 million each year (Penn, 2013). Rather than pursuing approximately \$1 billion in further repairs, the owners announced in February 2013 that the plant would be permanently shut down (Penn, 2013).

Other recent, isolated events such as shield building cracking and alkali-silica reaction (ASR)-induced degradation have increased the pressure for obtaining a better understanding of the condition of critical NPP structures. Furthermore, the 2011

Fukushima Dai-ichi nuclear accident has increased public concern regarding the safety of nuclear power.

A report by Performance Improvement International (2010) on the CR3 delamination identified several possible contributing factors, including weak aggregate and concrete, large tendon forces, and the detensioning scope and sequence for the steam generator replacement (SGR) opening. In order to determine how and when the CR3 PCC delamination occurred, a combination of experimental studies and finite element models are needed for exploring the potential causes.

1.3 Scope

This research addressed the objectives outlined in Section 1.1 in order to develop an understanding of the contributing factors to the development and propagation of delamination cracks in PCCs and prepare for extended NPP operation lives. An extensive literature review was conducted in order to identify cases of PCC delaminations, potential PCC degradation mechanisms, methods of representing nuclear containment buildings for experimental investigations, and properties related to heat generation and conduction in concrete that can result in tensile thermal stresses.

Two full-scale, planar mock-ups were constructed to represent a portion of the CR3 PCC where the SGR opening was prepared. The mock-ups were designed and constructed according to documented drawings of the CR3 PCC and reported details of the materials used. Unidentified or uncertain features, such as the possible usage of embedded formwork ties during construction of the CR3 PCC, were not included in the design of the mock-up.

Though the majority of the concrete pours for the CR3 PCC walls were 3 m (10 ft) high and nominally 6 m (20 ft) long (Progress Energy, 2009), the mock-ups were 2.64 m (104 in.) long in order to keep the weight within the 267-kN (30-ton) capacity of the overhead crane in the structural testing laboratory where the mock-ups were constructed.

A representative concrete mix design was used for the mock-ups based on the mix design used in the region of the SGR opening in the CR3 PCC, including the use of Type II moderate heat of hydration cement, an air-entraining admixture (AEA), and a water-reducing and retarding admixture (WRRET). Additionally, the limestone coarse aggregate used for the concrete for the mock-ups was obtained from Brooksville, Florida, the same city from which the limestone coarse aggregate for the CR3 PCC was sourced. Petrography studies of the CR3 PCC concrete have identified the coarse aggregate as an oolitic limestone (Naus, 2009), and investigations by Moreadith and Pages (1983) and Performance Improvement International (2010) into the properties of the concrete found that the aggregate had high porosity and high levels of soft particles. In concrete studies using Florida Ocala Limestone, higher specific heat capacity (Tia et al., 2010) and lower density (Ferraro, 2009) values have been noted relative to limestone from other areas of the United States. Due to the distinct characteristics of the limestone coarse aggregate used in the present research, the aggregate was referred to as limerock throughout this dissertation in order to distinguish it from limestone aggregate available elsewhere in the United States. As noted by Ferraro (2009), the term “limerock” is consistent with the nomenclature of the Florida concrete industry for Florida limestone aggregate.

Three series of specimens were prepared from the concrete for each mock-up: a series cured in a moist room at 23 ± 2 °C (73.5 ± 3.5 °F), a series match-cured to the temperature history measured near the front surface of the corresponding mock-up, and a series match-cured to the temperature history measured at the center of the corresponding mock-up. Tests for the compressive strength, splitting tensile strength, modulus of elasticity, and Poisson’s ratio were conducted on specimens from each of these series at ages ranging from 1 to 180 days, and tests for the coefficient of linear thermal expansion and thermal diffusivity were conducted on specimens cured in the moist room at 23 ± 2 °C (73.5 ± 3.5 °F).

Isothermal calorimetry was conducted on the cement paste in order to determine the apparent activation energy and hydration parameters, which were implemented in 3D finite element analysis of the second mock-up in COMSOL Multiphysics to model the heat generation in the concrete. The COMSOL model incorporated the results of the thermal property tests to model the heat transfer in the concrete and to the surroundings, and the results of the mechanical tests were incorporated to model the time- and temperature-dependent development of the mock-up concrete mechanical properties.

In addition to modeling the curing behavior of the mock-up, the 3600-kN (800-kip) post-tensioning loads applied by six horizontal and three vertical threaded post-tensioning rods were also applied in the COMSOL model. The model was also analyzed with the full 7228-kN (1625-kip) post-tensioning force in the CR3 PCC tendons. Parametric modeling was conducted to identify the influence of material and design parameters on the resulting tensile stresses in the plane of the horizontal ducts. After tensioning and detensioning the mock-ups, shear-wave tomography was conducted on the front face of the mock-ups.

This research did not investigate pressurization of the mock-up, and no dynamic loadings representative of seismic or impact loads were applied. Factors such as corrosion of post-tensioning tendons and stress relaxation were not studied. The mock-ups were constructed and kept in a facility exposed to ambient temperatures and humidity with brief daily exposure to direct sunlight. The influence of elevated temperatures inside the PCC during reactor operation or simulating a loss-of-coolant accident was not investigated.

Due to the planar geometry of the mock-ups, the tensile radial stresses developed by the circumferential post-tensioning tendons of the CR3 PCC were not developed in the mock-ups. In order to account for flexure of the mock-ups due to the eccentricity of the horizontal post-tensioning loads, substantial reinforcement was added towards the back of the mock-ups that was not present in the CR3 PCC.

1.4 Organization of Dissertation

- Chapter 2 provides background information on PCCs in the U.S. and a review of the documented PCC delaminations. A literature review of PCC degradation mechanisms and previous PCC mock-ups is presented, and areas requiring further research are identified. Properties related to heat generation and transfer in concrete are reviewed, and methods of testing for and estimating the values of the properties are discussed.
- Chapter 3 provides design and material details of the experimental mock-ups and presents the temperature histories of the two mock-ups. The variation of the temperature profiles through the thickness of the mock-ups was used with the modulus of elasticity and coefficient of thermal expansion values to determine the thermal stresses in the mock-ups as functions of time. The strains measured through the thickness of the second mock-up are also presented from the time of concrete setting through the full post-tensioning and detensioning sequences.
- Chapter 4 discusses the determination of the hydration properties of the cement paste used for the mock-ups and the development of the mechanical and thermal properties with respect to chronological and equivalent age. Literature functions for modeling the development of the concrete properties were compared with the experimental results.
- Chapter 5 presents thermal analysis of the second mock-up in ConcreteWorks (Texas Department of Transportation, 2010) and COMSOL Multiphysics 5.2 (COMSOL Group, 2015) for comparison with the experimental behavior. Mechanical analysis of the mock-up conducted in COMSOL was presented for determination of the tensile stresses in the plane of the horizontal post-tensioning ducts.

- Chapter 6 presents the results of parametric modeling of the second mock-up in COMSOL Multiphysics and discusses the influence of material and design parameters on the tensile stresses in the plane of the horizontal ducts.
- Chapter 7 presents the results of nondestructive evaluation of the two mock-ups using shear-wave tomography and comparison of the results with behavior measured in the mock-ups and predicted by finite element analysis.
- Chapter 8 provides a summary of the conclusions of the research and presents recommendations for analyzing PCCs for evaluation of the risk for delaminations and for selecting material and design parameters that reduce the risk for delaminations.
- The appendices provide calculations and derivations of values and models used in the body of the dissertation, complete tabulated results of experimental testing, and one-way analysis of variance (ANOVA) of the results. A list of all references for the dissertation is also provided.

CHAPTER 2

LITERATURE REVIEW

2.1 Nuclear Reactors and Containments

The designs of nuclear reactors and containments have consistently evolved as a result of efforts to improve the efficiency of construction and operation and to ensure safety. The Information Digest of the U.S. Nuclear Regulatory Commission (2015) states that, amongst the 99 licensed reactors in the U.S., about 80 different designs have been used. Generally, the reactor type and capacity guide the selection of containment type, resulting in a similarly large number of containment designs. As a result of the diversity of these structures, their management is increasingly challenging as they age.

2.1.1 Nuclear Reactor Types

Thermal nuclear reactors use heat generated by the reactor core to boil water, generating steam that flows to the turbines and turn an electric generator. In a commercial boiling water reactor (BWR), a single coolant loop is used, and the water for the steam turbines is boiled directly by the reactor core. In a commercial pressurized water reactor (PWR), the primary coolant loop is pressurized to prevent boiling of the water when heated by the reactor core. The pressurized, heated water flows to the steam generator, where heat transfer boils the water in a second loop and the resulting steam is directed to the turbines. Of the 99 licensed commercial reactors in the U.S., 65 reactors are PWRs, and CR3 was a PWR as well (U.S. Nuclear Regulatory Commission, 2015). Most of these PWRs, including CR3, have a large dry containment that houses the reactor, steam generators, and other major plant equipment and prevents the release of radiation. The large internal volume of these containments limits the increase in pressure when the temperature rises in accident scenarios.

2.1.2 Progression of Containment Design

A wide variety of containment types have been developed and employed at U.S. NPPs. Before the late 1960s, the primary material used for containments was steel—typically a carbon-manganese-silicon steel (Klamerus et al., 1996)—and the relatively small sizes of the reactors up to that point would have made steel the economically preferable material even if effective designs for concrete containments had been developed (Steigermann and Tan, 1969). However, as increasingly larger PWRs were constructed, steel containment vessels became comparatively expensive due to the cost of stress-relieving liner plates greater than 1½ in. thick, resulting in concrete containment structures becoming economically feasible alternatives (Steigermann and Tan, 1969). Unlike steel containments, which require an external reinforced concrete shield building, concrete containments serve as the final barrier to the release of radiation while also shielding the reactor from the exterior environment. According to Mehta et al. (1977), the Connecticut Yankee plant, commissioned in 1968, marked the shift from spherical steel containments to cylindrical concrete containments for PWRs.

A report by Dunn et al. (2011) states that the U.S. currently has 55 PWRs and 11 BWRs with concrete containment buildings. Of those, 36 PWRs and two BWRs have PCCs; the remaining concrete containments are reinforced concrete (Hessheimer and Dameron, 2006). The two BWR PCCs have fundamentally distinct structures from the large dry PWR PCCs, which are discussed in more detail in the next section.

2.1.3 Post-Tensioned Concrete Containment Details

A major consideration in the design of PCCs is the protection of the post-tensioning system from degradation. Grouted or bonded tendons are used in many PCCs in several countries, including France, Belgium, South Korea, China, and Canada (U.S. Nuclear Regulatory Commission, 2012c). In contrast, only two PCCs in the U.S. have bonded prestressing systems: Robinson Unit 2 has grouted, vertical prestressing bars, and

Three Mile Island Unit 2, which is no longer in operation, has grouted prestressing tendons (Shah and Hookham, 1998). The remaining U.S. PCCs utilize unbonded tendons coated with corrosion-inhibiting wax or grease, enabling the tendons to be examined, retensioned, and replaced as necessary.

In addition to the prestressing system, PCCs also have conventional reinforcement to provide localized stabilization and to minimize shrinkage and temperature effects. According to Steigelmann and Tan (1969), an advantage of PCCs over reinforced concrete containments (RCCs) is that the prestressing generally enables the walls to be 6 to 12 in. thinner and reduces the congestion in the concrete due to greater spacing of reinforcing and prestressing elements. Congestion of the reinforcing steel is particularly a concern around the equipment hatch for both RCCs and PCCs.

In contrast to Figure 2.1, which indicates no clear trend in the containment material type in the U.S., Table 2.1 shows that there was a gradual transition in the geometry and prestressing systems of U.S. PCCs. The first licensed U.S. commercial reactor with a prestressed containment, R.E. Ginna in 1969, was prestressed only vertically; the circumferential (hoop) and dome reinforcement was provided by conventional bars (Rochester Gas & Electric Corporation, 2002). Vertical prestressing increases the horizontal shear capacity of the concrete, reducing the amount of vertical reinforcement required and enabling thinner walls (Steigelmann and Tan, 1969).

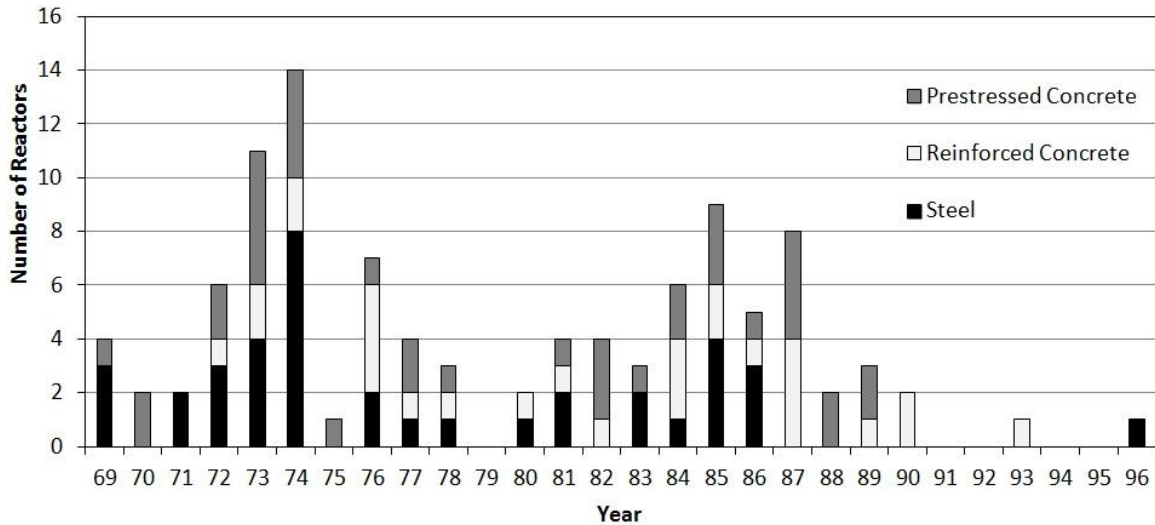


Figure 2.1: Containment types of currently licensed U.S. commercial nuclear power reactors by year of issuance of initial operating license. Data from NRC Information Digest 2010-2011 (U.S. Nuclear Regulatory Commission, 2010).

Table 2.1: Prestressed concrete containment types of currently licensed U.S. commercial pressurized water reactors by year of issuance of initial operating license. Cell shading corresponds to the numbers 1, 2, 3, and 4. Data from NRC Information Digest 2010-2011 (U.S. Nuclear Regulatory Commission, 2010); containment groupings from Naus et al. (1996).

PCC Type	Year																			Total		
	69	70	71	72	73	74	75	76	77	78	79	80	81	82	83	84	85	86	87		88	89
No buttresses (vertical only)	1	1			1																	3
6-buttress, shallow dome		1		2	4	3		1	1													12
4-buttress, shallow dome														1								1
3-buttress, shallow dome						1	1		1	1			1				1		2	1		9
3-buttress, hemispherical dome														1	1	1	2	1	2	1	2	11
Total	1	2	0	2	5	4	1	1	2	1	0	0	1	2*	1	1*	3	1	4	2	2	36*

* Two U.S. BWRs (LaSalle 1, 1982, and LaSalle 2, 1984) have prestressed concrete containments (Mark II), but those structures are fundamentally different and are not included in this table.

Two more reactors with vertically prestressed containments were licensed in the early 1970s, but biaxially prestressed containments quickly became the primary PCC type. The earlier biaxially prestressed containments had 6 buttresses for anchoring the hoop tendons, each of which spanned 120°, as shown in Figure 2.2a. At each hoop tendon elevation, a pair of tendons was located on opposite sides of the PCCs, and the pairs were

rotated 60° at each successive elevation so that the entire circumference of the structure was post-tensioned.

According to Wahl (1968), the use of more than 6 buttresses would have left insufficient space for the larger containment penetrations, particularly the equipment hatch. The prestressing tendons of the shallow dome were anchored to a large ring girder at the top of the cylindrical wall, as shown in Figure 2.2b. Through at least 1983, the BBRV system of button-headed wires was used in most PCCs built in the U.S., with 0.25-in. (6.35-mm) wires used predominantly except for cases of 0.28-in. (7-mm) 163-wire tendons (Ashar and Naus, 1983).

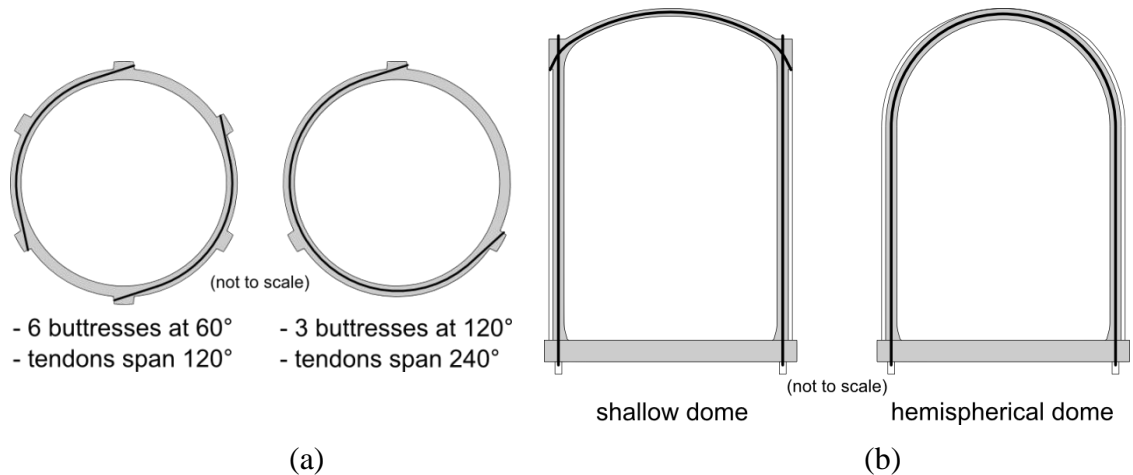


Figure 2.2: Diagrams of PCC geometry and tendon arrangement in (a) plan and (b) section

Because these containments have nearly 1000 tendons anchored at a variety of locations on the structure, the installation, tensioning, and corrosion-proofing of the prestressing system was a time-consuming process (Halligan, 1976; Naus, 1986). The increased capacity of newer reactors required larger containments, and a transition was made to 3-buttress containments with larger tendons spanning 240°, resulting in a substantial reduction in number of tendons (Halligan, 1976). Further reductions in tendon

count were accomplished by extending the vertical tendons through a hemispherical dome and down the other side of the cylindrical wall. The hemispherical domes of these later PCCs obviated the need for the massive ring girder, greatly simplifying the structure.

According to Naus et al. (1996), the concrete used in the containments of PWRs typically is produced using ASTM C150 Type II Portland cement, which can be more resistant to sulfate attack than Type I cement. Type II cement also has a lower heat of hydration than Type I, which is important for mitigating thermal shrinkage and possible cracking due to the thick walls of the containment. The concrete typically contains air-entraining admixtures and curing agents and has appropriate natural aggregates to prevent common mechanisms of degradation.

Each concrete containment building in the U.S. has an interior steel liner to serve as a leaktight vapor barrier (Steigelmann and Tan, 1969). The liner is typically between ¼ and ½ in. (6.3 and 13 mm) thick, and its contribution to the strength of the containment is neglected in design and analysis. However, degradation of the liner can substantially impair the ability of the containment structure to maintain leaktightness (Naus, 2007). The steel liner also serves as a permanent form for the interior of the concrete wall and is typically constructed in 9- to 10-ft-high rings (Steigelmann and Tan, 1969).

2.1.4 Crystal River 3 Nuclear Power Plant

CR3 is a 838-MWe PWR located in Crystal River, Florida, 80 miles north of Tampa (U.S. Nuclear Regulatory Commission, 2012a). The construction permit for CR3 was issued on September 25, 1968; concrete placement for the containment walls and the dome was completed in 1973 and 1974, respectively; and post-tensioning was completed in 1975 (Performance Improvement International, 2010). The operating license was issued on December 3, 1976, with commercial operation beginning on March 13, 1977.

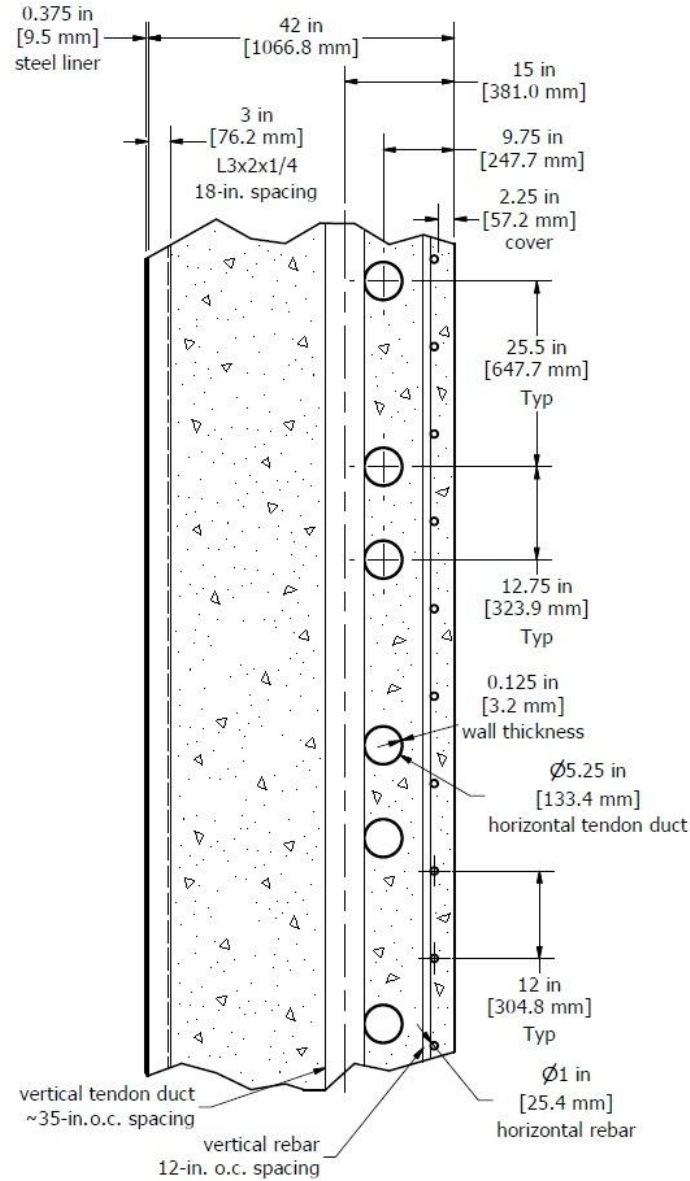
2.1.4.1 Containment Structure

The CR3 reactor and steam generators are housed in a large dry containment building maintained at ambient pressure. The containment building is a cylindrical, shallow-domed, post-tensioned concrete structure with an interior steel liner. The outside diameter of the containment is 41.78 m (137 ft 0.75 in) with a wall thickness of 1.07 m (42 in.), as shown in the representative section of the containment wall in Figure 2.3. The containment has six equally spaced vertical buttresses at which the wall thickness is 1.78 m (5 ft 10 in.).

The walls are post-tensioned by 282 hoop tendons and 144 vertical tendons, and the dome is post-tensioned by 123 tendons in a three-way configuration. Each tendon consists of 163 7-mm- (0.28-in.)-diameter low relaxation steel wires and has a guaranteed ultimate strength of 10.39 MN (2,335 kips). The tendons are greased (unbonded) and housed inside galvanized steel pipes with a 5.25-in. (133.4-mm) outer diameter; the specified minimum inner diameter and wall thickness were 127 and 1.7 mm (5.0 and 0.065 in.), respectively (Gilbert Associates, 1970), and wall thicknesses of 2.0 and 3.2 mm (0.08 and 0.125 in.) have been indicated in post-delamination analysis (Performance Improvement International, 2010). The hoop tendons are centered at a depth of 248 mm (9.75 in.) from the surface of the wall with on-center spacing alternating between 324 and 647 mm (12.75 and 25.5 in.), and each hoop tendon spans a nominal 120° of the structure and is anchored to the buttresses. The vertical tendons are centered at a depth of 381 mm (15 in.) with 0.89-m (2.93-ft) on-center spacing, corresponding to an angular spacing of 2.5°, and are anchored to the ring girder and beneath the flat foundation mat in a tendon access gallery. The 41 dome tendons in each layer are spaced at 76.2-cm (30-in) center-to-center intervals and are anchored to the ring girder.

A 300-by-300-mm (12-by-12-in.) grid of #8 bars is located near the outer face of the wall with 57.2 mm (2.25 in.) of concrete cover. The steel liner is 9.5-mm (0.375-in.) thick, and L3x2x¼ steel angles are stitch welded to the liner at 457-mm (18-in.) spacing

to provide stiffness and to anchor the liner to the concrete. The interior face of the liner was painted, but the face in contact with the concrete was not painted (Hill, 2013); this is typical for concrete containments (Shah and Hookham, 1998).



Note: Displayed components are not necessarily in the same vertical plane
 Figure 2.3: Typical section of CR3 containment wall

2.1.4.2 Containment Concrete Design

The CR3 containment concrete was designed for a specified minimum 28-day compressive strength of 34.5 MPa (5000 psi) using ASTM C150-67 (1967) Type II

cement with moderate heat of hydration and no pozzolanic admixtures (Gilbert Associates, 1968). The project specifications did not indicate a minimum tensile strength, but design documents used the relationship shown in Eq. 2.1 to determine an allowable tensile stress of 1.5 MPa (212 psi) for concrete with a 28-day compressive strength of 5000 psi (Performance Improvement International, 2010). A 0.405 maximum water-to-cement ratio (w/c) was specified, and a report by Performance Improvement International (2010) on the delamination identified in 2009 states that the average w/c of the containment concrete was 0.41.

$$\begin{aligned} f_{tsp} &= 0.25\sqrt{f'_c} \quad [\text{MPa}] \\ f_{tsp} &= 3\sqrt{f'_c} \quad [\text{psi}] \end{aligned} \quad \text{Eq. 2.1}$$

Where,

$$\begin{aligned} f'_t &= \text{allowable tensile stress in concrete, MPa or psi} \\ f'_c &= \text{compressive strength of concrete, MPa or psi} \end{aligned}$$

The slump was initially specified to be 5 cm (2 in.) (Gilbert Associates, 1968) but was increased to 7.5 cm (3 in.) before concrete placement began (Performance Improvement International, 2010). Pour records indicate that batches of concrete with slumps of 8.5 cm (3.25 in.) or greater were rejected for overslump, and batches with slumps of 4.5 cm (1.75 in.) or lesser were rejected for being unworkable (Performance Improvement International, 2010). However, after the completion of the primary portions of the PCC walls, a letter from the Project Structural Engineer (Dobreff, 1973) indicated that 10-cm (4-in.) slumps measured at the pump discharge pipe and 11.5-cm (4.5-in.) slumps measured at the truck had previously been approved for acceptance.

Natural sand with a fineness modulus (FM) of 2.2 to 2.7 was used as the fine aggregate, and local Brooksville limestone (limerock) was used as the coarse aggregate with a specified maximum size of aggregate (MSA) of 19 mm (0.75 in.). Petrography studies identified the coarse aggregate as an oolitic limestone (Naus, 2009), and investigations by Moreadith and Pages (1983) and Performance Improvement

International (2010) into the properties of the containment concrete found the aggregate to be gap graded with high levels of soft particles and high porosity. Air entrainer was specified for 3 to 6% total air content by volume (Gilbert Associates, 1971), and ASTM C494 Type D water-reducing and retarding admixture was added to all structural concrete (Gilbert Associates, 1968). Progress Energy (2009) showed that the majority of the concrete pours for the CR3 PCC walls were 3 m (10 ft) high and nominally 6 m (20 ft) long. Details of the material properties of the CR3 PCC concrete are discussed in Section 2.3.1.

2.2 Post-Tensioned Concrete Containment Delaminations

Aside from CR3, reports of delaminations at two other PCCs have been identified: Turkey Point 3 in Homestead, Florida, and Kaiga Atomic Power Project Unit 1 in Kaiga, India.

2.2.1 Turkey Point 3 Dome Delamination

On June 17, 1970, approximately three months after the completion of concrete placement, delamination of the dome of the Turkey Point PCC was identified after concrete cracking and leakage of grease from the tendon ducts were noticed during the tensioning process for the 165 dome tendons, of which 110 had been completed according to the Containment Dome Report (1970). The report describes comparative studies of the properties of the Turkey Point 3 concrete and concrete constituents to those of four unidentified PCCs, noting that all properties were comparable except for the lower splitting tensile strength of the Turkey Point 3 concrete. The average result of eight direct tension tests, each conducted at an age of 31 days or more, was 352 psi, which the report stated was expectedly lower than the tensile strength determined by the splitting tensile strength test. In five of the eight direct tension tests, it was estimated that at least 90% of the aggregate fractured rather than separating from the hardened cement paste.

The maximum calculated radial tensile stress in the dome was 91.5 psi—approximately 25% of the measured direct tensile strength—adjacent to the outermost tendon ducts, leading to the conclusion that tensile stresses did not cause the delamination. Similarities noted between the delamination surface and the failure surfaces of the cylinders tested in compression contributed to the conclusion that the delamination resulted from large compression forces along the tendons. Unbalanced tendon loads were identified as a contributing factor.

Like the coarse aggregate used in the CR3 PCC, the aggregate used in the PCC of Turkey Point 3 was obtained from oolitic limestone in Florida. The results of petrographic analysis of the concrete noted no deficiencies in the concrete or aggregate.

2.2.2 Kaiga 1 Dome Delamination

Basu et al. (2001) reported that on May 13, 1994, the dome of the inner containment of Kaiga 1 delaminated and partially collapsed after tensioning approximately 1/3 of the dome tendons. Unlike U.S. PCCs, the concrete containment structure did not have a steel liner; the collapse may not have occurred if a stiffened steel liner was used. Loud sounds were heard for approximately 7 to 8 minutes during the event, which was attributed to radial tension and membrane compression in regions of low net concrete thickness due to overlapping tendon ducts.

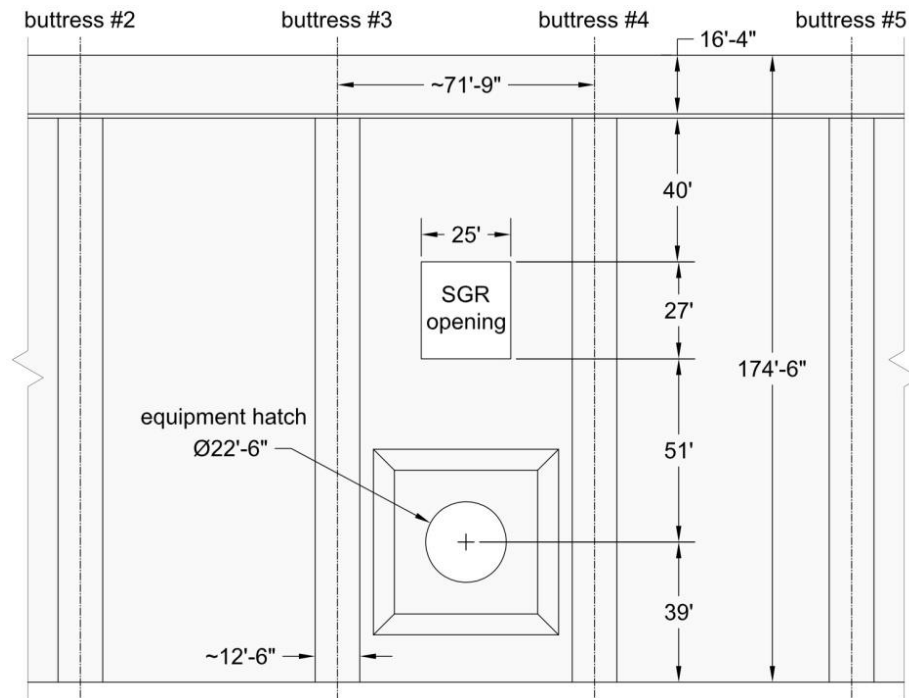
2.2.3 Crystal River 3 Dome Delamination

In addition to the previously mentioned delaminations, a delamination of the CR3 dome was identified on April 14, 1976, when workers were unable to fasten anchors to the exterior of the dome (Moreadith and Pages, 1983; Naus, 2009). Though the delamination was identified approximately two years after the placement of the dome concrete and one year after the completion of post-tensioning, construction records showed that a loud noise, apparently from the containment building, occurred on

December 4, 1974, prior to completion of the post-tensioning (Naus, 2009). Since visual inspection of the structure identified no damage, neither the engineer nor the NRC was made aware of the event (Naus, 2009), but the noted noise and vibrations may have been caused by the dome delamination that was later identified. Investigation of the delamination concluded that radial tension and biaxial membrane compression in concrete with lower-than-expected tensile strength resulted in the cracking (Moreadith and Pages, 1983) . The delaminated concrete was replaced and radial reinforcement was grouted into the concrete beneath the delamination to tie the new and substrate concrete together.

2.2.4 Crystal River 3 Bay 34 Delamination

On September 26, 2009, CR3 was shut down for a scheduled refueling outage, during which the steam generators were to be replaced as part of a power uprate (Performance Improvement International, 2010). In order to replace the steam generators, a rectangular opening 7.6 m (25 ft) wide by 8.2 m (27 ft) high was to be created in the PCC wall in bay 34, i.e., the bay between buttresses #3 and #4, as shown in Figure 2.4. The opening was approximately 40 feet above the equipment hatch and was horizontally centered in the bay.



Note: Horizontal dimensions are approximate due to unfolding of curved surface
 Figure 2.4: Diagram of unfolded elevation showing the SGR opening location

Steam generator replacement (SGR) procedures were not discussed in the Code (ASME, 1995), and, therefore, no standardized process existed. All of the previous 34 SGR projects at U.S. NPPs had been completed successfully by either Bechtel or The Steam Generating Team (SGT), and at least 13 of those projects involved cutting into the containment, with the remainder using the equipment hatch (Penn, 2011). For the CR3 SGR, Progress Energy chose to self-manage the project and hired multiple companies with no experience at NPPs with their assigned tasks.

On September 30, 2009, hydrodemolition of the SGR opening area began, and on October 2, 2009, a delamination was identified approximately 9 to 10 in. beneath the concrete surface, generally in the vertical plane of the hoop tendon ducts (Performance Improvement International, 2010). According to the U.S. Nuclear Regulatory Commission (2011b), the steel liner and the inner 32 in. of concrete appeared to be unaffected by the delamination. Figure 2.5 shows a photograph of the delamination, and

Figure 2.6 shows a photograph of bay 34 of CR3 with an overlay indicating the extent of the delamination as determined by NDE work, core drilling, and fiberscope examination.

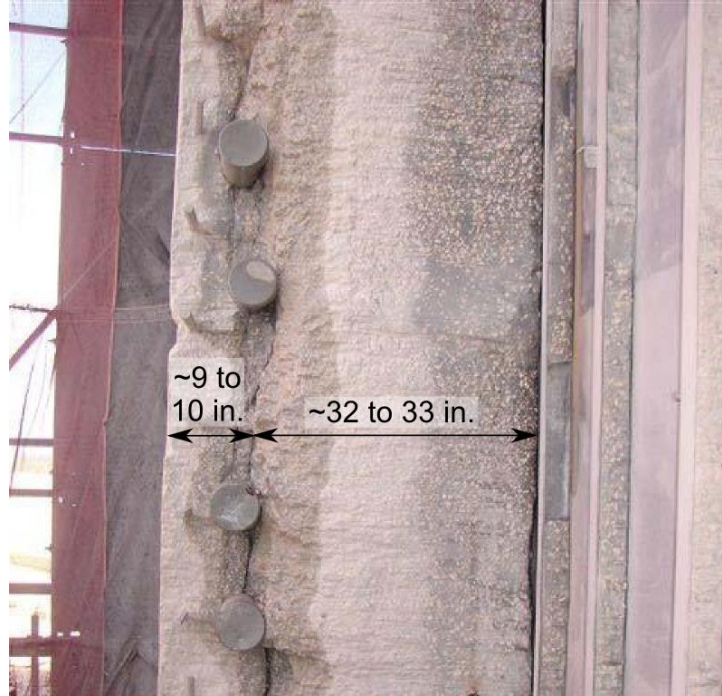


Figure 2.5: Photograph of delamination after removal of concrete for SGR opening (Performance Improvement International, 2010)

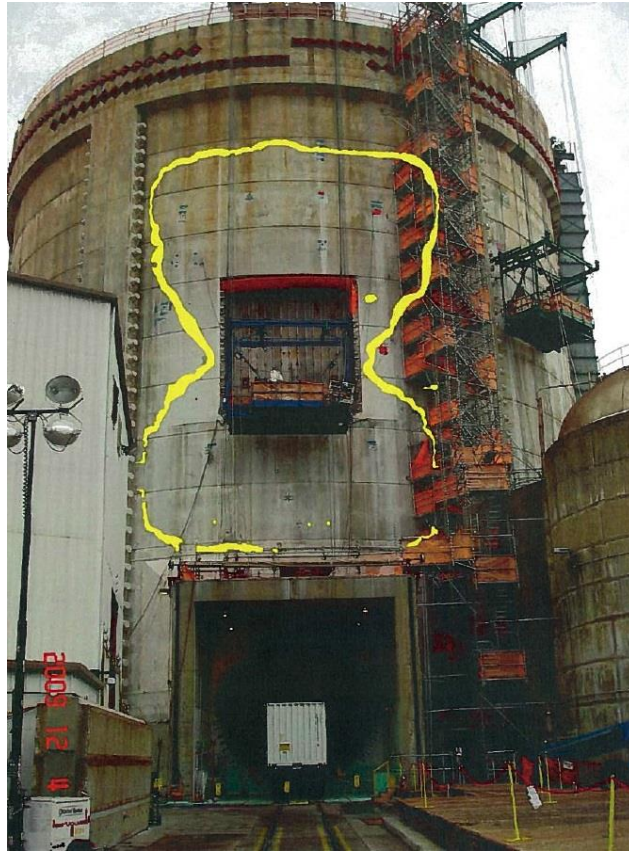


Figure 2.6: Photograph of bay 34 with overlay indicating the extent of the delamination (Performance Improvement International, 2010)

A photograph taken during the hydrodemolition demonstration on September 30 revealed that a crack was present between two exposed hoop tendons (Performance Improvement International, 2010). The volume of concrete removed at that time was only about 0.5% of the total volume of concrete to be removed for the SGR opening, indicating that the concrete removal was probably not the primary cause of the delamination.

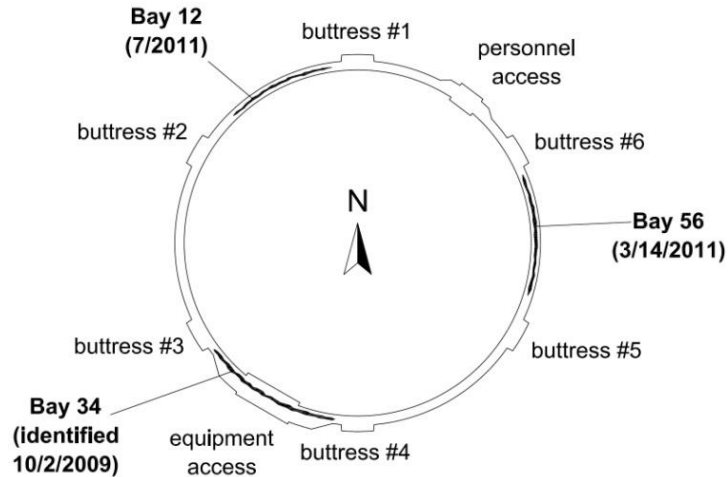
Post-delamination analysis, discussed more thoroughly in Section 2.3, concluded that a root cause of the delamination was the sequence and scope of the detensioning process, which developed large stresses at the interface between tensioned and detensioned tendons (Performance Improvement International, 2010). Furthermore, the root-cause analysis indicated that the tendon stresses, radial stresses, design for

concentration factors, concrete strength properties, and aggregate properties contributed to the delamination.

Similar to the CR3 dome repair, the selected repair approach for the delaminated wall involved replacing the delaminated concrete and grouting radial reinforcement into the concrete behind the delamination to tie the new and substrate concrete together. However, prior to removing the delaminated concrete, additional hoop and vertical tendons were detensioned (Wheeler, 2011), and all tendons were to be retensioned after placement of the repair concrete.

2.2.5 Crystal River 3 Bay 56 and Bay 12 Delaminations

After replacing the delaminated concrete in bay 34 of the CR3 PCC, a sudden delamination occurred in bay 56 following retensioning pass 100 of 112 on March 14, 2011 (Wheeler, 2011; Hill, 2012a). Though retensioning and other work was stopped following this event, bay 12 delaminated approximately four months later in July 2011 (Hill, 2012b). Figure 2.7 shows the orientation of the affected bays. According to Howard Hill, a CR3 consultant that was not at the containment when the delaminations occurred, field personnel reported that both of these delaminations were clearly indicated by sudden loud noise and building vibrations (Hill, 2012a, 2012b). In order to decrease the stress concentrations in the concrete surrounding the hoop tendon ducts, the forces in the vertical tendons were decreased by 25% from the original anchor load, and no problems have been identified since.



Note: Delaminations are not drawn to scale
 Figure 2.7: Plan diagram showing locations and date of occurrence or identification of CR3 wall delaminations

Previously scheduled to resume operation in April 2011, the plant never reopened and bays 12 and 56 remain delaminated (Wheeler, 2011). With cost estimates ranging from \$1.49 billion to \$3.49 billion and estimated project durations ranging from 31 to 96 months (Carr, 2012), the owners announced on February 5, 2013, that the reactor would be permanently shut down rather than pursuing repairs (Penn, 2013).

2.3 Investigation of Crystal River 3 Bay 34 Delamination

Following the identification of the CR3 bay 34 delamination in 2009, impulse-response scans were conducted on each of the bays to determine the extent of the delamination. Figure 2.8 shows the delaminated region as identified by impulse-response testing and confirmed by core bores. Multiple iterations of concrete mix designs were used for the CR3 PCC, but by estimating the area of the delaminated region from the diagram, it was approximated that 85-90% of the delamination occurred in a portion of the CR3 PCC in which mix design DM-5-Mod was used. This mix design is shown in Table 2.2.

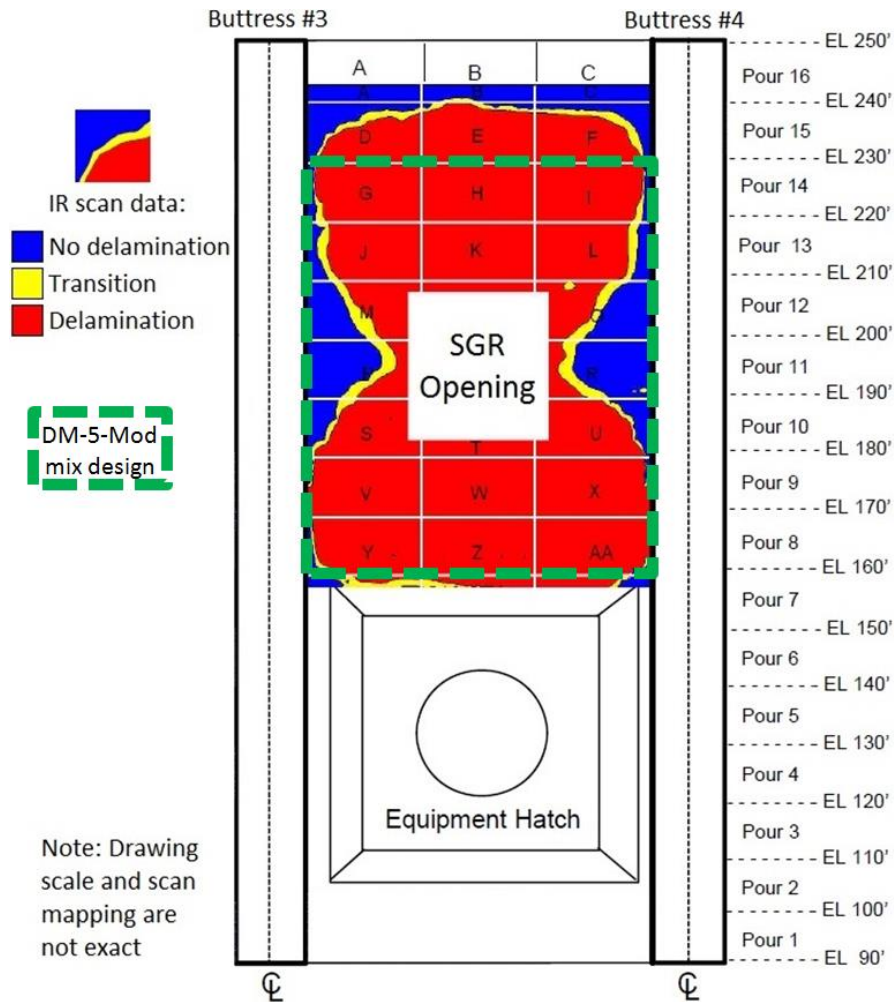


Figure 2.8: Diagram (Progress Energy, 2009) of delaminated region of CR3 PCC with outline of portion of bay in which mix design DM-5-Mod was used as indicated by Performance Improvement International (2010)

Table 2.2: Primary concrete mix design (saturated-surface dry) used in delaminated region of CR3 PCC (Performance Improvement International, 2010)

Material	Measure per unit concrete volume	
	Weight (lb/yd ³)	Mass (kg/m ³)
Water	276	164
Cement	682	405
Coarse aggregate	1800	1068
Fine aggregate	1100	653
	Volume (fl. oz./yd ³)	Volume (mL/m ³)
Water reducer/retarder	21.0	812
Air entrainer	4.7	182

2.3.1 Concrete Material Properties

The material properties of the CR3 PCC concrete were determined by testing standard-cured cylinder specimens prepared during original concrete placement and cores taken from the PCC after the delamination was identified in 2009.

2.3.1.1 Compressive Strength

Sets of 150-by-300-mm (6-by-12-in.) cylinders were prepared from each batch of concrete and standard-cured in accordance with ASTM C31-69 (1969) to be tested for acceptance and quality control. Based on tests of pairs of these cylinders, the average compressive strength of the concrete at 7, 28, and 90 days was 31.6, 41.6, and 46.6 MPa (4,581, 6,029, and 6,756 psi), respectively, with 64 cylinders reported for both 7 and 28 days and 63 cylinders reported for 90 days (Performance Improvement International, 2010).

Post-delamination cores were tested to evaluate the mechanical properties of the concrete when the delamination was identified, approximately 36 years after concrete placement. The diameter of the tested cores was 102 mm (4 in.), and since no ACI 214.4R-03 correction factors were applied, the lengths of the cores were likely between 178 and 213 mm (7 and 8.4 in.) to conform with the 1.75-to-2.1 range of length-to-diameter ratio (L/D) values permitted by ASTM C42-04 (2004).

The average compressive strength f_c of all cores was 50.9 MPa (7,385 psi), well above the design strength of 34.5 MPa (5000 psi). The average compressive strength reported for 18 core specimens taken from regions of the PCC with concrete mix design DM-5-Mod was 53.1 MPa (7707 psi) with a standard deviation of 4.4 MPa (634 psi). This average strength is slightly higher than that of all cores.

2.3.1.2 Tensile Strength

The average splitting tensile strength f_{tsp} measured for all cores was 4.14 MPa (600 psi), well above the allowable tensile stress of 1.5 MPa (212 psi) determined via Eq. 2.1 (Performance Improvement International, 2010). The average splitting tensile strength reported for 10 core specimens taken from regions of the PCC with concrete mix design DM-5-Mod was 4.1 MPa (594 psi) with a standard deviation of 0.4 MPa (59 psi). This average splitting tensile strength is slightly less than that of all cores.

Several empirical relationships between compressive strength and splitting tensile strength have been proposed. ACI 318-08 (2008) provides Eq. 2.2 based on tests of 28-day specimens conducted by Hanson (1961). For the average compressive strength of all cores, Eq. 2.2 gives a splitting tensile strength of 4.0 MPa (580 psi), slightly lower than the value measured for the cores. For the cores from the regions with concrete mix DM-5-Mod, Eq. 2.2 gives a splitting tensile strength of 4.1 MPa (588 psi), matching the value measured for the cores.

Performance Improvement International (2010) stated that the best fit was obtained using the relationship given in Eq. 2.3, which was provided by the Comité Euro-International du Béton/International Federation for Prestressing (CEB/FIP) and gives a splitting tensile strength of 4.14 MPa (600 psi) for all cores, matching the measured value. For the cores from the regions with concrete mix DM-5-Mod, Eq. 2.3 gives a splitting tensile strength of 4.2 MPa (624 psi), slightly higher than the measured value. The good fit of the values measured on the cores with the empirical relationships suggests that the tensile strength of the CR3 PCC was not particularly deficient.

$$\begin{aligned} f_{tsp} &= 0.56\sqrt{f'_c} \quad [\text{MPa}] \\ f_{tsp} &= 6.7\sqrt{f'_c} \quad [\text{psi}] \end{aligned} \quad \text{Eq. 2.2}$$

$$\begin{aligned} f_{tsp} &= 0.3(f'_c)^{\frac{2}{3}} \quad [\text{MPa}] \\ f_{tsp} &= 1.6(f'_c)^{\frac{2}{3}} \quad [\text{psi}] \end{aligned} \quad \text{Eq. 2.3}$$

Where,

$$\begin{aligned} f_{tsp} &= \text{splitting tensile strength, MPa or psi} \\ f'_c &= \text{specified compressive strength, MPa or psi} \end{aligned}$$

The average direct tensile strength f_t of all tested core specimens was 3.12 MPa (453 psi), and the average value for 3 core specimens taken from a region of the PCC with concrete mix design DM-5-Mod was 3.15 MPa (457 psi) (Performance Improvement International, 2010). In both cases, the direct tensile strengths are approximately 75% of the corresponding splitting tensile strengths. Per Neville (2011), direct tensile strength tends to be about 89 to 95% of the splitting tensile strength; the lower direct tensile strength of the cores was attributed to the soft and highly porous aggregate, to which the direct tensile strength is more sensitive (Performance Improvement International, 2010). However, the average measured direct tensile strength of cores from bay 34 was approximately 10% lower than that of cores from an adjacent bay and bay 61 (Performance Improvement International, 2010). The 10% decrease in tensile strength matches the 10% standard deviation for the entire population of measurements.

ACI 224.2R-92 (1997) and ACI 209R-92 (2008) provide the empirical relationship amongst unit weight, compressive strength, and direct tensile strength shown in Eq. 2.4. The average unit weight of the cores was 2515 kg/m³ (157 lb/ft³) (Performance Improvement International, 2010), so Eq. 2.4 yields a direct tensile strength of 2.53 MPa (358 psi) for all cores. The lowest direct tensile strength measured on the cores was 2.4 MPa (350 psi) (Performance Improvement International, 2010), slightly less than the value from the empirical relationship, but the average core values were well above the empirical relationship. This suggests that the measured tensile strength of the PCC concrete was satisfactory, but the lower values in bay 34 indicate that the bay may have been more susceptible to cracking.

$$\begin{aligned} f_t &= 0.0069\sqrt{w_c f'_c} \quad [\text{MPa}] \\ f_t &= 0.33\sqrt{w_c f'_c} \quad [\text{psi}] \end{aligned} \quad \text{Eq. 2.4}$$

Where,

- f_t = direct tensile strength, MPa or psi
- w_c = unit weight of concrete, kg/m³ or lb/yd³
- f'_c = compressive strength of concrete, MPa or psi

2.3.1.3 Modulus of Elasticity and Poisson's Ratio

The average modulus of elasticity E_c of 22 tested cores was 23.8 GPa (3,450 ksi), but the average Poisson's ratio ν for all tested cores was not available from Performance Improvement International (2010). The average modulus of elasticity of 12 core specimens taken from a region of bay 61 (opposite bay 34) with concrete mix design DM-5-Mod was 24.7 GPa (3,579 ksi) with a standard deviation of 2.1 GPa (302 ksi), and the average Poisson's ratio of the 12 cores was 0.18 with a standard deviation of 0.02. An average modulus of elasticity of 26.9 GPa (3,900 ksi) and Poisson's ratio of 0.24 were reported for cores from an area of the SGR opening for which concrete mix design DM-5-Mod was used, but the number of specimens included in the average was not identified.

ACI 318-08 (2008) provides Eq. 2.5 for calculating the modulus of elasticity from the compressive strength and unit weight of the concrete. With an average unit weight of 2515 kg/m³ (157 lb/ft³), Eq. 2.5 predicts a modulus of elasticity of 38.7 GPa (5,579 ksi) for all cores and 39.8 GPa (5,700 ksi) for cores taken from regions of the PCC with concrete mix design DM-5-Mod. The measured values of modulus of elasticity are approximately 62% of the corresponding estimated values, whereas ACI 318 states that measured values are typically within 80 to 120% of the estimated values. ACI 318 notes that the modulus of elasticity of the aggregate influences the modulus of elasticity of the concrete, and Performance Improvement International (2010) stated that the weak aggregate would have a greater effect on the modulus of elasticity than the compressive strength, potentially contributing to the relatively low modulus of elasticity values for the concrete.

$$\begin{aligned}
 E_c &= 0.043w_c^{1.5}\sqrt{f'_c} \quad [\text{MPa}] \\
 E_c &= 33w_c^{1.5}\sqrt{f'_c} \quad [\text{psi}]
 \end{aligned}
 \tag{Eq. 2.5}$$

Where,

$$\begin{aligned}
 E_c &= \text{modulus of elasticity of concrete, MPa or psi} \\
 w_c &= \text{unit weight of concrete, kg/m}^3 \text{ or lb/yd}^3 \\
 f'_c &= \text{compressive strength of concrete, MPa or psi}
 \end{aligned}$$

Based on a unit weight of approximately 2230 kg/m³ (144 lb/ft³), Eq. 2.6 is provided by ACI 318-08 as a simplification of Eq. 2.5 for normalweight concrete. Since the assumed unit weight is lower than that of the cores, this relationship predicts lower values for modulus of elasticity: 33.5 GPa (4,898 ksi) for all cores and 34.2 GPa (5,004 ksi) for cores taken from regions of the PCC with concrete mix design DM-5-Mod. Therefore, the measured values are approximately 72% of the corresponding estimated values using Eq. 2.6, still lower than would be expected.

$$\begin{aligned}
 E_c &= 4700\sqrt{f'_c} \quad [\text{MPa}] \\
 E_c &= 57,000\sqrt{f'_c} \quad [\text{psi}]
 \end{aligned}
 \tag{Eq. 2.6}$$

2.3.1.4 Properties Related to Thermal Strains

The coefficient of thermal expansion of the CR3 PCC concrete was determined to be 11.7 $\mu\epsilon/^\circ\text{C}$ (6.5 $\mu\epsilon/^\circ\text{F}$), and thermal conductivity values of 1.73 W/m·K (1.00 Btu/hr·ft·°F) and 43 W/m·K (25 Btu/hr·ft²·°F) were identified for concrete and steel, respectively (Performance Improvement International, 2010). However the sources of these values was not available in the report. Additionally, 0.75 was used as a conservative estimate of the degree of restraint K , for mid-thickness concrete in regions of the bays away from the buttresses (Performance Improvement International, 2010).

2.3.2 Air Content

The final specifications (Gilbert Associates, 1971) for the CR3 concrete required that all structural concrete contain entrained air for a total air content of 3 to 6% by

volume. The air-entraining admixture used for the concrete was Darex AEA, and its producer, W. R. Grace, states that typical Darex AEA dosages range from 30 to 200 mL/100 kg (0.5 to 3 fl. oz./100 lb) of cement (2007). Mix design DM-5-Mod called for an addition rate of 35 mL/100 kg (0.53 fl. oz./100 lb) of cement, but pour cards for that region indicate that the AEA dosage was increased to 44 mL/100 kg (0.68 fl. oz./100 lb) of cement (Performance Improvement International, 2010).

Concrete pour data (Performance Improvement International, 2010) available for most of bay 34 and bay 61 includes air content measurements of the freshly mixed concrete, though the procedure for determining the air content was not identified. Gravimetric (ASTM C138), volumetric (ASTM C173), and pressure (ASTM C231) methods for measuring air content of freshly mixed concrete may provide different results depending on aggregate density, and the measured air content may differ from that of the hardened concrete due to factors including the methods of placement and consolidation. For the six available measurements from pours in the region of the delamination, the average air content was 3.30% with a standard deviation of 0.27 percentage points. When also considering 14 measurements from pours with the same mix design in bay 61, the average air content was 3.45% with a standard deviation of 0.31 percentage points.

Following the delamination detected in 2009, Wilson (2009a) performed petrographic analysis in accordance with ASTM C856-04 (2004) on half of two cores from the delaminated region and half of a core from a region that had not delaminated. According to a later report (Wilson, 2009b), one of the core halves from the delaminated region measured 95 mm (3.75 in.) in diameter and 178 to 203 mm (7 to 8 in.) in length; the dimensions of the other specimens were not indicated. The air content was estimated to be approximately 2 to 3%, but the method used to determine the air content and the samples to which the estimate applied were not stated. Noting some clustering of air voids around the some of the coarse aggregate and areas lacking entrained air, the air-

void system was described as somewhat uneven. Later analysis by Wilson (2009b), using the modified point count method from ASTM C457-08d, determined an air content of 3.1% for the core half from the delaminated region with the previously stated dimensions.

Brown (2009) performed petrographic analysis in accordance with ASTM C856-04 (2004) on a saw-cut core from the delaminated region. The entrained and total air content were estimated to be 1 to 2% and 2 to 4%, respectively, though the methods used to determine these values were not stated. Some large voids measuring 4 to 10 mm (0.16 to 0.4 in.) were identified, and the void distribution was characterized as moderately non-uniform. The specimen measured 95 mm (3.75 in.) in diameter and 197 mm (7.75 in.) in length, and Wilson (2009a) suggests that the specimen analyzed by Brown may have been the other half of one of core halves analyzed by Wilson.

Following the CR3 dome delamination detected in 1976, Erlin (1976) performed petrographic analysis of a concrete fragment from the delaminated region. The fragment measured approximately 127 mm (5 in.) in length with a maximum thickness of 19 mm (0.75 in.). No estimation of the entrained air content was provided, but the total air content was estimated to be 5.5%, and the air-void system was deemed to be effective for preventing freeze-thaw damage. The method used to determine the air content was not identified, sample preparation was not described, and whether the petrographic examination was done in accordance with ASTM C856 was not stated.

Though still within the specified range, the 5.5% air content identified by Erlin is notably higher than that measured in the concrete in the region of the wall delamination. The mix design reported to have been used for the dome called for an air-entraining admixture dosage of 39 mL/100 kg (0.60 fl. oz./100 lb) of cement, which is less than the dosage used in the region of the wall delamination. Records of air content measurements of the fresh concrete for the dome were not found, but 11 measurements for pours at the top of bay 61, where the same mix design was reported to have been used, had an average

air content of 3.33% with a standard deviation of 0.20 percentage points. These statistics closely match those for the concrete used in the region of the delamination.

The higher air content measured by Erlin may be due to changes in the mix design used for the dome or to different methods of measuring the air content. Also, as discussed in a literature review by Du and Folliard (2005), differences in mixing, pumping, vibration, and consolidation can result in changes in air content and the air-void system for otherwise identical concrete mixes.

2.3.3 Discussion on Delaminations

Based on the root-cause analysis of the CR3 bay 34 delamination identified in 2009, Progress Energy concluded that the delamination occurred during the detensioning process in preparation for creating the SGR opening (U.S. Nuclear Regulatory Commission, 2011b), and Roger Hannah, NRC Region II Sr. Public Affairs Officer, has stated that there were no indications of the delamination prior to the scheduled refueling outage (Wheeler, 2011). However, the Kaiga dome delamination and the CR3 bay 56 and bay 12 delaminations were clearly indicated by noise and building vibrations, and a similar report of structural agitation prior to the completion of tensioning the CR3 dome may correspond to the dome delamination that was later identified. In contrast, there have been no such reports attributed to the bay 34 delamination, and it was not until several inches of the PCC concrete had been removed for the SGR opening that any unusual conditions were noticed (Performance Improvement International, 2010). If the onset of the bay 34 delamination lacked the salience of the other CR3 delaminations, it seems plausible that the bay 34 delamination may have developed differently, and it is possible that the delamination may have been present prior to the detensioning process or that the detensioning process may have exacerbated an existing degradation. Since the onset of the bay 34 delamination lacked the salience of the other CR3 delaminations, the present work investigated the hypothesis that the bay 34 delamination developed differently and

considered the possibility that the delamination may have been present prior to the detensioning process or that the detensioning process may have exacerbated an existing degradation.

If the bay 34 delamination was present prior to any work to create the SGR opening, similar cracks may be undetected in other PCCs. Tests of the CR3 concrete have indicated lower-than-average tensile strength in bay 34 that likely contributed to the delamination, but extended reactor operations may subject other containments to long-term degradations that could cause similar reductions in concrete strength. Therefore, the following section provides a review of these degradation mechanisms in relation to PCCs for determination of their potential contribution to the development of delaminations.

2.4 Mechanisms of Degradation of Post-Tensioned Concrete Containments

Many of the problems experienced at U.S. NPPs have been due to poor detailing, construction, or quality control and were detected either during construction or early in the life of the containment. These incidences include containment dome delaminations at Turkey Point 3 and Crystal River 3 (Sections 2.2.1 and 2.2.3, respectively); extensive voids beneath prestressing bearing plates at Calvert Cliffs 1 and 2; anchor head failures at Bellefonte, Byron, and Farley Units 1 and 2; and excessive honeycombing and air voids in Marble Hill Units 1 and 2 (Naus, 1986). In each of these cases, the affected concrete regions were replaced and additional precautions were taken to avoid reoccurrences.

After some initial problems early in the life of many reactors, most were able to continue operation for decades without major problems arising. However, as the structures continue to age, there is increasing likelihood of long-term degradation becoming a critical factor for operation. The following sections provide a review of the literature on potential mechanisms of degradation in PCCs. Mass concrete effects and methods of monitoring PCCs for degradation are also reviewed.

2.4.1 Concrete Drying Shrinkage and Creep

The loss of water from concrete and the subsequent decrease in volume is defined as concrete drying shrinkage. When restraint to shrinkage is provided by reinforcement or other parts of the structure, the resulting tensile stresses in the concrete can cause cracking that can increase the ability of other mechanisms of degradation to penetrate and affect the concrete (Naus, 2007). In a report by Krauss (1994) including a survey of American NPPs, the most common cause of concrete cracking was drying shrinkage, with nearly half of the responding plants reporting such cracking. However, this report did not specify which concrete elements were affected and whether they were part of the safety-related structure. Shah and Hookham (1998) suggested that the reported cases were not part of the containment structure since there had been no significant damage reports due to concrete shrinkage. Drying shrinkage usually occurs early in the life of a concrete structure, and since the newest reactor in the U.S. began operation in 1996, it is unlikely that shrinkage will result in significant damage in the future (Krauss, 1994; U.S. Energy Information Administration, 2010). However, the leaktight steel liner on the interior surface of concrete containment buildings results in substantial water retention in the thick concrete walls, so extended durations of drying shrinkage may occur.

Creep is the gradual deformation of a material resulting from long-term stresses. In PCCs, the continuous compressive force in the concrete generated by the prestressing tendons contributes to creep, but containment building measurements have typically shown that creep has been limited to within the predicted values. No cases of excessive shrinkage or creep have been identified at U.S. NPPs, but even slight reductions in the concrete volume can decrease the prestressing force throughout the containment, potentially impairing its structural capacity (Shah and Hookham, 1998).

2.4.2 Stress Relaxation

A controlling factor in the design of PCCs is the ability of the prestressing system to maintain compressive concrete stresses at high internal pressures that are possible during critical accident scenarios. Thus, monitoring prestress losses is important for long-term operation of NPPs. Regulatory Guide 1.35.1 by the U.S. Nuclear Regulatory Commission (1990a) recommends and describes the calculation of graphical tolerance bands for prestress losses so that prestress forces measured during inspections can be compared with predicted values. Depending on the design and the properties of the materials, stress relaxation of the tendons can account for as much as 60% of the predicted loss.

In U.S. PCC construction, sufficient time is typically provided between the casting of concrete and the prestressing of tendons to allow a significant percentage of the assumed long-term shrinkage to occur (U.S. Nuclear Regulatory Commission, 1990a). For example, the post-tensioning of the CR3 PCC was completed at least one full year after the containment walls were completed. This helps reduce the extent of prestressing losses, and losses due to stress relaxation in U.S. PCCs have typically been within the anticipated range described in RG 1.35.1 (Shah and Hookham, 1998). However, cases of substantial prestressing losses attributed to unexpectedly high levels of prestressing steel relaxation have occurred. Ashar et al. (1994b) reported that, at one PCC, the prestressing forces in many hoop tendons 3 years after initial tensioning were found to be lower than the values expected to occur 40 years after tensioning. In addition to stress relaxation, cited causes included improperly calibrated jacks, concrete creep, and poor quality control during tensioning. At presumably the same plant, similarly low forces due to excessive stress relaxation were measured in the vertical tendons 13 years after initial tensioning. Other cases of excessive prestress losses after 20 to 25 years have been identified, but the ability to retension unbonded tendons reduces the long-term severity of these losses (Shah and Hookham, 1998).

2.4.3 Thermal Loading

The effects of elevated temperatures and freeze-thaw cycles on hardened concrete have been studied for nuclear containments and are presented in the following sections. Mass concrete thermal effects, which have not been as thoroughly documented for nuclear containments, are discussed in Section 2.4.8.

2.4.3.1 Elevated Temperatures

Because the basic function of a nuclear reactor is to generate heat, nuclear containments may be exposed to considerable thermal loads. If severe enough, the increase in temperature can reduce the strength of the steel in the containment and cause cracking and spalling of the concrete, especially if the thermal load is cycled. High temperatures are particularly detrimental to prestressing tendons because the heat can alter the microstructural formations created during the heat-treating process, preventing them from regaining their initial strength, even after cooling (Naus, 2007). The thick walls of concrete containment buildings provide a high thermal inertia that slows the progression of heat through the section depth. Even at temperature conditions characteristic of a fire, the concrete may keep the steel temperatures low enough to delay the loss of strength. However, if the temperature increases too quickly, the concrete could spall and expose the conventional reinforcement.

For long-duration temperature exposures in containments, ACI 349-06 (2007) specifies a maximum concrete surface temperature of 66 °C (150 °F), but local temperature exposures are permitted up to 93 °C (200 °F). For short-term events, such as accidents, a maximum concrete surface temperature of 177 °C (350 °F) is specified, but local areas are permitted to reach 343 °C (650 °F). After such exposure conditions, however, the structure is to be examined for serviceability defects according to ACI 349.1R-07 (2007).

Tests by Hanson et al. (1987) have indicated that the highest temperatures expected to occur in a concrete containment building, approximately 177° to 204 °C (350° to 400 °F), have minimal effects on the ultimate pressure capacity of the structure. According to Hessheimer and Dameron (2006), the pressure capacity would only be reduced if temperatures near 370° to 427 °C (700° to 800 °F) were maintained in the concrete long enough to heat up the reinforcement or prestressing tendons. Even though containment buildings at older plants may experience higher local temperatures because the penetrations for piping are not cooled, there have been no reports of significant damage due to thermal loads (Shah and Hookham, 1998).

Analysis by Anderson (2007) of data collected at Swedish PCCs similar to those in the U.S. indicates that there may be a strong relationship between the temperature increase at the beginning of reactor operation and the rate of prestressing loss in the tendons. Data from lift-off tests conducted during in-service inspections are shown in Figure 2.9. The apparent increase in force between some data points occurs because the measured tendons are selected randomly for each in-service inspection. Therefore, this figure is primarily effective for identifying trends and comparing the general behavior of the containments. While the other reactors shown in the figure began operation 4-5 years after prestressing, the Ringhals 2 reactor began operation about 1 year after prestressing and has the only containment showing noticeably greater losses than the controls for both vertical and horizontal tendons. Because higher temperatures increase shrinkage, creep, and relaxation, it was proposed that the earlier operation of Ringhals 2, accompanied by the temperature increase from approximately 20 °C (68 °F) to about 30 to 45 °C (86 to 113 °F), was the primary contribution to the greater prestress losses.

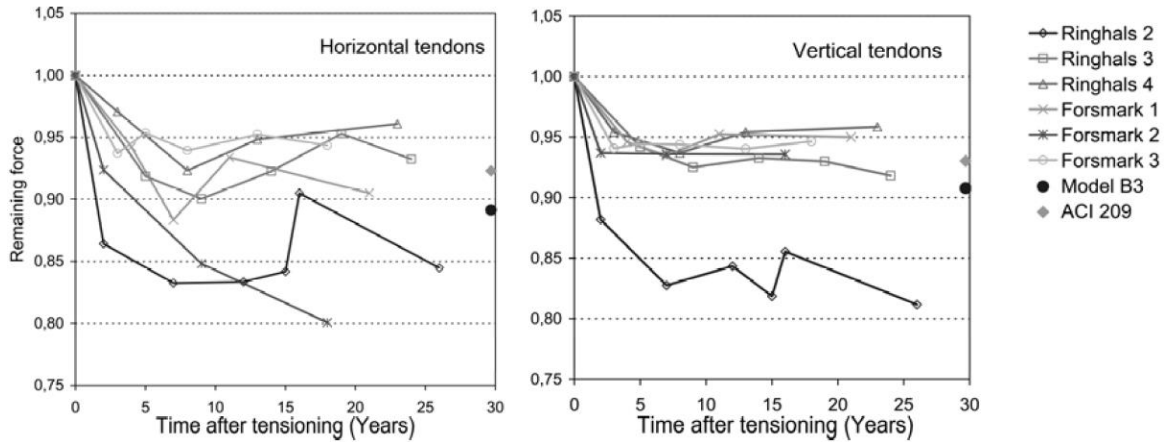


Figure 2.9: Remaining prestressing force from lift-off tests normalized by initial prestressing force. Each point represents the average of all values obtained at the containment at the corresponding inspection. Horizontal (left) and vertical tendons (right) (Anderson, 2007).

At the Forsmark 1 reactor (included in Figure 2.9), Glötzl gauges were installed during construction at the ends of some of the prestressing tendons. Shown on a logarithmic timescale (Figure 2.10), the data from these gauges shows a noticeable increase in the rate of prestress loss that coincides with the beginning of reactor operation about 5 years after initial tensioning. This behavior has not been investigated at other PCCs, so its implications are uncertain.

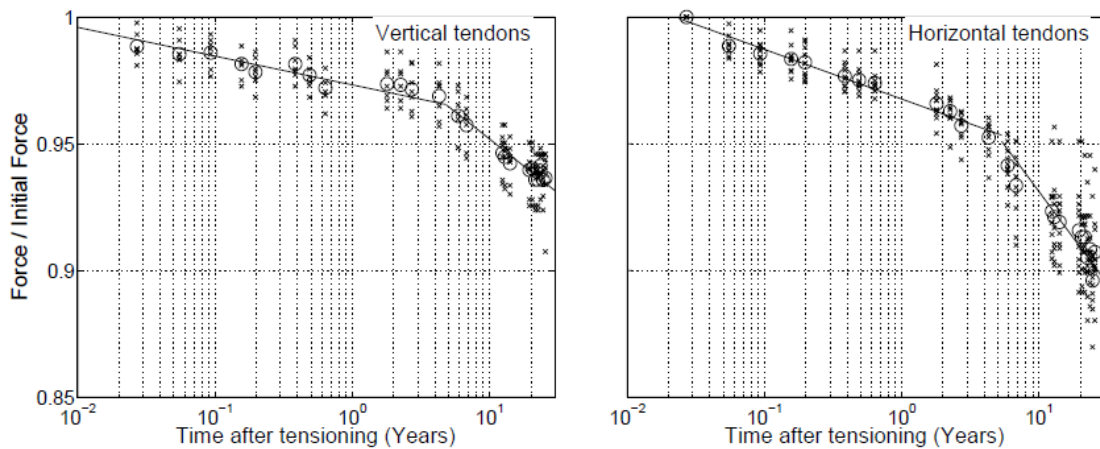


Figure 2.10: Remaining force from gauges normalized by initial force (logarithmic timescale) (Anderson, 2007).

2.4.3.2 Freeze-Thaw Cycling

If highly saturated concrete has insufficient entrained air in the cement paste or has highly porous aggregates, freeze-thaw cycles can result in internal expansion and eventual cracking, scaling, or disintegration of the concrete (Mather, 1979; Naus, 2007). The low water-cement ratio and the air-entraining admixtures typically used in containment buildings minimize the potential for damage from freeze-thaw cycles by forming small, closely spaced voids in the concrete that permit the release of hydraulic pressure during freezing (Mehta and Monteiro, 2006). In the proper climate, however, external surfaces that accumulate moisture could still be susceptible. A large area of the dome of one U.S. containment building spalled due to substantial freeze-thaw damage, requiring the replacement of concrete up to 230 mm (9 in.) deep in certain areas (IAEA, 1998; Naus et al., 1998; Shah and Hookham, 1998).

2.4.4 Carbonation

Carbonation is the process in which calcium hydroxide and carbon dioxide react to form calcium carbonate (calcite) and water (Chang and Chen, 2005). This reaction alters the concrete microstructure and decreases the porosity, but the resulting decrease in the alkalinity of the concrete is typically of most concern. The pH of the pore solution of non-carbonated concrete normally ranges between 12.5 and 13.5, which creates a passive layer protecting steel reinforcement from corrosion (Saetta et al., 1993). The pH decreases to approximately 8.3 in fully carbonated concrete, making the reinforcement vulnerable to corrosion.

Carbonation typically progresses slowly in quality concrete, estimated at a rate of about 1 mm (0.04 in.) per year, but the rate is a function of the humidity and concrete porosity (Naus, 2007). The most likely location of carbonation in NPPs is at the surfaces of concrete inside the containment building, where the low humidity and high temperature are favorable conditions for carbonation. Since the interior surfaces of

concrete containment buildings are lined with steel, this is not a likely source of degradation for PCCs.

As a result of the decreased porosity, carbonated concrete has higher compressive strength and modulus of elasticity than non-carbonated concrete (Chang and Chen, 2005). However, carbonation is usually limited to a thin layer of the surface zone, so the resulting changes in mechanical properties are negligible for the thick walls of PCCs (Naus, 2007).

Through petrographic analysis of three cores from the CR3 PCC, Wilson (2009a) measured a carbonation depth of 6.4 to 12.7 mm (0.25 to 0.50 in.) from the exterior surface. In similar analysis, Brown (2009) measured a carbonation depth of 4.1 to 5.1 mm (0.16 to 0.20 in.) from the outer surface. This extent of carbonation after 35 years has negligible mechanical impact on the 1.07-m-thick (42-in.-thick) PCC wall and is still approximately 44.5 mm (1.75 in.) from the steel reinforcement. In both studies, negligible carbonation was identified on the fractured core surfaces from the delamination.

2.4.5 Steel Corrosion

2.4.5.1 Corrosion of Conventional Reinforcement

Amongst the potential mechanisms of degradation of conventional reinforcement, corrosion is identified as the most detrimental to the durability of NPP concrete structures (Naus, 2007). Corrosion causes metallic iron to react and produce ferric oxide (rust), resulting in an increased volume that can cause cracking and spalling. This process reduces the cross-sectional area, and therefore capacity, of the steel and reduces the ductility and composite action of reinforced concrete. General corrosion occurs uniformly along the affected element, whereas pitting corrosion is localized, decreasing the cross-sectional area in isolated regions while leaving most of the element unaffected. Corrosion

cannot occur without the presence of both water and oxygen, and the alkaline nature of concrete protects the steel by causing the formation of a passive iron oxide film on the reinforcement. Though corrosion is not stopped by the passive layer, the rate of corrosion in the presence of the film is negligible: $0.1 \mu\text{m}$ (4×10^{-5} in.) per year according to ACI 222R-01 (2001).

Steel in reinforced concrete becomes vulnerable to corrosion when depassivation occurs by carbonation or chloride diffusion. A concrete pH value of 9.5 is considered to be the threshold for corrosion, but the interaction of carbonation and chloride diffusion can result in depassivation at higher pH values and lower chloride concentrations (Naus, 2007). The low permeability of concrete containment buildings delays the onset of corrosion, which could take about 100 years with carbonation, after which visible concrete damage could take another 5 to 20 years to occur (Shah and Hookham, 1998).

2.4.5.2 Corrosion of Prestressed Tendons

The protection of the prestressing tendons used in PCCs is important because the high-strength steels used to fabricate the tendons are more susceptible to corrosion than plain carbon steels (Ashar and Naus, 1983). Furthermore, the use of small-diameter wires stressed to approximately 70% of their GUTS increases the susceptibility to corrosion. In prestressed containments with bonded tendons, the portland cement grout injected into the ducts protects the tendons from corrosion. Similarly, the tendons of unbonded structures are protected by the microcrystalline wax (petrolatum) or grease in the ducts. In addition to providing corrosion protection, the grease decreases the friction factor by about 50 percent, enabling the use of longer tendons and requiring fewer anchorage points on the structure (Ashar et al., 1994a). Also, the unbonded tendons can be relaxed, inspected for corrosion, and re-tensioned or replaced.

In some plants with shallow-domed PCCs, pitting corrosion has been detected near the bottom anchors of the vertical tendons (Shah and Hookham, 1998). The problem

has been attributed to the buildup of rain water on the dome and top of the ring girder due to clogged drains. The water eventually seeps through the top anchor and settles at the bottom of the tendon. Corrosion was detected in some of the vertical tendons of the secondary shield wall at Oconee 2 and 3, and in addition to replacing the tendons, the bottom grease caps were redesigned to allow water drainage (Naus, 1986).

In the reactor vessel at Fort St. Vrain, corrosion of prestressing wires was caused by the presence of acids formed by microbial attack on the anticorrosion grease (Naus, 1986). The corrosion was detected during regular tendon surveillance, and most of the corrosion was found near the top anchors of the vertical tendons. After stopping the degradation by filling the ducts with inert nitrogen, it was determined that the vessel still had sufficient capacity for operation.

At one plant, corrosion was identified on some grease can and bearing plate surfaces of the prestressing system, but no tendon corrosion was noted (Gregor and Hookham, 1993). At Zion Unit 2, pitting corrosion developed on the prestressing wires prior to installation due to improper storage and handling on the site (Naus, 1986).

The results of finite element analyses of a typical U.S. PCC with prestressing losses caused by tendon corrosion, anchor corrosion, and other forms of degradation suggest that the containment building capacity in a loss of coolant accident is negligibly affected by the corrosion of vertical tendons (Smith, 2001), matching the results of a separate 1:4-scale mock-up experiment (discussed in more detail in Section 2.5.3) (Hessheimer, 2003). It was suggested, however, that the vertical tendons may be critical for the integrity of the structure in other loading conditions that were not analyzed. The greatest capacity losses in the finite element analysis were caused by the failure of mid-height hoop tendons due to corrosion. However, assumptions were made in the finite element model that could have impacted the results: the friction in the vertical tendons was neglected, the possibility of other forms of degradation in the non-corroded tendons was ignored, and the hoop tendons were modeled as bonded tendons though only two

U.S. PCCs have bonded tendons. In the tests on the 1:4-scale mock-up, the losses due to wobble friction in the vertical tendons were greater than expected (Hessheimer, 2003), indicating that the absence of friction in the finite element model may have affected the results more than expected.

Due to the redundancy in the design of U.S. PCCs, the loss of individual tendons due to corrosion is typically not a concern; many tendons would need to fail before a decrease in capacity could be identified (Shah and Hookham, 1998). Corrosion of the tendon ducts could contribute to cracking in the plane of the post-tensioning, but the ducts and tendons that were removed for the SGR opening at CR3 showed no signs of corrosion (Performance Improvement International, 2010), and chloride profiles of the PCC indicated that no significant chloride ingress had occurred.

2.4.5.3 Corrosion of Steel Liner

The steel liner and its anchorages in the containment wall are also susceptible to corrosion, particularly by chlorides in the concrete. Since the liners are often less than 13 mm (0.5 in.) thick, there is very little tolerance for material loss. Because through-thickness corrosion prevents the liner from establishing a leaktight boundary, corrosion is seen as the primary threat to the long-term performance of steel liners in PCCs (Naus et al., 1996). Containment liners typically receive a protective coating on the exposed inner surface, but the surface in contact with the concrete is usually left untreated and therefore vulnerable to corrosion that is difficult to detect until substantial degradation has occurred (Shah and Hookham, 1998).

A study conducted between 1999 and 2009 identified four cases of through-thickness liner corrosion in reinforced concrete containments due to foreign objects embedded in the concrete (Dunn et al., 2011; Petti et al., 2011). The embedded objects were items from the construction of the containment: a worker's glove, the handle of a wire brush, and pieces of wood (Figure 2.11). During an outage for a steam generator

replacement at one of these plants, corrosion was also found on the outer surface of a liner following hydrodemolition of the concrete. Embedded wood was found in the containments of four other reactors, but no apparent corrosion had developed. Since each of the through-thickness corrosion cases were observed many years after the affected reactors began operation and there is currently no efficient means of detecting the embedded objects, it is likely that similar incidences of liner corrosion will occur in other containments as well.

An earlier survey received three reports of corrosion of structural steel and containment liners, though no clarification was given as to whether the structural steel or the liner was affected in each case. In multiple French 900-MW reactor containments, pitting corrosion was observed at the bottom of the 6.3-mm-thick (0.25-in.-thick) steel liners at the interface with the lower floor (Nucleonics Week, 1991). As this degradation was consistent within the series of reactors, it was attributed to poor detailing around the affected area.

Braverman (1992) reported that at least one U.S. NPP has an impressed current cathodic protection system connected to the prestressing system, rebars, and steel liner, preventing corrosion of these elements by supplying a current that reduces the net anodic current. At least two U.S. NPPs have foundation piles connected to a similar system for corrosion protection.



Figure 2.11: Embedded wood found in containment concrete at Beaver Valley Unit 1 after removal of corroded liner (Dunn et al., 2011).

2.4.6 Alkali-Aggregate Reactions

The predominant mechanism of degradation amongst the alkali-aggregate reactions is the alkali-silica reaction (ASR), in which alkalis and hydroxyls in the portland cement react with certain siliceous components of the aggregate in the presence of moisture to form a calcium alkali-silicate gel (Naus, 2007). This gel absorbs water and expands, resulting in cracking. Because exposure to water is necessary for the gel expansion, the damage is often seen in parts of structures below grade in areas with a high water table, so below-grade portions of containment buildings may be susceptible (Shah and Hookham, 1998). Similar expansion and cracking result from the alkali-carbonate reaction (ACR), but no gel is formed.

Before the first U.S. containment buildings were constructed, ASTM tests were available to identify aggregates likely to cause ASR: ASTM C227-50 Test for Potential Alkali Reactivity of Cement-Aggregate Combinations, a lengthy mortar bar expansion test; ASTM C289-52 Test for Potential Reactivity of Aggregates (Chemical Method), a rapid chemical test; and ASTM C295-56 Practice for Petrographic Examination of Aggregates for Concrete (Frohnsdorff et al., 1978; Shah and Hookham, 1998). By

avoiding the use of reactive aggregates, containment buildings resistant to ASR were constructed. However, field observations and laboratory testing by Stark (1980) showed deficiencies in the earlier ASTM tests for reactive aggregates, so ASR-induced degradation is still a potential hindrance to long-term durability. Additionally, higher alkali contents of current cements and the scarcity of quality aggregate sources in many areas of the U.S. have increased the potential for ASR to impact future containment structures (Naus, 2007).

The onset of ASR-induced degradation has been observed from as early as 5 to 10 years to as long as 40 years into the life of a structure. It was thought that because no occurrences of ASR had been reported at any U.S. NPPs, the majority of which have been in operation for more than 30 years, ASR might not be a critical factor for U.S. containment buildings. However, ASR-induced degradation was recently detected in below-grade walls of an electrical tunnel at Seabrook Station in Seabrook, New Hampshire, resulting in decreased compressive strength of the concrete (Roberts, 2011). Out of five other safety-related structures that were tested at Seabrook Station, including the reinforced concrete containment building, evidence of ASR was identified in four. The investigation into the extent of the degradation is ongoing.

Erlin (1976) performed petrographic analysis of a concrete fragment from the CR3 dome delamination and did not detect the presence any reactive components or the alkali-silica gel. In analysis by Wilson (2009a) following the CR3 PCC delamination detected in 2009, localized evidence of ASR was detected in one of the two cores from the delaminated region, but a later report by Wilson (2009b) indicated that the amount of material present was too small to positively identify as ASR. Brown (2009) did not detect any evidence of ASR in a saw-cut core from the CR3 PCC delamination.

2.4.7 Sulfate Attack

Sulfate attack occurs as a result of high concentrations of hydrated calcium aluminates in the cement paste reacting with dissolved sulfates present in the environmental moisture, though the inclusion of sources of sulfate in the concrete mix can also contribute (Mather, 1979). Sulfate attack may result in ettringite and gypsum formation in the concrete or the progressive breakdown of the cement compounds, resulting in loss of strength, concrete expansion, and cracking (Mehta and Monteiro, 2006; Naus, 2007).

The use of Type II portland cement in U.S. NPPs minimizes the likelihood of sulfate attack on concrete containment structures. However, even if the concentration of sulfates is less than the limit for Type II cement, groundwater can build up quantities of precipitated sulfate salts in the concrete that, when later dissolved, would be capable of gradually breaking down the cement compounds in the long-term (Clifton, 1991; Cohen and Mather, 1991). Therefore, even though damage from sulfate attack has not been reported at any U.S. containments, it is still cited as a major potential source of containment degradation.

Petrographic analysis by Brown (2009) following the identification of the CR3 PCC delamination in 2009 identified no signs of sulfate attack, and the low permeability of the concrete and the absence of sulfate sources near CR3 limit the susceptibility to sulfate attack (Performance Improvement International, 2010).

2.4.8 Mass Concrete Effects

For concrete members with large dimensions, the heat of hydration is generated more quickly at early ages than it is able to escape from the member, resulting in higher temperatures at the center of the member compared to temperatures at the surface. If the temperature difference is large enough, thermal stresses will cause surface cracking that can be detrimental to the durability of the structure.

Another concern regarding the temperature rise in large concrete members is the susceptibility to delayed ettringite formation (DEF). In this form of sulfate attack, the sulfate is present within the cement paste rather than in the environment. Ettringite decomposes at the high temperatures, releasing sulfate ions that are adsorbed by the calcium silicate hydrate of the cement paste (Mehta and Monteiro, 2006). Expansion and potential cracking result when the sulfate is later desorbed and new ettringite is formed. Concrete temperatures exceeding approximately 70 °C (158 °F) have been identified as the critical factor in the occurrence of DEF (Taylor et al., 2001; Gajda, 2007).

2.4.8.1 Criteria and Restrictions for Mass Concrete

Various definitions of mass concrete have been presented by professional organizations and state departments of transportation (DOTs). ACI Concrete Terminology (American Concrete Institute, 2013) defines mass concrete as “any volume of structural concrete in which a combination of dimensions of the member being cast, the boundary conditions, the characteristics of the concrete mixture, and the ambient conditions can lead to undesirable thermal stresses, cracking, deleterious chemical reactions, or reduction in the long-term strength as a result of elevated concrete temperature due to heat from hydration.” ACI 207.2R-07 indicates that concrete members with a minimum dimension of at least 460 mm (18 in.) are generally evaluated for mass concrete effects. For most bridge components, the Florida Department of Transportation (FDOT) Structures Manual (2015) requires mass concrete considerations when the minimum dimension of a placement is greater than 914 mm (3 ft) and the volume-to-surface area ratio (V/SA) is greater than 305 mm (1 ft).

ACI 301-10 specifies that the maximum concrete temperature after placement not exceed 70 °C (158 °F) and that the maximum temperature difference in the concrete not exceed 19 °C (35 °F) as measured between the center of mass of the placement and the center of the nearest exterior surface. Gajda and VanGeem (2002) note that project

specifications may limit the maximum temperature to as low as 57 °C (135 °F). The maximum temperature limits are generally established in consideration of DEF, which can occur at concrete temperatures greater than 70 °C (158 °F) (Taylor et al., 2001; Gajda, 2007).

Since the cementitious materials content and admixtures influence the rate and extent of heat of hydration, criteria have also been established to control mix designs for mass concrete applications. Gajda (2007) suggested that concrete with cementitious materials content exceeding 355 kg/m³ (600 lb/yd³) of concrete be considered mass concrete, though Tia et al. (2010) note that different cement types generate different amounts of heat and that concrete typically releases less heat when supplementary cementitious materials (SCMs) are used to replace some portion of the cement (Malhotra and Mehta, 1996). For mass concrete applications, ACI 301-10 specifies the use of moderate- or low-heat hydraulic cement or the use of portland cement with Class F fly ash and/or slag.

The criteria and restrictions for mass concrete amongst 18 state DOTs tabulated by Tia et al. (2010) vary widely: the minimum dimensions for classification as mass concrete ranged from 0.9 to 2.0 m (3 to 6.5 ft), and the maximum permissible placement temperatures, curing temperatures, and temperature differentials ranged between 18 and 27 °C (65 and 80 °F), 71 and 85 °C (160 to 185 °F), and 15 and 28 °C (27 to 50 °F), respectively.

The CR3 PCC design meets many of the previously described criteria for mass concrete considerations. The 1.07-m (42-in.) thickness exceeds the ACI guidelines and FDOT requirement for minimum cross-sectional dimension, and the V/SA for a typical pour was calculated in Appendix A.1 to be 351 mm (13.8 in.), exceeding the FDOT limit. The cement content of 405 kg/m³ (682 lb/yd³) of concrete also exceeds the guideline from Gajda (2007). However, analysis that was conducted following the identification of

the PCC delamination in 2009 did not thoroughly account for the effects of mass concrete behavior on the early-age behavior and property development of the concrete.

2.4.8.2 Methods of Limiting Mass Concrete Effects

Two primary criteria for reducing differential volume changes in mass concrete are limiting the temperature of the freshly mixed concrete and limiting the temperature difference that develops due to the heat of hydration. Volume change can also be reduced by selecting an aggregate with a lower coefficient of thermal expansion, which will result in a concrete with a lower coefficient of thermal expansion.

Efforts to limit the temperature difference typically begin with trying to limit the heat of hydration for the concrete mix by selecting low-heat cements, such as Type IV, Type II, and some Type V portland cements, and using supplementary cementitious materials (SCMs), such as fly ash or slag, that reduce the generation of heat (Gajda, 2007). Admixtures for reducing water content, increasing slump, delaying setting time, and entraining air are often used in mass concrete applications. However, none of these effects directly contribute to decreased concrete temperatures in large mass concrete placements; decreased concrete temperatures will only be attained with water-reducing admixtures if the cement content is also reduced.

Without any precooling, the initial temperature of concrete when placed in the forms is approximately 3 to 6 °C (5 to 10 °F) higher than the ambient air temperature (Gajda, 2007). A unit increase or decrease of the initial concrete temperature has the same effect on the maximum concrete temperature after placement, so precooling the freshly mixed concrete is an effective way to limit the maximum temperature (Gajda, 2007). Precooling can be applied to individual components of the concrete or the entire concrete mix, but water is the easiest to cool. Additionally, part of the mixing water can be added as ice, reducing the concrete temperature even further by consuming heat when changing phase from ice to water.

Methods of reducing the maximum temperature difference in the concrete include using internal cooling pipes and insulating the exposed concrete surfaces. Internal cooling pipes bring heat away from the concrete interior, reducing the maximum temperature and the temperature difference in the concrete. In contrast, insulation increases the concrete surface temperature by slowing the release of heat to the environment, resulting in a lower temperature difference in the concrete. Even without explicit insulation, wooden formwork can insulate the concrete and slow the loss of heat. The procedures for concrete curing and form removal for the CR3 PCC specified that forms be kept in place for at least 1 day or that a concrete compressive strength of at least 500 psi be developed prior to formwork removal, and the record for the uppermost region of the delamination indicates that the formwork was still in place 9 days after concrete placement (McGillivray, 1973).

As mentioned in Section 2.1.4.2, the concrete for the CR3 PCC contains Type II portland cement and limerock coarse aggregate, which typically has a low coefficient of thermal expansion. Though an ASTM C494 Type D water-reducing and retarding admixture was included, the cement content was kept relatively high for a w/c of 0.41. Three pour cards for the concrete mix design used in most of the delaminated region of bay 34 indicate that ice was substituted for 12 to 19% of the total water content, whereas a pour card for the uppermost region of the delamination, where a different mix design was used, indicates that ice was substituted for 40% of the total water content (Performance Improvement International, 2010). The recorded range of ambient temperatures during concrete placement was 14 to 21 °C (58 to 70 °F), and the recorded range of concrete temperatures during placement was 10 to 16 °C (50 to 60 °F), below the specified maximum temperature of 21 °C (70 °F) (Gilbert Associates, 1968; Performance Improvement International, 2010).

The concrete curing and form removal card for the uppermost region of the delamination indicates that the concrete was to be continuously sprinkled and ponded for

at least 7 days with an ambient temperature no less than 10 °C (50 °F) (McGillivray, 1973). Though moist curing is generally beneficial for the mechanical properties of concrete, sprinkling the concrete with water will cool the surface, resulting in a greater temperature difference unless the water is heated.

2.4.8.3 Non-Uniform Properties

Due to the temperature gradient in mass concrete members, hydration progresses at different rates in different regions of the member. The concrete at the center of the member, subjected to higher temperatures, will have a much higher maturity at any given time than concrete nearer the surface, which cures at a lower temperature. All other factors being constant, the more mature concrete will typically have higher compressive strength, tensile strength, and modulus of elasticity at early ages. In a PCC, the non-uniform modulus of elasticity through the thickness of the wall will result in a non-uniform distribution of circumferential compressive stresses that has not been thoroughly investigated in the literature. The present work considers the influence that high early-age temperatures and non-uniform concrete property development have on the mechanical behavior of PCCs.

2.4.9 Monitoring Prestressed Concrete Containments for Degradation

According to the U.S. Nuclear Regulatory Commission (2011a), U.S. containments are required to be designed such that all of the critical areas of the containment can be periodically inspected and that an appropriate plan for surveillance of the structure can be developed. Many NPPs follow the inspection programs recommended by the NRC Regulatory Guides (U.S. Nuclear Regulatory Commission, 1976, 1990a, 1990b), though different methods are accepted as long as they provide sufficient evidence of satisfactory integrity of NPP structures.

For exposed concrete surfaces, visual inspection can identify excessive levels of concrete shrinkage, concrete spalling, or steel corrosion. Naus et al. (1996) reports that ultrasonic pulse velocity measurement is a commonly used NDE technique for detecting subsurface cracks or voids and estimating the concrete quality. The identification of cracks is often the first indicator of many forms of degradation in reinforced concrete structures, and the type of degradation can often be determined from the characteristics of the cracking. Concrete core samples can be used for in-situ compressive strength testing, petrographic studies, and chemical analyses. These tests can provide evidence of chemical degradation or poor quality of the concrete. Visual examination of cores can aid in the detection of cracks and voids and the identification of reinforcement corrosion.

For PCCs with unbonded tendons, Regulatory Guide 1.35 (U.S. Nuclear Regulatory Commission, 1976) recommends inservice inspections (ISIs) of the containment structure one, three, and five years after the initial structural integrity test of the containment and every five years thereafter. For each inspection, representative tendons should be randomly selected from subgroups of hoop, vertical, and dome tendons. Revision 2 of Regulatory Guide 1.35 states that one tendon from each group of the initial ISI may be kept constant for subsequent ISIs in order to develop a consistent history; Revision 3 (U.S. Nuclear Regulatory Commission, 1990b) encourages this practice. Regulatory Guide 1.35.1 (U.S. Nuclear Regulatory Commission, 1990a) states that the forces in the selected tendons should be measured by liftoff testing or load cells, and the measured changes can be compared with the predicted values to monitor prestress losses.

One tendon from each of the previously identified groups should be removed and examined for degradation such as corrosion, and tensile tests of at least three samples from the removed tendon should be conducted. Extra wires were intentionally included in selected tendons for these tests (Steigermann and Tan, 1969). The tendon anchorage assembly and surrounding concrete for the selected tendons should be visually inspected

for corrosion and voids. Revision 3 also suggests that the exterior surface of the containment be examined for areas of surface defects or grease leakage. To check for sheathing filler grease leakage or grease cap deformations of the vertical tendons, all of the bottom grease caps should be inspected.

The sheathing filler grease from all of the sample tendons should be tested according to the appropriate standards for water content, reserve alkalinity, concentrations of water-soluble chlorides, nitrates, and sulfides. The volume of grease removed and replaced from any sheathing should be monitored to identify internal grease leakage into the containment wall.

The inspection of steel liners typically involves visual examination of the exposed surface. As discussed in Section 2.3.5.3, it is difficult to identify liner corrosion that initiates on the concrete side of the liner, so supplemental nondestructive examination methods may be used in situations where specific sites of possible degradation have been identified (Naus et al., 1996).

Bekowich (1968) discusses an instrumentation program for monitoring multiple PCCs that were being constructed in the U.S., but no results of the studies were provided, and no follow-up references have been identified.

2.5 Containment Mock-Ups

In order to appropriately design a mock-up for investigation of the mechanisms contributing to the CR3 PCC delamination detected in 2009, a review of the literature on containment mock-ups was conducted. The following sections focus on mock-ups of concrete containments and cover a variety of scales and test methods.

2.5.1 Early Testing

In the 1970s, many scale models of concrete reactor vessels were pressure tested to failure (Hessheimer and Dameron, 2006). Though reactor vessels have thicker walls

and higher internal pressures than containment buildings, these tests contributed to the evaluation methodology for later containment tests.

In the 1980s, tests were conducted on small-scale steel containment mock-ups in the US by Horschel and Blejwas (1983) and Horschel and Clauss (1984) and in Germany by Krieg et al. (1984) and Goller et al. (1987) investigating the containment response to overpressurization. These early tests demonstrated the benefits of scale model testing for comparison with analytical predictions and predictions of containment response and failure modes, particularly the weakening influence of discontinuities at containment penetrations.

2.5.2 1:6-Scale Reinforced Concrete Containment Mock-Up

A 1:6-scale reinforced concrete mock-up was tested at Sandia National Laboratories in July 1987. The model included the steel liner and representative containment penetrations, and over 1200 strain gages, displacement transducers, and other sensors were installed for data collection. After initial low-pressure tests, the mock-up was pressurized with nitrogen gas until failure, resulting in leakage through tears in the steel liner and cracks in the concrete (Horschel, 1992). Similar to the earlier steel containment mock-ups, strain concentrations near the containment penetrations resulted in the critical liner tear and many smaller tears along anchor studs near the penetrations. In a review of posttest analyses of the 1:6-scale mock-up, von Riesemann and Parks (1995) observed that, though strain concentrations were anticipated at the penetrations, the anchor studs were expected to fail before the liner tore.

Weatherby and Clauss (1989), Lambert (1993), and Spletzer et al. (1995) conducted follow-up investigations of the liner and anchor stud behavior on steel-lined, uniaxially loaded specimens presented in Figure 2.12. The results showed that the failure of the studs versus the failure of the liner was controlled by the magnitude of preload

forces in the liner, but the simplified local mock-ups were unable to reproduce the behavior of the 1:6-scale mock-up of the entire containment.

Hanson et al. (1987) conducted follow-up tests related to the 1:6-scale containment mock-up by constructing full-scale mock-ups of specific regions of the containment where critical liner behavior had been observed or was expected, typically at connection and penetration details as shown in Figure 2.13. Each region was modeled as a flat panel, some with initial flaws, and loaded with the expected biaxial loads that would be experienced during overpressurization of containment building. The loads were applied to individual rebars and liner edges rather than the concrete. The results of these tests displayed the desired “leak before break” behavior for concrete containments and contributed to the prediction methodology for liner tearing and leakage in concrete containments (Hessheimer and Dameron, 2006).

A prestressed concrete specimen and a reinforced concrete specimen from this series were tested and analyzed to investigate potential thermal buckling of the steel liner during accident conditions, during which the maximum expected surface temperatures are approximately 177 to 204 °C (350 to 400 °F). For both specimens, the low tensile capacity of the cracked concrete was unable to restrain the thermal expansion of the liner, so no liner buckling occurred. The results indicated that increased temperatures had little impact on the ultimate pressure capacity of either containment type.

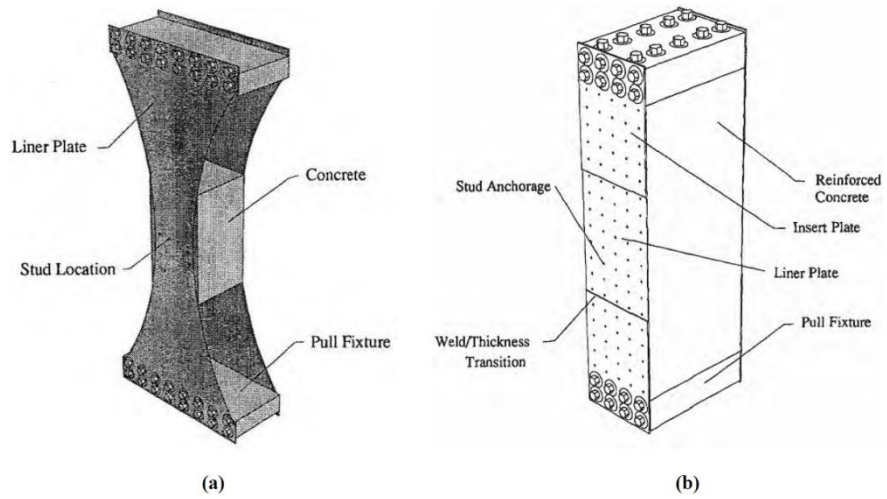


Figure 2.12: Uniaxial specimens for strain concentration and liner tear studies (Hessheimer and Dameron, 2006)

Typical Prestressed Containment

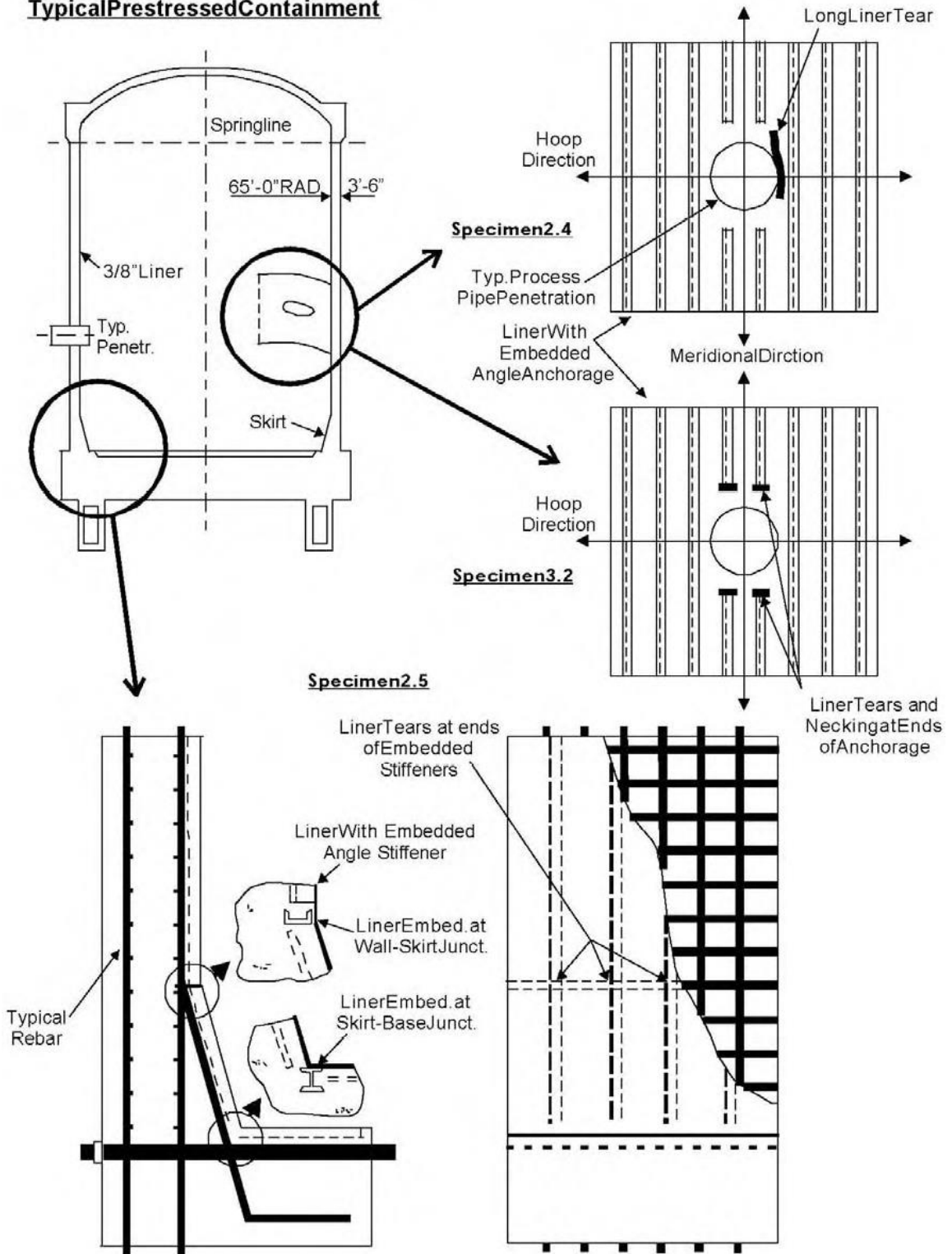


Figure 2.13: Panel mock-ups for investigation of liner behavior at local regions of containment (Hessheimer and Dameron, 2006).

2.5.3 1:4-Scale Prestressed Concrete Containment Mock-Up (Ohi-3)

The largest documented scale model of a full containment was the 1:4-scale model of the Japanese Ohi-3 PCC (Hessheimer, 2003). The containment was scaled uniformly to the extent possible, but rather than directly scaling individual rebars, they were spaced and sized to match the reinforcing ratio closely. The number and size of the wires in the unbonded prestressing tendons were scaled and prestressed so that the net anchor forces at the limit state test were representative of the expected forces after 40 years of operation of the prototype.

The tendons were brushed with an anti-corrosion coating rather than greased because of the relatively short five-year life of the model and for ease of instrumentation placement; more than half of the instruments were damaged during tensioning. Additional sensors were installed to monitor the strain, displacement, forces, temperatures, and pressures throughout the mock-up. Initial low-pressure testing confirmed the leaktightness of the containment and the calibration of the sensors, and then a series of increasing pressure tests were performed until sudden rupture of the containment at 3.63 times the design pressure.

Pretest finite element analyses included an axisymmetric model of the entire structure, local models of the major penetrations, and a cylindrical model of the mid-height region with buttresses and penetrations included (Hessheimer and Dameron, 2006). Comparison of the results from each of the models revealed slight differences in the behavior depending on the detail of the model. The cylindrical model displayed considerable circumferential bending adjacent to each buttress, which the axisymmetric model could not represent. The local models of the penetrations and the cylindrical model also displayed notable strain concentrations at the penetrations and buttresses, another result that the axisymmetric model was unable to represent.

Prior to testing the 1:4-scale mock-up, seventeen analysts were provided with the mock-up information and asked to independently model the behavior analytically. Luk

(2000) reported that the results of this round-robin analysis varied regarding the prediction of failure mode, global behavior near failure, and some local strains near penetrations (Figure 2.14). The predicted elastic response was fairly consistent amongst the analyses.

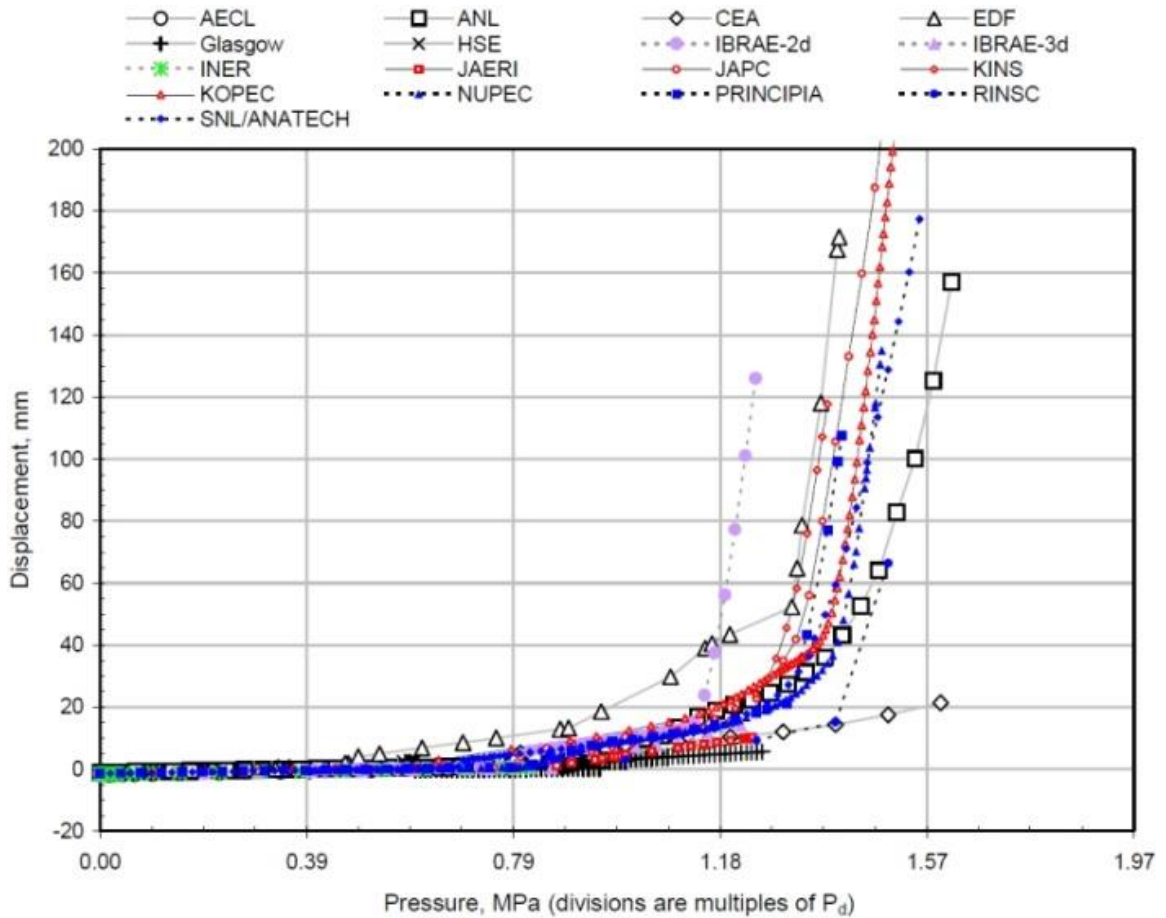


Figure 2.14: Predictions of radial displacement at mid-height of cylinder wall vs. internal pressure (Luk, 2000).

Posttest analysis showed that the axisymmetric pretest model accurately predicted circumferential strains and the response at the junction between the cylinder wall and the base, indicating that such simplified analyses can successfully be used for representation of global behavior during overpressure scenarios (Hessheimer and Dameron, 2006). The multiple phases of analysis for this 1:4-scale mock-up also provided insight regarding the

accuracy of various tendon modeling methods, with a contact friction surface between the tendons and the concrete being most preferable. When friction surfaces and friction ties are impractical for the analysis, an average stress, determined from friction loss calculations, should be uniformly used along the tendons instead (Hessheimer and Dameron, 2006).

2.5.4 1:10-Scale Prestressed Concrete Containment Mock-Up (Sizewell-B)

Similar to the 1:4-scale mock-up, the Sizewell-B 1:10-scale mock-up tested in 1989 was also a cylindrical, hemispherical domed, biaxially prestressed containment (Twidale and Crowder, 1991). The tendons consisted of seven-wire strands sheathed in a plastic coating rather than preformed ducts, which prevented tendon sliding and resulted in strain gradients along the tendons. Because of the difficulty of welding and fabricating a 1:10-scale liner plate, a rubber bladder was used to prevent leakage during the series of hydrostatic pressurization tests. Four cycles up to 1.15 times the design pressure were followed by an ultimate pressure test. Increased uplift of the base slab was observed at the fourth low pressure cycle, and the ultimate pressure test was terminated with only a small extent of cylinder reinforcement yielding due to extensive inelastic deformation of the base slab. Posttest finite element analysis (Hessheimer and Dameron, 2006) with bonded tendons matched the observed response of the model better than analysis with unbonded tendons, suggesting that the tendon coating may have altered the behavior of the structure. Similar to the 1:4-scale analysis, axisymmetric modeling of the 1:10-scale mock-up was satisfactory for modeling global response but was ineffective for modeling local effects.

2.5.5 Non-Uniform 1:3-Scale Mock-Up (MAEVA)

Granger et al. (2001a, 2001b) tested a non-uniformly scaled model of the biaxially prestressed containment cylinder of Civaux 2 in France in 1997. The radius of the mock-

up was 1/3 that of the Civaux 2 containment, but the thickness of the wall was maintained so that, in addition to mechanical behavior, accurate interpretation of thermal and hydraulic behavior would be possible during pressurization by air and an air-steam mixture. Though not evaluated in other mock-ups, the temperature loads in a containment were predicted to affect the pressure at which leakage begins relative to the ultimate pressure. Rather than modeling the dome, the unlined cylinder was enclosed by a flat circular base and cover with neoprene pads to allow radial motion while maintaining airtightness. However, this interface caused difficulties for maintaining leaktightness, and the final results of the experiment have not been published.

2.5.6 Mock-Ups for Seismic Testing

Beginning in the late 1980s, a series of seismic tests for scaled containment models were conducted using the large-scale shake table at the Tadotsu Engineering Laboratory in Japan. Nakamura et al. (1996, 1997) conducted tests on 1:10-scale curved segments of a biaxially prestressed concrete containment with 1:8-scale wall thickness and varying liner dimensions. Later tests were conducted on a biaxially prestressed concrete cylinder by Sasaki et al. (1999) and a reinforced concrete cylinder by Sasaki et al. (2001a, 2001b) at the same scales as the curved specimen. For simplicity, a large mass was attached to the top of the cylinders rather than constructing the dome. The goals of these tests were to evaluate the performance of the containment structures when subjected to seismic loads and to establish reference results to which analytical methods could be compared and improved upon.

The curved specimens exhibited consistent behavior despite varying liner thicknesses, and no instances of failure or pull-out of the liner anchors were observed. The prestressed concrete cylinder was subjected to the extreme design earthquake motion and experienced no shift in natural frequency, indicating that it had maintained its structural integrity. Furthermore, the containment maintained leaktightness until collapse

at five times the extreme design earthquake motion. While subjected to nine times the extreme design earthquake motion, the reinforced concrete cylinder failed almost simultaneously in shear near the lower drywell access penetrations and in flexure at the bottom of the cylinder. The ability to maintain integrity at such large motions was seen as evidence of the conservative design of the structures.

Though the testing of each of the models at increasing seismic motions enabled the observation of damage accumulation in the models, it complicated the analytical simulation because cumulative analysis of each motion was required.

Okamoto et al. (1995) conducted a pressurization test on a 1:10-scale reinforced concrete model of a rectangular boiling-water reactor building subjected to lateral loads representative of seismic motion. At the design level earthquake motion, narrow, distributed shear cracks developed in the walls, and a small amount of air leakage, well within limits, was detected. As the amount of air leakage decreases with increasing wall thickness, the results of this test indicated that full-scale concrete nuclear power plant structures would be able to maintain leaktightness, even when subjected to large earthquakes.

2.5.7 Representative Structural Volume Mock-Ups (PACE)

A series of tests proposed by Electricité de France (EDF) investigated concrete damage evolution and its effect on the permeability of pressurized containments using models of representative portions of the containment walls rather than the entire structure. These full-scale “representative structural volumes” (RSVs) excluded local details such as buttresses and penetrations but included typical wall curvature, prestressing, and reinforcement. The finite element analyses and experimental modeling of these RSVs of French prestressed concrete containments were presented as alternatives to tests on fully modeled containments.

Jason et al. (2005, 2007) conducted the PACE 1300 analysis of the containment of a French 1300 MWe nuclear reactor. The full-scale RSV incorporates the typical horizontal, vertical and transverse reinforcement and typical horizontal and vertical prestressed tendons of the prototype containment. The boundary conditions of the analytical model restrained the RSV as if it were part of a global containment model, and the weight of the structure above the RSV was accounted for. Pressure was applied radially on the interior face of the RSV, and tensile stresses were applied to the top face to account for the uplift pressure on the dome. Mechanical degradation of the model was simulated, resulting in damage along the middle vertical tendon that propagated through the thickness and part of the height of the RSV.

The PACE 1450 study included parallel experimental and analytical modeling of the containment of a French 1450 MWe nuclear reactor. Similar to the PACE 1300 analysis, the full-scale RSV tested by Herrmann et al. (2008, 2009) contained the typical horizontal, vertical and transverse reinforcement of the prototype (Figure 2.15). Horizontal prestressing was also included, but the tendons were not grouted (all French containments have grouted tendons). Vertical prestressing was modeled indirectly by steel cushions applying uniform pressure to the top and bottom faces. A single rigid vertical duct was included, but no prestressing was applied through it.

Optical fiber strain sensors and temperature sensors were embedded in the RSV, and eight microphones were embedded to detect the initiation of cracks. Displacement transducers measured the displacement of the edges of the RSV to provide information on the global behavior, and the force in each prestressing tendon was recorded by load cells.

To accurately represent the behavior of a containment cylinder, the boundary conditions of the experimental setup (Figure 2.16) allowed radial displacement of the RSV. As pressure was applied to the inner face of the RSV, the circumferential supports adjusted and applied corresponding tensile forces to facilitate the desired displacements

at the boundaries. The setup for this experiment cost approximately 1 million Euros (\$1.3 million) and was chosen over the cost of a closed ring pressure chamber with an inner radius of 71'-10" (21.9 m) and thickness of 3'-11" (1.2 m) with boundary conditions that would enable radial displacement.

The first three test cycles were pressurized with incrementally decreased prestress forces representative of an aging containment. Fourth and fifth cycles were planned for severe accident pressure with 60% of the initial prestressing force, with leakage detection provided during the fifth cycle. Internal strain measurements during the first three cycles matched the shape of the pressure and external force profiles. During the first two runs, the RSV experienced no circumferential tensile stresses, so only passive elongation occurred as the compressive stress decreased due to the internal pressurization. Tensile stresses were developed for the first time during the third cycle, and radial cracks developed, though none extended through the entire section and leakage detection was not necessary.

Jason et al. (2010) conducted analytical modeling of the PACE 1450 experiment. Two models were developed to compare the behavior when the tendons were modeled by 1D trusses and when they were modeled by explicit 3D elements for the tendons. Very little damage occurred during prestressing, and no further nonlinearities were developed until the final load step, when damage developed at the top of the model near the vertical tendon and propagated down the structure until heavy cracking resulted in partial unloading. These results suggest that rigid tendon ducts may contribute to containment cracking. The damage in the analysis with 1D truss elements was localized to the tendon area, whereas the damage in the analysis with 3D elements was more complex and propagated to the inner surface and one of the hoop tendons. The 1D truss modeling is typically used for industrial applications because of the complicated meshing and computation cost of explicit modeling of the tendons.

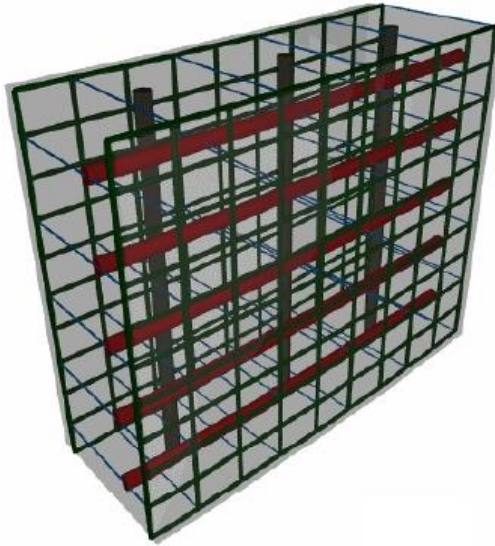


Figure 2.15: Rendering of an RSV with tendons and reinforcement shown Jason et al. (2005).



Figure 2.16: Experimental setup for PACE 1450 (Herrmann et al., 2008).

2.5.8 Discussion on Containment Mock-Ups

The review of mock-ups in the previous sections indicates that most of the experimental modeling of containment buildings has focused on the leaktightness of the structures while subjected internal pressure loads representative of accident scenarios.

Understanding this behavior is important because it relates directly to the ability of a containment to perform one of its primary functions of preventing the release of radioactive materials. These tests tend to focus on the development of cracks through the thickness of the containment wall. However, no tests have been identified in the literature that examining the development of delaminations parallel to the surface of the containment wall.

Due to the size of the PCCs of commercial nuclear reactors, most mock-ups are scale representations of the actual structures. Multiple mock-ups of entire PCCs have been tested, but analysis has indicated that axisymmetric models are able to representatively capture the global behavior of the structure, so using mock-ups of representative structural volumes (RSVs) is a practical approach to investigating PCC behavior. The feasibility of constructing full-scale RSVs versus entire containments is also beneficial for consideration of properties or phenomena, such as thermal effects in mass concrete applications, that do not scale well.

Planar mock-ups of local regions of PCCs with initial flaws have not been post-tensioned and have been loaded in tension to represent pressurization loads. Only the PACE 1450 mock-up was representatively curved and post-tensioned, but the set-up required for the boundary conditions increased the cost considerably relative to the simpler case of a post-tensioned planar specimen.

2.6 Heat of Hydration of Cementitious Materials

In order to model the thermal behavior of mass concrete applications, information about the generation of heat of hydration is needed. Due to the temperature dependence of the hydration reactions in cementitious materials, numerous parameters are needed to holistically model the time- and temperature-dependent development of heat in mass concrete.

2.6.1 Heat of Complete Hydration

Lea (1935) investigated the relationship between the four primary cement phases (C_3S , C_2S , C_3A , and C_4AF) and the strength, volume change, and heat of hydration of cements in order to determine the extent to which the properties could be considered additive according to the unit contribution of the individual compounds to the property and the mass ratio of the corresponding compounds in terms of total cement content. Whereas strength and volume change were not found to exhibit clearly additive behavior, the additive nature of the component heats of hydration was supported. Three sets of data were analyzed: component heats of hydration data obtained at 3, 7, 28, 90, and 180 days by Woods et al. (1932), in which the clinker and cement were produced specifically for the investigation; component heats of hydration data obtained at 7, 28, 90, and 265 days by Davis et al. (1933), in which the cements were burnt under similar conditions, ground to the same fineness, and had the same gypsum content in order to limit the influence of those variables on the properties; and component heats of complete hydration determined by Lerch and Bogue (1934). In all three cases, the heats of hydration were determined by the heat of solution method addressed in ASTM C186 (2005). Lea noted that, except for C_4AF , the component heats of hydration were roughly consistent amongst the studies.

Lerch and Bogue (1934) found that the heats of complete hydration measured for the primary cement phases and free CaO , MgO , and SO_3 could be used to calculate, with good agreement, the total heat of complete hydration of the cement according to the cement composition. Schindler (2004) adapted the component heats of complete hydration in Lerch and Bogue (1934) into Eq. 2.7 for the total heat of hydration per unit mass of cement. Though separate empirical equations have been developed for various parameters depending on the determination of cement composition according to Rietveld analysis in accordance with ASTM C1365 (2012) or oxide analysis and Bogue calculations in accordance with ASTM C150 (2011), Eq. 2.7 has been used for both methods in predictive software (Riding, 2007).

$$H_{cem} = 500p_{C_3S} + 260p_{C_2S} + 866p_{C_3A} + 420p_{C_4AF} + 624p_{SO_3} + 1186p_{FreeCaO} + 850p_{MgO} \quad \text{Eq. 2.7}$$

Where,

- H_{cem} = total heat of hydration of cement at 100% hydration, J/g
- p_{C_3S} = mass ratio of C₃S in terms of total cement content
- p_{C_2S} = mass ratio of C₂S in terms of total cement content
- p_{C_3A} = mass ratio of C₃A in terms of total cement content
- p_{C_4AF} = mass ratio of C₄AF in terms of total cement content
- p_{SO_3} = mass ratio of SO₃ in terms of total cement content
- $p_{FreeCaO}$ = mass ratio of free CaO in terms of total cement content
- p_{MgO} = mass ratio of MgO in terms of total cement content

Eq. 2.7 was extended by Schindler and Folliard (2005) to incorporate the influence of ground-granulated blast-furnace slag (GGBFS) and fly ash and by Riding et al. (2012) to incorporate the influence of silica fume, resulting in Eq. 2.8 for the total heat of hydration of cementitious materials at complete hydration. The CaO content of the fly ashes was used to account for the varying contributions of different classes (C and F) and sources of ashes. The ultimate cumulative heat of hydration of concrete could then be determined according to Eq. 2.9 based on the cementitious materials content of the concrete.

$$H_u = H_{cem}p_{cem} + 461p_{slag} + 1800p_{FACaO}p_{FA} + 330p_{SF} \quad \text{Eq. 2.8}$$

Where,

- H_u = total heat of hydration of cementitious materials at 100% hydration, J/g
- p_{cem} = cement mass ratio in terms of total cementitious content
- p_{slag} = slag mass ratio in terms of total cementitious content
- p_{FACaO} = CaO mass ratio in fly ash
- p_{FA} = fly ash mass ratio in terms of total cementitious content
- p_{SF} = silica fume mass ratio in terms of total cementitious content

$$H_T = H_u C_c \quad \text{Eq. 2.9}$$

Where,

- H_T = total heat of hydration of concrete at 100% hydration, J/m³
- C_c = cementitious materials content per unit volume of concrete, g/m³

2.6.2 Degree of Hydration

The degree of hydration α is defined as the ratio between the amount of cement that has reacted and the original amount of cement, but due to difficulty in determining when all of the material has reacted, the degree of hydration has been approximated indirectly using various parameters, such as the heat of hydration, the amount of chemically bound water, and chemical shrinkage (van Breugel, 1997). Since the principal cement compounds react at different rates and release different amounts of heat per unit mass (Woods et al., 1932; Davis et al., 1933; Davis et al., 1934), the degree of hydration of cement has been evaluated according to superposition of the degree of hydration of the individual cement phases weighted according to mass ratio (Parrott et al., 1990). However, Parrott et al. (1990) measured a nearly linear relationship between the heat of hydration of cement and the degree of hydration, particularly for $\alpha > 0.4$, for which the relationship was independent of the cement type. D'Aloia and Chanvillard (2002) noted that comparable values are obtained for degree of hydration determined by heats of the individual phases and heat of the cement, and van Breugel (1998) noted that, even in the case of blended cements, the amount of heat generated seems to be an effective parameter for characterizing the degree of hydration. Accordingly, Eq. 2.10 can be used to determine the degree of hydration as a function of the cumulative heat of hydration.

$$\alpha(t) = \frac{H(t)}{H_T} \quad \text{Eq. 2.10}$$

Where,

- $\alpha(t)$ = degree of hydration at time t
- $H(t)$ = cumulative heat of hydration at time t , J/m³
- H_T = total heat of hydration of concrete at 100% hydration, J/m³

2.6.3 Influence of Temperature on Hydration

The rate of heat of hydration and, therefore, the degree of hydration $\alpha(t)$ and the cumulative heat of hydration $H(t)$ in Eq. 2.10 are influenced by the temperature of the concrete at time t . The Arrhenius equation, presented in two equivalent forms in Eq. 2.11

(Glasstone et al., 1941), governs the temperature dependence of chemical reaction rates. According to the equation, the reaction rate k increases with increasing temperature T ; the proportionality constant A and activation energy E_a can be considered constant for a given reaction for small to moderate temperature ranges (Glasstone et al., 1941). The activation energy represents the minimum energy needed for reactants to undergo a particular chemical reaction, and though the hydration of cementitious materials involves the simultaneous reactions of multiple minerals with varying reaction rates (Kada-Benameur et al., 2000), the Arrhenius equation has been shown to apply to the hydration of cement with an “apparent” activation energy for the combined system of reactions (Schindler, 2004). Through tests over wide ranges of isothermal curing temperatures, the apparent activation energy of cement has been determined to be independent of temperature (Ma et al., 1994; Schindler, 2004).

$$\ln k = \ln A - \frac{E_a}{\bar{R}T}$$

$$k = A \exp\left(-\frac{E_a}{\bar{R}T}\right)$$

Eq. 2.11

Where,

- k = reaction rate constant
- A = proportionality constant
- E_a = activation energy, J/mol (Btu/lbmol)
- \bar{R} = universal gas constant, 8.3144 J/mol·K (1.986 Btu/lbmol·°R)
- T = temperature, K (°R)

2.6.4 Nurse-Saul Maturity Function

Due to the temperature dependence of the rate of hydration, identical batches of concrete at the same age but curing at different temperatures will have different maturities, which ASTM C1074 (2011) defines as “the extent of development of a property of a cementitious mixture.” McIntosh (1949) proposed that the relative time- and temperature-dependent strength development could be approximated by taking the product of the concrete age and the concrete temperature above a datum temperature,

suggested to be $-1.1\text{ }^{\circ}\text{C}$ ($30\text{ }^{\circ}\text{F}$), but the experimental results did not support the effectiveness of this approach.

Nurse (1949) also proposed a similar approach but did not incorporate a datum temperature and used the curing chamber temperatures rather than the concrete temperature for calculations. The general alignment of the relative strength development results according to the approach was the first indication that the effects of concrete age and temperature on strength development could be estimated by their product (Carino, 2004).

Saul (1951) applied the same function as McIntosh but recommended a datum temperature of $-10.5\text{ }^{\circ}\text{C}$ ($13\text{ }^{\circ}\text{F}$), below which strength gain would not occur. Saul introduced the term “maturity” to define the behavior described by the function, shown in Eq. 2.12, and determined that concretes with the same maturity, regardless of age and temperature history, had roughly equal strength. Saul noted that Eq. 2.12 was not valid when the concrete temperature increased too quickly: if the temperature reached 50 or $100\text{ }^{\circ}\text{C}$ (122 or $212\text{ }^{\circ}\text{F}$) within the first 2 or 6 hours, respectively, the function underestimated early-age strength gain, and the late-age strength was reduced. Eq. 2.12 is referred to as the Nurse-Saul maturity function, and the result is called the temperature-time factor (Carino, 2004).

$$M(t) = \int_0^t (T_c - T_o) dt$$

$$M(t) = \sum_0^t (T_c - T_o) \Delta t$$

Eq. 2.12

Where,

- $M(t)$ = temperature-time factor at age t , $^{\circ}\text{C}$ -day or $^{\circ}\text{C}$ -hr ($^{\circ}\text{F}$ -day or $^{\circ}\text{F}$ -hr)
- t = chronological age, day or hr
- T_c = average concrete temperature during interval, $^{\circ}\text{C}$ ($^{\circ}\text{F}$)
- T_o = datum temperature, $^{\circ}\text{C}$ ($^{\circ}\text{F}$)

Citing ACI 306R-78 Cold Weather Concreting, Carino (1984) stated that the traditional value for datum temperature T_o in North America was $-10\text{ }^{\circ}\text{C}$ ($14\text{ }^{\circ}\text{F}$). However, Carino determined distinct datum temperature values appropriate for ordinary portland cement (OPC) concrete without admixtures in different environmental curing conditions: $-4\text{ }^{\circ}\text{C}$ ($25\text{ }^{\circ}\text{F}$) for curing between 0 and $20\text{ }^{\circ}\text{C}$ (32 and $68\text{ }^{\circ}\text{F}$) and $9\text{ }^{\circ}\text{C}$ ($48\text{ }^{\circ}\text{F}$) for curing between 20 and $40\text{ }^{\circ}\text{C}$ (68 and $104\text{ }^{\circ}\text{F}$). ASTM C1074-11 (2011) recommends a datum temperature of $0\text{ }^{\circ}\text{C}$ ($32\text{ }^{\circ}\text{F}$) for concrete with Type I cement and without admixtures curing between 0 and $40\text{ }^{\circ}\text{C}$ (32 and $104\text{ }^{\circ}\text{F}$). ASTM C1074 also provides a method of experimentally determining the datum temperature based on the strength development of 50-mm (2-in.) mortar cubes curing in water baths at three temperatures.

2.6.5 Equivalent Age (Arrhenius) Maturity Function

Based on the temperature history of the concrete of interest, the equivalent age approach converts the true curing age t of the concrete to an equivalent age t_e for isothermal curing at a reference temperature T_r . The concept is based mathematically on Eq. 2.13, which accounts for the different reaction rates due to the different curing temperatures (Carino, 1984). As shown in Eq. 2.14, the derivative of Eq. 2.13, the ratio of the equivalent and true time increments is equal to the ratio of the reaction rates at time t . This relationship is called the age conversion factor and allows the conversion of the time interval at concrete temperature T_c to its equivalent interval at reference temperature T_r (Carino, 1984).

$$t_e = \int_0^t \frac{k(T_c)}{k(T_r)} dt \quad \text{Eq. 2.13}$$

$$\frac{dt_e}{dt} = \frac{k(T_c)}{k(T_r)} \equiv f(T_c) \quad \text{Eq. 2.14}$$

Where,
 t_e = equivalent age at reference temperature T_r , hr

$$\begin{aligned}
t &= \text{chronological age, hr} \\
k(T_c) &= \text{reaction rate constant at concrete temperature } T_c \\
k(T_r) &= \text{reaction rate constant at reference temperature } T_r \\
T_c &= \text{concrete temperature, K} \\
T_r &= \text{reference temperature, K} \\
f(T_c) &= \text{age conversion factor determined at concrete temperature } T_c
\end{aligned}$$

Due to the previously described limitations of the Nurse-Saul function, other methods of determining concrete maturity were developed as alternatives. The use of the Arrhenius equation for determination of equivalent age for concrete applications was proposed by Hansen and Pedersen (1977) by defining the reaction rates in Eq. 2.14 according to the Arrhenius equation (Eq. 2.11), resulting in the age conversion factor given in Eq. 2.15. Inserting this Arrhenius age conversion factor into Eq. 2.13 yields Eq. 2.16 and its discretized form in Eq. 2.17, which ASTM C1074-11 (2011) provides as the equivalent age maturity function for use in estimating concrete strength as a function of temperature history. Hansen and Pedersen (1977) used 20 °C (68 °F) for the reference temperature T_r , but ASTM C1074-11 (2011) states that any reported reference temperature may be used for determining the equivalent age. Since standard curing in accordance with ASTM C192 (2013) is conducted at 23.0 ± 2.0 °C (73.5 ± 3.5 °F), 23 °C (73.5 °F) is often used as the reference temperature.

Gajda (2007) notes that the Nurse-Saul maturity function doesn't account for the acceleration of maturity at higher temperatures, typically resulting in underestimations of strength development at temperatures common in mass concrete applications. In contrast, the Arrhenius maturity function accounts for the non-linear increase in maturity at elevated temperatures and the material-specific temperature dependence of the concrete. Tank and Carino (1991) found the Arrhenius maturity function to be more accurate than the Nurse-Saul maturity function for modeling the temperature-dependence of concrete strength development with isothermal curing at 10, 23, and 40 °C (50, 73, and 104 °F).

$$f(T_c) \equiv \frac{k(T_c)}{k(T_r)} = \frac{A \exp\left(-\frac{E_a}{RT_c}\right)}{A \exp\left(-\frac{E_a}{RT_r}\right)} = \exp\left(\frac{E_a}{R}\left(\frac{1}{T_r} - \frac{1}{T_c}\right)\right) \quad \text{Eq. 2.15}$$

$$t_e(T_r) = \int_0^t \exp\left(\frac{E_a}{R}\left(\frac{1}{T_r} - \frac{1}{T_c}\right)\right) dt \quad \text{Eq. 2.16}$$

$$t_e(T_r) = \sum_0^t \exp\left(\frac{E_a}{R}\left(\frac{1}{T_r} - \frac{1}{T_c}\right)\right) \Delta t \quad \text{Eq. 2.17}$$

Where,

$t_e(T_r)$ = equivalent age at reference curing temperature T_r , hr

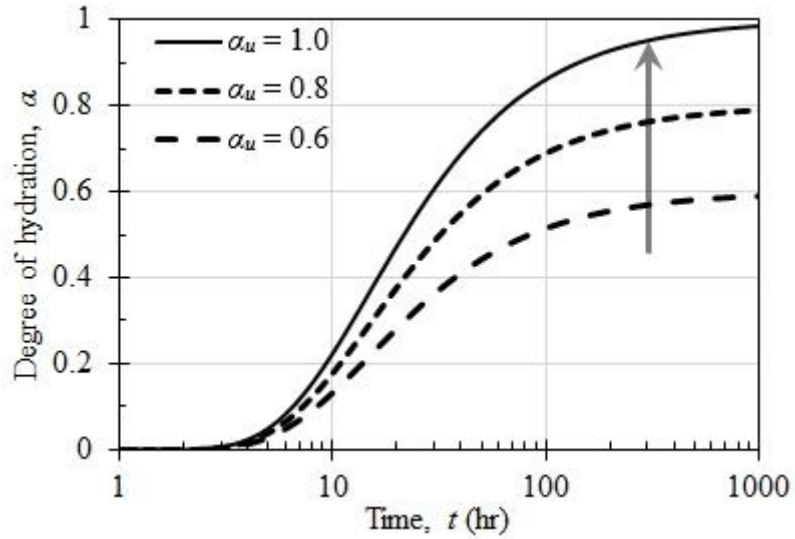
2.6.6 Three-Parameter Model for Degree of Hydration

Hansen and Pedersen (1985) found that a three-parameter exponential function provided a good approximation of the cumulative heat of hydration as a function of equivalent age and presented Eq. 2.18 for the degree of hydration based on the relation given in Eq. 2.10. Pane and Hanson (2002) confirmed the accuracy of the three-parameter model for representing the sigmoidal progression of hydration. Figure 2.17 shows the influence of the three hydration parameters, α_u , τ , and β , on the degree of hydration curve. The ultimate degree of hydration α_u linearly scales the degree of hydration α ; higher values of α_u correspond to higher degrees of hydration at any equivalent age t_e . The hydration time parameter τ inversely scales the time variable of the degree of hydration; higher values of τ correspond to delayed acceleration of hydration and slower rates of hydration. The hydration shape parameter β affects the slope of the degree of hydration curve; higher values of β correspond to delayed, shorter time periods of more rapid hydration, whereas lower values of β correspond to longer periods of more gradual hydration.

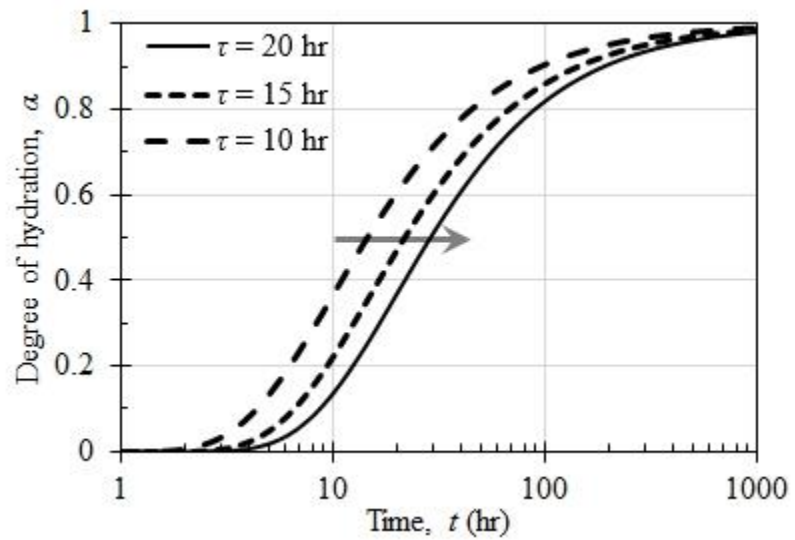
$$\alpha(t_e) = \alpha_u \exp\left(-\left[\frac{\tau}{t_e}\right]^\beta\right) \quad \text{Eq. 2.18}$$

Where,

- $\alpha(t_e)$ = degree of hydration at equivalent age t_e
- α_u = ultimate degree of hydration
- τ = hydration time parameter, hr
- t_e = equivalent age, hr
- β = hydration shape parameter

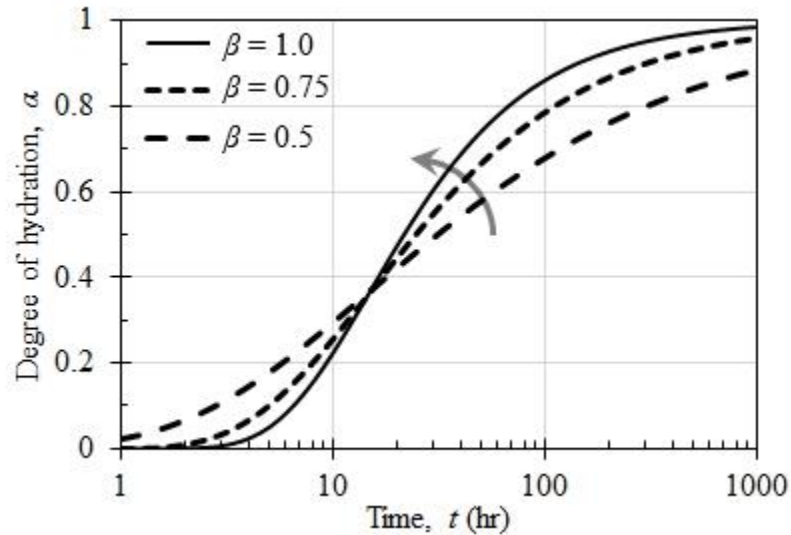


(a) Influence of increasing ultimate degree of hydration α_u ; $\tau = 15$ hr, $\beta = 1.0$



(b) Influence of increasing hydration time parameter τ ; $\alpha_u = 1.0$, $\beta = 1.0$

Figure 2.17: Influence of hydration parameters on the progression of hydration



(c) Influence of increasing hydration shape parameter β ; $\alpha_u = 1.0$, $\tau = 15$ hr
Figure 2.17 (continued)

2.6.7 Hydration Parameters

The ultimate degree of hydration α_u accounts for the fact that, when hydration ceases, the degree of hydration α is not necessarily 1. Though theoretically impossible, Poole et al. (2011) determined values of α_u greater than 1 by curve-fitting isothermal calorimetry data with Eq. 2.18. The authors noted that the results were based on extrapolation of 44 to 100 hours of calorimetry data rather than complete hydration and that the degree of hydration data was determined according to Eq. 2.10 using the empirical relations for total heat release provided in Eq. 2.7 and Eq. 2.8.

Noting that, even when cured in water, hardened concrete generally contains unhydrated cement, Mills (1966) measured the weight of chemically bound water in cement pastes and mortars upon the cessation of hydration to determine the ultimate degree of hydration, and Eq. 2.19 was developed empirically to estimate the ultimate degree of hydration α_u as a function of w/c. According to Eq. 2.19, Mills (1966) notes that complete hydration is impossible for w/c < 6.25. Van Breugel (1997) acknowledges the improvements of Eq. 2.19 relative to alternative determinations of the ultimate degree of hydration but emphasizes that it does not account for the cement type or fineness,

noting that the ultimate degree of hydration increases with increasing fineness. Through multivariate regression analysis of semi-adiabatic calorimetry results for 150-by-300-mm (6-by-12-in.) concrete cylinders, Schindler and Folliard (2005) extended Eq. 2.19 to incorporate the influence of fly ash and slag on the ultimate degree of hydration, resulting in Eq. 2.20.

$$\alpha_u = \frac{1.031 \cdot w/c}{0.194 + w/c} \quad \text{Eq. 2.19}$$

Where,

α_u = ultimate degree of hydration
 w/c = water-to-cement ratio

$$\alpha_u = \frac{1.031 \cdot w/cm}{0.194 + w/cm} + 0.50p_{FA} + 0.30p_{slag} \leq 1.0 \quad \text{Eq. 2.20}$$

Where,

w/cm = water-to-cementitious materials ratio
 p_{FA} = fly ash mass ratio in terms of total cementitious content
 p_{slag} = slag mass ratio in terms of total cementitious content

Also using semi-adiabatic calorimetry of concrete cylinders, Riding et al. (2012) developed Eq. 2.21 by testing a wide range of ASTM C150 (2011) cement types, SCMs, and chemical admixtures, extending the application of Eq. 2.19 beyond the concrete pavement materials for which Eq. 2.20 and a comparable model by Ge (2005) were primarily developed. Eq. 2.21 is applicable for cement phase composition data determined by Rietveld analysis of cement X-ray diffraction results in accordance with ASTM C1365 (2012); Riding et al. (2012) also provided an analogous equation for cement composition data based on oxide analysis and Bogue calculations in accordance with ASTM C150 (2011). Fly ash, ASTM C494 (2013) Type B and D water reducer/retarder, and ASTM C494 (2013) Type F polycarboxylate high-range water reducer were found to decrease the ultimate degree of hydration; per ANOVA, the influences of the other tested SCMs and chemical admixtures were not warranted for inclusion in Eq. 2.21.

$$\alpha_u = \frac{1.031 \cdot w/cm}{0.194 + w/cm} + \exp \left(\begin{array}{l} -0.297 - 9.73 \cdot p_{C_4AF} \cdot p_{cem} \\ -325 \cdot p_{Na_2O_{eq}} \cdot p_{cem} \\ -8.90 \cdot p_{FA} \cdot p_{FACaO} \\ -331 \cdot WRRET - 93.8 \cdot PCHRWR \end{array} \right) \quad \text{Eq. 2.21}$$

Where,

w/cm = water-to-cementitious materials ratio

p_{cem} = cement mass ratio in terms of total cementitious content

p_{C_4AF} = mass ratio of C₄AF in terms of total cement content

$p_{Na_2O_{eq}}$

= mass ratio of alkalis as Na₂O equivalent in terms of total cement content

p_{FA} = fly ash mass ratio in terms of total cementitious content

p_{FACaO} = fly ash CaO mass ratio in terms of total fly ash content

$WRRET$

= ASTM C494 (2013) Type B and D water reducer/retarder, percent solids by mass per mass of cementitious material

$PCHRWR$

= ASTM C494 (2013) Type F polycarboxylate high-range water reducer, percent solids by mass per mass of cementitious material

Eq. 2.22 and Eq. 2.23 are models for the hydration time parameter τ developed by Schindler and Folliard (2005) and Riding et al. (2012), respectively, and Eq. 2.24 and Eq. 2.25 are models for the hydration shape parameter β developed by Schindler and Folliard (2005) and Riding et al. (2012), respectively. Eq. 2.23 and Eq. 2.25 are applicable for cement phase composition data determined by Rietveld analysis of cement X-ray diffraction results in accordance with ASTM C1365 (2012); Riding et al. (2012) also provided analogous equations for cement composition data based on oxide analysis and Bogue calculations in accordance with ASTM C150 (2011). The latter models accounts for a wide range of ASTM C150 (2011) cement types, SCMs, and chemical admixtures, however, the cement fineness was found to have insignificant effect on the parameters contrary to the earlier models by Schindler and Folliard. Experimentally, increasing dosages of WRRET were found to significantly increase τ and β while slightly reducing α_u , and these effects were incorporated into the respective models (Riding et al., 2012).

$$\tau = 66.78 \cdot p_{C_3A}^{-0.154} \cdot p_{C_3S}^{-0.401} \cdot Blaine^{-0.804} \cdot p_{SO_3}^{-0.758} \cdot \exp(2.187 \cdot p_{slag} + 9.50 \cdot p_{FA} \cdot p_{FACaO}) \quad \text{Eq. 2.22}$$

$$\tau = \exp \left(\begin{array}{l} 2.95 - 0.972 \cdot p_{C_3S} \cdot p_{cem} + 152 \cdot p_{Na_2O} \cdot p_{cem} \\ + 1.75 \cdot p_{slag} + 4.00 \cdot p_{FA} \cdot p_{FACaO} \\ - 11.8 \cdot ACCL + 95.1 \cdot WRRET \end{array} \right) \quad \text{Eq. 2.23}$$

$$\beta = 181.4 \cdot p_{C_3A}^{0.146} \cdot p_{C_3S}^{0.227} \cdot Blaine^{-0.535} \cdot p_{SO_3}^{0.558} \cdot \exp(-0.647 \cdot p_{slag}) \quad \text{Eq. 2.24}$$

$$= \exp \left(\begin{array}{l} \beta \\ - 0.418 + 2.66 \cdot p_{C_3A} \cdot p_{cem} - 0.864 \cdot p_{slag} \\ + 108 \cdot WRRET + 32.0 \cdot LRWR + 13.3 \cdot MRWR \\ + 42.5 \cdot PCHRWR + 11.0 \cdot NHRWR \end{array} \right) \quad \text{Eq. 2.25}$$

Where,

p_{Na_2O} = mass ratio of Na₂O in terms of total cement content

$ACCL$ = ASTM C494 Type C accelerator, percent solids by mass per mass of cementitious material

$Blaine$ = Blaine value, specific surface area of cement, m²/kg

$LRWR$ = ASTM C494 (2013) Type A water reducer, percent solids by mass per mass of cementitious material

MRW = ASTM C494 (2013) Type A and F midrange water reducer, percent solids by mass per mass of cementitious material

R

$NHRWR$ = ASTM C494 (2013) Type F naphthalene sulfonate high-range water reducer, percent solids by mass per mass of cementitious material

2.6.8 Determining Apparent Activation Energy

In order to calculate the equivalent age according to Eq. 2.16 or Eq. 2.17, the apparent activation energy E_a of the cementitious mixture must be determined. This can be accomplished using the Arrhenius equation (Eq. 2.11), which can be expressed in slope-intercept form as shown in Eq. 2.26 as the natural logarithm of the reaction rate constant $\ln(k)$ varying linearly with the reciprocal of the absolute temperature $1/T$ with the slope equal to the negative of the apparent activation energy E_a divided by the universal gas constant \bar{R} . The graphical presentation of $\ln(k)$ versus $1/T$ data is called an Arrhenius plot. ASTM C1074-11 (2011) provides an experimental method to determine

reaction rate constants k by measuring the strength development of mortar cubes curing at different temperatures T . Ma et al. (1994) approximated the reaction rate as the maximum linear slope of the acceleratory portion of the isothermal cumulative heat curve. With an Arrhenius plot of this data, the apparent activation energy can be calculated by dividing the negative of the slope of the simple linear regression by the universal gas constant \bar{R} . For testing at two temperatures, say, T_c and T_r for consistency, the slope would be determined as shown in Eq. 2.27.

$$\ln(k) = \left(-\frac{E_a}{\bar{R}}\right)\left(\frac{1}{T}\right) + \ln(A) \quad \text{Eq. 2.26}$$

$$\left[M = -\frac{E_a}{\bar{R}}\right] = \frac{\ln(k(T_c)) - \ln(k(T_r))}{\frac{1}{T_c} - \frac{1}{T_r}} = \frac{\ln\left(\frac{k(T_c)}{k(T_r)}\right)}{\frac{1}{T_c} - \frac{1}{T_r}} \quad \text{Eq. 2.27}$$

Where,

M = slope of the simple linear regression of the Arrhenius plot, K

A modified ASTM C1074 method for determining the apparent activation energy was developed by Schindler (2004) using the hydration time parameter τ from the three-parameter degree of hydration model (Eq. 2.18) and the age conversion factor (Eq. 2.14). In the method, isothermal calorimetry is conducted on cementitious pastes to measure the rate of heat release at different temperatures, and the three-parameter model is used to fit the experimental degree of hydration data determined using Eq. 2.7 to Eq. 2.10. Due to temperature fluctuations as the specimens are inserted into the calorimeter, the first hour of data is often discarded (Poole et al., 2007). Additionally, since the apparent activation energy of cement hydration has been shown to be relatively constant when the degree of hydration α is between 0.1 and 0.5 (Kada-Benameur et al., 2000), the isothermal calorimetry data used for determining the activation energy has been limited to values of $\alpha \leq 0.5$ (Jayapalan et al., 2014).

Since the three-parameter model is expressed as a function of equivalent age at the reference curing temperature T_r , the hydration time parameter τ in the model also

corresponds to the reference curing temperature and can appropriately be labelled τ_r , as shown in Eq. 2.28 for the degree of hydration α_c when curing at T_c . In consideration of the equivalent age maturity method, which only adjusts time t and can therefore only affect the hydration time parameter τ , the ultimate degree of hydration α_u and the hydration shape parameter β are conceptually independent of the temperature for the same cementitious mix (Schindler, 2004).

$$\alpha_c(t_e) = \alpha_u \exp\left(-\left[\frac{\tau_r}{t_e}\right]^\beta\right) \quad \text{Eq. 2.28}$$

Where,

$$\begin{aligned} \alpha_c(t_e) &= \text{degree of hydration at temperature } T_c \text{ at equivalent age } t_e \\ \tau_r &= \text{hydration time parameter at reference temperature } T_r \end{aligned}$$

For isothermal conditions, the age conversion factor (Eq. 2.14) no longer needs to be expressed incrementally with respect to time, and the age conversion factor $f(T_c)$ for converting the chronological age of a mix curing at T_c to an equivalent age at T_r can be expressed as given in Eq. 2.29. Accordingly, the degree of hydration at temperature T_c can be expressed as a function of chronological age t as shown in Eq. 2.30. In order to incorporate, as shown in Eq. 2.31, the hydration time parameter τ_c determined at concrete temperature T_c , the hydration time parameter τ_c must equal the hydration time parameter τ_r divided by the age conversion factor $f(T_c)$, as shown in Eq. 2.32.

$$\begin{aligned} f(T_c) &\equiv \frac{k(T_c)}{k(T_r)} = \frac{t_e}{t} \\ t_e &= f(T_c) \cdot t \end{aligned} \quad \text{Eq. 2.29}$$

$$\alpha_c(t) = \alpha_u \exp\left(-\left[\frac{\tau_r}{f(T_c) \cdot t}\right]^\beta\right) \quad \text{Eq. 2.30}$$

Where,

$$\alpha_c(t) = \text{degree of hydration at temperature } T_c \text{ at chronological age } t$$

$$\alpha_c(t) = \alpha_u \exp\left(-\left[\frac{\tau_c}{t}\right]^\beta\right) \quad \text{Eq. 2.31}$$

Where,

$$\tau_c = \text{hydration time parameter at concrete temperature } T_c$$

$$\begin{aligned}\tau_c &= \frac{\tau_r}{f(T_c)} \\ f(T_c) &= \frac{\tau_r}{\tau_c}\end{aligned}\tag{Eq. 2.32}$$

From observation of Eq. 2.29 and Eq. 2.32, an inverse relationship is seen between the hydration time parameters τ_i and the reaction rates $k(T_i)$ as expressed by the age conversion factor. As curing temperature T_c is increased relative to reference temperature T_r , the reaction rate $k(T_c)$ increases relative to $k(T_r)$, which increases the age conversion factor $f(T_c)$ and the equivalent age t_e relative to the chronological age t . In contrast, the inversion of the hydration time parameter means that as T_c is increased relative to T_r , τ_c decreases relative to τ_r , conceptually indicating a reduction in the delay of hydration at T_c per the behavior shown in Figure 2.17b.

As shown in Eq. 2.33, the age conversion factor $f(T_c)$ in Eq. 2.29 and Eq. 2.32 can be substituted into Eq. 2.27 for the slope of the Arrhenius plot. Rearranging the τ terms results in Eq. 2.34, which has the form of the slope of the natural logarithm of the hydration time parameter $\ln(\tau)$ as a function of the reciprocal of the absolute temperature $1/T$. Accordingly, the modified ASTM C1074 method uses the hydration time parameters τ_i determined at multiple temperatures T_i to develop a simple linear regression for the previously described function, the slope of which is multiplied by the universal gas constant to calculate the apparent activation energy per Eq. 2.34.

$$M = -\frac{E_a}{\bar{R}} = \frac{\ln\left(\frac{k(T_c)}{k(T_r)}\right)}{\frac{1}{T_c} - \frac{1}{T_r}} = \frac{\ln(f(T_c))}{\frac{1}{T_c} - \frac{1}{T_r}} = \frac{\ln\left(\frac{\tau_r}{\tau_c}\right)}{\frac{1}{T_c} - \frac{1}{T_r}}\tag{Eq. 2.33}$$

$$\frac{E_a}{\bar{R}} = \frac{\ln\left(\frac{\tau_c}{\tau_r}\right)}{\frac{1}{T_c} - \frac{1}{T_r}} = M'\tag{Eq. 2.34}$$

Where,

M' = slope of the linear regression of the natural logarithm of the hydration time parameter $\ln(\tau)$ as a function of the reciprocal of the absolute temperature $1/T$, K

Poole et al. (2007) noted that determination of the reaction rate according to the linear slope method by Ma et al. (1994) could be subjective due to difficulty in identifying the linear portion of the cumulative heat evolution curve for certain cementitious mixes. The modeled results of the modified ASTM C1074 method were found to be comparable to those of an incremental method that applies the linear slope method incrementally over a selected time period, and the modified ASTM C1074 method was deemed more methodical than the linear or incremental methods.

For cementitious mixtures containing inert nanoparticles, Jayapalan et al. (2014) measured greater apparent activation energy values using the linear slope method than the modified ASTM C1074 method, but the measured trend of increasing apparent activation energy values with increasing nanoparticle dosage was similar for both methods.

2.6.9 Influence of Activation Energy on Rate of Hydration

According to the Arrhenius equation (Eq. 2.11), the activation energy determines the temperature sensitivity of the hydration reaction (Schindler, 2004). However, the qualitative relationship between the activation energy and the temperature sensitivity of the reaction rate is not often addressed. Carino (1984) and Jayapalan et al. (2014) stated that increasing activation energy increases the temperature sensitivity of the reaction rate, and this behavior is confirmed by the increased temperature sensitivity of age conversion factor (Eq. 2.15) for higher values of activation energy, as shown in Figure 2.18. This influence of the activation energy on the conversion age factor was described by Carino (1984) and Carino (2004). Since the age conversion factor is defined by the ratio of the reaction rates at different temperatures, an increase in the age conversion factor with increasing activation energy indicates greater relative variation of the reaction rate with respect to temperature. The Arrhenius plot in Figure 2.19a illustrates the temperature sensitivity of the reaction rate: the greater the magnitude of the slope and, therefore,

activation energy, the greater the relative temperature sensitivity of the reaction rate. However, by plotting the natural logarithm of the reaction rates $\ln(k)$, proportional rather than absolute behavior is illustrated. In contrast, Figure 2.19b shows the same data without taking the natural logarithm of the reaction rates, and the rates are seen to vary over a narrower absolute range as the activation energy increases. This suggests that greater values of activation energy reduce the absolute temperature sensitivity of the reaction rate.

Figure 2.19 also shows that, at all temperatures, increased activation energies correspond to reduced reaction rates, which can be understood from observation of the Arrhenius equation (Eq. 2.11). Therefore, increasing activation energy decreases the magnitude and absolute temperature sensitivity of the reaction rate but increases the relative temperature sensitivity of the reaction rate. Since the relative reaction rates are utilized in the age conversion factor and the determination of equivalent age, the relative behavior is of greater interest in the present study. In practice, greater absolute temperature sensitivity may be observed for higher values of activation energy due to change in the proportionality constant A , which is not used in maturity methods and therefore is typically not addressed in terms of influence.

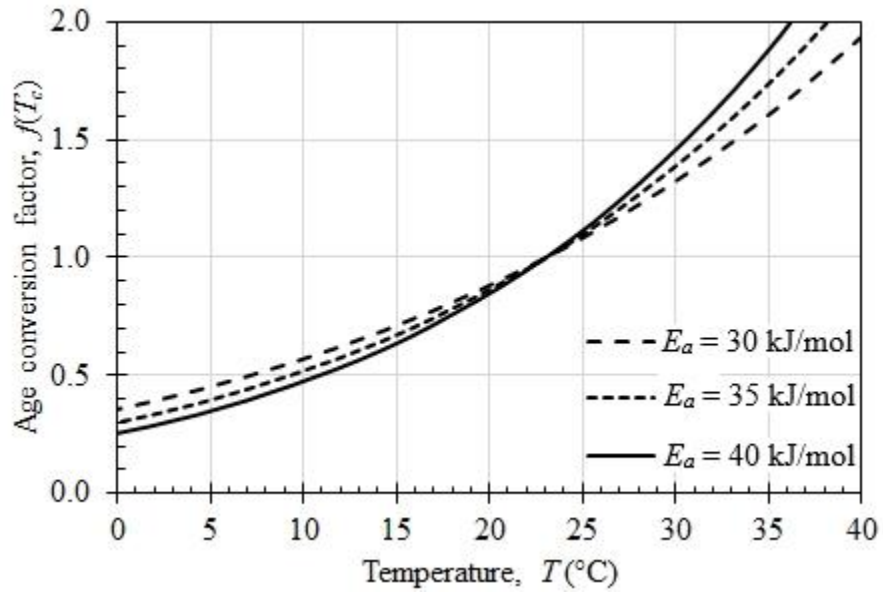
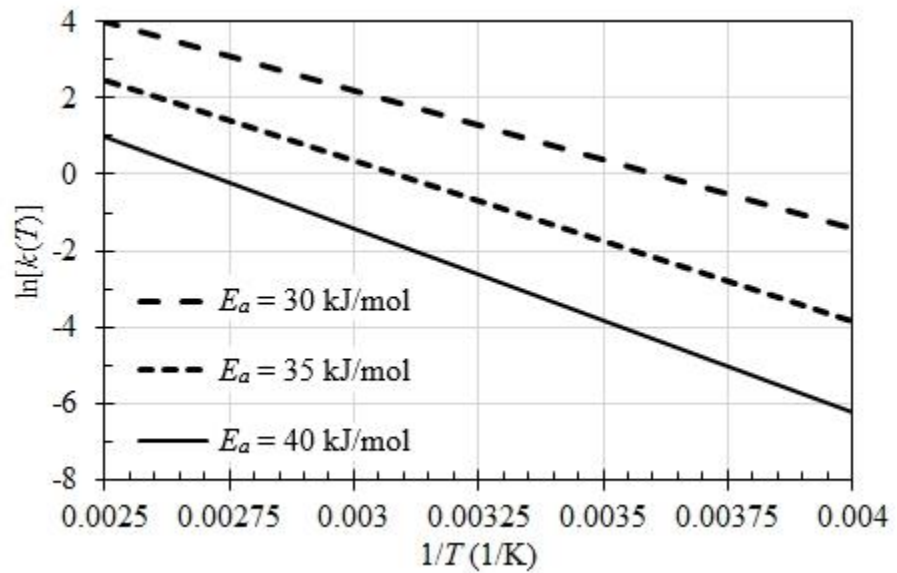
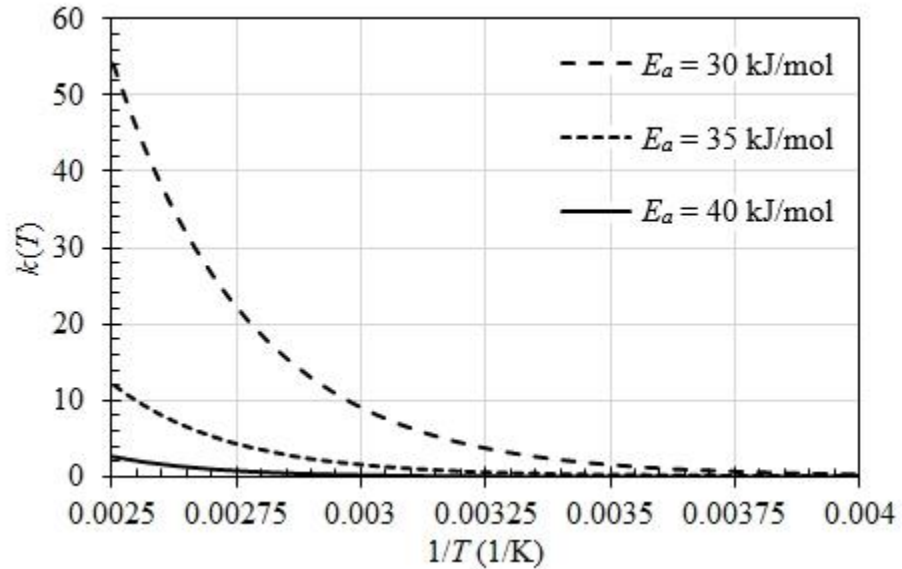


Figure 2.18: Influence of activation energy on age conversion factor; $T_r = 23$ °C (73.4 °F); 1 kJ/mol = 429.9 Btu/lbmol



(a) Arrhenius plot for 250-to-400-K temperature range



(b) Natural logarithm of reaction rate as function of reciprocal of temperature
 Figure 2.19: Influence of activation energy on reaction rate constant; $A = 450$

2.6.10 Literature Values for Apparent Activation Energy

Literature values for the apparent activation energy of cementitious systems vary widely. Carino (2004) presented literature values of apparent activation energy ranging from 41 to 47 kJ/mol (18,000 to 20,000 Btu/lbmol) for various types of cement pastes, mortar, and concrete tested via strength or heat of hydration. With the addition of 50 and 70% GGBFS to cement paste, values of 49 and 56 kJ/mol (21,000 and 24,000 Btu/lbmol), respectively, were reported. Carino and Tank (1992) tested concrete cylinders and obtained a value of 38.7 kJ/mol (16,600 Btu/lbmol) for concrete w/c values of 0.45 and 0.6 with Type I cement and a retarding admixture. Ma et al. (1994) measured an experimental apparent activation energy of 39.0 kJ/mol (16,800 Btu/lbmol) for portland cement and values of 26.7, 30.4, and 49.3 kJ/mol (11,500, 13,000, and 21,200 Btu/lbmol) for blended cements with fly ash, silica fume, and slag, respectively.

Due to the dependence of apparent activation energy on various parameters, numerous models have been proposed for estimating apparent activation energy. Hansen and Pedersen (1977) recommended the apparent activation energy model shown in Eq.

2.35 for use with the equivalent age maturity method based on compressive strengths of concrete specimens cured at temperatures ranging between -10 and 80 °C (14 and 176 °F). Jonasson et al. (1995) recommended the model shown in Eq. 2.36 for use with Standard Swedish cements. Both of these models indicate that, for the values that are influenced by temperature, the apparent activation energy decreases with increasing temperature, but other contributing factors such as the composition and fineness of the cementitious materials are not considered.

$$E_a(T_c) = \begin{cases} 33,500 & \text{if } T_c \geq 20 \text{ }^\circ\text{C} \\ 33,500 + 1470(20 - T_c) & \text{if } T_c < 20 \text{ }^\circ\text{C} \end{cases} \quad \text{Eq. 2.35}$$

$$E_a(T_c) = 44,066 \left(\frac{30}{10 + T_c} \right)^{0.45} \quad \text{Eq. 2.36}$$

Where,

$$\begin{aligned} E_a(T_c) &= \text{apparent activation energy at concrete temperature } T_c, \text{ J/mol} \\ T_c &= \text{concrete temperature, } ^\circ\text{C} \end{aligned}$$

Through multivariate regression analysis of isothermal calorimetry results for various cement pastes, Schindler (2004) developed Eq. 2.37, which accounts for cement composition and fineness, and proposed the apparent activation energy modification factor presented in Eq. 2.38 based on the previously mentioned experimental apparent activation energy values reported by Ma et al. (1994) for blended cements with Class F fly ash and GGBFS.

$$E_a = 22,100 \cdot p_{C_3A}^{0.30} \cdot p_{C_4AF}^{0.25} \cdot Blaine^{0.35} \quad \text{Eq. 2.37}$$

Where,

$$\begin{aligned} p_i &= \text{mass ratio of } i\text{-th compound in terms of total cement content} \\ Blaine &= \text{Blaine value, specific surface area of cement, m}^2/\text{kg} \end{aligned}$$

$$f_E = 1 - 1.05p_{FA}(1 - 2.5p_{FACaO}) + 0.40p_{slag} \quad \text{Eq. 2.38}$$

Where,

$$\begin{aligned} f_E &= \text{apparent activation energy modification factor} \\ p_{FA} &= \text{fly ash mass ratio in terms of total cementitious content} \\ p_{FACaO} &= \text{fly ash CaO mass ratio in terms of total fly ash content} \\ p_{slag} &= \text{slag mass ratio in terms of total cementitious content} \end{aligned}$$

Riding et al. (2011) extended the approach utilized in Schindler (2004) to pastes with various cement types, SCMs, and chemical admixtures. Through multivariate regression analysis of the experimental data, Eq. 2.39 was developed for the apparent activation energy of cementitious systems as a function of the cement chemistry, SCMs, and chemical admixtures. Eq. 2.39 is applicable for cement phase composition data determined by Rietveld analysis of cement X-ray diffraction results in accordance with ASTM C1365 (2012); Riding et al. (2012) also provided an analogous equation for cement composition data based on oxide analysis and Bogue calculations in accordance with ASTM C150 (2011). Poole et al. (2011) and Riding et al. (2012) found that air-entraining admixtures had no effect on hydration parameters or apparent activation energy, whereas water-reducing and retarding admixtures were found to decrease the apparent activation energy. Poole et al. (2011) found that, independent of the cement composition, glucose-based WWRET slightly lowered the apparent activation energy and lignosulfonate-based WRRET significantly lowered the apparent activation energy. However, Riding et al. (2011) observed that the mixtures that deviated significantly from the model presented in Eq. 2.39 had relatively high dosages of ASTM C494 Type B and D low-range water-reducer/retarder or high content of GGBFS or Class C fly ash, and the deviation was attributed to the unique hydration behavior of the mixes containing those admixtures or SCMs. Riding et al. also noted that, for a given dosage, chemical admixtures may influence cement paste and concrete differently, so the direct applicability of the results to concrete mixtures may be limited.

$$\begin{aligned}
 E_a &= 39,200 + 1,069,000 \cdot [p_{C_3A} \cdot p_{cem} (p_{CaSO_4 \cdot xH_2O} + p_{K_2SO_4}) \cdot p_{cem}] \\
 &\quad - 12.2 \cdot Blaine + 12,400 p_{FA} \cdot p_{FA-CaO} + 12,000 p_{slag} \\
 &\quad - 53,300 p_{SF} - 3,020,000 \cdot WRRET - 343,000 \cdot ACCL
 \end{aligned} \quad \text{Eq. 2.39}$$

2.6.11 Heat Generation and Temperature Change

When curing under adiabatic conditions, the temperature change in concrete can be determined according to Eq. 2.40 (Jonasson et al., 1994). According to Eq. 2.9 and Eq. 2.10, the cumulative heat of hydration of the concrete per unit volume at time t is given by Eq. 2.41 such that the rate of heat generation can be expressed as shown in Eq. 2.42. Taking the derivative with respect to time of the three-parameter model of the degree of hydration as expressed in Eq. 2.30 yields Eq. 2.43, and the time- and temperature-dependent rate of heat generation can finally be expressed as shown in Eq. 2.44.

$$\frac{dT}{dt} = \frac{Q_H}{\rho c_p} = \frac{dH}{dt} \left(\frac{1}{\rho c_p} \right) \quad \text{Eq. 2.40}$$

Where,

$$\begin{aligned} T &= \text{concrete temperature, } ^\circ\text{C} \\ Q_H &= \text{rate of heat generation, W/m}^3 \\ \rho &= \text{concrete density (unit weight), kg/m}^3 \\ c_p &= \text{concrete specific heat capacity, J/kg}\cdot\text{K} \\ H &= \text{cumulative heat of hydration of concrete, J/m}^3 \end{aligned}$$

$$H(t) = H_u C_c \alpha(t) \quad \text{Eq. 2.41}$$

Where,

$$\begin{aligned} H_u &= \text{total heat of hydration of cementitious materials at 100\%} \\ &\text{hydration, J/g} \\ C_c &= \text{cementitious materials content per unit volume of concrete,} \\ &\text{g/m}^3 \end{aligned}$$

$$Q_H = \frac{dH}{dt} = H_u C_c \frac{d\alpha}{dt} \quad \text{Eq. 2.42}$$

$$\begin{aligned} \frac{d\alpha}{dt} &= \frac{\alpha_u \beta}{t_e} \left(\frac{\tau}{t_e} \right)^\beta \exp \left(- \left[\frac{\tau}{t_e} \right]^\beta \right) \frac{dt_e}{dt} \\ &= \frac{\alpha_u \beta}{t_e} \left(\frac{\tau}{t_e} \right)^\beta \exp \left(- \left[\frac{\tau}{t_e} \right]^\beta \right) \exp \left(\frac{E_a}{R} \left(\frac{1}{T_r} - \frac{1}{T_c} \right) \right) \end{aligned} \quad \text{Eq. 2.43}$$

$$Q_H(t) = H_u C_c \alpha(t_e) \left(\frac{\tau}{t_e} \right)^\beta \left(\frac{\beta}{t_e} \right) \exp \left(\frac{E_a}{R} \left(\frac{1}{T_r} - \frac{1}{T_c} \right) \right) \quad \text{Eq. 2.44}$$

2.7 Thermal Properties of Concrete

In addition to the generation of heat due to the hydration of cementitious materials, the properties governing the transfer of heat through concrete and the resulting thermal strains are significant in mass concrete applications. The following sections discuss the specific heat capacity, thermal conductivity, thermal diffusivity, and coefficient of linear thermal expansion of concrete, including literature values and experimental methods of determination.

2.7.1 Specific Heat Capacity

The specific heat capacity c of a material is defined by ASTM E1142-14b (2014) as the amount of heat needed to raise the temperature of a unit mass of the material by 1 °C (°F). In turn, the specific heat of a material is defined as the ratio of the specific heat capacity of the material to that of a reference material, typically water, at the same temperature. Because the specific heat capacity of water is 1.0 cal/g·°C (1.0 Btu/lb·°F), the specific heat capacity of a material is numerically equivalent to the dimensionless specific heat when expressed in units of cal/g·°C (Btu/lb·°F) (U.S. Army Corps of Engineers, 1973a). In the SI system, specific heat capacity is expressed in units of J/kg·K, obtained by multiplying units of cal/g·°C (Btu/lb·°F) by the conversion factor 4186.8 J/cal. The subscripts p and v are used to indicate the specific heat capacity determined at constant pressure (c_p) or volume (c_v), respectively.

2.7.1.1 Typical Values

The specific heat capacity values presented in Table 2.3 are representative for a wide range of concrete mix designs and curing conditions. Stating that the specific heat capacity of normalweight concrete is not significantly influenced by aggregate mineralogy and temperature, ACI 207.2R-07 (2007) gives a range of 840 to 1050 J/kg·K (0.20 to 0.25 Btu/lb·°F). Tatro (2006) reports a smaller range of values for normal

temperatures: 920 to 1000 J/kg·K (0.22 to 0.24 Btu/lb·°F). Tia et al. (2010) reported a volumetric heat capacity of 2,675,596 J/m³·K for concrete containing Florida Ocala limestone aggregate; the density (unit weight) of the concrete was not provided, but assuming a density of 2323 kg/m³ (145 lb/ft³) yields a specific heat capacity of 1,152 J/kg·K (0.275 Btu/lb·°F), within the reported 1100-to-1200-J/kg·K (0.26-to-0.29-Btu/lb·°F) range and greater than most of the typical values presented in Table 2.3.

Table 2.3: Specific heat capacity values of concrete

Specific Heat Capacity, c_p		Reference
J/kg·K	Btu/lb·°F	
800–1200	0.2–0.3	Mindess et al., 2003
837	0.200	Janna, 2000
840–1050	0.20–0.25	ACI 207.2R-07, 2007
880	0.21	Incropera et al., 2007
920–1000	0.22–0.24	Tatro, 2006

Table 2.4 presents literature values of specific heat capacity for the components of concrete. RILEM TC 42-CEA (1982) reported the specific heat capacity of cement and most aggregates is approximately 800 J/kg·K (0.19 Btu/lb·°F), which coincides reasonably with the values given in Table 2.4. The specific heat capacity of water is approximately 5 times that of the other components in concrete, and the U.S. Bureau of Reclamation (1940) determined this to be the case for a wide range of temperatures and aggregate types. Accordingly, the U.S. Bureau of Reclamation measured generally increasing values for concrete as the original water content in the mix was increased from 4 to 8% of the concrete weight. For dry concrete, Janna (2000) reported a specific heat capacity of 837 J/kg·K (0.200 Btu/lb·°F), which is at the low end of the literature values listed for concrete. As shown in Figure 2.20, Osborne et al. (1939) measured the specific heat capacity of water to be relatively constant with respect to temperature: despite the

curvature, the range of specific heat capacities is only 39.5 J/kg·K (0.009 Btu/lb·°F), less than 0.1% of the values.

Table 2.4: Specific heat capacity values of concrete components

Material	Specific Heat Capacity, c_p		Reference
	J/kg·K	Btu/lb·°F	
Cement	840	0.19	Van Breugel, 1980
Cement (CEM III/C 32.5)	857	0.20	De Schutter and Taerwe, 1995
Water	4186.8	1.00	U.S. Army Corps of Engineers, 1973a
Limestone (Salem)	810	0.19	Incropera et al., 2007
Sand	800	0.19	Incropera et al., 2007

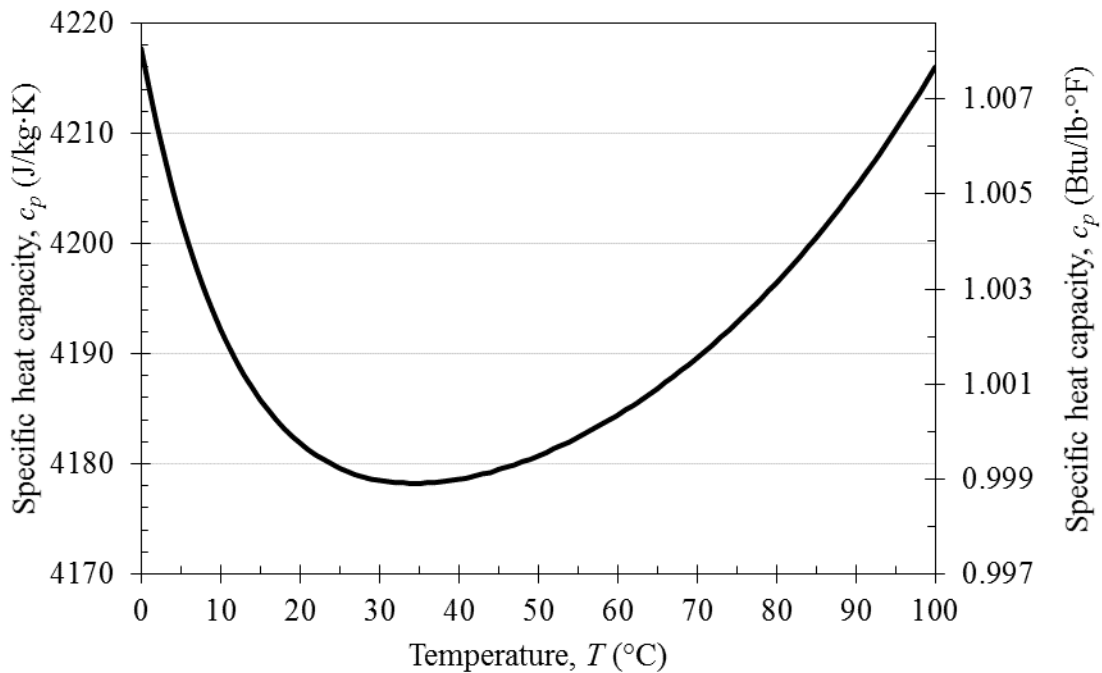


Figure 2.20: Specific heat capacity of water as a function of temperature at 1 atm (101.325 kPa) pressure (Osborne et al., 1939)

Mindess et al. (2003) states that the specific heat capacities of aggregates vary little with mineralogy, and the U.S. Bureau of Reclamation (1940) found that values for concretes containing different aggregate types, each averaged from tests ranging from 10

to 66 °C (50 to 150 °F), varied within a narrow range of about 963 to 1030 J/kg·K (0.230 to 0.245 Btu/lb·°F). Testing concrete containing Florida Ocala Limestone, Tia et al. (2010) measured specific heat capacity values at early ages ranging from 1100 to 1200 J/kg·K (0.26 to 0.29 Btu/lb·°F). Those values were noted to be higher than examples in ACI 207.2R-07 (2007) of concrete containing limestone aggregate with specific heat capacities ranging from 925 to 1054 J/kg·K (0.22 to 0.25 Btu/lb·°F) at temperatures from 10 to 66 °C (50 to 150 °F). For the same temperatures, the U.S. Bureau of Reclamation (1940) reported a similar range of 925 to 1100 J/kg·K (0.221 to 0.262 Btu/lb·°F) for the concrete containing limestone aggregate. Tia et al. attributed the higher specific heat capacity values to the distinct characteristics of the Florida Ocala Limestone relative to aggregate available elsewhere in the U.S.

Increases in specific heat capacity as a function of temperature were presented in ACI 207.2R-07 (2007) for numerous mass concrete applications with various coarse aggregate types, averaging 920, 970, and 1040 J/kg·K (0.22, 0.23, and 0.25 Btu/lb·°F) for 10, 38, and 66 °C (50, 100, and 150 °F), respectively. Book and Barnoff (1973) measured a 20% increase in specific heat capacity of uncured concrete as a result of temperature increasing from 24 to 78 °C (75 to 175 °F), and ACI 517.2R-80 (1980) notes that the higher water content before the completion of hydration appears to contribute to the rapid rise of specific heat capacity with temperature. Accordingly, Khan et al. (1998) measured increasing specific heat capacity of concrete for temperatures increasing from 30 to 70 °C (86 to 158 °F), but the relative increase was approximately 4.5 times greater for saturated concrete than oven-dried concrete, which seems unexpected considering the roughly constant specific heat capacity of water with respect to temperature. The U.S. Bureau of Reclamation (1940) reported a 20% increase in the specific heat capacity of concrete as the temperature increased from 10 to 66 °C (50 to 150 °F) and found the influence of temperature to be consistent for all concrete tested. RILEM TC 42-CEA (1982) cited work by Löfquist showing, at all ages, an approximately 3% increase in specific heat

capacity of cement paste for each 10-°C (18-°F) increase in temperature from 25 to 55 °C (77 to 131 °F).

Some sources have found the specific heat capacity of cement paste and concrete to be constant with age. Rilem TC 42-CEA (1982) cites work by Löfqvist that measured an insignificant decrease in specific heat capacity of cement paste from 1180 to 1160 J/kg·K (0.282 to 0.277 Btu/lb·°F) from 3 to 10 days after casting. Similarly, the U.S. Bureau of Reclamation (1940) measured no significant change in the specific heat capacity of concrete between 3 and 180 days after casting.

However, others have measured decreasing values with age. Testing concrete, Brown and Javaid (1970) measured a linear 23% decrease with time from 1151 to 888 J/kg·K (0.275 to 0.212 Btu/lb·°F) between 6 hours and 7 days after casting. Testing cement pastes between 1 and 7 days after casting, De Schutter and Taerwe (1995) developed a linear regression of specific heat capacity as function of degree of hydration, roughly logarithmic with time. Accounting for aggregate content, the regression was converted to values for concrete, giving a 13% decrease from 1150 to 1000 J/kg·K (0.275 to 0.239 Btu/lb·°F) with increasing hydration, and they suggested that the decrease in specific heat capacity was due to the conversion of water during hydration.

Like De Schutter and Taerwe, van Breugel (1980) developed a model for specific heat capacity, given in Eq. 2.45, which varies as a linear function of degree of hydration. However, this model accounts for the temperature of the concrete and the mixture proportions according to the principle of superposition with respect to the relative mass content of each component. Schindler (2002) found the model to provide reasonable results for a representative mix design based on literature values for specific heat capacities of the components.

$$c_p = \frac{1}{m} (m_c \alpha_H c_{p(cef)} + m_c (1 - \alpha_H) c_{p(c)} + m_a c_{p(a)} + m_w c_{p(w)}) \quad \text{Eq. 2.45}$$

Where,

- c_p = specific heat capacity of concrete, J/kg·K
- m = total mass of concrete mixture, kg
- m_c = mass of cement content, kg
- m_a = mass of aggregate content, kg
- m_w = mass of water content, kg
- α_H = degree of hydration
- $c_{p(cef)}$ = fictitious specific heat capacity of hydrated cement, defined in Eq. 2.46, J/kg·K
- $c_{p(c)}$ = specific heat capacity of cement, J/kg·K
- $c_{p(a)}$ = specific heat capacity of aggregate, J/kg·K
- $c_{p(w)}$ = specific heat capacity of water, J/kg·K

$$c_{p(cef)} = 8.4T + 339 \quad \text{Eq. 2.46}$$

Where,

- T = temperature of concrete, °C

2.7.1.2 Experimental Methods

Calorimeters are used to measure heat and temperature data for experimental determination of specific heat capacity (Tatro, 2006). Some methods are based on the conservation of energy described in the first law of thermodynamics, according to which an isolated system maintains constant internal energy. In such a system, when two substances at different temperatures are mixed, the amount of heat lost by the warmer substance is equal to the amount of heat gained by the cooler substance.

In the procedure specified by CRD-C 124-73 (U.S. Army Corps of Engineers, 1973a), a sample of dry aggregate or concrete is weighed and placed in a wire basket for submersion in either a hot or cold constant-temperature bath until reaching thermal equilibrium. Immediately after removal from the bath, the moist sample and basket are weighed in order to determine the mass of carry-over water transferred from the bath to the calorimeter. The basket and sample are then submerged in a calorimeter containing water at room temperature, and the temperature change of the water in the calorimeter is recorded at 1-minute intervals. The process is repeated for a reference specimen with known specific heat capacity in order to calculate, per Eq. 2.47, a water-equivalent mass

of the calorimeter to account for the influence of the heat gained or lost by the calorimeter. The mean specific heat capacity of the sample is then calculated using Eq. 2.48.

$$m_e = \frac{c_{ref}m_{ref}T_{ref} + c_w m_o T_{ref} + c_b m_b T_{ref}}{c_w T_w} - m_w \quad \text{Eq. 2.47}$$

Where,

- m_e = water-equivalent mass of calorimeter, kg (lb)
- m_{ref} = mass of reference specimen, kg (lb)
- m_o = mass of carry-over water, kg (lb)
- m_b = mass of wire basket, kg (lb)
- m_w = mass of water in calorimeter, kg (lb)
- $c_{p(ref)}$ = specific heat capacity of reference specimen, J/kg·K (Btu/lb·°F)
- $c_{p(w)}$ = specific heat capacity of water, J/kg·K (Btu/lb·°F)
- $c_{p(b)}$ = specific heat capacity of wire basket, J/kg·K (Btu/lb·°F)
- T_{ref} = temperature change of reference specimen, K (°F)
- T_w = maximum temperature change of water in calorimeter, K (°F)

$$c_p = \frac{(m_w + m_e)c_w T_w - (m_o c_w + m_b c_b)T_s}{m_s T_s} \quad \text{Eq. 2.48}$$

Where,

- $c_{p(s)}$ = mean specific heat capacity of sample, J/kg·K (Btu/lb·°F)
- m_s = mass of reference specimen, kg(lb)
- T_s = temperature change of reference specimen, K (°F)

De Schutter and Taerwe (1995) measured the specific heat capacity of cement paste using a nested two-bath calorimeter and monitoring the temperature history of the interior bath in response to heat inputs of known magnitude. The calorimeter was first calibrated without the sample by measuring the temperature increase ΔT_1 due to heat input E_1 . The specimen was then submerged in the interior bath, and the temperature increase ΔT_2 due to heat input E_2 was measured. In order to account for the influence of the heat of hydration and the presence of a temperature spike immediately after applying the heat input, the linear portion of the temperature history after the heat input was extrapolated to the time immediately preceding the heat input for determination of ΔT_2 . The specific heat capacity of the sample was then calculated according to Eq. 2.49, which

is based on the change in the amount of heat required to increase the temperature due to the addition of the sample.

$$c_p = \frac{1}{m} \left(\frac{E_2}{\Delta T_2} - \frac{E_1}{\Delta T_1} \right) \quad \text{Eq. 2.49}$$

Where,

- c_p = specific heat capacity of sample, J/kg·K (Btu/lb·°F)
- m = mass of sample, kg (lb)
- E_2 = heat input with sample, J (Btu)
- E_1 = heat input without sample, J (Btu)
- ΔT_2 = temperature increase with sample, K (°F)
- ΔT_1 = temperature increase without sample, K (°F)

In contrast to the preceding methods, in which the sample is directly submerged in a liquid in the calorimeter, ASTM D2766-95 (2009) utilizes a sample container, allowing the testing of materials such as cement that would react with water. The test can be conducted for multiple temperatures over a range of interest in order to determine specific heat capacity as a function of temperature. In order to calibrate the calorimeter and to account for the enthalpy change in the calorimeter due to the sample container, the empty sample container is heated to equilibrium in a tube furnace at temperature T_f and is then transferred to an adiabatic calorimeter at fixed initial temperature T_c . The process is repeated at the same furnace and initial calorimeter temperatures with the sample in the container, and the enthalpy changes ΔH_c and ΔH_T in the calorimeter for the empty container and the container with the specimen, respectively, are calculated. The calibration and sample measurements are repeated for furnace temperatures T_f evenly distributed over the temperature range of interest.

The net enthalpy change per mass of the sample $\Delta H_s = (\Delta H_T - \Delta H_c)/m$ is calculated for each furnace temperature difference $\Delta T = T_f - T_c$. A power function for ΔH_s with respect to the temperature difference ΔT is obtained by curve-fitting, and differentiation of the power function with respect to furnace temperature T_f yields an

equation for specific heat capacity of the sample as a linear function of T_f over the range of temperatures tested.

O'Neill (1966) presented a method of determining specific heat capacity by differential scanning calorimetry (DSC), in which an empty container and a test specimen in a container are subjected to a linear increase in temperature, and the difference in heat flow rate into the two containers is measured as a function of temperature. A calibration curve for the same temperature program is obtained by measuring the difference in heat flow rate into an empty container and a container with a standard specimen for which the specific heat capacity is known over the desired temperature range. A baseline heat flow rate curve is obtained for the same temperature program by testing two empty containers, and the calorimetric differentials between the baseline and both the test specimen and calibration curves equal the heat flow rates into the respective specimens. Since the heat flow rate into a material during a linear temperature increase is proportional to the instantaneous specific heat capacity of the material, the specific heat capacity of the test specimen can then be determined by scaling the known specific heat capacity of the standard specimen according to the ratio of the two calorimetric differentials.

ASTM E1269-11 (2011) provides a standardized method for determining specific heat capacity via differential scanning calorimetry using a synthetic sapphire (α -aluminum oxide) disk as the standard specimen. The recommended maximum specimen size is approximately 50 mg, so the method is not ideal for highly heterogeneous materials. If the same containers are used for the baseline measurements and the test specimen or standard specimen measurements, the specific heat capacity of the material can be calculated as a function of temperature according to Eq. 2.50.

$$c_{p(s)}(T) = c_{p(st)}(T) \frac{D_s(T)m_{st}}{D_{st}(T)m_s} \quad \text{Eq. 2.50}$$

Where,

$c_{p(s)}$ = specific heat capacity of test specimen at temperature of interest, J/kg·K (Btu/lb·°F)

- $c_{p(st)}$ = specific heat capacity of sapphire standard at temperature of interest, J/kg·K (Btu/lb·°F)
- D_s = calorimetric differential between test specimen and baseline heat flow rate curves, mW (Btu/hr)
- D_{st} = calorimetric differential between sapphire standard and baseline heat flow rate curves, mW (Btu/hr)
- m_{st} = mass of sapphire standard, mg (lb)
- m_s = mass of test specimen, mg (lb)

2.7.2 Thermal Conductivity

Thermal conductivity λ is a measure of the rate at which heat is conducted through a material and is defined by Fourier's law of heat conduction, given in one-dimensional form in Eq. 2.51 (Carman and Nelson, 1921). Based on this relation, thermal conductivity is the ratio of heat flux density to the temperature gradient causing the heat flux or, similarly, the heat flux per unit area per unit temperature gradient (ACI207.2R-07). In metric (SI) units, thermal conductivity is measured in W/m·K. However, in U.S. customary (Imperial) units, thermal conductivity is often measured in Btu·in./hr·ft²·°F. For consistency of the units in both systems, thermal conductivity will be reported in U.S. customary (Imperial) units of Btu/hr·ft·°F, obtained by dividing values given in Btu·in./hr·ft²·°F by 12 in./ft.

$$q_x = \frac{Q_x}{A_x} = -\lambda \frac{dT}{dx} \quad \text{Eq. 2.51}$$

Where

- q_x = heat flux density in positive x -direction, W/m² (Btu/hr·ft²)
- Q_x = heat flux in positive x -direction, W (Btu/hr)
- A_x = area of heat flux normal to x -direction, m² (ft²)
- λ = thermal conductivity, W/m·K (Btu/hr·ft·°F)
- T = temperature, °C (°F)
- x = coordinate in three-dimensional Cartesian space, m (ft)

2.7.2.1 Typical Values

At typical mass concrete temperatures and high moisture contents, ACI 207.2R-07 (2007) reports a thermal conductivity range of 1.9 to 4.5 W/m·K (1.1 to 2.6 Btu/hr·ft·°F) for concretes containing various aggregate types. For concrete containing limestone aggregate, a range of 2.6 to 3.3 W/m·K (1.5 to 1.9 Btu/hr·ft·°F) is given. Tatro (2006) reports values of 2.2 and 3.2 W/m·K (1.25 and 1.83 Btu/hr·ft·°F) at normal temperatures for moist concrete containing limestone aggregate, and Tia et al. (2010) determined a value of 2.2 W/m·K (1.25 Btu/hr·ft·°F) for concrete containing Florida limestone aggregate based on experimentally determined thermal diffusivity and specific heat capacity values and using Eq. 2.53 in Section 2.7.3. A thermal conductivity of 1.73 W/m·K (1.00 Btu/hr·ft·°F) was identified for the CR3 PCC concrete, but the source of the value was not identified, and the value is lower than the typically reported values for concrete (Performance Improvement International, 2010).

As shown in Table 2.5, typical thermal conductivity values of concrete components are unique, and the relative proportions of these components influence the thermal conductivity of the concrete mix (Mindess, 2003). Kim et al. (2003) measured the thermal conductivity of concrete with varying mix designs and curing conditions and identified linear trends that would be expected from the relative thermal conductivities of the components. Increasing the content of aggregate, which has the highest thermal conductivity, resulted in a generally linear increase in concrete thermal conductivity. Increasing the w/c of cement paste reduced the thermal conductivity, and moist-cured concrete specimens had higher values than corresponding dry-cured specimens, in which air would replace a portion of the water volume. Accordingly, ACI 207.1R-05 (2012) notes that entrained air reduces thermal conductivity. Tatro (2006) also reported higher thermal conductivities for moist concrete, and Riding (2007) noted that mass concrete typically maintains a high moisture content at early ages.

Kim et al. also measured a slight increase in thermal conductivity as the fine aggregate fraction of the aggregate content was increased, and two possible causes were suggested: (1) the conductivity of the fine aggregate was higher than that of the coarse aggregate, or (2) the increased fine aggregate content resulted in a more uniform distribution of aggregate in the concrete. Like Kim et al., Carman and Nelson (1921) tested concrete with various aggregate volume ratios, but no significant difference in thermal conductivity was measured for the 100-to-200-°C (212-to-392-°F) test range, which was considered to be the more accurate set of results due to the number and consistency of the readings.

Table 2.5: Thermal conductivity values of concrete components

Material	Thermal Conductivity, λ		Reference
	W/m·K	Btu/hr·ft·°F	
Limestone	2.2–2.9	1.3–1.7	Zoldners, 1971
Cement paste*	1.0	0.58	Bentz, 2007
Water, 27 °C (80 °F)	0.613	0.354	Incropera et al., 2007
Air, 27°C (80 °F), atmospheric pressure	0.0263	0.0152	Incropera et al., 2007

*Cement pastes prepared with Cement and Concrete Reference Laboratory (CCRL) cement proficiency sample 152 with w/c of 0.3 and 0.4.

Testing at 20, 40, and 60 °C (68, 104, and 140 °F), Kim et al. (2003) measured a decrease in thermal conductivity with increasing temperature for concrete and cement paste specimens, and Zoldners (1971) reported that the thermal conductivity of rock typically decreases with increasing temperature. In contrast, Carman and Nelson (1921) identified negligible or inconsistent change in conductivity when testing different temperature gradients. Mindess et al. (2003) states that, for normal climatic temperatures, the thermal conductivity of concrete is independent of temperature.

Carman and Nelson found the age of the concrete to have a negligible effect on the thermal conductivity, and they noted that the slight decrease measured at later ages may have been caused by reduction of the moisture content. Measuring statistically

insignificant variation in thermal conductivity of cement pastes for the tested variables, Bentz (2007) determined that a constant value of $1.0 \text{ W/m}\cdot\text{K}$ ($0.58 \text{ Btu/hr}\cdot\text{ft}\cdot^\circ\text{F}$) would be a sufficient estimate at all degrees of hydration for cement pastes with w/c of 0.3 and 0.4 and either saturated or sealed curing conditions. Kim et al. (2003) also found that the thermal conductivities of cement paste, mortar, and concrete were independent of age. The U.S. Bureau of Reclamation (1940) measured a gradual 4% increase in thermal conductivity of concrete between 3 and 180 days after casting, and van Breugel (1980) reported that the thermal conductivity of concrete varies within a narrow range with increasing hydration. However, van Breugel (1998) cited instances of significantly increasing and decreasing thermal conductivity with hydration.

Brown and Javaid (1970) measured a 30% decrease from 2.176 to $1.515 \text{ W/m}\cdot\text{K}$ (1.257 to $0.875 \text{ Btu/hr}\cdot\text{ft}\cdot^\circ\text{F}$) between 6 hours and 7 days after casting, but they noted that heat of hydration may have influenced the results during the first 24 hours. For normal-strength concrete, Khan et al. (1998) measured a similar 33% decrease between an initial value of $1.73 \text{ W/m}\cdot\text{K}$ ($1.00 \text{ Btu/hr}\cdot\text{ft}\cdot^\circ\text{F}$) during the first 48 hours after casting and a final value of $1.16 \text{ W/m}\cdot\text{K}$ ($0.67 \text{ Btu/hr}\cdot\text{ft}\cdot^\circ\text{F}$) at 28 days. They compensated for heat of hydration by measuring the temperature rise at the center of control specimens with no artificial heating. In accordance with CRD-C 44-63 (U.S. Army Corps of Engineers, 1963) and assuming constant density, De Schutter and Taerwe (1995) calculated a 21% decrease in thermal conductivity of concrete as a function of degree of hydration based on experimentally determined trends for specific heat capacity (-13%) and thermal diffusivity (-9%).

Based on the decreasing trends for thermal conductivity with increasing hydration in the literature, Schindler (2002) proposed Eq. 2.52, which corresponds to a linear 25% decrease in thermal conductivity with increasing hydration, similar to a logarithmic decrease in time for common cement types. Riding (2007) also used this equation for modeling thermal conductivity.

$$\lambda(\alpha_H) = \lambda_u(1.33 - 0.33\alpha_H) \quad \text{Eq. 2.52}$$

Where,

- λ = thermal conductivity, W/m·K (Btu/hr·ft·°F)
- λ_u = ultimate thermal conductivity of mature concrete, W/m·K (Btu/hr·ft·°F)
- α_H = degree of hydration.

2.7.2.2 Experimental Methods

Thermal transmission properties, such as thermal conductivity, can be measured in accordance with ASTM C177-13, in which steady-state heat flux through flat slab specimens is measured using a guarded-hot-plate apparatus. The specimens are placed between constant-temperature heating and cooling plates in the apparatus, and the thermal conductivity is calculated using Eq. 2.51 with measurements of the cross-sectional area of the heat flux, the heat input, the temperatures of the plates, and the specimen thickness.

Whereas ASTM C177-13 allows direct determination of thermal conductivity, ASTM C518-10 (2010) is a comparative method that requires specimens of known thermal conductivity for calibration of the apparatus. Like C177, specimens are sandwiched between constant-temperature heating and cooling plates, but heat flux transducers are used to measure the heat flux through the specimen.

CRD-C 45-65 (U.S. Army Corps of Engineers, 1965) provides a method of measuring the thermal conductivity of lightweight insulating concrete but is applicable to materials with thermal conductivities between 0.09 and 0.72 W/m·K (0.05 and 0.42 Btu/hr·ft·°F). The specimen, with a nominal 25-mm (1-in.) thickness, sits on a heating plate, and an evaporator containing boiling n-pentane serves as the cooling plate on the top face of the specimen.

Carman and Nelson (1921) measured the thermal conductivity of long cylindrical specimens by generating heat through an electrical coil along the axis of the cylinder and measuring the temperature at two radial distances from the axis using embedded

thermocouples. They noted that 14 to 16 hours of heating were required before constant temperatures were obtained for taking measurements.

In contrast to the preceding steady-state methods, in which constant temperature profiles are obtained and the corresponding heat flux and temperature gradient are measured, transient methods measure the change in temperature as a function of time due to the generated heat flux. Because steady-state conditions are not required, the tests can be completed in significantly less time. Brown and Javaid (1970) tested curing concrete in a set-up similar to that described in ASTM C518-10, but the thermal conductivity could be determined from approximately 15 minutes of transient-state testing. Like Carman and Nelson, Khan et al. (1998) tested cylindrical concrete specimens with heating coils along the cylinder axis, but measurements were completed in less than 9 minutes for each test. Using a commercial thermal conductivity measuring device, Kim et al. (2003) measured the thermal conductivity of concrete specimens within 60 seconds.

Tatro (2006) states that thermal conductivity is usually calculated from experimentally determined values of thermal diffusivity and specific heat capacity because the latter properties are typically easier to measure than thermal conductivity, and CRD-C 44-63 (1963) specifies this approach for determining thermal conductivity of normalweight concrete. The relationship amongst these properties is discussed in Section 2.7.3.

2.7.3 Thermal Diffusivity

Thermal diffusivity κ is defined by ASTM E1461-13 (2013) as the thermal conductivity λ divided by the volumetric heat capacity ρc_p , which is the product of the density ρ and the specific heat capacity at constant pressure c_p . This relationship for thermal diffusivity is given in Eq. 2.53 and indicates that thermal diffusivity measures the ability of a material to conduct thermal energy relative to its ability to store thermal energy. Per Eq. 2.53, thermal diffusivity increases as the thermal conductivity increases

or the volumetric heat capacity decreases, corresponding to more rapid transfer of heat or greater temperature change per unit heat, respectively. Therefore, larger values of thermal diffusivity correspond to higher rates of temperature change through the material or more rapid “flow” of temperature (Carman and Nelson, 1921). Accordingly, in mass concrete applications, larger values of thermal diffusivity would reduce the temperature differential in the concrete by increasing the rate at which the temperatures of the interior and near-surface concrete equalized.

$$\kappa = \frac{\lambda}{\rho c_p} \quad \text{Eq. 2.53}$$

Where,

- κ = thermal diffusivity, m²/s (ft²/hr)
- λ = thermal conductivity, W/m·K (Btu/hr·ft·°F)
- ρ = density, kg/m³ (lb/ft³)
- c_p = specific heat capacity at constant pressure, J/kg·K (Btu/lb·°F)

2.7.3.1 Literature Values

Reported values of thermal diffusivity of concrete vary widely. A range of 0.6 to 2.0×10^{-6} m²/s (0.02 to 0.08 ft²/hr) for typical concrete was given by Mindess et al. (2003). Much of the variation is due to the coarse aggregate type used in the concrete, and ACI 207.2R-07 provides a value of 1.28×10^{-6} m²/s (0.051 ft²/hr) for concrete containing limestone coarse aggregate. Concrete containing Florida Ocala limestone, which is known to have higher porosity and lower density than limestone from other areas of the United States (Ferraro, 2009), exhibited an 18% increase in thermal diffusivity from 0.70 to 0.83×10^{-6} m²/s (0.027 to 0.032 ft²/hr) when tested from 1 to 28 days after mixing (Tia et al., 2010).

As shown in Table 2.6, the reported variation of thermal diffusivity as a function of hydration has been inconsistent in the literature. The U.S. Bureau of Reclamation (1940) measured negligible variation in thermal diffusivity of concrete between 3 and 180 days, with the maximum increase relative to the 3-day value being 2.0% at 60 days.

However, the testing would have missed changes that occurred during the first two days of curing. Chirdon et al. (2007) measured an 11% increase in thermal diffusivity of mortar during testing from 2 to 24 hours, after which the value remained consistent through testing up to 7 days. Similarly, Hansen et al. (1982) measured a 12% increase in cement paste. However, others have identified a decrease in thermal diffusivity of concrete with time. De Schutter and Taerwe (1995) measured a roughly linear decrease of about 9% as a function of degree of hydration, and Brown and Javaid (1970) measured a decrease of 16% from 6 hours to 7 days. Perumal (2008) measured a decrease of 32% between 10 and 20 hours after casting, followed by constant values through 60 hours, but the thermal diffusivity values are significantly lower than those reported by others, and no comparison with the literature was provided.

De Schutter and Taerwe (1995) explained that the decrease in diffusivity should be expected due to the decrease in free water and porosity with increasing degree of hydration, and they noted that the thermal conductivity decreases more than specific heat capacity, so that with constant concrete density, as measured by the U.S. Bureau of Reclamation (1940) between 3 and 180 days, the diffusivity would decrease according to Eq. 2.53. However, Ferraro (2009) noted that the sealed specimens tested by De Schutter and Taerwe would be susceptible to self-desiccation, which would further decrease the free water and likely slow the transfer of heat in the specimens as hydration continued, resulting in decreased diffusivity and conductivity measurements.

Table 2.6: Thermal diffusivity trends ($1 \text{ m}^2/\text{s} = 38,750 \text{ ft}^2/\text{hr}$)

Thermal Diffusivity, κ ($\text{m}^2/\text{s} \times 10^{-6}$)		Change (%)	Ages of Variation	Description	Reference
Initial	Final				
0.70	0.83	+18	1 to 28 days	Concrete; Florida limestone aggregate	Tia et al., 2010
0.60	0.67	+11	2 to 24 hours	Mortar	Chirdon et al., 2007
1.22	1.11	-9	1 to 14 days	Concrete; linear regression as function of degree of hydration	De Schutter and Taerwe, 1995
0.93	0.79	-16	6 hours to 7 days	Concrete	Brown and Javaid, 1970
0.28	0.19	-32	10 to 20 hours	Concrete	Perumal, 2008

2.7.3.2 Theoretical Solutions for Transient Heat Conduction

The methods for experimentally determining the thermal diffusivity of concrete are based upon the theoretical solutions for transient heat conduction of a body subjected to a heating or cooling medium and the first-order approximations of those solutions for the temperature at the center of the body. For a cylindrical body with a length-to-diameter ratio similar to that of most standard concrete cylindrical specimens, the solution consists of components for longitudinal and radial heat flow. An overview of these theoretical solutions and approximations is provided in the following sections in order to identify the assumptions that are made in the selected experimental methods and as a basis for comparing the methods.

2.7.3.2.1 Solution for Infinite Plane Slab

The general partial differential equation governing heat flow in a body with no internal heat generation and constant thermal diffusivity is given in Eq. 2.54, known as the heat equation (Ingersoll et al., 1948). Many of the experimental methods assume that

the rate of heat of hydration is constant or zero during testing, allowing a term for the rate of internal heat generation to be excluded from Eq. 2.54.

$$\frac{\partial T}{\partial t} = \kappa \nabla^2 T \quad \text{Eq. 2.54}$$

Where,

$$\begin{aligned} T &= \text{temperature at point of interest in body, } ^\circ\text{C} \\ t &= \text{time, s} \\ \kappa &= \text{thermal diffusivity, m}^2/\text{s} \end{aligned}$$

In Cartesian coordinates, Eq. 2.54 is expressed as shown in Eq. 2.55. In the theoretical case of an infinite plane slab or analogous body in which heat only flows in one direction, say, the x direction, Eq. 2.55 can be simplified to Eq. 2.56. An example of a physical representation of this case is a large finite slab in which the point of interest is thermally remote from all but two parallel faces.

$$\frac{\partial T}{\partial t} = \kappa \left(\frac{\partial^2 T}{\partial x^2} + \frac{\partial^2 T}{\partial y^2} + \frac{\partial^2 T}{\partial z^2} \right) \quad \text{Eq. 2.55}$$

$$\frac{\partial T}{\partial t} = \kappa \frac{\partial^2 T}{\partial x^2} \quad \text{Eq. 2.56}$$

Where,

$$x, y, z = \text{coordinates in three-dimensional Cartesian space, m}$$

The theoretical solutions for transient heat conduction of a body at uniform temperature T_i subjected to a heating or cooling medium at constant temperature $T_\infty \neq T_i$ are commonly given in terms of the dimensionless temperature θ^* , which is defined in Eq. 2.57 as the temperature difference $\theta(t) \equiv T(t) - T_\infty$ divided by the initial temperature difference $\theta_i \equiv T_i - T_\infty$. The dimensionless temperature decreases monotonically from 1 to 0 as the temperature T at the point of interest in the body changes from the initial temperature T_i to the temperature T_∞ of the medium. The dimensionless temperature can be conceptualized as the normalized temperature difference between the point of interest in the body and the medium.

$$\theta^* \equiv \frac{\theta(t)}{\theta_i} = \frac{T(t) - T_\infty}{T_i - T_\infty} \quad \text{Eq. 2.57}$$

Where,

- θ^* = dimensionless temperature
- θ = time-dependent temperature difference, K
- θ_i = initial temperature difference, K
- T = temperature at point of interest in body, °C
- T_∞ = medium temperature, °C
- T_i = initial body temperature, °C

Similarly, Eq. 2.58 defines the Fourier number Fo , which is sometimes referred to as dimensionless time. For a plane slab of thickness $2L$, the characteristic length L_c is taken as the half-thickness L , resulting in the Fourier number Fo_p for plane slabs given in Eq. 2.59.

$$Fo \equiv \frac{\kappa t}{L_c^2} \quad \text{Eq. 2.58}$$

Where,

- Fo = Fourier number
- κ = thermal diffusivity, m²/s
- t = time, s
- L_c = characteristic length, m

$$Fo_p = \frac{\kappa t}{L^2} \quad \text{Eq. 2.59}$$

Where,

- Fo_p = Fourier number for plane slab
- L = half-thickness of plane slab, m

Eq. 2.60 defines the dimensionless spatial coordinate x^* , for which $x^* = 0$ is the midplane of the slab and $x^* = 1$ is the surface of the slab.

$$x^* = \frac{x}{L} \quad \text{Eq. 2.60}$$

Where,

- x^* = dimensionless spatial coordinate
- x = distance from midplane of slab, m
- L = half-thickness of plane slab, m

Lastly, Eq. 2.61 defines the Biot number Bi , which indicates the thermal resistance within the body relative to the thermal resistance of the body-medium interface. At higher values of convective heat transfer coefficient h , sometimes referred to

as the film coefficient, heat transfers more readily between the body and the medium. For $Bi \gg 1$, the temperature gradient in the body is much greater than that between the surface and the medium. The Biot number Bi_p for plane slabs is given in Eq. 2.62.

$$Bi \equiv \frac{hL_c}{\lambda} \quad \text{Eq. 2.61}$$

Where,

$$\begin{aligned} Bi &= \text{Biot number} \\ h &= \text{convective heat transfer coefficient, W/m}^2\cdot\text{K} \\ \lambda &= \text{thermal conductivity, W/m}\cdot\text{K} \end{aligned}$$

$$Bi_p = \frac{hL}{\lambda} \quad \text{Eq. 2.62}$$

Where,

$$Bi_p = \text{Biot number for plane slab}$$

Using these dimensionless parameters, the exact theoretical solution for an infinite plane slab is given in Eq. 2.63 (Newman, 1936).

$$\theta_p^* = \sum_{n=1}^{\infty} C_n \exp(-\zeta_n^2 Fo_p) \cos(\zeta_n x^*) \quad \text{Eq. 2.63}$$

Where,

$$\begin{aligned} \theta_p^* &= \text{dimensionless temperature of plane slab} \\ C_n &= \text{coefficient defined in Eq. 2.64} \\ \zeta_n &= \text{positive roots of Eq. 2.65, rad} \end{aligned}$$

$$C_n = \frac{4 \sin(\zeta_n)}{2\zeta_n + \sin(2\zeta_n)} \quad \text{Eq. 2.64}$$

$$\zeta_n \tan \zeta_n = Bi_p \quad \text{Eq. 2.65}$$

The convective heat transfer coefficient h is influenced by the temperature difference at the interface and the thermodynamic properties of the medium (Low et al., 1991). For a surface heated or cooled by contact with water, Ingersoll et al. (1948) reports the convective heat transfer coefficient h ranging from 300 to 17,000 W/m²·K (50 to 3000 Btu/hr·ft²·°R). In certain cases, the convective heat transfer coefficient is assumed to be infinite ($h = \infty$) such that the temperature T_s at the surface of the body changes suddenly

to the medium temperature T_∞ when subjected to the medium (Olson and Schultz, 1942). Forced convection, such as by a circulating bath, can increase h , and Baïri et al. (2007) state that submerging a specimen in a stirred fluid conducive to heat transfer with the specimen achieves high values of h for which the assumption is reasonable. As discussed in Section 2.7.3.3, many of the experimental methods are based on calculations that utilize this assumption, but the discrepancy between this assumption and the actual boundary conditions is a motivation for methods developed more recently.

Assuming an infinite convective heat transfer coefficient, the boundary condition is changed to $T_s = T_\infty$, and T_∞ is replaced with T_s in Eq. 2.57. With $h = \infty$, the Biot number is also infinite ($Bi = \infty$), and the roots of Eq. 2.65 are $\zeta_n = (2n - 1)\pi/2$. Therefore, the coefficient C_n simplifies to Eq. 2.66, and evaluated at the midplane ($x^* = 0$), Eq. 2.63 becomes Eq. 2.67.

$$C_n = \frac{4 (-1)^{(n-1)}}{\pi (2n - 1)} \quad \text{Eq. 2.66}$$

$$\theta_p^*|_{x^*=0} = \sum_{n=1}^{\infty} C_n \exp\left(-\left(\frac{\pi}{2}(2n - 1)\right)^2 Fo_p\right) \quad \text{Eq. 2.67}$$

Heisler (1947) found that this infinite series solution given in Eq. 2.63 converges rapidly and that, for $Fo_p > 0.2$, the first term accurately approximates the solution. Accordingly, Eq. 2.68 gives the first-term approximation of Eq. 2.67.

$$\theta_p^*|_{x^*=0} = \frac{4}{\pi} \exp\left(\frac{-\pi^2 Fo_p}{4}\right) \quad \text{Eq. 2.68}$$

2.7.3.2.2 Solution for Infinite Right Cylinder

In the theoretical case of an infinite right cylinder or analogous body in which only radial heat transfer occurs, the general partial differential equation for heat flow given in Eq. 2.54 is expressed with radial coordinates as shown in Eq. 2.69.

$$\frac{\partial T}{\partial t} = \kappa \left(\frac{\partial^2 T}{\partial r^2} + \frac{1}{r} \frac{\partial T}{\partial r} \right) = \frac{\kappa}{r} \frac{\partial}{\partial r} \left(r \frac{\partial T}{\partial r} \right) \quad \text{Eq. 2.69}$$

Where,
 r = radial coordinate, m

For an infinite right cylinder, the characteristic length L_c is taken as the radius R of the cylinder. Therefore, the previously defined Fourier number (Eq. 2.58), dimensionless spatial coordinate (Eq. 2.60), and Biot number (Eq. 2.61) can be expressed for an infinite cylinder as in Eq. 2.70, Eq. 2.71, and Eq. 2.72, respectively.

$$Fo_c = \frac{\kappa t}{R^2} \quad \text{Eq. 2.70}$$

Where,
 Fo_c = Fourier number for infinite right cylinder
 R = radius of cylinder, m

$$r^* = \frac{r}{R} \quad \text{Eq. 2.71}$$

Where,
 r^* = dimensionless radial coordinate
 r = radial coordinate, m

$$Bi_c = \frac{hR}{\lambda} \quad \text{Eq. 2.72}$$

Where,
 Bi_c = Biot number for infinite cylinders

Using these parameters, the exact theoretical solution for an infinite right cylinder is given in Eq. 2.73 (Newman, 1936).

$$\theta_c^* = \sum_{n=1}^{\infty} D_n \exp(-\varphi_n^2 Fo_c) J_0(\varphi_n r^*) \quad \text{Eq. 2.73}$$

Where,
 θ_p^* = dimensionless temperature of plane slab
 D_n = coefficient defined in Eq. 2.74
 φ_n = positive roots of Eq. 2.75, rad
 $J_m(\cdot)$ = Bessel function of the first kind defined in Eq. 2.76 for non-negative integer order m

$$D_n = \frac{2}{\varphi_n} \frac{J_1(\varphi_n)}{J_0^2(\varphi_n) + J_1^2(\varphi_n)} \quad \text{Eq. 2.74}$$

$$\varphi_n \frac{J_1(\varphi_n)}{J_0(\varphi_n)} = Bi_c \quad \text{Eq. 2.75}$$

The Bessel function of the first kind of non-negative integer order m is defined in Eq. 2.76 as given by Gray and Mathews (1895), who also provided tabulated values of $J_0(x)$ and $J_1(x)$.

$$J_m(x) = \sum_{k=0}^{\infty} \frac{(-1)^k \left(\frac{x}{2}\right)^{2k+m}}{k! (m+k)!} \quad \text{Eq. 2.76}$$

For $Bi = \infty$, the positive roots φ_n satisfy $J_0(\varphi_n) = 0$ and are tabulated with the corresponding values of $J_1(\varphi_n)$ by Gray et al. (1922). With $J_0(\varphi_n) = 0$, Eq. 2.74 can be simplified to Eq. 2.77. Evaluating Eq. 2.73 at the axis ($r^* = 0$), $J_0(0) = 1$ and the expression simplifies to Eq. 2.78.

$$D_n = \frac{2}{\varphi_n J_1(\varphi_n)} \quad \text{Eq. 2.77}$$

$$\theta_c^*|_{r^*=0} = \sum_{n=1}^{\infty} D_n \exp(-\varphi_n^2 Fo_c) \quad \text{Eq. 2.78}$$

Like the infinite series solution for plane slabs, Heisler (1947) found that the solution for infinite cylinders is accurately approximated by the first term of the series for $Fo_c > 0.2$. Accordingly, Eq. 2.79 gives the first-term approximation of Eq. 2.78.

$$\theta_c^*|_{r^*=0} = \frac{2}{\varphi_1 J_1(\varphi_1)} \exp(-\varphi_1^2 Fo_c) \quad \text{Eq. 2.79}$$

Where,

$$\begin{aligned} \varphi_1 &= 2.40483 \text{ rad} \\ J_1(\varphi_1) &= 0.51915 \end{aligned}$$

The convergence of the first-term approximations for infinite cylinders (Eq. 2.79) and infinite slabs (Eq. 2.68) with the respective theoretical solutions (Eq. 2.78 and Eq. 2.67) is illustrated in Figure 2.21. The theoretical curves were obtained computationally using sixth-order approximations of the solutions, and the results were confirmed with tabulated values of the numerical solutions given by Olson and Schultz (1942). The first-term approximation for θ_c converges to within 5 and 1% of the theoretical solution at Fo values of 0.107 and 0.171, respectively. Similarly, the first-term approximation for θ_s converges to within 5 and 1% of the theoretical solution at Fo values of 0.098 and 0.178, respectively, supporting the conclusions by Heisler.

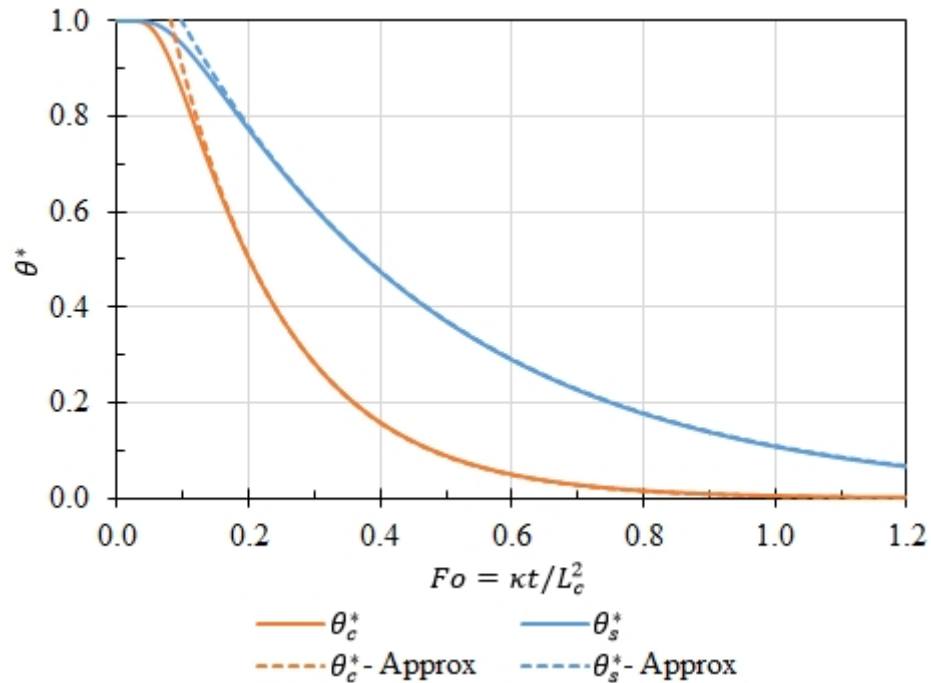


Figure 2.21: Convergence of first-term approximations with theoretical solutions for dimensionless temperature at the axis of an infinite right cylinder and midplane of an infinite plane slab

2.7.3.2.3 Solution for Short Right Cylinder

Olson and Schultz (1942) noted that a cylinder with a total length that is less than four times the diameter ($2L/D < 4$) should usually be analyzed as a finite cylinder, for

which both the radial effect of the cylindrical surface and the slab effect of the parallel circular faces contribute to the heat transfer. Therefore, the general partial differential equation for heat flow given in Eq. 2.54 is expressed in radial and longitudinal coordinates in Eq. 2.80 for a short cylinder.

$$\frac{\partial T}{\partial t} = \kappa \left(\frac{\partial^2 T}{\partial r^2} + \frac{1}{r} \frac{\partial T}{\partial r} + \frac{\partial^2 T}{\partial x^2} \right) \quad \text{Eq. 2.80}$$

Where,

$$\begin{aligned} r &= \text{radial coordinate, m} \\ x &= \text{longitudinal coordinate, m} \end{aligned}$$

Newman (1936) proved that the solutions for two- and three-dimensional problems can be expressed as the product of the solutions of the corresponding one-dimensional problems. Therefore, the solution for the short cylinder is obtained as the product of the solutions for the infinite right cylinder and infinite plane slab as shown in Eq. 2.81. The first-term approximation evaluated at the center of gravity of the cylinder, with $r^* = 0$ and $x^* = 0$, is given in Eq. 2.82.

$$\theta_{sc}^* = \theta_c^* \times \theta_p^* \quad \text{Eq. 2.81}$$

Where,

$$\theta_{sc}^* = \text{dimensionless temperature of short cylinder}$$

$$\theta_{sc}^* |_{(r^*, x^*)=(0,0)} = \frac{8}{\pi \varphi_1 J_1(\varphi_1)} \exp \left(-\varphi_1^2 Fo_c - \frac{\pi^2 Fo_p}{4} \right) \quad \text{Eq. 2.82}$$

Substituting the corresponding Fourier number expressions from Eq. 2.59 and Eq. 2.70 into Eq. 2.82 yields Eq. 2.83.

$$\theta_{sc}^* |_{(r^*, x^*)=(0,0)} = \frac{8}{\pi \varphi_1 J_1(\varphi_1)} \exp \left(-\kappa t \left(\frac{\varphi_1^2}{R^2} + \frac{\pi^2}{4L^2} \right) \right) \quad \text{Eq. 2.83}$$

Taking the natural logarithm of both sides of Eq. 2.83, differentiating with respect to time t , and rearranging the terms yields Eq. 2.84 for thermal diffusivity κ of the body

based on the first-term approximation for the temperature at the center of gravity of a short right cylinder.

$$\kappa = \frac{-1}{\left(\frac{\varphi_1^2}{R^2} + \frac{\pi^2}{4L^2}\right)} \frac{d \ln \theta_{sc}^*}{dt} = \frac{-\ln(10)}{\left(\frac{\varphi_1^2}{R^2} + \frac{\pi^2}{4L^2}\right)} \frac{d \log \theta_{sc}^*}{dt} \quad \text{Eq. 2.84}$$

Similarly, by letting T_1 and T_2 be the temperatures at times t_1 and t_2 , respectively, dividing Eq. 2.83 at time t_1 by itself at t_2 yields Eq. 2.85. Taking the natural logarithm of both sides and rearranging yields Eq. 2.86, which is a slightly different form of Eq. 2.84 for calculating the thermal diffusivity.

$$\frac{T_1 - T_s}{T_2 - T_s} = \exp\left(\kappa(t_2 - t_1) \left(\frac{\varphi_1^2}{R^2} + \frac{\pi^2}{4L^2}\right)\right) \quad \text{Eq. 2.85}$$

$$\kappa = \frac{-1}{\left(\frac{\varphi_1^2}{R^2} + \frac{\pi^2}{4L^2}\right)} \frac{\ln\left(\frac{T_2 - T_s}{T_1 - T_s}\right)}{(t_2 - t_1)} = \frac{-\ln(10)}{\left(\frac{\varphi_1^2}{R^2} + \frac{\pi^2}{4L^2}\right)} \frac{\log\left(\frac{T_2 - T_s}{T_1 - T_s}\right)}{(t_2 - t_1)} \quad \text{Eq. 2.86}$$

For a short right cylinder with known radius R , half-length L , initial body temperature T_i , and surface temperature T_s , the temperature history $T(t)$ at the center of gravity of the cylinder can be used with Eq. 2.84 or Eq. 2.86 to experimentally determine the thermal diffusivity κ of the body.

Eq. 2.84 and Eq. 2.86 can be rewritten for infinite cylinders by taking the limit as L approaches infinity, resulting in Eq. 2.87 and Eq. 2.88 in which the $\pi^2/4L^2$ term has become zero. These equations for thermal diffusivity are based on the first-term approximation for the temperature at the axis of an infinite cylinder and are applicable when the slab heat transfer effect of the cylinders is negligible.

$$\kappa = -\left(\frac{R}{\varphi_1}\right)^2 \frac{d \ln \theta_{sc}^*}{dt} = -\ln(10) \left(\frac{R}{\varphi_1}\right)^2 \frac{d \log \theta_{sc}^*}{dt} \quad \text{Eq. 2.87}$$

$$\kappa = -\left(\frac{R}{\phi_1}\right)^2 \frac{\ln\left(\frac{T_2 - T_s}{T_1 - T_s}\right)}{(t_2 - t_1)} = -\ln(10) \left(\frac{R}{\phi_1}\right)^2 \frac{\log\left(\frac{T_2 - T_s}{T_1 - T_s}\right)}{(t_2 - t_1)} \quad \text{Eq. 2.88}$$

2.7.3.3 Experimental Methods

From observation of Eq. 2.84 and Eq. 2.86, it can be seen that, for the first-term approximation of the temperature at the center of a cylinder, the slope of $\log \theta^*$ or $\log(T(t) - T_s)$ with respect to time t is directly related to the first-term approximation of thermal diffusivity κ by a coefficient that depends only on the dimensions of the specimen. This behavior is utilized in many of the experimental methods for determining thermal diffusivity by calculating the slope of the roughly linear portion of the experimental θ^* curve.

The procedure for CRD-C 36-73 (1973b) details the determination of the thermal diffusivity of a 152-by-305-mm (6-by-12-in.) cylinder, but functions for determining the thermal diffusivity of prisms and cylindrical specimens of other dimensions via the same procedure are provided as well. A thermocouple is embedded in the center of mass of the specimen, and the specimen is heated in boiling water until the temperature at the center of the specimen reaches 100 °C (212 °F). The specimen is then placed in a constant-temperature bath of running cool water such that all surfaces of the specimen are exposed to the water. The temperature of the cooling bath is not specified, but based on the recording requirements of the procedure, the temperature should be no more than 33 °C (92 °F). The time t and temperature difference $\theta(t) = T(t) - T_\infty$ between the center of the specimen and the bath are recorded at 60-second intervals for values of θ from 67 to 4 K (120 to 8 °R). The heating and cooling process is conducted twice for each specimen.

From the recorded temperature history, the times t_1 and t_2 at which $\theta_1 = T_1 - T_\infty = 44$ K (80 °R) and $\theta_2 = T_2 - T_\infty = 11$ K (20 °R), respectively, are used in Eq. 2.86 to calculate the thermal diffusivity κ . With radius $R = 76$ mm (3 in.) and half-length $L = 152$

mm (6 in.), Eq. 2.86 simplifies to Eq. 2.89 for SI units and Eq. 2.90 for US customary (Imperial) units. The form of Eq. 2.90 matches that given in CRD-C 36-73 (U.S. Army Corps of Engineers, 1973b), and the conversion factor between the two unit systems for thermal diffusivity is $1 \text{ m}^2/\text{s} = 38,750 \text{ ft}^2/\text{hr}$.

$$\kappa = \frac{0.00125191}{t_2 - t_1} \quad \text{Eq. 2.89}$$

Where,

- κ = thermal diffusivity, m^2/s
- t_1 = time when $\theta_1 = 44 \text{ K}$ ($80 \text{ }^\circ\text{R}$), s
- t_2 = time when $\theta_2 = 11 \text{ K}$ ($20 \text{ }^\circ\text{R}$), s

$$\kappa = \frac{0.812278}{t_2 - t_1} \quad \text{Eq. 2.90}$$

Where,

- κ = thermal diffusivity, ft^2/hr
- t_1 = time when $\theta_1 = 44 \text{ K}$ ($80 \text{ }^\circ\text{R}$), min
- t_2 = time when $\theta_2 = 11 \text{ K}$ ($20 \text{ }^\circ\text{R}$), min

CRD-C 36-73 acknowledges that the thermal diffusivity value obtained from Eq. 2.90 is a first-order approximation but notes that, for 152-by-305-mm (6-by-12-in.) cylinders, the result is generally sufficiently accurate. Although the assumption of $Bi = \infty$ such that the surface temperature T_s is immediately equal to the bath temperature T_∞ is utilized in arriving at Eq. 2.89 and Eq. 2.90, the procedure does not acknowledge this assumption or address its applicability for concrete.

In order to avoid artificially increasing the maturity of early-age specimens prior to testing, Ferraro (2009) utilized a modified CRD-C 36-73 method, determining the thermal diffusivity using the temperature history of specimens initially at $23 \text{ }^\circ\text{C}$ ($73 \text{ }^\circ\text{F}$) for standard curing and then heated in a hot water bath. Ferraro cites results in an unpublished report indicating that there was negligible difference in the thermal diffusivity values obtained using the CRD-C 36-73 method, in which the specimens are

cooled during the test segment, and the modified method, in which the specimens are heated during the test segment.

The procedure developed by De Schutter & Taerwe (1995) is similar to CRD-C36-73 except that the bath and initial specimen temperatures are not prescribed and the tested specimens were sealed. The relationship between the slope of $\log(T(t) - T_s)$ as a function of time t and the thermal diffusivity is noted but not quantified, so insufficient details are provided for the method used to calculate the thermal diffusivity. Furthermore, there is no mention of whether the slope of the linear portion of the curve is determined by linear regression or by a pair of points, such as in CRD-C 36-73.

Low et al. (1991) provided a method of calculating the thermal diffusivity from the temperature history at the center of cylindrical specimens using graphs of the first-term approximations of the theoretical solutions for short cylinders. Curves were provided for specimens with radius $R = 50$ mm (2 in.), lengths ranging from 50 to 200 mm (2 to 8 in.), and thermal conductivities representative of construction materials. A thermal diffusivity value is determined for heating and cooling segments at $\theta^* = 0.8, 0.5,$ and 0.2 using the times to reach those dimensionless temperatures, the specimen length, and the appropriate graphs. The average of the six values gives the thermal diffusivity of the specimen.

The various specimen lengths are handled by using a length correction factor that normalizes the curves to that of a specimen with reference length $2L = 200$ mm (8 in.). However, this factor is based on a plot in which the linear portions of three of the six curves, including that of the reference length, have values of $Fo < 0.2$, for which the first-term approximations have not converged with the exact solutions. Low et al. attribute the poorer alignment of the normalized curves at values of $\theta^* > 0.8$ to the error in the first-term approximation at those values of Fo , but the accuracy of the linear regions roughly spanning $\theta^* = 0.2$ to 0.8 is not addressed for the same values of Fo .

As noted in the discussion following Eq. 2.65, the convective heat transfer coefficient h is commonly assumed to be infinite for the experimental determination of thermal diffusivity of concrete. Low et al. note that h depends on the temperature difference at the interface between the specimen and heating/cooling medium and then show that the range of temperature differences tested doesn't have a significant impact on the dimensionless temperature history. However, the handling of h to arrive at the simplified solution is not discussed. Theoretical curves showing the influence of thermal conductivity are provided, but the only dependence of the exact solution and the first-order approximation on thermal conductivity is in the Biot number. If the convective heat transfer coefficient is assumed to be infinite ($h = \infty$), Biot number is also infinite ($Bi = \infty$), meaning that both the Biot number and the solution are independent of thermal conductivity. This suggests that the curves provided by Low, which depend on thermal conductivity, do not assume that h is infinite.

Methods developed more recently have accounted for the various assumptions involved in the preceding derivations and methods by applying different thermal inputs or recording different temperature histories. Like De Schutter and Taerwe, Ukrainczyk (2009) tested sealed specimens, but instead of assuming that the surface temperature of the specimen immediately changes to that of the heating/cooling medium, the temperature was recorded at the center of the specimens and at the inside surface of the containers. The thermal diffusivity was then determined numerically based on the temperature histories at the two locations. The rate of heat of hydration was assumed to be sufficiently constant during the tests such that Eq. 2.54 would be valid.

Perumal (2008) experimentally determined the thermal diffusivity of curing concrete by measuring the thermal response at the center of a fresh concrete sample in a 150-by-300-mm (6-by-12-in.) cylindrical container in an oven rather than a water bath. The temperature in the oven was gradually cycled between 30 and 70 °C (86 and 158 °F) while maintaining a 5-K (9-°R) temperature difference between the oven and the center

of the specimen during each heating or cooling segment. The adiabatic temperature rise of a different specimen of the same concrete was measured concurrently in order to account for the heat of hydration, and the constant temperature differential in the specimen during each segment of the test was used as a boundary condition in the determination of the thermal diffusivity.

In order to minimize the variation of temperature-dependent thermal properties during the testing of hydrating cement mortar, Chirdon et al. (2007) developed a method to measure the thermal diffusivity over a small temperature range. The exposed face of an insulated rectangular specimen was subjected to an oscillating boundary temperature via alternating water baths at 35 and 50 °C (95 and 122 °F), and the temperature in the specimen was recorded at two distances from the exposed face. The ratio of the peak amplitudes or the time-lag between peak amplitudes at the two recording locations could be used to determine the thermal diffusivity. Chirdon et al. found that the method was effective during hydration because the frequency of the temperature oscillation was high enough that the rate of heat generation could be considered constant during each cycle.

2.7.3.4 Initial Temperature Differential

Eq. 2.84 and Eq. 2.86 suggest that the determination of the thermal diffusivity κ is independent of the initial specimen temperature T_i and the initial temperature difference θ_i . In theoretical analysis, Low et al. (1991) showed graphically that, for cylinders with radius $R = 50$ mm (2 in.), half-length $L = 31.75$ mm (1.25 in.), and a minimum temperature of 30 °C (86 °F), initial temperature differences ranging from 10 to 40 K (18 to 72 °R) had negligible influence on the dimensionless temperature history θ^* as a function of $\log(Fo)$, and the slopes of the curves appeared qualitatively uniform. Their results were confirmed experimentally by constant thermal diffusivity results for hardened cement paste specimens with initial temperature differences ranging from 10 to 30 K (18 to 54 °R).

De Schutter and Taerwe (1995) showed numerically that, for thermal diffusivity testing at early ages, the heat of hydration influences the results when small temperature differences are applied, and they imply that 5 or 10 K (9 or 18 °R) be the minimum initial temperature difference applied when testing via submersion in a constant-temperature water bath.

2.7.3.5 Discussion of Short and Infinite Cylinders

Since the method used by De Schutter and Taerwe (1995) to calculate the thermal diffusivity was not given, an effort was made to calculate the thermal diffusivity using Eq. 2.84 knowing that the cylinder radius R was 50 mm (2 in.) and assuming that the cylinder half-length L was 100 mm (4 in.). Data were sampled from a figure in De Schutter and Taerwe displaying an experimental dimensionless temperature history $\theta^*(t)$ is plotted in Figure 2.22 with a regression of the linear portion of the plot. Though not evident in the sampled data, as θ^* decreased below 0.1 in the original figure, scatter began appearing in the data. With the given radius, assumed half-length, and exponential regression slope of -10.0447 hr^{-1} , Eq. 2.84 yields a thermal diffusivity of $1.09 \times 10^{-6} \text{ m}^2/\text{s}$ ($0.0422 \text{ ft}^2/\text{hr}$), which is lower than the minimum value plotted by De Schutter and Taerwe.

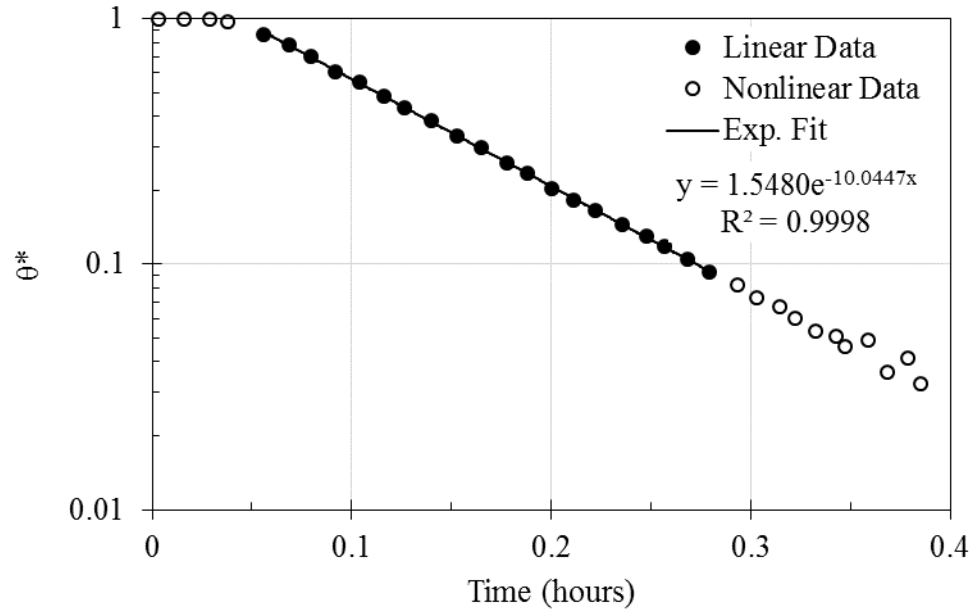
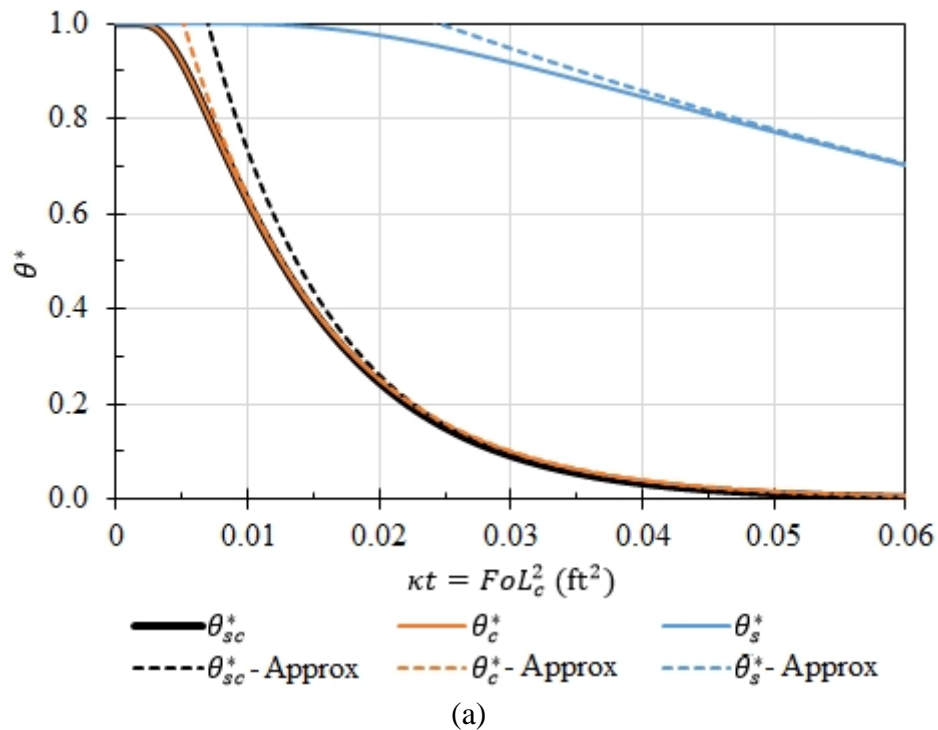


Figure 2.22: Dimensionless temperature history data sampled from diffusivity test in De Schutter and Taerwe (1995)

Noting that the cylinder lengths were not identified and that the temperature history was recorded at the cylinder axis rather than at the volumetric center of the cylinder, the above calculation was repeated for the case of an infinite cylinder. Using Eq. 2.87 with the known radius and the sampled data, the thermal diffusivity was calculated to be $1.21 \times 10^{-6} \text{ m}^2/\text{s}$ ($0.0467 \text{ ft}^2/\text{hr}$), which fits well with the diffusivity results plotted by De Schutter and Taerwe at lower degrees of hydration.

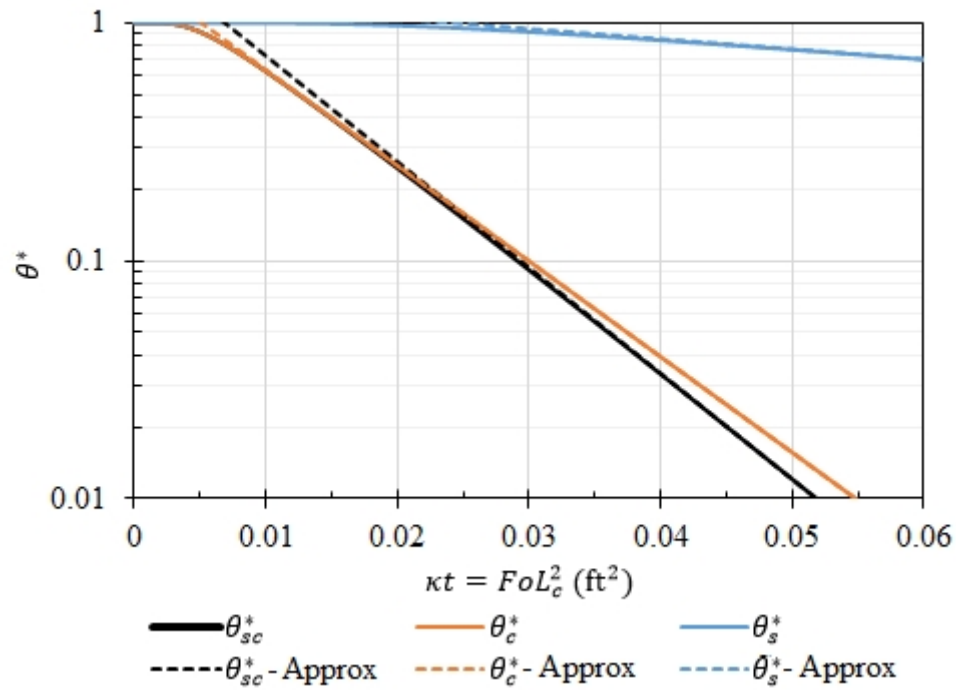
For common lab-prepared cylindrical concrete specimens with half-length $L = 2R$, the assumption of an infinite cylinder and use of Eq. 2.87 results in an increase in calculated thermal diffusivity by a factor of $(\pi/4\phi_1)^2 \approx 10.7\%$ relative to the result of Eq. 2.84. Figure 2.23 shows the contribution of the cylindrical and slab heat transfer effects on the dimensionless temperature at the center of such a specimen. The plots are shown for a 152-by-305-mm (6-by-12-in.) cylinder, but the curves scale proportionally along the abscissa for different specimen sizes with half-length $L = 2R$.

Of note in Figure 2.23 is that the cylindrical heat transfer effect largely governs the behavior of the specimen; approximately 50% of the temperature change has occurred before any visible contribution from the slab effect begins. Figure 2.23a shows that the first-term approximation of θ_c^* converges with θ_{sc}^* at lower values of κt than the first-term approximation of θ_{sc}^* , suggesting that the assumption of an infinite cylinder is appropriate for cylinders with $L = 2R$. However, Figure 2.23b shows that the first-term approximation of θ_c^* diverges from θ^* at later values when the slab effect begins to contribute. The first-term approximation of θ_c^* is within 5 and 1% of θ_{sc}^* over κt ranges of 0.007 to 0.024 ft² and 0.011 and 0.015 ft², respectively. In contrast, the first-term approximation of θ_{sc}^* converges within 5 and 1% of θ_{sc}^* at κt values of 0.025 and 0.044 ft², respectively, and as κt increases, θ_{sc}^* approaches the approximation asymptotically (Olson and Jackson, 1942).



Note: (1 m²/s = 38,750 ft²/hr)

Figure 2.23: Dimensionless temperature history at the center of a 152-by-305-mm (6-by-12-in.) cylinder as a function of κt with the ordinate shown (a) linearly and (b) logarithmically



(b)
Figure 2.23 (continued)

Since the slope of θ_{sc}^* is not constant, the point or range of values for which the slope is taken will impact the determination of the thermal diffusivity. At $\kappa t = 0.013 \text{ ft}^2$, the slope of θ_{sc}^* is equal to that of the first-term approximation of θ_c^* , and as κt increases, the slope of θ_{sc}^* approaches that of its first-term approximation asymptotically. Since the slope of the experimental θ^* curve is used to determine the thermal diffusivity, the measured thermal diffusivity will depend on the range of temperature data collected. Noting that the slopes of the two approximations bound the slope of the theoretical solution and differ by about 10%, it may be reasonable to calculate the thermal diffusivity using the two approximations as bounds for the experimental value.

As an example, CRD-C 36-73 specifies that the slope of the experimental curve be taken between points where $\theta_1 = 44 \text{ K}$ (80 °R) and $\theta_2 = 11 \text{ K}$ (20 °R). The maximum allowable bath temperature is $\theta_\infty = 33 \text{ °C}$ (92 °F), for which the first-term approximation

of θ_{sc}^* yields (via Eq. 2.86) a thermal diffusivity that is 7.6% lower than the theoretical value and the first-term approximation of θ_c^* yields (via Eq. 2.88) a thermal diffusivity that is 2.23% higher than the theoretical value. The lowest possible bath temperature without solvents or pressurization is 0 °C (32 °F), for which the first-term approximation of θ_{sc}^* yields a thermal diffusivity that is 5.2% lower than the theoretical value and the first-term approximation of θ_c^* yields a thermal diffusivity that is 4.89% higher than the theoretical value. Therefore, throughout the entire range of possible bath temperatures for CRD-C 36-73, the first-term approximation for θ_c^* overestimates the thermal diffusivity but yields more accurate values than the approximation for θ_{sc}^* that is used in the standard, which underestimates the thermal diffusivity.

These results indicate that, with a known thermal diffusivity, the first-term approximation for an infinite cylinder provides a better approximation than the corresponding approximation for a short cylinder of the temperature at the center of a cylinder with half-length $L = 2R$ for the first 84% of the temperature change, and the absolute difference for the remainder of the temperature change is not significant since the dimensionless temperature is so small. The first-term approximation for a short cylinder provides a better estimate of the thermal diffusivity at later times, but the ability to obtain smooth data at those times is uncertain. Therefore, for experimental determination of the thermal diffusivity of concrete, using cylindrical specimens with $L/R > 2$ may be preferable due to the reduced influence of the slab heat transfer effects and, therefore, the greater precision of the first-term approximation of θ_c^* for a wider range of experimental θ^* values.

2.7.4 Coefficient of Linear Thermal Expansion

The coefficient of linear thermal expansion (CTE) is an important thermal property for mass concrete because it governs the dimensional change of concrete due to changes in temperature. ASTM E228-11 (2011) defines the CTE as the ratio of thermal

strain to the temperature change that is causing the strain, so higher values of CTE indicate greater thermal strain for a given temperature change. The following sections discuss typical values of CTE for concrete, particularly concrete containing limestone coarse aggregate, and common methods of measuring the CTE of concrete.

2.7.4.1 Literature Values

The CTE of concrete is largely dependent on the amount and CTE of coarse aggregate in the concrete (ACI 207.1R-05, 2012). Won (2005) found that the CTE of concrete decreases linearly with increasing coarse aggregate content. Due to the high CTE of cement paste, the cement content can also influence the CTE of concrete, but for typical ranges of cement contents, the aggregate type has a greater influence (Mindess et al., 2003).

The moisture content of concrete has been found to have a significant influence on the measured CTE of concrete due to hygrothermal expansion. Meyers (1940) subjected concrete specimens to varying humidity environments and found that the measured CTE of fully dried and fully saturated specimens was lower than that of specimens with intermediate moisture contents. Testing cement paste with $w/c = 0.22$ and 0.4 , Zoldners (1971) measured maximum CTE values when the moisture content was about 65-70% for concrete aged up to 6 months. At these ages, the peak CTE was about double the minimum values at oven-dried or saturated conditions, but this effect would be reduced for concrete due to the aggregate. After 16 years, the CTE peaks decreased in magnitude and shifted to lower moisture contents of about 45-50%.

Table 2.7 provides values of CTE reported in the literature for concrete containing limestone coarse aggregate. The $11.7\text{-}\mu\epsilon/\text{°C}$ ($6.5\text{-}\mu\epsilon/\text{°F}$) CTE reported for the CR3 PCC concrete is higher than all of the other identified values for concrete containing limestone aggregate (Performance Improvement International, 2010). Varying trends in early-age CTE variation have also been observed. Won (2005) measured generally constant values

of concrete CTE testing daily from 1 to 21 days. Khan et al. (1998) also measured consistent values for normal-strength concrete with limestone aggregate tested at 16 hours, 24 hours, and 28 days after casting. For ordinary Portland cement concrete with Florida Ocala Limestone coarse aggregate, Tia et al. (2010) measured a 1-day CTE of $9.2 \mu\epsilon/^\circ\text{C}$ ($5.1 \mu\epsilon/^\circ\text{F}$), which increased to approximately $10.0 \mu\epsilon/^\circ\text{C}$ ($5.6 \mu\epsilon/^\circ\text{F}$) by 7 days and remained constant through 28 days. Testing sealed, high-performance concrete with limestone coarse aggregate, Cusson and Hoogeveen (2006) measured an initial decrease in CTE between approximately 12 and 24 hours after setting to a minimum value of $6.0 \mu\epsilon/^\circ\text{C}$ ($3.3 \mu\epsilon/^\circ\text{F}$), followed by a gradual increase through 7 days to approximately $8.7 \mu\epsilon/^\circ\text{C}$ ($4.8 \mu\epsilon/^\circ\text{F}$). Kada et al. (2002) measured similar CTE behavior for sealed concrete with limestone-based coarse aggregate and a w/c of 0.30, but for w/c of 0.35 and 0.45, the CTE was constant following the decrease at about 8 to 12 hours with no later increase. Book and Barnoff (1973) measured a 90% decrease in concrete CTE during the first 10 hours after mixing, followed by constant values through 3 days. Kada et al. and Glisic (2000) note that, at the relevant temperatures for curing concrete, the CTE of water is significantly higher than that of the other concrete components and the hydrated cement products, resulting in the high CTE values measured soon after mixing that decrease rapidly as hydration progresses.

The increasing CTE values measured on sealed specimens may have been caused by self-desiccation of the specimens (Cusson and Hoogeveen, 2006). As noted previously, the measured CTE of concrete increases as the moisture content decreases from a saturated to intermediate moisture content, and the ages at which the increases in CTE were measured coincide with the decrease in internal relative humidity of sealed cement paste measured by Lura et al. (2003).

Table 2.7: Coefficient of linear thermal expansion values for concrete containing limestone coarse aggregate

Concrete Coefficient of Linear Thermal Expansion		Coarse Aggregate Description	Reference
$\mu\epsilon/^\circ\text{C}$	$\mu\epsilon/^\circ\text{F}$		
5.4–8.6	3.0–4.8	Limestone	ACI 207.4R-93, 1998
6.91	3.84	Georgia limestone	Kim, 2012
7.77–8.47	4.32–4.71	Texas limestone	Won, 2005
7.80	4.34	Limestone	Federal Highway Administration, 2011
8.18	4.54	Limestone	Jahangirnejad et al., 2009
9.16–9.97	5.09–5.54	Florida Ocala Limestone	Tia et al., 2010
9.76–10.44	5.43–5.80	Porous limestone	Alungbe et al., 1992
9.50–10.00	5.3–5.6	Limestone	Khan et al., 1998
10.48–11.05	5.82–6.14	Dense limestone	Alungbe et al., 1992
11.7	6.5	Brooksville limestone (limerock)	Performance Improvement International, 2010

Varying trends in CTE values at later ages have also been observed. Alungbe et al. (1992) measured insignificant change in CTE values of moist-cured, water saturated specimens tested at 28 and 90 days. In contrast, Jahangirnejad et al. (2009) found that concrete CTE values measured at 90, 180, and 365 days were statistically significantly higher than values measured at 28 days for several aggregate types, including limestone. Kim (2012) measured decreasing CTE values between 28 and 120 days for lab-prepared specimens containing granite and dolomite aggregate and for cored concrete pavement specimens containing granite aggregate.

2.7.4.2 Experimental Methods

Several test methods have been developed for determining the CTE of concrete. The most widely used method is AASHTO T 336, which was used by all but one state Department of Transportation (DOT) as recently as 2012 (Tanesi et al., 2012). The Texas Department of Transportation (TxDOT) uses Tex-428-A, a modified version of the AASHTO T 336 procedure based on findings by Won (2005). In an interlaboratory study

conducted by the Federal Highway Administration (FHWA) (Crawford et al., 2010), thirteen of the fifteen research laboratories and universities used AASHTO T 336. The study did not identify the two laboratories that used Tex-428-A, but TxDOT was one of the study participants. In preliminary tests by the FHWA, the precision of an older method by the Army Corps of Engineers, CRD-C 39-81, was found to be lower than that of the AASHTO methods (Tanesi et al., 2010).

Generally, the test methods require the specimens to be submerged in water during the tests, but the moisture content of concrete has been found to influence the measured CTE due to hygrothermal expansion. Meyers (1940) subjected concrete specimens to varying humidity environments and found that the measured CTE of fully dried and fully saturated specimens was lower than that of specimens with intermediate moisture contents. Testing cement paste with $w/c = 0.22$ and 0.4 , Zoldners (1971) measured maximum CTE values when the moisture content was about 65-70% for concrete aged up to 6 months. At these ages, the peak CTE was about double the minimum values at oven-dried or saturated conditions, but this effect would be reduced for concrete due to the aggregate. After 16 years, the CTE peaks decreased in magnitude and shifted to lower moisture contents of about 45-50%.

In order to limit the influence of these hygrothermal effects during testing and improve consistency amongst results (Jahangirnejad et al., 2009), the test methods typically require that specimens be submerged in limewater prior to testing to ensure saturation. For comparison, general descriptions of the three predominant test methods are provided in the following sections; further details are given in the corresponding standards.

2.7.4.2.1 CRD-C 39-81

The U.S. Army Corps of Engineers test method for measuring the CTE of concrete is CRD-C 39-81 (1981). The procedure involves measuring the change in length

of saturated concrete specimens over a temperature range of 5 to 60 °C (40 to 140 °F), though the moisture condition of the specimens and the temperature range of the test can be modified to better suit the conditions of interest. The method details the use of separate isothermal water baths for the two test temperatures, but other methods of heating and cooling the specimens to thermal equilibrium at the test temperatures are also permitted. Various methods of measuring length change, including horizontal length comparators and embedded strain gauges, are permitted.

When testing saturated specimens, they should be submerged in water for at least 48 hours before testing. The initial gauge lengths of the specimens are measured, and the specimens are placed in the heating or cooling environment. Once thermal equilibrium is achieved, the lengths of the specimens are measured. If needed, the specimens can be removed from the thermal environment for measurement, but the readings should be taken promptly to minimize the influence of ambient conditions on the specimens. The specimens are then transferred to the remaining thermal environment, and the final length measurements are taken after thermal equilibrium is achieved. The CTE is then calculated according to Eq. 2.91.

$$\alpha_T = \frac{\Delta L}{L_g \Delta T} \quad \text{Eq. 2.91}$$

Where,

- α_T = coefficient of linear thermal expansion, $\varepsilon/^\circ\text{C}$ ($\varepsilon/^\circ\text{F}$)
- ΔL = length change of specimen, mm (in.)
- L_g = gauge length, mm (in.)
- ΔT = temperature difference between length readings, $^\circ\text{C}$ ($^\circ\text{F}$)

2.7.4.2.2 AASHTO TP 60 and AASHTO T 336

In contrast to CRD-C 39-81, the AASHTO method requires that the specimens be continuously submerged in a water bath that cycles through the specified temperature range of 10 to 50 °C (50 to 122 °F). Each specimen is placed in a submersible fixture that measures the change in length while the specimen is submerged, but the thermal

deformation of the specimen fixture must be accounted for, requiring a calibration specimen with a known CTE. AASHTO TP 60 (AASHTO, 2007) identified 304 stainless steel as a suitable material for calibrating the specimen fixtures and listed the CTE of 304 stainless steel as $17.3 \mu\epsilon/^\circ\text{C}$ ($9.6 \mu\epsilon/^\circ\text{F}$). As a result, many labs used 304 stainless steel and the given CTE value when calibrating the fixtures for the AASHTO TP 60 procedure. All fifteen of the labs participating in the FHWA interlaboratory study on CTE used 304 stainless steel calibration specimens, and all but one used the given CTE value.

The CTE of 304 stainless steel calibration specimens used by FHWA were later measured in accordance with ASTM E228-06 by two independent laboratories. The CTE was found to vary with temperature, and for the 10-to-50- $^\circ\text{C}$ (50-to-122- $^\circ\text{F}$) range of AASHTO TP 60, the measured CTE was approximately $15.8 \mu\epsilon/^\circ\text{C}$ ($8.8 \mu\epsilon/^\circ\text{F}$), about 9% lower than the value stated in AASHTO TP 60 (Tanesi et al., 2010). From a reference temperature of 20 $^\circ\text{C}$ (68 $^\circ\text{F}$), the measured CTE approached the given $17.3\text{-}\mu\epsilon/^\circ\text{C}$ ($9.6\text{-}\mu\epsilon/^\circ\text{F}$) value as the temperature approached 300 $^\circ\text{C}$ (572 $^\circ\text{F}$), well beyond the AASHTO TP 60 test range.

As a result of these findings, an updated test method, AASHTO T 336 (AASHTO, 2009), was approved in 2009 with requirements that calibration specimens be tested by a third-party laboratory for CTE in accordance with ASTM E228 or ASTM E289 over the 10-to-50- $^\circ\text{C}$ (50-to-122- $^\circ\text{F}$) range.

The AASHTO T 336 test is conducted on cylinders or cores with a diameter of 100 mm (4 in.) and sawn to a length of 177.8 ± 2.54 mm (7.0 ± 0.1 in.). Tests are conducted on at least two specimens from each concrete mixture, and the specimens must be submerged in a limewater storage tank at 23 ± 2 $^\circ\text{C}$ (73 ± 4 $^\circ\text{F}$) for at least 48 hours prior to testing and until the weight of the surface-dried specimens increases by less than 0.5% over a 24-hour interval.

The length of each saturated specimen is measured at room temperature, then each specimen is placed in a specimen fixture with a device for measuring length change and placed in the temperature-controlled bath. The bath is cycled from room temperature through the following sequence:

- cooled to 10 °C (50 °F)
- heated to 50 °C (122 °F)
- cooled 10 °C (50 °F)

At each set temperature, once the specimens have reached thermal equilibrium, the temperature of the water and the length of the specimen are recorded. The CTE for each specimen and temperature change segment is calculated according to Eq. 2.91. The heating and cooling segments are repeated until two consecutive CTE measurements for each specimen are within $0.3 \mu\epsilon/^\circ\text{C}$ ($0.2 \mu\epsilon/^\circ\text{F}$), and the CTE for each specimen is reported as the average of the CTE values measured on the final two segments.

2.7.4.2.3 *Tex-428-A*

The Tex-428-A (Texas Department of Transportation, 2011) procedure generally follows the AASHTO T 336 procedure, and with proper programming and data collection, the CTE can be calculated in accordance with both methods during a single test. Whereas the AASHTO T 336 method uses the total change in length of the specimens over the temperature range to determine CTE, the Tex-428-A method uses the average rate of length change with respect to temperature to determine CTE.

The specimens are submerged in a temperature-controlled bath and cycled through the same temperature sequence, but temperature, displacement, and time readings are taken at 1-minute intervals during the entire test. For each specimen, the displacement is plotted as a function of temperature during the heating and cooling segments, and the slopes of the linear regressions of the two segments are used to calculate the CTE for each segment according to Eq. 2.92. Though not stated in Tex-428-

A, the method (Won, 2005) on which Tex-428-A is based excluded from regression analysis the data for temperatures outside the 15-to-45-°C (59-to-113-°F) temperature range because of inconsistent temperature gradients in the specimens outside that range.

$$\alpha_T = \frac{M}{L_g} + C_f \quad \text{Eq. 2.92}$$

Where,

- α_T = coefficient of linear thermal expansion, $\epsilon/^\circ\text{C}$ ($\epsilon/^\circ\text{F}$)
- M = slope of the linear regression, $\text{mm}/^\circ\text{C}$ ($\text{in.}/^\circ\text{F}$)
- L_g = gauge length, mm (in.)
- C_f = correction factor for thermal deformation of specimen fixture, $\epsilon/^\circ\text{C}$ ($\epsilon/^\circ\text{F}$)

Similar to AASHTO T 336, the heating and cooling segments are repeated until two consecutive CTE measurements for each specimen are within $0.5 \mu\epsilon/^\circ\text{C}$ ($0.3 \mu\epsilon/^\circ\text{F}$) of each other, and the CTE for each specimen is taken as the average of the CTE values measured on the final two segments. Unlike AASHTO T 336, however, the heating and cooling segments are also repeated until the CTE values of each specimen are within $0.5 \mu\epsilon/^\circ\text{C}$ ($0.3 \mu\epsilon/^\circ\text{F}$) of each other. The average CTE value of the tested specimens is reported as the final CTE value for the test.

2.7.4.2.4 Test Sequence

In contrast to the AASHTO T 336-11 and Tex-428-A testing sequences, the manual (Pine Instrument Company, 2011) for commercial equipment available for these tests recommends beginning by heating the bath and submerged specimens from room temperature to 50°C (122°F) before proceeding with the first segment of the tests. The initial temperature increase and resulting expansion of the specimen is said to allow the specimens to settle in the fixtures before displacement measurements are recorded during the test segments, potentially reducing the number of test segments required for convergence of results. Since alternating tests segments of heating and cooling are conducted until consecutive CTE values are within tolerance, the selection of the initial

test segment should not impact the results of the AASHTO T 336 and Tex-428-A methods.

CHAPTER 3

INFLUENCE OF MASS CONCRETE THERMAL BEHAVIOR ON DEVELOPMENT OF CONCRETE PROPERTIES

3.1 Introduction

For concrete members with large dimensions, the heat of hydration is generated more quickly at early ages than it is able to escape from the member, resulting in higher temperatures at the center of the member compared to temperatures at the surface. If the temperature difference is large enough, thermal stresses will cause surface cracking that can be detrimental to the durability of the structure.

Another concern regarding the temperature rise in large concrete members is the susceptibility to delayed ettringite formation (DEF). In this form of sulfate attack, the sulfate is present within the cement paste rather than in the environment. Ettringite decomposes at the high temperatures, releasing sulfate ions that are adsorbed by the calcium silicate hydrate of the cement paste (Mehta and Monteiro, 2006). Expansion and potential cracking result when the sulfate is later desorbed and new ettringite is formed. Concrete temperatures exceeding approximately 70 °C (158 °F) have been identified as the critical factor in the occurrence of DEF (Taylor et al., 2001; Gajda, 2007).

The present research investigates the potential that these mass concrete effects contributed to the extensive laminar cracking (delamination) identified in the Crystal River 3 post-tensioned concrete containment building in 2009, after which the nuclear power plant never resumed operation and was permanently shut down in 2013.

3.1.1 Criteria and Restrictions for Mass Concrete

Various definitions of mass concrete have been presented by professional organizations and state departments of transportation (DOTs). *ACI Concrete Terminology* (American Concrete Institute, 2013) defines mass concrete as “any volume of structural concrete in which a combination of dimensions of the member being cast, the boundary conditions, the characteristics of the concrete mixture, and the ambient conditions can lead to undesirable thermal stresses, cracking, deleterious chemical reactions, or reduction in the long-term strength as a result of elevated concrete temperature due to heat from hydration.” ACI 207.2R-07 indicates that concrete members with a minimum dimension of at least 460 mm (18 in.) are generally evaluated for mass concrete effects. For most bridge components, the Florida Department of Transportation (FDOT) *Structures Manual* (2015) requires mass concrete considerations when the minimum dimension of a placement is greater than 914 mm (3 ft) and the volume-to-surface area ratio (V/SA) is greater than 305 mm (1 ft).

ACI 301-10 specifies that the maximum concrete temperature after placement not exceed 70 °C (158 °F) and that the maximum temperature difference in the concrete not exceed 19 °C (35 °F) as measured between the center of mass of the placement and the center of the nearest exterior surface. Gajda and VanGeem (2002) note that project specifications may limit the maximum temperature to as low as 57 °C (135 °F). The maximum temperature limits are generally established in consideration of DEF, which can occur at concrete temperatures greater than 70 °C (158 °F) (Taylor et al., 2001; Gajda, 2007).

Since the cementitious materials content and admixtures influence the rate and extent of heat of hydration, criteria have also been established to control mix designs for mass concrete applications. Gajda (2007) suggested that concrete with cementitious materials content exceeding 355 kg/m³ (600 lb/yd³) of concrete be considered mass concrete, though Tia et al. (2010) note that different cement types generate different

amounts of heat and that concrete typically releases less heat when supplementary cementitious materials (SCMs) are used to replace some portion of the cement (Malhotra and Mehta, 1996). For mass concrete applications, ACI 301-10 specifies the use of moderate- or low-heat hydraulic cement or the use of portland cement with Class F fly ash and/or slag.

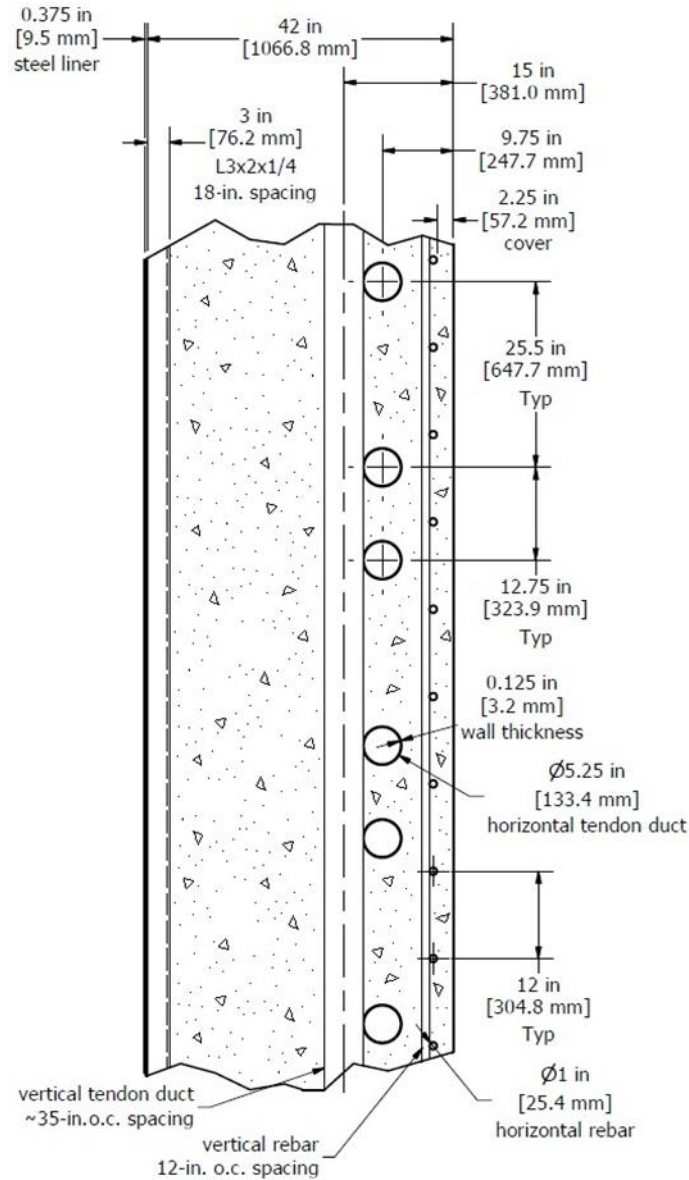
The criteria and restrictions for mass concrete amongst 18 state DOTs tabulated by Tia et al. (2010) vary widely: the minimum dimensions for classification as mass concrete ranged from 0.9 to 2.0 m (3 to 6.5 ft), and the maximum permissible placement temperatures, curing temperatures, and temperature differentials ranged between 18 and 27 °C (65 and 80 °F), 71 and 85 °C (160 to 185 °F), and 15 and 28 °C (27 to 50 °F), respectively.

3.1.2 Crystal River 3 Containment Building

3.1.2.1 Structure

The reactor and steam generators of the Crystal River 3 nuclear power plant are housed in a cylindrical, shallow-domed, post-tensioned concrete containment building (PCC) with an interior steel liner. A representative section of the PCC wall is shown in Figure 3.1. The concrete walls are generally 1.07 m (42 in.) thick and have a 300-by-300-mm (12-by-12-in.) grid of #8 bars located near the outer surface with 57.2 mm (2.25 in.) of concrete cover. Greased, unbonded post-tensioning tendons were housed inside galvanized steel pipes with a 133.4-mm (5.25-in.) outer diameter; the specified minimum inner diameter and wall thickness were 127 and 1.7 mm (5.0 and 0.065 in.), respectively (Gilbert Associates, 1970), and wall thicknesses of 2.0 and 3.2 mm (0.08 and 0.125 in.) have been indicated in post-delamination analysis (Performance Improvement International, 2010).

The circumferential (hoop) tendons are centered at a depth of 248 mm (9.75 in.) from the surface of the wall with on-center spacing alternating between 324 and 647 mm (12.75 and 25.5 in.), and the vertical tendons are centered at a depth of 381 mm (15 in.) with 0.89-m (2.93-ft) on-center spacing, corresponding to an angular spacing of 2.5°. The steel liner is 9.5-mm (0.375-in.) thick, and L3x2x¼ steel angles are stitch welded to the liner at 457-mm (18-in.) spacing to provide stiffness during concrete placement and to anchor the liner to the concrete. Progress Energy (2009) shows that the majority of the concrete pours for the CR3 PCC walls were 3 m (10 ft) high and nominally 6 m (20 ft) long.



Note: Displayed components are not necessarily in the same vertical plane
 Figure 3.1: Typical section of CR3 PCC wall

3.1.2.2 Materials

The primary concrete mix design used in the region of the delamination identified in 2009 is shown in Table 3.1 and was designated as “DM-5-Mod.” The cement content of 405 kg/m³ (682 lb/yd³) of concrete is relatively high, exceeding by 14% the 355-kg/m³ (600-lb/yd³) guideline from Gajda (2007) for consideration as mass concrete. The concrete was designed for a specified minimum 28-day compressive strength of 34.5

MPa (5000 psi) using ASTM C150-67 Type II cement with moderate heat of hydration and no pozzolanic admixtures (Gilbert Associates, 1968). Table 2 gives the ASTM C150-67 limits that are unique for Type II cement with moderate heat of hydration along with the modern ASTM C150-11 limits applicable to the cement used in the present experimental work. Additionally, ASTM C150-67 required a minimum average Blaine fineness of 280 m²/kg (152 yd²/lb) for Type II cement, and the project specifications required a maximum fineness of 400 m²/kg (217 yd²/lb) (Gardner, 1974).

Table 3.1: Primary concrete mix design (saturated-surface dry) used in delaminated region of the CR3 PCC (Performance Improvement International, 2010)

Material	Measure per unit volume concrete	
	Mass (kg/m ³)	Weight (lb/yd ³)
Water	164	276
Cement	405	682
Coarse aggregate	1068	1800
Fine aggregate	653	1100
	Volume (mL/m ³)	Volume (fl. oz./yd ³)
Water reducer/retarder	812	21.0
Air entrainer	182	4.7

Table 3.2: ASTM C150 limits for Type II cement with moderate heat of hydration

ASTM Standard	Chemical Requirements (%)						Heat of hydration, ¹ (J/g)	
	SiO ₂ , min	Al ₂ O ₃ , max	Fe ₂ O ₃ , max	C ₃ A, max	C ₃ S + C ₃ A, max	C ₃ S + 4.75C ₃ A, max	7 days, max	28 days, max
C150-67	21.0	6.0	6.0	8	58	-	293	335
C150-11	-	6.0	6.0 ²	8	-	100 ²	290	-

¹These limits only apply if specifically requested

²Does not apply when heat of hydration limit is specified

The project specifications did not indicate a minimum tensile strength, but design documents used the relationship shown in Eq. 3.1 to determine an allowable tensile stress of 1.5 MPa (212 psi) for concrete with a 28-day compressive strength of 5000 psi

(Performance Improvement International, 2010). A 0.405 maximum water-to-cement ratio (w/c) was specified, and a report by Performance Improvement International (2010) on the delamination identified in 2009 states that the average w/c of the containment concrete was 0.41.

$$\begin{aligned} f_{tsp} &= 0.25\sqrt{f'_c} \quad [\text{MPa}] \\ f_{tsp} &= 3\sqrt{f'_c} \quad [\text{psi}] \end{aligned} \quad \text{Eq. 3.1}$$

Where,

$$\begin{aligned} f'_t &= \text{allowable tensile stress in concrete, MPa or psi} \\ f'_c &= \text{compressive strength of concrete, MPa or psi} \end{aligned}$$

Table 3.3 presents the composition of the cement used for the CR3 PCC as reported in 1974, and the Blaine fineness of the cement was determined to be 401 m²/kg (218 yd²/lb) (Gardner, 1974). Though the cement was slightly finer than specified, it was deemed acceptable for use. The sulfate-to-aluminate molar ratio (SO₃/Al₂O₃) was 0.69, greater than the 0.45 value above which cement has been found to be susceptible to DEF (Heinz et al., 1999).

Based on the composition, the total heat of complete hydration of the cement was determined to be 436 J/g (188 Btu/lb) of cement using Eq.7 in Section 2.6.1. Natural sand with a fineness modulus (FM) of 2.2 to 2.7 was used as the fine aggregate, and local Brooksville limestone (limerock) was used as the coarse aggregate with a specified maximum size of aggregate (MSA) of 19 mm (0.75 in.). Petrography studies identified the coarse aggregate as an calcareous, oolitic limestone (Naus, 2009), and investigations by Moreadith and Pages (1983) and Performance Improvement International (2010) into the properties of the containment concrete found the aggregate to be gap graded with high levels of soft particles and high porosity. Darex AEA, an air-entraining admixture (AEA) conforming to ASTM C260 (2011), was used to obtain a specified total air content of 3 to 6% by volume (Gilbert Associates, 1971), and Daratard HCF, an ASTM C494 (2013)

Type D water-reducing and retarding admixture (WRRET), was added at a dosage rate of 200 mL/100 kg (3.08 fl.oz./100 lb) cement (Gilbert Associates, 1968).

Table 3.3: Oxide analysis and phase composition of CR3 PCC cement (Gardner, 1974)

Oxide Analysis and Phase Composition (percent by mass)										
SiO ₂	Al ₂ O ₃	Fe ₂ O ₃	CaO*	MgO	SO ₃	LOI	C ₃ S	C ₂ S	C ₃ A	C ₄ AF
22.45	4.42	2.93	63.97	1.09	2.52	1.80	48.8	27.6	6.8	8.9

*CaO content was back-calculated from the reported C₃S content

Three pour cards for the concrete mix shown in Table 3.1 indicate that ice was substituted for 12 to 19% of the total water content by mass (McGillivray, 1973), and the recorded range of concrete temperatures during placement was 10 to 16 °C (50 to 60 °F) (Performance Improvement International, 2010), below the specified maximum temperature of 21 °C (70 °F) (Gilbert Associates, 1968). The concrete was to be continuously sprinkled and ponded for at least 7 days with an ambient temperature no less than 10 °C (50 °F), and the procedures for concrete curing and form removal for the CR3 PCC specified that forms be kept in place for at least 1 day or that a concrete compressive strength of at least 500 psi be developed prior to formwork removal (McGillivray, 1973). The record for the uppermost region of the delamination, where a concrete mix different from that shown in Table 3.1 was used, indicates that the formwork was still in place 9 days after concrete placement (McGillivray, 1973).

3.1.2.3 Properties

Sets of 150-by-300-mm (6-by-12-in.) cylinders were prepared from each batch of concrete and standard-cured in accordance with ASTM C31-69 (1969) to be tested for acceptance and quality control. Based on tests of pairs of these cylinders for the mix shown in Table 3.1, the average compressive strength of the concrete at 7, 28, and 90 days was 31.6, 41.6, and 46.6 MPa (4,581, 6,029, and 6,756 psi), respectively, with 64

cylinders reported for both 7 and 28 days and 63 cylinders reported for 90 days (Performance Improvement International, 2010). Since factors such as the consolidation and curing temperature of the in-place concrete are not necessarily consistent with the standard-cured specimens, these strengths serve as indicators of the potential strength of the concrete rather than the actual strength of the in-place strength (Neville, 2001).

Post-delamination cores were tested to evaluate the mechanical properties of the concrete when the delamination was identified, approximately 36 years after concrete placement. The diameter of the tested cores was 102 mm (4 in.), and since no ACI 214.4R-03 correction factors were applied, the lengths of the cores were likely between 178 and 213 mm (7 and 8.4 in.) to conform with the 1.75-to-2.1 range of length-to-diameter ratio (L/D) values permitted by ASTM C42-04 (2004). The average density of the cores was 2515 kg/m³ (157 lb/ft³), and the average of 13 reported percent void values was 15.0% (Performance Improvement International, 2010).

The average compressive strength f_c of all cores was 50.9 MPa (7,385 psi), well above the design strength of 34.5 MPa (5000 psi). The average compressive strength reported for 18 core specimens taken from regions of the PCC with the mix shown in Table 3.1 was 53.1 MPa (7707 psi) with a standard deviation of 4.4 MPa (634 psi). This average strength is slightly higher than that of all cores.

Table 3.4 presents the previously discussed compressive strength development of the CR3 PCC concrete specimens and the relative strength at each age. For comparison, Table 3.5 presents the compressive strength development of concrete made with Type II cement at a content of 335 kg/m³ (564 lb/yd³) of concrete and an MSA of 38 mm (1.5-in.) (U.S. Bureau of Reclamation, 1981). The tests were conducted on 150-by-300-mm (6-by-12-in.) cylinder specimens that were moist-cured at 21 °C (70 °F) until testing.

At each age, the CR3 PCC specimens have greater strengths than the reference specimens, likely due to the greater cement content of the CR3 PCC concrete. The 7-day strength of the CR3 PCC specimens is also a higher percentage of the late-age strength

than that of the reference specimens, indicating that the CR3 PCC concrete exhibited relatively rapid early-age strength gain and slower late-age strength gain. Beyond the first 7 days, the relative strength gain of the CR3 PCC specimens is approximately half that of the reference specimens. For example, the relative strength gain between 28 and 90 days for the CR3 PCC specimens was 12 %, approximately half the corresponding 25% gain for the reference specimens. Comparing the relative strength gain for the 7-, 28-, and 90-day results, as well as the 36-year cores for CR3 and the 5-year specimens for the reference concrete, the rate of strength gain for the CR3 PCC specimens varied between 45% and 53% of that of the reference specimens. The only exception was the relative strength gain between 90 days and the 36-year cores for CR3 and between 90 days and 5 years for the reference specimens, for which the CR3 rate was about 64% of the reference specimens.

This difference may have been due to the significantly longer time period over which the cores were able to develop strength. Additionally, 100-by-200-mm (4-by-8-in.) cylinders, with the same diameter as the cores, have been shown to have strengths up to 5% greater than corresponding 150-by-300-mm (6-by-12-in.) cylinders, though for strengths between 20 and 60 MPa (2900 and 8700 psi) the difference can reasonably be neglected (Day, 1994). In contrast, ASTM C42-13 (2013) states that the compressive strength of cores tends to be less than that of corresponding standard-cured cylinders of the same age and notes that there is no uniform relationship between the compressive strength of the two specimens types. A factor of 1.06 is often applied to core strengths to account for anticipated strength reductions due to damage occurring during the drilling process (ACI 214.4R-03), though no factor was applied to the reported core results. Furthermore, ACI 318-08 permits compressive strength results of core tests to indicate satisfactory in-place concrete ACI 318-08 permits compressive strength results of core tests to indicate satisfactory in-place concrete “if the average of three cores is at least 85 percent of f'_c and if no single core is less than 75 percent of f'_c .” Performance

Improvement International (2010) also notes that the 4.37-MPa (634-psi) standard deviation of the cores indicates a relatively wide spread of the measured cores strengths, likely due to variations in the concrete batches, varying orientation of the cores, and environmental exposure of the different regions of the structures from which the cores were taken. With all of these factors, it is difficult to directly compare the core results with those of the standard-cured specimens from CR3 and with those in Table 3.5.

Table 3.4: Compressive strength development of CR3 PCC concrete specimens

Age	Compressive Strength, f_c (psi)	Relative Compressive Strength (%)			
		f_c/f_{c-7}	f_c/f_{c-28}	f_c/f_{c-90}	$f_c/f_{c-cores}$
7 days	4581	100	76	68	59
28 days	6029	132	100	89	78
90 days	6756	147	112	100	88
36 years (cores)	7707	168	128	114	100

Table 3.5: Compressive strength development of concrete made with Type II cement (U.S. Bureau of Reclamation, 1981)

Age		f_c (psi)	Relative Compressive Strength (%)			
(days)	(years)		f_c/f_{c-7}	f_c/f_{c-28}	f_c/f_{c-90}	$f_c/f_{c-5years}$
7	-	2550	100	61	49	40
14	-	3400	133	81	65	53
28	-	4200	165	100	80	66
90	-	5250	206	125	100	82
180	-	5650	222	135	108	88
365	1	5950	233	142	113	93
730	2	6200	243	148	118	97
1825	5	6400	251	152	122	100

The average splitting tensile strength f_{tsp} measured for all cores was 4.14 MPa (600 psi), well above the allowable tensile stress of 1.5 MPa (212 psi) determined via Eq. 3.1 (Performance Improvement International, 2010). The average splitting tensile strength reported for 10 core specimens taken from regions of the PCC with the mix

shown in Table 3.1 was 4.1 MPa (594 psi) with a standard deviation of 0.4 MPa (59 psi). This average splitting tensile strength is slightly less than that of all cores.

The average direct tensile strength f_t of all tested core specimens was 3.12 MPa (453 psi), and the average value for 3 core specimens taken from a region of the PCC with concrete mix design DM-5-Mod was 3.15 MPa (457 psi) (Performance Improvement International, 2010). In both cases, the direct tensile strengths are approximately 75% of the corresponding splitting tensile strengths. Per Neville (2011), direct tensile strength tends to be about 89 to 95% of the splitting tensile strength; the lower direct tensile strength of the cores was attributed to the soft and highly porous aggregate, to which the direct tensile strength is more sensitive (Performance Improvement International, 2010). However, the average measured direct tensile strength of cores from bay 34 was approximately 10% lower than that of cores from an adjacent bay and bay 61 (Performance Improvement International, 2010). The 10% decrease in tensile strength matches the 10% standard deviation for the entire population of measurements.

The average modulus of elasticity E_c of 22 tested cores was 23.8 GPa (3,450 ksi), but the average Poisson's ratio ν for all tested cores was not available from Performance Improvement International (2010). The average modulus of elasticity of 12 core specimens taken from a region of bay 61 (opposite bay 34) with the mix shown in Table 3.1 was 24.7 GPa (3,579 ksi) with a standard deviation of 2.1 GPa (302 ksi), and the average Poisson's ratio of the 12 cores was 0.18 with a standard deviation of 0.02. An average modulus of elasticity of 26.9 GPa (3,900 ksi) and Poisson's ratio of 0.24 were reported for cores from an area of the SGR opening for which the mix shown in Table 3.1 was used, but the number of specimens included in the average was not identified. The 0.24 Poisson's ratio is well above the typical range of 0.15 to 0.20 for concrete (Mehta and Monteiro, 2006), but no additional information was provided. Whereas the modulus

of elasticity increases with time, Poisson's ratio has been shown to be independent of curing conditions and age (Higginson, 1961; Oluokun et al, 1991).

The coefficient of thermal expansion (CTE) of the CR3 PCC concrete was determined to be $11.7 \mu\epsilon/^\circ\text{C}$ ($6.5 \mu\epsilon/^\circ\text{F}$), and thermal conductivity values of $1.73 \text{ W/m}\cdot\text{K}$ ($1.00 \text{ Btu/hr}\cdot\text{ft}\cdot^\circ\text{F}$) and $43 \text{ W/m}\cdot\text{K}$ ($25 \text{ Btu/hr}\cdot\text{ft}^2\cdot^\circ\text{F}$) were identified for concrete and steel, respectively (Performance Improvement International, 2010). However, these CTE and thermal conductivity values are outside of typical ranges for concrete with limestone aggregate, and the source or method of determining these values was not stated. Additionally, 0.75 was used as a conservative estimate of the degree of restraint K_r for mid-thickness concrete in regions of the bays away from the buttresses (Performance Improvement International, 2010).

3.1.2.4 Post-Tensioning

According to concrete pour data for bays 12 and 34 of the CR3 PCC and a diagram of the pour locations (Performance Improvement International, 2010), the final primary concrete pour for the PCC walls was on March 3, 1973, at the top of bay 12. Serhan and Adler (1997) documented the original sequence of tendon tensioning for the CR3 PCC and indicated that post-tensioning began on August 30, 1974, approximately 16 months after the final concrete pour for the PCC walls. The 16-month delay was likely due to the construction timeline rather than consideration of concrete strength gain; as shown in Table 3.4, the CR3 PCC concrete had an average 28-day strength of 5752 psi, 15% greater than the 5000-psi specified strength. Serhan and Adler (1997) indicated that, except for four tendons that had to be retensioned, tensioning of the vertical tendons of the CR3 PCC was completed before tensioning of the horizontal tendons began.

As part of the SGR opening process for the CR3 PCC, the tendons in the region of the SGR opening were detensioned. The two vertical tendons at the center of the opening were removed first, then two more vertical tendons were removed (Performance

Improvement International, 2010). The final four tendons to be removed were horizontal tendons, but the sequence of removing the other tendons has not been identified.

3.2 Objective

The CR3 PCC design meets many of the previously described criteria for mass concrete considerations. The 1.07-m (42-in.) thickness exceeds the ACI guidelines and FDOT requirement for minimum cross-sectional dimension, and the V/SA for a typical pour was calculated in Appendix A.1 to be 351 mm (13.8 in.), exceeding the FDOT limit. Furthermore, the cement content of 405 kg/m³ (682 lb/yd³) of concrete exceeds by 14% the guidelines of ACI 301-05 and Gajda for consideration as mass concrete. Despite these factors, analysis that was conducted following the identification of the PCC delamination in 2009 did not thoroughly account for the effects of mass concrete behavior on the early-age behavior and property development of the concrete.

This research investigated the thermal behavior of the CR3 PCC at early ages via temperature and strain monitoring of full-scale mock-ups of a portion of the CR3 PCC. The influence of that behavior on the development of the concrete properties was investigated by experimental determination of mechanical and thermal properties of specimens cured in accordance with ASTM C192-13a at 23 ± 2 °C (73.5 ± 3.5 °F) and two sets of specimens match-cured with the temperature of the mock-up concrete. These results were incorporated into analysis of the mock-up strains to identify potential cracking.

3.3 Experimental Work

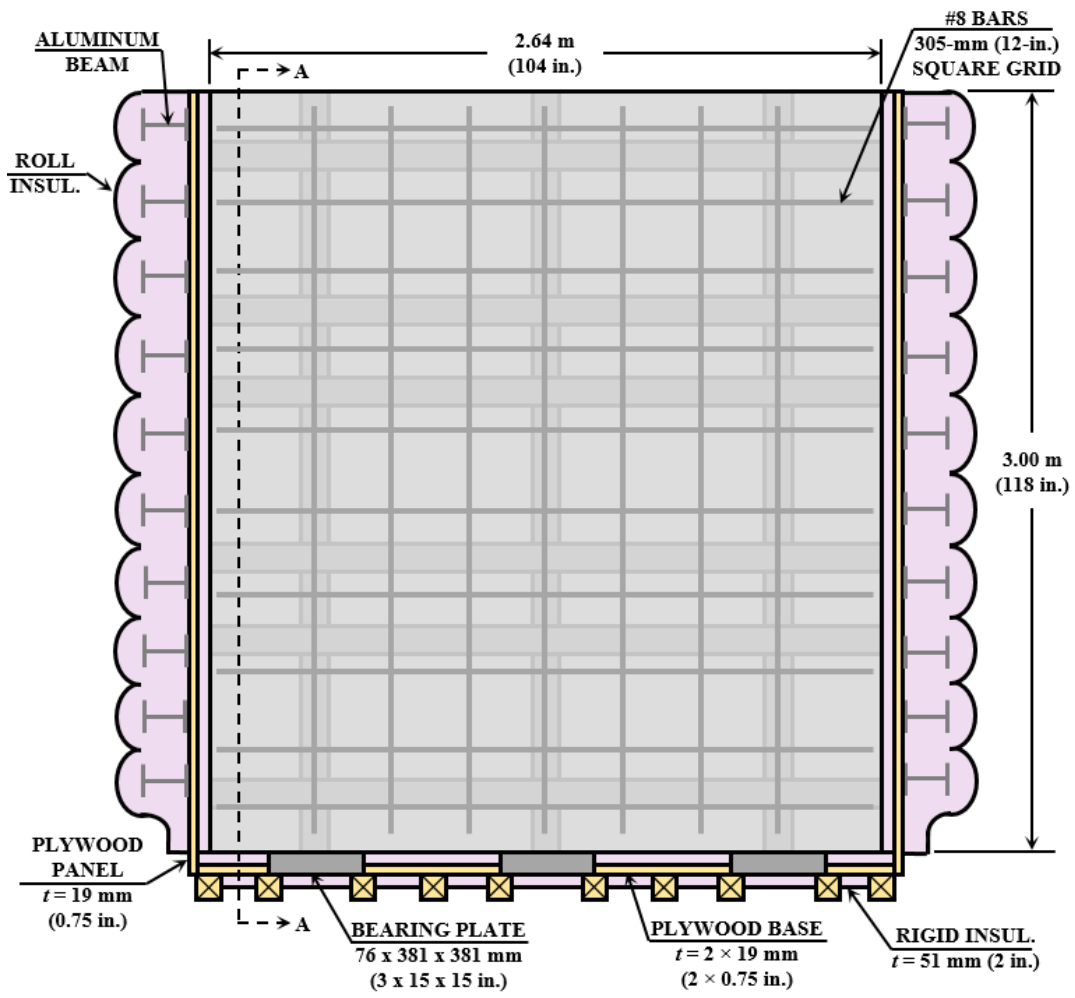
The following sections discuss the experimental approach for investigation of the mass concrete behavior of the CR3 PCC. Details are provided on the full-scale mock-ups of the CR3 PCC, the materials used in the experimental work, and the tests for characterization of the properties of the mock-up concrete.

3.3.1 Mock-Ups

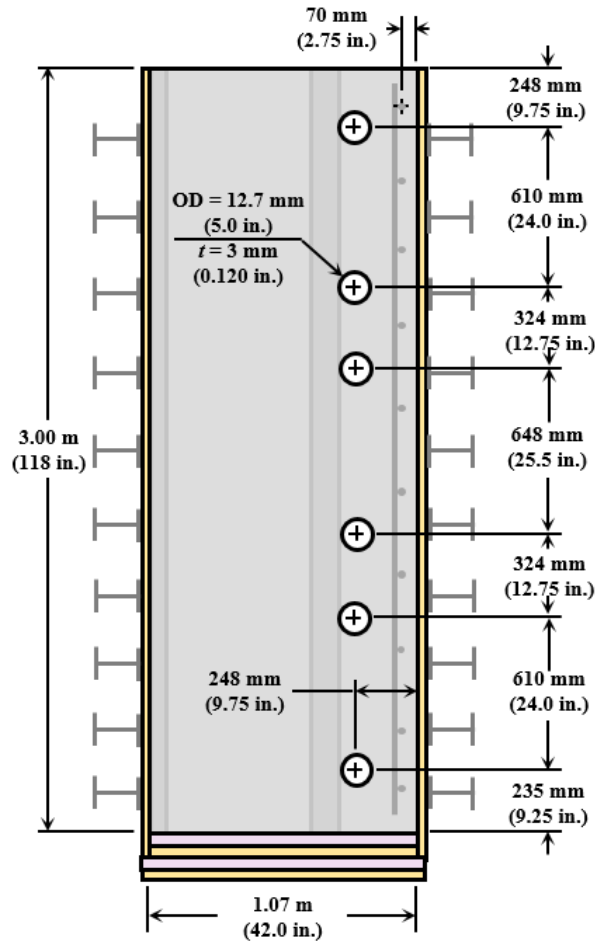
In order to investigate the mass concrete behavior of a representative CR3 PCC pour, two full-scale planar mock-ups of a portion of the PCC were constructed and monitored with strain and temperature gauges. The mock-ups were prepared and kept in a facility exposed to ambient temperatures and humidity with brief daily exposure to direct sunlight. Plan, front elevation, and section drawings of the mock-ups as cast and cured are shown in Figure 3.2, Figure 3.3, and Figure 3.4, respectively. The mock-ups maintain the 1.07-m (42-in.) wall thickness of the CR3 PCC, and the 3.00-m (118-in.) height of the mock-ups is comparable to the 3.05-m (10-ft) height of typical CR3 PCC pours. The 2.64-m (104-in.) length of the mock-ups is slightly less than half the 6-m (20-ft) length of typical CR3 PCC pours.

The mock-ups contain six horizontal and three vertical post-tensioning ducts with representative spacing. With an outer diameter of 12.7 mm (5.0 in.) and wall thickness of 3 mm (0.120 in.), the welded carbon steel tubes used for the post-tensioning ducts in the mock-ups are slightly smaller than and of comparable thickness to those used in the CR3 PCC. Due to the smaller diameter, the vertical ducts were shifted 6 mm (0.25 in.) towards the front of the mock-ups to maintain contact with the horizontal ducts as in the CR3 PCC. A nominal 300-by-300-mm (12-by-12-in.) grid of #8 bars is located near front face of the mock-ups with 57.2 mm (2.25 in.) of concrete cover; due to post-tensioning reinforcement at the ends of the mock-ups, the actual spacing of the #8 bars varies. The A36 steel plate at the back of the mock-ups with stitch-welded L3x2x¼ steel angles at 457-mm (18-in.) spacing is representative of the CR3 PCC liner.

In order to thermally simulate a longer wall, 50-mm-thick (2-in.-thick) polystyrene rigid foam insulation with an R-value of 1.7 m²·K/W (10 ft²·°F·hr/Btu) was attached to the interior of the left and right ends of the formwork, and 165-mm-thick (6.25-in.-thick) paper-faced fiberglass roll insulation with an R-value of 3.3 m²·K/W (19



Note: Post-tensioning anchorage reinforcement is not shown
 Figure 3.3: Front elevation drawing of mock-ups as cast and cured



Note: Post-tensioning anchorage reinforcement not shown
 Figure 3.4: Section A-A (see Figure 3.3) drawing of mock-ups as cast and cured

The location and orientation of 153-mm (6-in.) vibrating wire strain gauges and temperature gauges in the mock-ups are shown in Figure 3.5 and Figure 3.6. Each low-modulus strain gauge had a nominal range of $3000 \mu\epsilon$ and contained a thermistor to measure temperature at the center of the gauge length. The CTE of the gauges was $12.2 \mu\epsilon/^\circ\text{C}$ ($6.78 \mu\epsilon/^\circ\text{F}$) and was used to correct for thermal strain of the gauges themselves. Twelve series of six transverse gauges, arranged in three rows and four columns in the front elevation of the mock-ups (Figure 3.5c), allowed measurement of strain and temperature profiles through the thickness of the mock-ups. The vertical and horizontal

gauges parallel with the post-tensioning ducts allowed comparison of the post-tensioning strains with expected values for the applied post-tensioning loads.

Temperature gauges were located at depths of 51 and 127 mm (2 and 5 in.) from the front face of the mock-ups and 76 and 127 mm (3 and 5 in.) from the steel liner at the back side of the mock-ups for of the series of transverse gauges. These gauges were used to determine the degree of restraint K_r , defined by ACI 207.2R-07 as “the ratio of actual stress resulting from volume change to the stress that would result if completely restrained.” In accordance with ACI 301-10, a temperature probe was located at a depth of 51 mm (2 in.) from the center of the front face of the mock-ups, and a second probe was located at the center of mass of the mock-ups, 533 mm (21 in.) from the front face. In addition to recording temperature at these locations for determining the maximum temperature difference in the mock-up concrete, each of these probes was connected to a match-curing tank containing standard cylinder specimens prepared from the same concrete as the mock-ups.

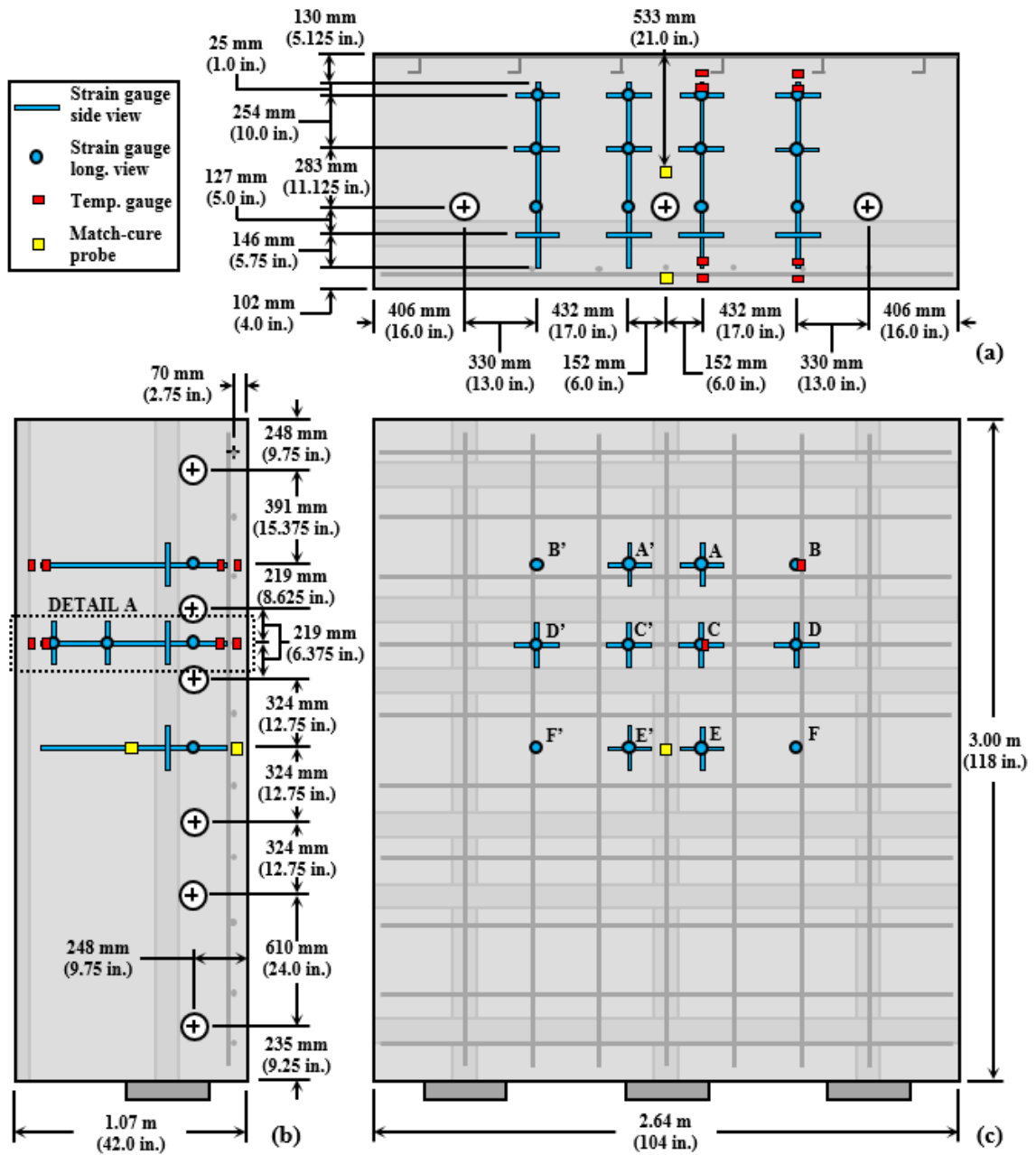


Figure 3.5: Drawings of gauge location and orientation: (a) plan, (b) side elevation, (c) front elevation

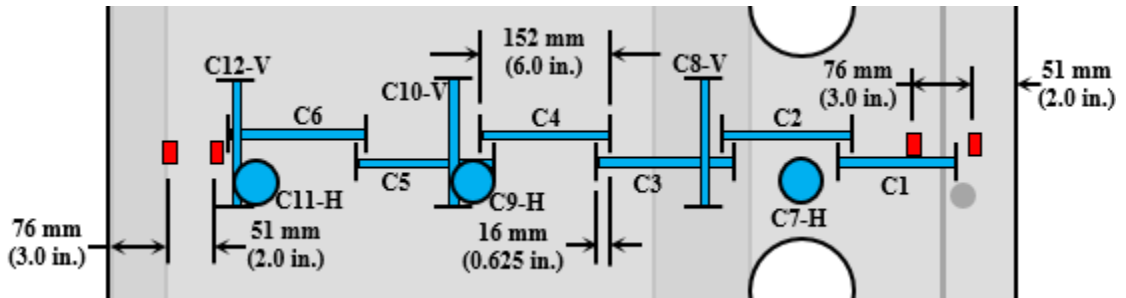


Figure 3.6: Detail A (see Figure 3.5) of series of transverse gauges

3.3.2 Post-Tensioning

The mock-ups were post-tensioned using 75-mm (3-in.) threaded post-tensioning rods with an ultimate tensile strength of 1030 MPa (150 ksi) and a guaranteed ultimate tensile strength (GUTS) of 7088 MPa (1028 kips). Details of the anchorage system for the threaded rods are shown in Figure 3.7. Load cells with nominal 76-mm (3-in.) lengths were fabricated from seamless, hot-rolled 4140/4142 annealed steel tubing with an outer diameter of 152 mm (6 in.) and a wall thickness of 32 mm (1.25 in.). With a cross-sectional area of $1.21 \times 10^4 \text{ mm}^2$ (18.7 in²) and a yield stress f_y of 413 MPa (60 ksi), the yield capacity of each load cell was 4980 kN (1120 kips). Therefore, for a 3600-kN (800-kip) load, the applied longitudinal stress was 296 MPa (43 ksi) or $0.72f_y$.

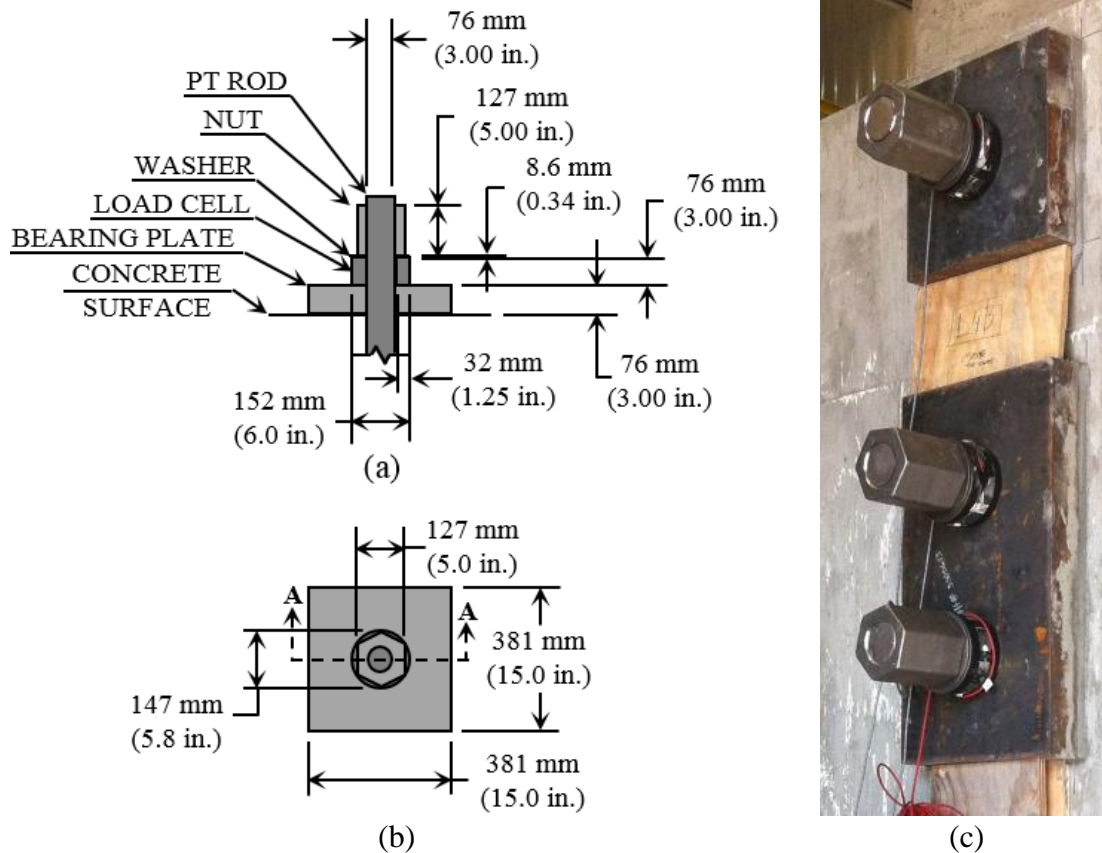
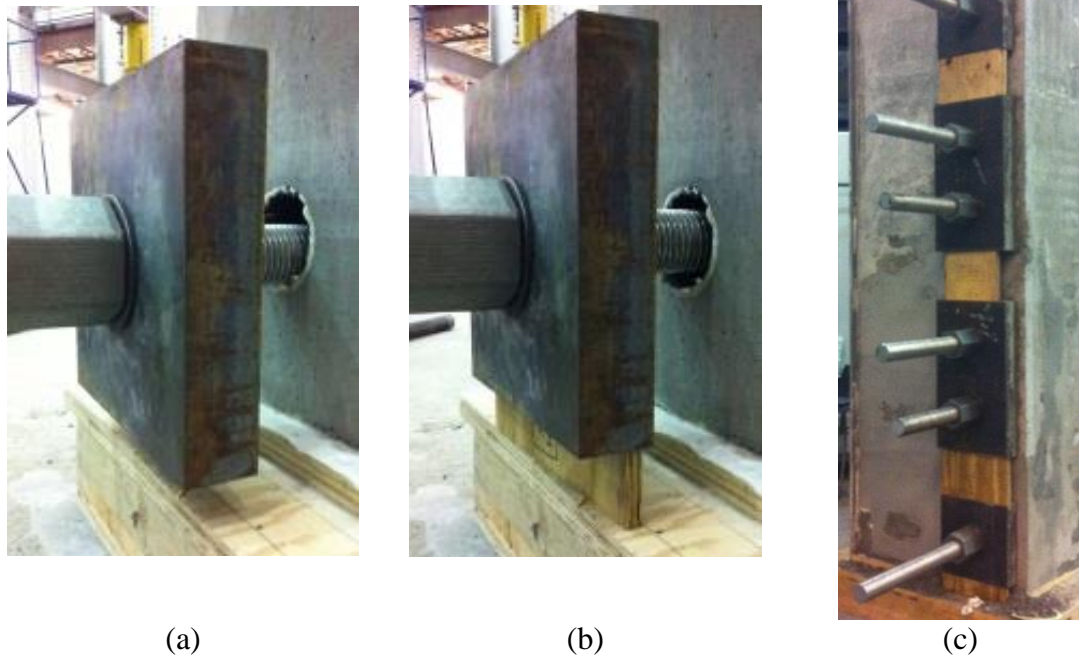


Figure 3.7: Post-tensioning anchorage system (a) Section A-A, (b) elevation, and (c) picture

The A36 steel bearing plates used for the mock-up were 76 mm (3 in.) thick. The plates for the three vertical rods and the top and bottom horizontal rods were 381-mm (15-in.) squares. Due to the 324-mm (12.75-in.) spacing of the pairs of remaining rods, four 406-by-730-mm (16-in.-by-28.75-in.) two-hole plates spanning the paired rods were used for the remaining rods. In order to center the horizontal post-tensioning rods within the ducts and reduce the likelihood of friction losses along the length of the rod, plywood spacers were used to support the bearing plates as they were tightened against the concrete wall as shown in Figure 3.8.



(a) (b) (c)
 Figure 3.8: (a) Post-tensioning rod resting on duct embedded in concrete, (b) plywood spacer beneath bearing plate lifting rod to center of duct, and (c) full stack of plates and plywood spacers against the concrete

As shown in Figure 3.3, the concrete for the main block of the mock-up was cast directly onto the three bottom bearing plates of the vertical post-tensioning rods. The remaining eleven bearing plates were placed after formwork removal, and a non-shrink, cementitious grout was used to ensure uniform and level bearing between the plates and the concrete. The grout was mixed with a handheld drill and paddle mixer attachment and had a 0.12 water-to-grout mass ratio with a dry-pack consistency.

The grout was applied to the concrete surface behind the bearing plate, the plates were hammered against the grout to flatten the grout surface, and the nuts were tightened to ensure that the plates were perpendicular to the rods. The bearing plates at each end of each horizontal rod or pair of rods were grouted simultaneously. Figure 3.9 shows the grouting sequence for the top bearing plate for one of the vertical rods.

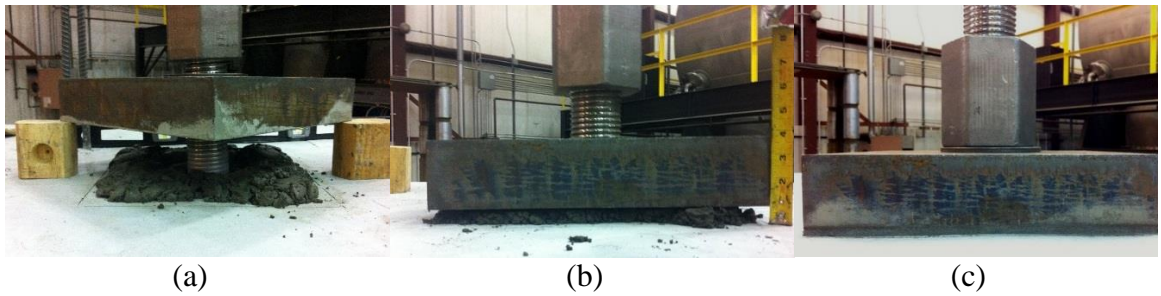


Figure 3.9: (a) Fresh grout placed on concrete surface beneath bearing plate, (b) bearing plate lowered onto grout, and (c) finished grout after hammering bearing plate and tightening nut

As shown in Table 3.6, the measured flow of the grout was 33% as tested in accordance with ASTM C1437-13, except that the flow was measured after 5 drops of the flow table in 3 seconds in accordance with ASTM C1107-14. The least flowable grout consistency defined by ASTM C1107-14 is plastic consistency, which is classified by a flow of 100 to 125%, so the grout used for the bearing plates could be considered non-plastic. Since ASTM C1107-14 does not specify a sample preparation procedure for compressive strength of non-plastic grouts, the grout was prepared and tested in accordance with ASTM C109-13 with appropriate modifications prescribed in ASTM C1107-14 for plastic grouts, to which the tested grout was most similar. The results from six 2-inch cube specimens tested for compressive strength at 28 days, the age at which post-tensioning began, are shown in Table 3.7. The average compressive strength of the specimens was 12,610 psi.

Table 3.6: Results of flow test for cementitious grout used for bearing plates

Reading	Base Diameter		Flow
	(in)	(mm)	
1	5.229	132.82	31%
2	5.389	136.87	35%
3	5.352	135.94	34%
4	5.246	133.26	31%
Average	5.304	134.72	33%
St. Dev.	0.078	1.99	2%

Table 3.7: Results of compression tests on cementitious grout specimens

Specimen	Ultimate Load (kips)	Compressive Strength (psi)
1	51.84	12,960
2	48.48	12,120
3	52.40	13,100
4	47.60	11,900
5	51.44	12,860
6	50.88	12,720
Average	50.44	12,610
St. Dev.	1.94	486

The post-tensioning and detensioning sequences for the mock-ups are illustrated in Figure 3.10 and were based on the original sequence of tendon tensioning for the CR3 PCC in the center region of the SGR opening and the detensioning sequence for preparation of the SGR opening (Serhan and Adler, 1997). During tensioning and detensioning, load cell readings were taken every 10 seconds and gauge readings were taken every 30 seconds.

Each rod was jacked in five steps of approximately 600 kN (135 kips) each followed by a final step of approximately 890 kN (200 kips) so that the rods could be locked off at approximately 3600 kN (800 kips), as shown in Figure 3.11. Before locking off each rod, the nut at the end with the jack was tightened using a wrench and mallet in order to minimize the seating losses. The horizontal rods were tensioned approximately 55 hours after the vertical rods, and the mock-up was fully post-tensioned for approximately 7.5 days before complete detensioning.

The 75-mm (3-in.) rods used for post-tensioning the mock-up were the largest available. Multi-strand systems with larger capacities were considered, but due to the relatively short 2.64-m (104-in.) horizontal post-tensioning length, the expected 6-mm (0.25-in.) wedge seating would have resulted in a loss of approximately 1350 kN (300 kips), making the post-tensioning rods a more effective approach.

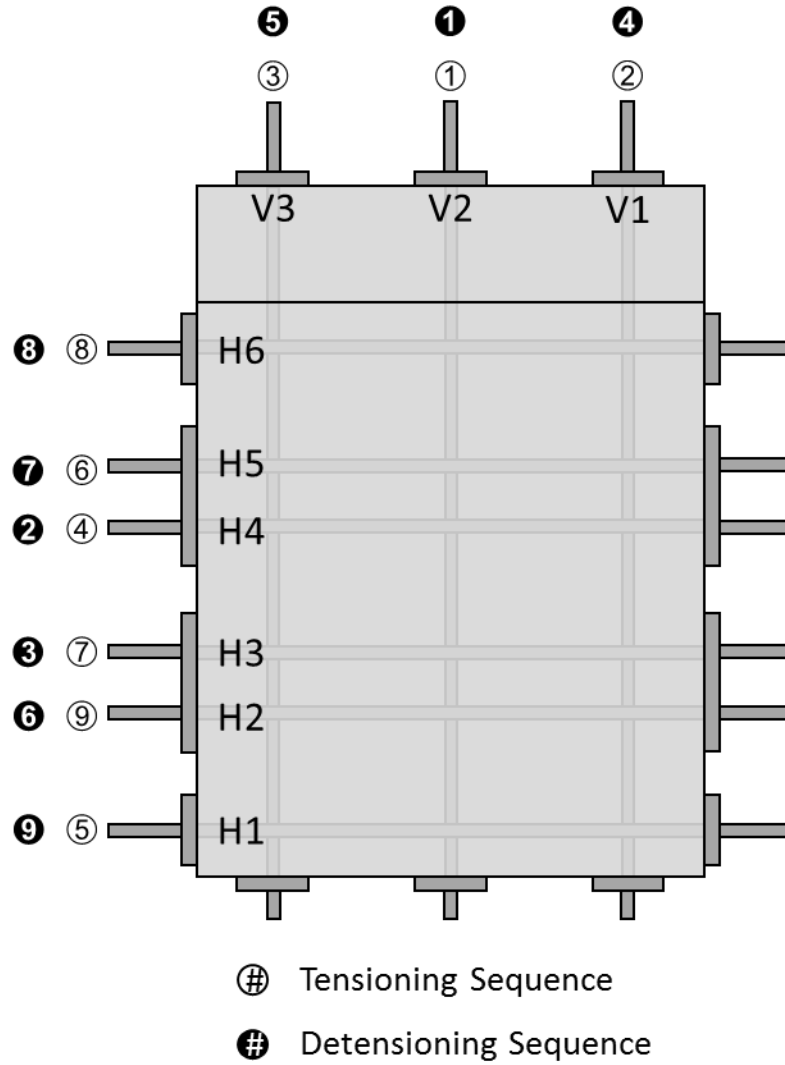


Figure 3.10: Identification of post-tensioning rods and post-tensioning and detensioning sequences

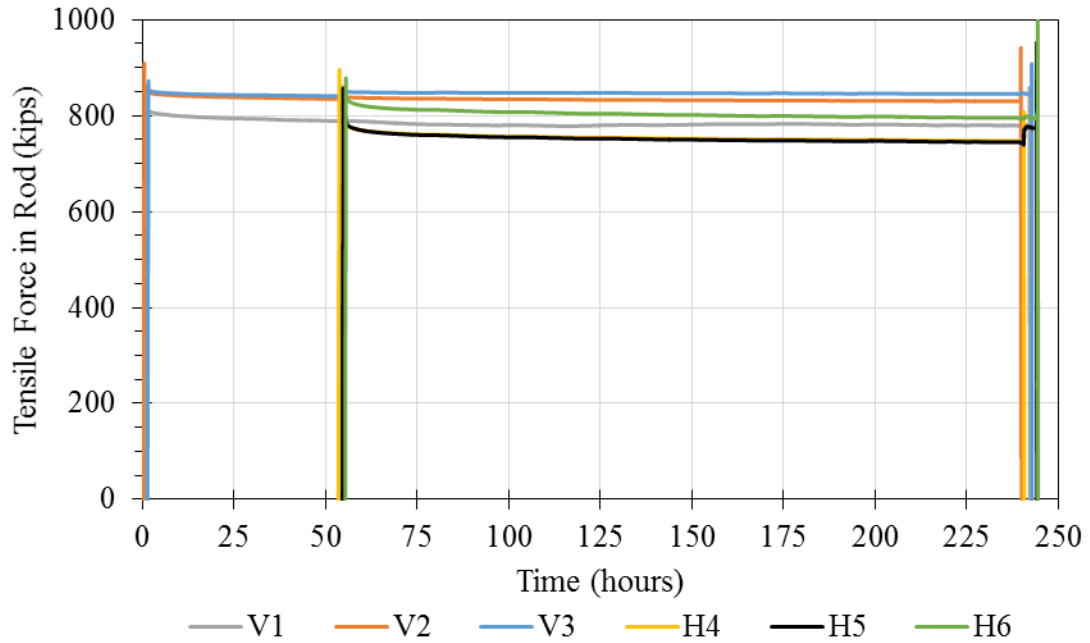


Figure 3.11: Tensile forces in post-tensioning rods

3.3.3 Materials

In order to represent the CR3 PCC concrete, the mix design shown in Table 3.1 was used for the mock-up concrete. The w/c was 0.40 with a specified slump of 72 to 127 mm (3 to 5 in.) and a specified minimum 28-day compressive strength of 34.5 MPa (5000 psi). As discussed in the following sections, materials were selected to match those used in the CR3 PCC.

The slumps of the concrete from the two trucks for the first mock-up were determined to be 102 and 108 mm (4.0 and 4.25 in.) in accordance with ASTM C143-12 (2012), and the slumps for the second mock-up were determined to be 121 and 133 mm (4.75 and 5.25 in.). The density (unit weight) of the concrete from the first truck for the second mock-up was determined to be 2,276 kg/m³ (142.1 lb/ft³) in accordance with ASTM C138-12 (2012).

3.3.3.1 Cement

The cement used for the mock-ups was an ASTM C150-11 Type I/II low-alkali (LA) cement from the Buzzi Unicem USA plant in Chattanooga, Tennessee. Though not indicated by the producers, the cement also met the standard composition and physical requirements of ASTM C150-11 listed in Table 3.2 for Type II moderate heat of hydration (MH) cement. Table 3.8 presents the oxide analysis results as determined by chemical analysis in accordance with ASTM C114-11b (2011) and the phase composition as determined by Bogue calculations in accordance with ASTM C150-11 and by Rietveld analysis in accordance with ASTM C1365-06 (2012). Based on the composition, the total heat of complete hydration of the cement was determined to be 465 J/g (200 Btu/lb) of cement using Eq.7 in Section 2.6.1, 29 J/g (12 Btu/lb) greater than that of the CR3 PCC cement. The Blaine fineness of the cement was determined in accordance with ASTM C204-11 to be 373 m²/kg (202 yd²/lb), 28 m²/kg (16 yd²/lb) less than the value measured for the cement used for the CR3 PCC, meaning the difference in heat release may not be as great as predicted by the total heats of complete hydration.

Table 3.8: Oxide analysis and phase composition of mock-up cement

Oxide Analysis* (percent by mass)										
SiO ₂	Al ₂ O ₃	Fe ₂ O ₃	CaO	MgO	SO ₃	(Na ₂ O) _e	TiO ₂	Mn ₂ O ₃	fCaO	LOI
19.41	4.59	3.89	62.14	2.07	2.63	0.69	0.25	0.22	0.12	2.43
Phase Composition (percent by mass)										
Method	C ₃ S	C ₂ S	C ₃ A	C ₄ AF	C ₃ S + C ₃ A		C ₃ S + 4.75C ₃ A			
Bogue Calculation	61.6	9.2	5.6	11.8	67.1		88.1			
Rietveld analysis	63.6	14.0	2.3	13.2	65.9		74.4			

*oxides contributing less than 0.1% of the total content are not reported

Figure 3.12 through Figure 3.14 present a summary of C₃S, C₃A, and 7-day heat of hydration data for Type II cements reported in various cement surveys since the 1950s

(Clifton and Mathey, 1971; Gebhardt, 1995; Tennis, 1999; Tennis and Bhatta, 2006) and seven current Type II cements available from various producers in the U.S.

Figure 3.12 shows that since 1994 most Type II cements have exceeded the 58% $C_3S + C_3A$ limit given by ASTM C150-67 for Type II cement with moderate heat of hydration, which was the cement type that was specified for the CR3 PCC. The increase over time is due to the increasing C_3S content of the cement; Figure 3.13 shows that C_3A content has not varied significantly, and the same 8% limit on C_3A content is present in the current specifications for Type II cement. The modern composition limit for moderate heat of hydration is $C_3S + 4.75 \cdot C_3A = 100\%$ (ASTM C150-11, 2011).

Per Table 3.8, the $C_3S + C_3A$ content of the cement used for the mock-ups as determined by Rietveld analysis is 65.9%, slightly greater than the 63.5% average of current cements shown in Figure 3.12. The cements with lower C_3S plus C_3A contents were not available locally and would not have been practical to transport for use at a ready mix plant for the concrete volume needed for the mock-ups.

Figure 3.14 shows the increasing trend of heat of hydration as determined in accordance with ASTM C186 (2005). As in Figure 3.12, cements produced since 1994 have typically had 7-day heats of hydration greater than the ASTM C150-11 moderate heat of hydration limit of 290kJ/g, which only applies if specifically requested. This indicates that modern Type II cements, even when meeting the modern requirements for moderate heat of hydration, may have different hydration behavior than the cement used in the CR3 PCC concrete. Though the cumulative 7-day heats of hydration were not provided for the CR3 PCC or mock-up cements, the total heats of complete hydration per unit mass of cement were estimated according to Eq. 7 in Section 2.6.1 to be 436 and 465 J/g (187 and 200 Btu/lb) for the CR3 PCC and mock-up cements, respectively.

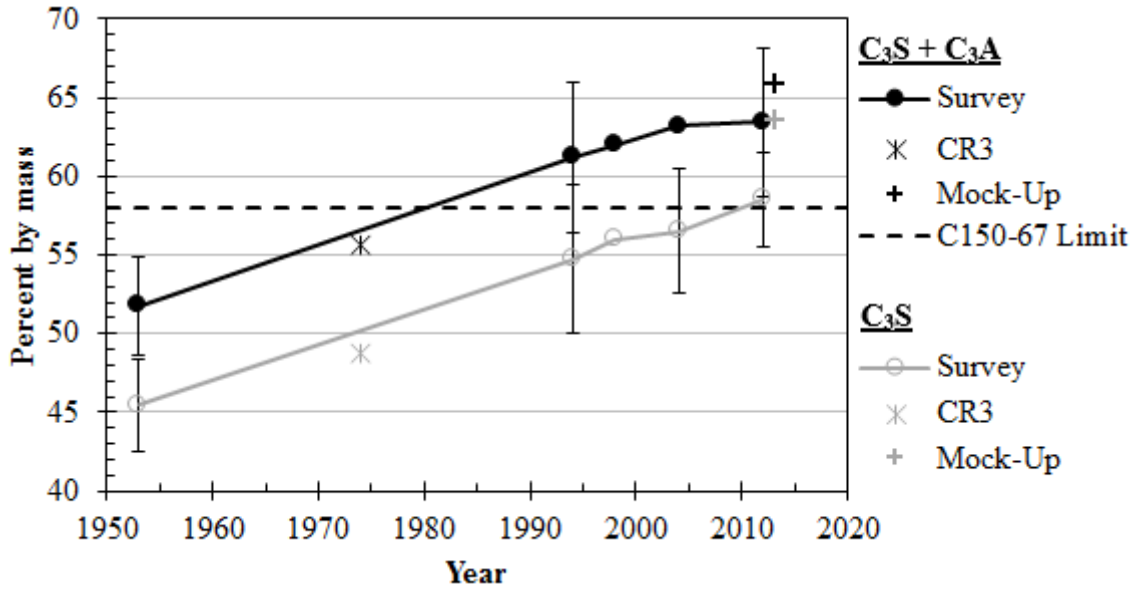


Figure 3.12: C₃S and C₃S plus C₃A contents of cements produced in different years

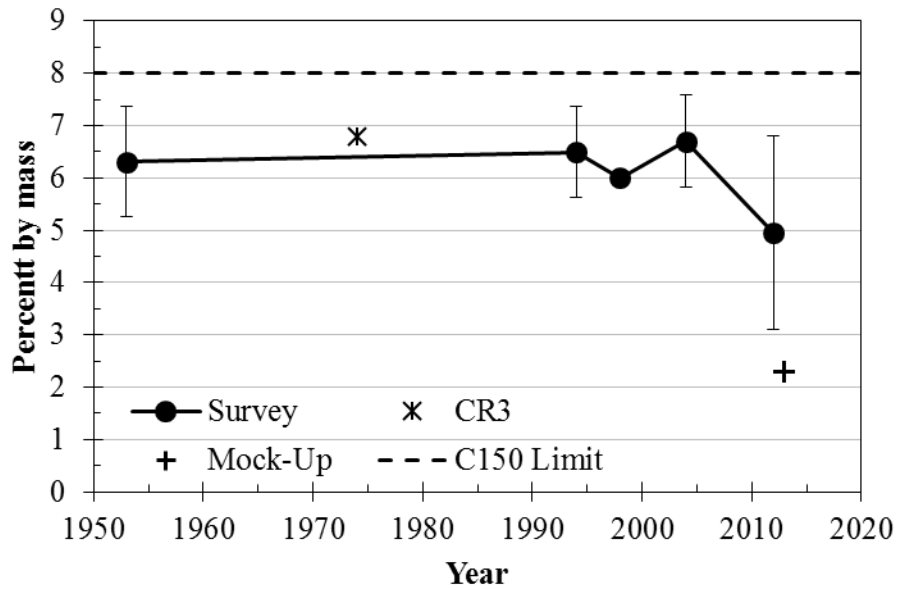


Figure 3.13: C₃A content of cements produced in different years

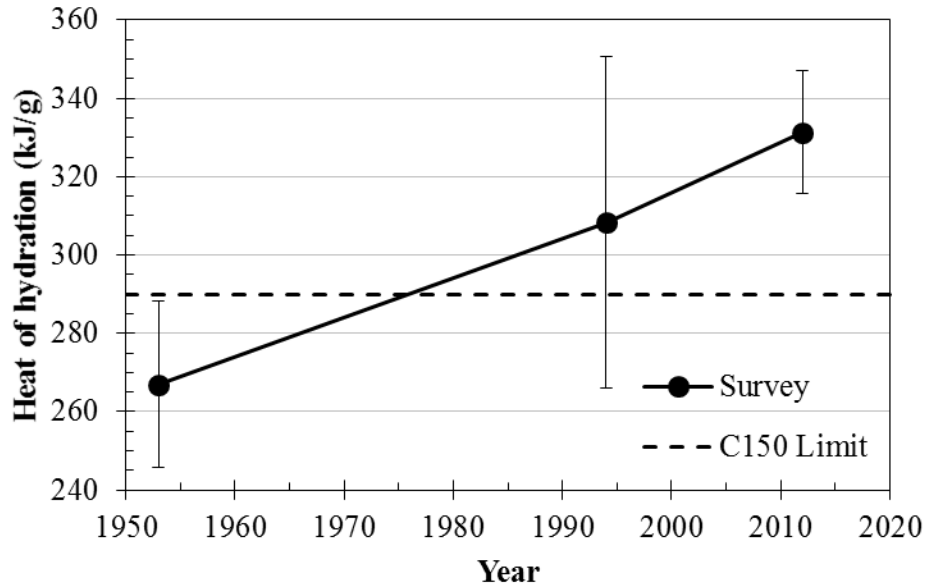


Figure 3.14: Cumulative 7-day heat of hydration of cements produced in different years

3.3.3.2 Coarse Aggregate

The coarse aggregate was ASTM C33 (2013) #67 limerock from the CEMEX quarry in Brooksville, Florida, the city from which the coarse aggregate for the CR3 PCC was sourced. The gradation curve for the limerock aggregate is shown in Figure 3.15, and the absorption capacity, oven-dry specific gravity, and SSD specific gravity were determined in accordance with ASTM C127-12 (2012) to be 6.13%, 2.301, and 2.442, respectively.

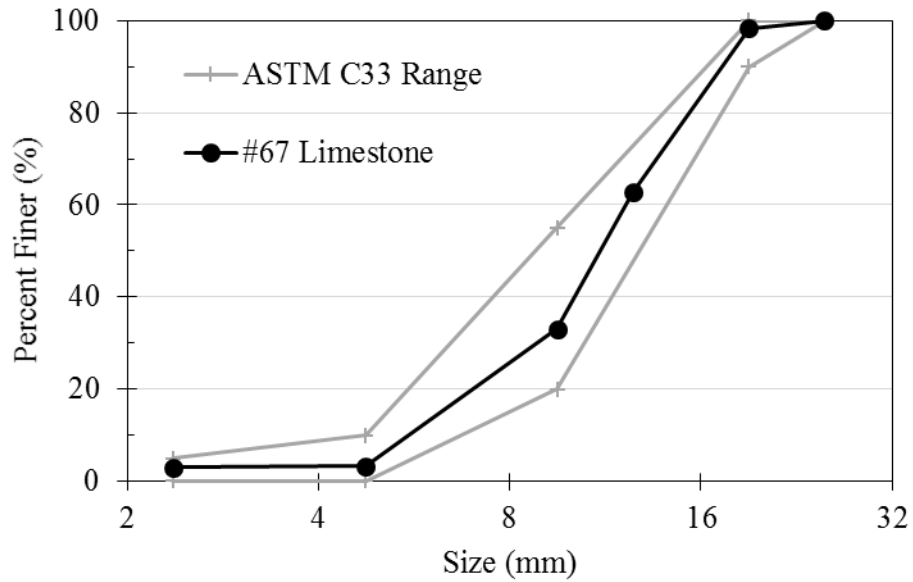


Figure 3.15: Gradation curve of limerock coarse aggregate (1 in. = 25.4 mm)

3.3.3.3 Fine Aggregate

The fine aggregate was natural silica sand from Lambert Materials in Shorter, Alabama, meeting the physical and chemical requirements of ASTM C33 (2013). The gradation curve for the sand is shown in Figure 3.16, and the fineness modulus was determined in accordance with ASTM C136-06 (2006) to be 2.65, within the 2.2-to-2.7 range of the fine aggregate used for the CR3 PCC concrete. The absorption capacity and SSD specific gravity were determined in accordance with ASTM C128-12 (2012) to be 0.53% and 2.634, respectively.

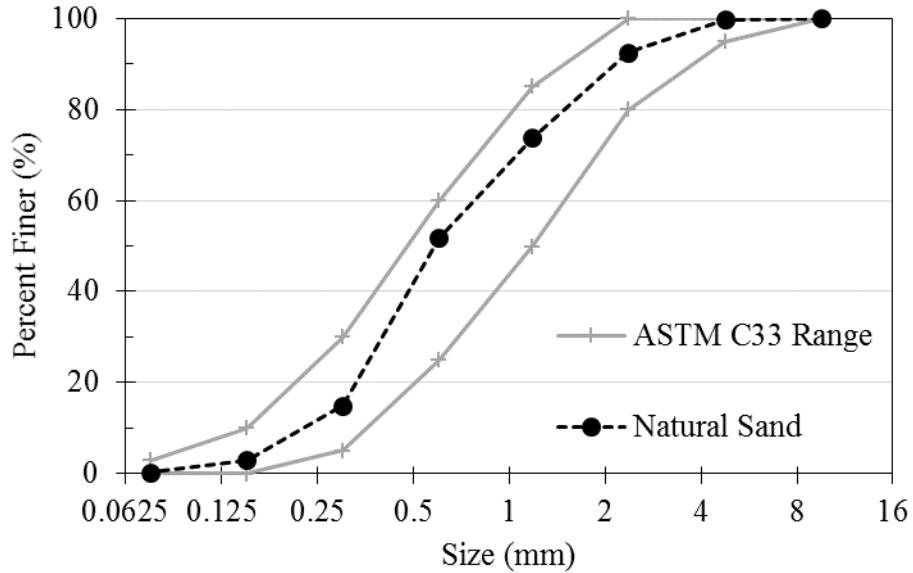


Figure 3.16: Gradation curve of natural silica sand (1 in. = 25.4 mm)

3.3.3.4 Admixtures

As in the CR3 PCC, Darex AEA was used as the AEA for the mock-up concrete. Daratard HC, a modern version of the Daratard HCF admixture used in the CR3 PCC concrete, was used as the WRRET. Both admixtures are produced by W.R. Grace and are compatible for use together.

3.3.4 Property Characterization

The following sections discuss the curing conditions of the test specimens and the experimental tests conducted to characterize the properties of the mock-up concrete.

3.3.4.1 Curing Conditions

Standard cylinder specimens were prepared from the mock-up concrete for experimental testing to characterize the properties of the mock-up concrete. The specimens were grouped into three series according to the curing conditions to which they were subjected. A series of control specimens was cured in accordance with ASTM

C192-13a (2013) in a moist room at a temperature of 23 ± 2 °C (73.5 ± 3.5 °F), matching the curing condition of the standard-cured specimens used for testing compressive strength of the CR3 PCC concrete. A second series of specimens was match-cured with the temperature of the concrete at a depth of 51 mm (2 in.) from the center of the front face of the mock-ups, and a third series was match-cured with the temperature of the concrete at the center of mass of the mock-ups. The match-cured specimens were submerged in temperature-controlled storage tanks containing water saturated with calcium hydroxide in accordance with ASTM C511-13 (2013). The locations of the match-curing temperature probes in the mock-ups are shown in Figure 3.5, and specimens in one of the match-curing storage tanks are shown in Figure 3.17.

Except for specimens from the second truck of the second mock-up, which were only subjected to standard curing, specimens tested for compressive strength, splitting tensile strength, modulus of elasticity, and Poisson's ratio were subjected to all three curing conditions. All other tests were conducted on standard-cured specimens.



Figure 3.17: Specimens in match-curing storage tank

3.3.4.2 Mechanical Properties

Tests for compressive strength, splitting tensile strength, modulus of elasticity, and Poisson's ratio were conducted 1, 2, 3, 7, 10, 14, 28, 90, and 180 days after casting. The compressive strength and splitting tensile strength were measured in accordance with ASTM C39-12 (2012) and ASTM C496-11 (2011), respectively, on sets of four 100-by-200-mm (4-by-8-in.) cylinders at each age and curing condition. The modulus of elasticity and Poisson's ratio were measured in accordance with ASTM C469-10 (2010) on sets of three 150-by-300-mm (6-by-12-in.) cylinders at each age and curing condition, and the compressive strength of each cylinder was determined in accordance with ASTM C39-12 after the loadings for modulus of elasticity and Poisson's ratio were completed.

3.3.4.3 Coefficient of Linear Thermal Expansion

Three methods of determining the coefficient of linear thermal expansion (CTE) were conducted: CRD-C 39-81, AASHTO T 336, and Tex-428-A. For each method, standard-cured specimens from the first mock-up were tested at 1, 2, 3, 7, 14, 28, 56, and 90 days after casting, except that a set was also tested at 10 days in accordance with CRD-C 39-81. Each specimen was tested only once so that variations in maturity due to thermal cycling during the test would not influence later test results.

The specimens were cured in accordance with ASTM C192-13a in a moist room. In order to ensure consistent moisture content and prevent hygrometric expansion during testing, the specimens were placed in a limewater storage tank inside the moist room for at least the final 48 hours before testing to ensure that the specimens were fully saturated. The specimens tested at 1 and 2 days were moved into the limewater storage tank at 12 hours, demolded at 16 hours, and kept in the limewater storage tank until testing.

For consistency, the specimens were subjected to the same temperature sequence for all tests three test methods:

- 23 ± 2 °C (73 ± 4 °F)

- 50 °C (122 °F)
- 10 °C (50 °F)
- 50 °C (122 °F)

As discussed in Section 2.7.4.2.4, this sequence follows the suggestion of the manual for the commercial equipment used for the AASHTO T 336 and Tex-428-A test methods.

3.3.4.3.1 CRD-C 39-81

The CRD-C 39-81 test method was conducted on 150-by-300-mm (6-by-12-in.) cylinders. Each specimen had two pairs of diametrically opposite embedded inserts spanning nominal 254-mm (10-in.) gauge lengths for measuring longitudinal length change with a 254-mm (10-in.) demountable mechanical (DEMEC) gauge with a precision of ± 0.0025 mm (0.0001 in.). The molds used for preparing the specimens and the use of the DEMEC gauge to measure the gauge lengths of the specimens are shown in Figure 3.18.

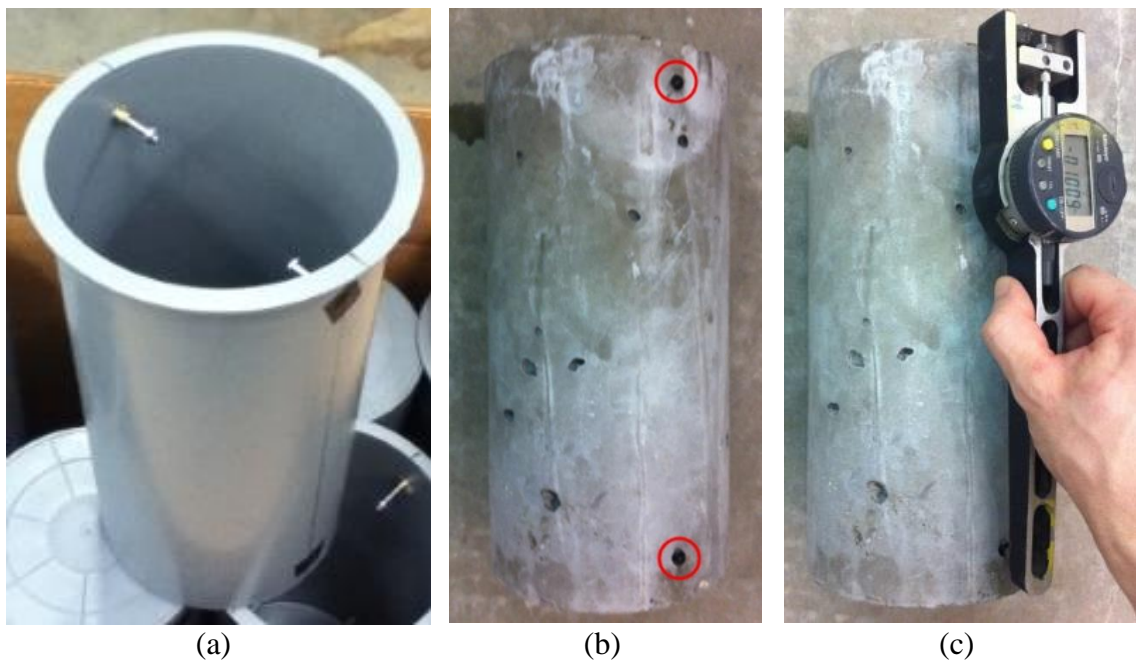


Figure 3.18: Specimens for CTE testing in accordance with CRD-C 39-81: (a) cylinder mold with inserts, (b) specimen with embedded inserts circled in red, and (c) reading taken with DEMEC gauge

Specimens from both trucks were tested at 7, 14, 28, 56, and 90 days after casting, and specimens from one of the two trucks were tested at 1, 2, 3, and 10 days after casting. The specimens were tested in triplicate except at 1 day after casting, when the inserts for one of the specimens were outside the range of the DEMEC gauge and only two specimens could be measured.

For each length measurement, the specimens were removed from the limewater storage tank or constant-temperature bath and promptly measured in air with the DEMEC gauge. The specimens were then returned to the same storage tank or bath, and measurements were repeated at the same temperature until the change in each length between successive readings at 1-hour intervals was less than or equal to 0.0051 mm (0.0002 in.). The final length measurements were recorded for the corresponding temperature condition, the specimens were transferred to the next constant-temperature bath, and the process was repeated for all temperature conditions.

The change in length for each side of each specimen over the tested temperature range was taken as the average of the change in length over the cooling and heating segments. The CTE for each specimen was calculated as the average of the apparent CTE values for each side as determined according to Eq. 91 in Section 2.7.4.2.1. The results are reported as the average and standard deviation of the three specimens tested for each truck at each age.

3.3.4.3.2 AASHTO T 336 and Tex-428-A

The AASHTO T 336 and Tex-428-A methods for determining CTE were conducted using commercial equipment (Pine Instrument AFCT2 Coefficient of Thermal

Expansion (CTE) of Hydraulic Cement Concrete System) available at the Georgia Department of Transportation (GDOT) Office of Materials and Research. The specimen fixtures were made of a corrosion-resistant alloy and had submersible LVDTs for measuring length change. The fixture calibration standard was AISI 410 stainless steel with a CTE of $10.296 \mu\epsilon/^\circ\text{C}$ ($5.720 \mu\epsilon/^\circ\text{F}$) over the test temperature range as determined in accordance with ASTM E228. The test set-up is shown in Figure 3.19.



Figure 3.19: Set-up for AASHTO T 336 and Tex-428-A CTE testing

The tests were conducted on pairs of 100-mm-by-200-mm (4-by-8-in.) cylinders from the first truck of the first mock-up sawn to lengths of $177.8 \pm 2.54 \text{ mm}$ ($7.0 \pm 0.1 \text{ in.}$). After the specimens reached saturation at room temperature, the length of each

specimen was measured in accordance with ASTM C1542 (2010) except that the lengths were recorded to the nearest 0.1 mm (0.004 in.) rather than the nearest 0.25 mm (0.01 in.).

The water temperature, taken as the average reading of two temperature sensors, and the change in length of the specimens were recorded every 60 seconds until completion of the test. The measured temperature change and length change for each segment were used with the length of the specimen at room temperature to calculate the CTE according to Eq. 91 in Section 2.7.4.2.1.

The raw temperature and length change data collected during the AASHTO T 336 test was also used to determine the CTE in accordance with Tex-428-A using EQ92 in Section 2.7.4.2.3. However, since the program operating the equipment was not set up for Tex-428-A, the specified inter-specimen CTE tolerance of $0.5 \mu\epsilon/^\circ\text{C}$ ($0.3 \mu\epsilon/^\circ\text{F}$) was not used as criteria for completion of the test. Additionally, only the values between 15 and 45 °C (59 to 113 °F) were used in regression analysis, as recommended by Won (2005).

3.3.4.4 Time of Final Setting

The time of final setting approximates the time of complete solidification and the beginning of hardening, during which mechanical strength develops (Mehta and Monteiro, 2006). As the concrete would begin sustaining stress at this time, the time of final setting was used to help establish the time at which the strain gauges in the mock-up would be tared.

Dodson (1994) demonstrated that, for mortars screened from concrete, the times of initial and final setting decreased as the temperature at which the specimens were tested increased. This indicates that the results of testing for time of setting at room temperature would not necessarily be indicative of the setting behavior of the mock-up concrete with rapidly increasing temperatures over the first several hours after the beginning of concrete placement. Christensen (2006) found that the time of the maximum

rate of change of concrete temperature with respect to time correlated well with times of final setting of companion mortar specimens tested in accordance with ASTM C403. Therefore, the rate of temperature change of the mock-up concrete as measured by the embedded gauges was used to assist in determination of the time at which the gauges would be tared.

3.3.4.5 Density, Percent Absorption, and Percent Voids of Hardened Concrete

Three 100-by-200-mm (4-by-8-in.) cylinders were prepared from both trucks for the second mock-up for determination of the density, percent absorption, and percent permeable voids in accordance with ASTM C642-13 (2013) for comparison with values reported for cores taken from the CR3 PCC in 2009. At an age of 180 days, the bottom 51 mm (2 in.) of each cylinder was cut off with a wet saw, and the subsequent 51 mm (2 in.) of each cylinder was cut and used as a test specimen with a nominal volume of 4.12×10^5 mm³ (25.1 in.³).

3.3.4.6 Statistical Analysis

One-way analysis of variance (ANOVA) was conducted on all sets of property data to test the null hypothesis that, for each mock-up and curing condition and at each age, the mean value of the given property of the concrete from the two trucks was the same. A significance level of $\alpha = 0.05$ (5%) was used for all statistical analysis, and if the null hypothesis could not be rejected according to the significance level, the results for the two trucks were combined. Complete property results and ANOVA p-values are provided in Appendix B.

3.4 Results and Discussion

3.4.1 Density, Percent Absorption, and Percent Voids of Hardened Concrete

The SSD bulk density of the hardened concrete for the second mock-up was determined to be 2,283 kg/m³ (142.5 lb/ft³), similar to the measured density of the fresh concrete. The apparent density was determined to be 2,558 kg/m³ (159.7 lb/ft³), slightly higher than the 2515-kg/m³ (157-lb/ft³) density reported for the cores. The average permeable voids volume was 16.9%, also higher than the 15.0% reported for the cores. Results of the density, percent absorption, and percent permeable voids are tabulated in Appendix B.1.

3.4.2 Naming Convention

Each mock-up required two trucks of concrete, and the companion specimens for each mock-up were exposed to three curing conditions. In the figures, tables, and discussion that follow, the first term in each label is a Roman numeral indicating the mock-up for which the concrete was used: “I” indicates the first mock-up, and “II” indicates the second mock-up.

The terms “Fog,” “Ext,” and “Int” refer to the curing condition of the specimens. “Fog” specimens were cured in a moist room at 23 ± 2 °C (73.5 ± 3.5 °F), “Ext” specimens were match-cured with the temperature of the concrete near the center of the front face of the mock-ups, and “Int” specimens were match-cured with the temperature of the concrete at the center of mass of the mock-ups.

The final numerical term indicates the ready-mix truck from which the specimens were obtained: “1” indicates the first truck for the identified mock-up, and “2” indicates the second truck for the identified mock-up. Therefore, “II-Ext-1” identifies specimens from the second mock-up that were match-cured to the near-surface temperature of the mock-up concrete and were obtained from the first truck for that pour. When the final

numeral is not provided, the label refers to concrete from both trucks of the given mock-up and curing condition.

The label “CR3” refers to the standard-cured 150-by-300-mm (6-by-12-in.) concrete cylinders tested for acceptance and quality control of the DM-5-Mod concrete used in the CR3 PCC, and the label “Cores” refers to cores measuring 102 mm (4 in.) in diameter taken from the region of delaminated DM-5-Mod concrete and tested by Performance Improvement International (2010) as-received in 2009-2010 at an age of approximately 36 years.

3.4.3 Mock-Up Temperatures

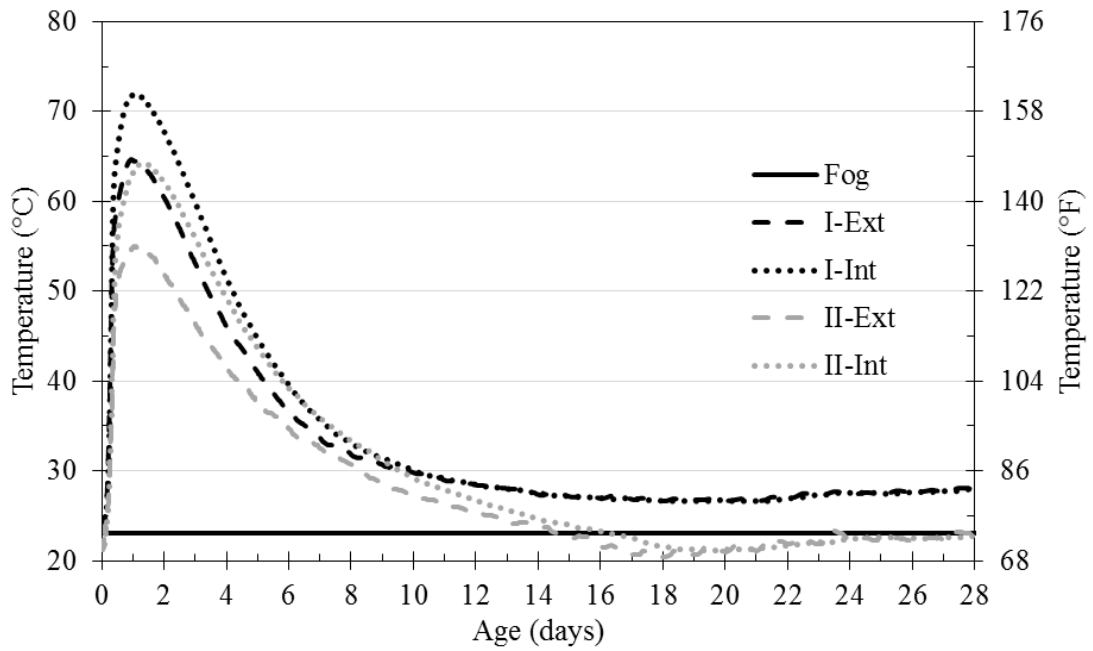
Figure 3.20 shows the temperature histories recorded at the center and near the surface of the two mock-ups, the same histories to which the match-curing specimens were matched, and the 23-°C (73.5-°F) curing temperature of the “Fog” specimens. The initial temperature of the concrete at the time of placement was 25.5 and 22.5 °C (77.9 and 72.5 °F) for the first and second mock-up, respectively, close to the measured ambient temperatures of 26 and 21 °C (79 and 70 °F), respectively. This behavior is consistent with ACI 207.2R-07, which indicates that the temperature of concrete at the time of placement can be approximated as being equal to or slightly greater than the average ambient temperature.

The maximum recorded temperature in the first mock-up was 71.9 °C (161 °F) approximately 24 hours after concrete placement, and the maximum temperature difference was 7.5 °C (45.5 °F) approximately 30 hours after placement. The maximum recorded temperature in the second mock-up was 64.7 °C (148 °F) approximately 28 hours after placement, and the maximum temperature difference was 10.4 °C (50.7 °F) approximately 49 hours after placement. Therefore, the first mock-up exceeded the 70-°C (158-°F) maximum temperature limit specified by ACI 301-10 and may have been susceptible to DEF, but neither mock-up exceeded the 19-°C (35-°F) maximum

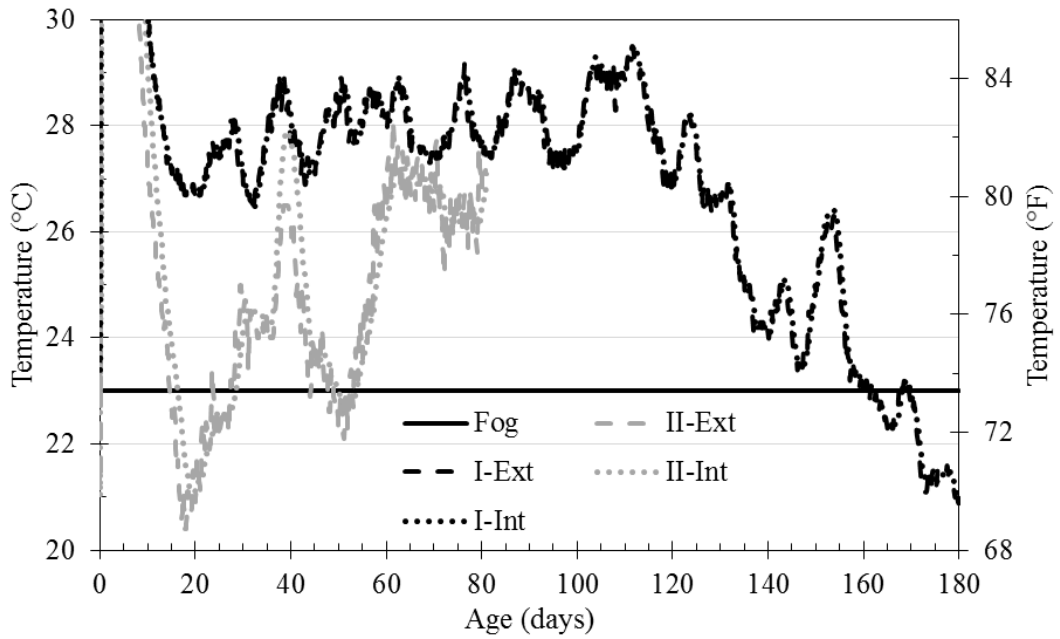
temperature difference specified by ACI 301-10. The higher temperatures in the first mock-up were likely related to the lower slump of the concrete, which may have had a slightly lower water content than that of the second mock-up.

In contrast to the large-magnitude temperature changes shown in Figure 3.20a during the first 14 days of curing, Figure 3.20b shows that relatively little variation occurred at later ages and ambient conditions controlled the temperature. For each mock-up, the similar temperatures near the surface and at the center of the mock-ups at later ages suggest that the presence of the post-tensioning ducts, which were only covered while the forms were in place and during post-tensioning, increased the influence of the ambient conditions on the temperatures of the concrete at the interior of the mock-ups. After hydration has slowed, the concrete surface temperature is typically similar to that of the air when not directly exposed to sunlight or other heat sources, whereas the variation of the interior concrete temperature may be only 10% of that of the surface concrete temperature (ACI 207.2R-07). The lack of consistent direct sunlight on the mock-ups also contributed to the limited temperature difference between the surface and interior concrete.

Due to seasonal variations, the second mock-up cured in generally lower ambient temperatures, which may have contributed to the lower temperatures values and larger temperature variation measured in the second mock-up.



(a)



(b)

Figure 3.20: Concrete specimen curing temperature histories through (a) 28 days and (b) 180 days

The temperature profile through the thickness of the second mock-up as measured by the C gauges at the time of maximum temperature differential is shown in Figure 3.21. The balance line is the value of the average temperature across the section so that the compressive and tensile stresses due temperatures greater than and less than the balance line sum to zero. Based on the quadratic fit of the temperature profile, the temperature of the balance line was determined to be 58.2 °C (137 °F) in Appendix A.5. The depth of the internal stress block d_s , where the quadratic fit intersects the balance line, was determined to be 236 mm (9.3 in.). For the 2.64-m (104-in.) length of the mock-up, the length-to-depth ratio L/d_s of the stress block was 11.2 at this time. Using this value as the length-to-height ratio L/H and taking the surface to be the full height H from the point of restraint, the degree of restraint K_r at the center of the front of the mock-up was estimated to be 0.77 according to ACI 207.2R-07.

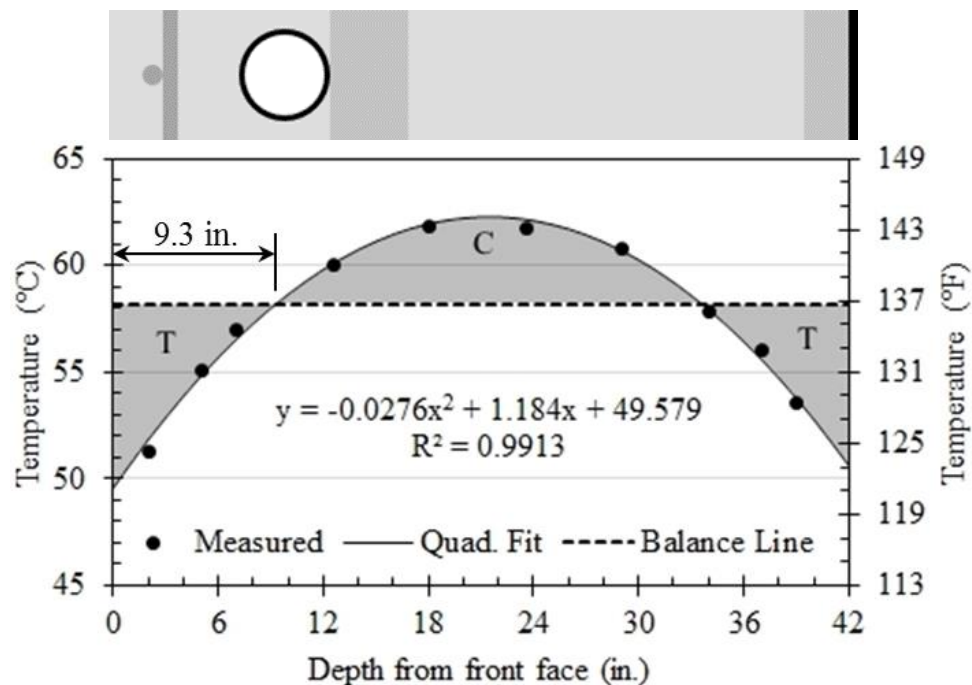
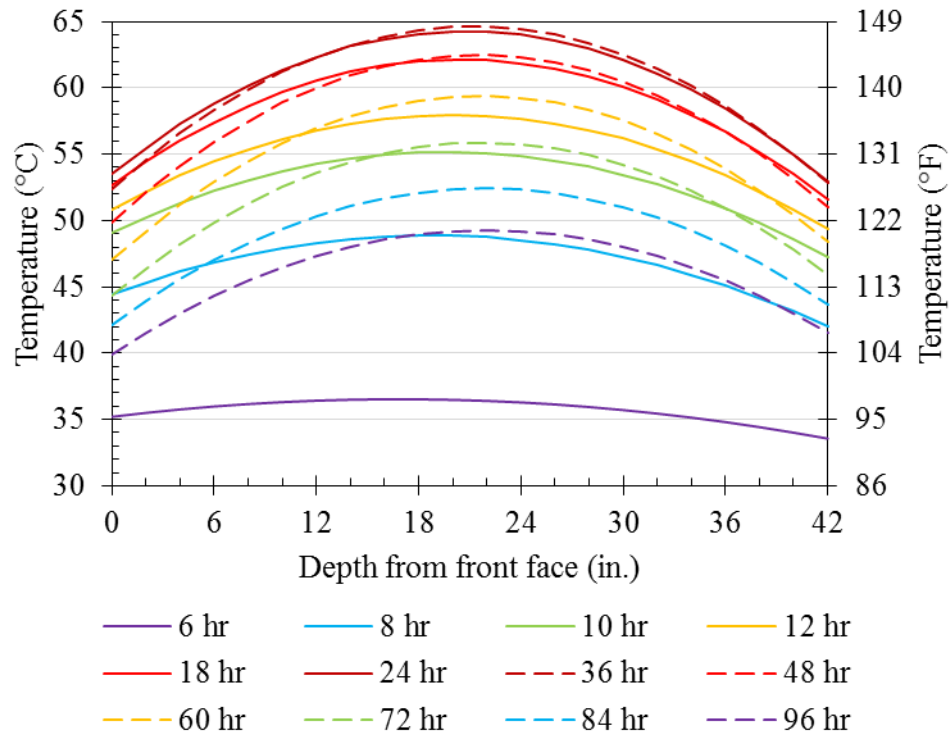


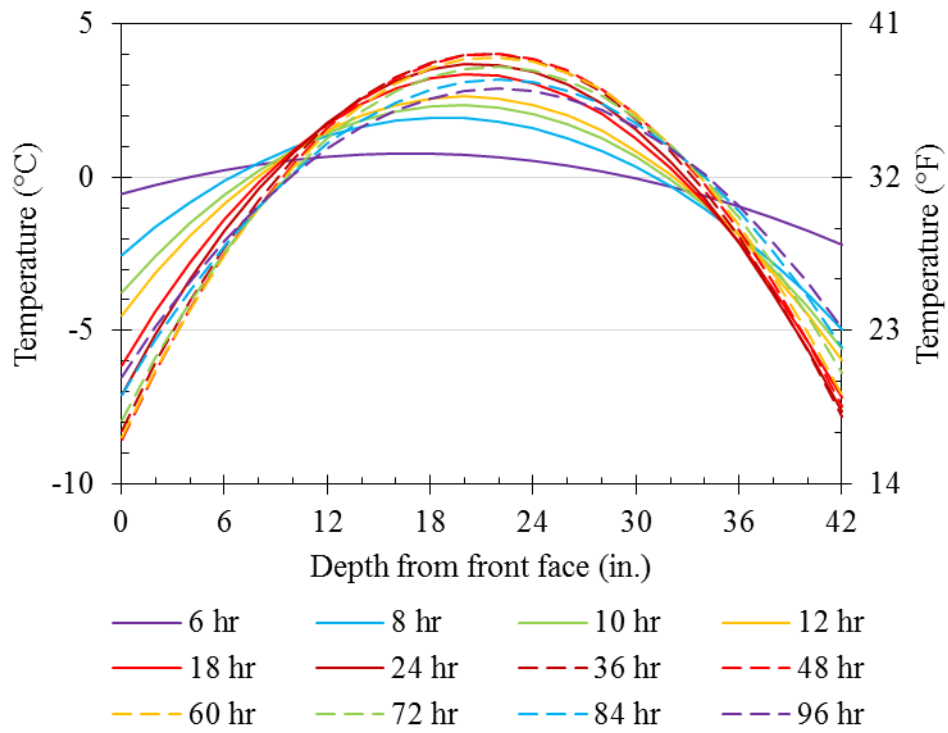
Figure 3.21: Section detail and temperature profile through thickness of second mock-up measured by C gauges at time of maximum temperature differential

The temperature profiles in Figure 3.22 show the variation of the temperature in the C gauges during the first 4 days of curing. At 6 hours, the temperature profile was relatively flat, with little variation in temperature. As the temperature increased rapidly during the first 24 hours, more curvature developed in the temperature profiles, with the temperature at the center of the mock-up increasing more rapidly than the temperatures near the surfaces. Little change occurred between 24 and 36 hours, and during the gradual decrease in temperature through 96 hours, the temperature profile began slowly flattening out again.

As shown in Figure 3.22b, the temperatures towards the front of the mock-up were higher than those towards the back at early ages, but by 18 hours, the parabolic form of the temperature profiles had shifted to the center of the thickness of the mock-up. The lower temperatures at the back of the mock-up were likely due to the steel liner, which would have drawn heat away from the concrete as it was being placed more rapidly than the plywood in contact with the front face. The variation in the depth of the internal stress block due to the varying temperature profiles resulted in slight variation of the degree of restraint as shown in Figure 3.36 in Section 3.4.8; as the depth of the stress block increased with time, the degree of restraint decreased, contributing to lower stresses if all other factors were constant.



(a)



(b)

Figure 3.22: Quadratic regressions of temperature profiles through thickness of second mock-up shown with (a) actual magnitudes and (b) balance lines shifted to 0 °C (32 °F)

Temperature contours at midheight of the second mock-up are shown in Figure 3.23. The vertical axis indicates the depth from the front face of the mock-up, and the horizontal axis indicates the horizontal distance from the vertical midplane of the mock-up. As the concrete temperature was rising during the first day, the temperature was asymmetric across the midplane of the mock-up, with slightly higher temperatures centered towards the left side as shown in Figure 3.23a at 12 hours. This behavior may have been caused by the non-uniform placement of concrete from the first ready-mix truck in order to avoid displacing the gauges at the center of the mock-up. If more concrete from the first truck was placed in the left side of the form than the right, the temperature would have begun rising earlier on the left side due to the larger volume of concrete and earlier initiation of hydration in the concrete at that height on the left side.

However, by 24 hours (Figure 3.23b), when the concrete temperatures approached maximum values, the temperature contours became more uniform along the length of the mock-up. Between 24 and 36 hours, the temperature contours were relatively consistent. As shown in Figure 3.23c at 48 hours, the contours remained relatively uniform along the length as the temperatures decreased. At 96 hours (Figure 3.23d), the temperature contour was still mostly uniform along the length except for a small region of slightly higher temperatures just left of the center of the mock-up. Aside from the asymmetry during the first day, the temperature contours suggest that the variation of the temperature at any time in the region of the mock-up with the gauges was generally one-dimensional and primarily dependent on the depth from the concrete surface. This behavior also suggests that, by insulating the ends of the mock-ups, the temperatures in the region of the gauges are comparable to what would have been measured for a mock-up measuring the full 6-m (20-ft) length of typical CR3 PCC pours rather than the 2.64-m (104-in.) length of the mock-ups.

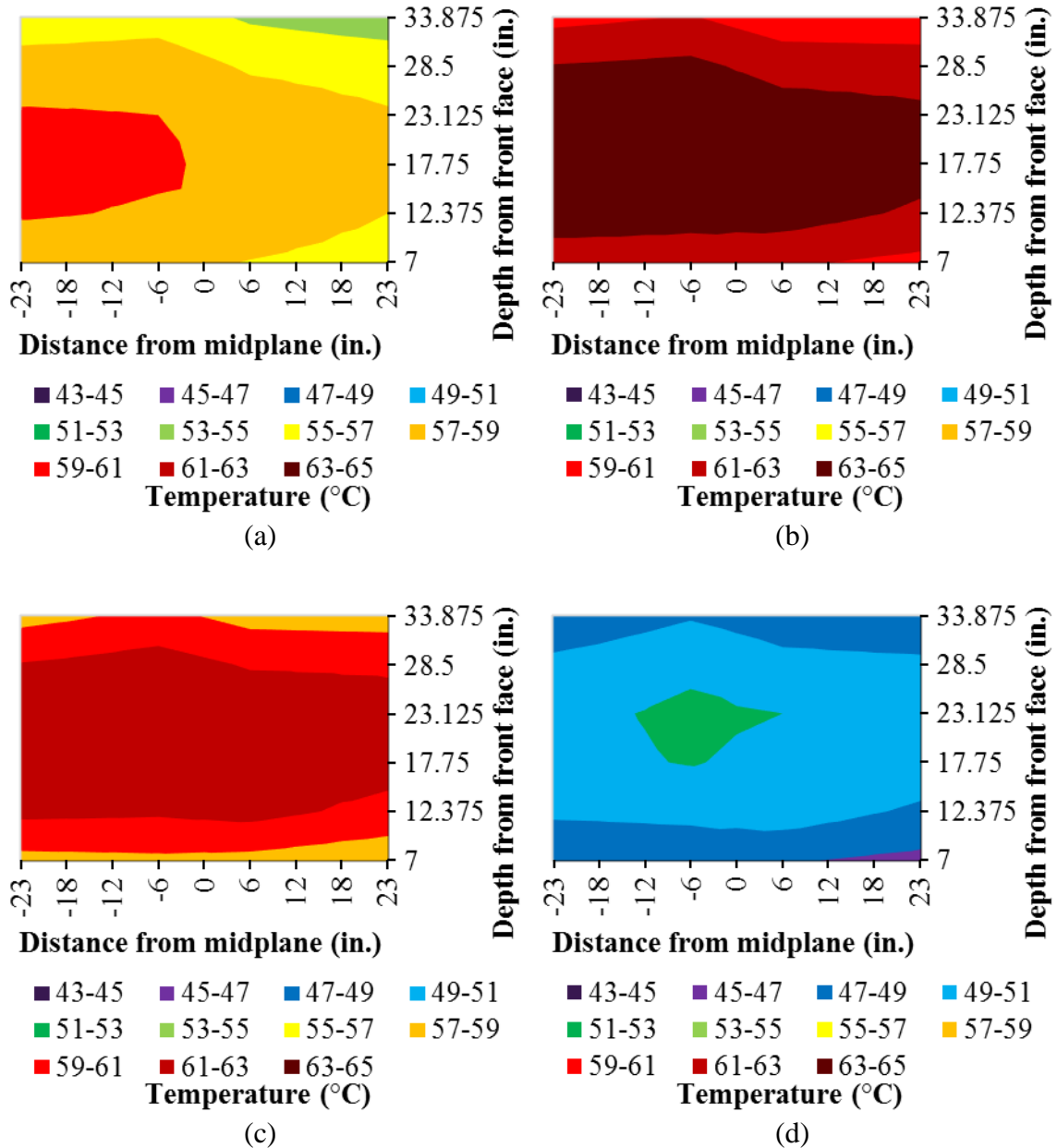


Figure 3.23: Temperature contours at midheight of second mock-up at (a) 12 hours (b) 24 hours (c) 48 hours, and (d) 96 hours after concrete placement began

3.4.5 Mechanical Properties

The following sections discuss the results of the tests for the mechanical properties of the mock-up concrete. Except for the compressive strength and modulus of elasticity results of the II-Fog concrete, the results for the two trucks for each mechanical property and curing condition were combined based on ANOVA results.

3.4.5.1 Compressive Strength

The compressive strength results for the mock-up concrete are shown in Figure 3.24 and Table 3.9. Whereas the results for the first mock-up are shown as the average of the two trucks for each curing condition, the results for the II-Fog specimens for the second mock-up are shown separated by truck due to statistical significance of the two sets of data per ANOVA and rejection of the null hypothesis that the two sets of data were from the same set. The complete results are presented in Appendix B.2.

At 7, 28, and 90 days, the compressive strength of the first mock-up concrete was lower than that of the standard-cured 150-by-300-mm (6-by-12-in.) cylinders tested for the CR3 PCC concrete, particularly at the later ages. At 28 days, the I-Fog specimens achieved an average compressive strength of 35.9 MPa (5,203 psi) with a sample standard deviation s_s of 0.92 MPa (133 psi). According to Eq. 3.2 from ACI 318-08, the required average compressive strength f'_{cr} of the I-Fog specimens would have been 35.7 MPa (5,179 psi) for the design strength of 34.5 MPa (5000 psi), meaning the specimens would have met the design requirements for the CR3 PCC concrete. In contrast, the I-Ext and I-Int specimens had 28-day strengths of 34.0 and 30.9 MPa (4,927 and 4,481 psi), respectively, and would not have met the design requirements. Each set of specimens tested for the second mock-up developed sufficient 28-day strength to meet the design requirements according to Eq. 3.2.

$$\begin{aligned} f'_{cr} &= \max \left\{ \begin{array}{l} f'_c + 1.34s_s \\ f'_c + 2.33s_s - 3.5 \end{array} \right. \quad [\text{MPa}] \\ f'_{cr} &= \max \left\{ \begin{array}{l} f'_c + 1.34s_s \\ f'_c + 2.33s_s - 500 \end{array} \right. \quad [\text{psi}] \end{aligned} \quad \text{Eq. 3.2}$$

Where,

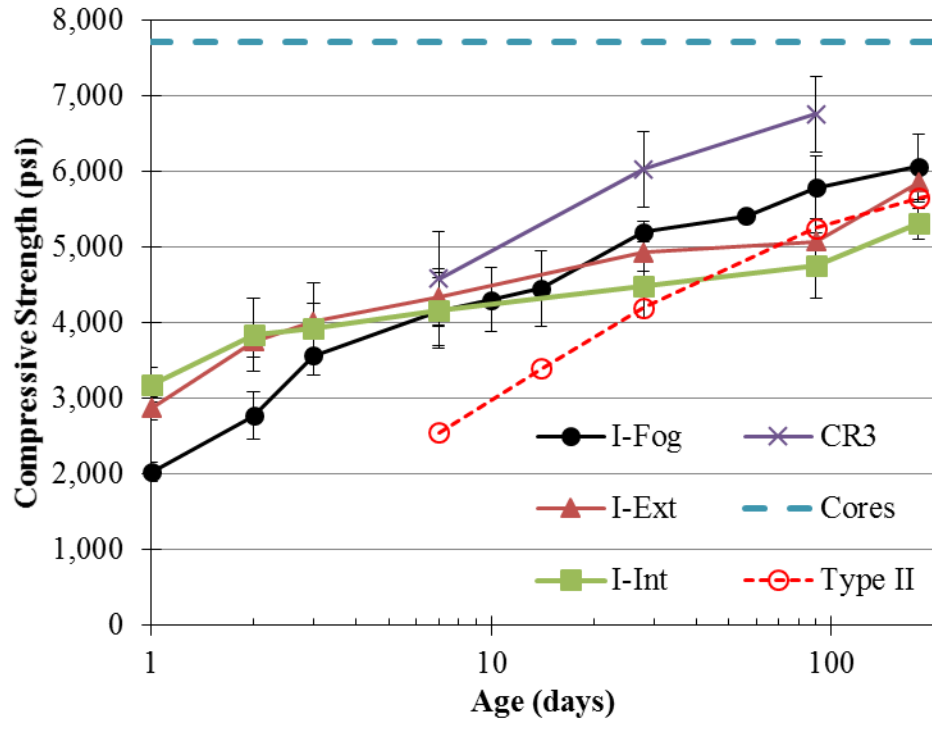
$$\begin{aligned} f'_{cr} &= \text{required average compressive strength, MPa (psi)} \\ f'_c &= \text{specified compressive strength, MPa (psi)} \end{aligned}$$

For each curing condition and age, the strength of the concrete for the second mock-up was greater than that of the first. The II-Fog-2 specimens had similar strengths

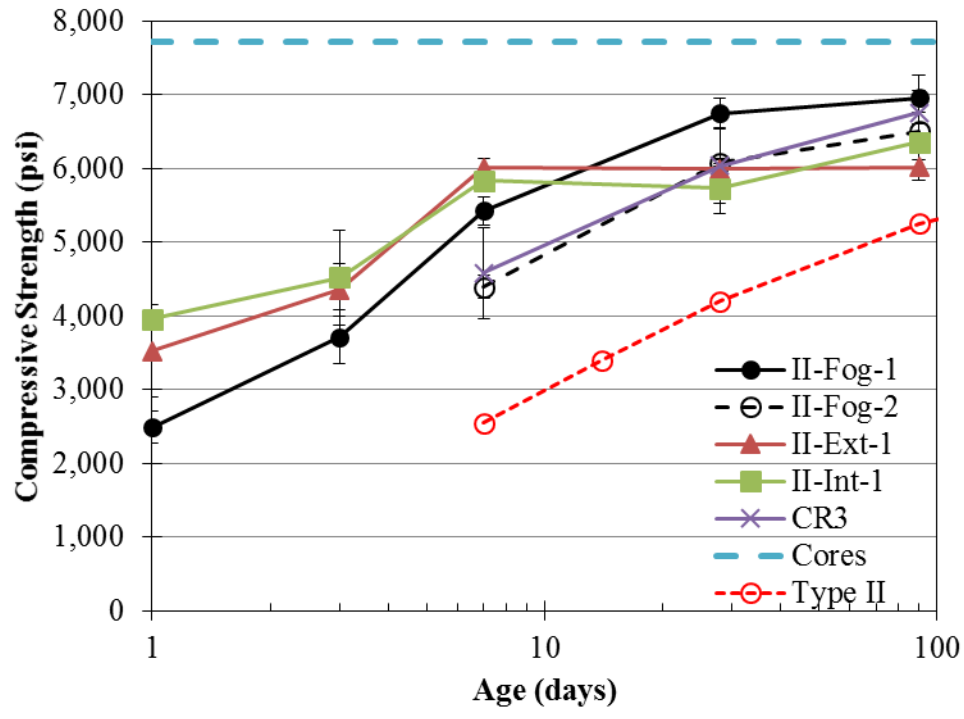
to those tested for the CR3 PCC at 7, 28, and 90 days, and the II-Ext and II-Int specimens had strengths slightly lower than the CR3 specimens at 28 and 90 days. All specimens had strengths lower than the 53.1-MPa (7707-psi) average strength of the post-delamination core specimens of DM-5-Mod concrete.

For both mock-ups, the development of the compressive strength exhibits the crossover effect. For the first mock-up, the I-Int specimens had the highest strength and the I-Fog specimens had the lowest strength over the first two days, but at 28 days and beyond, the I-Fog specimens had the highest strength and the I-Int specimens had the lowest strength. Similar behavior was observed for the second mock-up, though the II-Ext specimens didn't surpass the II-Int specimens until after 28 days. The rapid early increase in strength at higher temperatures is due to more rapid hydration at higher temperatures, but the microstructure of the resulting cement paste is not as uniform, resulting in regions of weakness that limit strength (Mehta and Monteiro, 2006; Mindess et al., 2003).

The sample standard deviation s_s of the experimental specimens ranges from 0.15 MPa (22 psi) (I-Fog at 56 days) to 4.43 MPa (642 psi) (II-Int-1 at 28 days). Per ACI 214R-11, the 4.43-MPa (642-psi) standard deviation for 28-day compressive strength results meets the “fair” standard of concrete control for concrete with a specified compressive strength no greater than 5000 psi. With a standard deviation of 502 psi at 28 days, the CR3 cylinders met the “good” standard of concrete control. However, most of the experimental tests had lower standard deviation values than the CR3 results; this may be due to the fact that the experimental results were obtained from two trucks of concrete, whereas the CR3 results were obtained from pairs of specimens from numerous different batches of concrete poured over a period of about 8 months. Performance Improvement International (2010) also notes an instance of potential testing error in the compressive strength results of the cylinders and suggests that other instances of error may have occurred.



Note: 1 MPa = 145 psi
(a)



Note: 1 MPa = 145 psi
(b)

Figure 3.24: Compressive strength of (a) first and (b) second mock-up concrete

Table 3.9: Compressive strength of the mock-up concrete

Batch ID	Measure	Compressive Strength (psi)									
		1-day	2-day	3-day	7-day	10-day	14-day	28-day	56-day	90-day	180-day
I-Fog	Avg.	2028	2774	3570	4151	4305	4454	5203	5412	5784	6066
	Std. Dev.	127	308	258	450	426	502	133	22	416	434
I-Ext	Avg.	2868	3749	4016	4336	-	-	4927	-	5072	5852
	Std. Dev.	149	202	507	385	-	-	255	-	303	250
I-Int	Avg.	3177	3841	3928	4169	-	-	4481	-	4755	5308
	Std. Dev.	227	486	329	498	-	-	408	-	430	200
II-Fog-1	Avg.	2486	-	3714	5421	-	-	6749	-	6953	-
	Std. Dev.	222	-	370	197	-	-	196	-	95	-
II-Fog-2	Avg.	-	-	-	4387	-	-	6073	-	6499	-
	Std. Dev.	-	-	-	157	-	-	50	-	258	-
II-Ext-1	Avg.	3522	-	4351	6003	-	-	5988	-	6018	-
	Std. Dev.	624	-	360	121	-	-	136	-	179	-
II-Int-1	Avg.	3950	-	4519	5833	-	-	5730	-	6355	-
	Std. Dev.	102	-	642	93	-	-	339	-	248	-
CR3	Avg.	-	-	-	4581	-	-	6029	-	6756	-
	Std. Dev.	-	-	-	619	-	-	502	-	498	-

Note: 1 MPa = 145 psi

3.4.5.2 Splitting Tensile Strength

The splitting tensile strength results for the mock-up concrete are shown in Figure 3.25 and Table 3.10. At 180 days, the match-cured specimens for the first mock-up had achieved the 4.10-MPa (594-psi) average splitting tensile strength of the post-delamination core specimens of DM-5-Mod concrete, whereas the I-Fog specimens achieved a splitting tensile strength of approximately (700 psi) by 90 days. In contrast, the 90-day splitting tensile strength of the specimens from all three curing conditions of the second mock-up similar to that of the cores. Whereas the splitting tensile strength of the I-Fog specimens increased by 2.24 MPa (325 psi) between 1 and 90 days, the strength of the II-Fog specimens increased by 0.97 MPa (141 psi) over the same period. The first mock-up specimens exhibited more clearly defined crossover effect behavior than the

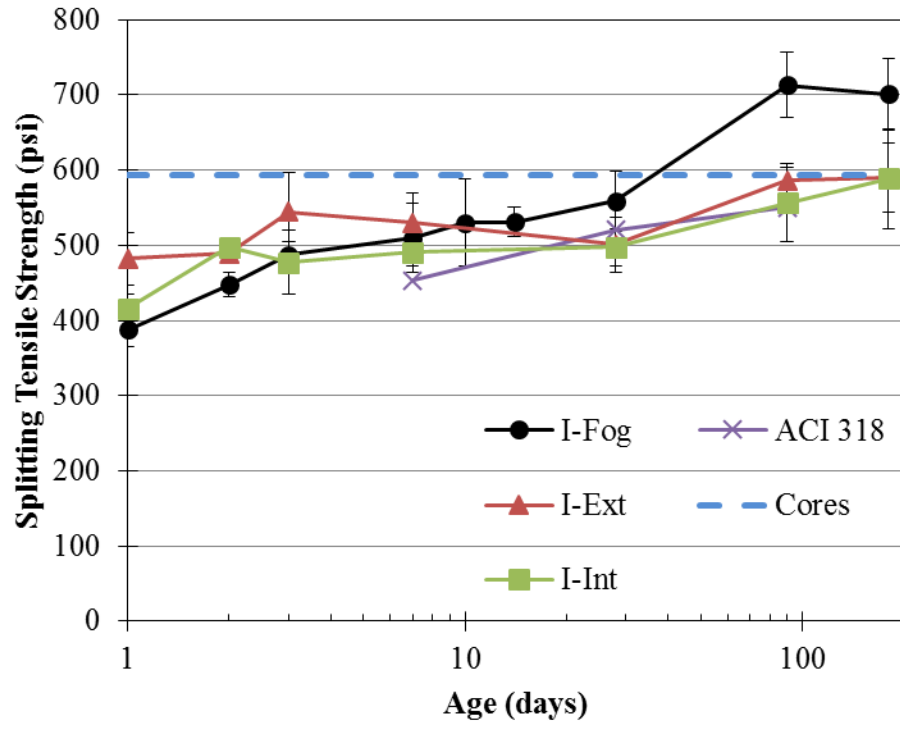
second mock-up, though for both mock-ups, the Int and Ext specimens tended to exhibit comparable strength at each age.

Figure 3.25 also shows the splitting tensile strengths predicted by Eq. 3.3, an empirical relationship between compressive strength and splitting tensile strength provided by ACI 318-08. Using the average compressive strengths of the CR3 PCC concrete at 7, 28, and 90 days, the tensile splitting strength of the CR3 PCC concrete is predicted by Eq. 3.3 to be 3.12, 3.59, and 3.80 MPa (453, 520, and 551 psi) at the respective ages. Except for the I-Ext and I-Int specimens at 28 days, each set of mock-up specimens at 7, 28, and 90 days equaled or exceeded the predicted splitting tensile strength for the CR3 PCC concrete.

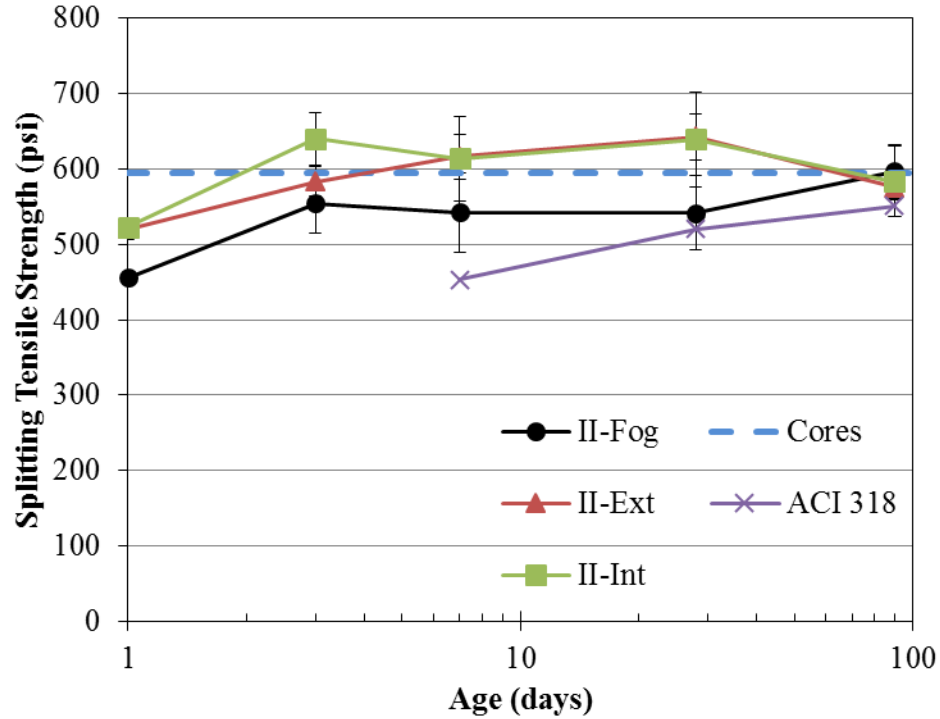
$$\begin{aligned} f_{tsp} &= 0.56\sqrt{f'_c} \quad [\text{MPa}] \\ f_{tsp} &= 6.7\sqrt{f'_c} \quad [\text{psi}] \end{aligned} \qquad \text{Eq. 3.3}$$

Where,

$$\begin{aligned} f_{tsp} &= \text{splitting tensile strength, MPa or psi} \\ f'_c &= \text{specified compressive strength, MPa or psi} \end{aligned}$$



Note: 1 MPa = 145 psi
(a)



Note: 1 MPa = 145 psi
(b)

Figure 3.25: Splitting tensile strength of (a) first and (b) second mock-up concrete

Table 3.10: Splitting tensile strength of the mock-up concrete

Batch ID	Measure	Splitting Tensile Strength (psi)								
		1-day	2-day	3-day	7-day	10-day	14-day	28-day	90-day	180-day
I-Fog	Average	388	448	487	510	530	531	559	713	701
	Std. Dev.	24	16	17	46	58	20	40	43	48
I-Ext	Average	482	489	544	530	-	-	500	586	590
	Std. Dev.	35	14	52	39	-	-	37	18	46
I-Int	Average	416	498	477	491	-	-	498	556	588
	Std. Dev.	19	6	43	19	-	-	25	52	67
II-Fog	Average	456	-	555	542	-	-	542	597	-
	Std. Dev.	7	-	40	53	-	-	50	36	-
II-Ext	Average	520	-	584	616	-	-	643	576	-
	Std. Dev.	13	-	20	30	-	-	30	18	-
II-Int	Average	523	-	641	613	-	-	640	583	-
	Std. Dev.	12	-	35	56	-	-	63	47	-

Note: 1 MPa = 145 psi

Figure 3.26 shows a failed I-Int-1 splitting tensile strength specimen tested at 1 day with approximately 70 to 80% of the coarse aggregate fractured along the plane of failure during testing. Typically, the aggregate is the strongest component material in concrete, especially at early ages when the cement paste has not developed substantial strength. Therefore, fracturing usually occurs around rather than through a significant portion of the aggregate at early ages. Similar fracturing of a large portion of the aggregate was also observed at early ages for the compressive strength specimens but is more clearly displayed in the splitting tensile strength specimens. The high rate of coarse aggregate fracture is consistent with the high content of soft and friable particles identified in the CR3 PCC coarse aggregate. Though the compressive and splitting tensile strengths of the concrete increased beyond the 1-day results due to strengthening of the cement paste between the aggregate particles, the failure of the aggregate at relatively early ages indicates that it limits the potential late-age strength of the concrete.



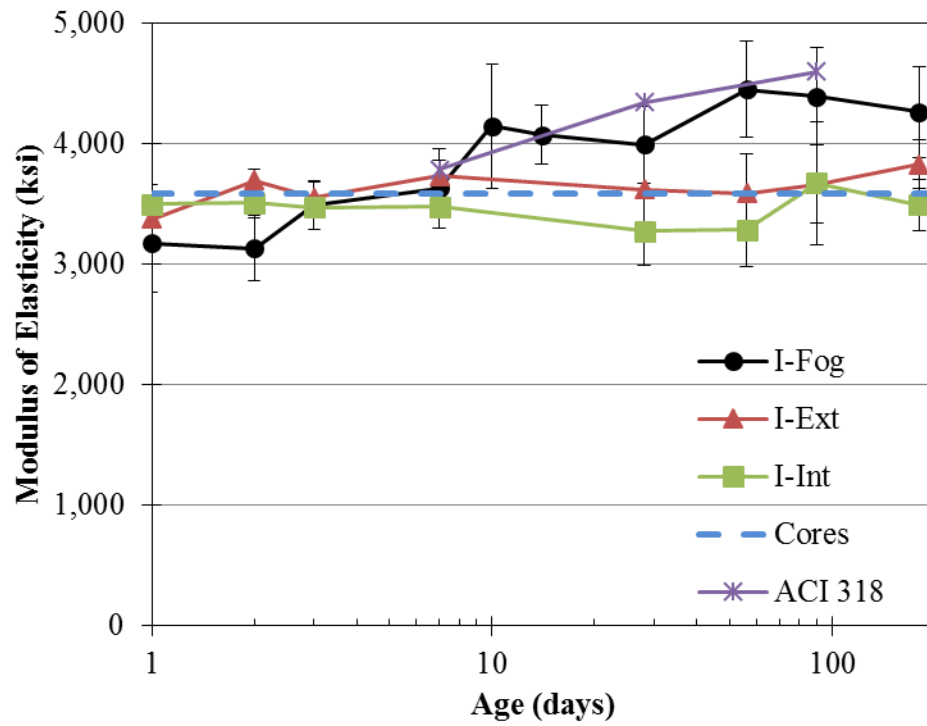
Figure 3.26: Failed I-Int-1 splitting tensile strength specimen tested at 1 day

3.4.5.3 Modulus of Elasticity

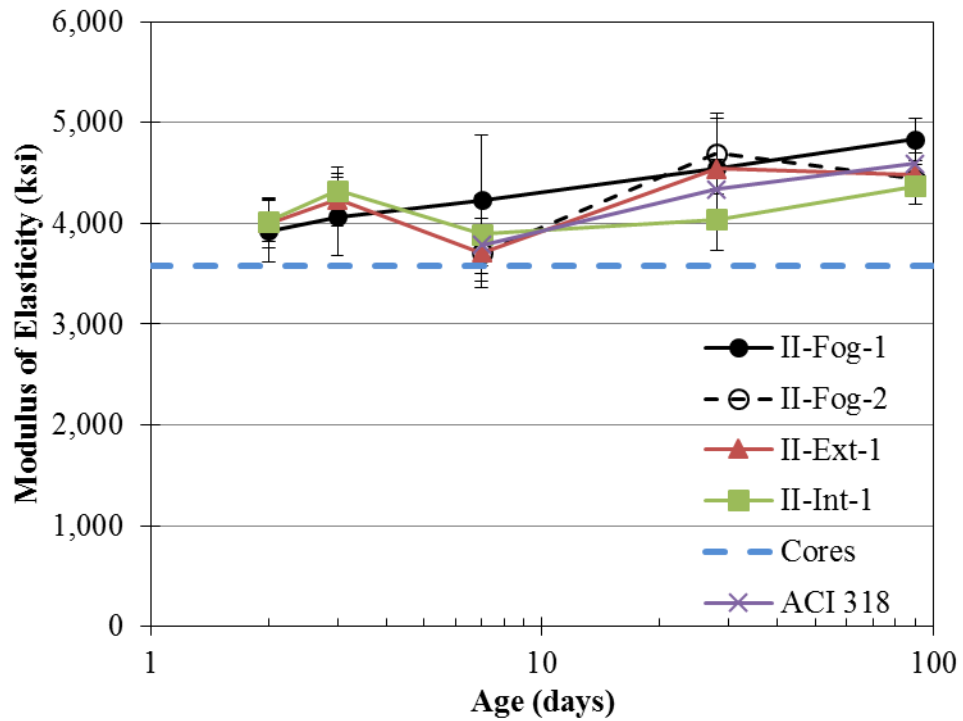
The modulus of elasticity results for the mock-up concrete are shown in Figure 3.27 and Table 3.11. Whereas the results for the first mock-up are shown as the average of the two trucks for each curing condition, the results for the II-Fog specimens for the second mock-up are shown separated by truck due to statistical significance of the two sets of data per ANOVA and rejection of the null hypothesis that the two sets of data were from the same set.

The values measured for the I-Ext specimens were generally slightly higher than those for the I-Int specimens, and both sets had generally consistent values at all ages, fluctuating around the 24.7-GPa (3,579-ksi) average modulus of elasticity of 12 post-delamination core specimens of DM-5-Mod concrete taken from bay 61 of the CR3 PCC. The crossover effect is more clearly observed in the results for the first mock-up, for which the modulus of elasticity of the I-Fog specimens increased by about 8.3 GPa (1200

ksi) over the first 90 days. In contrast, the lower 4.8-GPa (700-ksi) increase of the II-Fog specimens over the first 90 days results in less distinct crossover behavior. Except for the 7-day Ext specimens, the modulus of elasticity of the second mock-up specimens was greater than that of the first mock-up for the corresponding curing conditions and ages.



Note: 1 GPa = 145 ksi
(a)



Note: 1 GPa = 145 ksi
(b)

Figure 3.27: Modulus of elasticity of (a) first and (b) second mock-up concrete

Table 3.11: Modulus of elasticity of mock-up concrete

Batch ID	Meas-ure	Modulus of Elasticity (ksi)									
		1-day	2-day	3-day	7-day	10-day	14-day	28-day	56-day	90-day	180-day
I-Fog	Avg.	3,175	3,129	3,485	3,627	4,143	4,071	3,989	4,449	4,391	4,260
	s_s	407	270	203	325	513	242	321	402	403	377
I-Ext	Avg.	3,376	3,693	3,548	3,731	-	-	3,621	3,589	3,663	3,828
	s_s	82	97	136	127	-	-	359	320	321	200
I-Int	Avg.	3,496	3,507	3,469	3,475	-	-	3,271	3,281	3,671	3,489
	s_s	164	128	91	81	-	-	287	305	512	214
II-Fog	Avg.	-	3,929	4,068	3,968	-	-	4,622	-	4,641	-
	s_s	-	310	389	529	-	-	409	-	298	-
II-Ext-1	Avg.	-	4,006	4,240	3,709	-	-	4,546	-	4,488	-
	s_s	-	253	263	345	-	-	90	-	97	-
II-Int-1	Avg.	-	4,025	4,325	3,892	-	-	4,038	-	4,370	-
	s_s	-	208	241	385	-	-	305	-	12	-

Note: 1 GPa = 145 ksi

An empirical relationship for the modulus of elasticity based on the unit weight and compressive strength of the concrete is given in Eq. 3.4 (ACI 318-08), and this relationship was determined to be valid for ages greater than or equal to 12 hours (Oluokun et al., 1991).

Since the 2515-kg/m³ (157-lb/ft³) average unit weight reported for the CR3 PCC cores is similar to the 2,558-kg/m³ (159.7-lb/ft³) apparent density measured in accordance with ASTM C642, the reported unit weight is not likely representative of the unit weight of the fresh concrete, which includes the mass of the water and the volume of the water and air in the concrete. Therefore, the 2,276-kg/m³ (142.1-lb/ft³) unit weight of the fresh mock-up concrete was used in Eq. 3.4 with the corresponding compressive strengths to determine predicted modulus of elasticity values of 26.1, 29.9, and 31.7 GPa (3783, 4340, and 4595 ksi) at 7, 28, and 90 days, respectively, for the CR3 PCC concrete.

At the corresponding ages, the modulus of elasticity of the I-Fog specimens is slightly lower than the predicted values for the CR3 PCC concrete, but the general

behavior is comparable. At 28 and 90 days, the I-Ext and I-Int specimens have considerably lower values of modulus of elasticity than those predicted for the CR3 PCC concrete. In contrast, the modulus of elasticity values for the second mock-up are generally consistent with the predicted values at the corresponding ages, and a similar trend is present amongst all tested sets between 7 and 90 days.

$$\begin{aligned} E_c &= 0.043w_c^{1.5}\sqrt{f'_c} \quad [\text{MPa}] \\ E_c &= 33w_c^{1.5}\sqrt{f'_c} \quad [\text{psi}] \end{aligned} \quad \text{Eq. 3.4}$$

Where,

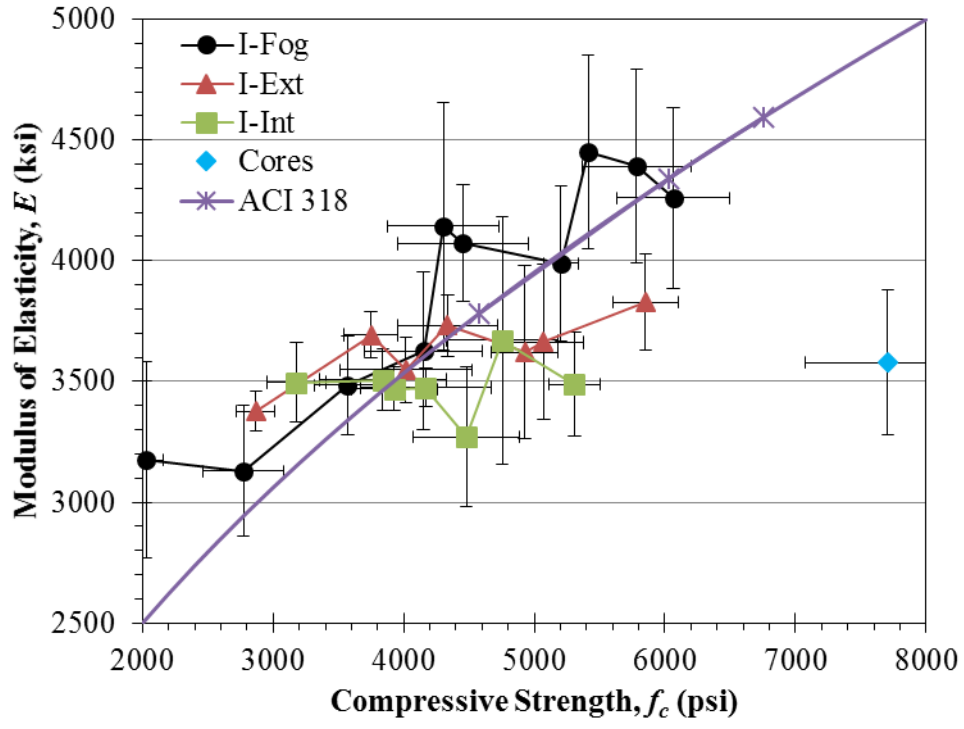
- E_c = modulus of elasticity of concrete, MPa or psi
- w_c = unit weight of concrete, kg/m³ or lb/yd³
- f'_c = compressive strength of concrete, MPa or psi

Figure 3.28 shows the relationship between the measured modulus of elasticity and compressive strength for each age and curing condition in comparison with the ACI 318 relationship (Eq. 3.4). For both mock-ups, the Fog specimens generally follow the curve predicted by ACI 318. Since the modulus of elasticity of the match-cured specimens from the first mock-up increased a relatively small amount, the I-Ext and I-Int curves have a lower slope and cross the ACI 318 curve at approximately 27.6-MPa (4000-psi) compressive strength and 24.1-GPa (3500-ksi) modulus of elasticity.

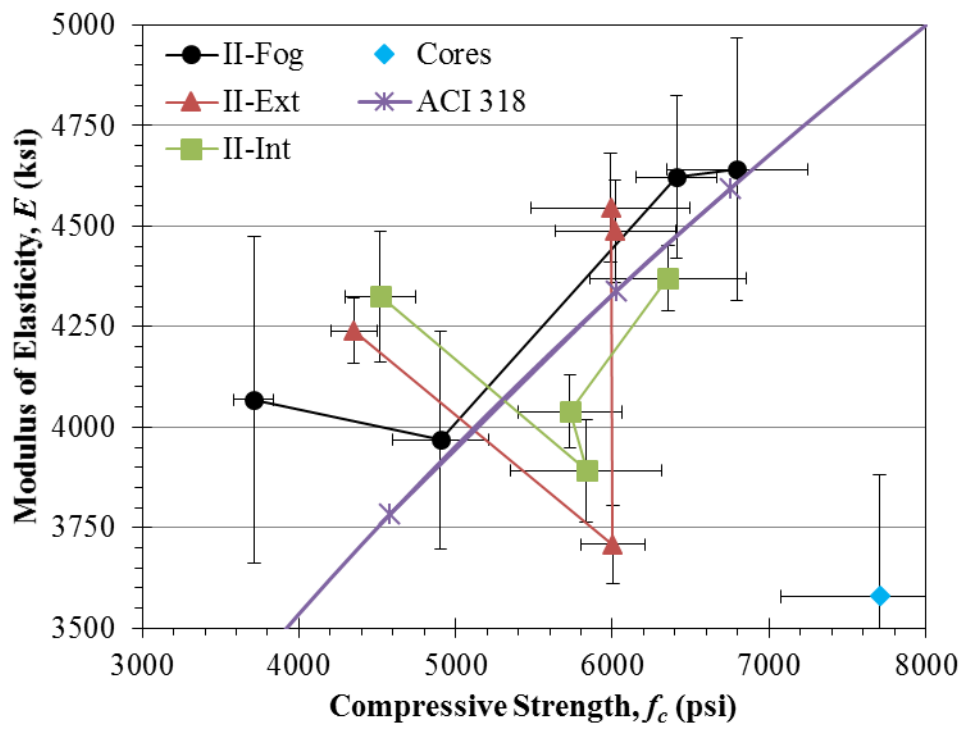
Aside from the left-most II-Fog point, which corresponds to 3-day values, the relationship between the modulus of elasticity and compressive strength of the II-Fog specimens is comparable to the ACI 318 prediction. The match-cured specimens for the second mock-up also deviate significantly from the ACI 318 prediction at early ages, and the later ages are more comparable to the ACI 318 prediction, but the general trend of the II-Ext and II-Int specimens is inconsistent with the predicted relationship.

The most significant outlier is the point for the post-delamination cores, which had an average compressive strength of 53.1 MPa (7707 psi) with a standard deviation of 4.4 MPa (634 psi) and an average modulus of elasticity of 24.7 GPa (3,579 ksi) with a standard deviation of 2.1 GPa (302 ksi). The modulus of elasticity is 73% of the 53.1-

GPa (4907-ksi) value predicted by Eq. 3.4, which, when overestimating, tends to be within 9.41% of the measured modulus of elasticity. This difference may have been caused by damage to the cores during drilling that affected the stiffness of the cores more than the strength. Additionally, as previously discussed, the numerous factors influencing core strengths may have influenced the predicted modulus of elasticity value.



(a)



(b)

Figure 3.28: Modulus of elasticity versus compressive strength for (a) first and (b) second mock-up concrete

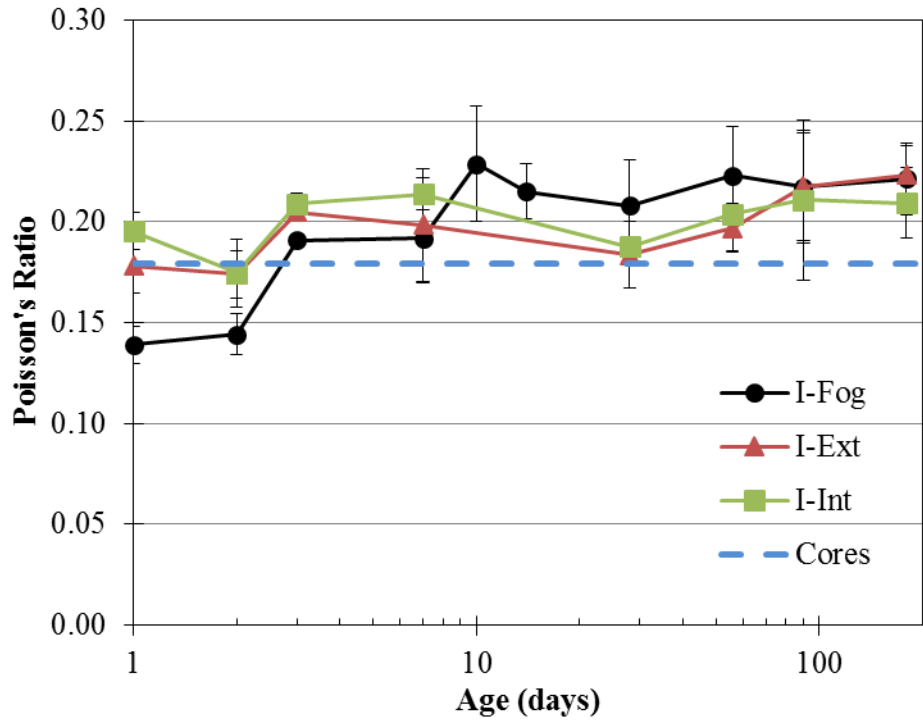
3.4.5.4 Poisson's Ratio

The Poisson's ratio results for the mock-up concrete are shown in Figure 3.29 and Table 3.12. The I-Fog specimens increased from an initial value of 0.14 at 1 day to a value of approximately 0.22 at 10 days, and was roughly constant for the remainder of testing. The II-Fog specimens exhibited a gradual increase from an initial value of 0.20 at 2 days to a maximum of 0.22 at 90 days. In contrast, the match-cured specimens for both mock-ups generally varied within the range of 0.18 to 0.22 with no distinct trend. Aside from the I-Fog specimens, the general consistency of the Poisson's ratio values for the different curing conditions and ages is consistent with the literature (Higginson, 1961; Oluokun et al, 1991).

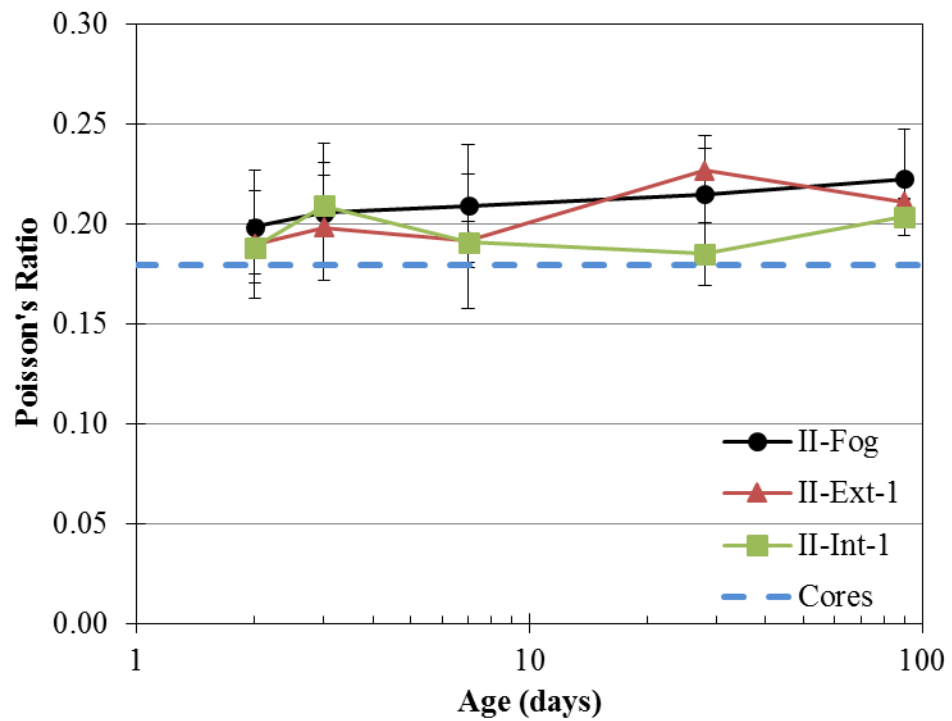
Most of the measured Poisson's ratio values were higher than the 0.18 average Poisson's ratio of 12 post-delamination core specimens of DM-5-Mod concrete taken from bay 61 of the CR3 PCC. Furthermore, many values were above the typical range of 0.15 to 0.20 for concrete (Mehta and Monteiro, 2006). However, the 0.24 average value reported for post-delamination cores taken from the region of the SGR opening with DM-5-Mod concrete suggests that the high values for the mock-up concrete may be representative.

The high values may have been caused by longitudinal microcracking during the loading, which would have increased the measured transverse strains and resulted in higher Poisson's ratio values. Such microcracking typically occurs at high stresses, leading to rapidly increasing Poisson's ratio values until failure (Persson, 1999). However, some of the mock-up specimens cracked longitudinally into halves during the loading segments before reaching 40% of the ultimate strength, indicating that microcracking may have been occurring at lower stresses and increasing the measured Poisson's ratio. Figure 3.30 shows a 7-day Ext specimen from the second mock-up that cracked during the first cycle of testing. Despite the planar crack, which did not coincide with any of the pin contacts of the compressometer, the specimen was able to sustain an

ultimate load of 582 kN (131 kips), corresponding to a strength of 32.0 MPa (4,634 psi). Such cracking at low stresses while still achieving reasonable strength results suggests that the behavior would not necessarily be evident in the original compressive strength results obtained for the CR3 PCC concrete.



(a)



(b)

Figure 3.29: Poisson's ratio of the (a) first and (b) second mock-up concrete

Table 3.12: Poisson's ratio of the mock-up concrete

Batch ID	Meas-ure	Poisson's Ratio									
		1-day	2-day	3-day	7-day	10-day	14-day	28-day	56-day	90-day	180-day
I-Fog	Avg.	0.14	0.14	0.19	0.19	0.23	0.22	0.21	0.22	0.22	0.22
	s_s	0.009	0.010	0.003	0.022	0.028	0.014	0.023	0.025	0.027	0.018
I-Ext	Avg.	0.18	0.17	0.20	0.20	-	-	0.18	0.20	0.22	0.22
	s_s	0.014	0.012	0.003	0.028	-	-	0.016	0.012	0.028	0.014
I-Int	Avg.	0.20	0.17	0.21	0.21	-	-	0.19	0.20	0.21	0.21
	s_s	0.009	0.017	0.005	0.008	-	-	0.021	0.018	0.040	0.017
II-Fog	Avg.	-	0.20	0.21	0.21	-	-	0.21	-	0.22	-
	s_s	-	0.028	0.025	0.031	-	-	0.029	-	0.025	-
II-Ext	Avg.	-	0.19	0.20	0.19	-	-	0.23	-	0.21	-
	s_s	-	0.027	0.026	0.034	-	-	0.011	-	0.001	-
II-Int	Avg.	-	0.19	0.21	0.19	-	-	0.18	-	0.20	-
	s_s	-	0.014	0.031	0.010	-	-	0.016	-	0.009	-



Figure 3.30: Cracked specimen from modulus of elasticity and Poisson's ratio testing

3.4.6 Coefficient of Linear Thermal Expansion

The following sections discuss the results of the tests for the CTE of the mock-up concrete according to the methods discussed in Section 3.3.4.4.

3.4.6.1 Army Corps CRD-C 39-81

The results of testing for CTE in accordance with Army Corps CRD-C 39-81 (1981) are shown in Figure 3.31 and Table 3.13. The average value of all specimens was $7.91 \mu\epsilon/^{\circ}\text{C}$ ($4.39 \mu\epsilon/^{\circ}\text{F}$) with a standard deviation of $1.86 \mu\epsilon/^{\circ}\text{C}$ ($1.03 \mu\epsilon/^{\circ}\text{F}$), and the values ranged from a minimum of $6.24 \mu\epsilon/^{\circ}\text{C}$ ($3.47 \mu\epsilon/^{\circ}\text{F}$) for truck 1 at 56 days to a maximum of $9.62 \mu\epsilon/^{\circ}\text{C}$ ($5.34 \mu\epsilon/^{\circ}\text{F}$) for truck 2 at 7 days.

For the null hypothesis that the concrete from the two trucks was the same, single-factor ANOVA results indicated that, for the ages at which specimens from both trucks were tested, the CTE values for specimens from the two trucks were not statistically unique at the 5% significance level. Furthermore, for the null hypothesis that the CTE for all specimens is the same at each age, single-factor ANOVA indicated that the CTE values at each age were not statistically unique at the 5% significance level. Therefore, the mean CTE of all specimens from both trucks at all ages, $7.91 \mu\epsilon/^{\circ}\text{C}$ ($4.39 \mu\epsilon/^{\circ}\text{F}$), can be considered representative of the entire population of CTE specimens.

The logarithmic regression shown in Figure 3.31 similarly indicates that, though widely varying, the data tends to be constant with time. The low coefficient of determination (R^2) value indicates that the regression provides a marginally better fit of the data than the mean of the data.

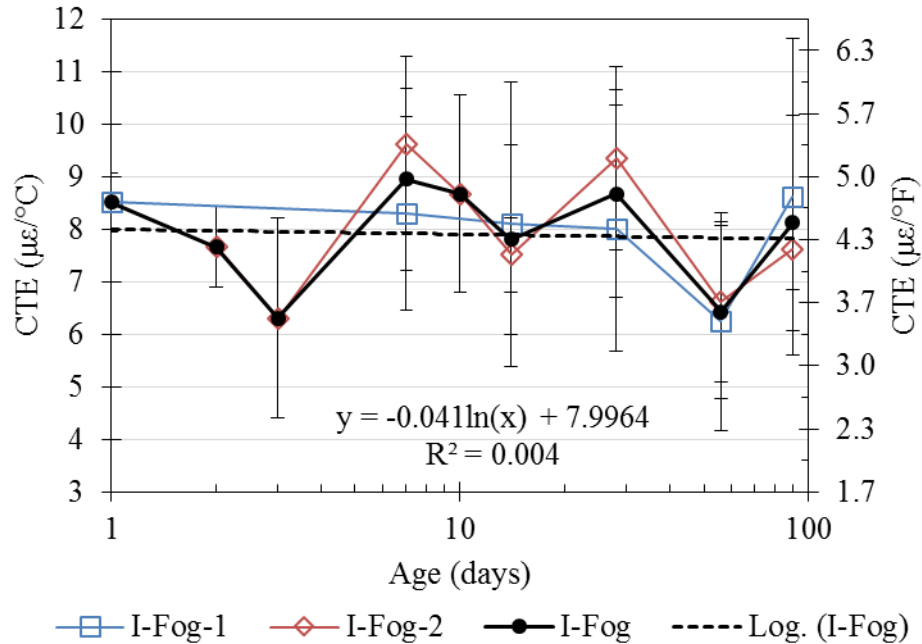


Figure 3.31: CTE results for concrete from the first mock-up tested in accordance with Army Corps CRD-C 39-81

Table 3.13: CTE results for concrete from the first mock-up tested in accordance with Army Corps CRD-C 39-81

Batch ID	Measure	Coefficient of Thermal Expansion, α_T ($\mu\epsilon/^\circ\text{C}$)									
		1-day	2-day	3-day	7-day	10-day	14-day	28-day	56-day	90-day	All
I-Fog-1	Average	8.51	-	-	8.29	-	8.09	8.01	6.24	8.62	7.93
	Std. Dev.	0.57	-	-	1.84	-	2.70	2.34	2.08	3.02	2.10
I-Fog-2	Average	-	7.66	6.30	9.62	8.67	7.51	9.34	6.62	7.62	7.92
	Std. Dev.	-	0.77	1.91	1.67	1.88	0.71	1.74	1.53	0.78	1.67
I-Fog	Average	8.51	7.66	6.30	8.96	8.67	7.80	8.68	6.43	8.12	7.92
	Std. Dev.	0.57	0.77	1.91	1.73	1.88	1.80	1.98	1.65	2.05	1.84
	p-value*	-	-	-	0.407	-	0.736	0.475	0.812	0.609	0.259

* p-value for single-factor ANOVA with significance level $\alpha = 0.05$ and the null hypothesis that the concrete from the two trucks is the same

3.4.6.2 AASHTO and Texas Method

The temperature history and corresponding length change for one of the 1-day specimens tested in accordance with AASHTO T336 are shown in Figure 3.32, and the

corresponding data used to calculate the CTE in accordance with the Texas method is shown in Figure 3.33. Rather than plotting the length change as a function of temperature, Figure 3.33 shows the specimen strain with the correction factor from Eq. 92 in Section 2.7.4.2.3 applied so that the slopes of the linear regressions equal the CTE for the corresponding segment of the test cycle. The average of the two slopes gives the CTE for the specimen: $8.32 \mu\epsilon/^\circ\text{C}$ ($4.62 \text{ }^\circ\text{F}$). The nonlinearity in the data at the extreme temperatures in Figure 3.33 justifies the 15-to-45- $^\circ\text{C}$ (59-to-113- $^\circ\text{F}$) temperature range for regression analysis.

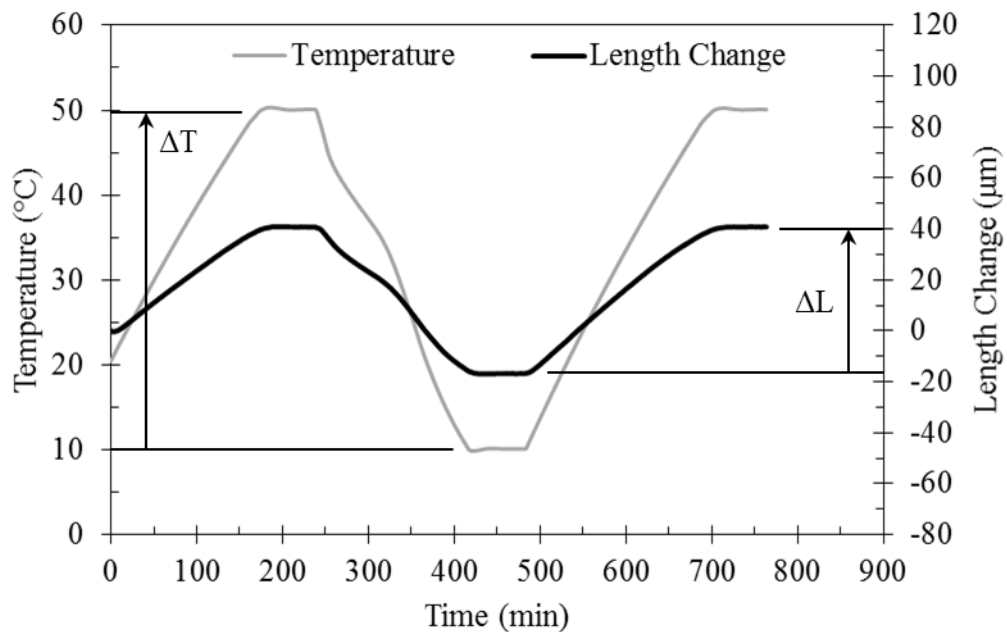


Figure 3.32: Length change and temperature histories for determination of CTE in accordance with AASHTO T 336

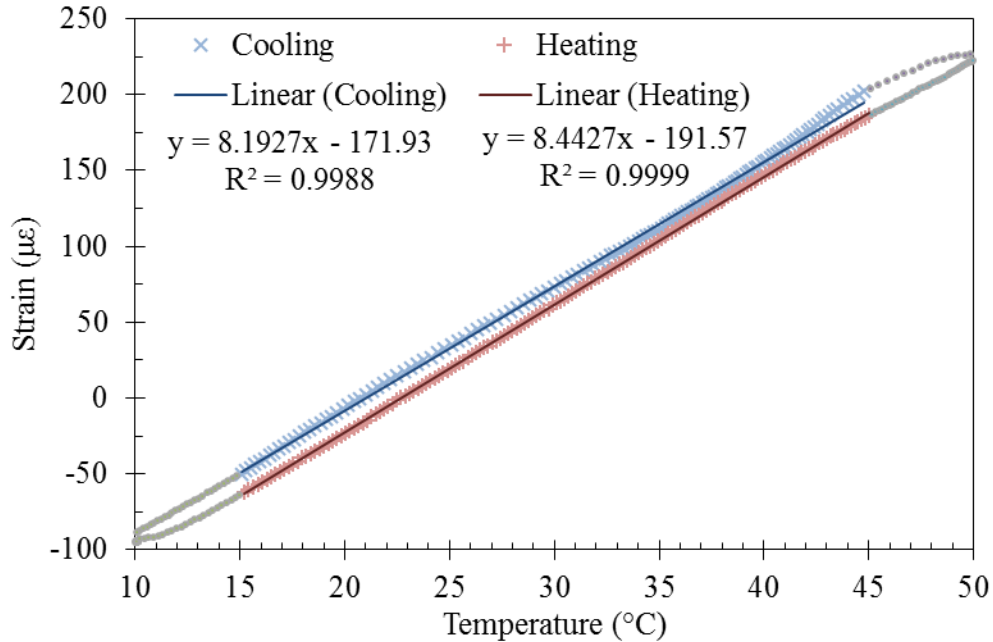


Figure 3.33: Strain as a function of temperature for determination of CTE in accordance with Tex-428-A

The results of testing for CTE in accordance with AASHTO T 336 and the Texas Method are shown in Figure 3.34 and Table 3.14. The CTE measured by the AASHTO method decreased gradually with age, ranging from a maximum of $7.99 \mu\epsilon/^{\circ}\text{C}$ ($4.44 \mu\epsilon/^{\circ}\text{F}$) at 2 days to a minimum of $7.15 \mu\epsilon/^{\circ}\text{C}$ ($3.97 \mu\epsilon/^{\circ}\text{F}$) at 56 days. The Texas Method results followed the trends of the AASHTO results but had slightly higher values at each age. The difference between the two tests ranged from 0.19 to $0.31 \mu\epsilon/^{\circ}\text{C}$ (0.11 to $0.17 \mu\epsilon/^{\circ}\text{F}$) at 1 and 14 days, respectively. For the null hypothesis that the CTE measured by the two methods was the same at each age, single-factor ANOVA results indicated that the CTE values were not statistically unique at the 5% significance level, but the limited sample size (two specimens) for each age is probably a contributing factor to those results.

The similar trends of the two test methods suggests that the results are not independent, and the comparable ranges in the data for both tests indicates that one method cannot necessarily be considered superior based on these results. Since the

AASHTO method is more widely used than the Army Corps and Texas methods (see Section 2.7.4.2) and the results of the AASHTO method are more precise than those of the Army Corps method, the AASHTO CTE results will be used for the remainder of the analysis.

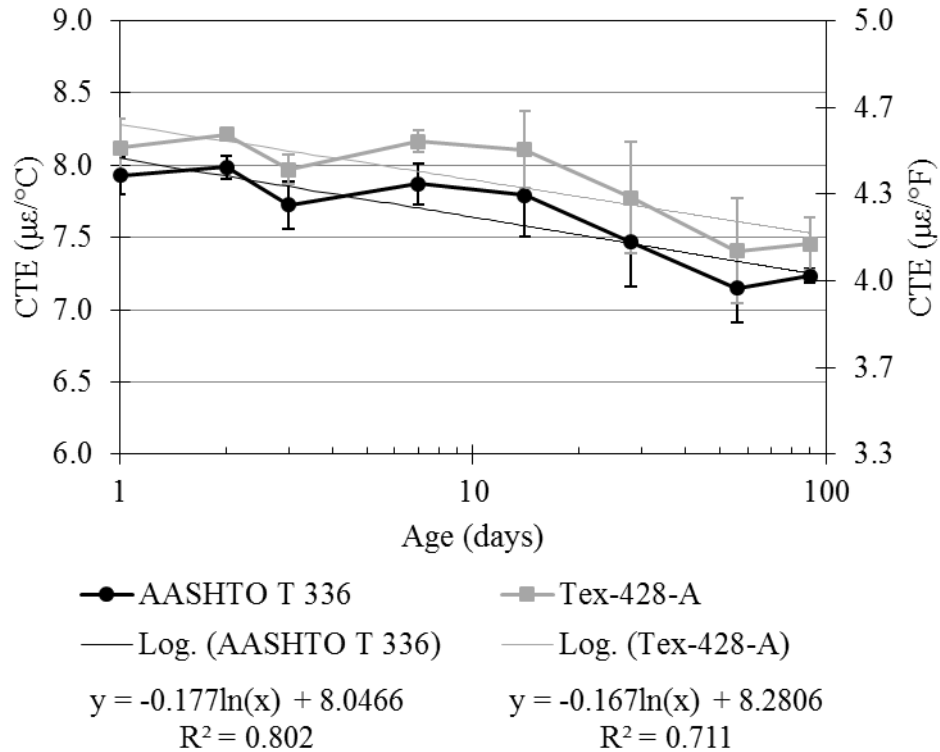


Figure 3.34: CTE results for concrete from the first truck of the first mock-up tested in accordance with AASHTO 336 and the Texas Method

Table 3.14: CTE results for concrete from the first truck of the first mock-up tested in accordance with AASHTO 336 and the Texas Method

Test Method	Measure	Coefficient of Thermal Expansion ($\mu\epsilon/^\circ\text{C}$)							
		1-day	2-day	3-day	7-day	14-day	28-day	56-day	90-day
AASHTO T 336	Average	7.93	7.99	7.72	7.87	7.79	7.47	7.15	7.23
	Range	0.26	0.16	0.33	0.28	0.58	0.61	0.47	0.10
Tex-428-A	Average	8.12	8.21	7.97	8.16	8.11	7.77	7.40	7.46
	Range	0.40	0.01	0.20	0.15	0.53	0.77	0.73	0.37
Difference		0.19	0.23	0.25	0.30	0.31	0.31	0.26	0.22
p-value*		0.505	0.105	0.328	0.204	0.508	0.597	0.616	0.361

* p-value for single-factor ANOVA with significance level $\alpha = 0.05$ and the null hypothesis that the CTE measured by the two test methods is the same

As discussed in Section 3.4.4 and shown in Figure 3.20, the concrete in both mock-ups returned to near-ambient temperatures within two weeks, and later variations were relatively negligible compared to the early-age hydration temperatures. Figure 3.35 shows that the decrease in measured CTE was minimal during the first 14 days and that most of the change in CTE happened after 14 days. The low coefficient of determination (R^2) value for the logarithmic regression over the first 14 days indicates that the regression does not provide a significantly better fit of the data than the average of the data. For the null hypothesis that the CTE over the first 14 days was constant, ANOVA with a significance level of 5% determined a p-value of 0.833, indicating that the CTE values measured over the first 14 days were not statistically unique.

The average CTE measured over the first 14 days was $7.86 \mu\epsilon/^\circ\text{C}$ ($4.37 \mu\epsilon/^\circ\text{F}$) with a standard deviation of $0.21 \mu\epsilon/^\circ\text{C}$ ($0.12 \mu\epsilon/^\circ\text{F}$). Over a temperature range of 50°C (90°F), representative of the temperature change in the mock-ups, these average and standard deviation values correspond to thermal strains of 393 and $10.5 \mu\epsilon$, respectively, indicating that the variation in CTE over the first 14 days is insignificant compared to the magnitude. Since the temperature change in the mock-up beyond 14 days is minimal, a constant CTE of $7.86 \mu\epsilon/^\circ\text{C}$ ($4.37 \mu\epsilon/^\circ\text{F}$) was used for analysis of the concrete at all ages.

This experimental CTE value is within the 5.4-to-8.6 $\mu\epsilon/^\circ\text{C}$ (3.0-to-4.8 $\mu\epsilon/^\circ\text{F}$) range given by ACI 207.4R-93 (1998) for concrete containing limestone coarse aggregate and is similar to the 7.80- $\mu\epsilon/^\circ\text{C}$ (4.34- $\mu\epsilon/^\circ\text{F}$) and 8.18- $\mu\epsilon/^\circ\text{C}$ (4.54- $\mu\epsilon/^\circ\text{F}$) values reported by the Federal Highway Administration (2011) and Jahangirnejad et al. (2009), respectively. As noted in Section 3.1.2.3, the 11.7- $\mu\epsilon/^\circ\text{C}$ (6.5- $\mu\epsilon/^\circ\text{F}$) CTE reported for the CR3 PCC concrete is notably higher than typical values reported in the literature, and the method of determining the value was not identified.

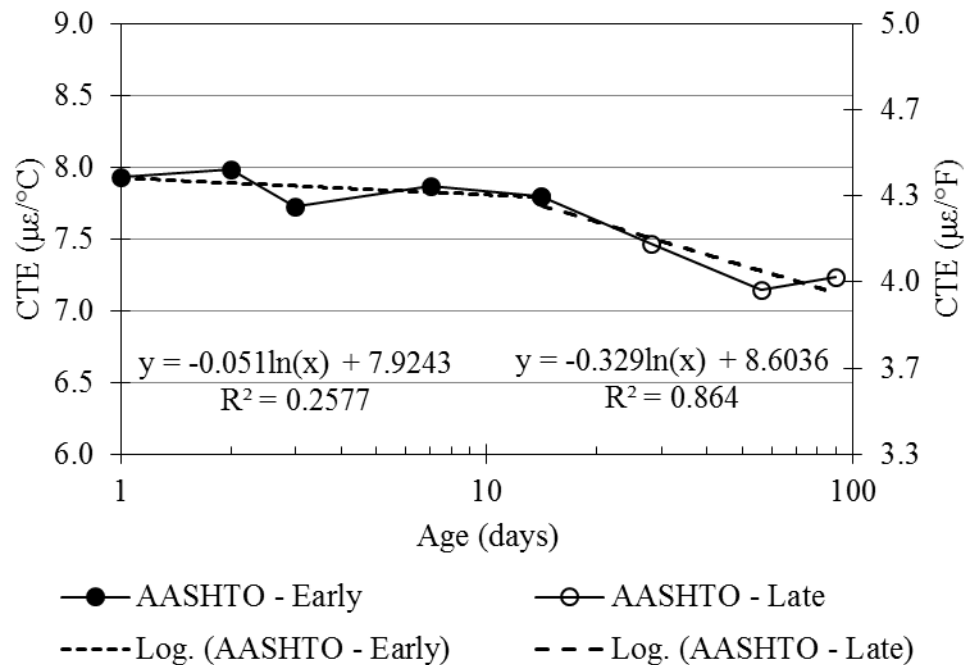


Figure 3.35: Piecewise-linear regression of AASHTO T 336 results with hinge at 14 days

3.4.7 Thermal Stresses

Eq. 3.5 was provided by Mehta and Monteiro (2006) for prediction of the thermal stresses in concrete due to temperature change. Due to the rapid rise in concrete temperatures during the first day, the effect of creep was minimized (ACI 207.2R-07), and the creep coefficient ϕ was conservatively taken to be zero. The time-dependent

degree of restraint K_r was determined according to the temperature profiles as discussed in Section 3.4.4, and the CTE was determined to be $7.86 \mu\epsilon/^\circ\text{C}$ ($4.37 \mu\epsilon/^\circ\text{F}$) as discussed in Section 3.4.7. For each mock-up, time-dependent values of the modulus of elasticity were determined via regression of the Ext and Int specimens together since there was little statistical difference between the sets of data.

$$\sigma_t = K_r \frac{E}{1 + \varphi} \alpha_T \cdot \Delta T \quad \text{Eq. 3.5}$$

Where,

- σ_t = tensile thermal stress, MPa (psi)
- K_r = degree of restraint
- E = elastic modulus
- φ = creep coefficient
- α_T = coefficient of thermal expansion
- ΔT = temperature change

With values normalized by the maximum value during the first 14 days, Figure 3.36 shows the relative influence of the degree of restraint, modulus of elasticity, and temperature difference on the calculated tensile thermal stress in the second mock-up. The most rapid change for each factor occurred during the first day, after which the relative variation of the degree of restraint and modulus of elasticity was small compared to the variation of the temperature difference. Generally, the variation of the thermal stresses during the first 14 days was largely governed by the temperature difference. The calculated thermal stresses for each mock-up are shown in Figure 3.37.

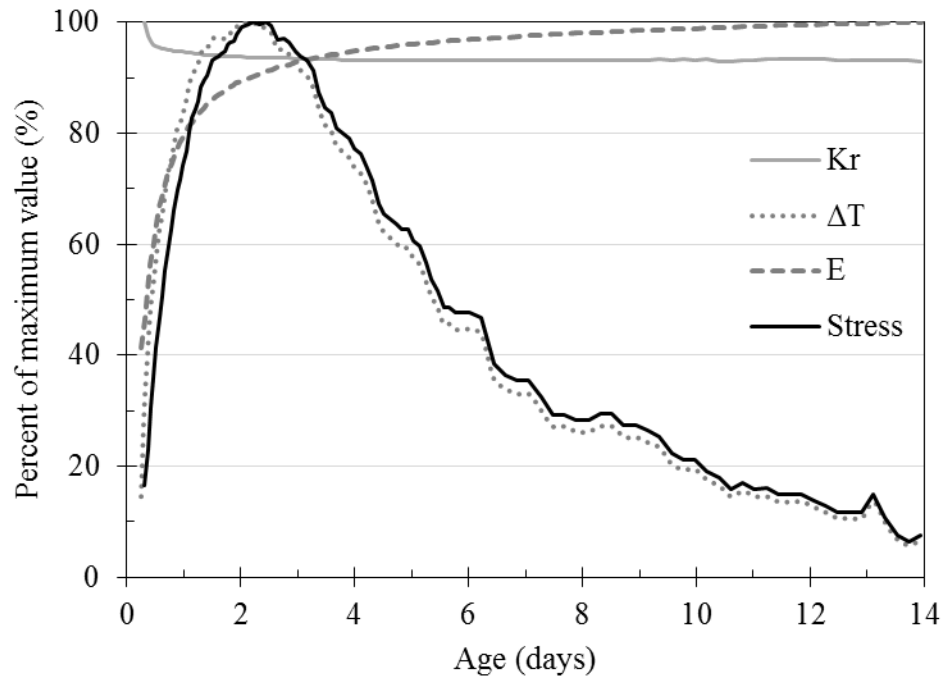


Figure 3.36: Degree of restraint, maximum temperature difference, modulus of elasticity, and tensile thermal stress of second mock-up normalized by maximum value during first 14 days

ACI 207.2R-07 recommends that direct tensile strength be used for analysis of thermal stress capacity and suggests that indirect tensile strengths, such as tensile splitting strength, be converted to predicted values of direct tensile strength. Per Neville (2011), direct tensile strength tends to be about 89 to 95% of the splitting tensile strength, and Figure 3.37 shows the match-cured splitting tensile strength results from Figure 3.25 multiplied by a factor of 0.9. Since the average direct tensile strength of the post-delamination CR3 PCC cores was approximately 75% of the average splitting tensile strength of the cores, the splitting tensile strength results multiplied by a factor of 0.75 are also shown in Figure 3.37. ACI 209R-92 (2008) provides the empirical relationship amongst unit weight, compressive strength, and direct tensile strength shown in Eq. 3.6, which was also used to predict the direct tensile strength as shown in Figure 3.37.

$$\begin{aligned}
 f_t &= 0.0069\sqrt{w_c f'_c} \quad [\text{MPa}] \\
 f_t &= 0.33\sqrt{w_c f'_c} \quad [\text{psi}]
 \end{aligned}
 \tag{Eq. 3.6}$$

Where,

- f_t = direct tensile strength, MPa or psi
- w_c = unit weight of concrete, kg/m³ or lb/yd³
- f'_c = compressive strength of concrete, MPa or psi

Figure 3.37a shows that the tensile thermal stress never exceeded the predicted tensile strength of the first mock-up concrete. The 1.14-MPa (165-psi) maximum stress at 31 hours was approximately 73% of the 1.55 MPa (225 psi) tensile strength predicted by the ACI equation (Eq. 3.6) at that time. At 15 hours, the 1.09-MPa (158-psi) tensile stress was 80% of the 1.36-MPa (197-psi) strength predicted by the ACI equation, the greatest stress-to-strength ratio for the first mock-up.

In contrast, the 1.61 MPa (234-psi) maximum tensile thermal stress, at approximately 53 hours, in the second mock-up was nearly 0.48 MPa (69 psi) greater than that in the first mock-up due to the larger temperature difference and the higher modulus of elasticity of the second mock-up. As a result, the tensile stress at that time is 88% of the 1.81-MPa (262-psi) direct tensile strength predicted by the ACI equation, the greatest stress-to-strength ratio for the second mock-up.

Of note in Figure 3.37 is that, after the first day, the direct tensile strength predicted by the ACI equation is approximately 50 to 55% of the strength predicted by Neville and 60 to 65% of that predicted by the relationship measured on the post-delamination CR3 PCC cores. The lower direct tensile strength of the cores was attributed to the soft and porous aggregate, which would similarly influence the mock-up concrete, but the ACI equation, based on the compressive strength, appears to underestimate the direct tensile strength of the concrete. Therefore, the results suggest that no early-age thermal cracking occurred in the mock-ups.

Riding (2007) developed a lognormal distribution for cracking probability as a function of the tensile stress-to-splitting tensile strength ratio (σ/f_{tsp}) of concrete

specimens. The maximum σ/f_{tsp} values during the first 14 days for the first and second mock-ups were 0.35 and 0.45, respectively, corresponding the cracking probabilities of less than 1 and 10%, respectively. Therefore, the likelihood that thermal cracking occurred in the mock-ups is very low.

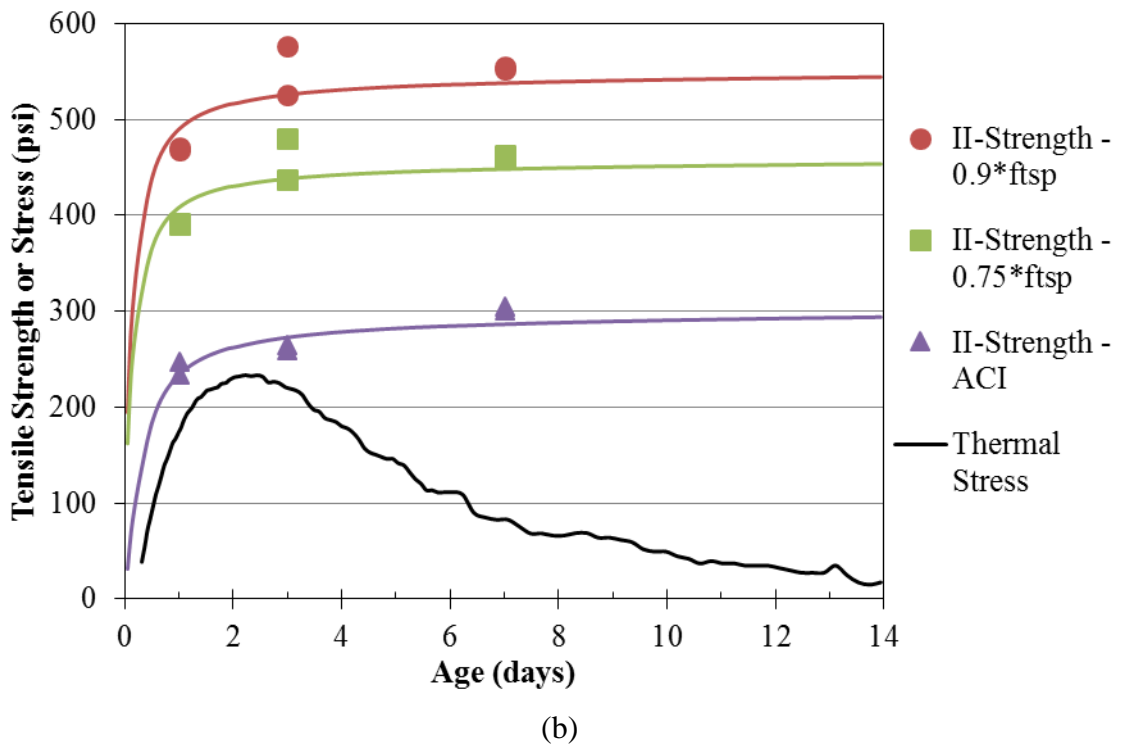
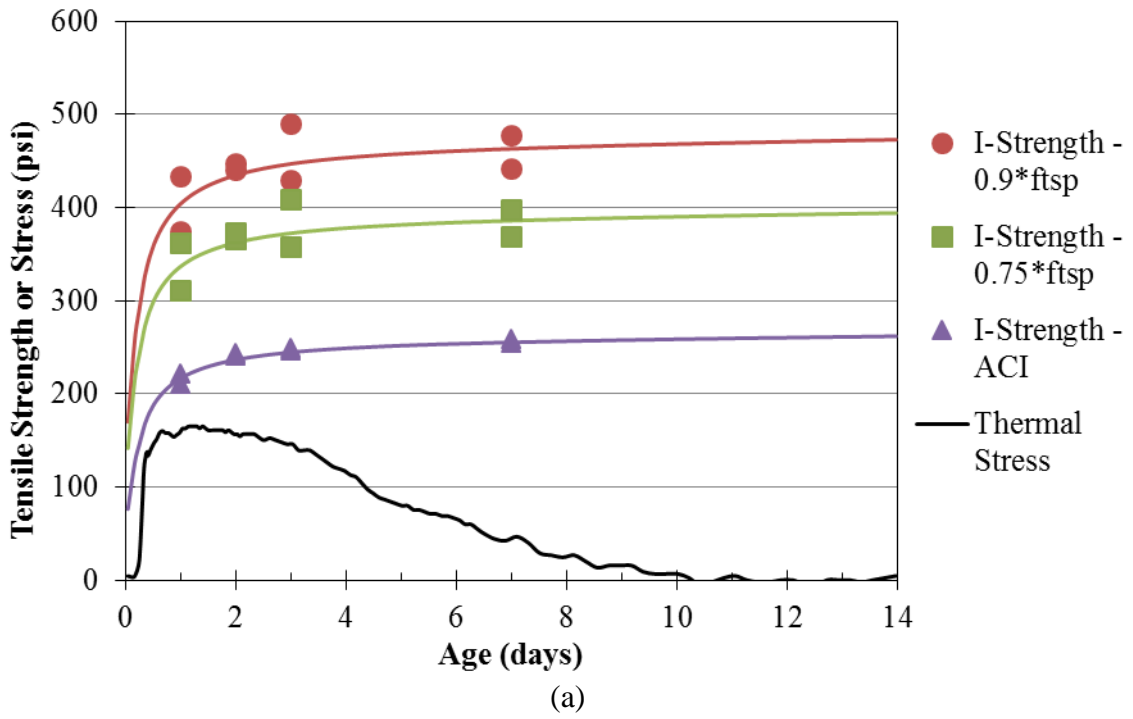


Figure 3.37: Thermal stresses and predicted direct tensile strength of (a) first and (b) second mock-up concrete

3.4.8 Mock-Up Strains

Figure 3.38 shows the rate of temperature change measured at a depth of roughly 533 mm (21 in.) from the front face of the second mock-up during the first 12 hours after concrete placement. The first two hours of data were deleted due to noise from the placement and consolidation of the fresh concrete. The maximum rate of temperature change measured by the E4, F4, E'4, and F'4 gauges (those at the lowest elevation in the mock-up) occurred approximately 5.5 hours after concrete placement began, whereas the maximum rate measured by the gauges at higher elevations occurred approximately 7 to 8 hours after concrete placement began. According to Christensen (2006), these times can be representative of the time of final setting of the concrete. The time between the two batches of concrete for the mock-up was approximately 1.5 to 2 hours, comparable to the 1.5 to 2.5 hours between maximum rates of temperature change.

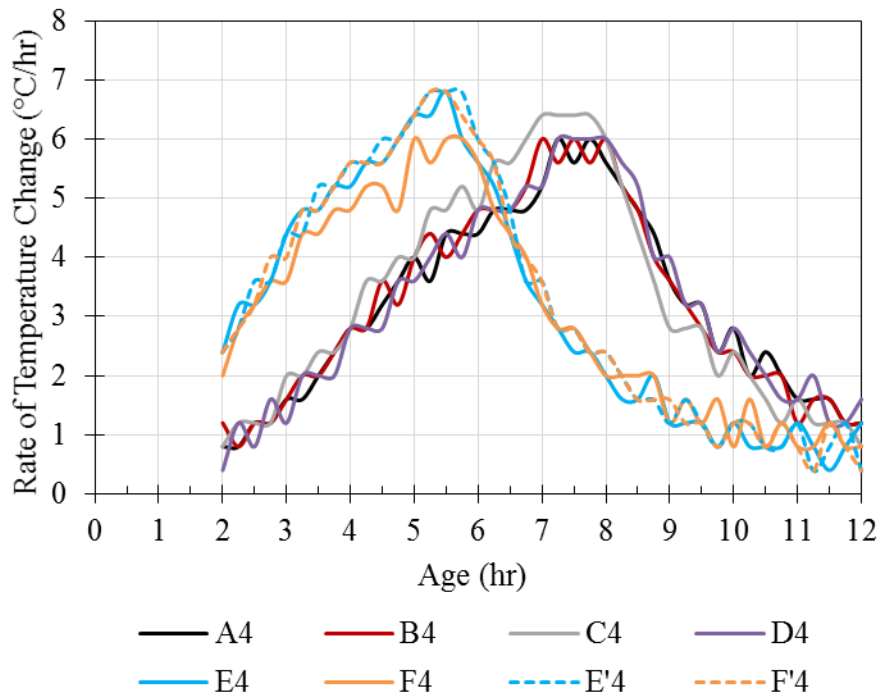


Figure 3.38: Rate of temperature change of second mock-up concrete

Figure 3.39 shows strains measured at a depth of roughly 533 mm (21 in.) from the front face of the second mock-up during the first 8 hours after concrete placement. Due to consolidation and settlement of the fresh concrete, unrepresentative strains were recorded during the first 3 hours. By 3.25 hours, the strain readings for the E4 and F4 gauges had stabilized, and the measured total tensile strain had begun increasing rapidly. Similarly, the measurements of the gauges at the higher elevations had stabilized by approximately 5 hours and rapidly increasing tensile strains were recorded. This behavior suggests that the concrete had obtained sufficient rigidity at these times to sustain stresses, and the 1.75 hours between the two times matches the times between the two batches of concrete and the maximum rates of temperature change. Therefore, the strains for the E, F, E', and F' gauges were zeroed at 3.25 hours, and the strains for all other gauges were zeroed at 5 hours, as shown in Figure 3.39.

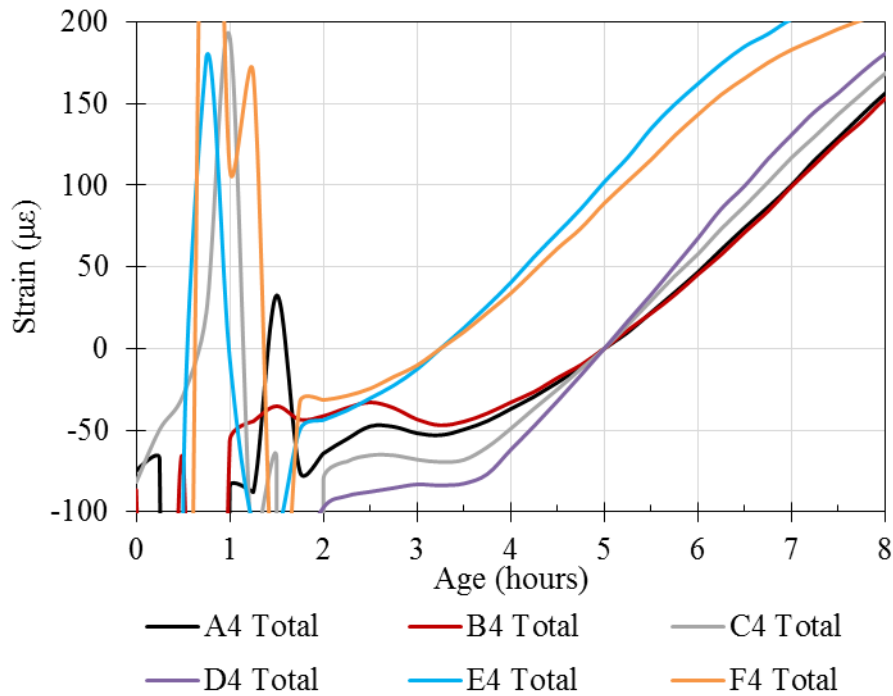


Figure 3.39: Total strains measured in mock-up during first 12 hours after beginning of concrete placement

Figure 3.40 shows the first 28 days of total strains measured by the same gauges as well as the thermal and non-thermal components of the measured strains. For each gauge, the thermal strain was determined using the experimentally determined concrete CTE of $7.86 \mu\epsilon/^\circ\text{C}$ ($4.37 \mu\epsilon/^\circ\text{F}$) and the temperature difference between the time of interest and the previously discussed zeroing times. Comparison of the strain types reveals that the thermal strain largely controlled the measured total strain behavior. As shown in Figure 3.41, after initial variability, thermal strain contributed to approximately 70 to 80% of the total strain through the first 30 hours, during which the temperature of the concrete was rising rapidly and both the thermal and non-thermal strains were increasing. After this period, however, the non-thermal strains were essentially constant, and decreasing temperatures at about 36 hours resulted in equal rates of total and thermal strain reduction, as seen in Figure 3.40.

The rapid rise in total and thermal strains was relatively consistent amongst the various gauge locations during the first 18 hours. After 1 day, the A4 and B4 thermal strains, measured nearest the top surface of the mock-up, began to decrease relative to the other gauges nearer the center of the mock-up, resulting in a difference in thermal strain between the two sets of gauges of approximately 50 to $75 \mu\epsilon$ between 2 and 6 days as the concrete cooled. After this period, the thermal strains converged as the concrete temperature became more uniform. By 9 days, the measured temperatures had returned to the values measured at the zeroing times, and the continued gradual drop in temperature resulted in negative thermal strains that stabilized at around -60 to $-70 \mu\epsilon$, comparable to the magnitude of the non-thermal strains and resulting in total strains of approximately 0 to $25 \mu\epsilon$.

In mass concrete applications, the high V/SA limits the escape of heat from the concrete during hydration, resulting in the high early-age temperatures. Similarly, the high V/SA limits the loss of moisture from mass concrete, resulting in negligible early-age drying shrinkage (Riding, 2007). Therefore, the positive non-thermal strains indicate

autogenous expansion. As previously noted, the non-thermal strains were essentially constant after the first 30 hours, consistent with ACI 207.1R-05 (2005), which states that such expansion typically occurs within the first 30 days if at all. Such autogenous expansion has been measured in many mass concrete structures, particularly dams (ACI 207.1R-05, 2005; Serafim and Guerreiro 1969).

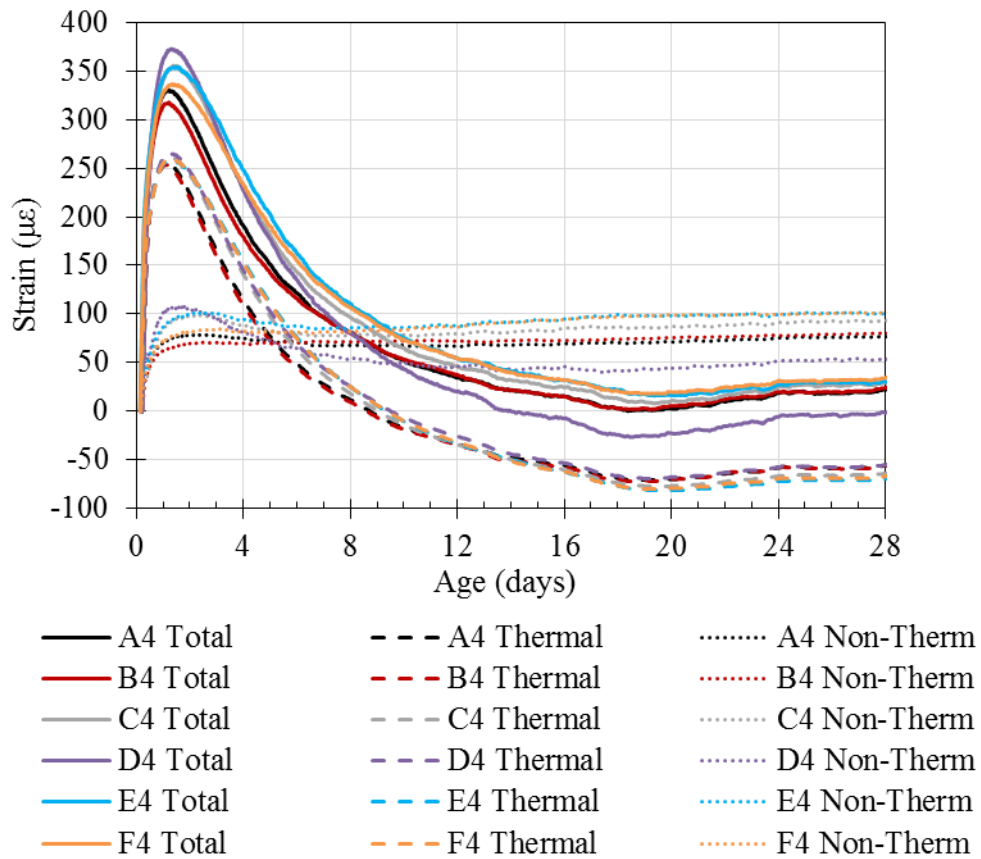


Figure 3.40: Total, thermal, and non-thermal strains measured in second mock-up during first 28 days

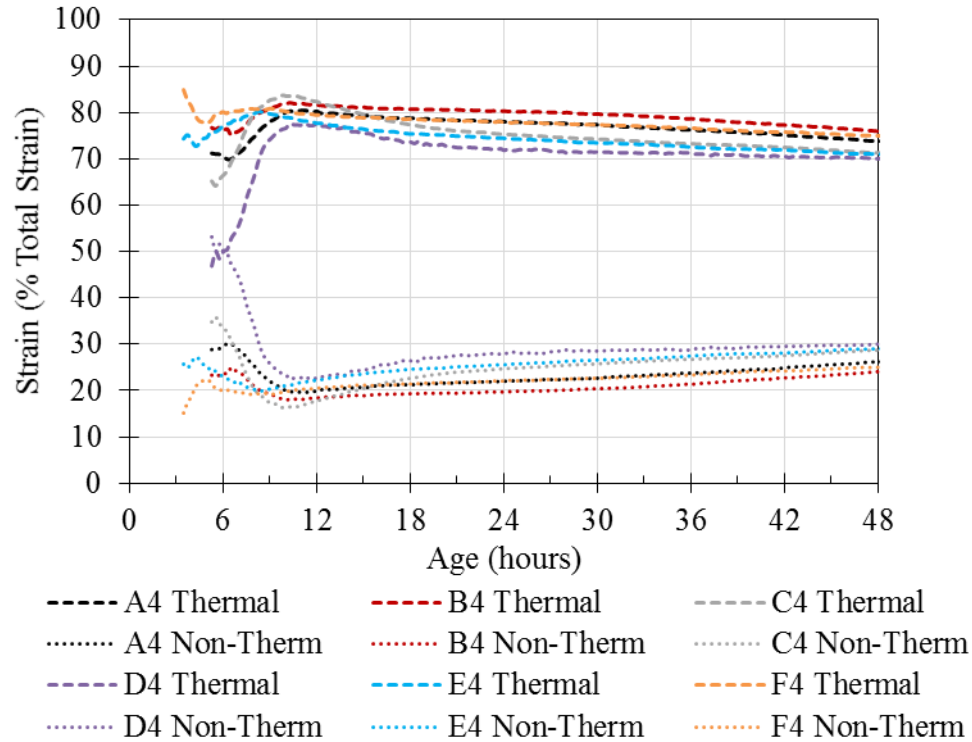


Figure 3.41: Thermal strain as a percentage of total strain over first 6 days

As shown in Figure 3.42, post-tensioning of the second mock-up began at 69 days. From regression of previously discussed results, the modulus of elasticity and splitting tensile strength of the second mock-up concrete at 69 days were determined to be 29.9 GPa (4343 ksi) and 4.27 MPa (619 psi), respectively. The post-tensioning strains shown in Figure 3.42 were generally consistent amongst the series of gauges in the mock-up and demonstrate the expected behavior of the mock-up. Following vertical post-tensioning at 69 days, the vertical gauge C'8-V measured a compressive strain of approximately 220 $\mu\epsilon$, whereas the other gauges, all perpendicular to the vertical load, measured smaller tensile strains. Based on the mock-up geometry and applied vertical force, a nominal compressive stress of 4.62 MPa (670 psi) was expected at the depth of the C'7-H gauges, which would result in a compressive strain of 154 $\mu\epsilon$ according to the 29.9-GPa (4343-ksi) modulus of elasticity. Though the predicted strain is about 25% of the measured value, the predicted value does not account for discontinuities, such as the

post-tensioning ducts, in the concrete that would contribute to higher local stresses and strains.

Horizontal post-tensioning was applied after 71 days, and the horizontal gauge C'7-H measured a 425- $\mu\epsilon$ compressive shift in strain from 30 to -385 $\mu\epsilon$. This compressive strain due to horizontal post-tensioning agrees with the predicted strain of 422- $\mu\epsilon$ based on the calculated nominal compressive stress of 12.6 MPa (1834 psi). For a Poisson's ratio of 0.20, the expected transverse tensile strain would be 84 $\mu\epsilon$, comparable to the 94- $\mu\epsilon$ tensile strain measured by vertical gauge C'8-V and transverse gauges C'1 and C'3. The greatest increase in tensile strain was measured in transverse gauge C'2, which crosses the plane of the horizontal post-tensioning tendons, where the CR3 PCC delamination was identified.

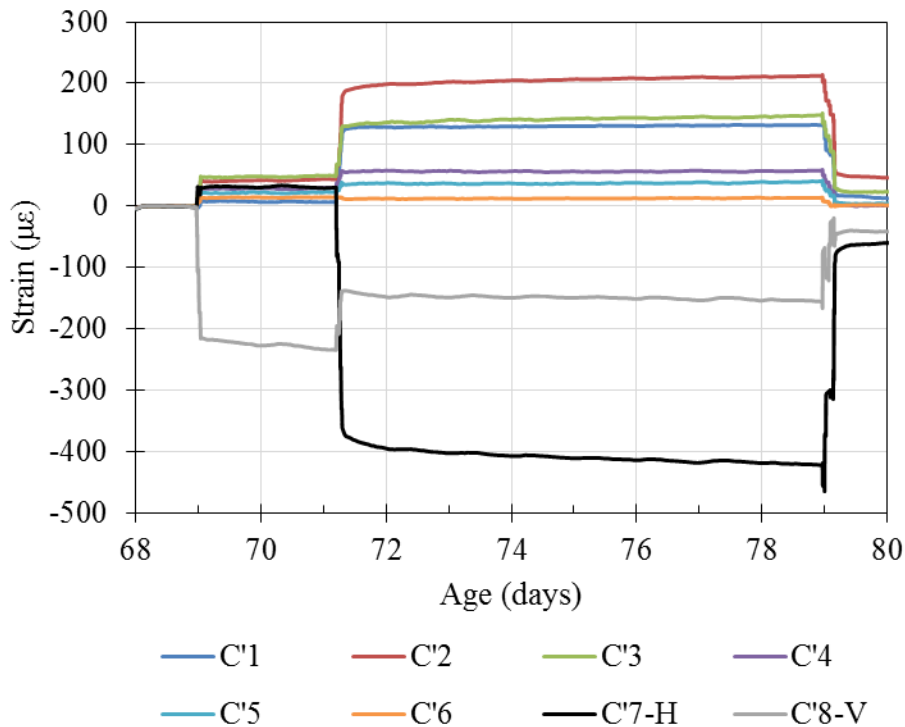
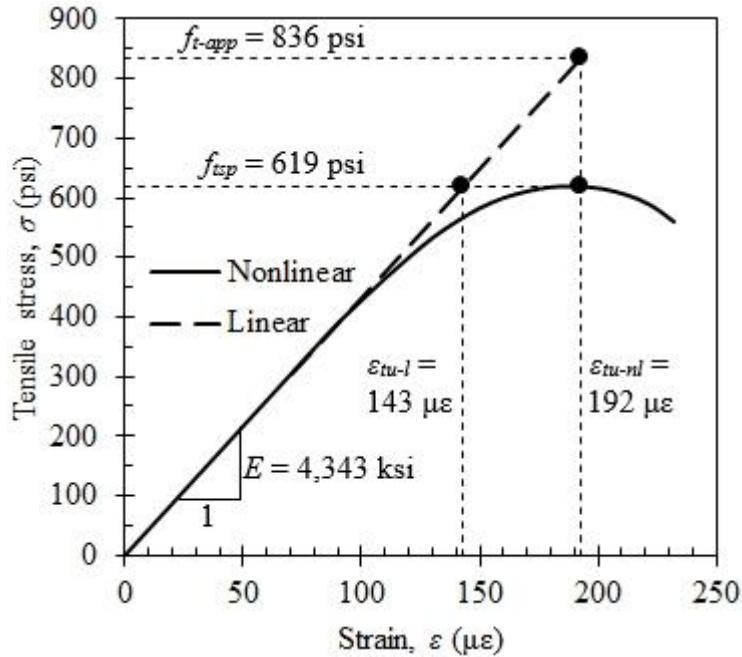


Figure 3.42: Post-tensioning strains measured in C' gauges of second mock-up

Based on the 4.27-MPa (619-psi) splitting tensile strength f_{tsp} and 29.9-GPa (4343-ksi) modulus of elasticity E of the concrete and assuming linear-elastic behavior, the ultimate tensile strain capacity ε_{tu-l} of the concrete was determined to be 143 $\mu\varepsilon$, lower than the 200 $\mu\varepsilon$ measured in gauge C'2 while the mock-up was fully post-tensioned, indicating potential for cracking. Figure 3.43 shows a hypothetical tensile stress-strain curve fitting these experimental values for the mock-up concrete. However, Figure 3.43 illustrates that the assumption of linear-elastic behavior to the tensile splitting strength f_{tsp} of 4.27 MPa (619 psi) underestimates the strain capacity for the nonlinear behavior of concrete. Noting this behavior and earlier work investigating conversion factors for determining an apparent tensile strength f_{t-app} , Raphael (1984) provided tensile strength equations accounting for the nonlinearity of concrete that were approximately 35% greater than the actual strength. Applying a factor of 1.35 to the mock-up splitting tensile strength f_{tsp} yields an apparent tensile strength f_{t-app} of 5.76 MPa (836 psi), corresponding to a nonlinear tensile strain capacity ε_{tu-nl} of 192 $\mu\varepsilon$. As this value is still less than the measured 200 $\mu\varepsilon$, cracking in the plane of the horizontal post-tensioning ducts may have occurred in the mock-up.

Furthermore, the 153-mm (6-in.) gauges measure average strain over the entire gauge length. Therefore, localized high strains or cracking across a gauge may not have been representatively measured, and a 200- $\mu\varepsilon$ measurement over 153 mm (6 in.) may include much higher strains over a shorter length. In order to better understand the concrete behavior in the plane of the ducts, finite element analysis of the loaded mock-up was conducted and is presented in Chapter 5.



Note: 1 MPa = 145 psi

Figure 3.43: Hypothetical stress-strain curve fitting mock-up concrete properties

3.5 Conclusions

The CR3 PCC met many criteria to be considered a mass concrete application, including geometric and material factors. Though the neither mock-up exceeded the 19-°C (35-°F) maximum temperature difference specified by ACI 301-10 and analysis of thermal stresses and tensile strengths suggested that early-age thermal cracking did not occur in the mock-ups, the high concrete temperatures during the first several days of curing were shown to influence the development of the mechanical properties relative to concrete cured at 23 °C (73.5 °F). Higher early-age compressive and tensile strengths and moduli of elasticity were measured for the match-cured specimens, but due to the crossover effect, the same properties were reduced relative to the standard-cured specimens after 7 to 10 days. In particular, reduced splitting tensile strengths at later ages make the concrete more susceptible to cracking during post-tensioning than would otherwise be expected by analysis of standard-cured specimens. Furthermore, since the temperature of the first mock-up concrete exceeded 70 °C (158 °F), the concrete may be

susceptible to DEF, which could cause future durability issues and reduced capacity in the future.

The early-age strain behavior of the mock-ups was largely governed by thermal strain, but the relatively uniform changes in temperature throughout both mock-ups limited tensile thermal stresses that could have caused cracking. After approximately 14 days, thermal and non-thermal strains were generally constant until post-tensioning, during which peak tensile strains were measured across the plane of the horizontal post-tensioning ducts. These strains exceeded the calculated linear-elastic strain capacity of the concrete, suggesting that the plane was susceptible to the laminar cracking identified in the CR3 PCC in 2009.

CHAPTER 4

MODELING CONCRETE PROPERTY DEVELOPMENT

4.1 Introduction

Cement hydration, the exothermic chemical reaction of cement and water, generates heat in concrete, which is an insulating material. The extent to which the heat escapes or accumulates within the concrete depends upon numerous concrete, environmental, and design parameters. Aspects of the concrete mixture design that influence thermal behavior include the cement composition and fineness, the cement content of the concrete, the water-to-cement ratio (w/c), the use of SCMs and chemical admixtures, and the thermal properties of the aggregate. Environmental factors that influence the thermal behavior include the ambient temperature, exposure to solar radiation, and wind speed. Design parameters that influence the thermal behavior include the initial concrete temperature at the time of placement, the minimum dimension of the members being cast, the use of internal cooling pipes, and the thermal properties of the material surrounding the concrete.

In larger members, heat generated near the center of the mass must travel a longer distance to reach the surface and be released, typically resulting in higher internal concrete temperatures. As discussed in Section 2.6.3, cement hydration typically accelerates at higher temperatures per the Arrhenius equation for reaction rate (Carino, 1984). Thermal conductivity governs the rate at which heat is transferred through the concrete, specific heat capacity governs the relationship between heat and temperature, and the coefficient of thermal expansion (CTE) governs the deformation of the concrete in response to temperature changes. Lastly, mechanical properties govern the stresses

developed due to thermal deformations and any external loads and determine the capacity of the concrete to sustain those stresses.

As discussed in Chapter 3, the Crystal River 3 (CR3) post-tensioned concrete containment building (PCC) meets many criteria for consideration as a mass concrete structure, for which thermal effects should be considered (ACI 301-10). Temperatures exceeding 70 °C (158 °F) were measured in a full-scale mock-up of the CR3 PCC curing in ambient conditions, and such elevated temperatures during the first few days of curing can influence the development of concrete properties, some of which are known to develop as functions of time and temperature (Carino, 1984; Waller et al., 2004). However, concrete specimens prepared for estimating the properties of in-place concrete are typically cured in accordance with ASTM C192 (2013) at 23 ± 2 °C (73.5 ± 3.5 °F).

In order to understand the influence of the mock-up temperatures on concrete property development, this chapter compares the results of tests on match-cured specimens with those of control specimens cured in accordance with ASTM C192. The results of these tests were compared with empirical models in the literature, and appropriate models and parameters were selected for implementation in finite element analysis of the mock-ups.

4.1.1 Objectives

The objectives of this chapter are to determine the cement hydration parameters and apparent activation energy for modeling the heat generation of the concrete used to produce the mock-ups, determine the thermal properties of the concrete for modeling heat transfer in the concrete and the thermal deformation of the concrete, and determine the mechanical properties for modeling the mechanical response of the concrete to thermal strains and post-tensioning loads. Additionally, the activation energy was utilized in the equivalent age maturity method in order to investigate the time- and temperature-dependent development of the measured properties and to identify potential

relationships between the properties under different curing conditions. Various empirical models in the literature were compared with the corresponding experimental results for identification of the optimum models and parameters for finite element analysis of the mock-ups.

4.2 Models for Concrete Properties

The following sections present and discuss empirical models for the prediction of hydration parameters and the development of mechanical and thermal properties of concrete. Literature models for hydration parameters and apparent activation energy of cementitious mixtures are discussed more thoroughly in Sections 2.6.7 and 2.6.10, respectively, and a detailed discussion of the literature on thermal properties of concrete is provided in Section 2.7.

4.2.1 Hydration Parameters

The three-parameter exponential model for degree of hydration given in Eq. 4.1 was proposed by Hansen and Pedersen (1985) for representing the sigmoidal progression of hydration with respect to time. Schindler and Folliard (2005) developed Eq. 4.2 for predicting the ultimate degree of hydration α_u as a function of the water-to-cementitious materials ratio and the fly ash and slag content of the cementitious mixture, and Riding et al. (2012) developed Eq. 4.3 to account for the influence of cement composition, SCMs, and chemical admixtures. Eq. 4.4 and Eq. 4.5 are models for the hydration time parameter τ developed by Schindler and Folliard (2005) and Riding et al. (2012), respectively, and Eq. 4.6 and Eq. 4.7 are models for the hydration shape parameter β developed by Schindler and Folliard (2005) and Riding et al. (2012), respectively.

$$\alpha(t_e) = \alpha_u \exp\left(-\left[\frac{\tau}{t_e}\right]^\beta\right) \quad \text{Eq. 4.1}$$

Where,

- $\alpha(t_e)$ = degree of hydration at equivalent age t_e
 α_u = ultimate degree of hydration
 τ = hydration time parameter, hr
 t_e = equivalent age, hr
 β = hydration shape parameter

$$\alpha_u = \frac{1.031 \cdot w/cm}{0.194 + w/cm} + 0.50p_{FA} + 0.30p_{slag} \leq 1.0 \quad \text{Eq. 4.2}$$

Where,

- α_u = ultimate degree of hydration
 w/cm = water-to-cementitious materials ratio
 p_{FA} = fly ash mass ratio in terms of total cementitious content
 p_{slag} = slag mass ratio in terms of total cementitious content

$$\alpha_u = \frac{1.031 \cdot w/cm}{0.194 + w/cm} + \exp \left(\begin{array}{l} -0.297 - 9.73 \cdot p_{C_4AF} \cdot p_{cem} \\ -325 \cdot p_{Na_2O_{eq}} \cdot p_{cem} \\ -8.90 \cdot p_{FA} \cdot p_{FACaO} \\ -331 \cdot WRRET - 93.8 \cdot PCHRWR \end{array} \right) \quad \text{Eq. 4.3}$$

Where,

- w/cm = water-to-cementitious materials ratio
 p_{cem} = cement mass ratio in terms of total cementitious content
 p_{C_4AF} = mass ratio of C₄AF in terms of total cement content
 $p_{Na_2O_{eq}}$
 = mass ratio of alkalis as Na₂O equivalent in terms of total cement content
 p_{FA} = fly ash mass ratio in terms of total cementitious content
 p_{FACaO} = fly ash CaO mass ratio in terms of total fly ash content
 $WRRET$
 = ASTM C494 (2013) Type B and D water reducer/retarder, percent solids by mass per mass of cementitious material
 $PCHRWR$
 = ASTM C494 (2013) Type F polycarboxylate high-range water reducer, percent solids by mass per mass of cementitious material

$$\tau = 66.78 \cdot p_{C_3A}^{-0.154} \cdot p_{C_3S}^{-0.401} \cdot Blaine^{-0.804} \cdot p_{SO_3}^{-0.758} \cdot \exp(2.187 \cdot p_{slag} + 9.50 \cdot p_{FA} \cdot p_{FACaO}) \quad \text{Eq. 4.4}$$

$$\tau = \exp \left(\begin{array}{l} 2.95 - 0.972 \cdot p_{C_3S} \cdot p_{cem} + 152 \cdot p_{Na_2O} \cdot p_{cem} \\ + 1.75 \cdot p_{slag} + 4.00 \cdot p_{FA} \cdot p_{FACaO} \\ - 11.8 \cdot ACCL + 95.1 \cdot WRRET \end{array} \right) \quad \text{Eq. 4.5}$$

$$\beta = 181.4 \cdot p_{C_3A}^{0.146} \cdot p_{C_3S}^{0.227} \cdot Blaine^{-0.535} \cdot p_{SO_3}^{0.558} \cdot \exp(-0.647 \cdot p_{slag}) \quad \text{Eq. 4.6}$$

$$= \exp \left(\frac{\beta}{-0.418 + 2.66 \cdot p_{C_3A} \cdot p_{cem} - 0.864 \cdot p_{slag} + 108 \cdot WRRET + 32.0 \cdot LRWR + 13.3 \cdot MRWR + 42.5 \cdot PCHRWR + 11.0 \cdot NHRWR} \right) \quad \text{Eq. 4.7}$$

Where,

p_{Na_2O} = mass ratio of Na₂O in terms of total cement content

$ACCL$ = ASTM C494 Type C accelerator, percent solids by mass per mass of cementitious material

$Blaine$ = Blaine value, specific surface area of cement, m²/kg

$LRWR$ = ASTM C494 (2013) Type A water reducer, percent solids by mass per mass of cementitious material

MRW = ASTM C494 (2013) Type A and F midrange water reducer, percent solids by mass per mass of cementitious material

$NHRWR$

= ASTM C494 (2013) Type F naphthalene sulfonate high-range water reducer, percent solids by mass per mass of cementitious material

4.2.2 Apparent Activation Energy

As discussed in Section 2.6.9, the apparent activation energy determines the temperature sensitivity of the hydration reaction rate (Schindler, 2004). Due to the dependence of apparent activation energy on various parameters, numerous models have been proposed for estimating the apparent activation energy of cementitious mixtures. Hansen and Pedersen (1977) recommended the apparent activation energy model shown in Eq. 4.8. Schindler (2004) developed Eq. 4.9 to account for cement composition and fineness and proposed the apparent activation energy modification factor for SCMs presented in Eq. 4.10. Riding et al. (2011) developed Eq. 4.11 for the apparent activation energy of cementitious systems as a function of the cement chemistry, SCMs, and chemical admixtures.

$$E_a(T_c) = \begin{cases} 33,500 & \text{if } T_c \geq 20 \text{ }^\circ\text{C} \\ 33,500 + 1470(20 - T_c) & \text{if } T_c < 20 \text{ }^\circ\text{C} \end{cases} \quad \text{Eq. 4.8}$$

Where,

$E_a(T_c)$ = apparent activation energy at concrete temperature T_c , J/mol

T_c = concrete temperature, °C

$$E_a = 22,100 \cdot p_{C_3A}^{0.30} \cdot p_{C_4AF}^{0.25} \cdot Blaine^{0.35} \quad \text{Eq. 4.9}$$

Where,

p_i = mass ratio of i -th compound in terms of total cement content

$Blaine$ = Blaine value, specific surface area of cement, m²/kg

$$f_E = 1 - 1.05p_{FA}(1 - 2.5p_{FACaO}) + 0.40p_{slag} \quad \text{Eq. 4.10}$$

Where,

f_E = apparent activation energy modification factor

p_{FA} = fly ash mass ratio in terms of total cementitious content

p_{FACaO} = fly ash CaO mass ratio in terms of total fly ash content

p_{slag} = slag mass ratio in terms of total cementitious content

$$\begin{aligned} E_a &= 39,200 + 1,069,000 \cdot [p_{C_3A} \cdot p_{cem} (p_{CaSO_4 \cdot xH_2O} + p_{K_2SO_4}) \cdot p_{cem}] \\ &\quad - 12.2 \cdot Blaine + 12,400p_{FA} \cdot p_{FA-CaO} + 12,000p_{slag} \\ &\quad - 53,300p_{SF} - 3,020,000 \cdot WRRET - 343,000 \cdot ACCL \end{aligned} \quad \text{Eq. 4.11}$$

4.2.3 Development of Concrete Mechanical Properties

The following sections present models for the development or evolution of concrete mechanical properties with respect to the age, degree of hydration, or compressive strength of the concrete. The curves predicted by the models tend to have generally consistent forms for each property, typically varying solely by the values of parameters selected through regression analysis of experimental data or the way in which certain factors are accounted for in the model.

4.2.3.1 Compressive Strength

Two common models for the development of concrete compressive strength with respect to equivalent age are given in Eq. 4.12 and Eq. 4.13. The hyperbolic strength gain model (Eq. 4.12) was derived by Carino (1984) and accounts for the induction period before the beginning of strength development. The 3-parameter exponential model (Eq. 4.13) for strength gain was proposed by Hansen and Pedersen (1985) and is analogous to the 3-parameter model for cumulative heat of hydration and degree of hydration.

$$f_c(t_e) = f_{cu} \frac{k_r(t_e - t_{e0})}{1 + k_r(t_e - t_{e0})} \quad \text{Eq. 4.12}$$

$$f_c(t_e) = f_{cu} \exp\left(-\left(\frac{\tau}{t_e}\right)^\beta\right) \quad \text{Eq. 4.13}$$

Where,

f_c	=	compressive strength, MPa (psi)
f_{cu}	=	ultimate compressive strength, MPa (psi)
k_r	=	rate constant at reference temperature, day ⁻¹
t_e	=	equivalent age, day
t_{e0}	=	time after mixing at which strength gain begins, day
τ	=	time parameter, day
β	=	shape parameter

4.2.3.2 Splitting Tensile Strength

Though both tensile and compressive strength of concrete increase with concrete age, the ratio of tensile strength to compressive strength decreases with age (Mindess et al., 2003). Based on regression analyses of experimental data, numerous power law relationships between the splitting tensile strength and compressive strength of concrete have been proposed. ACI 318-08 gives the relation shown in Eq. 4.14 with a coefficient of 0.56 MPa (6.7psi) and a power of 0.5, and the parameters for a few other power law relations are given in Table 4.1. The CEB-FIP Model Code for Concrete Structures 1990 (1991) and Raphael (1984) both recommended a power of 2/3, though the 0.3 MPa (1.576 psi) coefficient of the former results in values approximately 4% lower than the 0.313 MPa (1.7 psi) coefficient of the latter. The function suggested by Raphael is given in Eq. 4.15. In a reevaluation of existing functions and series of experimental results, Oluokun (1991) suggested a coefficient of 0.214 MPa (1.38 psi) and a power of 0.69 for optimum accuracy.

$$\begin{aligned} f_{tsp} &= 0.56(f_c)^{0.5} \quad [\text{MPa}] \\ f_{tsp} &= 6.7(f_c)^{0.5} \quad [\text{psi}] \end{aligned} \quad \text{Eq. 4.14}$$

$$\begin{aligned} f_{tsp} &= 0.313(f_c)^{2/3} \quad [\text{MPa}] \\ f_{tsp} &= 1.7(f_c)^{2/3} \quad [\text{psi}] \end{aligned} \quad \text{Eq. 4.15}$$

Where,

$$\begin{aligned} f_{tsp} &= \text{splitting tensile strength, MPa or psi} \\ f_c &= \text{compressive strength of concrete, MPa or psi} \end{aligned}$$

Table 4.1: Power law relationship parameters for splitting tensile strength as function of compressive strength

Source	Coefficient, a		Power, b
	(MPa)	(psi)	
ACI 318-08 (2008)	0.56	6.7	0.5
CEB-FIP (1991)	0.3	1.576	2/3
Raphael (1984)	0.313	1.7	2/3
Oluokun (1991)	0.214	1.38	0.69

Note: Conversion of coefficient for MPa from psi: $a_{\text{MPa}} = 145^b \cdot \frac{a_{\text{psi}}}{145}$

Since the relative rate of increase in compressive strength is greater than that in tensile strength, the compressive-to-tensile splitting strength (f_c/f_{tsp}) ratio increases with age. Accordingly, Zain et al. (2002) plotted high-performance concrete f_c/f_{tsp} ratio values with respect to compressive strength and identified a linear relationship of the form shown in Eq. 4.16 with positive slope a and intercept b . By rearranging the terms in Eq. 4.16, the splitting tensile strength could be expressed as a function of the compressive strength in the form shown in Eq. 4.17. Additional relationships between compressive and splitting tensile strength are presented in Artoglu et al. (2006).

$$\frac{f_c}{f_{tsp}} = af_c + b \quad \text{Eq. 4.16}$$

$$f_{tsp} = \frac{f_c}{af_c + b} \quad \text{Eq. 4.17}$$

4.2.3.3 Modulus of Elasticity

An empirical relationship for the modulus of elasticity based on the unit weight and compressive strength of the concrete is given in Eq. 4.18 (ACI 318-08), and this

relationship was determined to be valid for ages greater than or equal to 12 hours (Oluokun et al., 1991). For the 2,276-kg/m³ (142.1-lb/ft³) unit weight of the fresh mock-up concrete, Eq. 4.18 can be simplified to Eq. 4.19.

$$\begin{aligned} E_c &= 0.043w_c^{1.5}\sqrt{f_c} \quad [\text{MPa}] \\ E_c &= 33w_c^{1.5}\sqrt{f_c} \quad [\text{psi}] \end{aligned} \quad \text{Eq. 4.18}$$

$$\begin{aligned} E_c &= 4,670\sqrt{f_c} \quad [\text{MPa}] \\ E_c &= 55,900\sqrt{f_c} \quad [\text{psi}] \end{aligned} \quad \text{Eq. 4.19}$$

Where,

- E_c = modulus of elasticity of concrete, MPa or psi
- w_c = unit weight of concrete, kg/m³ or lb/yd³
- f_c = compressive strength of concrete, MPa or psi

Analogous to the 3-parameter degree of hydration model, the exponential function shown in Eq. 4.20 for the modulus of elasticity as a function of equivalent age was proposed by Larson and Jonasson (2003). They noted that, using Eq. 4.20, the modeled behavior during the first day changed significantly when data prior to 1 day of age was not included in the regression analysis, predicting earlier strength development than would be expected.

$$E_c(t_e) = E_u \exp\left(-\left(\frac{\tau}{t_e}\right)^\beta\right) \quad \text{Eq. 4.20}$$

Where,

- E_c = modulus of elasticity of concrete, MPa (psi)
- E_u = ultimate modulus of elasticity, MPa (psi)
- t_e = equivalent age, day
- τ = time parameter, day
- β = shape parameter

4.2.3.4 Poisson's Ratio

The Poisson's ratio of concrete has been considered independent of concrete age (Higginson, 1961; Oluokun et al., 1991), with values typically varying between 0.15 and 0.20 (Mehta and Monteiro, 2006). However, De Schutter and Taerwe (1996) noted that,

similar to water, the Poisson's ratio of fresh concrete is approximately 0.50, so the Poisson's ratio of concrete must change during hardening. Additionally, De Schutter and Taerwe noted lower values at early ages, including the 6-hour results in Oluokun et al. (1991), suggesting that Poisson's ratio decreases from an initial value of 0.50 to a minimum value before increasing to an ultimate value for the hardened concrete. De Schutter and Taerwe developed the model given in Eq. 4.21 for the evolution of Poisson's ratio as a function of the degree of hydration, and the model is shown in Figure 4.1 along with the two components of the model. The exponential component governs the initial decrease from 0.50, and the sine component governs the increase from the minimum value to the long-term value of 0.18 for the hardened concrete.

$$v(\alpha_H) = 0.18 \sin\left(\frac{\pi\alpha_H}{2}\right) + 0.5e^{-10\alpha_H} \quad \text{Eq. 4.21}$$

Where,

- v = Poisson's ratio
- α_H = degree of hydration

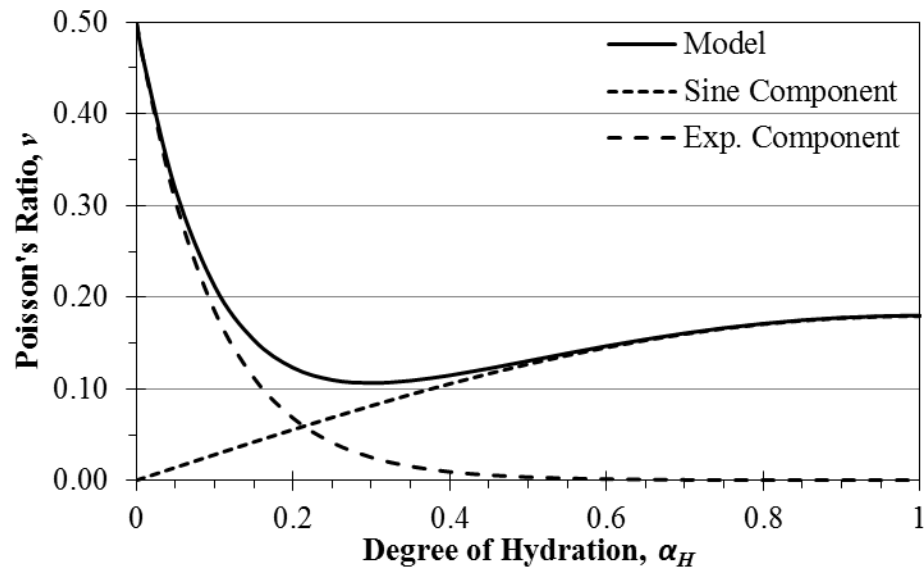


Figure 4.1: De Schutter and Taerwe (1996) Poisson's ratio model for concrete

4.2.4 Concrete Thermal Properties

Whereas the models for development of concrete mechanical properties tend to exhibit comparable behavior, trends identified for thermal properties in the literature have varied widely. As discussed in Section 2.7, researchers have identified direct, indirect, and independent relationships between concrete thermal properties and concrete age and temperature. Therefore, the determination of functions for the thermal properties of the mock-up concrete was largely based on the experimental results for each property rather than implementing trends identified in the literature. The exception is the specific heat capacity, for which van Breugel (1980) developed the model given in Eq. 4.22 which varies as a linear function of degree of hydration. The model accounts for the temperature of the concrete and the mixture proportions according to the principle of superposition with respect to the relative mass content of each component. Schindler (2002) found the model to provide reasonable results for a representative mix design based on literature values for specific heat capacities of the components.

$$c_p = \frac{1}{m} (m_c \alpha_H c_{p(cef)} + m_c (1 - \alpha_H) c_{p(c)} + m_a c_{p(a)} + m_w c_{p(w)}) \quad \text{Eq. 4.22}$$

Where,

- c_p = specific heat capacity of concrete, J/kg·K
- m = total mass of concrete mixture, kg
- m_c = mass of cement content, kg
- m_a = mass of aggregate content, kg
- m_w = mass of water content, kg
- α_H = degree of hydration
- $c_{p(cef)}$ = fictitious specific heat capacity of hydrated cement, defined in Eq. 4.23, J/kg·K
- $c_{p(c)}$ = specific heat capacity of cement, J/kg·K
- $c_{p(a)}$ = specific heat capacity of aggregate, J/kg·K
- $c_{p(w)}$ = specific heat capacity of water, J/kg·K

$$c_{p(cef)} = 8.4T + 339 \quad \text{Eq. 4.23}$$

Where,

- T = temperature of concrete, °C

4.3 Experimental Methods

The following sections discuss the experimental approach for developing model parameters for finite element analysis of the mock-ups. Details are provided on the tests for determining the hydration properties, specific heat capacity, and thermal diffusivity of the mock-up concrete. The experimental mock-ups, post-tensioning system, and materials used were discussed in Section 3.3.

4.3.1 Hydration Properties

Isothermal calorimetry was conducted using an eight-channel microcalorimeter at 15, 25, 35, 45, and 55 °C (59, 77, 95, 113, and 131 °F) to determine the hydration parameters and activation energy of the cement paste in the mock-ups in accordance with the modified ASTM 1074 method discussed in Section 2.6.8. The mix designs of the calorimetry cement pastes are shown Table 4.2. In addition to the representative cement paste with the AEA and WRRET dosage rates shown in Table 1 in Section 3.1.2.2, the plain portland cement (PC) paste, paste with AEA, and paste with WRRET were tested in order to determine the influence of the admixtures. The pastes were prepared with 60.00 g (0.1323 lb) of cement and 24.28 g (0.0535 lb) of water and admixtures, with water replacing the admixtures on a one-to-one mass basis when the admixtures were not used. All samples were tested in duplicate.

Using least-squares regression, the three-parameter degree of hydration model (Eq. 18) given in Section 2.6.6 was fit to the experimental degree of hydration data, obtained by integrating the rate of heat release with time and dividing by 465 J/g (200 Btu/lb), the total heat of complete hydration, as discussed in Section 2.6.2. As in Jayapalan et al. (2014), the data to which the three-parameter model was fit ranged from the time of minimum power preceding the acceleratory phase to the time at which the degree of hydration α was 0.5. Using the hydration parameters determined at each temperature, average values of α_u and β were determined for each mix, and values of τ

were recalculated for each mix and temperature using the average α_u and β values for each cement. The τ values and corresponding temperatures were then used to determine the apparent activation energy of each mix according to Eq. 34 in Section 2.6.8.

Table 4.2: Mix designs for calorimetry samples

Mixture	Cement	Water SG = 1.0	AEA SG = 1.02		WRRET SG = 1.1725	
	Mass (g)	Mass (g)	Vol (μ L)	Mass (g)	Vol (μ L)	Mass (g)
PC	60.00	24.28	-	-	-	-
PC+AEA	60.00	24.25	27	0.03	-	-
PC+WRRET	60.00	24.14	-	-	120.5	0.14
PC+AEA+WRRET	60.00	24.11	27	0.03	120.5	0.14

4.3.2 Specific Heat Capacity

The specific heat capacities of the cement, coarse aggregate, and fine aggregate used in the mock-up were measured via differential scanning calorimetry (DSC) in accordance with ASTM E1269-11 (2011), and the specific heat capacities of these component materials were used to determine the specific heat capacity of the concrete according to Eq. 45 in Section 2.7.1. The cement was tested as received, whereas fine and coarse aggregate particles were pulverized with a mortar and pestle until passing a #200 (75- μ m, 0.0029-in.) sieve. Figure 4.2 shows this sequence for the coarse aggregate. The three materials were oven-dried for 24 hours at 105 °C (221 °F) and were cooled at room temperature for 2 hours prior to testing. Three samples with nominal 25-mg (5.5×10^{-5} -lb) masses were tested for each material. Non-hermetic aluminum pans and lids were used to contain the samples, and a 25.65-mg (5.655×10^{-5} -lb) synthetic sapphire (α -aluminum oxide) disk was used as the standard specimen. The calorimeter was programmed to equilibrate at -40 °C (-40 °F) and maintain the temperature for 4 minutes, then increase the temperature at a rate of 20 °C/min (36 °F/min) to 120 °C (248 °F), and then maintain the temperature for 4 minutes to complete the test. The calorimeter was

purged with dry nitrogen at a flow rate of 50 mL/min (1.7 fl. oz./min) throughout each test. The full set-up is shown in Figure 4.3.

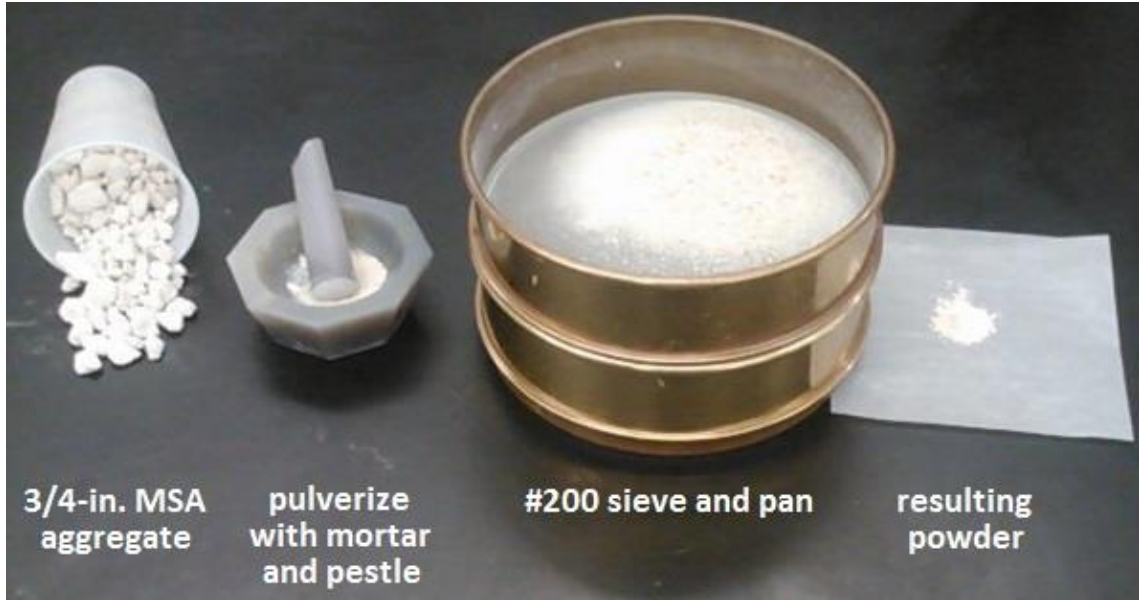


Figure 4.2: Coarse aggregate sample preparation for differential scanning calorimetry

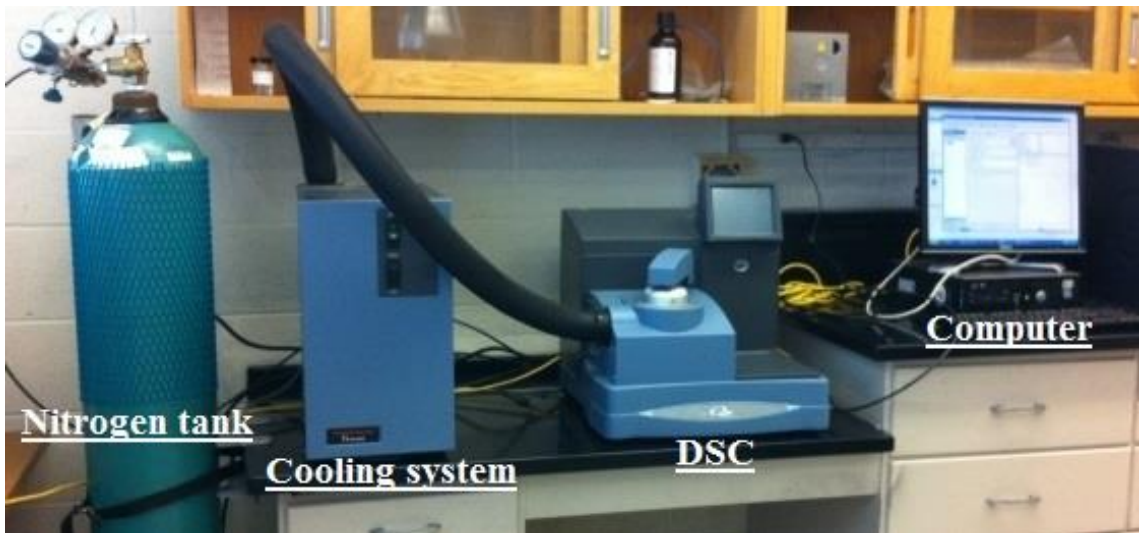


Figure 4.3: Full set-up for differential scanning calorimetry

4.3.3 Thermal Diffusivity

Thermal diffusivity was measured experimentally by a method similar to the modified CRD-C36-73 procedure utilized by Ferraro (2009). A Type-T thermocouple was embedded at the volumetric center of each 150-by-300-mm (6-by-12-in.) concrete cylinder during casting, and the specimens were cured in a moist room maintained at 23 ± 2 °C (73.5 ± 3.5 °F) and 100% relative humidity until needed for testing 1, 2, 3, 7, 10, 14, 28, 56, and 90 days after casting. Specimens were prepared with concrete from both trucks for the first mock-up and were tested in triplicate. Since the test involved thermal cycling that would alter the maturity of the concrete, each specimen was only used once.

At the appropriate testing age, the specimens were submerged in a constant-temperature circulating water bath at 50 °C (122 °F), and the temperature at the center of each specimen was recorded at 15-second intervals until stabilization at the bath temperature. The specimens were then submerged in a separate constant-temperature bath at 10 °C (50 °F) until stabilization at the bath temperature. Finally, the specimens were returned to the circulating water bath at 50 °C (122 °F), and the temperature at the center of each specimen was recorded at 15-second intervals until stabilization at the bath temperature.

For each temperature history, the linear regression of $\ln(\theta^*(t))$ was taken for values of time $t \geq 1500$ seconds and $\theta^* \geq 0.05$. For a 150-by-300-mm (6-by-12-in.) cylinder with a thermal diffusivity of 0.77×10^{-6} m²/s (0.030 ft²/hr), which is within the range of values measured by Tia et al. (2010) for concrete containing Florida limestone aggregate, $t \geq 1500$ corresponds to $Fo_c \geq 0.2$, for which the first-term approximation of the solution for transient heat conduction in an infinite cylinder has converged with the exact solution (Heisler, 1947). The slope of the linear regression was used in Eq. 81 in Section 2.7.3 to calculate a thermal diffusivity value for each temperature history, and the thermal diffusivity for each specimen was taken as the average of the values for the two temperature histories.

4.3.4 Statistical Analysis

One-way analysis of variance (ANOVA) was conducted on all sets of property data to determine whether the sets of data would be combined for further analysis in the sections that follow, and the detailed results of this analysis are presented in Appendix B.2. A significance level of $\alpha = 0.05$ (5%) was used for all statistical analysis. The null hypotheses were tested in the order listed below, and if a given null hypothesis could not be rejected according to the significance level, the tested sets of data were combined for subsequent analyses.

1. For each mock-up and curing condition and at each age, the mean value of the given property of the concrete from the two trucks was the same.
2. For each mock-up and at each age, the mean value of the given property for the Ext and Int curing conditions was the same.
3. For each curing condition and at each age, the mean value of the given property for the two mock-ups was the same.
4. For the Ext and Int curing conditions, the mean value of the given property was the same at all ages.

4.4 Results and Discussion

In the sections that follow, the hydration kinetics of the cement paste used in the mock-up concrete are analyzed, and the determined apparent activation energy value is used to determine the equivalent age of the match-cured concrete specimens. The compressive strength, splitting tensile strength, modulus of elasticity, and Poisson's ratio of the mock-up concrete are then investigated with respect to chronological and equivalent age, and models for the development of each mechanical property are presented and discussed for implementation in time- and temperature dependent finite element modeling. Lastly, the specific heat capacity and thermal diffusivity results are presented and discussed, and the thermal conductivity is determined as a function of

specific heat capacity, thermal diffusivity, and concrete density. The coefficient of linear thermal expansion (CTE) results were discussed in Section 3.4.7, and a constant CTE of $7.86 \mu\epsilon/^\circ\text{C}$ ($4.37 \mu\epsilon/^\circ\text{F}$) was used for analysis of the concrete at all ages.

4.4.1 Hydration Kinetics

The results of isothermal calorimetry at 25°C (77°F) are shown in Figure 4.4. As expected, the addition of WRRET resulted in delayed heat evolution through the first 20 hours and a 2-hour delay of the peak rate of heat evolution. As a result of the retardation, the cumulative heat of hydration of the pastes with WRRET was reduced relative to those without WRRET at all plotted times. The maximum difference in cumulative heat was 45 J/g at approximately 8.5 hours, coinciding with the intersection of the curves, and the difference reduced to 14 J/g by 20 hours, after which rates of heat release were comparable and the cumulative heats began gradually converging. The addition of WRRET also resulted in a 0.3-mW/g (5%) increase in the peak rate of heat evolution. In contrast, the addition of AEA did not influence the hydration behavior of the pastes, matching trends reported in the literature (Poole et al., 2011; Riding et al., 2012).

As shown in Figure 4.5a, the addition of WRRET slightly increased the peak rate of heat evolution at each temperature except 15°C (59°F). However, this effect was insignificant compared to the influence of increasing temperature, which resulted in progressively larger increases in peak rate of heat evolution. Figure 4.5b shows that increasing temperatures decreased the time to the peak rate of heat evolution and generally reduced the delay due to the addition of WRRET. The addition of AEA had no clear influence at any of the tested temperatures.

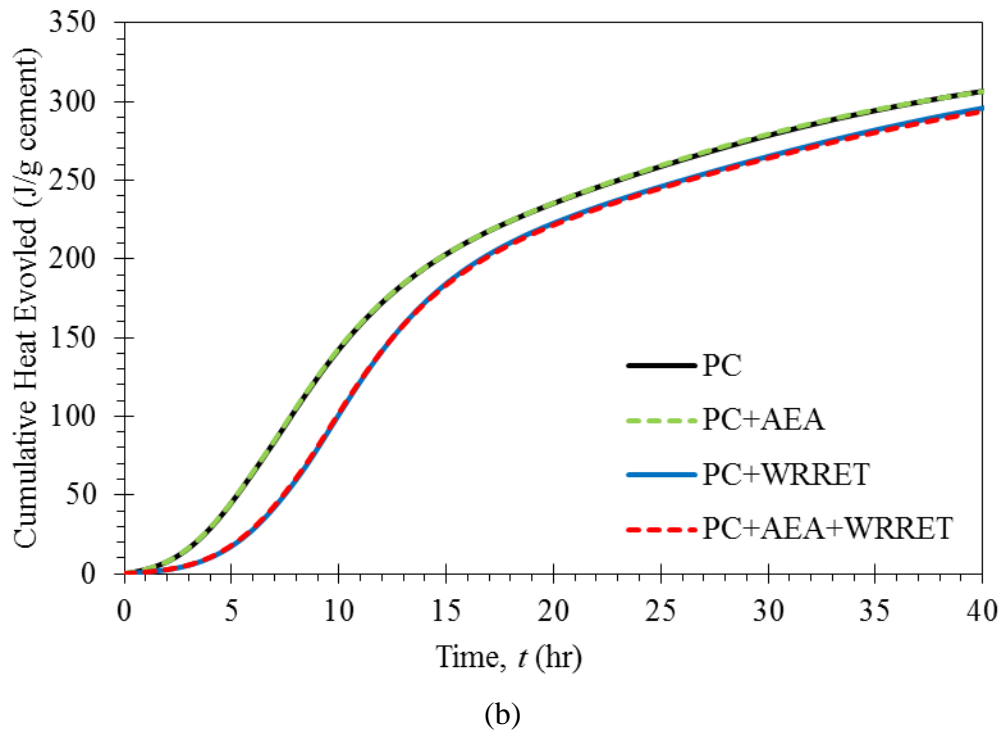
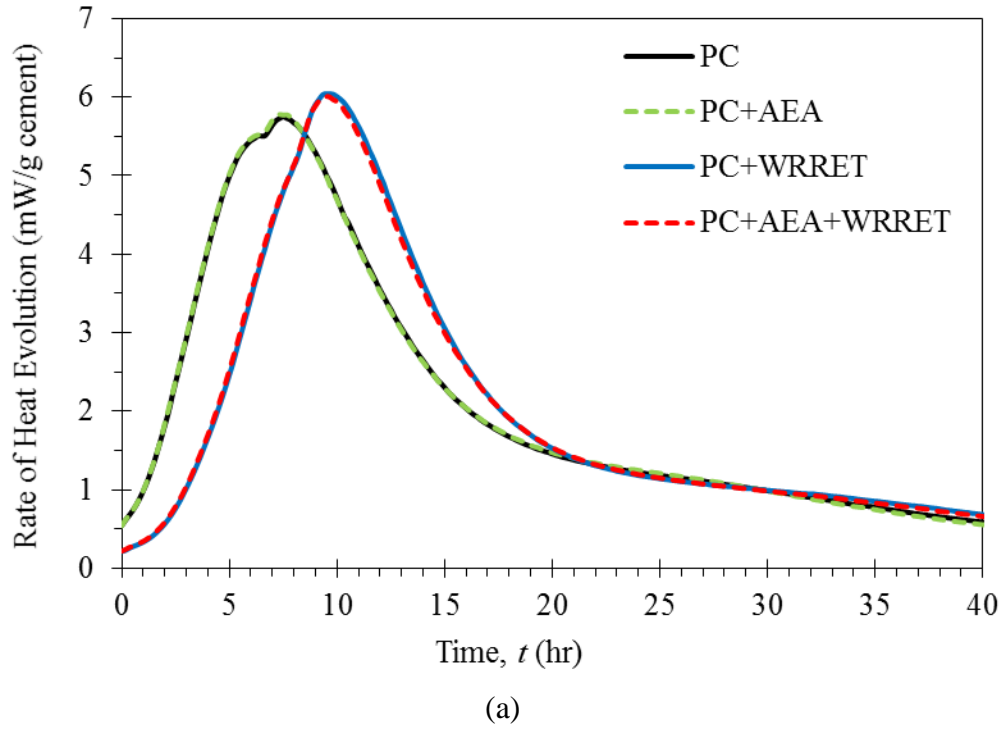
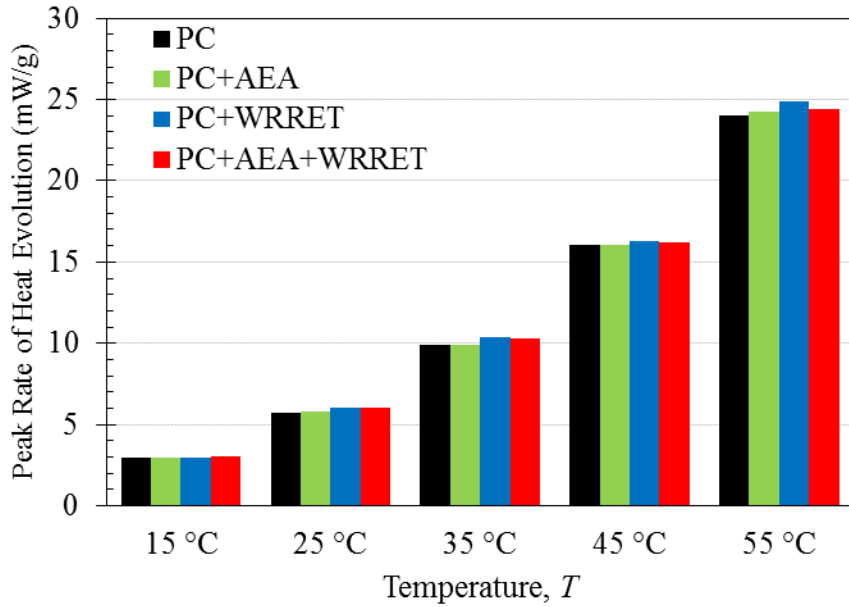
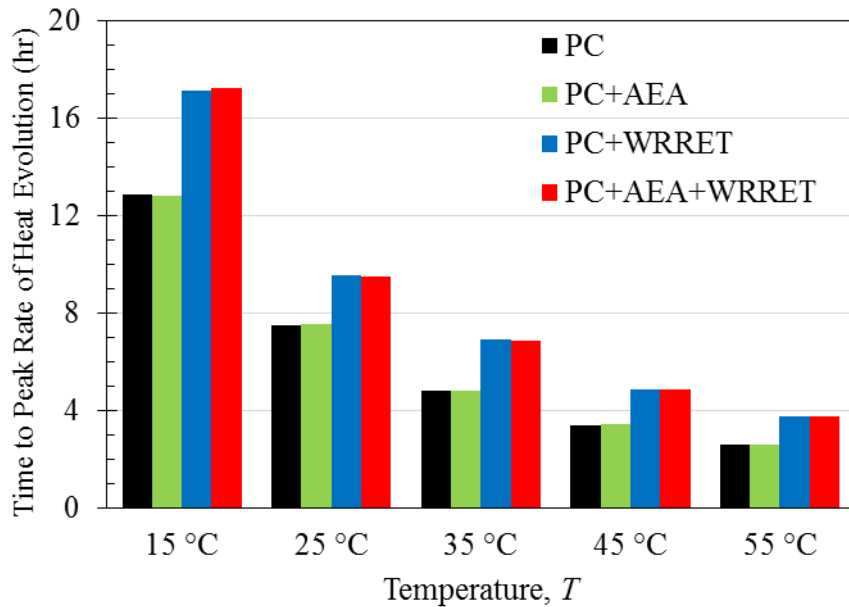


Figure 4.4: (a) Rate of heat evolution and (b) cumulative heat of hydration of representative mock-up cement pastes at 25 °C (77 °F)



(a)

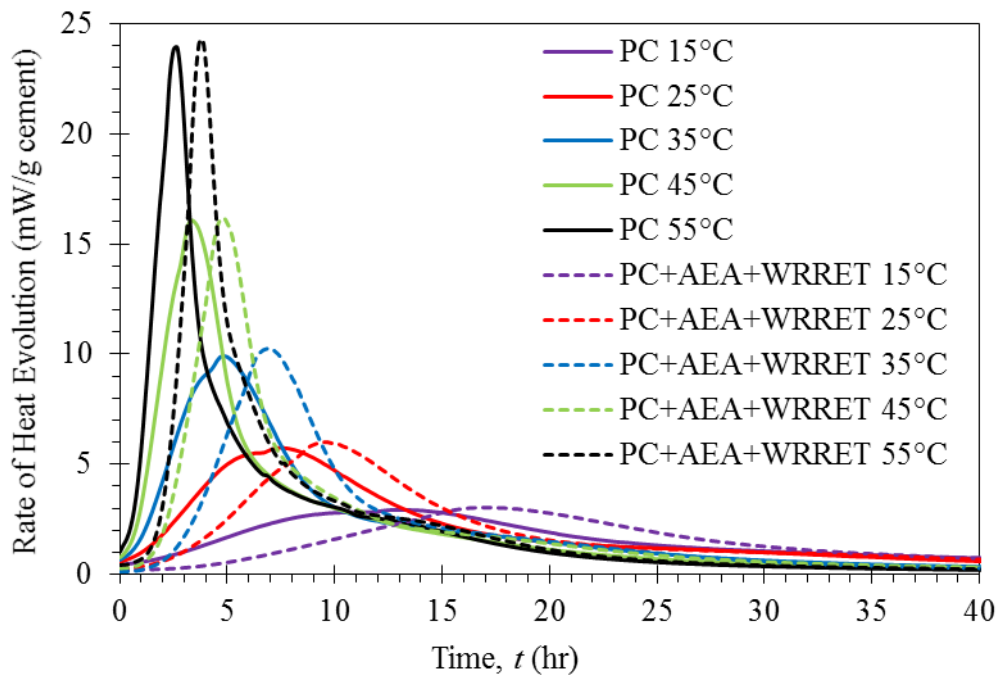


(b)

Figure 4.5: (a) Peak rates of heat evolution and (b) times to peak rate of heat evolution for tested cement pastes

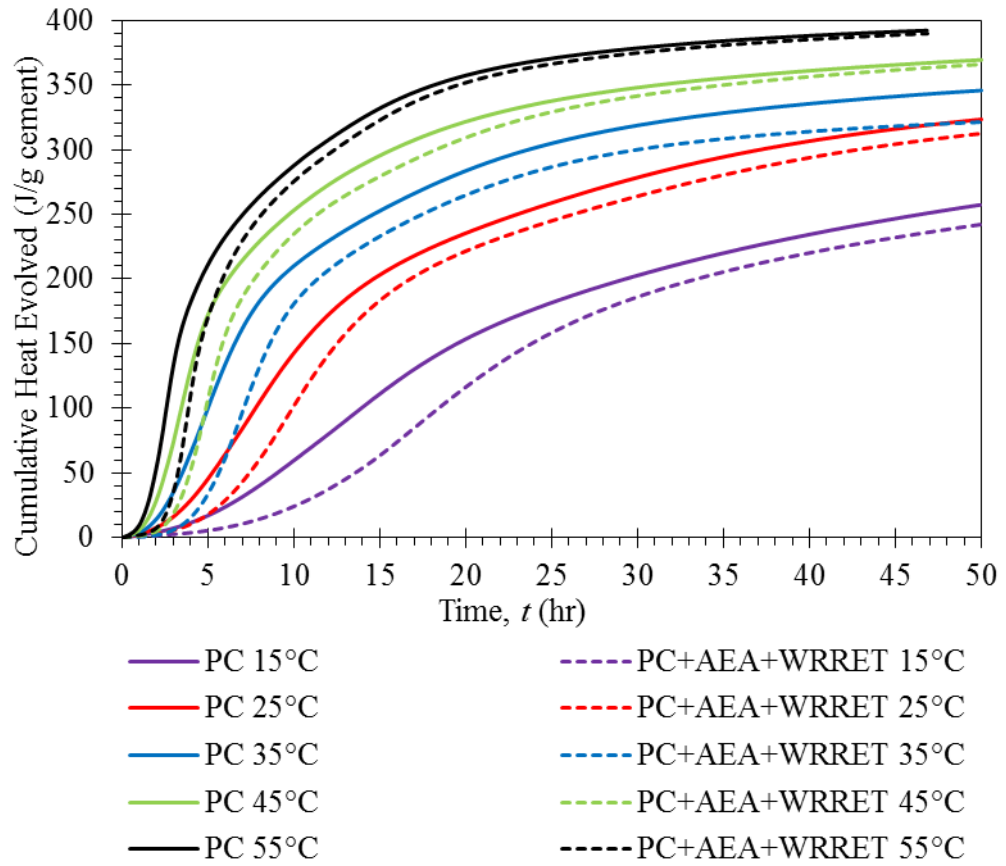
Since the trends for the influence of AEA and WRRET were consistent at each testing temperature, only the calorimetry curves of the plain cement pastes and the pastes

with both admixtures are presented in Figure 4.6, which shows the calorimetry results at all five tested temperatures. In addition to the effects identified in Figure 4.5, Figure 4.6a shows that higher temperatures result in narrower peaks and that the addition of AEA and WRRET does not significantly alter the shapes of the power curves aside from the initial delay of the acceleratory period. As shown in Figure 4.6b, the cumulative heat of hydration is increased by higher temperatures, though the curves tend to converge at later ages. The time delay in cumulative heat due to the addition of WRRET is also reduced at higher temperatures, corresponding to the reduced time to the peak rate of heat evolution in identified in Figure 4.5b and Figure 4.6a. Figure 4.6c shows that the paste with both admixtures tested at 15 °C (59 °F) achieved a degree of hydration of 0.5 at approximately 45 hours, whereas the same paste at 55 °C (131 °F) achieved the same degree of hydration at approximately 7 hours.

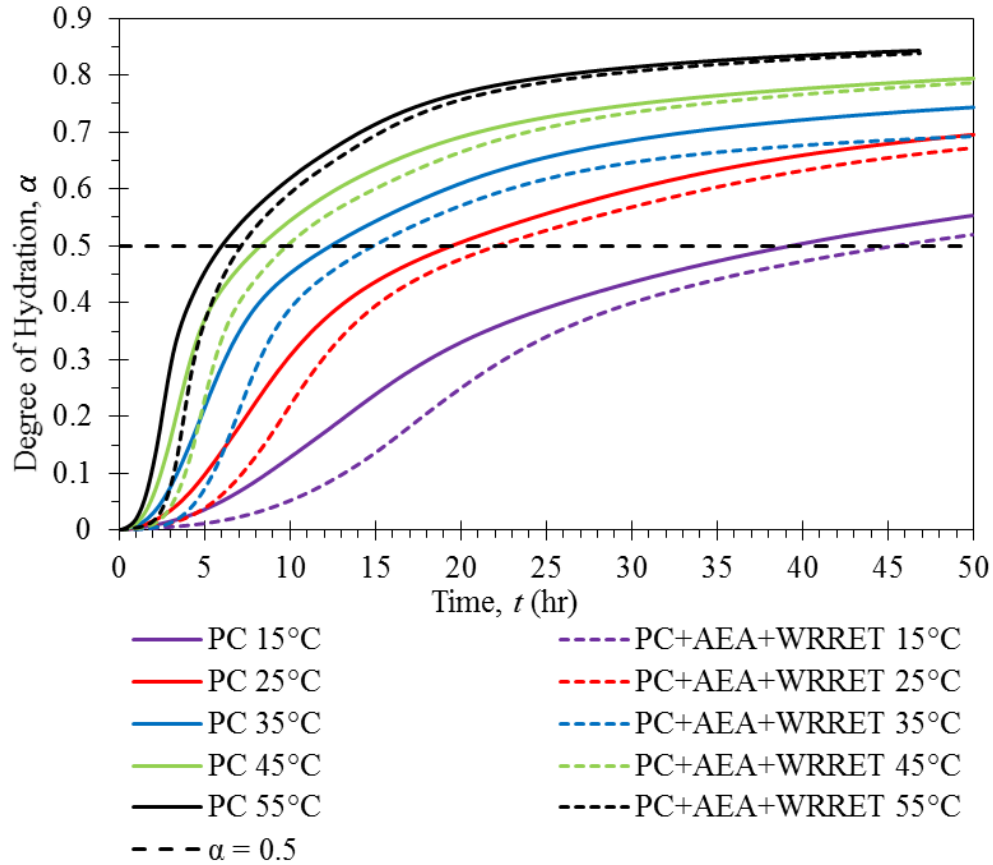


(a)

Figure 4.6: (a) Rate of heat evolution, (b) cumulative heat of hydration, and (c) degree of hydration of representative mock-up cement pastes



(b)
Figure 4.6 (continued)



(c)
Figure 4.6 (continued)

The variation of the natural logarithm of the hydration time parameter $[\ln(\tau)]$ as a function of the reciprocal of the absolute temperature ($1/T$) is shown in Figure 4.7 for the plain cement paste and for the paste with both admixtures. The apparent activation energy was calculated for each mixture using the corresponding curves and the calculation described in Section 2.6.8. From the regression in Figure 4.7, the hydration time parameter for the paste with both admixtures was determined to be 12.53 hr at an absolute temperature of 296.15 K (533.07 °R), corresponding to the 23-°C (73.5-°F) reference temperature used for determining the equivalent age in Section 4.4.2 according to Eq. 28 in Section 2.6.8.

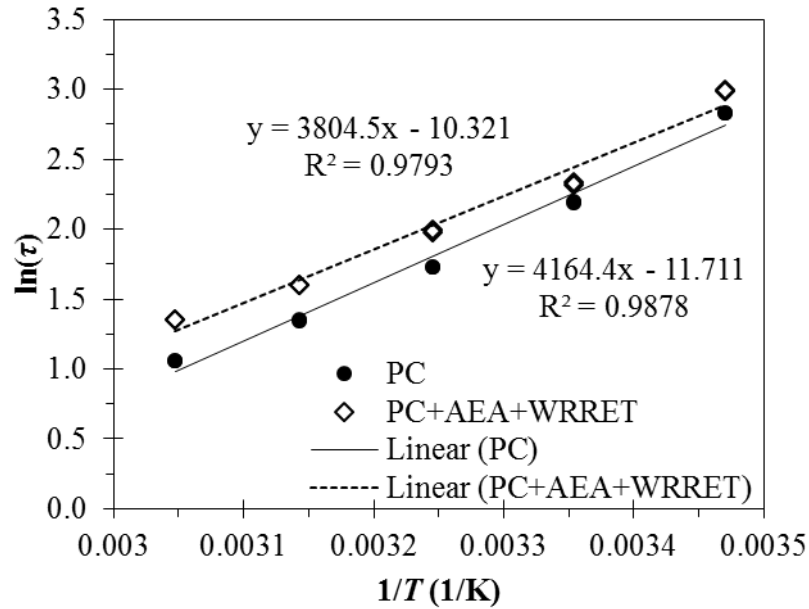


Figure 4.7: Variation of the natural logarithm of the hydration time parameter $[\ln(\tau)]$ as a function of the reciprocal of the absolute temperature ($1/T$)

The apparent activation energy E_a , ultimate degree of hydration α_u , hydration shape parameter β , and reference temperature hydration time parameter τ_r for the mock-up cement paste are shown in Table 4.3, and the resulting three-parameter degree of hydration model for the mock-up cement paste with both admixtures is given in Eq. 4.24. Since the addition of AEA did not influence the calorimetry curves, the negligible effect on the activation energy and the hydration parameters is expected. The addition of WRRET reduced the apparent activation energy and ultimate degree of hydration and increased the hydration shape and time parameters. These trends for the two admixtures are consistent with the literature (Poole et al., 2011; Riding et al., 2012).

Table 4.4 provides values obtained from empirical models in the literature using the cement composition as determined by Rietveld analysis and the admixture dosages when incorporated in the models. Since the concrete temperature is greater than 20 °C (68 °F) at all times (see Figure 22 in Section 3.4.4), the apparent activation energy determined according to the model by Hansen and Pedersen (1977) given in Eq. 4.8

would be 33,500 J/mol (14,400 Btu/lbmol), which is between the values for the plain cement paste and the paste with both admixtures. The apparent activation energy predicted by the model (Eq. 4.9) developed by Schindler (2004), which accounts for cement composition and fineness, is 7% greater than the experimentally determined value, and the value predicted by the model (Eq. 4.11) developed by Riding et al. (2011), which accounts for admixtures in addition to cement composition and fineness, is 4% greater than the experimentally determined value.

Riding et al. (2011) tested WRRET dosage rates ranging from 0.52 to 4.24 mL/kg of cementitious material and noted that mixes with relatively high dosages of WRRET deviated significantly from the model. The dosage rate of 2.0 kg/mL used in the mock-up cement is not high, but Riding et al. (2011) also noted that different types of admixtures meeting the same ASTM C494 classification could result in different values of apparent activation energy from those predicted by the models.

As mentioned in Section 2.6.7, Schindler and Folliard (2005) and Riding et al. (2012) developed the models for hydration parameters via semi-adiabatic calorimetry of concrete specimens. However, Riding et al. (2011) noted that, for a given dosage, chemical admixtures may influence cement paste and concrete differently. Therefore, the direct applicability of the models to isothermal calorimetry results for the cement pastes tested in the present work may be limited, but the values are still useful for comparison. The models by Schindler and Folliard (2005) and Riding et al. (2012) overestimated the ultimate degree of hydration by 10% and 13%, respectively, underestimated the hydration shape parameter by 75% and 64%, respectively, and overestimated the hydration time parameter by 55 and 47%, respectively. Since the model by Schindler and Folliard (2005) does not account for admixtures, the differences between the experimental results and the model predictions may be due to the effect of WRRET, which Riding et al. (2012) found to significantly increase β while slightly reducing α_u . Though the model by Riding et al.

accounts for admixtures, high dosages of retarder were noted to potentially decrease the accuracy of the model.

$$\alpha(t_e) = 0.633 \exp\left(-\left[\frac{12.53}{t_e}\right]^{2.081}\right) \quad \text{Eq. 4.24}$$

Table 4.3: Experimentally determined apparent activation energy and hydration parameters of mock-up cement paste

Mixture	E_a		Hydration parameters		
	(J/mol)	(Btu/lbmol)	α_u	β	τ_r (hr)
PC	34,625	14,886	0.722	1.338	10.50
PC+AEA	34,224	14,714	0.728	1.339	10.42
PC+WRRET	31,610	13,590	0.638	2.097	12.59
PC+AEA+WRRET	31,632	13,600	0.633	2.081	12.50

Table 4.4: Literature model values for apparent activation energy and hydration parameters of mock-up cement paste with AEA and WRRET (PC+AEA+WRRET)

Source	E_a		Hydration parameters		
	(J/mol)	(Btu/lbmol)	α_u	β	τ_r (hr)
Schindler (2004)	33,971	14,604	-	-	-
Riding et al. (2011)	32,900	14,144	-	-	-
Schindler and Folliard (2005)	-	-	0.697	0.520	19.36
Riding et al. (2012)	-	-	0.714	0.756	18.39

4.4.2 Concrete Maturity

With the mock-up temperature histories and the activation energy of the mock-up cement paste, the maturity indices of the first mock-up specimens shown in Figure 4.8 were determined. A datum temperature of 0 °C (32 °F) was used for the Nurse-Saul temperature-time factor (TTF) (see Appendix A.3 for discussion of the datum temperature), and a reference temperature of 23 °C (73.4 °F), matching the curing temperature of the Fog specimens, was used for the Arrhenius equivalent age. Since the

Fog specimens were cured at a constant temperature, the corresponding maturity indices are linear and serve as the baseline to which the match-cured specimens are compared. The vertical axes for the two maturity indices in Figure 4.8 were scaled so that the results for the Fog specimens were collinear, allowing comparison of the maturities predicted by both methods. The Arrhenius equivalent age function predicts higher maturities than the Nurse-Saul temperature-time factor, consistent with the literature stating that the Nurse-Saul maturity function underestimates the maturity when the concrete temperature rises too rapidly (Saul, 1951; Gajda, 2007). This suggests that the Arrhenius equivalent age better models the temperature effects of the mock-up concrete, and the equivalent age alone is used in all further analysis.

Figure 4.9 shows the equivalent age of the concrete specimens for the two mock-ups. Due to the higher temperatures, the first mock-up concrete has higher maturity than the corresponding concrete in the second mock-up. However, the maturity of the near-surface concrete of the first mock-up (I-Ext) is similar to that of the concrete at the center of the second mock-up (II-Int).

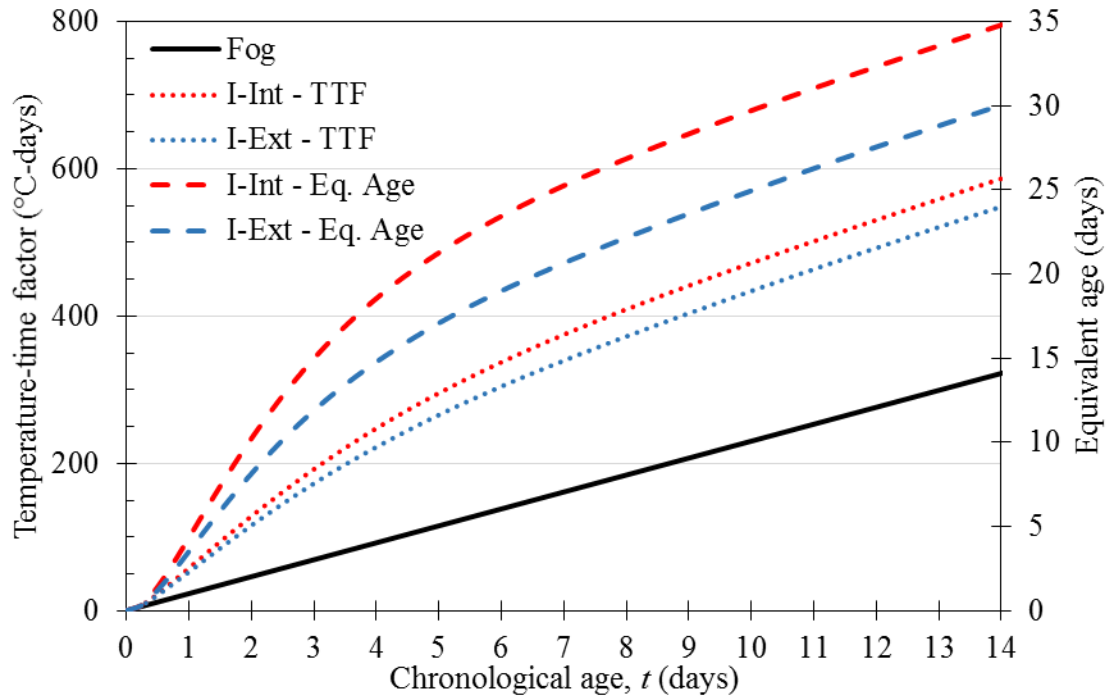


Figure 4.8: Maturity indices of concrete specimens for first mock-up

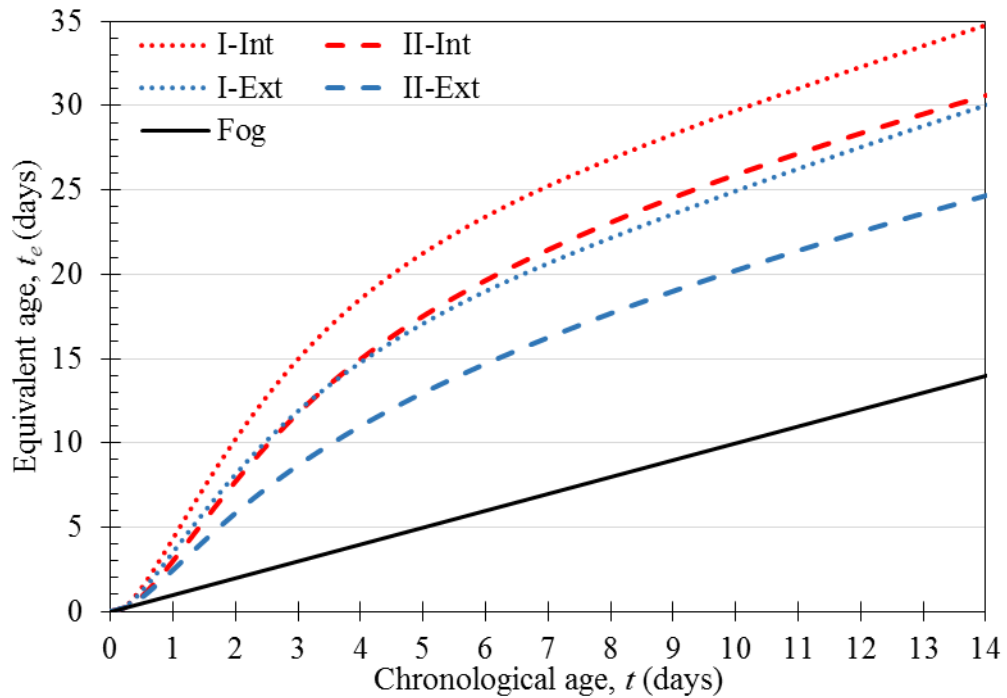
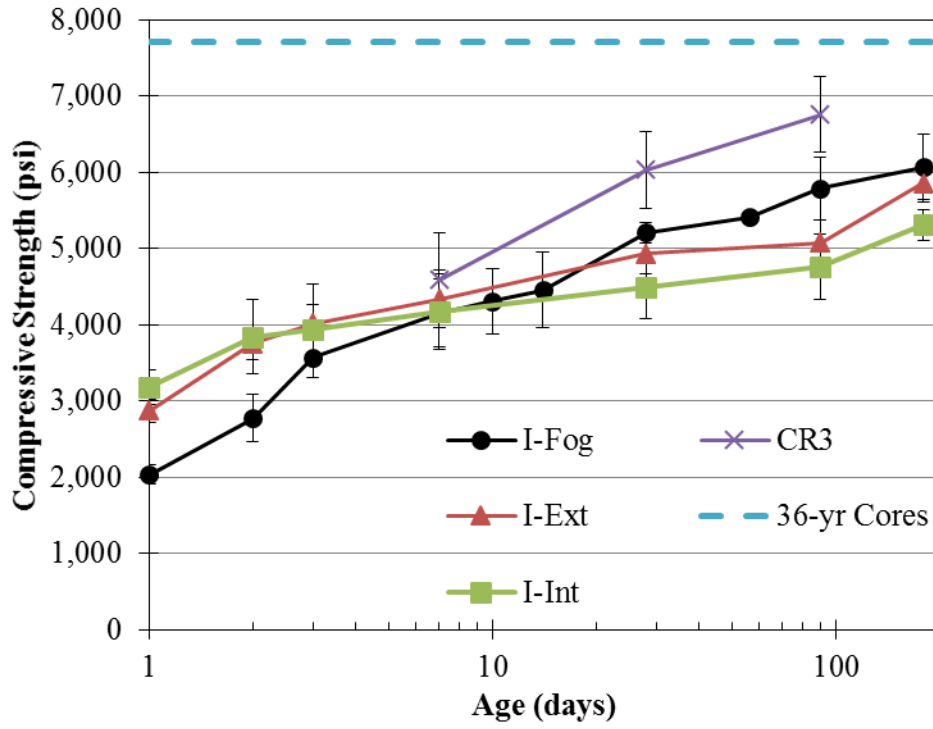


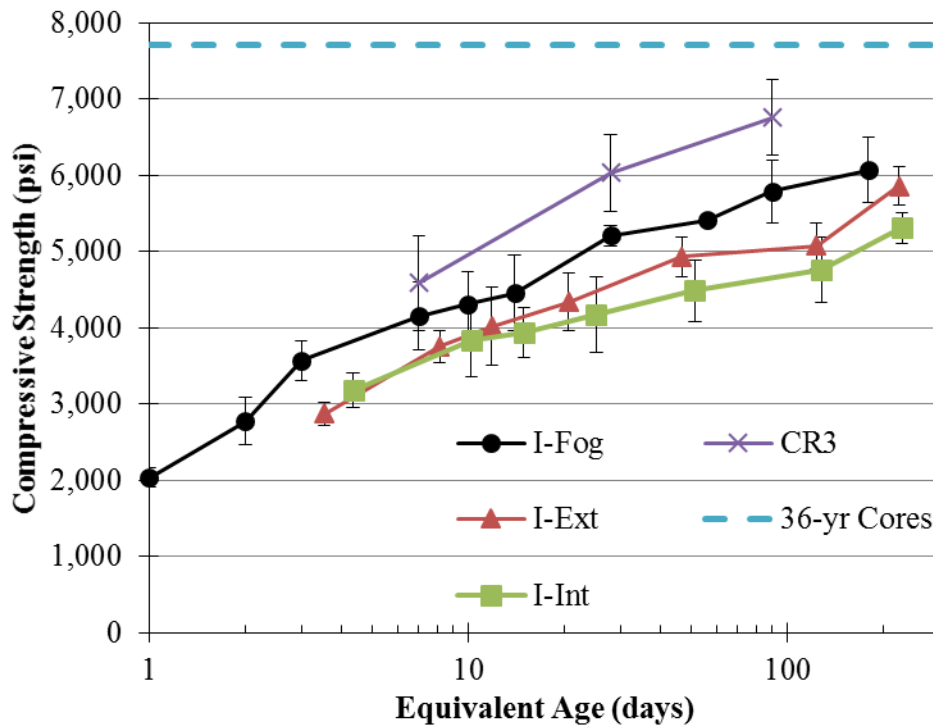
Figure 4.9: Equivalent age of concrete specimens for each mock-up

4.4.3 Compressive Strength

The measured compressive strength results for the first and second mock-up are shown in Figure 4.10 and Figure 4.11, respectively. As shown in Figure 4.10b and Figure 4.11b, the equivalent age results do not exhibit the crossover effect seen in the chronological age results in Figure 4.10a and Figure 4.11a. Instead, the early strength gains of the Ext and Int concrete due to the high temperatures at early ages are shifted to later equivalent ages, resulting in the Ext and Int concrete having generally lower strengths at comparable equivalent ages. The reduced strength of the Ext and Int concrete is due to the rapid hydration of the cement at the higher early-age temperatures; curing at temperatures as low as 4 °C (39 F) has been shown to result in maximum ultimate strengths, whereas curing at higher temperatures has been shown to result in a nonuniform microstructure with regions of weakness that limit strength (Mehta and Monteiro, 2006; Mindess et al., 2003). Above approximately 45 °C (113 °F), changes to the chemical and physical structure of the hydrated cement also contribute to decreased ultimate strengths (Mindess et al., 2003). Since the concrete temperatures matched ambient conditions after approximately 14 days, the relative time shift of the maturity at later ages is reduced, resulting in comparable slopes of the Fog, Ext, and Int curves and validating the equivalent age maturity method. The higher strength of the second mock-up concrete compared to the first mock-up concrete is likely due to the lower concrete temperatures of the second mock-up during curing and the better consolidation of the specimens for the second mock-up.



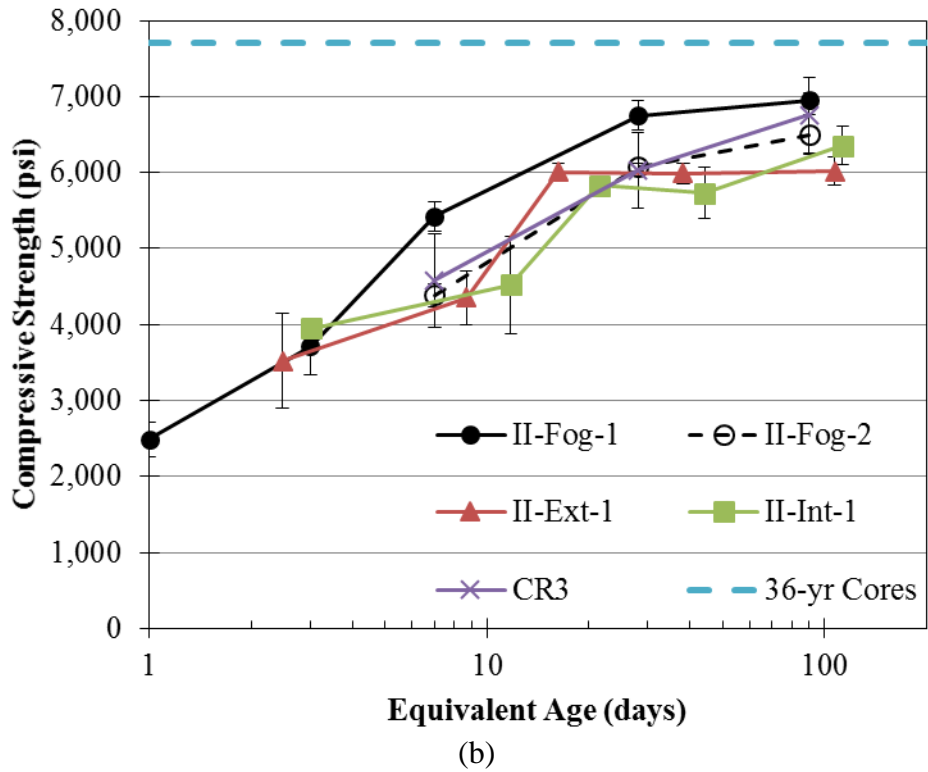
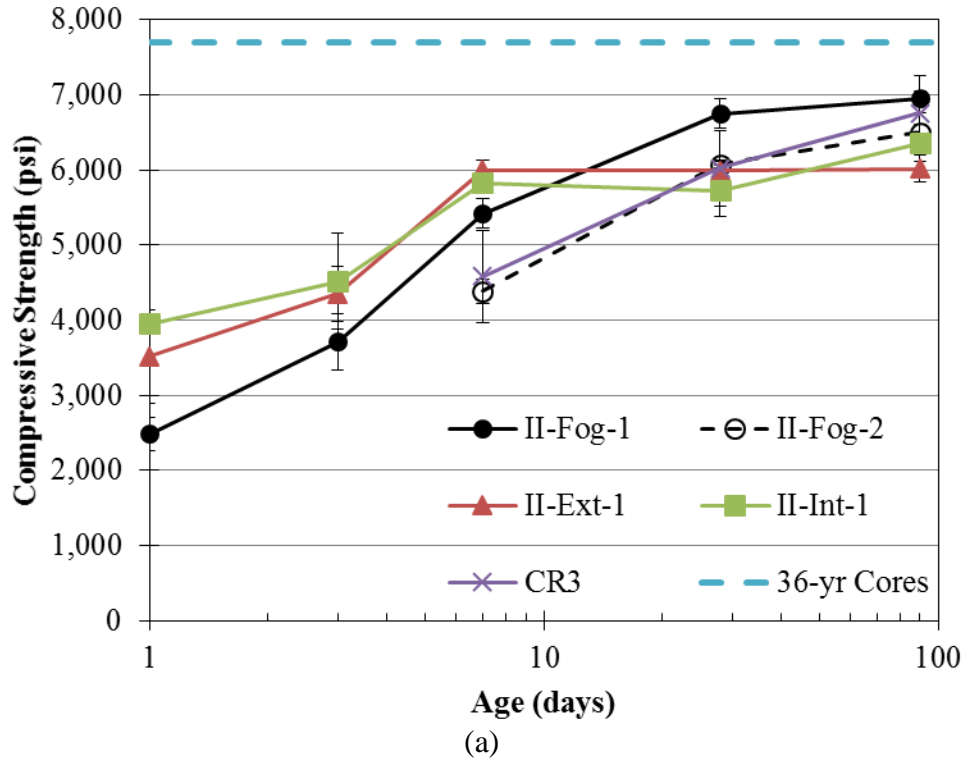
(a)



(b)

Note: 1 MPa = 145 psi

Figure 4.10: Compressive strength of first mock-up concrete as function of (a) chronological age and (b) equivalent age



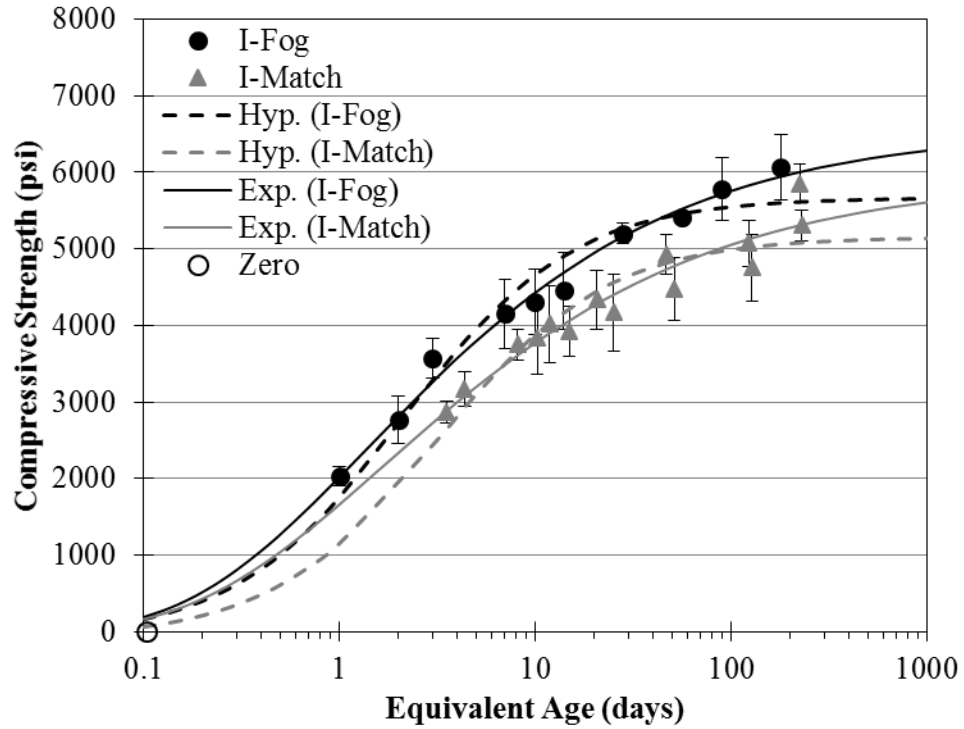
Note: 1 MPa = 145 psi

Figure 4.11: Compressive strength of second mock-up concrete as function of (a) chronological age and (b) equivalent age

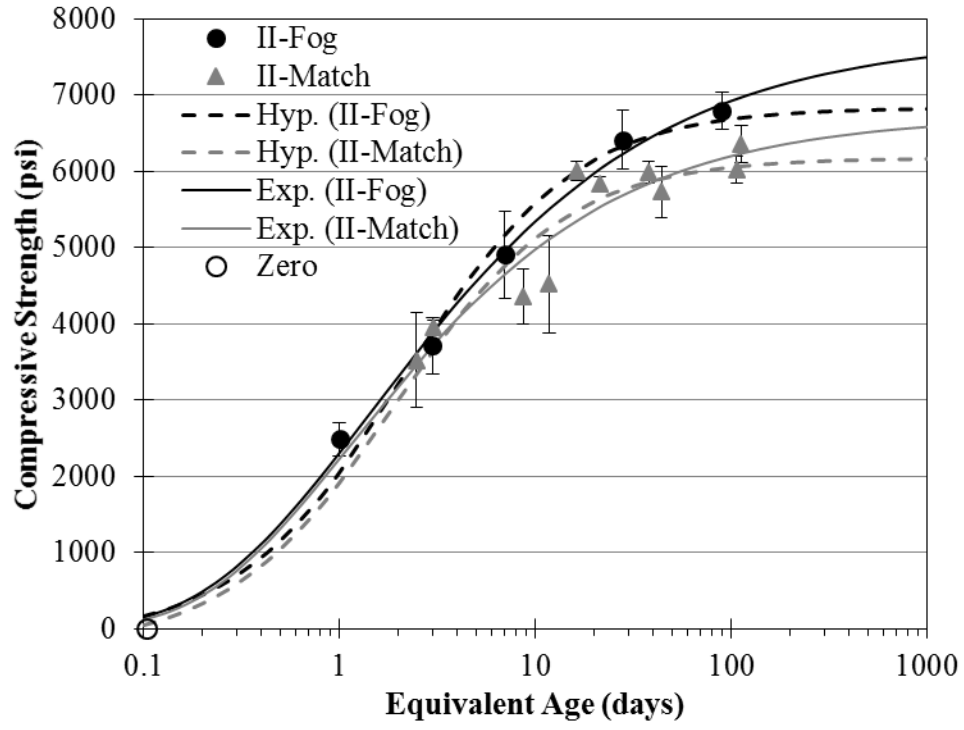
Based on ANOVA results discussed in Appendix B.2 indicating that, for each mock-up, the difference in compressive strength of the Ext and Int concrete at matching ages was not statistically significant, the Ext and Int results for each mock-up were combined for modeling. The compressive strength of the fog- and match-cured specimens for the two mock-ups is shown in Figure 4.12 as a function of equivalent age. The hyperbolic strength gain and 3-parameter exponential regressions of the experimental data are also shown in Figure 4.12, and the parameters and coefficients of determination (R^2) for each case are presented in Table 4.5. An initial compressive strength “result” of zero was added at 2.5 hours (0.10 days) for regression analysis to account for the lack of compressive strength of fresh concrete.

The general behavior of the hyperbolic and exponential models are comparable: rapid strength development during the first several days, followed by gradually slower strength gain. In each case, the coefficient of determination was greater than 0.95, though the values for the exponential model were greater than those of the corresponding hyperbolic models.

By approximately 200 days, the hyperbolic model exhibits asymptotic behavior, whereas the exponential model predicts continued strength development at a decreasing rate. Table 4.6 shows the modeled compressive strength values for each mock-up and curing condition at 90 days and extrapolated to 36 years. The relative increase of the hyperbolic models ranges between 2.3 and 3.6%, whereas the relative increase of the exponential models ranges between 8.6 and 16.3%.



(a)



(b)

Note: 1 MPa = 145 psi

Figure 4.12: Compressive strength as a function of equivalent age of fog- and match-cured specimens from (a) first and (b) second mock-up

Table 4.5: Parameters for compressive strength development

Series	Hyperbolic Parameters			R^2
	f_{cu} (psi)	k_r (day ⁻¹)	t_{e0} (day)	
I-Fog	5,675	0.466	0.0360	0.9743
II-Fog	6,842	0.448	0.0459	0.9893
I-Match	5,161	0.306	0.0548	0.9524
II-Match	6,171	0.491	0.0838	0.9555
Series	Exponential Parameters			R^2
	f_{cu} (psi)	τ (day)	β	
I-Fog	6,567	1.412	0.476	0.9925
II-Fog	7,771	1.465	0.511	0.9960
I-Match	5,941	1.714	0.448	0.9722
II-Match	6,736	1.197	0.563	0.9621

Table 4.6: Modeled compressive strength of mock-up concrete at 90 days and 36 years

Model	Series	Compressive strength (psi)		Increase (%)
		90 days	36 years	
Hyperbolic	I-Fog	5543	5674	2.4
	II-Fog	6676	6841	2.5
	I-Match	4980	5160	3.6
	II-Match	6034	6170	2.3
Exponential	I-Fog	5719	6483	14.4
	II-Fog	6880	7697	11.9
	I-Match	5015	5834	16.3
	II-Match	6170	6700	8.6

As shown in Table 4 in Section 3.1.2.3, the relative increase in measured compressive strength of the CR3 PCC concrete was 14% between 90-day standard specimens and 36-year cores. This suggests that the greater increase in the exponential model gives a better representation of the late-age compressive strength development of the mock-up concrete.

Furthermore, as shown in Table 5 in Section 3.1.2.3, the relative increase in compressive strength of typical concrete made with Type II cement between 90 days and 5 years is 22%. Though that increase is greater than any predicted by the models, it suggests that the relatively negligible late-age strength gain predicted by the hyperbolic model underestimates the actual strength gain.

Figure 4.13 compares the hyperbolic and exponential models for the compressive strength development of the CR3 PCC concrete and typical concrete made with Type II cement (U.S. Bureau of Reclamation, 1981), and the corresponding parameters and coefficients of determination are provided in Table 4.7. For both sets of data, the exponential curve provides a better prediction of the late-age strength development. In the case of the CR3 PCC concrete, the curves were developed from regression of the data through 90 days and extrapolated through 20,000 days (about 55 years). The exponential curve provides a better estimate of the strength of the 36-year (about 13,000 days) cores from the CR3 PCC than the hyperbolic curve. Based on these findings, the exponential model was used in analysis, and the models for the match-cured specimens from the first and second mock-up are given in Eq. 4.25 and Eq. 4.26, respectively.

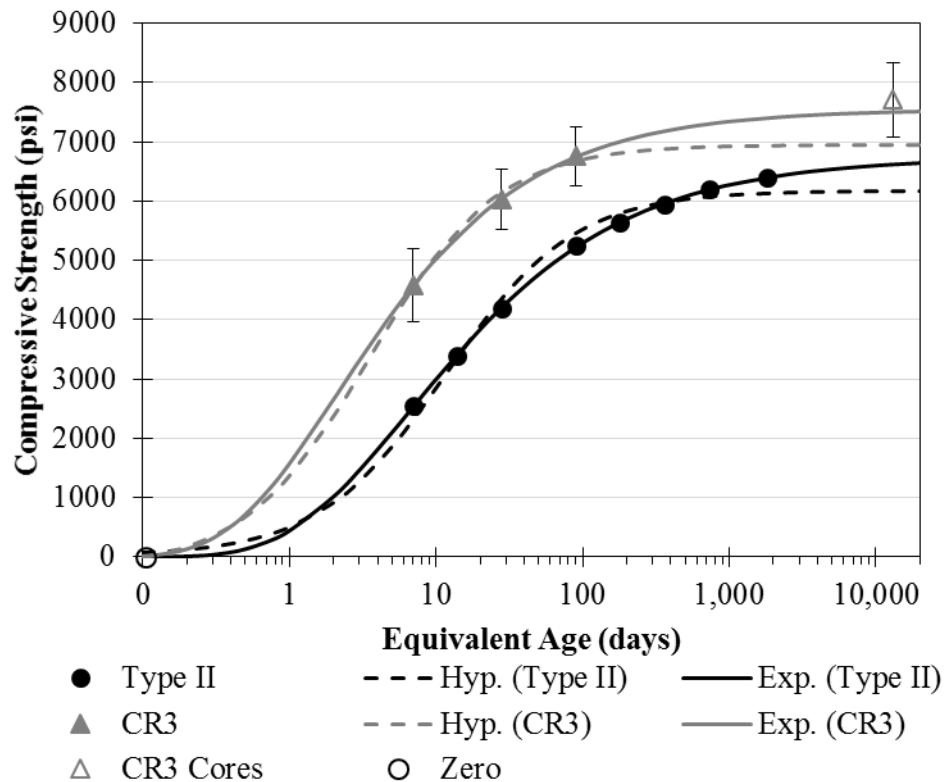


Figure 4.13: Compressive strength development of CR3 PCC concrete and typical concrete made with Type II cement (U.S. Bureau of Reclamation, 1981)

Table 4.7: Parameters for compressive strength development of CR3 PCC concrete and typical concrete made with Type II cement (U.S. Bureau of Reclamation, 1981)

Series	Hyperbolic Parameters			R^2
	f_{cu} (psi)	k_r (day ⁻¹)	t_{e0} (day)	
Type II	6179	0.0852	-0.0527	0.9933
CR3	6948	0.2737	0.1025	0.9992
Series	Exponential Parameters			R^2
	f_{cu} (psi)	τ (day)	β	
Type II	6745	6.712	0.5256	0.9999
CR3	7549	2.151	0.5857	1.0000

$$f_{c-I-Match}(t_e) = 41.0 \exp\left(-\left(\frac{1.714}{t_e}\right)^{0.448}\right) \quad [\text{MPa}]$$

$$f_{c-I-Match}(t_e) = 5,941 \exp\left(-\left(\frac{1.714}{t_e}\right)^{0.448}\right) \quad [\text{psi}]$$

Eq. 4.25

$$f_{c-II-Match}(t_e) = 46.4 \exp\left(-\left(\frac{1.197}{t_e}\right)^{0.563}\right) \quad [\text{MPa}]$$

$$f_{c-II-Match}(t_e) = 6,736 \exp\left(-\left(\frac{1.197}{t_e}\right)^{0.563}\right) \quad [\text{psi}]$$

Eq. 4.26

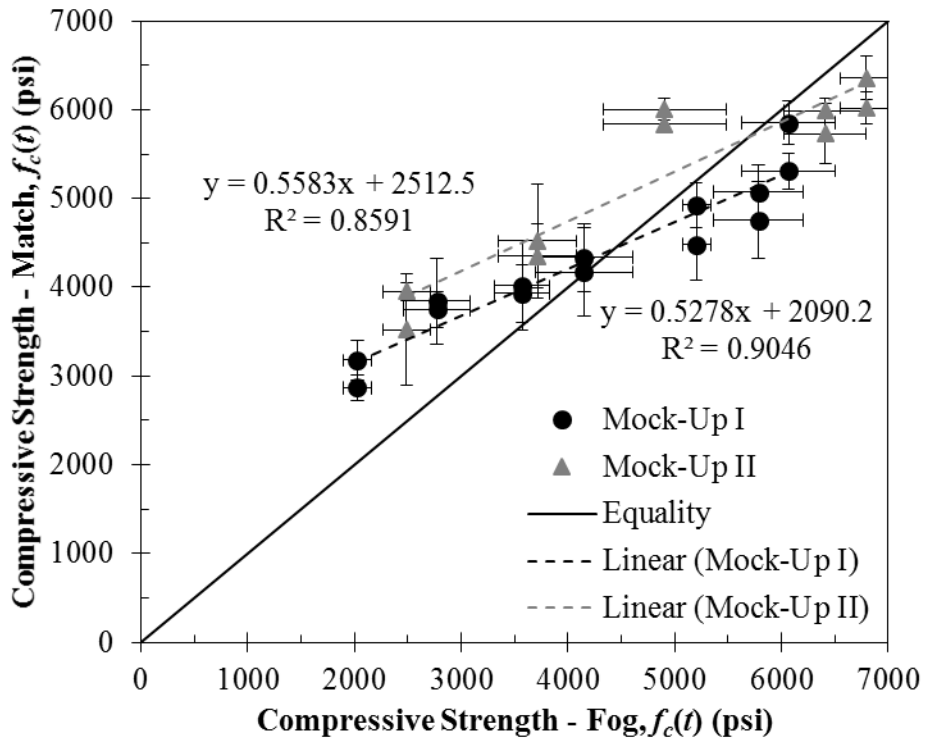
Where,

- f_{c-I} = compressive strength of first mock-up concrete, MPa or psi
- f_{c-II} = compressive strength of second mock-up concrete, MPa or psi
- t_e = equivalent age, days

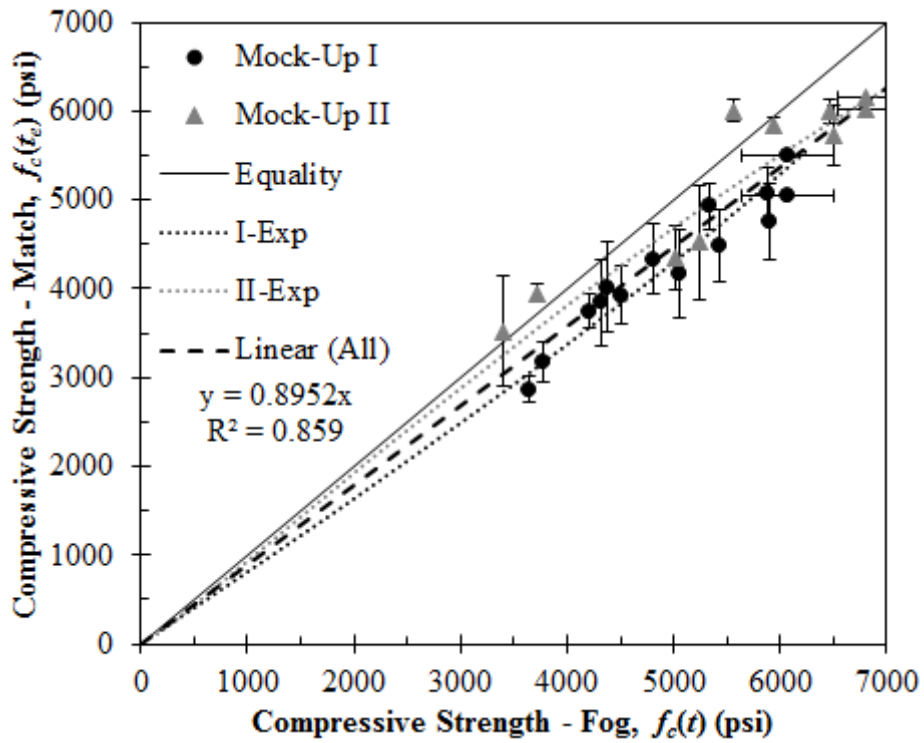
The compressive strengths of the fog- and match-cured specimens are compared at matching ages in Figure 4.14. Whereas tests were conducted at the same chronological ages for presentation in Figure 4.14a, the equivalent ages of the match-cured specimens at the times of testing did not match with the age of the fog-cured specimens, so linear interpolation was used to approximate compressive strength values at intermediate ages in Figure 4.14b. When compared according to chronological age in Figure 4.14a, the results from the two mock-ups are easily distinguished, and the linear regressions of the two sets of data are nearly parallel. The crossover effect is seen at about 31 MPa (4500 psi) for the first mock-up and 40 MPa (5750 psi) for the second mock-up. However, when compared according to the equivalent age in Figure 4.14b, the crossover effect is no longer present, and the two sets of data overlap more. The exponential model for both

mock-ups is nearly linear, and the linear regression through the origin for all of the data has a coefficient of determination of 0.859, very similar to that of the linear regression for the second mock-up in Figure 4.14a.

The slope of 0.8952 for the linear regression in Figure 4.14b indicates that, on average, the match-cured specimens have approximately 90% of the strength of the fog-cured specimens at the same equivalent age, whereas the maturity method conceptually predicts that the strengths should be equal. Since the reference temperature T_r for the equivalent age maturity method was selected to match the 23-°C (73.5-°F) curing temperature of the fog-cured specimens, the equivalent and chronological age of the fog-cured specimens are identical. Therefore, a reduction factor of 0.9 could be applied to the measured compressive strength of a fog-cured specimen at a given chronological age in order to obtain an estimate of the strength of a match-cured specimen at that equivalent age. This suggests that the compressive strength of the in-place mock-up concrete could be estimated without match-cured specimens by using compressive strength tests of fog-cured specimens and the equivalent age of the in-place concrete, which can be determined with the temperature history of the in-place concrete and the activation energy of the cement paste. Testing different concrete mixes with similar temperature histories would be necessary to establish the generality of the 90% relationship between fog- and match-cured specimens for comparable structures.



(a)



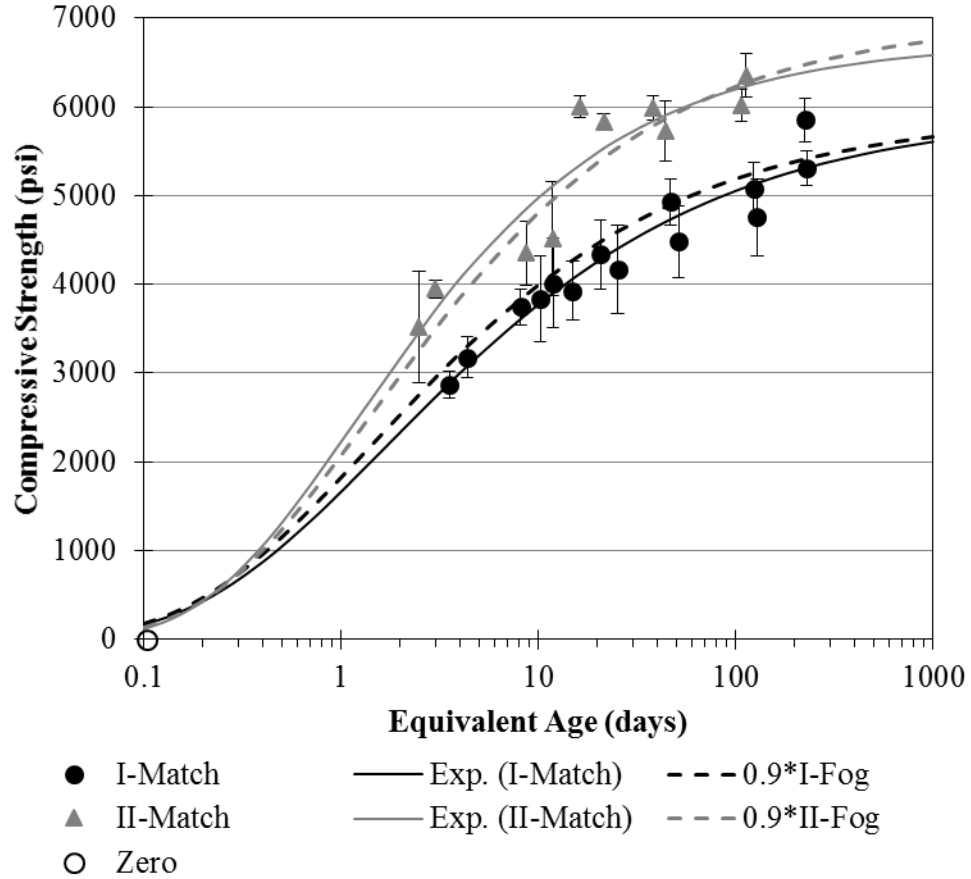
(b)

Note: 1 MPa = 145 psi; error bars are not shown for interpolated values

Figure 4.14: Compressive strength of match-cured specimens with respect to that of fog-cured specimens at same (a) chronological age and (b) equivalent age

Based on the 90% relationship shown in Figure 4.14, the compressive strengths of the match-cured specimens were replotted in Figure 4.15 with curves equal to 90% of the exponential functions for the fog-cured specimens at matching equivalent ages. The equations for these curves are given in Eq. 4.27 and Eq. 4.28, and the original exponential regressions given in Eq. 4.25 and Eq. 4.26 are shown in Figure 4.14 for comparison. The 90% curves are comparable to the original exponential curves, differing by less than 10% with the corresponding curve over the entire range. The coefficients of determination for the 90% curves were 0.9557 and 0.9569 for the first and second mock-up, respectively. Comparing with the values in Table 4.5, these coefficients of determination are less than the corresponding values for the original exponential regressions for the match-cured specimens but are comparable to the corresponding values for the hyperbolic regressions for the match-cured specimens. These results suggest that the 90% relationship provides a reasonable estimate of the development of the compressive strength of the match-cured mock-up concrete.

Though the 90% relationship likely varies based on the temperature history of the concrete, investigations into methods of quantifying this relationship based on the concrete temperature history would be useful because such methods would allow prediction of in-place concrete strengths using only standard-cured specimens rather than match-cured specimens.



Note: 1 MPa = 145 psi

Figure 4.15: Compressive strength as a function of equivalent age of match-cured specimens with comparison to 90% relationship

$$f_{c-I-Match}(t_e) = 40.8 \exp\left(-\left(\frac{1.412}{t_e}\right)^{0.476}\right) \quad [\text{MPa}] \quad \text{Eq. 4.27}$$

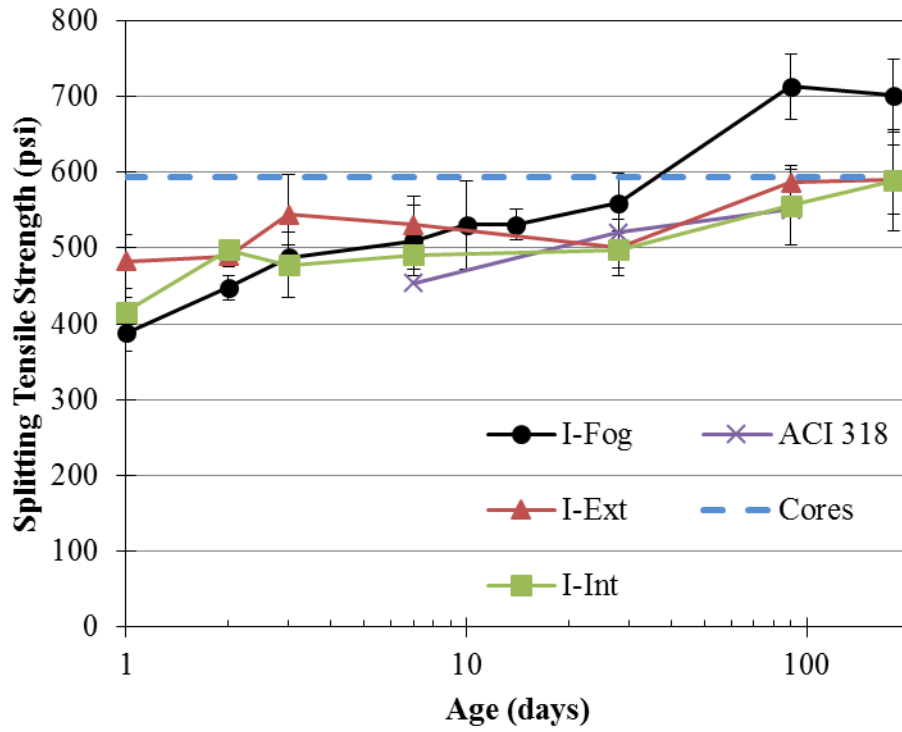
$$f_{c-I-Match}(t_e) = 5,910 \exp\left(-\left(\frac{1.412}{t_e}\right)^{0.476}\right) \quad [\text{psi}]$$

$$f_{c-II-Match}(t_e) = 48.2 \exp\left(-\left(\frac{1.470}{t_e}\right)^{0.511}\right) \quad [\text{MPa}] \quad \text{Eq. 4.28}$$

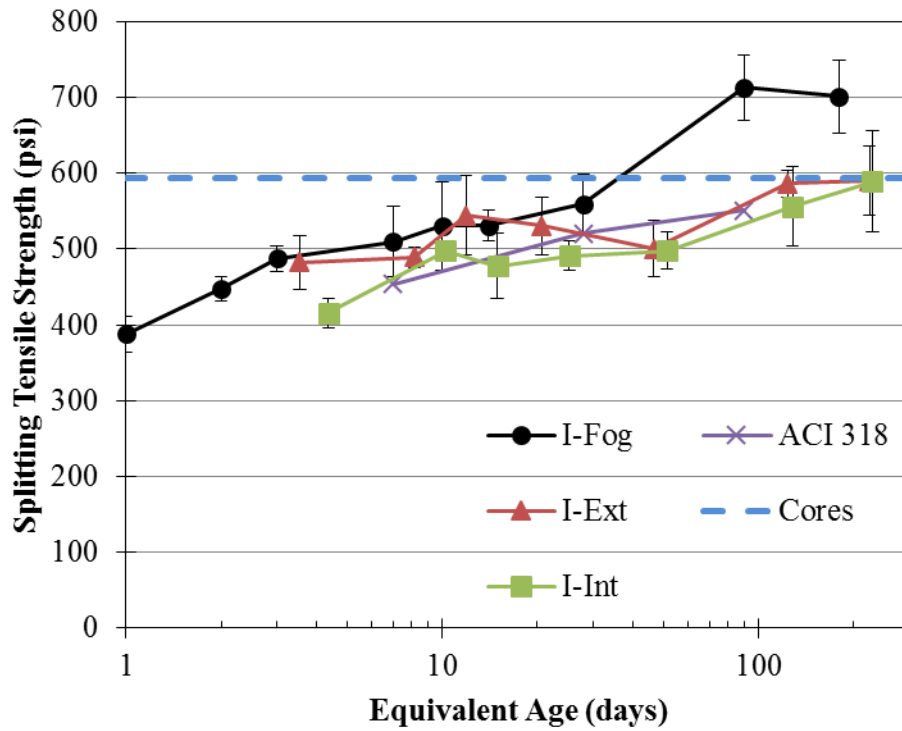
$$f_{c-II-Match}(t_e) = 6,994 \exp\left(-\left(\frac{1.470}{t_e}\right)^{0.511}\right) \quad [\text{psi}]$$

4.4.4 Splitting Tensile Strength

The splitting tensile strength results for the first and second mock-up are shown in Figure 4.16 and Figure 4.17, respectively. Though not as pronounced as in the case of compressive strength, the crossover effect exhibited with chronological age in Figure 4.16a is not exhibited with equivalent age in Figure 4.16b. Like the compressive strength results, the slopes of the maturity curves of the Fog, Ext, and Int splitting tensile strengths are closer than the slopes with chronological time. For the first mock-up, the splitting tensile strengths of the Ext and Int specimens were lower than the strengths of the Fog specimens at comparable equivalent ages, similar to the compressive strength behavior. However, the results for the second mock-up were more closely aligned, with comparable trends for the Fog, Ext, and Int concrete. Like the compressive strength, the higher splitting tensile strengths of the second mock-up concrete relative to the first mock-up concrete are likely due to the lower concrete temperatures of the second mock-up during curing and the better consolidation of the specimens for the second mock-up.



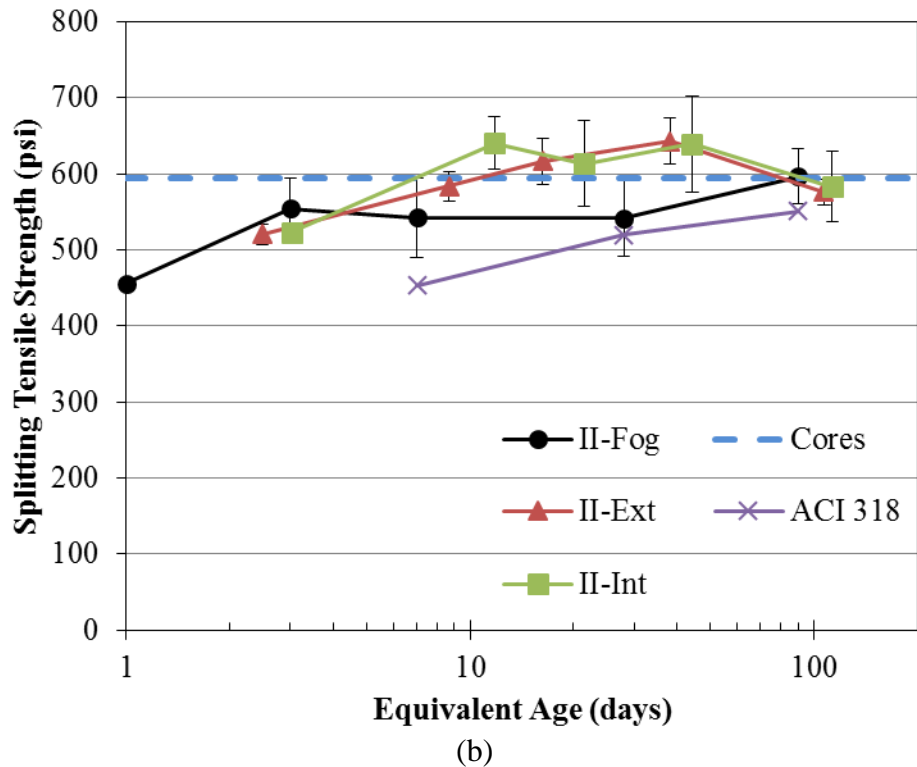
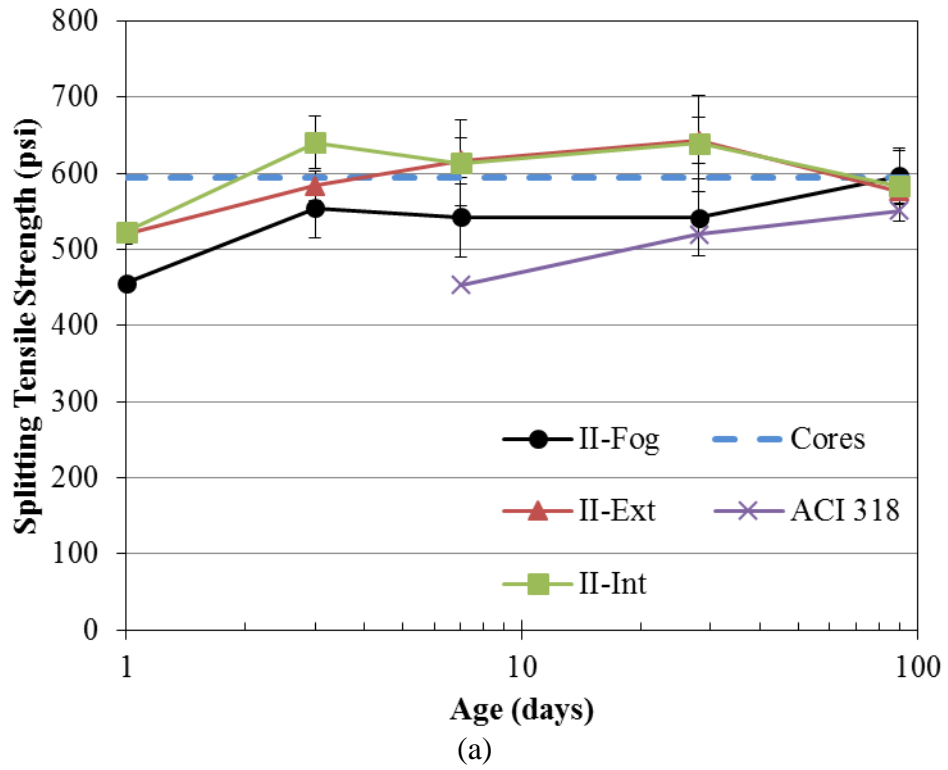
(a)



(b)

Note: 1 MPa = 145 psi

Figure 4.16: Splitting tensile strength of first mock-up concrete as function of (a) chronological age and (b) equivalent age



Note: 1 MPa = 145 psi

Figure 4.17: Splitting tensile strength of second mock-up concrete as function of (a) chronological age and (b) equivalent age

Based on ANOVA results discussed in Appendix B.2 indicating that, for each mock-up, the difference in splitting tensile strength of the Ext and Int concrete at matching ages was not statistically significant, the Ext and Int results for each mock-up were combined for modeling. The splitting tensile strength of the mock-up concrete is shown with respect to compressive strength in Figure 4.18 and with respect to equivalent age in Figure 4.19. Both figures also show the splitting tensile strengths predicted by the ACI 318 (2008) and Raphael (1984) relations (Eq. 4.14 and Eq. 4.15, respectively) and power law regressions of the splitting tensile strength of each series as a function of compressive strength. The power law relations are linear in the log-log plot (Figure 4.18a) with the form given in Eq. 4.29, but nonlinear least squares regression of the original power law form was used to determine each relation because taking the logarithm of the experimental results skews the data by reducing the error of larger values relative to smaller values.

$$\log(f_{tsp}) = b \log(f_c) + \log(a) \quad \text{Eq. 4.29}$$

Where,

- f_{tsp} = splitting tensile strength, psi
- f_c = compressive strength, psi
- b = power of power law relation
- a = coefficient of power law relation

The parameters for the power law regressions are given in Table 4.8 along with the coefficients of determination for each curve as a prediction of the observed splitting tensile strengths with respect to equivalent age. The regressions were determined with respect to equivalent age by incorporating the corresponding exponential functions for compressive strength from Table 4.5.

As shown in Figure 4.19, the tensile strengths predicted by the ACI and Raphael functions are lower than almost all of the corresponding experimental results. As discussed in Section 4.1.1, the values predicted by the CEB-FIP function are approximately 4% less than the Raphael function values, which are already lower than

the experimental results, so the CEB-FIP results are not presented. Similarly, the Oluokun (1991) function was nearly coincident with the Raphael function but with slightly lower values at early ages, so the Oluokun results are not presented either.

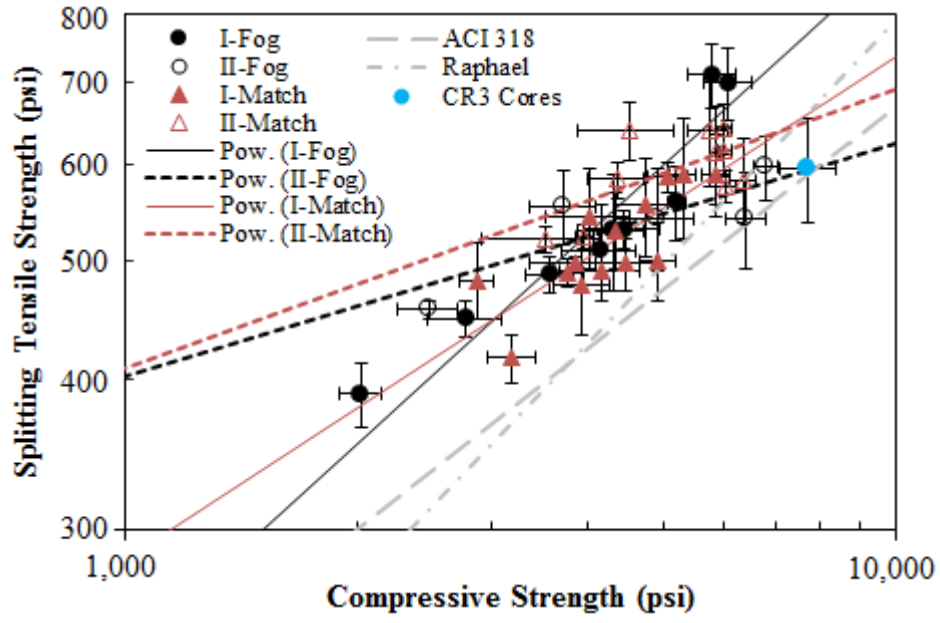
Since the splitting tensile strength for both the fog- and match-cured specimens is generally higher than predicted by the ACI and Raphael functions, the behavior is likely independent of the curing history. Performance Improvement International (2010) reported that the splitting tensile strength and compressive strength of cores taken from the CR3 PCC were consistent with the CEB-FIP relationship given in Table 4.1. However, the cores were taken approximately 36 years after concrete placement, and the literature models shown in Figure 4.19 were generally more consistent with the experimental results at later ages. No tensile strength testing was conducted on the CR3 PCC concrete at earlier ages.

A potential source of deviation from the literature models is the crushed limerock coarse aggregate used for the mock-up concrete. Mindess et al. (2003) stated that the use of crushed coarse aggregate seems to increase the concrete tensile strength more than the compressive strength, which would contribute to the higher tensile strengths than predicted by the compressive strength.

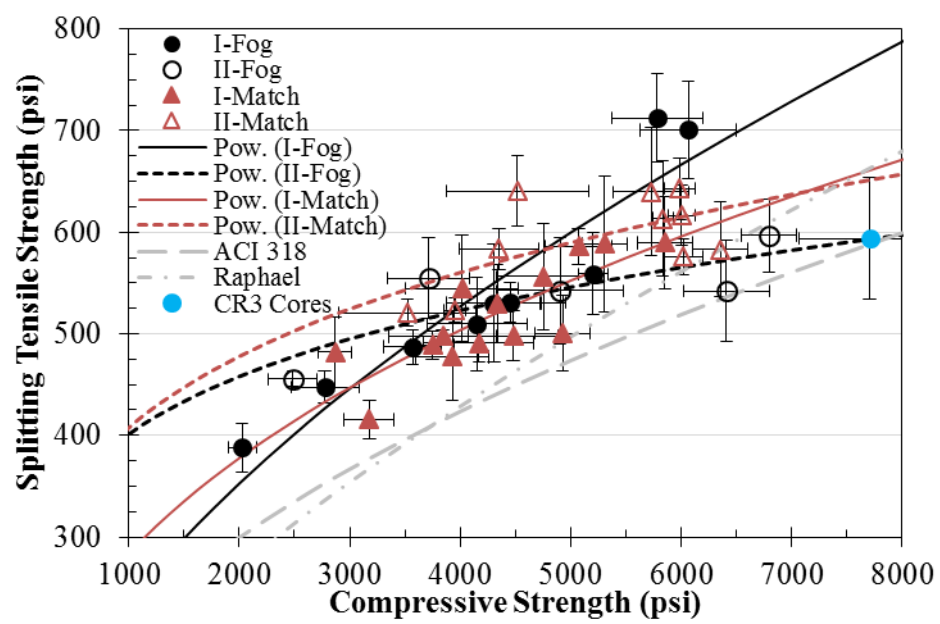
Lastly, since approximately 800 total tests specimens were prepared by several crews, the varying quality of the tested specimens may have influenced the relationship between the compressive and tensile strength. Several incompletely consolidated specimens were identified for the first mock-up, and Mindess et al. (2003) noted that such consolidation is more detrimental to the compressive strength than to the tensile strength. Therefore, these specimens could have contributed to artificially low compressive strength values without similarly decreasing the tensile strength values.

The relatively limited variation of the splitting tensile strength measurements for the second mock-up resulted in the power law regressions predicting unrealistically high tensile strengths during the first hours after concrete placement in Figure 4.19b.

Accordingly, the coefficients of determination for the power law for the second mock-up were lower than those for the first mock-up. Aside from the Fog specimens for the second mock-up, the power law regression yielded the highest coefficients of determination for each series of specimens. Furthermore, as discussed in Section 4.1.1, the relationship between splitting tensile strength and compressive strength is generally agreed to be well defined by a power law function. Therefore, the power law regressions shown in Figure 4.18 and Figure 4.19 with the parameters given in Table 4.8 will be used as baseline references to which further relations will be compared, and the curves will be labelled as “Reference” when presented in later figures.



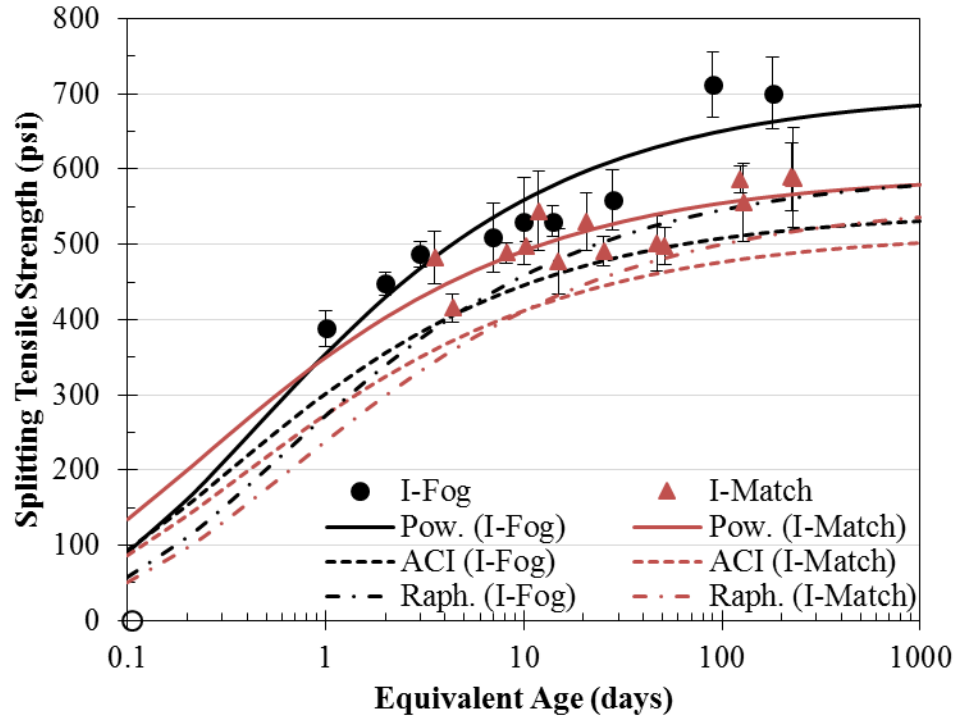
(a)



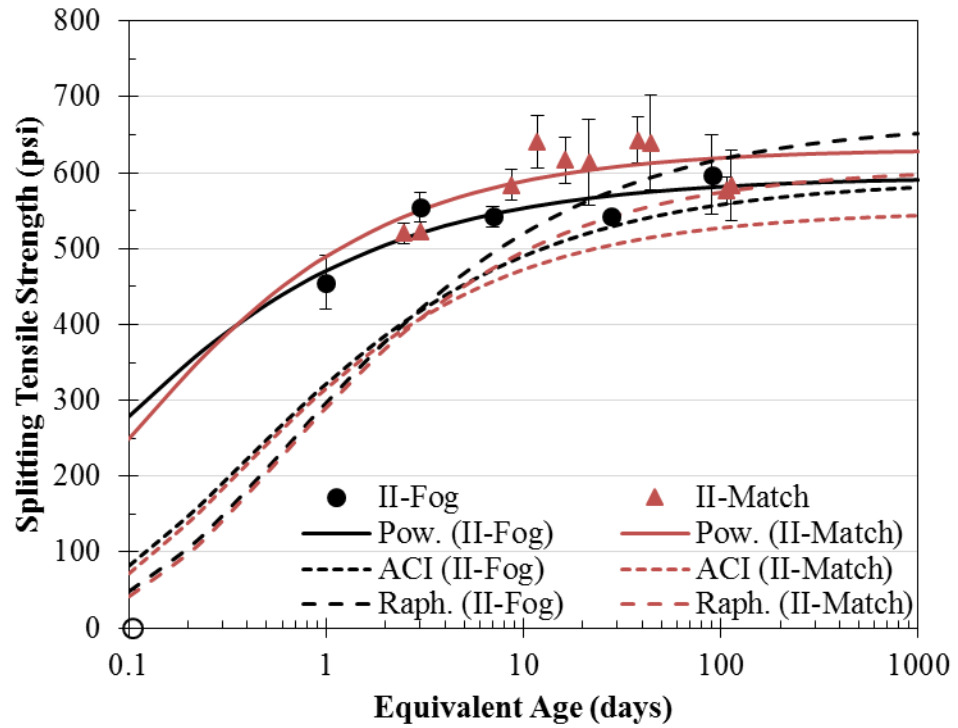
(b)

Note: 1 MPa = 145 psi

Figure 4.18: Splitting tensile strength with respect to compressive strength of all specimens shown on (a) log-log plot and (b) linear plot



(a)



(b)

Note: 1 MPa = 145 psi

Figure 4.19: Splitting tensile strength as a function of equivalent age of fog- and match-cured specimens from (a) first and (b) second mock-up

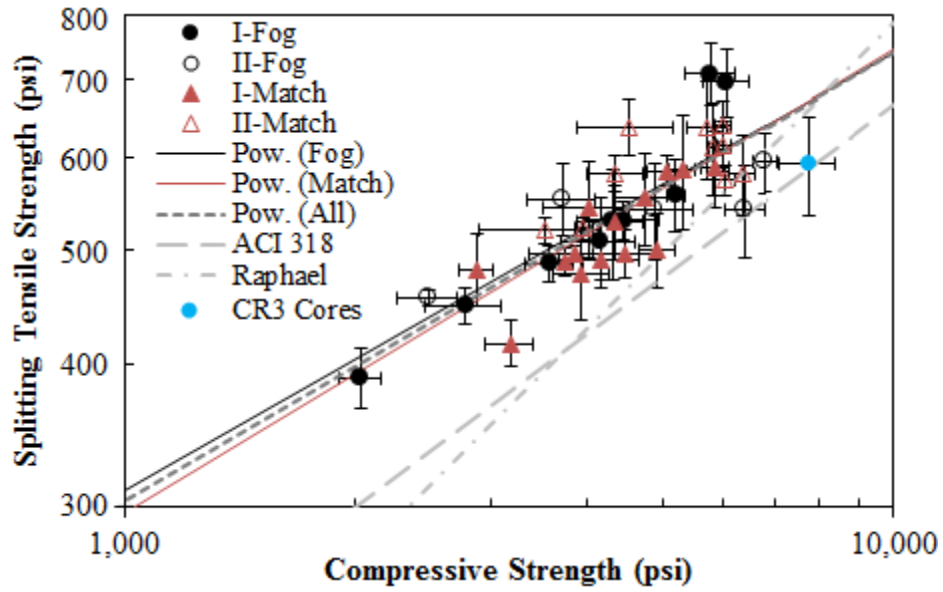
Table 4.8: Parameters for splitting tensile strength development as a power law function of compressive strength

Series	Power law parameters			Coefficient of determination, R^2		
	Coefficient, a		Power, b	Power law	ACI 318-08; Eq. 4.14	Raphael (1984); Eq. 4.15
	(for MPa)	(for psi)				
I-Fog	0.533	4.31	0.580	0.9359	0.6133	0.6994
II-Fog	1.91	106	0.192	0.6725	0.7981	0.8029
I-Match	0.876	16.1	0.415	0.8875	0.6171	0.7011
II-Match	1.80	83.2	0.230	0.7826	0.5829	0.7062

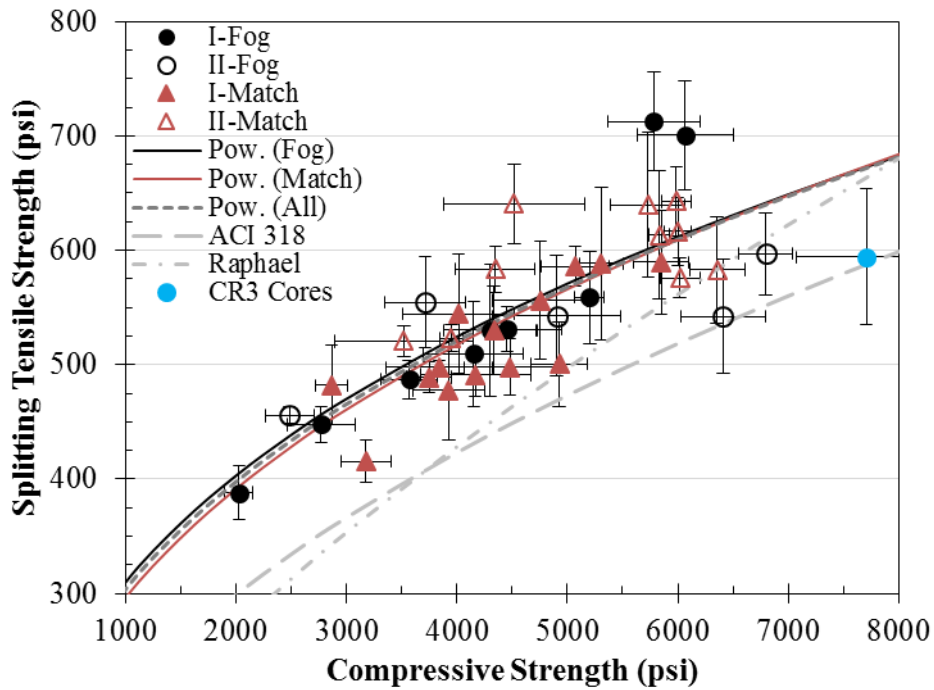
Note: Conversion of coefficient for MPa from psi: $a_{\text{MPa}} = 145^b \cdot \frac{a_{\text{psi}}}{145}$

As observed qualitatively in Figure 4.18 and quantitatively in Table 4.8, the power law regressions determined for each series are notably distinct. However, when power law regressions are conducted for the fog-cured specimens from both mock-ups, the match-cured specimens from both mock-ups, and all specimens, the resulting functions are similar as shown in Figure 4.20. This suggests that the regression for the fog-cured specimens can be used to approximate the relationship between the compressive and splitting tensile strength of the match-cured specimens. Therefore, the power law regression for the fog-cured specimens is indicated by “Power.F” in later plots and is given in Eq. 4.30.

$$\begin{aligned}
 f_{tsp-\text{Pow.F}} &= 1.02(f_c)^{0.380} \quad [\text{MPa}] \\
 f_{tsp-\text{Pow.F}} &= 22.4(f_c)^{0.380} \quad [\text{psi}]
 \end{aligned}
 \tag{Eq. 4.30}$$



(a)



(b)

Note: 1 MPa = 145 psi

Figure 4.20: Splitting tensile strength with respect to compressive strength of all specimens shown on (a) log-log plot and (b) linear plot

Figure 4.21 shows the compressive strength-to-splitting tensile strength (f_c/f_{tsp}) ratio with respect to compressive strength of all of the tested specimens. The f_c/f_{tsp} ratios range from approximately 5 to 12, and most of the results fall within the typical 7-to-12.5 range reported by Mindess et al. (2003). As noted in Section 4.1.1, the relative rate of increase in compressive strength is greater than that in tensile strength, resulting in the positive slope in Figure 4.21 corresponding to increasing f_c/f_{tsp} ratios with increasing compressive strength.

Regressions are shown in Figure 4.21 and Figure 4.22 for the fog-cured specimens from both mock-ups, for the match-cured specimens from both mock-ups, and for all specimens from both mock-ups. Zain et al. (2002) proposed taking the linear regression of the f_c/f_{tsp} ratios with respect to the compressive strength to obtain a relationship of the form shown in Eq. 4.16. The regressions shown in Figure 4.21 and Figure 4.22, however, were obtained from nonlinear regression of the original compressive and splitting tensile strength data as shown in Figure 4.22 using the expression shown in Eq. 4.17.

As in Figure 4.20, the three regressions in Figure 4.21 and Figure 4.22 are similar, suggesting that the linear relationship between the f_c/f_{tsp} ratio and the compressive strength is consistent for the mock-up concrete regardless of the curing history. The regression for the fog-cured specimens shown in Figure 4.21 and Figure 4.22 is given in Eq. 4.31 and is indicated by “Zain.F” in later plots. Similar to the power law regression for the fog-cured specimens (Eq. 4.30), Eq. 4.31 was used for modeling match-cured specimens to see how well the tensile strength of the match-cured specimens could be modeled using only the fog-cured results.

$$f_{tsp-Zain.F} = \frac{f_c}{0.169f_c + 2.86} \quad [\text{MPa}]$$

$$f_{tsp-Zain.F} = \frac{f_c}{(1.17 \times 10^{-3})f_c + 2.86} \quad [\text{psi}]$$

Eq. 4.31

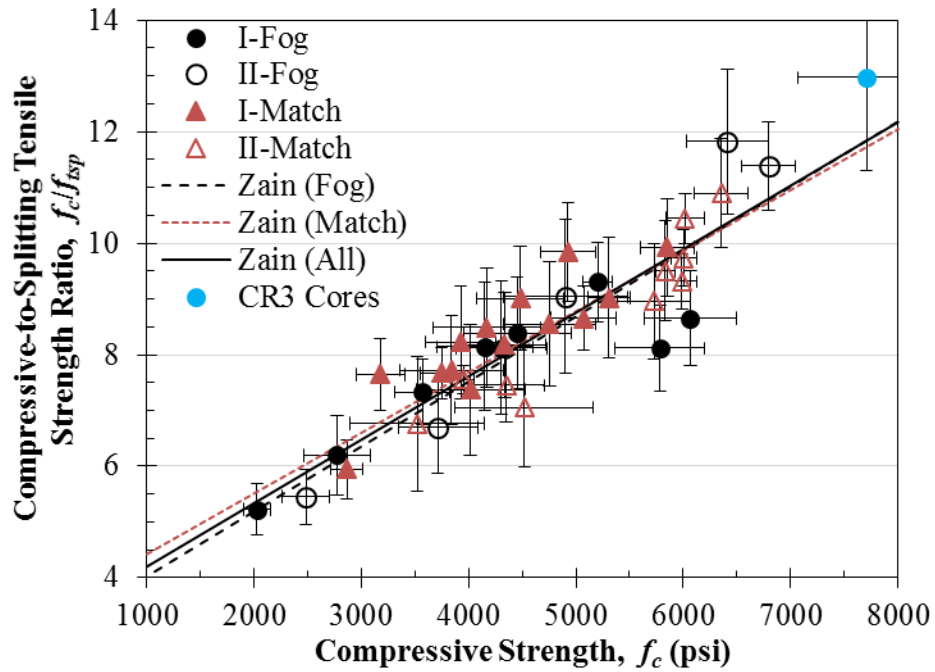


Figure 4.21: Compressive strength-to-splitting tensile strength (f_c/f_{tsp}) ratio with respect to compressive strength

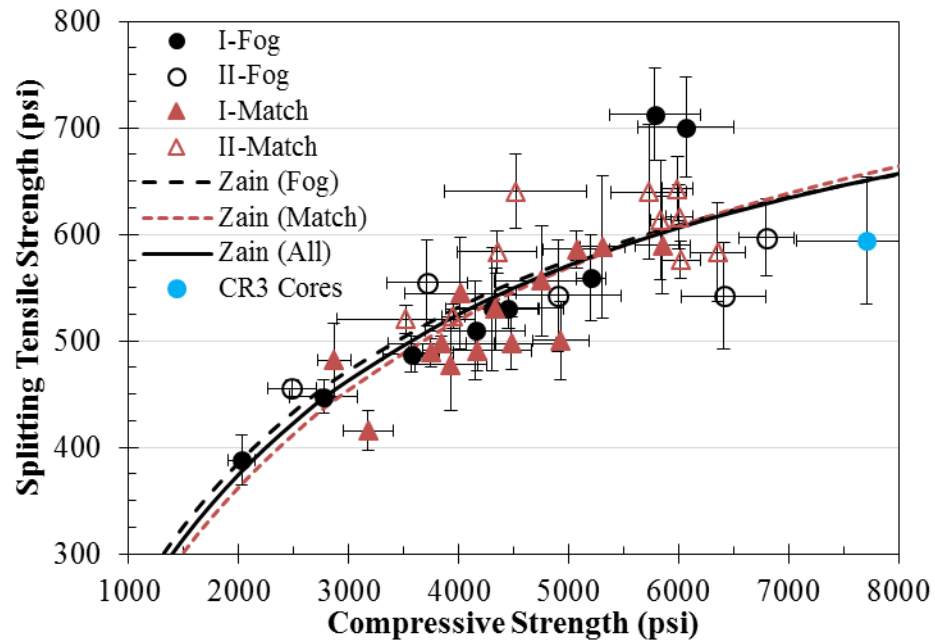
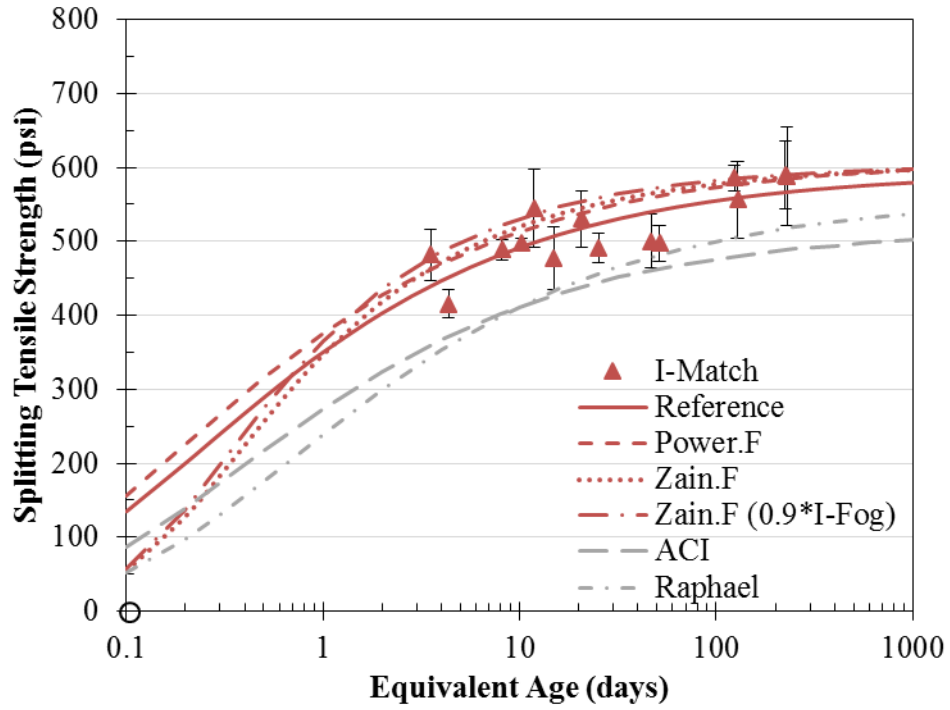


Figure 4.22: Splitting tensile strength with respect to compressive strength with Zain regressions

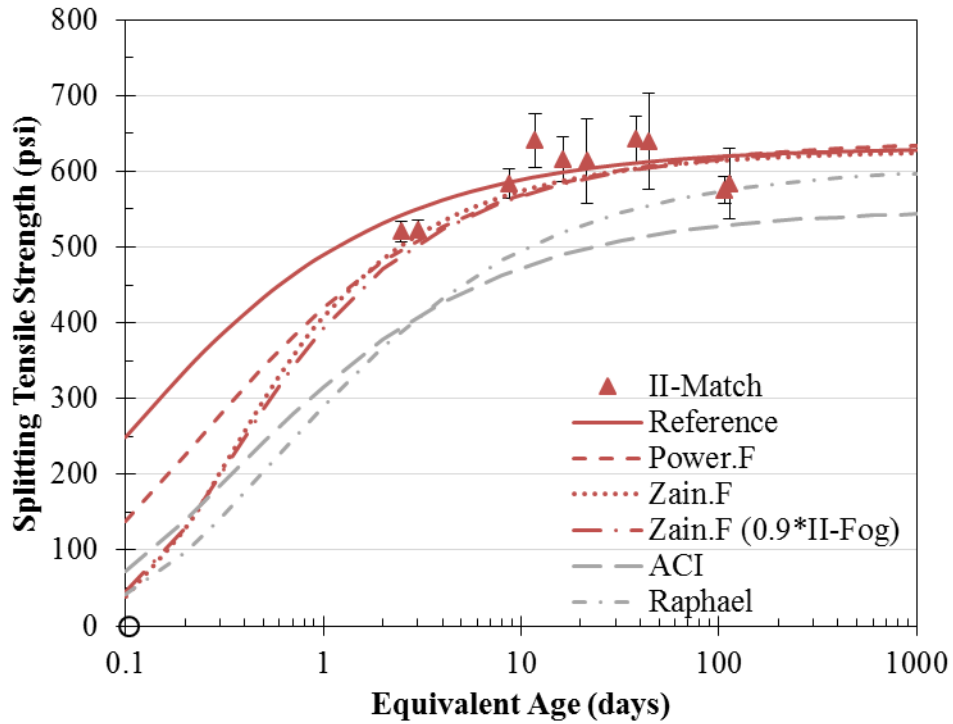
Figure 4.23 shows the experimental match-cured splitting tensile strengths with respect to equivalent age and the corresponding regressions from the previous analyses. As in Figure 4.19, the splitting tensile strength regressions were plotted with respect to equivalent age in Figure 4.23 by incorporating the corresponding exponential functions for compressive strength from Table 4.5. The coefficients of determination for each curve in Figure 4.23 are given in Table 4.9.

As discussed previously, the “Power.F” and “Zain.F” curves are based on the relationship between the compressive and splitting tensile strength of the fog-cured specimens rather than that of the match-cured specimens. However, the coefficients of determination for the “Power.F” curves are higher than those of the corresponding reference curves for two of the four cases, and the coefficients of determination for the “Zain.F” curves are higher than those of all other corresponding curves except for the I-Fog reference curve.

Graphically, the “Zain.F” curves predict very early tensile strengths consistent with the ACI 318 and Raphael functions and lower than the reference and “Power.F” curves. However, during the first day, the “Zain.F” curves increase rapidly and become more consistent with the reference and “Power.F” curves and the experimental data. These results indicate that the “Zain.F” model, based on the relationship between the compressive and tensile splitting strength of the fog-cured specimens, provides an accurate prediction of the splitting tensile strength of the match-cured specimens when only the compressive strength of the match-cured specimens is known.



(a)



(b)

Note: 1 MPa = 145 psi

Figure 4.23: Match-cured splitting tensile strengths with respect to equivalent age and corresponding regressions for (a) first and (b) second mock-up

Table 4.9: Coefficients of determination for regressions of splitting tensile strength with respect to equivalent age

Series	Coefficient of determination, R^2					
	Reference	Power.F	Zain.F	Zain.F (0.9·Fog)	ACI	Raphael
I-Fog	0.9359	0.8541	0.9187	-	0.6133	0.6994
II-Fog	0.6725	0.8592	0.9490	-	0.7981	0.8029
I-Match	0.8875	0.8439	0.9098	0.8835	0.6171	0.7011
II-Match	0.7826	0.9039	0.9630	0.9535	0.5829	0.7304

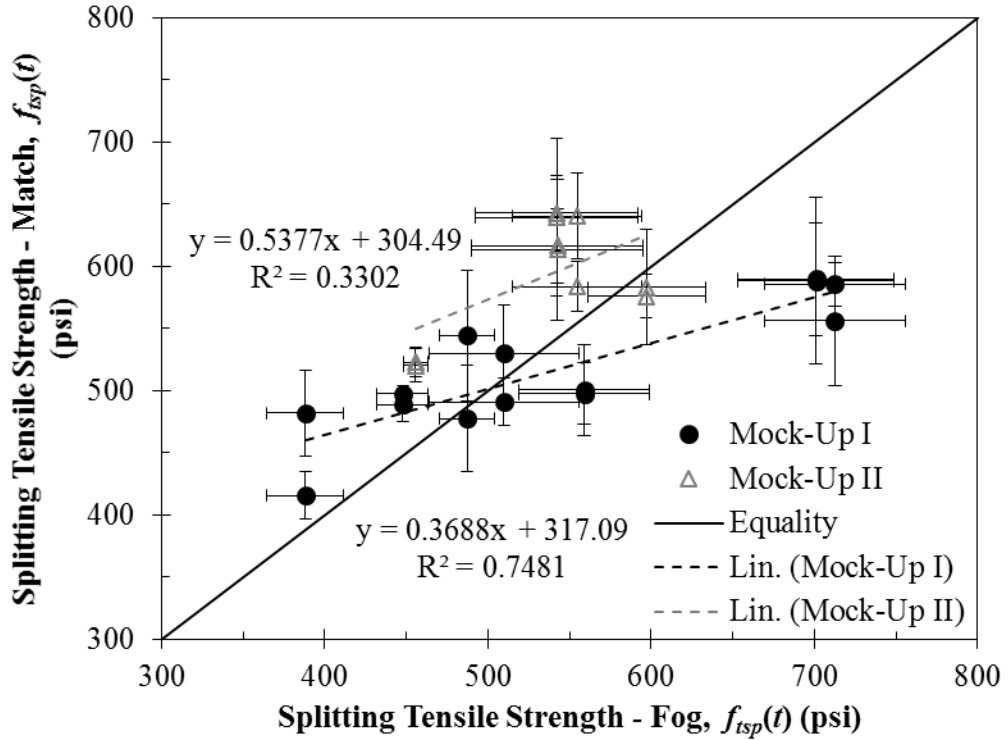
Also shown in Figure 4.23 is the “Zain.F” tensile strength function implemented with the match-cured compressive strength functions in Eq. 4.27 and Eq. 4.28 equal to 90% of the exponential functions for the fog-cured specimens from the corresponding mock-ups. These curves are based on the fog-cured compressive and tensile splitting strengths and are similar to the original “Zain.F” curves, differing by at most 7%. As shown in Table 4.9, the coefficients of determination for the “Zain.F” curves based on 90% of the I-Fog and II-Fog compressive strengths were slightly lower than the corresponding original “Zain.F” curves incorporating the match-cured compressive strengths. However, the coefficient of determination of the “Zain.F” model using 90% of the II-Fog compressive strength curve is higher than that of the reference curve for II-Match.

These results suggest that accurate predictions of the splitting tensile strength of match-cured mock-up concrete can be obtained using the fog-cured compressive and splitting tensile strengths. Whereas the relationship between the fog- and match-cured compressive strengths likely varies based on the concrete temperature history, the relationship between the compressive and tensile splitting strength seems to be independent of the temperature history. This indicates that splitting tension tests of fog-cured specimens are sufficient for predicting the splitting tensile strength of match-cured or in-place concrete given the compressive strength of the fog-cured specimens and either experimental or predicted values for the compressive strength of match-cured concrete.

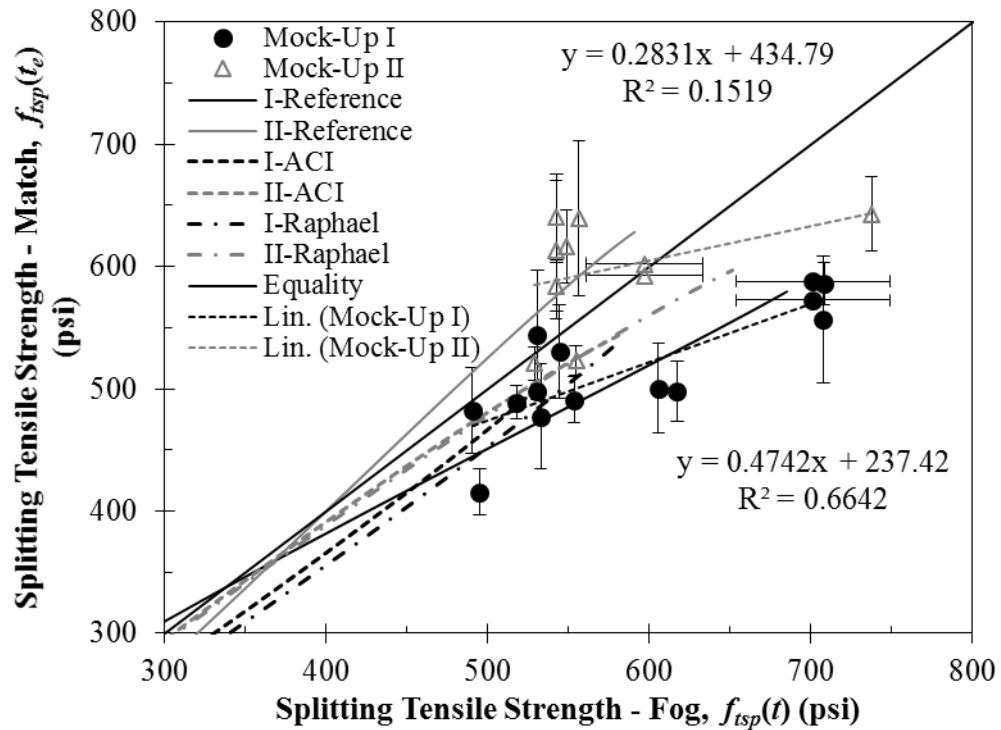
Analogous to the compressive strength results in Figure 4.14, the splitting tensile strength of the fog- and match-cured specimens are compared at matching ages in Figure 4.24. Tests were conducted at the same chronological ages for presentation in Figure 4.24a, and linear interpolation was used to approximate splitting tensile strengths at intermediate equivalent ages in Figure 4.24b.

Similar to the compressive strength results in Figure 4.14a, the splitting tensile strength results from the two mock-ups are easily distinguished when compared according to chronological age in Figure 4.24a, though the tensile strength results for the second mock-up don't exhibit clear linearity. The crossover effect is seen at about 3.5 MPa (510 psi) for the first mock-up, whereas the lack of consistent behavior for the second mock-up limits the clarity of a crossover point.

In contrast to the compressive strength results in Figure 4.14b, the tensile strength results for the two mock-ups are still distinct when compared according to equivalent age in Figure 4.24b. Whereas the results for the first mock-up are generally shifted below the line of equality, many of the results for the second mock-up are still above the line of equality, and no clear relationship between the fog- and match-cured tensile strengths can be identified amongst the various regressions.



(a)

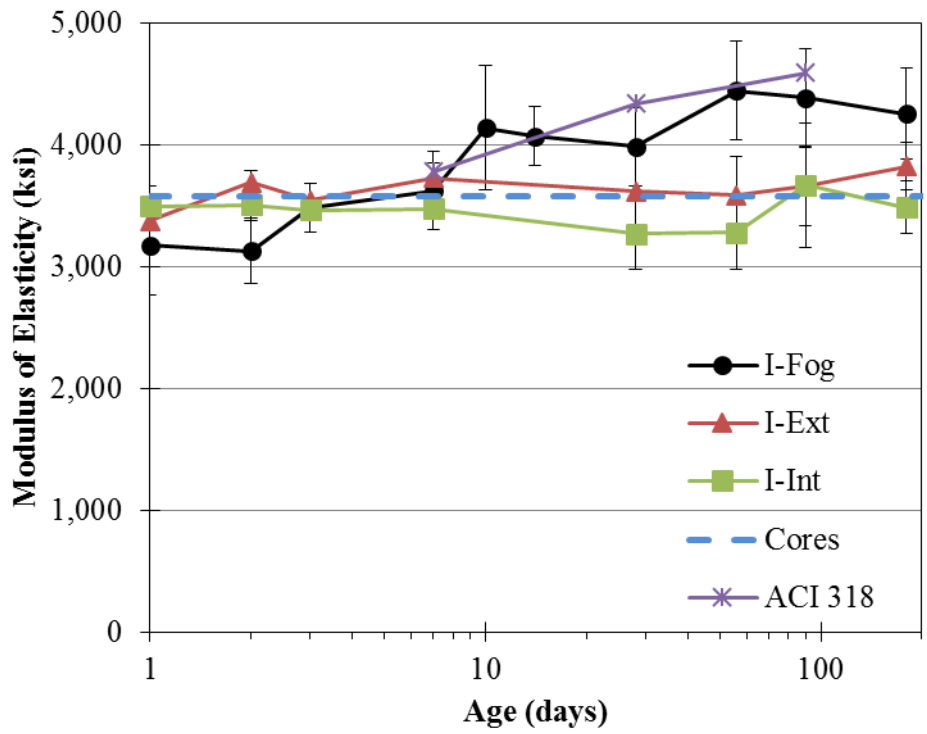


(b)

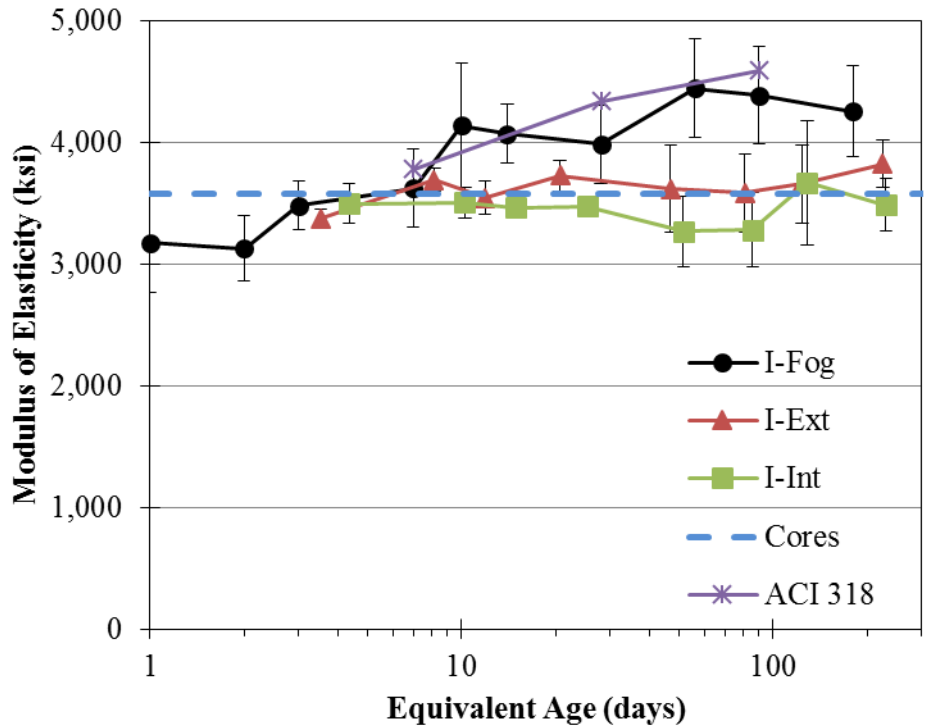
Note: 1 MPa = 145 psi; error bars are not shown for interpolated values
 Figure 4.24: Splitting tensile strength of match-cured specimens with respect to that of fog-cured specimens at same (a) chronological age and (b) equivalent age

4.4.5 Modulus of Elasticity

The modulus of elasticity results for the first and second mock-up are shown in Figure 4.25 and Figure 4.26, respectively. Like the splitting tensile strength results, the crossover effect is not as pronounced for the modulus of elasticity results as it is for the compressive strength results. However, in Figure 4.25b and Figure 4.26b, the Ext and Int results are shifted so that the modulus of elasticity is generally lower than that of the Fog specimens at each equivalent age. Whereas the trends of the Ext and Int curves for the second mock-up are comparable to that of the Fog specimens, the Ext and Int results for the first mock-up were determined to be statistically constant with respect to time in Appendix B.2 and are not similar to the Fog results for the first mock-up. Like the compressive strength and splitting tensile strength results, the higher modulus of elasticity of the second mock-up concrete relative to the first mock-up concrete is likely due to the lower concrete temperatures of the second mock-up during curing and the better consolidation of the specimens for the second mock-up.



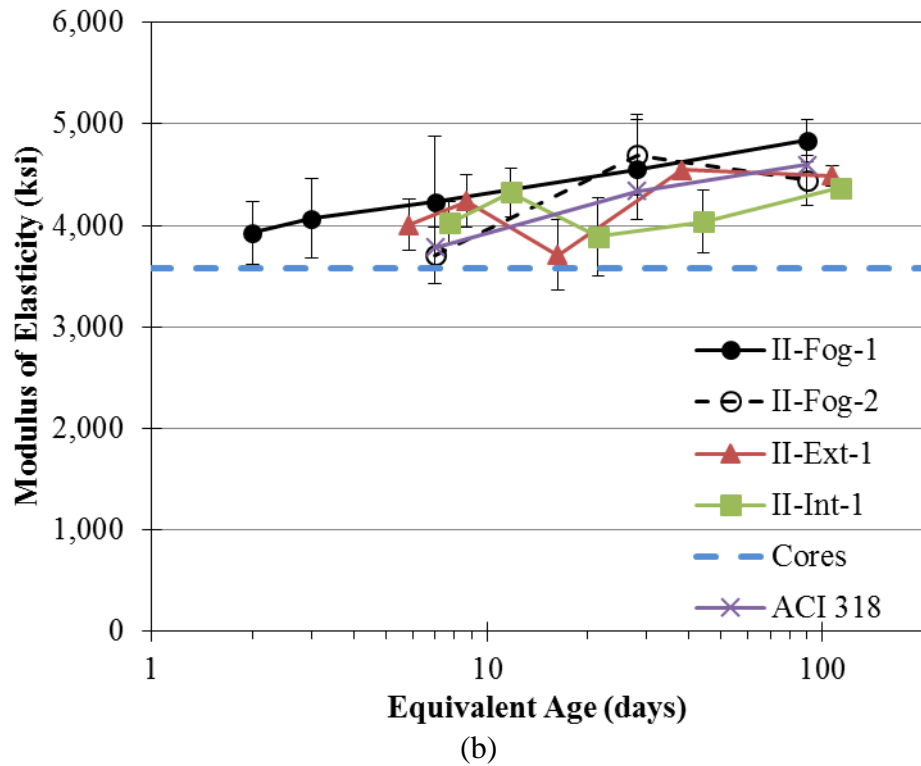
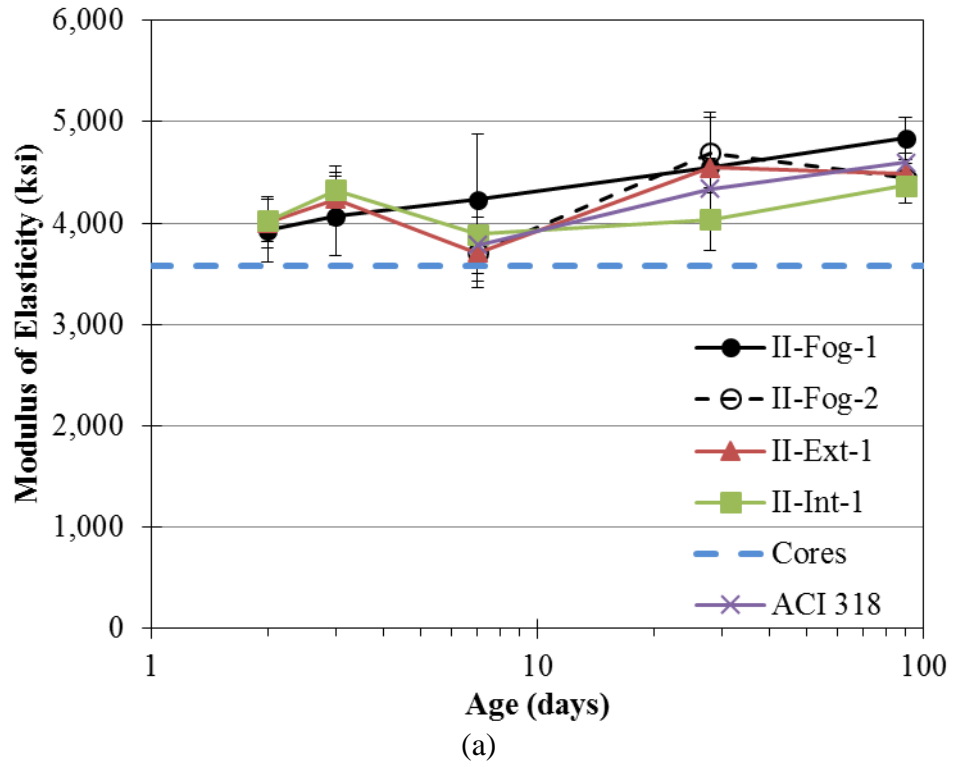
(a)



(b)

Note: 1 GPa = 145 ksi

Figure 4.25: Modulus of elasticity of first mock-up concrete as function of (a) chronological age and (b) equivalent age



Note: 1 GPa = 145 ksi

Figure 4.26: Modulus of elasticity of second mock-up concrete as function of (a) chronological age and (b) equivalent age

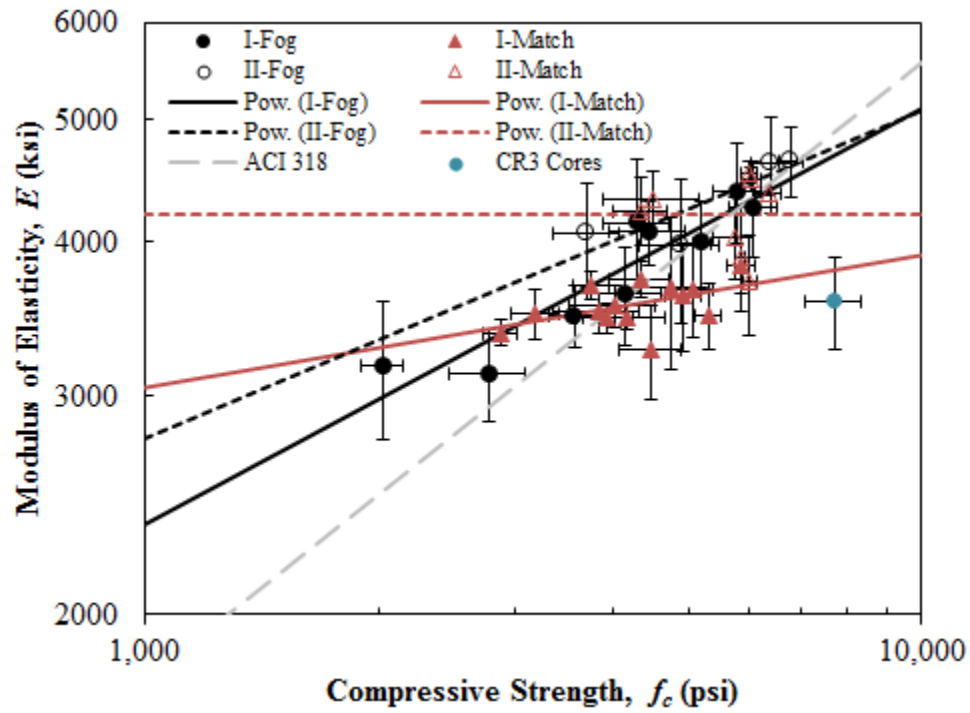
Based on ANOVA results discussed in Appendix B.2 indicating that, for each mock-up, the difference in modulus of elasticity of the Ext and Int concrete was not statistically significant, the Ext and Int results for each mock-up were combined for modeling. The modulus of elasticity of the mock-up concrete is shown with respect to the compressive strength in Figure 4.27. In the simplified form shown in Eq. 4.19 accounting for the unit weight of the mock-up concrete, the ACI 318-08 (2008) equation for the modulus of elasticity as a function of the compressive strength has the form of a power law relation with coefficient 4,670 for MPa (55,900 for psi) and power 0.5. Therefore, power law regressions were determined for each series of specimens using nonlinear least squares regression as discussed in Section 4.4.4. Similarly, power law regressions are shown in Figure 4.28 for the fog-cured specimens from both mock-ups, the match-cured specimens from both mock-ups, and all specimens from both mock-ups. The parameters and coefficients of determination for each of the power law regressions are given in Table 4.10.

As determined by the power of the functions, the slope of each regression is less than that of the ACI 318 relation in the log-log plots in Figure 4.27a and Figure 4.28a. As a result, the regressions predict higher moduli of elasticity for lower compressive strengths and lower moduli of elasticity for higher compressive strengths compared to the ACI relation. Figure 4.27 and Table 4.10 show that the power law regression for each series is relatively unique, though the regressions for the fog-cured specimens are more comparable to the ACI 318 function.

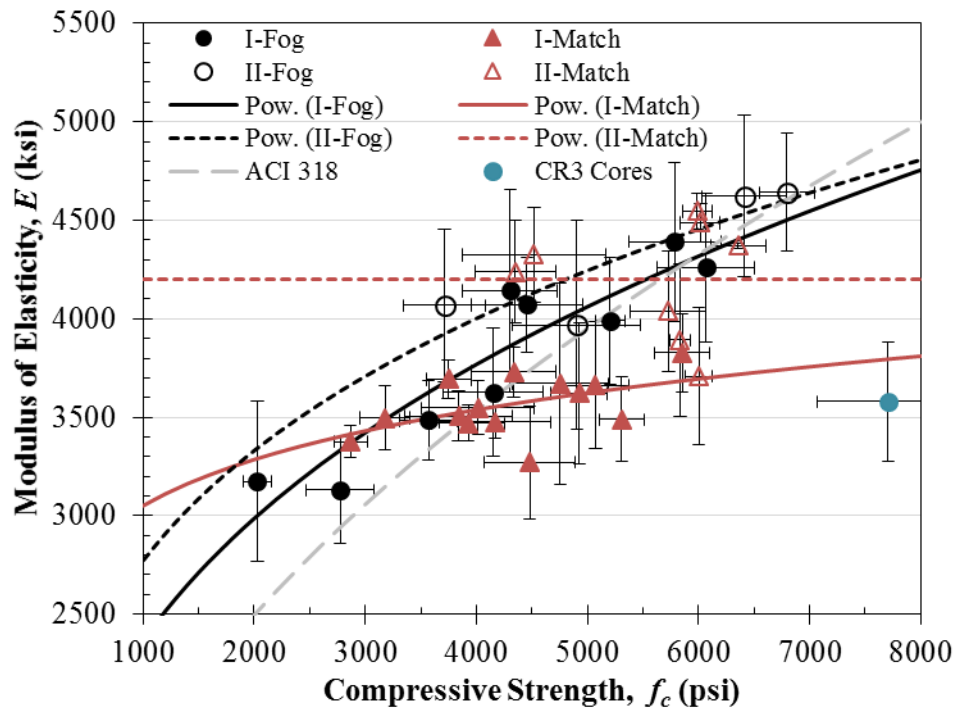
With a power of zero, the regression for the match-cured specimens from the second mock-up is equivalent to the average of the experimental modulus of elasticity values, resulting in the coefficient of determination of zero. Without setting a lower bound to prevent negative powers, the power law regression for that series yielded a negative power, predicting decreasing modulus of elasticity with increasing compressive strength. The regression for the math-cured specimens from the first mock-up is also

relatively constant over the plotted region compared to the ACI 318 function and the regressions for the fog-cured specimens. These results indicate that, compared to the fog-cured specimens and the ACI 318 prediction, the moduli of elasticity of the match-cured specimens reached late-age values more rapidly than the compressive strengths. Testing the match-cured specimens at chronological ages of less than one day would likely have yielded lower modulus of elasticity values that would allow better fitting of the data with the power law.

In contrast to the regressions for the individual series, the regressions for the combined series in Figure 4.28 are more uniform and are generally more consistent with the ACI function. However, the regression begin to deviate from each other upon reaching the compressive strengths of the experimental results, suggesting that the regression for the fog-cured specimens is not an ideal predictor of the modulus of elasticity of the match-cured specimens. However, the power law regression for the fog-cured specimens will be compared with other functions in later analyses in order to determine if the predicted modulus of elasticity values are comparable with respect to equivalent age.

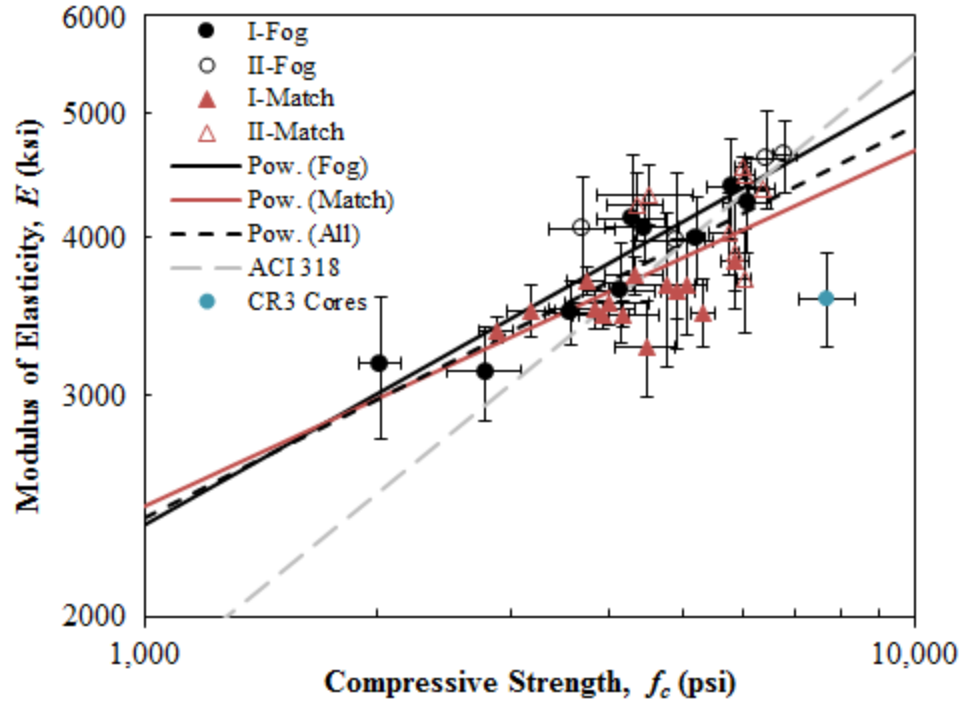


(a)

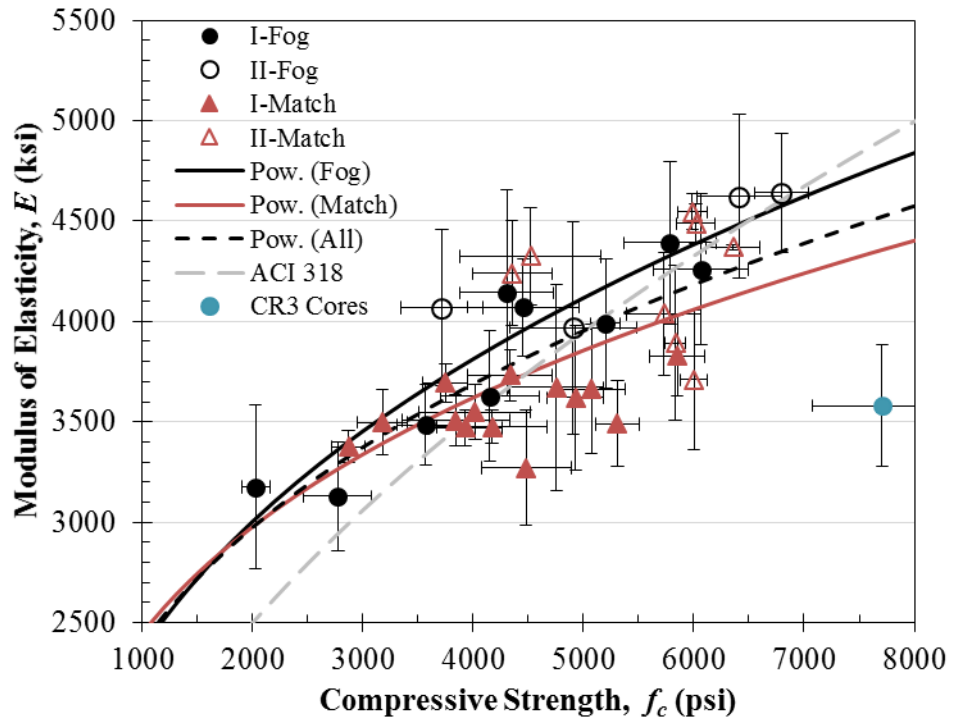


(b)

Figure 4.27: Modulus of elasticity with respect to compressive strength of all specimens with individual power law regressions shown on (a) log-log plot and (b) linear plot



(a)



(b)

Figure 4.28: Modulus of elasticity with respect to compressive strength of all specimens with combined power law regressions shown on (a) log-log plot and (b) linear plot

Table 4.10: Power law parameters and coefficients of determination for modulus of elasticity as function of compressive strength

Series	Power law parameters		Power, b	R^2
	Coefficient, a			
	(for GPa)	(for ksi)		
I-Fog	8.54	233	0.336	0.8458
II-Fog	11.7	447	0.264	0.7508
I-Match	17.1	1460	0.107	0.2440
II-Match	29.0	4201	0	0
Fog	8.41	220	0.344	0.8427
Match	9.79	349	0.282	0.3670
All	9.05	279	0.311	0.5325

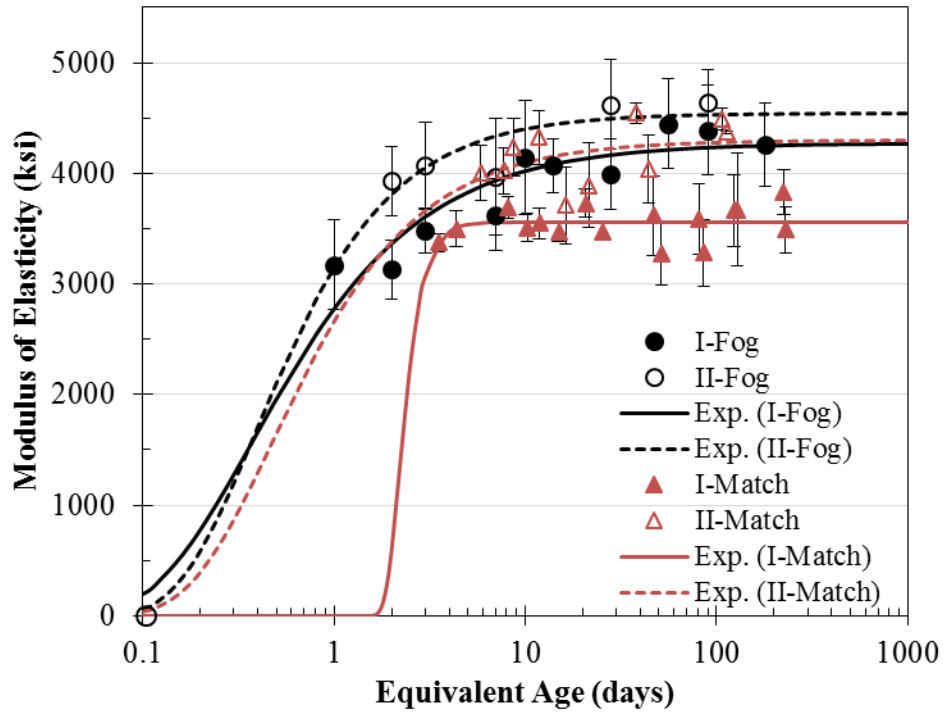
Note: Conversion of coefficient for GPa from ksi: $a_{\text{GPa}} = 145^b \cdot \frac{a_{\text{ksi}}}{145}$

The experimental modulus of elasticity results are shown with respect to equivalent age in Figure 4.29, and regressions for the three-parameter exponential function shown in Eq. 4.20 are included for the individual series in Figure 4.29a and for the combined series in Figure 4.29b. The parameters and coefficients of determination for each regression are given in Table 4.11. Qualitatively and quantitatively, the regressions for the individual series fit the experimental data well.

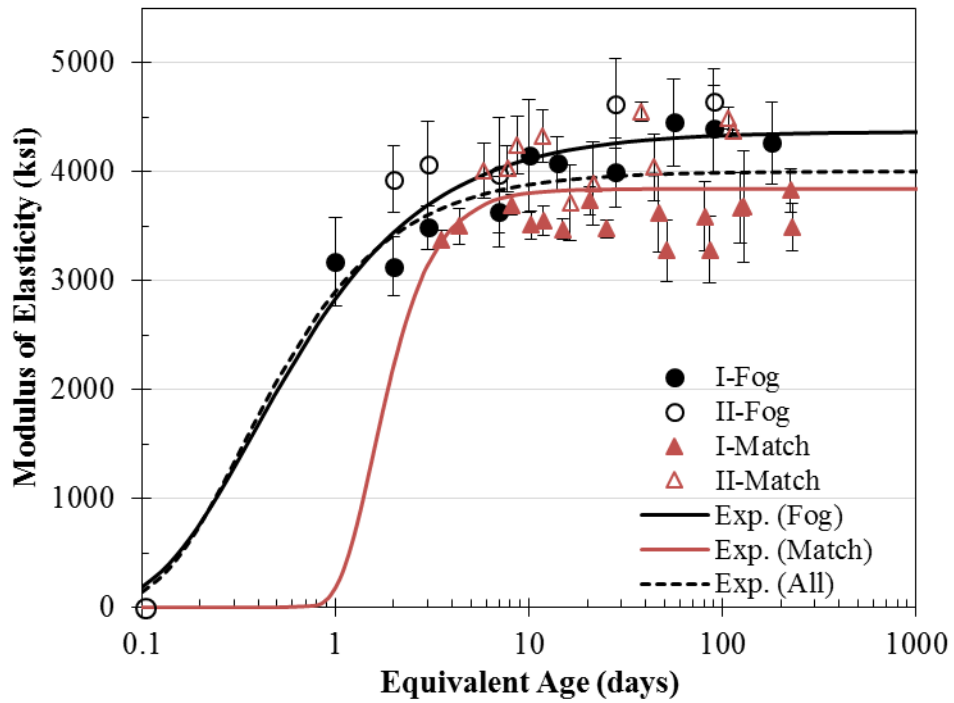
Per ANOVA results discussed in Appendix B.2, the modulus of elasticity of the match-cured concrete from the first mock-up was not significantly unique at any tested age and would be considered equal to the average of all experimental results as 24.5 GPa (3555 ksi). As shown in Figure 4.29a, the exponential model for the match-cured specimens from the first mock-up results predicts a constant modulus of elasticity within the first week. However, as shown in Table 4.11, relatively high time (τ) and shape (β) parameters are required to fit the data, resulting in the unrepresentative delay in the development of modulus of elasticity until two days after placement.

Whereas combining the series for power law regression analysis in Figure 4.28 resulted in a significant improvement in the uniformity of the curves, the exponential regressions of the combined series in Figure 4.29b are not as significantly different from

the original regressions for each series in Figure 4.29a. This suggests that the exponential function fits the data more consistently than the power law, even when the data are limited or somewhat inconsistent with the general form of the function. Similar to Figure 4.28, however, the regressions for the combined series in Figure 4.29b deviate from each other upon reaching the experimental results, indicating that the regression for the fog-cured specimens is not an ideal predictor of the modulus of elasticity of the match-cured specimens.



(a)



(b)

Figure 4.29: Modulus of elasticity with respect to equivalent age of all specimens with (a) individual and (b) combined exponential regressions

Table 4.11: Exponential function parameters and coefficients of determination for modulus of elasticity as function of equivalent age

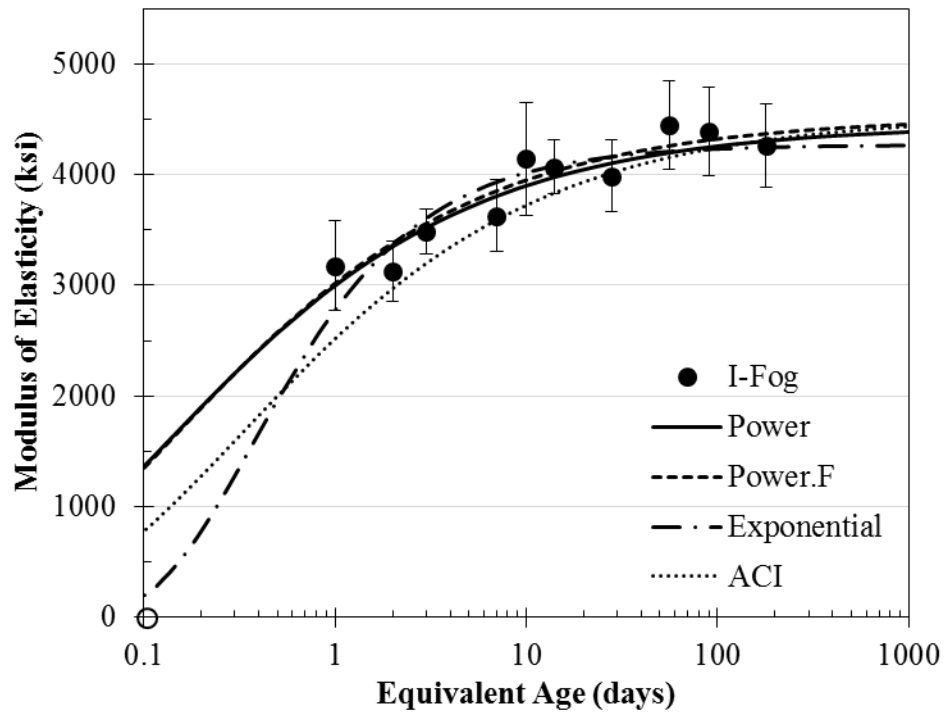
Series	Exponential function parameters			R^2	
	f_{cu}		τ (day)		
	(GPa)	(ksi)			
I-Fog	29.5	4273	0.3733	0.8526	0.9682
II-Fog	31.3	4544	0.3926	1.064	0.9881
I-Match	24.5	3559	2.199	6.144	0.9729
II-Match	29.7	4301	0.4824	0.9984	0.9651
Fog	30.1	4365	0.3785	0.8631	0.9467
Match	26.5	3840	1.569	2.479	0.8380
All	27.6	3996	0.3289	1.019	0.7672

The modulus of elasticity results for each series of specimens are shown in Figure 4.30 with the preceding regressions for comparison of the fits as functions of equivalent age, and the coefficient of determination for each regression is given in Table 4.12. The power law regression for fog-cured specimens is labeled “Power.F” in the plots; otherwise, each regression is specific to the displayed series of modulus of elasticity results and, when based on a relation between the modulus of elasticity and compressive strength, the corresponding power law function for the compressive strength as determined in Section 4.4.3.

The three-parameter exponential function has the highest coefficient of determination for each series. Furthermore, the exponential function appropriately models near-zero values early during the first day of curing while still following the trend of the experimental results. However, obtaining the exponential regressions requires experimental testing of each series since the curves were generally unique for each case, though the I-Fog and II-Match regressions were similar.

The ACI 318 relation, which was not based on any of the current modulus of elasticity results and depended only on the compressive strengths, generally provided good predictions of the behavior. For each series, the ACI 318 relation began with low modulus of elasticity values at very early ages, second only to the exponential regression in each case. Additionally, the coefficient of determination for the ACI 318 relation was

second only to that of the exponential regression in each case. This suggests that, in the absence of experimental results for modulus of elasticity, the ACI 318 relation provides reasonable estimates of the modulus of elasticity of the concrete when the compressive strength is known.



(a)

Figure 4.30: Modulus of elasticity with respect to equivalent age of (a) I-Fog, (b) II-Fog, (c) I-Match, and (d) II-Match specimens

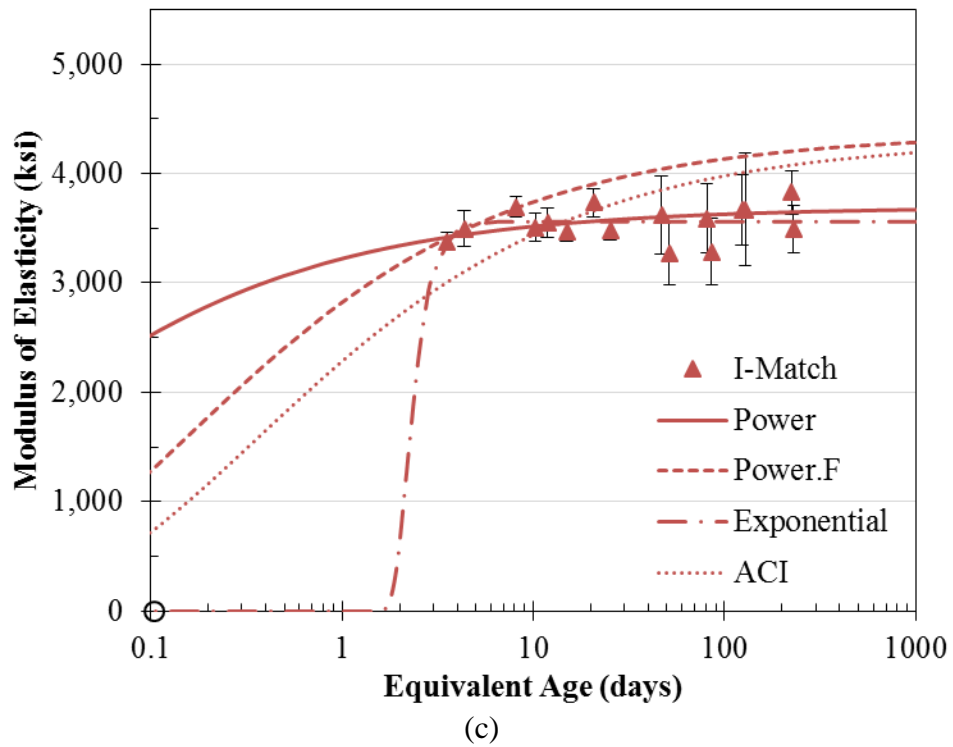
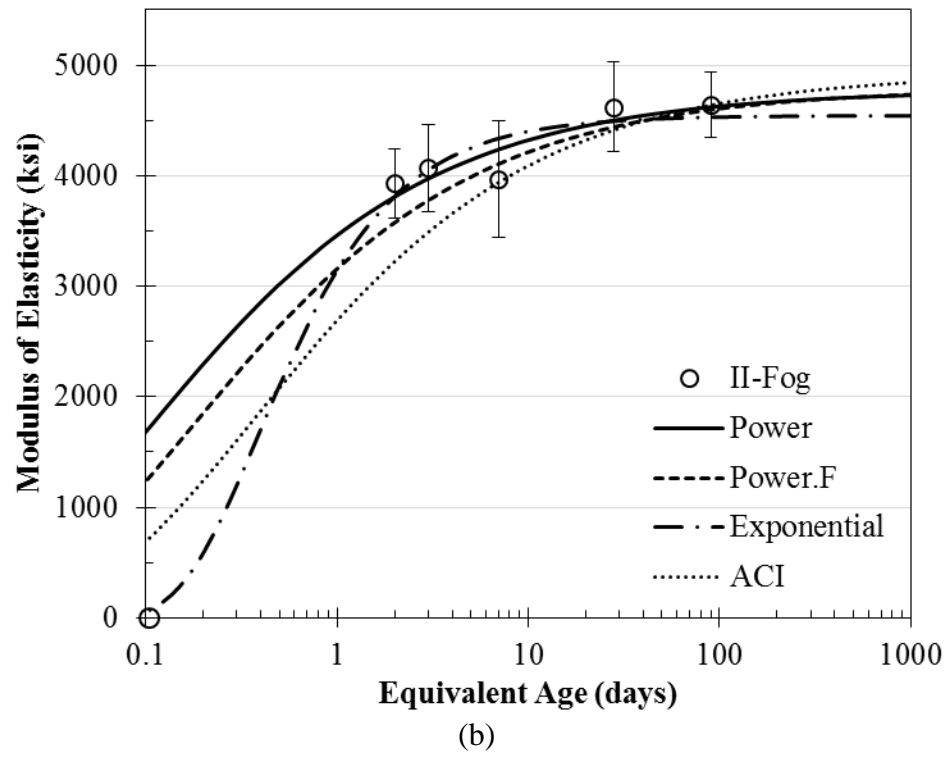
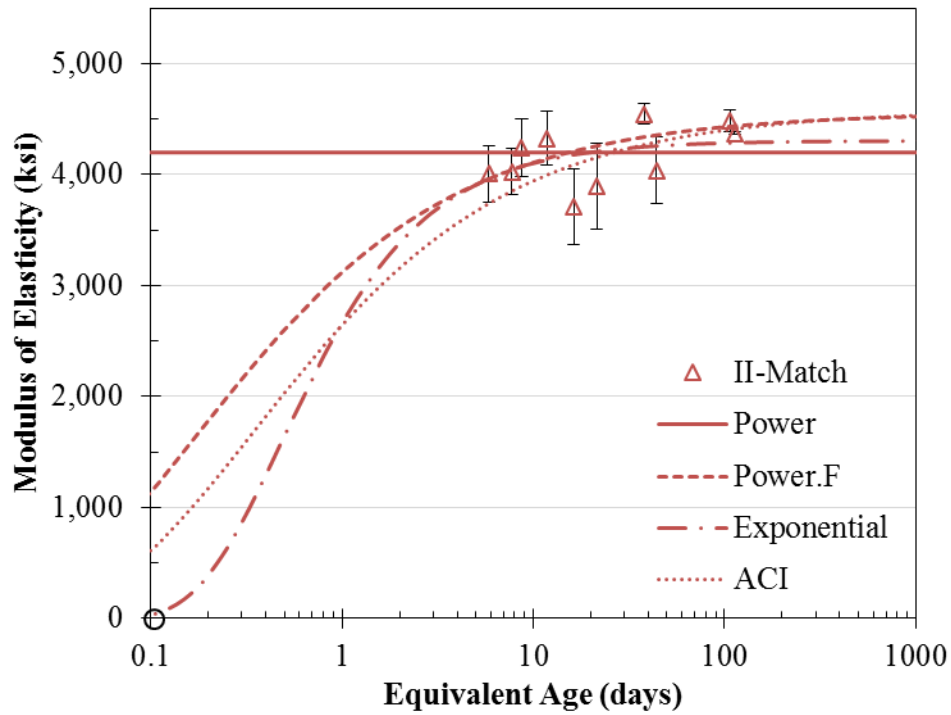


Figure 4.30 (continued)



(d)

Figure 4.30 (continued)

Table 4.12: Coefficients of determination for modulus of elasticity as function of equivalent age

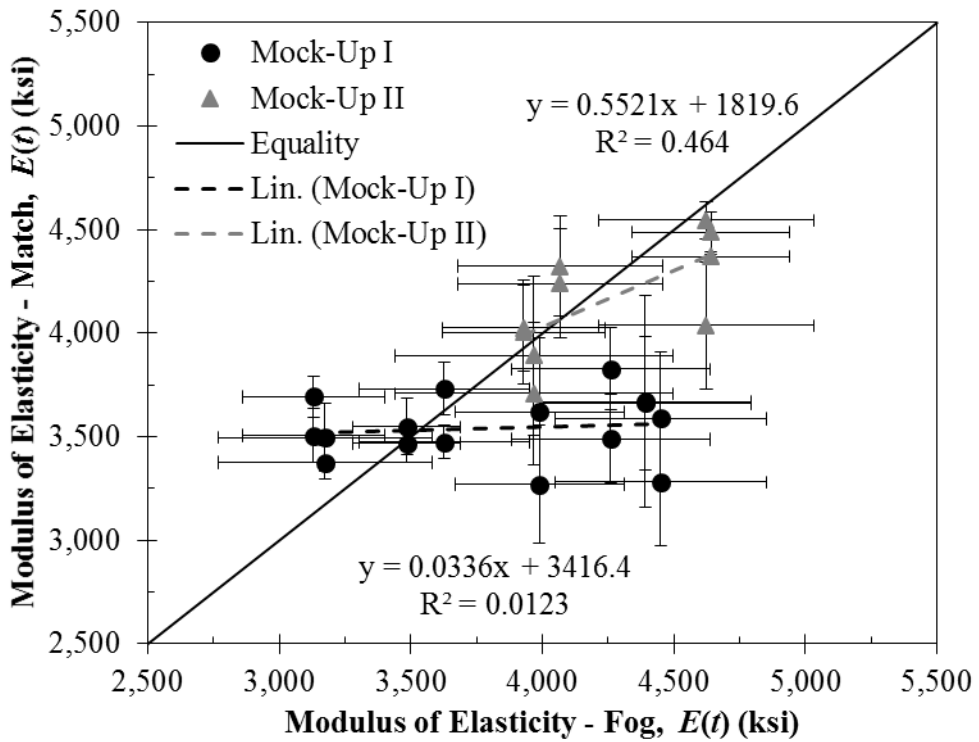
Series	Coefficient of determination, R^2			
	Power	Power.F	Exp.	ACI
I-Fog	0.8588	0.8629	0.9683	0.9016
II-Fog	0.8024	0.8790	0.9881	0.9095
I-Match	0.4408	0.5820	0.9729	0.7826
II-Match	0	0.8796	0.9651	0.9332

Analogous to the compressive strength results in Figure 4.14 and splitting tensile strength results in Figure 4.24, the modulus of elasticity results of the fog- and match-cured specimens are compared at matching ages in Figure 4.31. Tests were conducted at the same chronological ages for presentation in Figure 4.31a, and linear interpolation was used to approximate splitting tensile strengths at intermediate equivalent ages in Figure 4.31b.

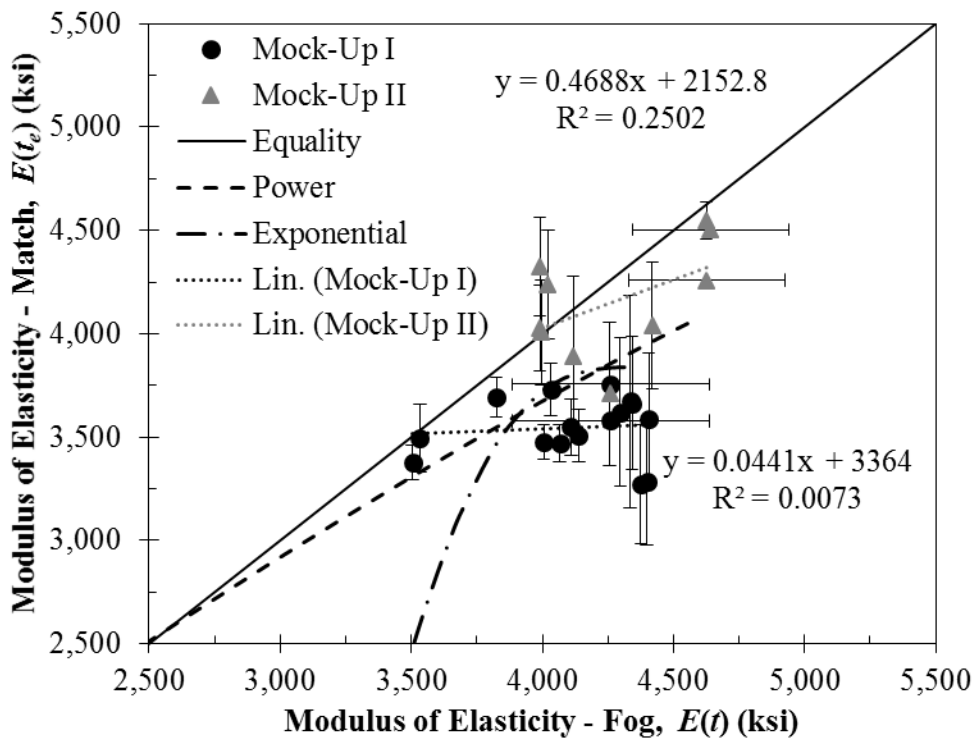
Similar to the compressive and splitting strength results, the modulus of elasticity results from the two mock-ups are generally distinct when compared according to

chronological age in Figure 4.31a. The crossover effect is seen at about 24 GPa (3,500 ksi) for the first mock-up. In contrast, the modulus of elasticity of the second mock-up concrete is roughly equal at the lowest values of approximately 28 MPa (4,000 ksi) before trending to lower values for the match-cured specimens as the modulus increases.

Like the splitting tensile strength results, the modulus of elasticity results for the two mock-ups are generally still distinct when compared according to equivalent age in Figure 4.31b. Nearly all of the results shifted below the line of equality, and the curve for the power law regressions is nearly linear, with the ratio of modulus of elasticity values for match- and fog-cured concrete decreasing from about 1.0 to 0.89 over the plotted range of values. However, the curve is not particularly representative of the experimental results, and, as was discussed previously, the power law regressions were not ideal for modeling the development of the modulus of elasticity of the mock-up concrete.



(a)



Note: 1 MPa = 145 psi; error bars are not shown for interpolated values

(b)

Figure 4.31: Modulus of elasticity of match-cured specimens with respect to that of fog-cured specimens at same (a) chronological age and (b) equivalent age

Due to the rapid development of modulus of elasticity for the mock-up concrete, testing within the first 24 hours of concrete placement is recommended for obtaining better early-age form in the regressions. Despite the absence of very early-age data, the three-parameter exponential function generally fits very well with the experimental modulus of elasticity results with respect to equivalent age. However, in the absence of experimental results for modulus of elasticity, the ACI 318 relation is recommended for predicting the modulus of elasticity based on known compressive strength values.

4.4.6 Poisson's Ratio

The results of all Poisson's ratio testing are presented collectively in Figure 4.32. As discussed in Appendix B.2, the average Poisson's ratio of 0.20 was determined to be statistically representative of all experimental results. However, as shown in Figure 4.32, the equation proposed by De Schutter and Taerwe (1996) (Eq. 4.21) underestimates the Poisson's ratio values measured experimentally for the mock-up concrete. Two factors contribute to this difference: (1) the average Poisson's ratio of the mock-up concrete was 0.20, higher than the 0.18 long-term value of the model, and (2) the ultimate degree of hydration of the mock-up cement was determined to be $\alpha_u = 0.633$, resulting in an approximately 16% decrease of the modeled long-term Poisson's ratio from 0.18 to 0.15. Therefore, in order to obtain an appropriate model for the mock-up concrete, least squares regression of all experimental Poisson's ratio results was conducted and a coefficient of 0.2387 was determined for the sine component of the model, resulting in the function shown in Eq. 4.32 and Figure 4.32. This model captures the initial decrease in Poisson's ratio, the intermediate minimum value, and the late-age average value of 0.20.

$$v(\alpha_H) = 0.2387 \sin\left(\frac{\pi\alpha_H}{2}\right) + 0.5e^{-10\alpha_H} \quad \text{Eq. 4.32}$$

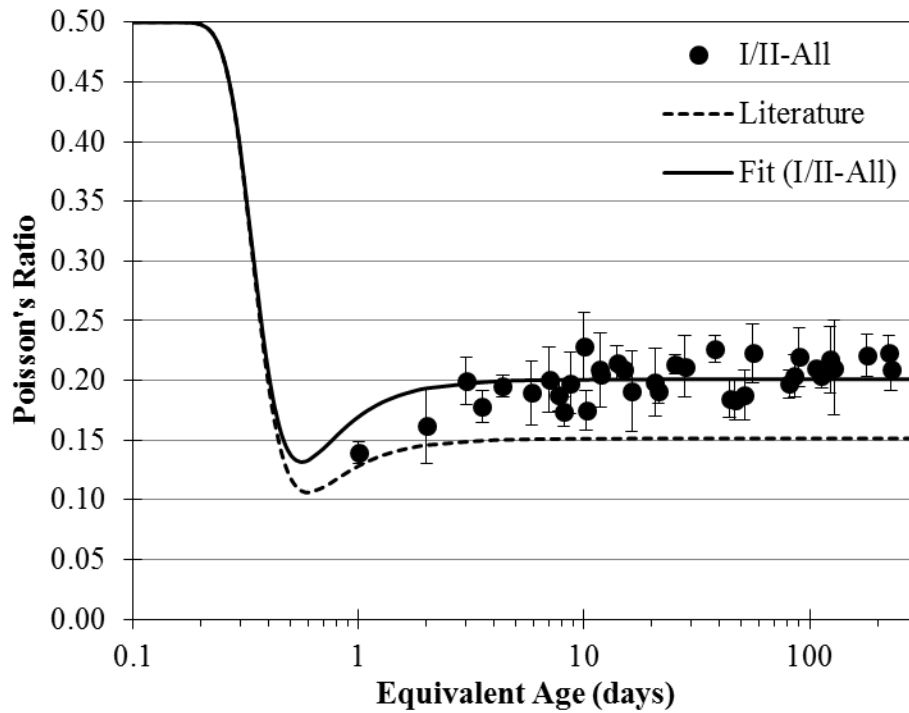


Figure 4.32: Poisson's ratio of all mock-up concrete specimens

Though the model proposed by De Schutter and Taerwe (1996) assumes a long-term Poisson's ratio of 0.18 for concrete, experimental testing is recommended to identify representative Poisson's ratio value for the concrete under investigation. The uniformity of the Poisson's ratio results among all series of specimens suggests that testing match-cured specimens is unnecessary when fog-cured specimens are tested. If the early-age variation of the Poisson's ratio is of interest, testing during the first few days, including during the first day, is recommended. However, if only the long-term value is of interest, testing after three days is recommended.

4.4.7 Specific Heat Capacity

The averages of the specific heat capacity curves determined for each material via differential scanning calorimetry are shown in Figure 4.33 for the nominal 20-to-75-°C

(68-to-167-°F) range of temperatures measured in the mock-up. The specific heat capacity of the fine aggregate exhibits linear dependency on temperature, whereas the specific heat capacity of the coarse aggregate exhibits nonlinearity at higher temperatures, and the specific heat capacity of the cement exhibits slight curvature throughout the temperature range. Since the variation from linear behavior is not significant over the temperature range of interest for any of the materials, linear regression analysis was conducted, and the resulting lines and corresponding equations are shown in Figure 4.33.

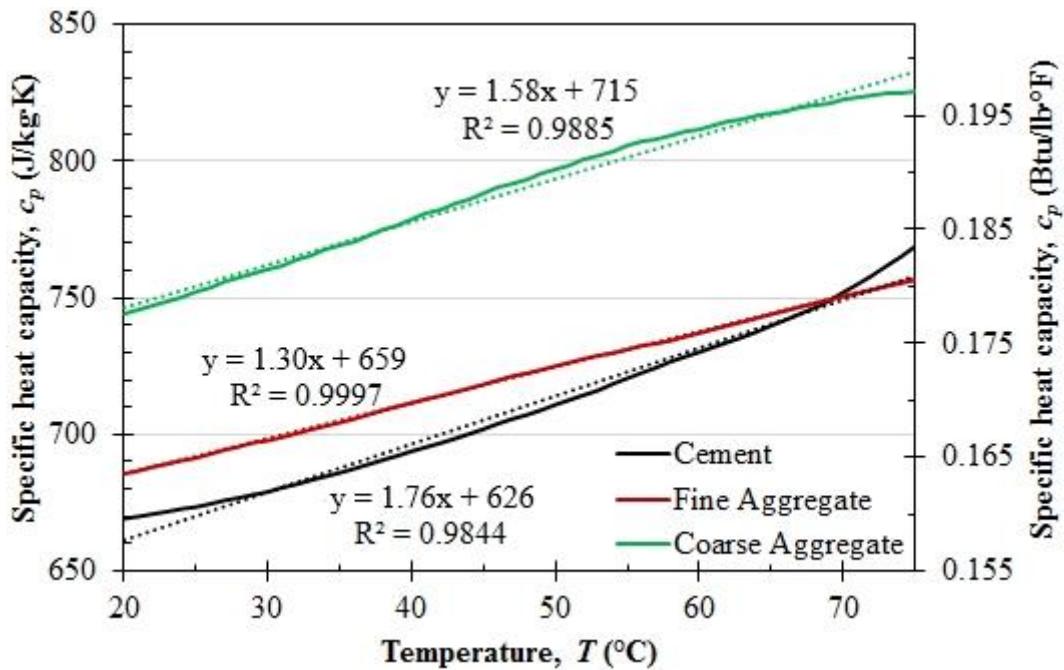


Figure 4.33: Specific heat capacities and linear regressions with respect to temperature

As discussed in Section 2.7.1, the specific heat capacity of water, in contrast to that of the cement and aggregates, is relatively constant over the temperature range of interest. Therefore, a constant value of 4186.8 J/kg·K (1.00 Btu/lb·°F) is used for modeling. The linear equations for specific heat capacity of the cement, fine aggregate, and coarse aggregate are given in Eq. 4.33, Eq. 4.34, and Eq. 4.35, respectively, and are

incorporated in Eq. 4.36 for the specific heat capacity of the concrete as a function of degree of hydration and temperature, based on the model developed by van Breugel (1980) and shown in Eq. 4.22. The determination of Eq. 4.36 is shown in Appendix A.4. Due to the relatively small masses used, the contribution of the admixtures to the specific heat capacity of the concrete is neglected.

$$c_{p(c)} = 1.76T + 626 \quad \text{Eq. 4.33}$$

$$c_{p(fa)} = 1.30T + 659 \quad \text{Eq. 4.34}$$

$$c_{p(ca)} = 1.58T + 715 \quad \text{Eq. 4.35}$$

Where,

- $c_{p(c)}$ = specific heat capacity of cement, J/kg·K
- $c_{p(fa)}$ = specific heat capacity of fine aggregate, J/kg·K
- $c_{p(ca)}$ = specific heat capacity of coarse aggregate, J/kg·K
- T = temperature, °C

$$c_p = 1.17\alpha_H T - 50.8\alpha_H + 1.42T + 932 \quad \text{Eq. 4.36}$$

Where,

- c_p = specific heat capacity of concrete, J/kg·K
- α_H = degree of hydration

Based on Eq. 4.36, the specific heat capacity curves for the mock-up concrete are shown in Figure 4.34. The specific heat capacity of the match-cured concrete was governed by the temperature of the concrete, with higher specific heat capacity values at higher temperature due to the behavior of the component materials shown in Figure 4.33. At the temperature of the Fog specimens, 23 °C (73.5 °F), the fictitious specific heat capacity of hydrated cement is 532 J/kg·K per van Breugel's model, 20% less than the 666-J/kg·K specific heat capacity of the cement at 23 °C per Figure 4.33. Therefore, the modeled decrease in specific heat capacity of the Fog specimens in Figure 4.34 is a result of the isothermal transition from unhydrated to hydrated cement.

Ranging from approximately 950 to 1055 J/kg·K, the modeled specific heat capacity values of the mock-up concrete are generally consistent with literature values for concrete. Though Tia et al. (2010) measured specific heat capacity values at early ages

ranging from 1100 to 1200 J/kg·K (0.26 to 0.29 Btu/lb·°F) for concrete containing Florida Ocala limestone coarse aggregate, those values were noted to be higher than examples in ACI 207.2R-07 (2007) of concrete containing limestone aggregate with specific heat capacities ranging from 925 to 1054 J/kg·K (0.22 to 0.25 Btu/lb·°F) at temperatures from 10 to 66 °C (50 to 150 °F).

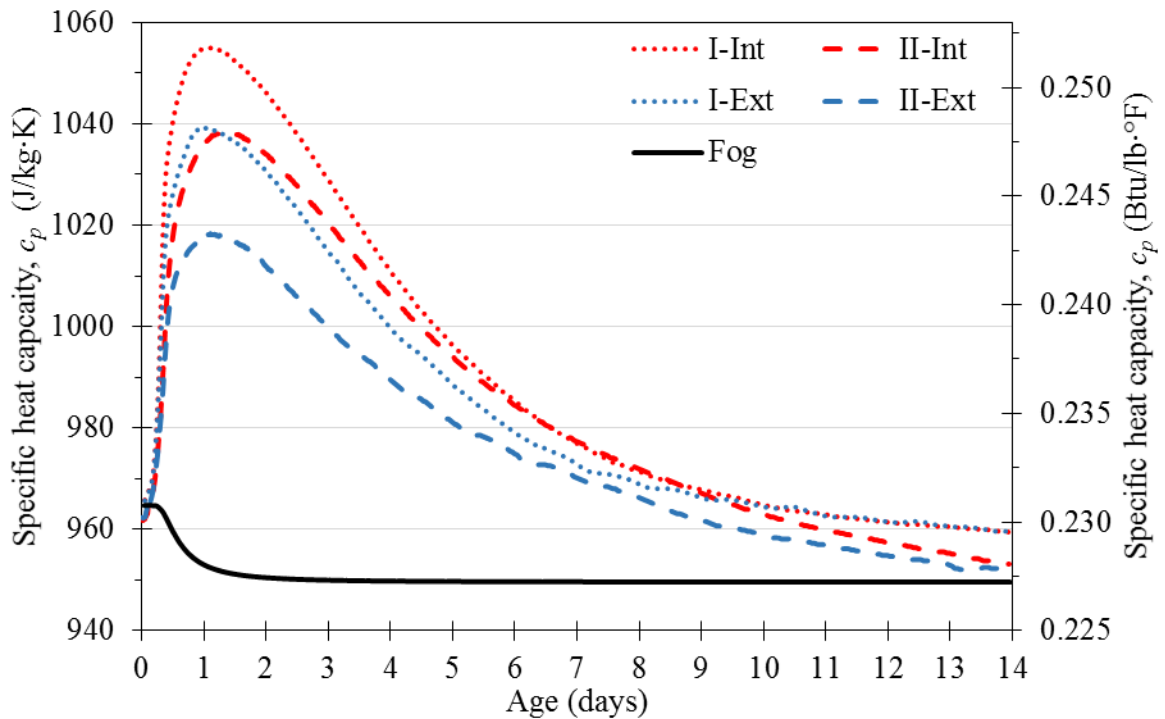


Figure 4.34: Specific heat capacity of mock-up concrete as function of age

4.4.8 Thermal Diffusivity

Figure 4.35 shows the dimensionless temperature history for a 14-day specimen during the second heating test segment. A linear trend is evident in the region of data for which $t \geq 1500$ seconds and $\theta^* \geq 0.05$ in the semi-log plot; outside of this region, curvature ($t < 1500$) or fluctuations ($\theta^* < 0.05$) in the data would influence the regression.

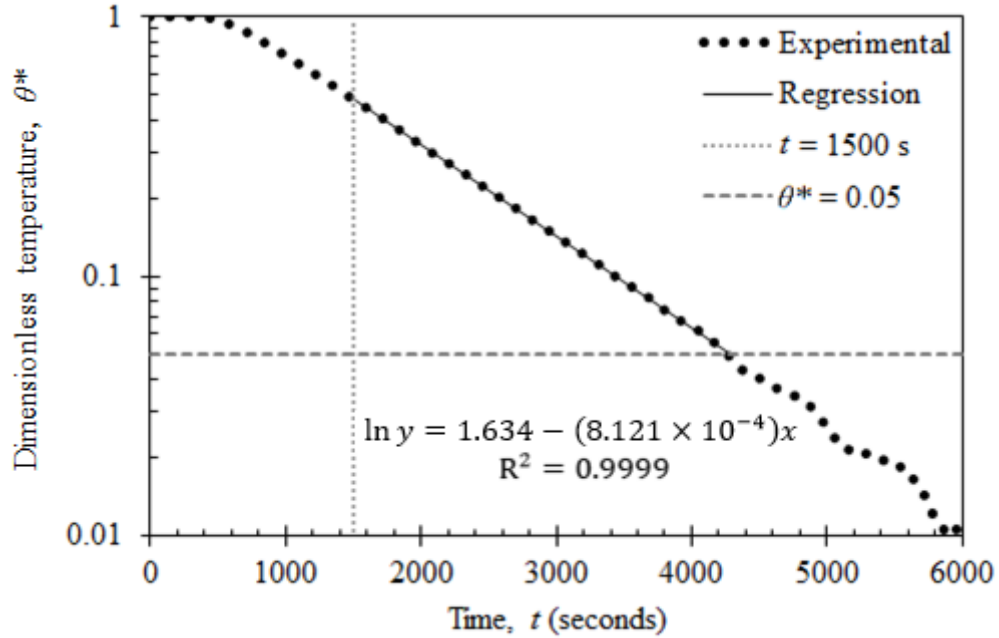


Figure 4.35: Dimensionless temperature history at center of specimen during thermal diffusivity testing

The results of the thermal diffusivity testing are shown in Figure 4.36 and in Table 22 in Appendix B.3. A generally logarithmic increase in thermal diffusivity was measured as a function of time, as shown in Eq. 4.37 from regression of the data from both trucks for the first mock-up. Applying this equation to the mock-up concrete according to the equivalent age results in Figure 4.37, which shows an earlier increase in thermal diffusivity for the higher-temperature concrete.

$$\kappa = (12.8 \times 10^{-9}) \ln(t) + 717 \times 10^{-9} \quad \text{Eq. 4.37}$$

Where,

- κ = thermal diffusivity, m²/s
- t = age, days

The experimental thermal diffusivity values ranged from 0.71 to 0.78 × 10⁻⁶ m²/s (0.028 to 0.030 ft²/hr), measured at 2 and 90 days, respectively. The results of Eq. 4.37 range from 0.72 to 0.77 × 10⁻⁶ m²/s (0.028 to .030 ft²/hr) for 1 to 90 days, an increase of 8%. All of these values are within the range measured by Tia et al. (2010) for

concrete containing Florida limestone aggregate, though they measured a greater increase in thermal diffusivity (18%) over a shorter testing range (1 to 28 days). Since the experimental method used in the present research was similar to that used by Tia et al., the increase in thermal diffusivity is not surprising. As noted by Ferraro (2009), the 9% decrease in thermal diffusivity measured by De Schutter and Taerwe (1995) may be due to self-desiccation of the sealed specimens that were tested.

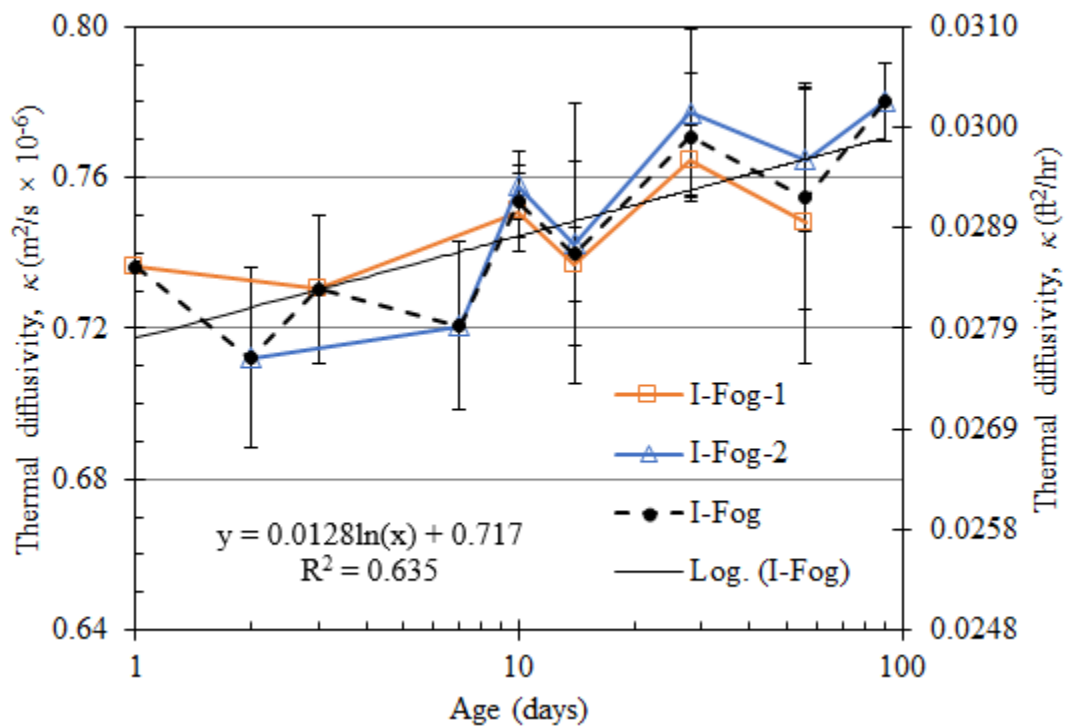


Figure 4.36: Thermal diffusivity results

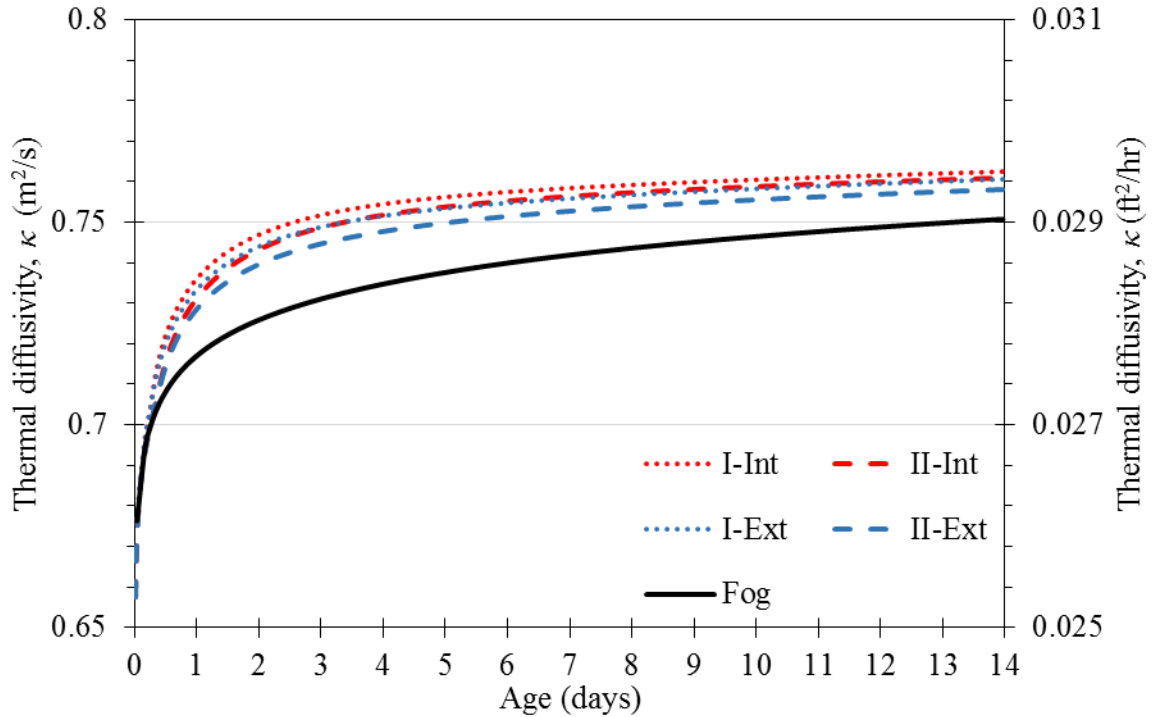


Figure 4.37: Thermal diffusivity of mock-up concrete per Eq. 4.37

As noted in Section 2.7.3.5 on short and infinite cylinders, Eq. 84 is used for determining the thermal diffusivity of short cylinders; using Eq. 87, the analogous equation for infinite cylinders, results in a thermal diffusivity 10.7% greater than that given by Eq. 84. If the results presented in Figure 4.36 were instead determined using Eq. 87 for infinite cylinders, the regression would be Eq. 4.38.

$$\kappa = (13.1 \times 10^{-9}) \ln(t) + 794 \times 10^{-9} \quad \text{Eq. 4.38}$$

Also noted in Section 2.7.3.5, the thermal diffusivity values determined by Eq. 84 (short cylinders) and Eq. 87 (infinite cylinders) underestimate and overestimate, respectively, the theoretical value. Figure 4.38 shows the experimental temperature history used to develop Figure 4.35 and the theoretical temperature histories for a 150-by-300-mm (6-by-12-in.) cylinder using the thermal diffusivity values determined when using Eq. 84 (short cylinder) and Eq. 87 (infinite cylinder). Aside from the initial

temperature increase, the experimental curve is generally bound by the two theoretical curves. This suggests that the two thermal diffusivity values could be used in modeling to obtain upper and lower limits on heat transfer behavior, and, by extension, that Eq. 4.38 and Eq. 4.37 could be used as upper and lower limits, respectively, for modeling heat transfer in curing concrete.

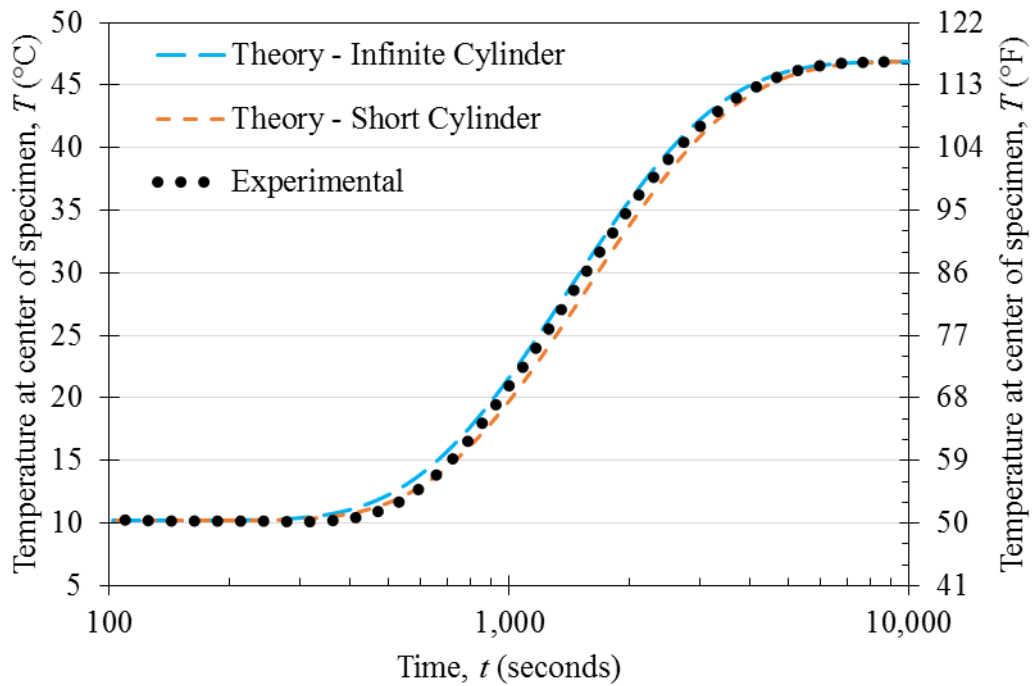


Figure 4.38: Temperature history at center of specimen during thermal diffusivity testing

4.4.9 Thermal Conductivity

Per Eq. 53 in Section 2.7.3, shown rearranged in Eq. 4.39, thermal conductivity is the product of thermal diffusivity, density, and specific heat capacity. Accordingly, the thermal conductivity of the mock-up concrete can be determined at any time as the product of the 2,276-kg/m³ (142.1-lb/yd³) density and the thermal diffusivity and specific heat capacity at that time, resulting in Figure 4.39.

$$\lambda = \kappa \rho c_p \quad \text{Eq. 4.39}$$

Where,

- λ = thermal conductivity, W/m·K (Btu/hr·ft·°F)
- κ = thermal diffusivity, m²/s (ft²/hr)
- ρ = density, kg/m³ (lb/ft³)
- c_p = specific heat capacity at constant pressure, J/kg·K (Btu/lb·°F)

Following an initial rapid increase consistent with the thermal diffusivity and specific heat capacity, maximum thermal conductivities of 1.75 and 1.78 W/m·K (1.01 and 1.03 Btu/hr·ft·°F) were calculated at approximately 40 hours for the Ext and Int concrete, respectively, of the first mock-up. The maximum calculated thermal conductivities for the second mock-up were 1.70 and 1.75 W/m·K (0.98 and 1.01 Btu/hr·ft·°F) for the Ext and Int concrete, respectively, at approximately 48 hours. The thermal conductivity then gradually decreased to 1.64 to 1.66 W/m·K (0.95 to 0.96 Btu/hr·ft·°F) at 14 days.

The calculated thermal conductivity values are lower than values reported in the literature. For concrete containing limestone aggregate, ACI 207.2R-07 (2007) reported typical values of 2.6 to 3.3 W/m·K (1.5 to 1.9 Btu/hr·ft·°F), whereas Tia et al. (2010) determined a value of 2.2 W/m·K (1.25 Btu/hr·ft·°F) for concrete containing Florida Ocala limestone aggregate based on experimentally determined thermal diffusivity and specific heat capacity values and using Eq. 4.39. Since the density and specific heat capacity measure for the mock-up concrete was consistent with general literature values, the lower thermal diffusivity of the mock-up concrete is the primary contributor to the lower calculated thermal conductivity values. However, the thermal diffusivity of the mock-up concrete was comparable to that measured by Tia et al. (2010) for concrete containing Florida Ocala limestone aggregate; the higher thermal conductivity calculated for that concrete was likely due to the higher specific heat capacity, which was noted to be greater than typical literature values.

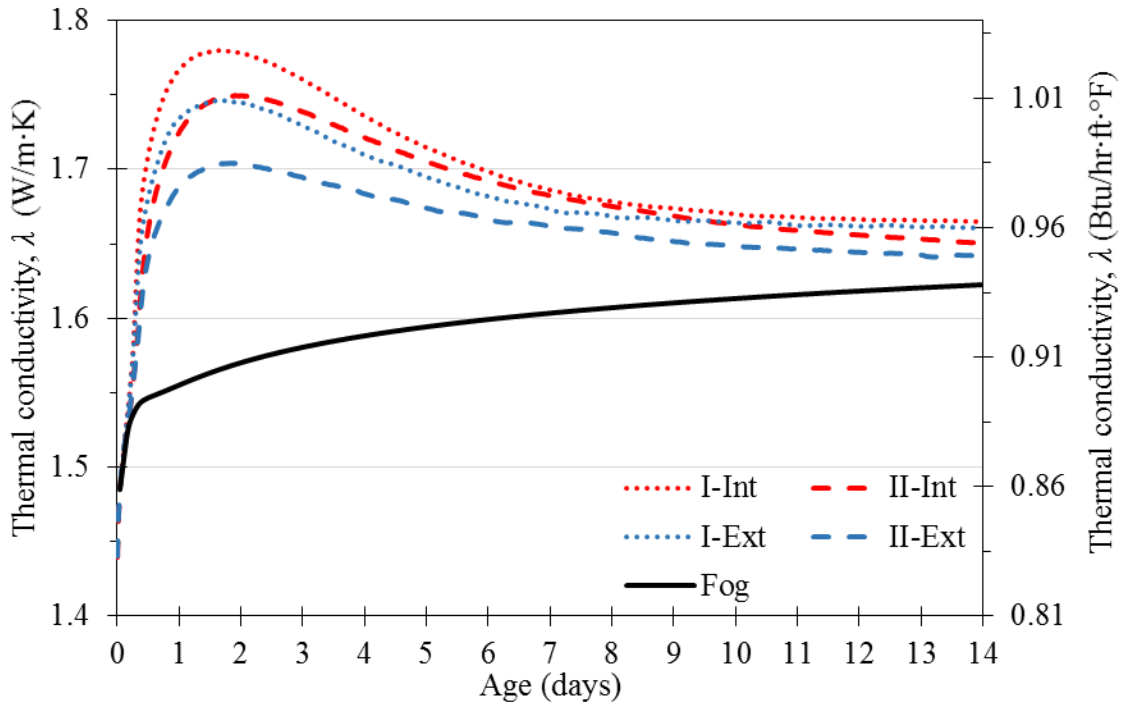


Figure 4.39: Calculated thermal conductivity values for mock-up concrete

4.5 Conclusions

The literature models for the apparent activation energy based on the cement composition and fineness were able to provide good estimates of the experimentally determined value. In contrast, the predicted hydration parameters, particularly the shape and time parameters, differed from the experimental values. However, the apparent activation energy generally has broader applications since it can be used in determining the equivalent age of concrete for prediction of the development of mechanical properties. Therefore, testing for the apparent activation energy and hydration parameters is likely unnecessary for most concrete applications, and the models can be utilized for predicting needed values.

The high early-age temperatures of the mock-up concrete were shown to reduce the compressive and splitting tensile strength and modulus of elasticity of the match-cured specimens compared to the fog-cured specimens at chronological ages greater than

10 days and at matching equivalent ages. In particular, the compressive strength of the match-cured specimens was found to be approximately 90% of the compressive strength of the fog-cured specimens at the same equivalent age. This suggests that the compressive strength of the in-place concrete can be estimated without match-cured specimens by using compressive strength tests of fog-cured specimens and the equivalent age of the in-place concrete, which can be determined with the temperature history of the in-place concrete and the activation energy of the cement paste. Though the 90% relationship likely varies based on the temperature history of the concrete, comparable structures would likely have similar concrete temperature histories, and the relationship may be valid. Investigations into methods of quantifying this relationship based on the concrete temperature history would be useful because such methods would allow prediction of in-place concrete strengths using only fog-cured specimens.

Though the experimental results for the splitting tensile strength and compressive strength of the mock-up concrete were not consistent with the power law relationships recommended in the literature, the relationships determined via regression analysis of the experimental results were shown to be consistent between the fog-cured and match-cured specimens. This indicates that the splitting tensile strength of match-cured concrete can be estimated using the relationship between splitting tensile strength and compressive strength of fog-cured specimens of the same concrete. Furthermore, if the 90% relationship is utilized to estimate the compressive strength of the match-cured concrete, the tensile strength of the match-cured concrete can be estimated without conducting any tests on match-cured specimens. Since the measured tensile strengths were greater than those predicted by the power law relationships recommended in the literature, using the ACI 318 model or other comparable models may be appropriate for obtaining a conservative estimate of the tensile strength in the absence of experimental data.

Though the three-parameter exponential model was able to fit each series of experimental results very well, its application would require testing the modulus of

elasticity at multiple ages for every concrete mix. Since the ACI 318 equation for modulus of elasticity provided reasonable predictions of the experimental results with respect to equivalent age, the ACI 318 relationship was recommended for use, particularly in the absence of modulus of elasticity data.

Due to wide variation of the trends identified for thermal properties in the literature, determination of appropriate values can be difficult without experimental testing. Since most thermal properties of concrete are heavily influenced by the coarse aggregate, identifying thermal property values for concretes containing the same or similar aggregates may be the most effective means of predicting the thermal properties.

CHAPTER 5

FINITE ELEMENT ANALYSIS

5.1 Introduction

Due to the previously identified influences of the thermal behavior on the properties of the mock-up concrete, thermal and mechanical analysis of the CR3 PCC was conducted to determine the influence of the high early-age temperatures on the late-age structural performance of the mock-up. Riding (2007) developed analysis software called ConcreteWorks that allows incorporation of experimental properties and parameters or automated determination of parameters based on information about the concrete mix design and components. Understandably, ConcreteWorks was developed with a focus on common concrete structures and construction practices and, therefore, has limited tailorability for modeling more complicated concrete members and unique environmental conditions. In contrast, COMSOL Multiphysics (COMSOL Group) allows full customization of the model components, parameters, and geometry, and in addition to thermal analysis, mechanical analysis of the response to externally applied loads can be conducted.

This chapter incorporates the previously determined thermal and mechanical properties for implementation in finite element analysis of the CR3 PCC mock-up. Thermal behavior predicted by ConcreteWorks and COMSOL models are compared with experimentally measured temperatures in the mock-up, and full thermal and mechanical analysis of the mock-up is conducted in COMSOL to study the structural response of the mock-up to post-tensioning loads and the resulting risk of tensile cracking in the plane of the ducts. Fracture mechanics analysis was not incorporated in the models, but qualitative cracking behavior of concrete is discussed in relation to the modeled tensile stresses.

5.1.1 Tensile Creep

The tensile strength of concrete is typically determined by short-term test methods such as the test for splitting tensile strength (ASTM C496-11). However, when concrete is subjected to tensile stresses for extended periods of time, failure can occur at stresses less than the determined short-term tensile strength. Bissonnette et al. (2007) identified a transition from linear to nonlinear creep behavior between tensile stresses of 50 to 67% of the direct tensile strength. At the higher stresses, progressive cracking resulted in increasing strain rates. Bissonnette et al. (2007) noted work by others (Illston, 1965; Domone, 1974; Al-Kubaisy and Young, 1975) indicating that increasing rates of creep begin at stresses of 60 to 85% of the direct tensile strength for various concretes and conditions.

Consistent with the preceding findings, Garas Yanni (2009) found that ultra-high performance concrete loaded in tension up to 60% of the direct tensile strength would not fail. However, when loaded at 70 or 80% of the direct tensile strength, the concrete would creep to failure.

As discussed in Section 3.1.2.3, direct tensile strength is typically lower than splitting tensile strength. Neville (2011) stated that direct tensile strength tends to be about 89 to 95% of the splitting tensile strength, and the direct tensile strength of cores taken from the CR3 PCC after the bay 34 delamination was identified in 2009 was approximately 75% of the splitting tensile strength (Performance Improvement International, 2010). Assuming the direct tensile strength of the mock-up concrete to be 75% of its splitting tensile strength, and assuming that tensile creep failure could occur at tensile stresses equal to approximately 70% of the direct tensile strength, the critical tensile stress for long-term post-tensioning loads in the mock-up would be approximately 50% of the splitting tensile strength of the concrete.

5.1.2 Objectives

The objectives of this chapter include identifying an effective means of modeling the CR3 PCC mock-up in order to investigate the influence of high early-age temperatures on the late-age structural behavior of the mock-up. The cracking potential of the mock-up under representative loads will be investigated and compared with experimental results, and the model will allow extension of the results to loading scenarios representative of the CR3 PCC. Additionally, the effects of compatibility between post-tensioning ducts and mass concrete will be studied, and the relative impact of thermal and post-tensioning stresses on the mock-up behavior will be determined.

5.2 ConcreteWorks Modeling

ConcreteWorks was used to develop a baseline model of the mock-up for comparison with the experimental early-age results. The program provides two-dimensional analysis of the mid-plane of a mass concrete member, assuming in the case of a rectangular column geometry that the column is of sufficient height that there is no out-of-plane temperature variation or heat transfer. As shown in Figure 5.1, one quarter of the modeled plane was analyzed using two orthogonal lines of symmetry, and the results are discretized into 36 points in a 6-by-6 grid. For the 2.64 m (104-in.) length and 1.07-m (42.0-in.) thickness of the mock-up, the grid spacing was 264 mm (10.4 in.) along the length of the wall and 107 mm (4.2 in.) through the thickness. The size of the differential control volumes being analyzed and the spacing of the result points could not be adjusted manually. Since the Ext gauges in the mock-ups were located at a depth of 51 mm (2.0 in.) from the front surface of the mock-ups, the ConcreteWorks results were interpolated between 0 and 107 mm (0 and 4.2 in.) for comparison with the Ext measurements. The linear interpolation is discussed in more detail in Section 5.2.2.1.

For thermal analysis, ConcreteWorks does not account for components embedded in the concrete member being analyzed. As a result, the post-tensioning ducts, rebar, and steel liner plate shown in the mock-up in Figure 5.1 were not incorporated in the model.

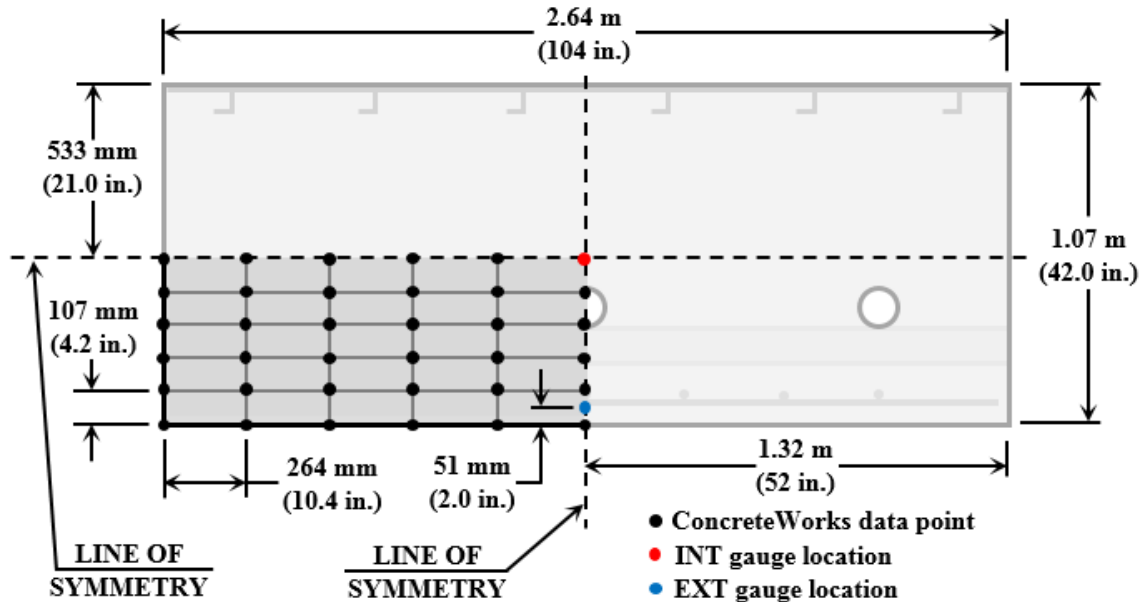


Figure 5.1: Plan view diagram of ConcreteWorks symmetries and results grid

5.2.1 Model Inputs

The following sections provide the ConcreteWorks inputs utilized for modeling the thermal behavior of the mock-ups. The selected parameters were based on information and results presented in greater detail in Chapters 3 and 4. Representative placement dates and times of May 13, 2014, at 10 am, and March 11, 2015, at 11 am were selected for the first and second mock-up, respectively, and Atlanta, Georgia was selected as the project location.

5.2.1.1 Mixture Proportion and Material Properties

The mock-up concrete mixture proportions were selected directly from Table 1 in Section 3.1.2.2. An air content of 3.3% was used based on the average of six available

measurements from CR3 pours in the region of the delamination discussed in Section 2.3.2. Options for mid-range water reducer and Type-B retarder were selected since a single option for ASTM C494 Type D water-reducing and retarding admixture (WRRET) was not available. ConcreteWorks can incorporate the selected chemical admixtures in the calculation of the hydration parameters based on the empirical models given by Eq. 21, Eq. 23, Eq. 25, and Eq. 39 in Section 2.6. However, as discussed later, experimentally determined parameters were manually entered, so the selection of the admixtures was not significant in this case.

Type I/II cement with a Blaine fineness of 373 m²/kg (202 yd²/lb) was selected, and the QXRD results presented in Table 8 in Section 3.3.3.1 were used for the cement composition inputs. Limestone coarse aggregate and siliceous river sand were selected for the aggregates, though information on gradation and specific gravity could not be specified. As given in Table 2 in Section 4.4.1 for the mock-up cement with both admixtures, the activation energy was determined to be 31,632 J/mol (13,600 Btu/lbmol), and the hydration parameters were determined to be 0.633 for the ultimate degree of hydration α_u , 2.081 for the hydration shape parameter β , and 12.50 hours for the hydration time parameter τ . These values and the 465-J/g (200-Btu/lb) total heat of complete hydration of the mock-up cement (Section 3.3.3.1) were entered for the hydration properties in ConcreteWorks.

The experimentally determined CTE of 7.86 $\mu\epsilon/^\circ\text{C}$ (4.37 $\mu\epsilon/^\circ\text{F}$) was used, and based on the thermal conductivity curve in Figure 27 in Section 4.4.6, an ultimate thermal conductivity value of 1.66 W/m·K (0.96 Btu/hr·ft·°F) was used. ConcreteWorks uses Eq. 52 in Section 2.7.2 to model thermal conductivity as a function of the degree of hydration, decreasing linearly to the ultimate thermal conductivity value. As shown in Figure 21 in Section 4.4.4, the specific heat capacities of the coarse and fine aggregate at 23 °C (73.4 °F) are 751 and 689 J/kg·K (0.179 and 0.165 Btu/lb·°F), respectively. Based on the mass contents of 1068 and 653 kg/m³ (1800 and 1100 lb/yd³) of concrete for the

coarse and fine aggregate, respectively, the composite specific heat capacity for the aggregate was determined to be 727 J/kg·K (0.174 Btu/lb·°F). ConcreteWorks uses the van Breugel (1980) model (Eq. 45 in Section 2.7.1.1) for degree of hydration- and temperature-dependent specific heat capacity of curing concrete, but it does not account for temperature-dependence of the specific heat capacity of the aggregates.

The equivalent age maturity function was used for development of the concrete properties, and, as discussed in Section 4.4.2, a reference temperature of 23 °C (73.4 °F) was selected to match the curing temperature of the Fog specimens. With the experimentally determined activation energy E_a of 31,632 J/mol (13,600 Btu/lbmol) and the universal gas constant \bar{R} equal to 8.3144 J/mol·K (1.986 Btu/lbmol·°R), the constant $Q = E_a/\bar{R}$ was determined to be 3804.5 K (6847 °R).

5.2.1.2 Curing, Formwork, and Environmental Conditions

The measured concrete placement temperatures of 25.5 and 22.5 °C (77.9 and 72.5 °F) were entered for the first and second mock-up, respectively, and the plywood forms were removed at a concrete age of 14 days (336 hours). The thickness of the form panels could not be specified, but other instances of plywood forms in the thesis (Riding, 2007) in which ConcreteWorks was developed used 19-mm (¾-in.) plywood, suggesting that that thickness may be used by default. No additional curing methods were applied after form removal.

Figure 5.2 shows the ambient temperatures recorded during the first 14 days of the two mock-ups. The temperature at each time for the first and second mock-up was recorded as the average of three and four temperature readings, respectively. Rather than importing the temperature data directly, the daily maximum and minimum temperatures were entered, and daily temperature variation between the corresponding values was modeled by ConcreteWorks. Since the concrete was cast inside an enclosed facility, the

maximum wind speed and maximum cloud cover were set to 0 m/s (0 mph) and 100%, respectively. The default inputs for relative humidity and yearly temperature were used.

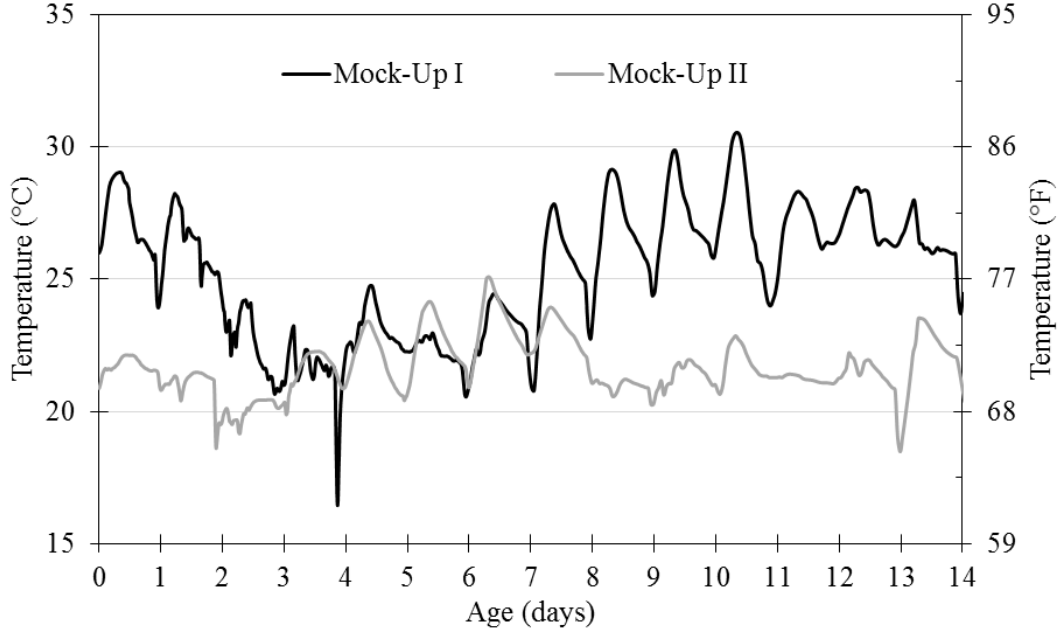


Figure 5.2: Ambient temperatures recorded during first 14 days for each mock-up

ConcreteWorks uses Eq. 5.1 to determine the convective heat transfer coefficient h for forced and free convection (ASHRAE, 1993). Per ASTM C680-14 (2014), the film temperature T_f can be taken as the average of the surface and ambient temperatures. The heat flow constant C is equal to 15.89 for vertical surfaces (ASHRAE, 1993), and the wind speed v_w is 0 m/s (0 mph) for the mock-up case of no wind.

$$h = 0.2782R_f C \left(\frac{1}{T_f + 17.8} \right)^{0.181} |T_s - T_a|^{0.266} \sqrt{1 + 2.8566v_w} \quad \text{Eq. 5.1}$$

Where,

- h = convective heat transfer coefficient, W/m²·K (Btu/hr·ft²·°F)
- R_f = forced convection surface roughness factor
- C = heat flow constant
- T_f = film temperature, °C (°F)
- T_s = surface temperature, °C (°F)
- T_a = ambient temperature, °C (°F)

v_w = wind speed, m/s (mph)

Clear et al. (2003) presented the forced convection surface roughness factors R_f derived by Walton (1983), including values of 1.00 for smooth surfaces such as glass, 1.13 for clear pine, and 1.52 for concrete. ConcreteWorks assumes a surface roughness of 1.00 for steel forms while in place and uses the 1.52 value for the concrete surface when the forms are removed. However, the value that ConcreteWorks uses for plywood forms is not indicated by Riding (2007). Furthermore, Riding (2007) does not state how the forced convection surface roughness factor is handled in ConcreteWorks in the case of no wind, as selected for the mock-up, for which forced convection should not be modeled. Incorporating the previously identified relations and constants and assuming that ConcreteWorks uses a plywood surface roughness of 1.30, between the 1.13 and 1.52 values for clear pine and concrete, Eq. 5.1 simplifies to Eq. 5.2. According to Eq. 5.1 and Eq. 5.2, the convective heat transfer coefficient h reaches a minimum value of zero when the surface and ambient temperatures are equal, and h increases as both the difference between and average of the surface and ambient temperatures increase.

$$h = 5.75 \left(\frac{2}{T_a + T_s + 35.6} \right)^{0.181} |T_s - T_a|^{0.266} \quad \text{Eq. 5.2}$$

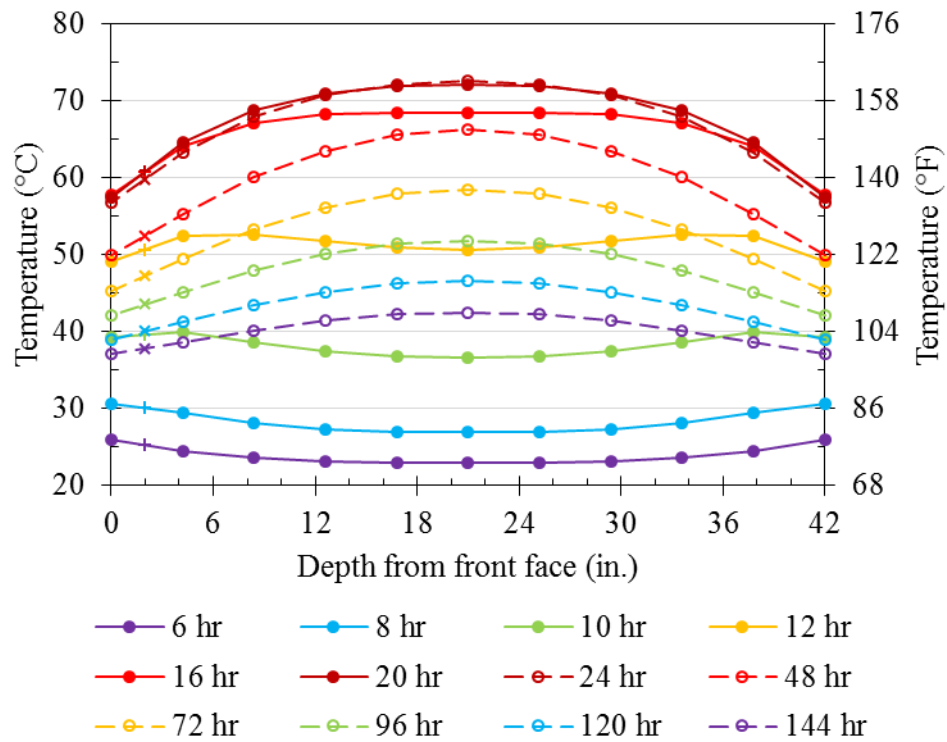
5.2.2 ConcreteWorks Results

The following sections present the results of the ConcreteWorks model of the second mock-up. The general thermal behavior predicted by the model is compared to that measured in the mock-up, and daily variations in temperature are investigated. Finally, limitations of the model are discussed.

5.2.2.1 General Behavior

The ConcreteWorks results for temperature variation along the line of symmetry through the thickness of the second mock-up are shown in Figure 5.3. At each age, the

modeled temperature profile had a generally parabolic form, and no significant changes in behavior were modeled between the surface and the nearest point at a depth of 107 mm (4.2 in.). Therefore, linear interpolation between the temperatures at the surface and at a depth of 107 mm (4.2 in.) was used to estimate the temperature at a depth of 51 mm (2 in.), matching the depth of the Ext gauges in the mock-ups.

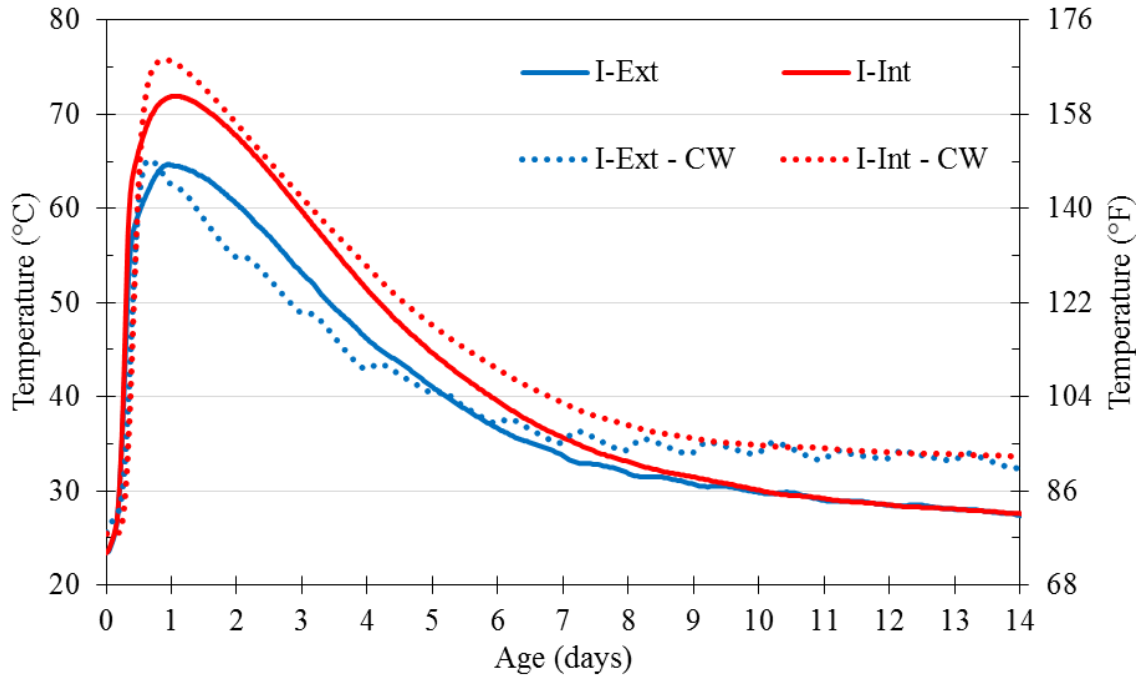


Note: 1 in. = 25.4 mm; interpolated points are indicated by + or ×
 Figure 5.3: Temperature variation modeled by ConcreteWorks along line of symmetry through thickness of mock-up between 6 and 144 hours after concrete placement and linearly interpolated values at a depth of 51 mm (2 in.)

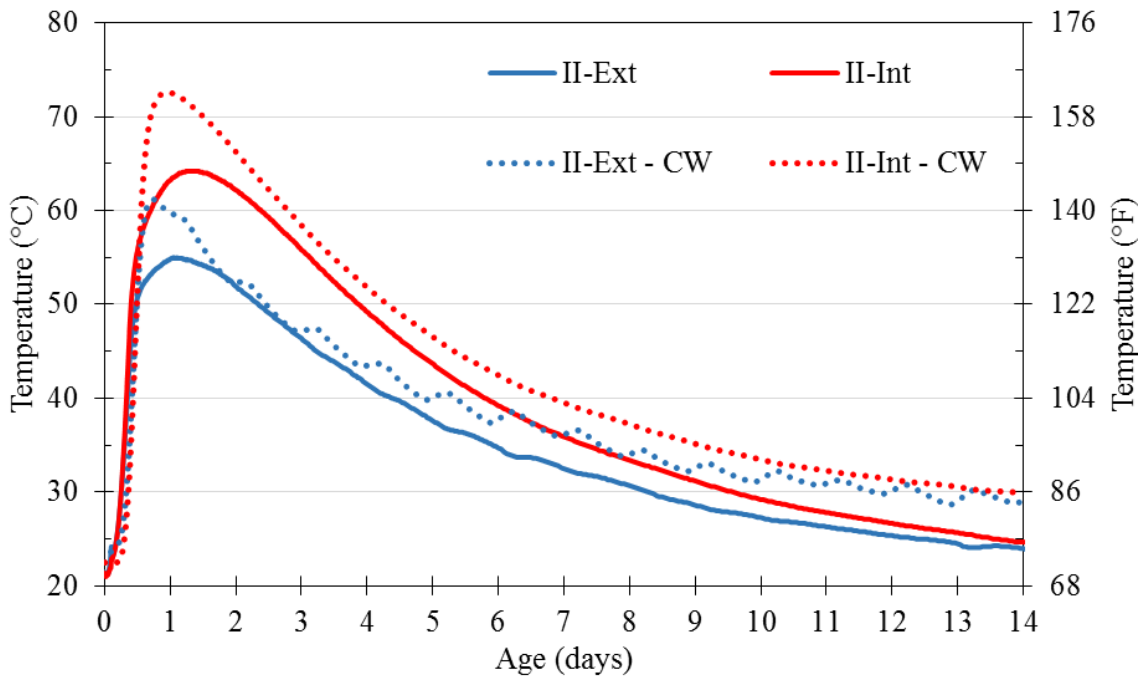
The temperature history results of the ConcreteWorks (CW) models for the two mock-ups are compared with the experimental results in Figure 5.4. For both mock-ups, the modeled initial temperature rise is consistent with the experimental results. However, the peak temperatures in the ConcreteWorks models are greater than the experimental values in all four cases, and the modeled peaks are also sharper than the experimental

peaks. Since the model assumes a geometry of a column with infinite height rather than the finite 3.00-m (118-in.) height of the mock-ups, cooling along the vertical axis is not accounted for and the slower cooling of the models is to be expected. Additionally, the influence of steel components embedded in the concrete, including the post-tensioning ducts, steel liner plate, and rebar, is not accounted for in the model; the higher conductivity of steel and the lack of heat generation in the volume occupied by the steel would contribute to lower temperatures in the mock-ups.

The modeled temperatures for the second mock-up are consistently greater than the experimental values after the initial temperature rise, and the maximum temperatures achieved are approximately 7 °C (13 °F) greater than the experimental peaks. In contrast, the maximum modeled temperatures for the first mock-up are closer to the experimental values, and the modeled temperatures near the surface are less than the experimental values between 1 and 5 days of age. This difference in behavior between the two mock-ups may have been due to greater water content in the second mock-up concrete, for which larger slumps were measured despite having the same mix design.



(a)



(b)

Figure 5.4: Experimental temperatures and corresponding ConcreteWorks (CW) results for (a) first and (b) second mock-up

5.2.2.2 Daily Variation

For both mock-ups, the ConcreteWorks results show greater sensitivity to diurnal temperature variation than the experimental results. Since the ConcreteWorks Ext values were determined by linear interpolation between nodes located at the surface and 107 mm (4.2 in.) from the surface, high daily variation at the surface may have artificially amplified the variation at the 51-mm (2.0-in.) depth of the Ext measurements. However, Figure 5.5 compares the temperatures measured in the Ext gauge in the second mock-up with the temperatures modelled by ConcreteWorks at the surface and at a depth 107 mm (4.2 in.) in addition to the interpolated Ext value. Figure 5.5 shows that the temperatures modeled by ConcreteWorks at a depth of 107 mm (4.2 in.) exhibit daily variation greater than that measured in the mock-up at the 51-mm (2.0-in.) depth of the Ext gauges, indicating that interpolation is not the primary contributing factor to the large diurnal temperature variation of the ConcreteWorks results.

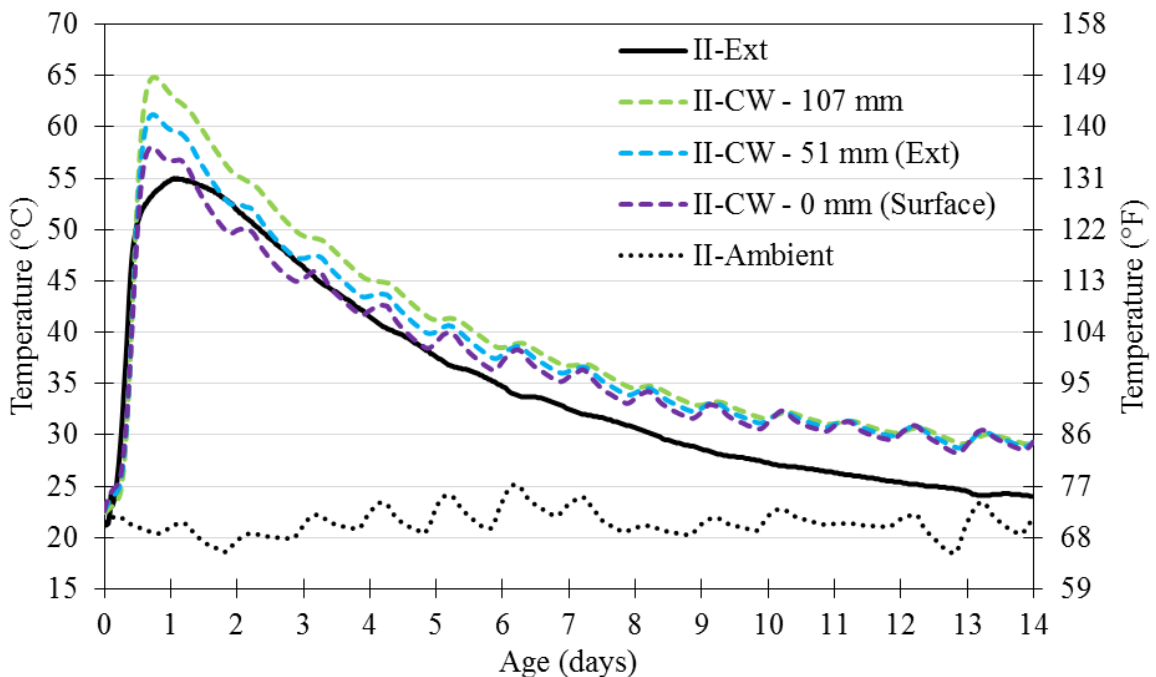


Figure 5.5: Second mock-up Ext temperatures and ConcreteWorks (CW) near-surface temperatures during first 14 days

Assuming that the variation of the ambient temperature can be represented by a sine wave and that the concrete is sufficiently thick so that the temperature variation farthest from the surface is negligible relative to that at the surface, the decrement of the temperature wave between two distances from the surface is given theoretically by Eq. 5.3 (Adams et al., 1976). Assuming that the temperature at the surface of the concrete is equal to the ambient temperature, Eq. 5.3 can be simplified to Eq. 5.4 for estimation of concrete temperature variation at any depth with known ambient temperature variation (ACI 207.2R-07). This simplification neglects the boundary layer temperature gradient at the concrete-air interface but provides an estimate of the upper bound of cyclical temperature variation within the concrete.

$$\frac{R_2}{R_1} = e^{-(x_2-x_1)\sqrt{\frac{\pi}{\kappa\gamma}}} \quad \text{Eq. 5.3}$$

Where,

- (ft)
- R_2 = amplitude of temperature wave at depth x_2 , °C (°F)
 - R_1 = amplitude of temperature wave at depth x_1 , °C (°F)
 - x = depth at which amplitude of temperature wave is measured, m
 - κ = thermal diffusivity, m²/day (ft²/day)
 - γ = period of the temperature wave, days

$$\frac{R_x}{R_0} = e^{-x\sqrt{\frac{\pi}{\kappa\gamma}}} \quad \text{Eq. 5.4}$$

Where,

- (ft)
- R_x = amplitude of temperature wave at depth x , °C (°F)
 - R_0 = amplitude of temperature wave at the surface ($x = 0$), °C (°F)
 - x = depth at which amplitude of temperature wave is measured, m
 - κ = thermal diffusivity, m²/day (ft²/day)
 - γ = period of the temperature wave, days

The thermal diffusivity of the plywood used for the forms was determined to be 0.190×10^{-6} m²/s (0.176 ft²/day) using Eq. 53 in Section 2.7.3 and the thermal conductivity, density, and specific heat capacity values of plywood provided in Section

5.4.1. Therefore, the decrement ratio of the daily temperature wave passing through the 19-mm (3/4-in.) thickness of the plywood forms was determined to be 0.77 using Eq. 5.4.

Similarly, the decrement ratio of the daily temperature wave through 51 mm (2 in.) of concrete—the depth of the Ext gauge—was determined to be 0.70 using the 7-day concrete thermal diffusivity of $0.742 \times 10^{-6} \text{ m}^2/\text{s}$ ($0.0286 \text{ ft}^2/\text{hr}$) determined from Eq. 25 in Section 4.4.5. The product of the plywood and concrete ratios is 0.54, indicating that the daily temperature variation of the concrete at the Ext gauges should be at most 54% of the ambient temperature variation.

As shown in Figure 5.6, the daily variation modeled by ConcreteWorks between 10 and 14 days of age for the second mock-up is relatively consistent between 1.0 and 1.5 °C (1.8 and 2.7 °F). In contrast, the daily ambient temperature variation ranges between nearly zero at 11 days to approximately 5 °C (9 °F) at 13 days. Therefore, the daily temperature variation in the ConcreteWorks model does not seem to depend solely on the ambient temperature variation. This is confirmed by Figure 5.7, which shows that, even with a constant ambient temperature of 21 °C (70 °F), ConcreteWorks models daily temperature variation for both sunny (0% cloud cover) and overcast (maximum 100% cloud cover) conditions. Since 100% cloud cover was selected as the maximum daily cloud cover for the mock-up models, the influence of solar radiation was reduced to the extent shown in Figure 5.7 rather than eliminated for simulation of concrete curing without any direct sunlight radiation.

Slight daily variations in the experimental Ext temperatures can be seen in Figure 5.4, but they are less than the 54% of the ambient temperature variation. This is attributed to the assumption that the temperature at the surface of the concrete is equal to the ambient temperature. By neglecting the boundary layer temperature gradient at the concrete-air interface, the influence of the ambient temperature on the concrete is amplified. Additionally, the heterogeneity of the concrete can influence the short-term

heat flow and resulting temperature measurements, particularly over a short distance such as 51 mm (2 in.).

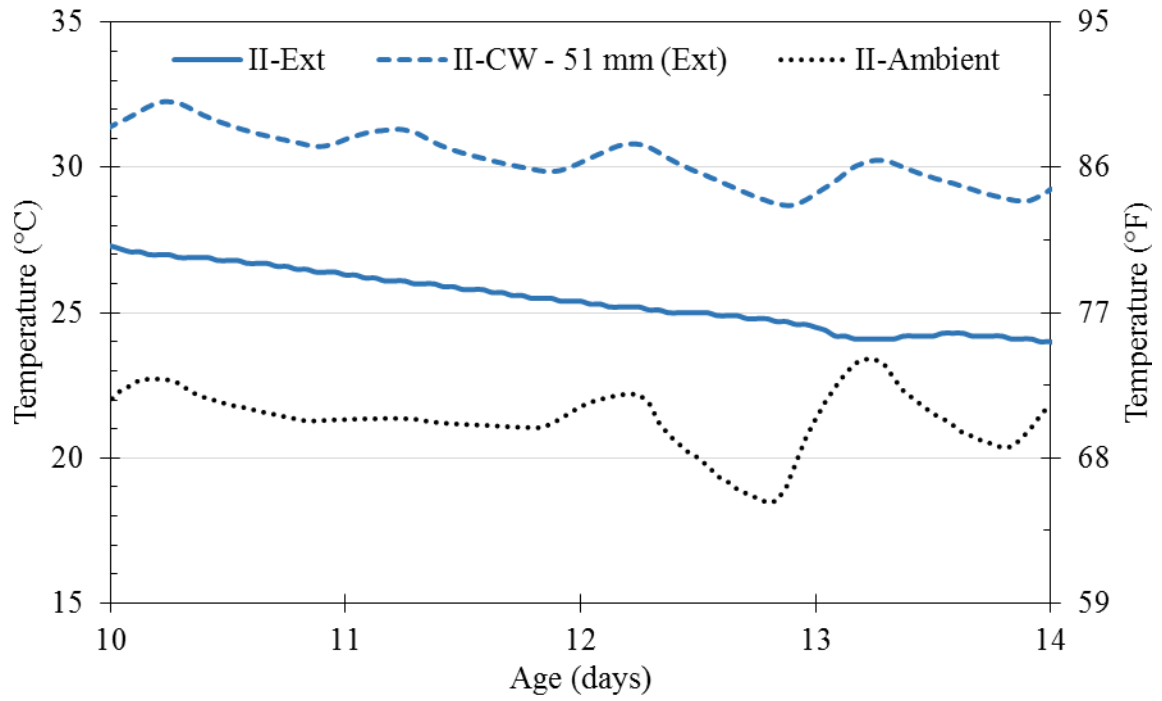


Figure 5.6: Comparison of experimental and modeled Ext temperature variation with ambient temperatures

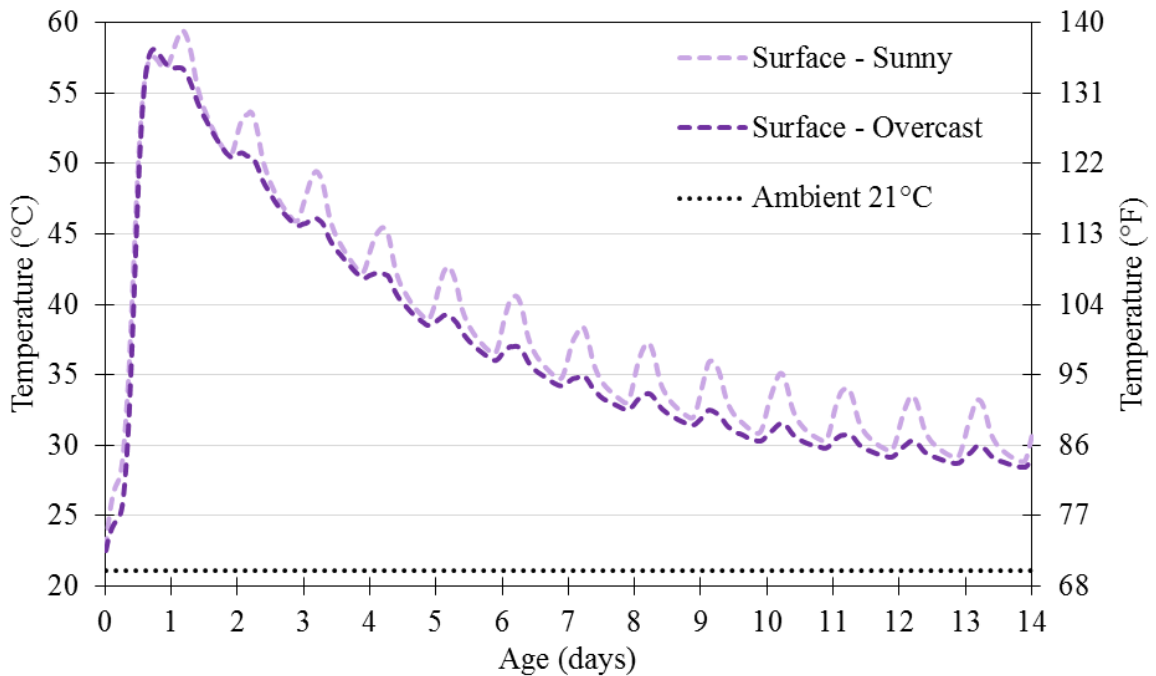


Figure 5.7: Concrete surface temperatures modeled in ConcreteWorks for constant ambient temperature of 21 °C (70 °F) and sunny and overcast conditions

5.2.2.3 Discussion

Though ConcreteWorks is useful for common concrete structures, some factors limit its utility for analysis of a unique concrete member such as the CR3 PCC mock-up. As discussed in Section 5.2.2.1, ConcreteWorks does not model out-of-plane heat transfer, so heat lost through the top and bottom faces of the mock-up was not accounted for. Additionally, the model does not account for the embedded steel components, which have higher thermal conductivity values than the concrete and transfer heat towards the surface of the mock-up more rapidly than the concrete.

Unlike typical structures that would be modeled in ConcreteWorks, the mock-ups were cast inside a facility exposed to ambient temperatures and humidity but with only brief daily exposure to sunlight. Therefore, the inability to limit direct solar radiation in ConcreteWorks resulted in greater daily temperature variation than measured in the mock-ups.

Though ConcreteWorks allows the selection of coarse and fine aggregate types, the gradation and specific gravity of the aggregates cannot be selected. As noted in Section 2.7, the Florida limerock aggregate used in the CR3 PCC and mock-up concrete has distinct thermal and mechanical properties compared to limestone aggregate available elsewhere in the U.S., but the only other aggregate input is the combined specific heat capacity. However, the van Breugel (1980) model used in ConcreteWorks for degree of hydration- and temperature-dependent specific heat capacity of curing concrete does not account for temperature-dependence of the specific heat capacity of the aggregates, which was shown in Figure 33 in Section 4.4.7.

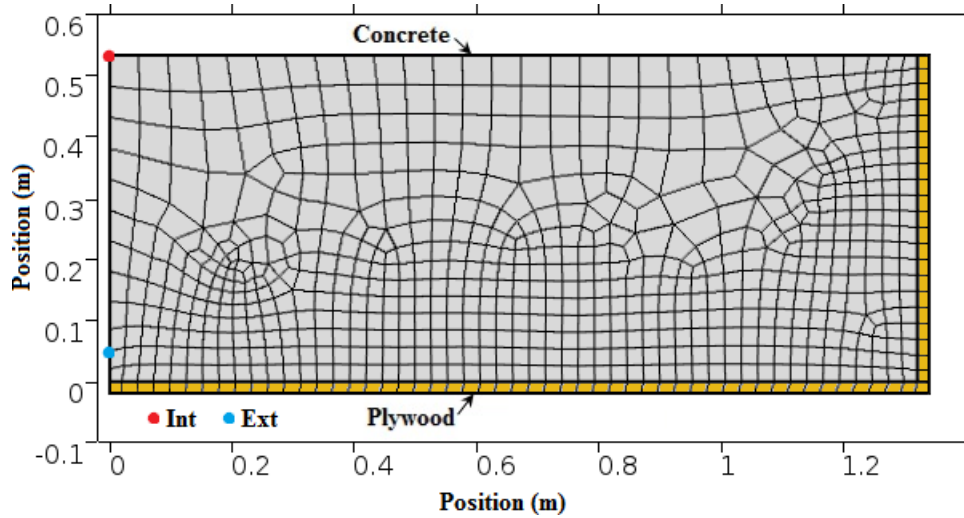
5.3 Replication of ConcreteWorks Results in COMSOL Multiphysics

Due to the limitations of ConcreteWorks for modeling the mock-up behavior, thermal analysis of the mock-up was conducted in COMSOL Multiphysics using the Heat Transfer in Solids physics. Before developing a three-dimensional, representative model of the mock-up, a two-dimensional COMSOL model using the ConcreteWorks inputs and parameters was developed in an attempt to replicate the ConcreteWorks results. This 2D COMSOL model and the results are discussed in the following sections.

5.3.1 Model Description

The geometry, mesh, and materials of the COMSOL model are shown in Figure 5.8. Like the ConcreteWorks model shown in Figure 5.1, one quarter of the modeled plane was analyzed using two orthogonal lines of symmetry. The 19-mm (0.75-in.) plywood forms were modeled as solids, and the model consisted of 717 rectangular domain elements and 188 boundary elements. The locations of the nodes used for comparison with the Int and Ext gauges are indicated in Figure 5.8. To match the ConcreteWorks model, the post-tensioning ducts, rebar, steel liner plate, and side insulation were not included. Whereas ConcreteWorks uses 5-minute time steps for the

entire duration of the analysis, 10-minute intervals were used for the first 28 hours of COMSOL analysis, followed by 60-minute intervals for the remainder of the 14-day analysis, during which temperature variation was more gradual.



Note: 1 m = 39.37 in.; using symmetry, front right quarter of mock-up modeled, whereas front left quarter was modeled in ConcreteWorks (Figure 5.1)
 Figure 5.8: Geometry, mesh, and materials for COMSOL model replicating ConcreteWorks

Matching the values listed in Section 5.2.1.1 for the ConcreteWorks model, Table 5.1 gives the parameters related to heat generation in the concrete as implemented in COMSOL. These values were used for all COMSOL models. The apparent activation energy E_a and reference temperature T_r were utilized in Eq. 5.5 to determine the equivalent age t_e at each node in the concrete as a function of time t and concrete temperature T_c . As in Hernandez-Bautista et al. (2014), Eq. 5.5 was implemented in COMSOL as a distributed ordinary differential equation (Eq. 5.6) in the concrete domain with initial values of t_e and dt_e/dt equal to zero. The hydration parameters α_u , τ , and β were used in Eq. 5.7 to determine the degree of hydration α at each node in the concrete as a function of the equivalent age t_e . Collectively, the parameters in Table 5.1, Eq. 5.6, and Eq. 5.7 were used in Eq. 5.8 to determine the volumetric rate of heat generation Q_H at

each node in the concrete as a function of the equivalent age t_e and concrete temperature T_c . Eq. 5.5, Eq. 5.7, and Eq. 5.8 were discussed in greater detail in Sections 2.6.5, 2.6.6, and 2.6.11, respectively.

$$t_e = \int_0^t \exp\left(\frac{E_a}{\bar{R}}\left(\frac{1}{T_r} - \frac{1}{T_c}\right)\right) dt \quad \text{Eq. 5.5}$$

$$\frac{dt_e}{dt} = \exp\left(\frac{E_a}{\bar{R}}\left(\frac{1}{T_r} - \frac{1}{T_c}\right)\right) \quad \text{Eq. 5.6}$$

$$\alpha(t_e) = \alpha_u \exp\left(-\left[\frac{\tau}{t_e}\right]^\beta\right) \quad \text{Eq. 5.7}$$

$$Q_H(t) = H_u C_c \alpha(t_e) \left(\frac{\tau}{t_e}\right)^\beta \left(\frac{\beta}{t_e}\right) \exp\left(\frac{E_a}{\bar{R}}\left(\frac{1}{T_r} - \frac{1}{T_c}\right)\right) \quad \text{Eq. 5.8}$$

Where,

- t_e = equivalent age, hr
- t = chronological age, hr
- T_c = concrete temperature, K
- $\alpha(t_e)$ = degree of hydration at equivalent age t_e
- Q_H = rate of heat generation, W/m³

Table 5.1: Parameters related to heat generation used in COMSOL

Parameter	Value	
	Metric (SI)	U.S. Customary (Imperial)
C_c Cementitious materials content per unit volume of concrete	405 kg/m ³	682 lb/yd ³
H_u Total heat of complete hydration	465 J/g	200 Btu/lb
E_a Apparent activation energy	31,632 J/mol	13,600 Btu/lbmol
\bar{R} Universal gas constant	8.3144 J/mol·K	1.986 Btu/lbmol·°R
α_u Ultimate degree of hydration	0.633	
β Hydration shape parameter	2.081	
τ Hydration time parameter	12.50 hr	
T_r Reference temperature	23 °C	73.5 °F

As discussed in Section 4.4.9, the thermal conductivity of the mock-up concrete was determined as a function of the thermal diffusivity, density, and specific heat

capacity. However, to match the implementation in ConcreteWorks (see Section 5.2.1.1), the thermal conductivity λ of the concrete was implemented in COMSOL according to Eq. 5.9 (Schindler, 2002) with an ultimate thermal conductivity λ_u of 1.66 W/m·K (0.96 Btu/hr·ft·°F).

$$\lambda(\alpha_H) = \lambda_u(1.33 - 0.33\alpha_H) \quad \text{Eq. 5.9}$$

Where,

- λ = thermal conductivity, W/m·K (Btu/hr·ft·°F)
- λ_u = ultimate thermal conductivity of mature concrete, W/m·K (Btu/hr·ft·°F)
- α_H = degree of hydration.

Specific heat capacity values for each concrete component as a function of temperature were presented in Section 4.4.7, but, to match the ConcreteWorks model, the original van Breugel (1980) model for specific heat capacity c_p of concrete (Eq. 5.10) was used with a constant value of 727 J/kg·K (0.174 Btu/lb·°F) for the aggregates. The specific heat capacity that ConcreteWorks uses for cement is not specified, so the 1140-J/kg·K (0.272-Btu/lb·°F) value reported by Mindess et al. (2003) and recommended by Schindler (2002) was used. Per the U.S. Army Corps of Engineers (1973a), 4186.8 J/kg·K (1.0 Btu/lb·°F) was used as specific heat capacity of water.

$$c_p = \frac{1}{m} (m_c \alpha_H c_{p(cef)} + m_c (1 - \alpha_H) c_{p(c)} + m_a c_{p(a)} + m_w c_{p(w)}) \quad \text{Eq. 5.10}$$

Where,

- c_p = specific heat capacity of concrete, J/kg·K
- m = total mass of concrete mixture, kg
- m_c = mass of cement content, kg
- m_a = mass of aggregate content, kg
- m_w = mass of water content, kg
- α_H = degree of hydration
- $c_{p(cef)}$ = fictitious specific heat capacity of hydrated cement, defined in Eq. 5.11, J/kg·K
- $c_{p(c)}$ = specific heat capacity of cement, J/kg·K
- $c_{p(a)}$ = specific heat capacity of aggregate, J/kg·K
- $c_{p(w)}$ = specific heat capacity of water, J/kg·K

$$c_{p(cef)} = 8.4T_c + 339 \quad \text{Eq. 5.11}$$

Where,
 T_c = temperature of concrete, °C

As in the ConcreteWorks model, 22.5 °C (72.5 °F) was entered for the initial concrete temperature, and 19-mm (¾-in.) plywood forms were kept in place for the entire 14-day (336-hour) period of analysis. ConcreteWorks provides the modeled ambient temperature with each 5-minute time step in the results, and the values were incorporated into COMSOL as a linear interpolation function. Similarly, the modeled daily solar radiation was sampled from ConcreteWorks and incorporated into COMSOL as a linear interpolation function. Per the discussion in Section 5.2.1.3, Eq. 5.2 was used to determine the convective heat transfer coefficient h for the vertical plywood surfaces with no wind and an assumed surface roughness factor R_f of 1.30.

The densities of the concrete and plywood were measured to be 2,276 and 521 kg/m³ (142.1 and 32.5 lb/ft³), respectively, and both values were used in the COMSOL model. Additionally, the thermal conductivity and specific heat capacity of the plywood were entered as 0.12 W/m·K (0.069 Btu/hr·ft·°) and 1215 J/kg·K (Btu/lb·°F), respectively, matching values reported by Incropera et al. (2007).

The net radiative heat flux q_r from a surface to its surroundings is governed by Eq. 5.12, which accounts for radiation from the surface and irradiation upon the surface from its surroundings. The emissivity ε of a material surface is the ratio, ranging from 0 to 1, of the thermal radiation emitted by the surface to that emitted by a blackbody at the same temperature (Incropera et al., 2007). Similarly, the spectral absorptivity α_s is the fraction, ranging from 0 to 1, of the spectral irradiation absorbed by the surface. Incropera et al. provided ranges of typical concrete and wood emissivity values of 0.88 to 0.93 and 0.82 to 0.92, respectively, at 27 °C (80 °F). ConcreteWorks uses 0.92 for concrete and wood, both within the provided ranges, so 0.92 was used as the surface emissivity ε of the mock-up concrete and plywood forms for modeling in COMSOL.

$$q_r = \varepsilon\sigma T_s^4 - \alpha_s\sigma T_a^4 \quad \text{Eq. 5.12}$$

Where,

- q_r = net radiative heat flux, W/m² (Btu/hr·ft²)
- ε = surface emissivity
- α_s = spectral absorptivity
- σ = Stefan-Boltzmann constant, 5.670373×10^{-8} W/m²·K⁴ (1.704×10^{-9} Btu/hr·ft²·°R⁴)
- T_s = surface temperature, K (°R)
- T_a = ambient temperature, K (°R)

In addition to being absorbed by a surface, incident radiation can be reflected by the surface or transmitted through the surface. The distribution of the irradiation amongst the three modes is determined by the absorptivity α_s , reflectivity ρ_s , and transmissivity t_s of the surface according to Eq. 5.13. For an opaque surface, the transmissivity t_s is zero, so that all of the irradiation is either absorbed or reflected by the surface. Though no reference values were provided as the basis of its selection, ConcreteWorks uses 0.6 for the spectral absorptivity α_s of wood (Riding, 2007), matching the value reported by Incropera et al. (2007) for concrete. Levinson and Akbari (2002) measured concrete reflectivity values of 0.41 to 0.77, which correspond to absorptivity values of 0.23 to 0.59. Those concrete absorptivity values were referenced for the use of 0.55 in ConcreteWorks (Riding, 2007).

$$\alpha_s + \rho_s + t_s = 1 \quad \text{Eq. 5.13}$$

Where,

- α_s = spectral absorptivity
- ρ_s = spectral reflectivity
- t_s = spectral transmissivity

5.3.2 Results

Figure 5.9 shows a comparison of the temperatures modeled by ConcreteWorks and COMSOL and the temperatures measured in the second mock-up. The COMSOL model effectively replicates the results of the ConcreteWorks model, reaching maximum temperatures of 71.6 and 60.5 °C (161 and 141 °F) at the Int and Ext locations, both within 1.5% of the 72.5- and 61.2-°C (163- and 142-°F) maximum temperatures in the

ConcreteWorks model at the corresponding locations. Additionally, the behavior of the Int and Ext curves are consistent between the models: both Int curves steadily decreased to approximately 30 °C (86 °F), whereas the Ext curves exhibited similar daily undulations while also gradually decreasing to approximately 30 °C (86 °F).

The differences between the two sets of results may be due to the different meshes and time steps used for the models and any errors in the assumptions made regarding parameters used in ConcreteWorks. The most notable differences between the sets of data occurred at the peaks and troughs of the curves, including the daily variation of the Ext data. Many of the plywood properties were assumed for COMSOL, and inconsistencies in those values could alter the way that daily variations in ambient temperature and radiation influence the concrete temperature.

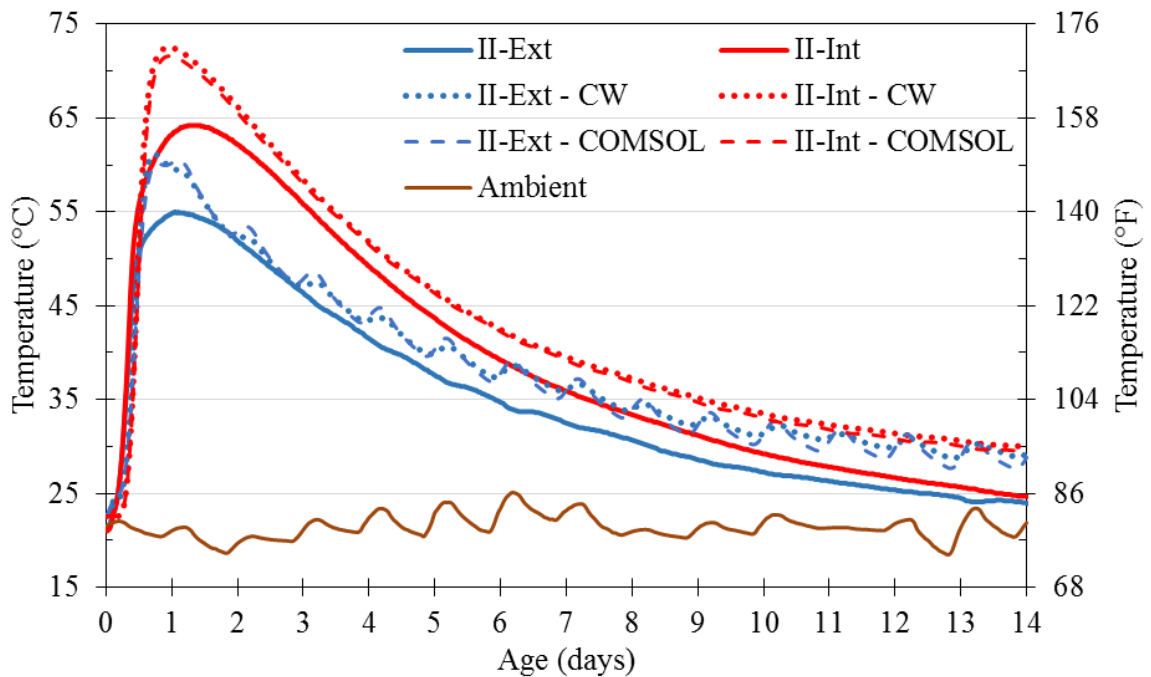


Figure 5.9: Experimental temperatures, corresponding ConcreteWorks (CW) results, and COMSOL Multiphysics results for matching ConcreteWorks

5.3.3 Discussion

The successful replication of the ConcreteWorks results in COMSOL Multiphysics validates the use of COMSOL for detailed thermal modeling of the mock-up. In particular, a representative model of the mock-up can be developed, incorporating the post-tensioning ducts, rebar, and steel liner plate embedded in the concrete, and the influence of these components can be identified in the temperature results. COMSOL also allows custom time- and temperature-dependent functions to be utilized for the concrete properties based on experimental results rather than constant values or fixed literature equations used in ConcreteWorks. Furthermore, the mechanical response of the mock-up to thermal and post-tensioning loads can be analyzed in COMSOL.

5.4 Representative Mock-Up Model in COMSOL Multiphysics

The following sections detail the development of a model in COMSOL Multiphysics representing the second mock-up. This model includes the embedded post-tensioning ducts, rebar, and steel liner plate in addition to the polystyrene rigid foam insulation applied to the narrow ends of the mock-up to simulate the longer lengths of the CR3 PCC pours. Commonalities and differences between the ConcreteWorks and COMSOL models are noted, and the results are compared with the measured temperatures in the second mock-up. Mechanical analysis of the thermal strains and subsequent post-tensioning loads was then conducted.

5.4.1 Determination of Model Symmetry

5.4.1.1 Model Description

Figure 5.10 illustrates the mock-up with the forms and rigid foam insulation that were in place during the first 14 days after concrete placement, and the vertical and horizontal planes of symmetry utilized for the final COMSOL model are identified. The

mock-up and forms are fully symmetric across the vertical plane of symmetry. Though the concrete and embedded components are symmetric across the horizontal plane, the bottom bearing plates and base formwork and insulation are not symmetric across the horizontal plane. Therefore, a preliminary model, shown in Figure 5.11, was developed to investigate the thermal behavior of the mock-up through the full height, utilizing only the vertical plane of symmetry. The vertical ducts, bottom bearing plates, and base formwork and insulation were modeled. However, components that are symmetric across the horizontal plane, such as the rebar, liner plate, and horizontal ducts, were not included in this preliminary model in order to highlight the influence of the asymmetric components. The symmetric components were included in the final model discussed in Section 5.5.2.

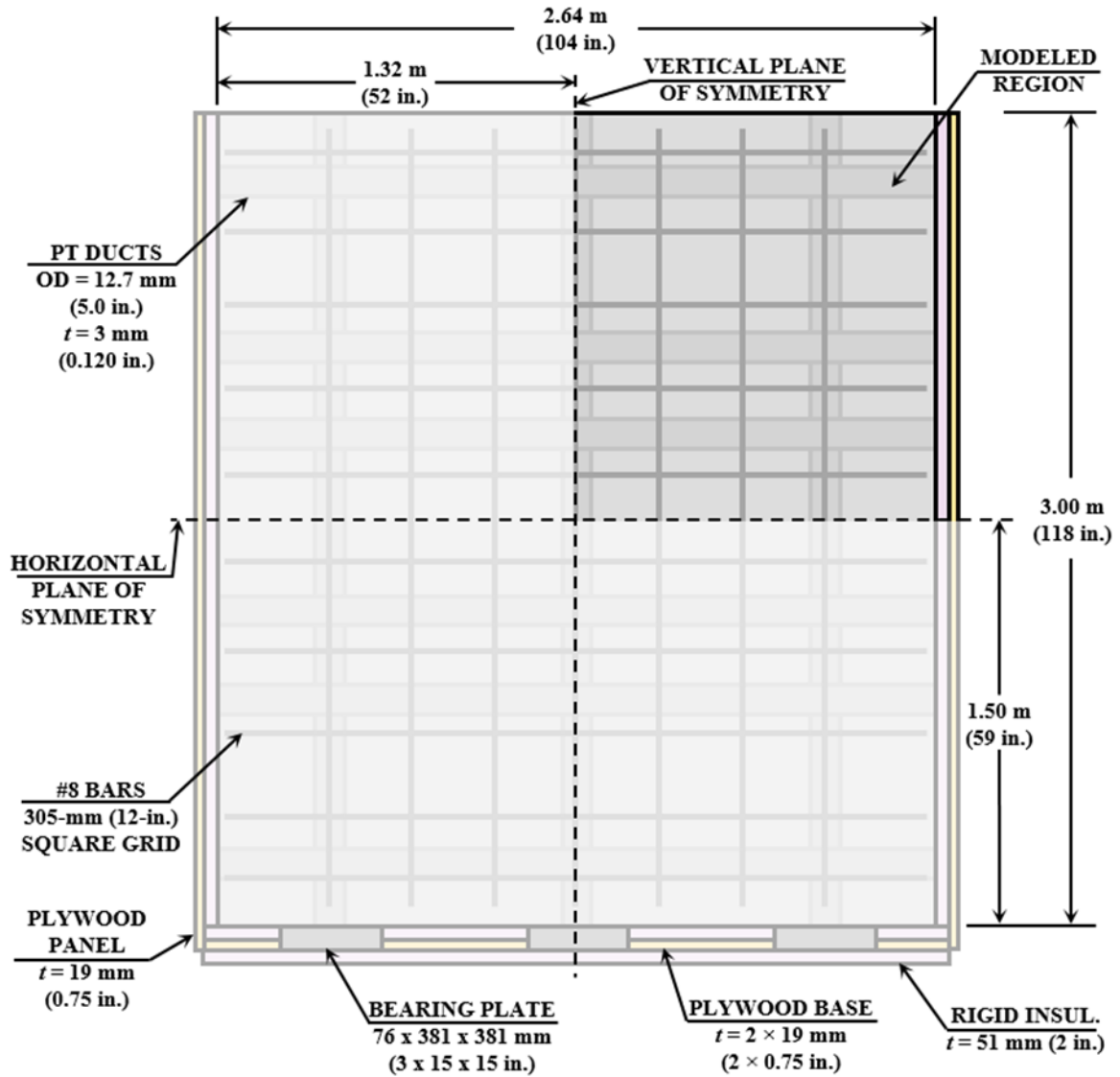


Figure 5.10: Planes of symmetry utilized in COMSOL model of mock-up

A plane symmetry boundary condition was applied to the entire front left face in Figure 5.11 to correspond to the vertical plane of symmetry in Figure 5.10. The modeled concrete, ducts, bearing plates, plywood forms, and rigid foam insulation are shown in Figure 5.11a and Figure 5.11b. The model consisted of 87,455 domain elements, 13446 boundary elements, 1,389 edge elements, and, as shown in Figure 5.11c, tetrahedral elements used due to the complexity of the geometry at the intersection of the ducts and

bearing plates. The steel ducts were modeled as shell elements with the 3-mm (0.120-in.) thickness of the actual ducts.

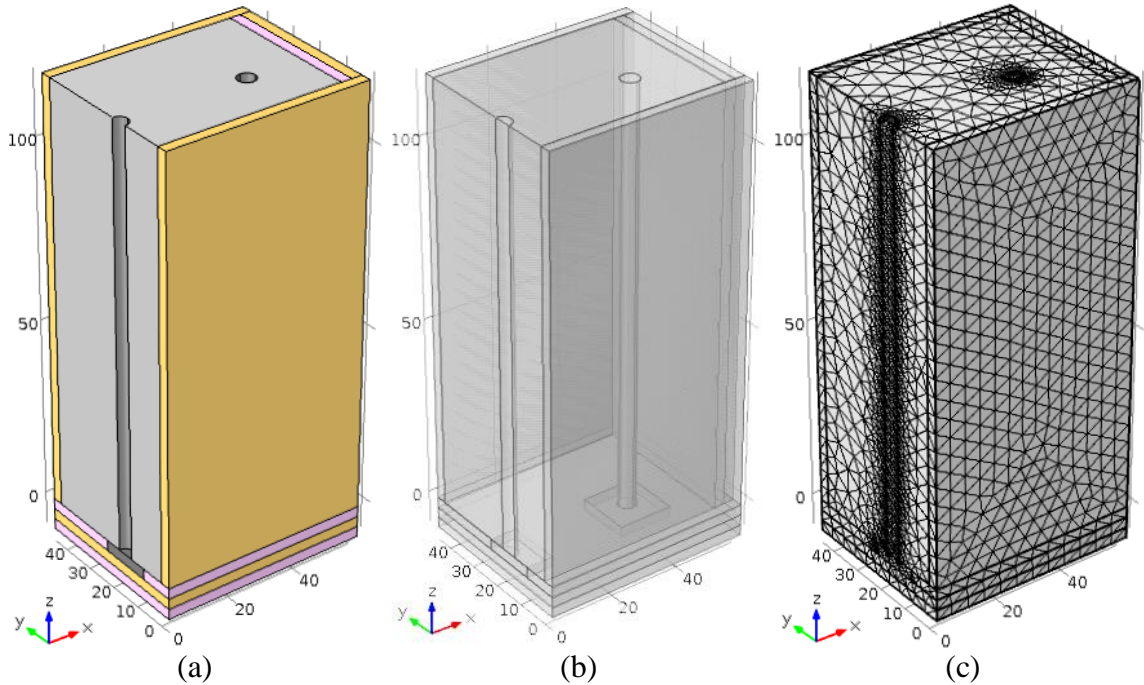


Figure 5.11: Preliminary COMSOL model of mock-up showing (a) materials, (b) embedded components, and (c) finite element mesh

5.4.1.2 Material Properties

As noted in Section 5.4.1, the values listed in Table 5.1 for the parameters related to heat generation were used for all COMSOL models. The same plywood density, thermal conductivity, and specific heat capacity values were also used. However, the 19-mm (0.75-in.) thickness and 0.12-W/m·K (0.069-Btu/hr·ft·°F) thermal conductivity of the plywood forms were multiplied by 4 in order to decrease the number of elements needed to model the forms while maintaining the appropriate conduction behavior through the forms. The same surface emissivity value of 0.92 was used for the concrete and wood, and 2276 kg/m³ (142.1 lb/ft³) was used as the concrete density, matching the previous models.

As noted in Section 5.4.1, the values listed in Table 5.1 for the parameters related to heat generation were used for all COMSOL models. The same plywood density, thermal conductivity, and specific heat capacity values were also used, and 0.92 was again used as surface emissivity for concrete and wood. Additionally, 2276 kg/m³ (142.1 lb/ft³) was used as the concrete density, matching the previous models.

However, the experimentally determined concrete CTE of 7.86 $\mu\epsilon/^\circ\text{C}$ (4.37 $\mu\epsilon/^\circ\text{F}$) and the experimentally determined functions for the concrete specific heat capacity and thermal diffusivity were used in this model. These functions were given in Eq. 36 in Section 4.4.7 and Eq. 37 in Section 4.4.8, respectively, and are reproduced here as Eq. 5.14 and Eq. 5.15. The concrete thermal conductivity was calculated from the thermal diffusivity, density, and specific heat capacity according to the relationship given in Eq. 5.16.

$$\kappa = (12.8 \times 10^{-9}) \ln(t) + 717 \times 10^{-9} \quad \text{Eq. 5.14}$$

Where,

κ = thermal diffusivity, m²/s
 t = age, days

$$c_p = 1.17\alpha_H T - 50.8\alpha_H + 1.42T + 932 \quad \text{Eq. 5.15}$$

Where,

c_p = specific heat capacity of concrete, J/kg·K
 α_H = degree of hydration

$$\lambda = \kappa \rho c_p \quad \text{Eq. 5.16}$$

Where,

λ = thermal conductivity, W/m·K (Btu/hr·ft·°F)
 κ = thermal diffusivity, m²/s (ft²/hr)
 ρ = density, kg/m³ (lb/ft³)
 c_p = specific heat capacity at constant pressure, J/kg·K (Btu/lb·°F)

The density of the polystyrene rigid foam insulation was measured to be 22.746 kg /m³ (1.42 lb/ft³), and thermal conductivity and specific heat capacity values of 0.030 W/m·K (0.017 Btu/ hr·ft·°F) (Owens Corning, 2001) and 1210 J/kg·K (0.289 Btu/lb·°F) (Incropera et al., 2007), respectively, were used for the rigid foam. Similar to the

plywood forms, the 51-mm (2-in.) thickness and the thermal conductivity of the rigid foam were multiplied by 2 in order to decrease the number of elements needed to model the foam while maintaining the appropriate conduction behavior through the foam.

5.4.1.3 Convective Heat Transfer Coefficient

In contrast to the single function (Eq. 5.1 in Section 5.2.1) used by ConcreteWorks to determine the convective heat transfer coefficient h for forced and free convection, COMSOL allows implementation of separate functions for various forced and free (or natural) convection cases. The convective heat transfer coefficient h for external free convection near a vertical wall, such as the vertical faces of the mock-up, is a function of the Rayleigh number Ra_L , which is a dimensionless number defined by Eq. 5.17 as the product of the dimensionless Grashof and Prandtl numbers, Gr_L and Pr . The Grashof number indicates the ratio of the buoyancy to viscous forces acting on a fluid and is defined by Eq. 5.18, and the Prandtl number is defined by Eq. 5.19 as the ratio of the kinematic viscosity or momentum diffusivity ν_k and thermal diffusivity κ of the fluid (Incropera et al., 2007). In each case, the fluid properties are calculated at the average of the surface and bulk fluid temperatures.

According to Eq. 5.19, small values of the Prandtl number ($Pr \ll 1$) indicate that thermal conduction is the primary mode of heat transfer due to the larger thermal diffusivity value, whereas large values of the Prandtl number ($Pr \gg 1$) indicate that convection is the primary mode of heat transfer due to the larger kinematic viscosity value. A Rayleigh number of 10^9 is typically identified as the transition between laminar and turbulent flow of the free convection boundary layer (Incropera et al., 2007); at lower Rayleigh numbers, the flow is laminar, and at higher Rayleigh numbers, the flow is turbulent.

$$Ra_L = Gr_L Pr = \frac{g\beta_T(T_s - T_\infty)L^3}{\nu_k \kappa} \quad \text{Eq. 5.17}$$

$$Gr_L = \frac{g\beta_T(T_s - T_\infty)L^3}{\nu_k^2} \quad \text{Eq. 5.18}$$

$$Pr = \frac{\nu_k}{\kappa} \quad \text{Eq. 5.19}$$

Where,

- Ra_L = Rayleigh number
- Gr_L = Grashof number
- Pr = Prandtl number
- g = acceleration due to gravity, 9.81 m/s² (32.2 ft/s²)
- β_T = coefficient of volumetric thermal expansion of fluid, roughly 1/T for ideal gases, 1/K (1/°R)
- T_s = surface temperature, K (°R)
- T_∞ = bulk temperature of fluid, K (°R)
- L = characteristic dimension, m (ft)
- ν_k = kinematic viscosity or momentum diffusivity of fluid, m²/s (ft²/s)
- κ = thermal diffusivity of fluid, m²/s (ft²/s)

Using the mock-up height of 3 m (118 in.) as the characteristic dimension, assuming a maximum temperature difference of 50 K (90 °R) between the surface and air, and using typical properties of air automatically implemented in COMSOL, the Rayleigh number was determined to be on the order of 10⁶, below the critical Rayleigh number of 10⁹ and indicative of laminar flow. For $Ra_L \leq 10^9$, COMSOL uses Eq. 5.20 to calculate the convective heat transfer coefficient h .

$$h = \frac{\lambda}{L} \left(0.68 + \frac{0.67 Ra_L^{1/4}}{\left(1 + \left(\frac{0.492 \lambda}{\mu c_p} \right)^{9/16} \right)^{4/9}} \right) \quad \text{Eq. 5.20}$$

Where,

- h = convective heat transfer coefficient, W/m²·K (Btu/hr·ft²·°F)
- λ = thermal conductivity of fluid, W/m·K (Btu/hr·ft·°F)
- μ = dynamic viscosity of fluid, W/m·K (Btu/hr·ft·°F)
- c_p = specific heat capacity of fluid at constant pressure, J/kg·K (Btu/lb·°F)

For the horizontal faces of the mock-up, the characteristic dimension is the “plate diameter,” which is defined as the area of the face divided by the perimeter (COMSOL, 2015). For the 2.64-m (104-in.) length and 1.07-m (42-in.) thickness of the mock-up, the plate diameter is 380 mm (15.0 in.). COMSOL uses Eq. 5.21 and Eq. 5.22 to calculate the convective heat transfer coefficient h for the top and bottom faces, respectively.

$$h = \frac{\lambda}{L} 0.54 \text{Ra}_L^{1/4} \quad \text{Eq. 5.21}$$

$$h = \frac{\lambda}{L} 0.27 \text{Ra}_L^{1/4} \quad \text{Eq. 5.22}$$

5.4.1.4 Results

The temperature results of the preliminary model are shown in Figure 5.12 and Figure 5.13. The influence of the steel post-tensioning ducts and the bearing plates is seen Figure 5.12 as they transfer heat towards the top and bottom surfaces more rapidly than the concrete. When the concrete is near its maximum temperature, as shown in Figure 5.12a at 24 hours, the temperatures at the plane of symmetry are nearly uniform for most of the height and thickness. Though the bottom bearing plate transfers heat further from the concrete, the effect is balanced by the base insulation so that the temperature gradients near the exposed top concrete face and insulated bottom face are comparable.

Figure 5.12b shows the modeled temperatures 60 hours after concrete placement as the mock-up cools. Due to the ducts transferring heat away from the warmer center towards the cooler surfaces, the maximum temperatures in the plane of symmetry shifted towards the back of the mock-up. Like the results at 24 hours, the temperature gradients near the top and bottom of the concrete are similar at 60 hours, and in both cases, the profile can reasonably be considered symmetric across a horizontal plane at mid-height.

Figure 5.13 shows the temperature profile through the thickness of the mock-up halfway between the two vertical post-tensioning ducts. Though not crossing the modeled

plane, the influence of the bottom bearing plates is demonstrated by the warmer temperatures towards the left in the base insulation. No clear influence of the ducts is shown, and, in contrast to Figure 5.12b, the maximum temperatures at 60 hours (Figure 5.13b) appear to be centered in the section. Though the temperature profile exhibits biaxial symmetry when the concrete was near its maximum temperature (Figure 5.13a) and as it cools (Figure 5.13b), the results in Figure 5.12b show that only the horizontal plane of symmetry is valid through the entire length of the mock-up.

Since the results of the preliminary model consistently exhibited symmetry across the horizontal plane at mid-height of the mock-up, that plane of symmetry was utilized in the final COMSOL model for thermal and mechanical analysis of the mock-up, as shown in Figure 5.10.

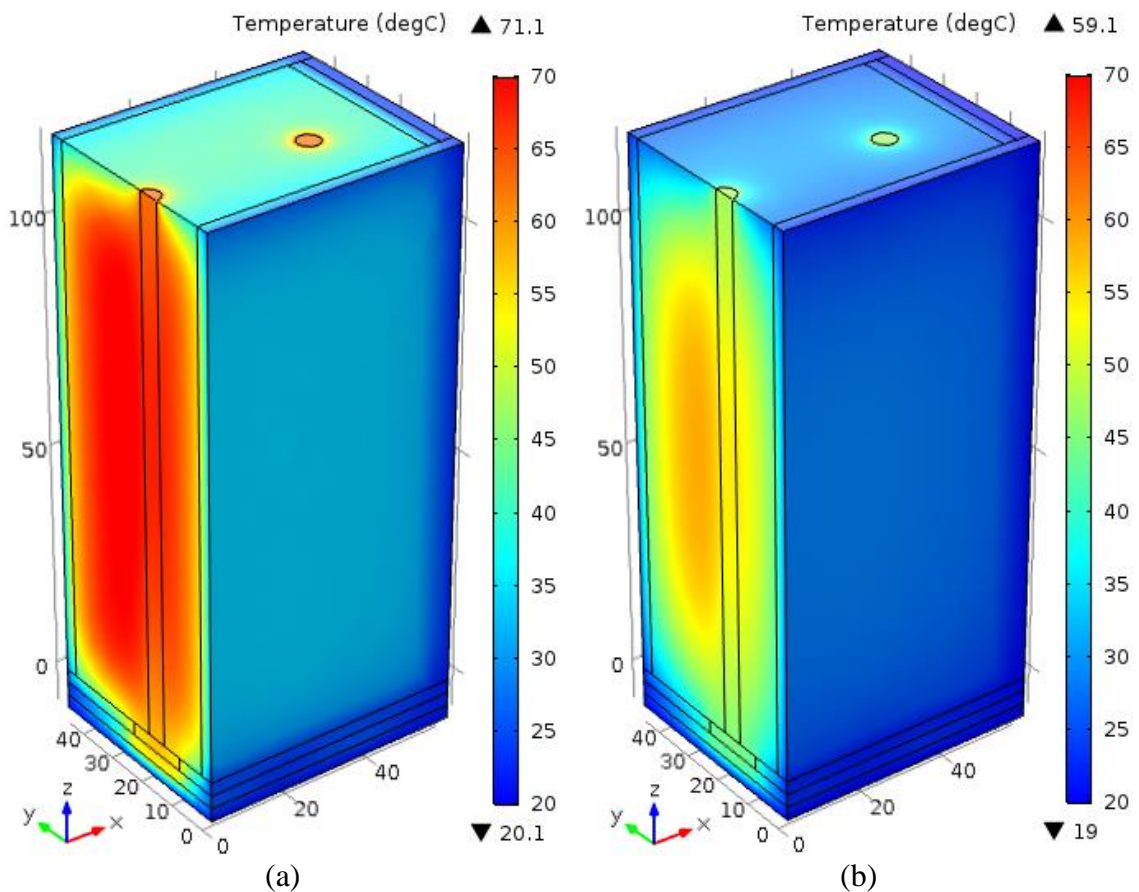


Figure 5.12: Preliminary modeled mock-up temperatures (a) 24 and (b) 60 hours after concrete placement

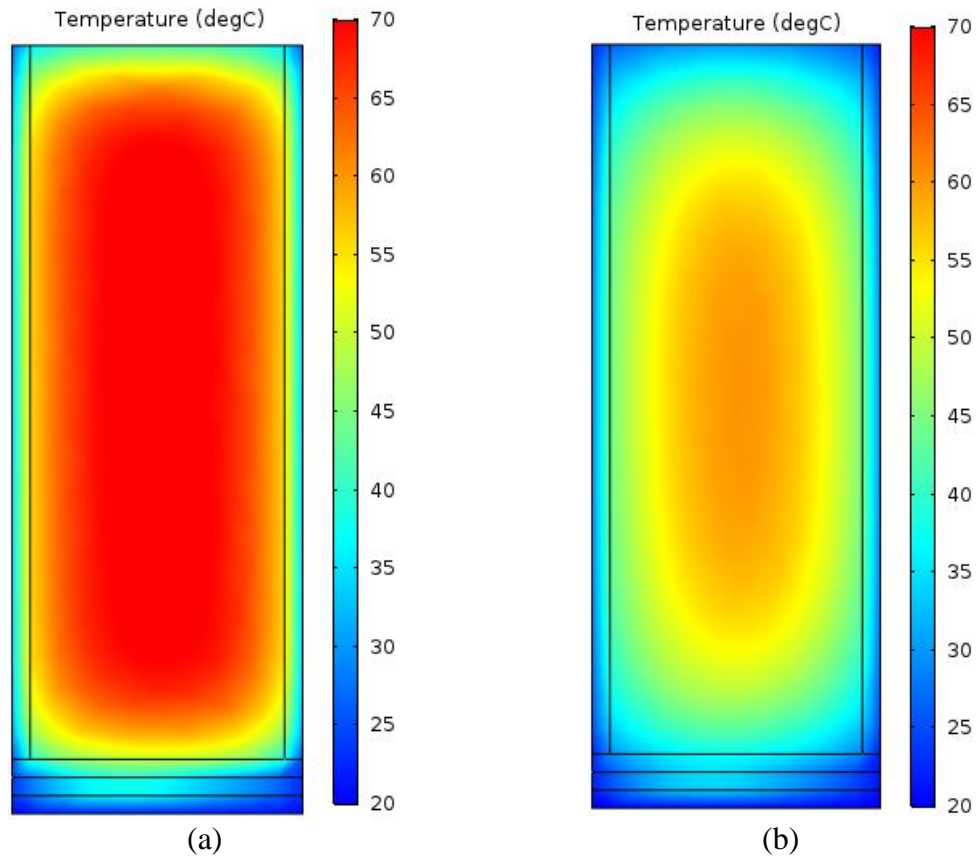


Figure 5.13: Preliminary mock-up temperature profiles modeled halfway between the vertical post-tensioning ducts (a) 24 and (b) 60 hours after concrete placement

5.4.2 Final Model

In order to understand the influence of the temperature history on the behavior of the mock-up, two separate analyses were conducted using the final COMSOL model. In the first analysis, the cement hydration was modeled, and the resulting thermal behavior influenced the development of the mechanical properties and the stress state in the concrete prior to post-tensioning. In the second method, the curing history was not accounted for, and all mechanical properties were based on results from fog-cured specimens evaluated at the chronological age of the concrete at the time of post-

tensioning. The following sections provide descriptions of the model and analyses conducted and identify the functions used for the mechanical properties for each case.

5.4.2.1 Model Description

The final COMSOL model is shown in Figure 5.14 and includes the representative vertical and horizontal post-tensioning ducts, rebar cage, steel plate liner, plywood forms, and rigid foam insulation. The concrete, forms, and insulation were modeled as solids, and the steel ducts and liner plate were modeled as shell elements with thicknesses matching the physical values. The rebar cage was located a depth of 83 mm (3.25 in.) from the front face of the mock-up, the average of the actual depths of the horizontal and vertical bars of the cage in experimental mock-up. Each rebar was modeled using truss elements, which are visible in Figure 5.14b, and the plane in which the rebar was modeled can be seen on the concrete surfaces in Figure 5.14a and Figure 5.14b.

The model consisted of 70,384 domain elements, 11,693 boundary elements, and 1,558 edge elements. As shown in Figure 5.14c, tetrahedral elements were used due to the complexity of the geometry near the intersections of the post-tensioning ducts.

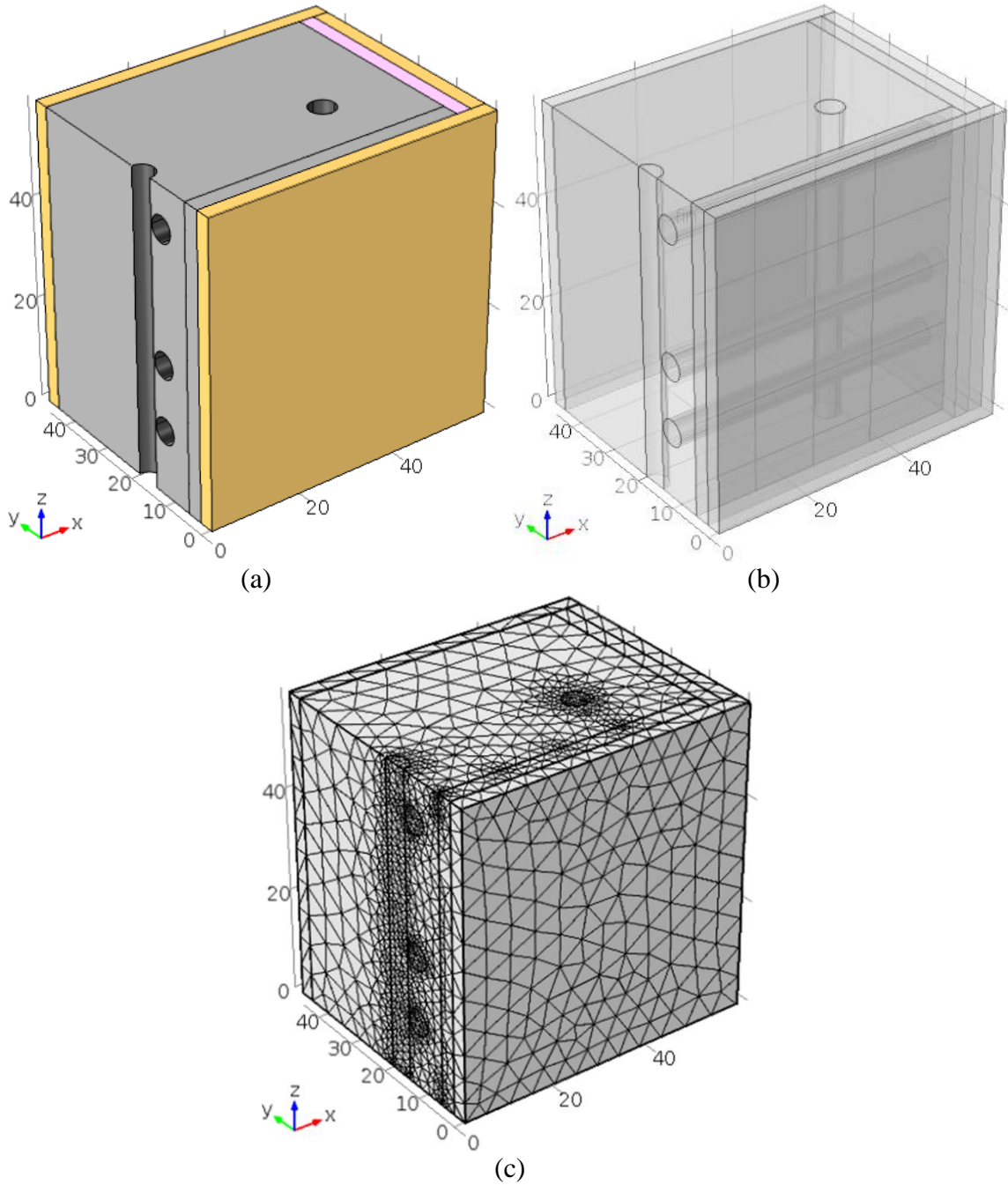


Figure 5.14: Diagrams of final COMSOL model showing (a) materials, (b) embedded components, and (c) finite element mesh

When accounting for the curing history, the analysis was conducted in three stages. First, hydration and the thermal response of the mock-up were modeled through 14 days, after which constant external ambient conditions were applied due to little

variation in the experimental mock-up temperatures after 14 days. Second, the mechanical response to the thermal behavior was modeled, beginning 5 hours after concrete placement to represent setting of the concrete and continuing until immediately before post-tensioning. Third, the post-tensioning loads were applied to the model at 69 days, matching the age at which the experimental mock-up was post-tensioned. During the first 15 hours, 30-minute intervals were used, followed by 1-hour intervals through 28 hours, 4-hour intervals through 14 days, and 48-hour intervals through 69 days.

When not accounting for the curing history, mechanical analysis of the post-tensioning loads was conducted in a single step using constant 69-day properties based on the results of tests on fog-cured specimens.

5.4.2.2. Functions for Mechanical Properties

The functions used for the concrete compressive strength, splitting tensile strength, modulus of elasticity, and Poisson's ratio are given in Eq. 5.23 through Eq. 5.26 for the analysis incorporating the mock-up curing history. The function for compressive strength (Eq. 5.23) was determined by exponential regression with respect to equivalent age of the results of match-cured specimens from the second mock-up and is reproduced from Eq. 26 in Section 4.4.3. The function for splitting tensile strength (Eq. 5.24) was based on the linear relationship between the compressive strength-to-splitting tensile strength (f_c/f_{tsp}) ratio and the compressive strength of the fog-cured specimens from both mock-ups. The function provided a good fit for the results of the match-cured specimens from both mock-ups and was given in Eq. 31 in Section 4.4.4. Like the compressive strength, the function for modulus of elasticity (Eq. 5.25) was determined by exponential regression with respect to equivalent age of the results of match-cured specimens from the second mock-up. The parameters for the function were given in Table 11 in Section 4.4.5. Lastly, the function for Poisson's ratio (Eq. 5.26) was based on the combined sine and exponential model proposed by De Schutter and Taerwe (1996). The function was

reproduced from Eq. 32 in Section 4.4.6 and was adjusted for the average measured late-age Poisson's ratio of 0.20 for all tested specimens.

$$f_c(t_e) = 46.4 \exp\left(-\left(\frac{1.197}{t_e}\right)^{0.563}\right) \quad [\text{MPa}]$$

$$f_c(t_e) = 6,736 \exp\left(-\left(\frac{1.197}{t_e}\right)^{0.563}\right) \quad [\text{psi}]$$
Eq. 5.23

$$f_{tsp}(t_e) = \frac{f_c(t_e)}{0.169f_c(t_e) + 2.86} \quad [\text{MPa}]$$

$$f_{tsp}(t_e) = \frac{f_c(t_e)}{1.17 \times 10^{-3}f_c(t_e) + 2.86} \quad [\text{psi}]$$
Eq. 5.24

$$E(t_e) = 29.7 \exp\left(-\left(\frac{0.4824}{t_e}\right)^{0.998}\right) \quad [\text{GPa}]$$

$$E(t_e) = 4301 \exp\left(-\left(\frac{0.4824}{t_e}\right)^{0.998}\right) \quad [\text{ksi}]$$
Eq. 5.25

$$\nu(\alpha_H) = 0.2387 \sin\left(\frac{\pi\alpha_H}{2}\right) + 0.5e^{-10\alpha_H}$$
Eq. 5.26

Where,

- f_c = compressive strength, MPa or psi
- f_{tsp} = splitting tensile strength, MPa or psi
- E = modulus of elasticity, GPa or ksi
- ν = Poisson's ratio
- t_e = equivalent age, days
- α_H = degree of hydration

The functions given in Eq. 5.27 and Eq. 5.28 were used to determine the compressive strength and modulus of elasticity, respectively, of the mock-up based on the results of tests on fog-cured specimens and neglecting the curing history. Analogous to Eq. 5.23 for the model accounting for curing history, Eq. 5.27 gives the compressive strength based on exponential regression with respect to equivalent age of the results of fog-cured specimens from the second mock-up. The parameters for the function were listed in Table 5 in Section 4.4.3. Similarly, the function for modulus of elasticity (Eq. 5.28) was determined by exponential regression with respect to equivalent age of the

results of match-cured specimens from the second mock-up. The parameters for the function were given in Table 11 in Section 4.4.5.

The same function for splitting tensile strength (Eq. 5.24) was used since the relationship between the compressive strength-to-splitting tensile strength (f_c/f_{isp}) ratio and the compressive strength was consistent for both curing conditions. Additionally, the same function for Poisson's ratio (Eq. 5.26) was used since the results were consistent for all tested specimens. Table 5.2 presents the results for each mechanical property evaluated at 69 days, the age at which the mock-up was post-tensioned. These value were used in analysis of the mock-up while neglecting the curing history.

$$f_c(t) = 53.6 \exp\left(-\left(\frac{1.465}{t}\right)^{0.511}\right) \quad [\text{MPa}]$$

$$f_c(t) = 7771 \exp\left(-\left(\frac{1.465}{t}\right)^{0.511}\right) \quad [\text{psi}]$$

Eq. 5.27

$$E(t) = 31.3 \exp\left(-\left(\frac{0.3926}{t}\right)^{1.064}\right) \quad [\text{GPa}]$$

$$E(t) = 4544 \exp\left(-\left(\frac{0.3926}{t}\right)^{1.064}\right) \quad [\text{ksi}]$$

Eq. 5.28

Where,

- f_c = compressive strength, MPa or psi
- E = modulus of elasticity, GPa or ksi
- t = chronological age, days

Table 5.2: Values of mechanical properties at 69 days based on fog-cured results

Mechanical Property	Value	
	Metric (SI)	U.S. Customary (Imperial)
Compressive strength, f_c	46.6 MPa	6758 psi
Splitting tensile strength, f_{isp}	4.33 MPa	628 psi
Modulus of elasticity, E	31.2 GPa	4525 ksi
Poisson's ratio, ν	0.20	

5.4.3 Results and Discussion

The following sections discuss the results of the COMSOL analysis of the mock-up. The modeled mock-up temperature histories are compared with those measured experimentally and those modeled by ConcreteWorks, and the impact of the curing history on the structural response of the mock-up to the post-tensioning loads is investigated.

5.4.3.1 Temperatures

The temperature results of the COMSOL model are shown in Figure 5.15 with the temperatures measured in the second mock-up and the temperatures modeled by ConcreteWorks. The initial temperature rise is consistent amongst the three pairs of data, but the shapes of the peaks for the modeled temperatures are sharper than those of the measured mock-up temperatures. The maximum temperatures in the COMSOL model were 69.7 and 59.3 °C (157.5 and 138.7 °F) at the Int and Ext locations, respectively, both approximately 5 °C (9 °F) warmer than the corresponding mock-up temperatures. After the initial rapid rise, the COMSOL temperatures were less than the ConcreteWorks results at all ages. The greater difference between the COMSOL and ConcreteWorks results for the Int peaks compared to the Ext peaks can be attributed to the influence of the post-tensioning ducts, which, as shown in Figure 5.12b, have a notable impact on the temperatures at the center of the mock-up.

In contrast to the ConcreteWorks results, the temperatures predicted by the COMSOL model were generally slightly less than the mock-up temperatures after the peak, but the COMSOL temperatures converged with the mock-up temperatures by the end of the first two weeks. The daily variation of the Ext results for the COMSOL model were consistent with the experimental results, exhibiting slight undulations but not to the extent of the ConcreteWorks results.

Since the ConcreteWorks and COMSOL models both predict sharper temperature peaks than the experimental data, the hydration parameters or apparent activation energy determined for the cement paste used in the mock-up may not be representative of the heat generation in the concrete. As discussed in Section 4.4.1, Riding et al. (2011) noted that, for a given dosage, chemical admixtures may influence the heat generation in cement paste and concrete differently. A slight broadening of the COMSOL peaks and an accompanied decrease in the maximum temperatures would result in the profiles matching well with the mock-up temperatures, suggesting that a slightly different hydration shape parameter β and hydration time parameter τ may be more appropriate for the concrete.

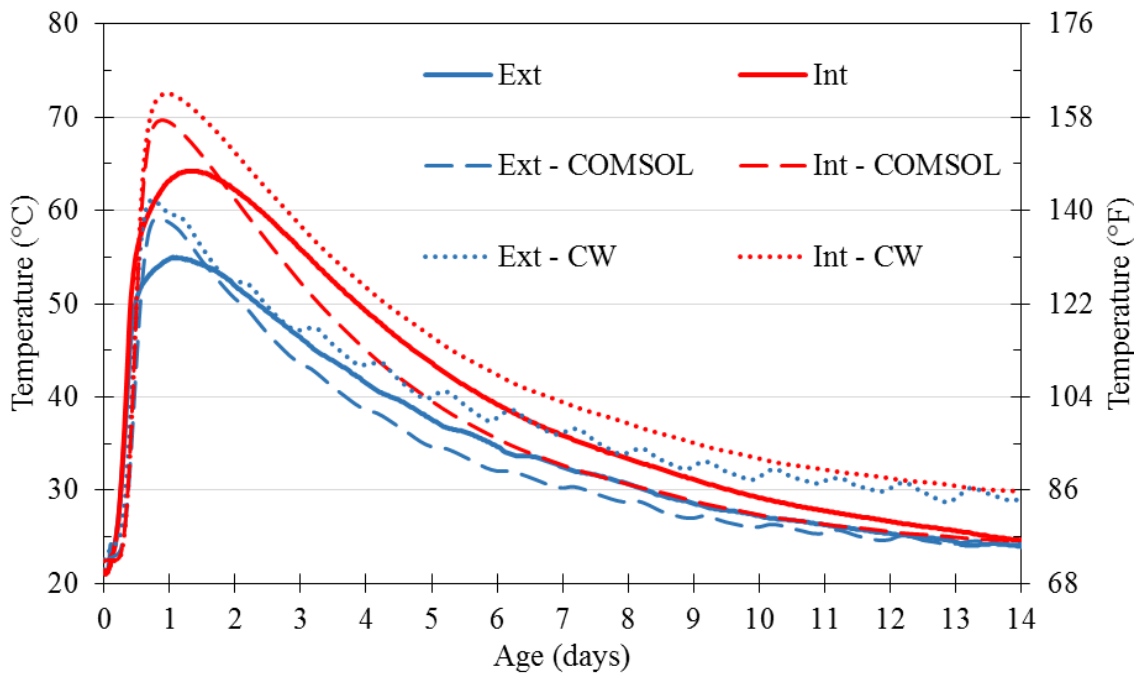


Figure 5.15: Experimental temperatures and temperatures modeled by COMSOL and ConcreteWorks (CW)

Though there are distinctions between the COMSOL predictions and the measured mock-up temperatures, the behavior predicted by the COMSOL model is more consistent with mock-up than the ConcreteWorks prediction. Though shown for only two

points, the COMSOL model develops spatial temperature distributions and tracks the spatial development of the thermal and mechanical properties accordingly. This behavior is utilized in the analysis accounting for the curing history of the mock-up.

5.4.3.2 Mock-Up Post-Tensioning Stresses

The figures presented in this section show results for the COMSOL model described in Section 5.5.2 with post-tensioning loads applied after 69 days of curing. Figure 5.16 shows the first principal stresses in the horizontal plane centered between the horizontal ducts spaced at 648 mm (25.5 in.) on center. In each figure showing stresses, the stress values for the color scale range from -4.1 MPa (-600 psi) for compression to 9.7 MPa (1400 psi) for tension. The consistent scale allows comparison of the stress profiles amongst the different views presented and loading scenarios analyzed. The range was selected so that all presented tensile stresses would be included and colored accordingly while limiting the influence of large compressive stresses, which are of less interest in the present investigation. Any compressive stresses exceeding -4.1 MPa (-600 psi) are represented by the deep blue indicated at -4.1 MPa (-600 psi). The values of the maximum and minimum stresses displayed in each figure are identified next to the ▲ and ▼ symbols, respectively.

As shown in Figure 5.16a, high tensile and compressive stresses developed around the vertical post-tensioning ducts. The maximum tensile stress was 6.5 MPa (944 psi), exceeding the measured tensile strength of the concrete, for which a maximum value of approximately 4.8 MPa (700 psi) was reported in Section 4.4.4. However, the stresses decrease rapidly with increasing distance from the ducts, and the areas away from the ducts generally have relatively low stresses.

The detail in Figure 5.16b includes deformation with an amplification factor of 230 and shows that the vertical duct is flattened by the horizontal post-tensioning loads. The deformation of the duct results in the compressive stresses extending from the duct

towards the front and back of the mock-up and the tensile stresses along the left and right sides of the duct and extending diagonally from the duct.

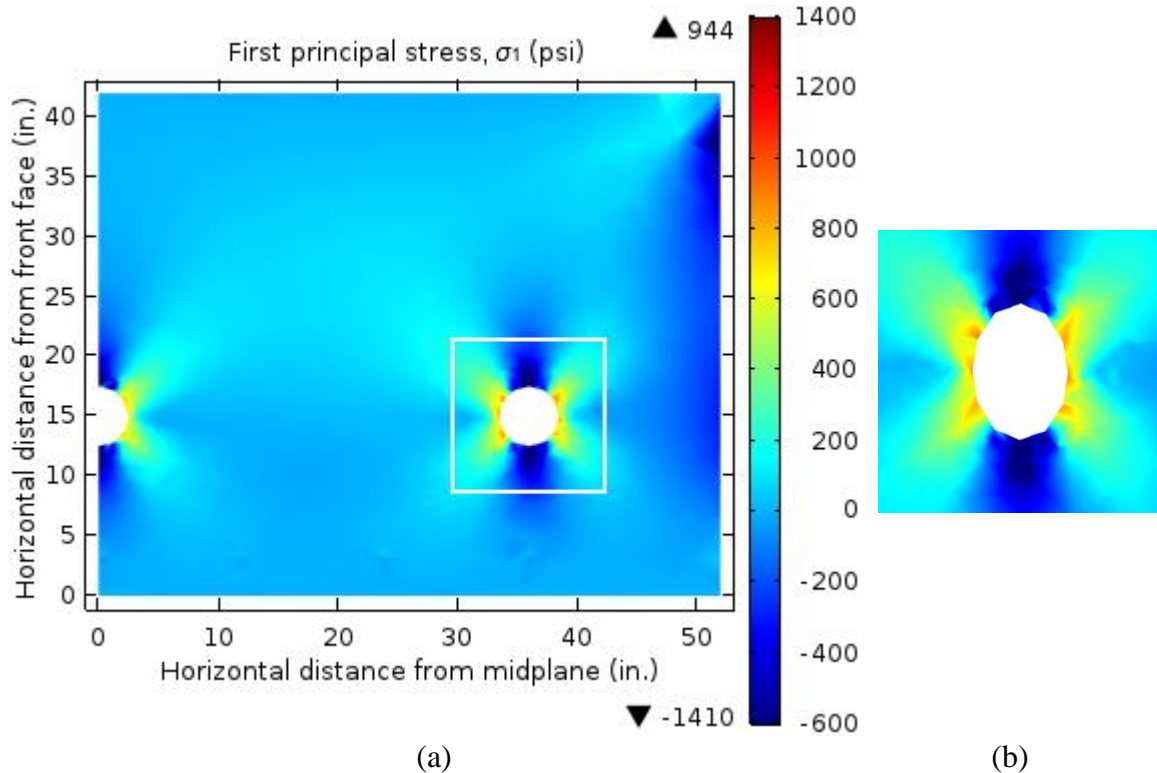


Figure 5.16: Plan view between horizontal ducts of modeled stresses in post-tensioned mock-up concrete, (a) full plan and (b) detail with deformation

In order to better understand the tensile cracking risk of the concrete, the stresses shown in Figure 5.16a were divided by the splitting tensile strength of the concrete at the same location, providing the first principal stress-to-splitting tensile strength ratio σ_1/f_{tsp} shown in Figure 5.17a. Analogous results are shown in Figure 5.17b for the horizontal plane at the top edge of a horizontal duct.

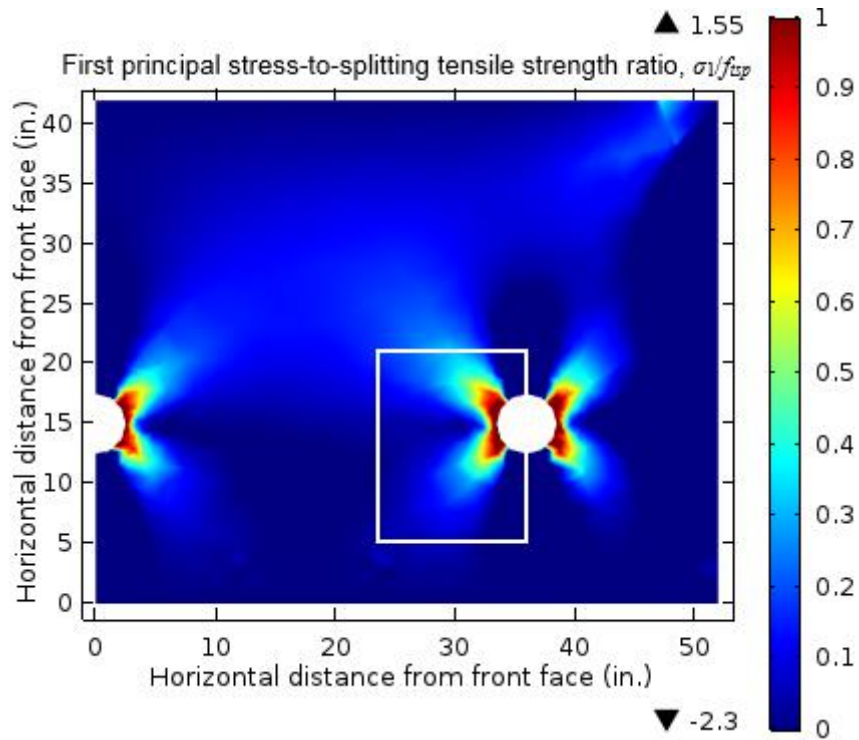
In each figure showing σ_1/f_{tsp} values, the ratios for the color scale range from 0 to 1. The range was selected so that all compressive stresses would be represented by deep blue and all tensile stresses greater than or equal to the splitting tensile strength would be represented by deep red. This allows quick identification of regions where tensile

cracking would be expected and allows comparison of the profiles amongst the different views presented and loading scenarios analyzed.

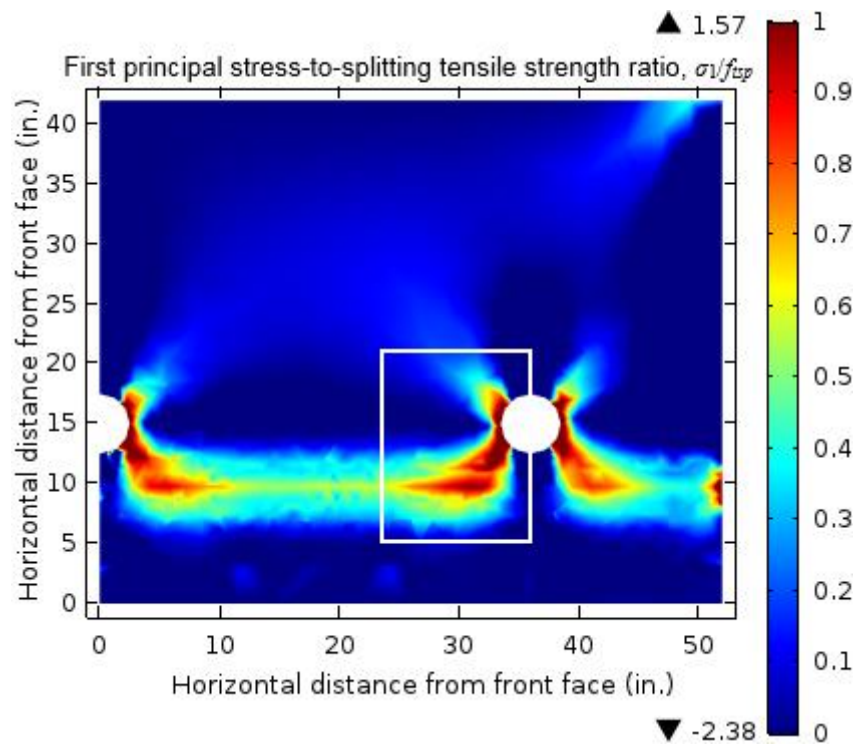
Figure 5.18 shows detail contours of the region adjacent to the vertical duct in Figure 5.17, where high σ_1/f_{tsp} values were predicted. In each figure showing detail contours of the σ_1/f_{tsp} values, the ratios for the contours range from 0 to 2.1 so that all presented tensile stresses would be included and colored accordingly.

As shown in Figure 5.17, cracking is expected along the left and right sides of the vertical ducts, and the high σ_1/f_{tsp} values extend along the horizontal duct when the plane of study approaches the horizontal ducts. Based on the potential for tensile creep failure at 50% of the tensile splitting strength, cracking would be expected along the edge of the horizontal duct as shown in Figure 5.17b except for the areas immediately in front of the vertical post-tensioning ducts, where the compressive stresses due to the flattening of the vertical duct limits the tensile stresses.

The details in Figure 5.18 show that maximum σ_1/f_{tsp} value along the vertical duct is approximately 1.6 both far from and near the horizontal ducts. However, the σ_1/f_{tsp} values decrease rapidly with increasing distance from the vertical ducts when away from the horizontal ducts. In contrast, σ_1/f_{tsp} values of approximately 1.0 extend along the horizontal duct in Figure 5.18b. These results indicate that tensile cracking could initiate along the edges of the post-tensioning ducts.



(a)



(b)

Note: Respective detail contours are shown in Figure 5.18

Figure 5.17: Plan views of modeled stress-to-splitting tensile strength ratio in post-tensioned mock-up concrete (a) between horizontal ducts and (b) at top edge of horizontal duct

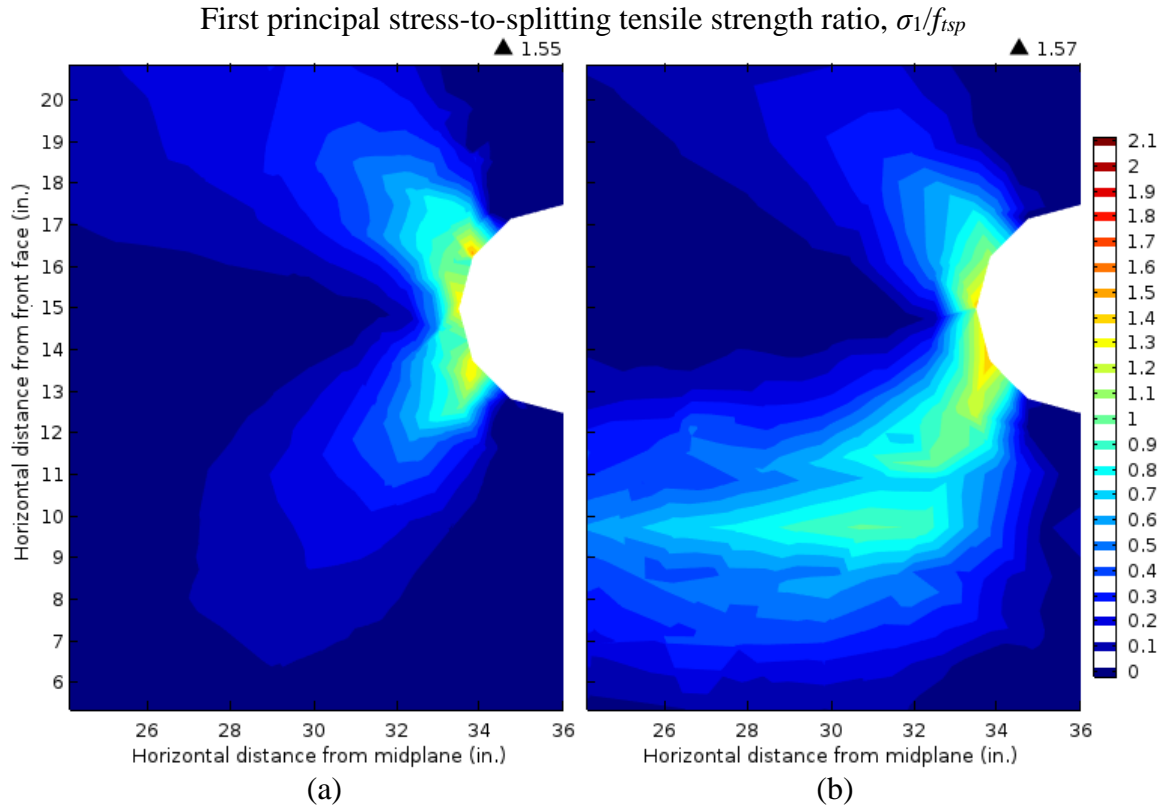


Figure 5.18: Plan details of modeled stress-to-splitting tensile strength ratio in post-tensioned mock-up concrete (a) between horizontal ducts and (b) at edge of horizontal duct

Figure 5.19 shows the first principal stresses in vertical planes through the thickness of the mock-up. The plane shown in Figure 5.19a is centered between the vertical ducts spaced at 914 mm (36 in.) on center and exhibits similar behavior to the horizontal plane shown in Figure 5.16a. The vertical post-tensioning loads flatten the horizontal ducts, resulting in compressive stresses extending horizontally from the ducts and tensile stresses extending diagonally from the ducts. Though the maximum tensile stress of 2.75 MPa (399 psi) in Figure 5.19a is approximately 40% of the maximum tensile stress near the vertical ducts in Figure 5.16a, the stress is approximately 57% of the maximum splitting tensile strength of the mock-up concrete and therefore susceptible to tensile creep failure.

In contrast, the maximum tensile stress in Figure 5.19b is 7.10 MPa (1030 psi), and comparably high tensile stresses extend along nearly the entire length of the vertical duct, interrupted only by the compressive stresses extending horizontally from the horizontal ducts. Similar to the behavior identified in the plan views, the tensile stresses decrease rapidly with increasing distance from the vertical duct, and the areas away from the ducts generally have relatively low stresses.

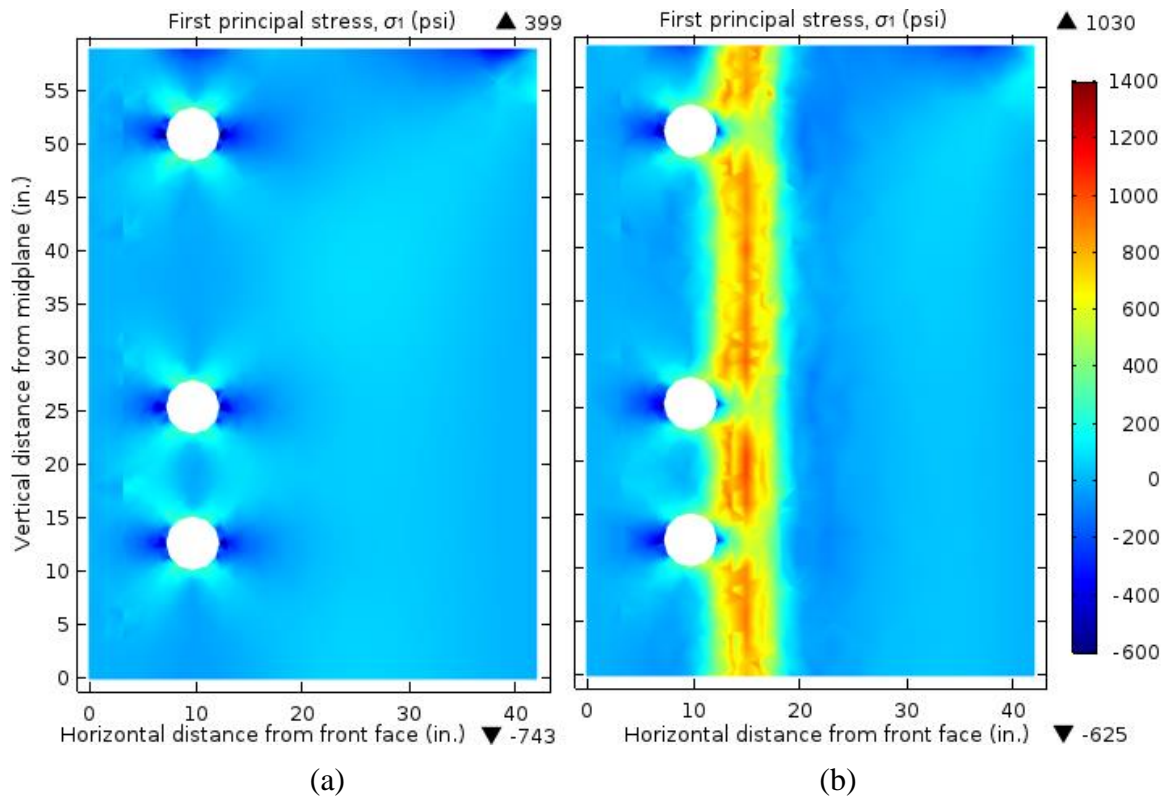
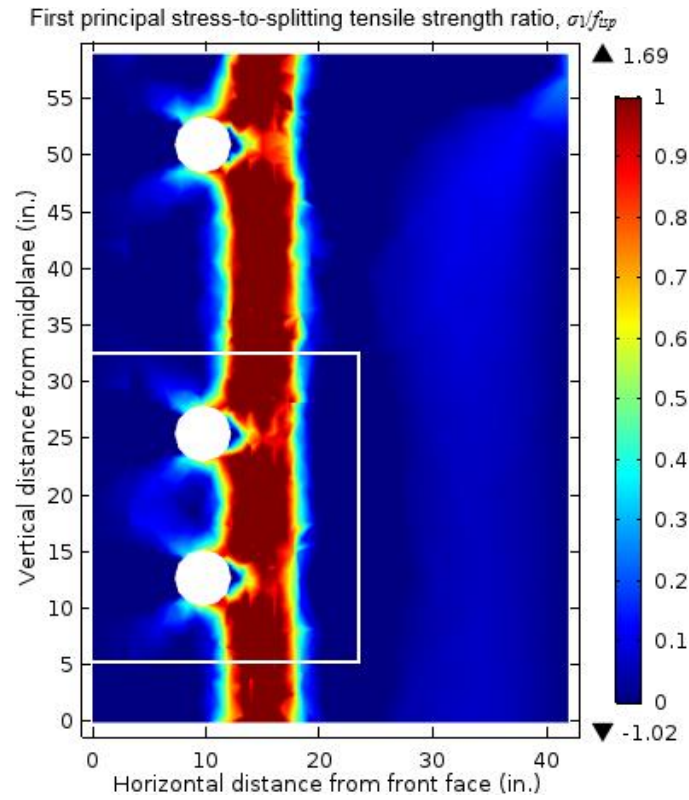


Figure 5.19: Transverse section view of modeled stresses in post-tensioned mock-up concrete (a) between vertical ducts and (b) at edge of vertical duct

Figure 5.20a illustrates the σ_1/f_{tsp} values in the vertical plane shown in Figure 5.19b, adjacent to the vertical duct. The σ_1/f_{tsp} values exceed 1.0 along nearly the entire length width of the vertical duct, indicating the cracking is very likely to initiate along the vertical ducts. As shown in Figure 5.20b, σ_1/f_{tsp} values comparable to the maximum of 1.69 extend along much of the length of the vertical duct. This behavior contrasts with

Figure 5.18b, in which the high σ_1/f_{tsp} values extended along the horizontal duct but decreased with increasing distance from the vertical duct.



(a)

Figure 5.20: Transverse section view of modeled stress-to-splitting tensile strength ratio in post-tensioned mock-up concrete at edge of vertical duct, (a) full section and (b) detail

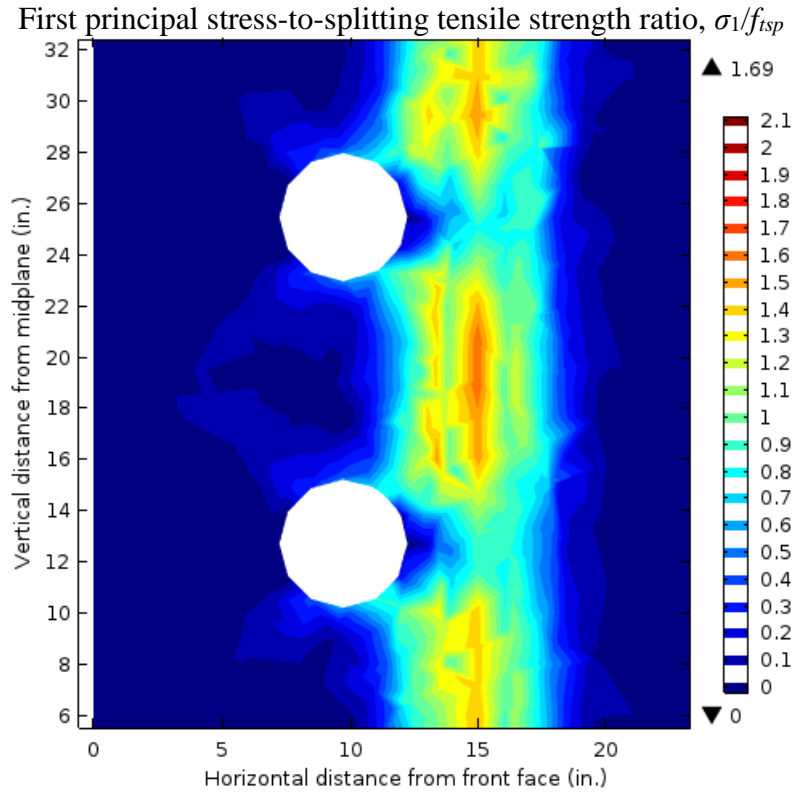


Figure 5.20 (continued)

Figure 5.21 shows the first principal stresses in the vertical plane of the horizontal ducts. The maximum tensile stresses of approximately 8.3 MPa (1200 psi) occur at the corners where the horizontal and vertical ducts overlap, and moderate tensile stresses extend along the tops and bottoms of the horizontal ducts and envelop areas of low tensile stresses or compressive stresses between the ducts.

Due to the flattening of the vertical ducts identified in Figure 5.16b, compressive stresses develop in line with the vertical ducts in Figure 5.21. The moderate tensile stresses extending diagonally from the vertical ducts in the plan view are seen on both sides of the compressive regions in Figure 5.21. As in the previous figures, the stresses decrease rapidly with increasing distance from the ducts.

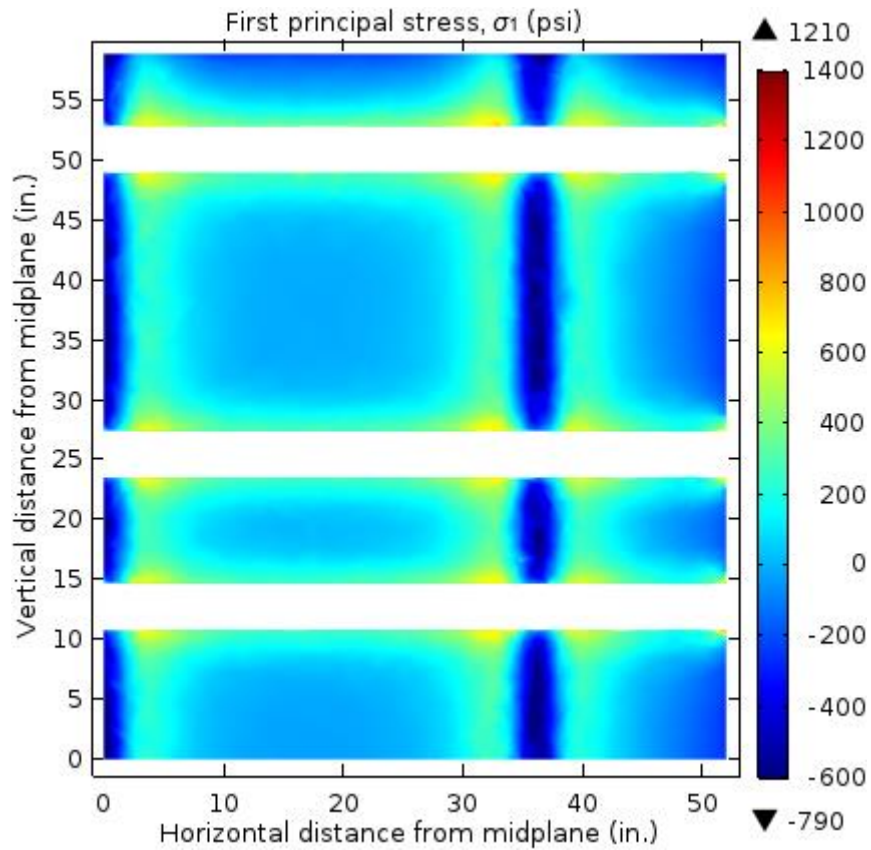


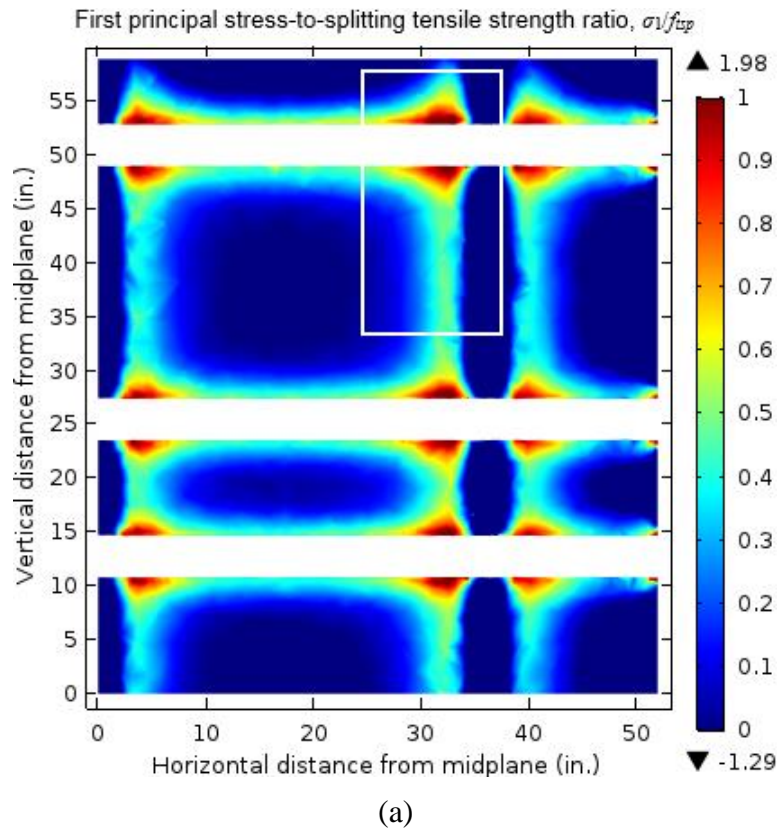
Figure 5.21: Longitudinal section view in plane of horizontal ducts of modeled stresses in post-tensioned mock-up concrete

Figure 5.22a shows the σ_1/f_{isp} values in the plane of the horizontal ducts, matching the location of Figure 5.21 and showing that the risk of crack initiation is high at the corners where the ducts overlap. Though moderate σ_1/f_{isp} values extend along the horizontal and vertical ducts, the stresses remote from the ducts are slightly tensile or compressive.

Figure 5.22b and Figure 5.22c show the σ_1/f_{isp} values in the plane of contact between the horizontal and vertical ducts and the plane of the vertical ducts, respectively. As the plane of study moves from the horizontal to vertical ducts, the concentration of high σ_1/f_{isp} values shifts increasingly to the vertical ducts. This behavior is also exhibited in the details in Figure 5.23. Though the highest σ_1/f_{isp} value, 1.98, occurs in the plane of the horizontal ducts (Figure 5.22a and Figure 5.23a), the stresses decrease so rapidly that

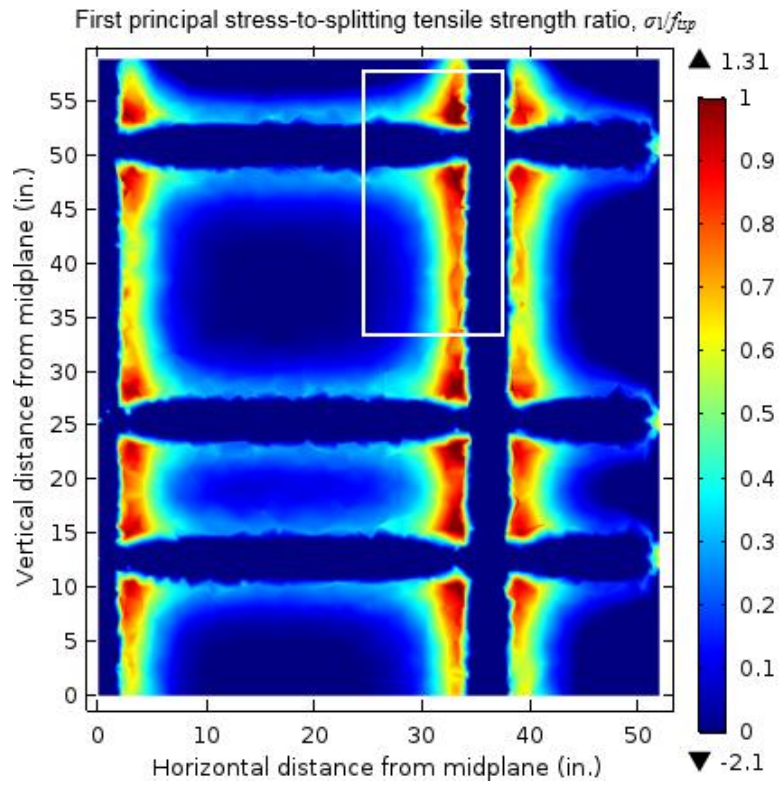
the high σ_1/f_{tsp} values in the plane of the vertical ducts are more extensive (Figure 5.22a and Figure 5.23a).

The high tensile stresses and σ_1/f_{tsp} values modeled near the post-tensioning ducts suggest that cracks were initiated in those regions of the mock-up and extended as much as 25 mm (1 in.) away from the ducts. However, fracture mechanics analysis would be needed to determine the extent of crack propagation into the regions of low tensile and compressive stresses between the ducts. This is discussed in Section 5.5.3.4.



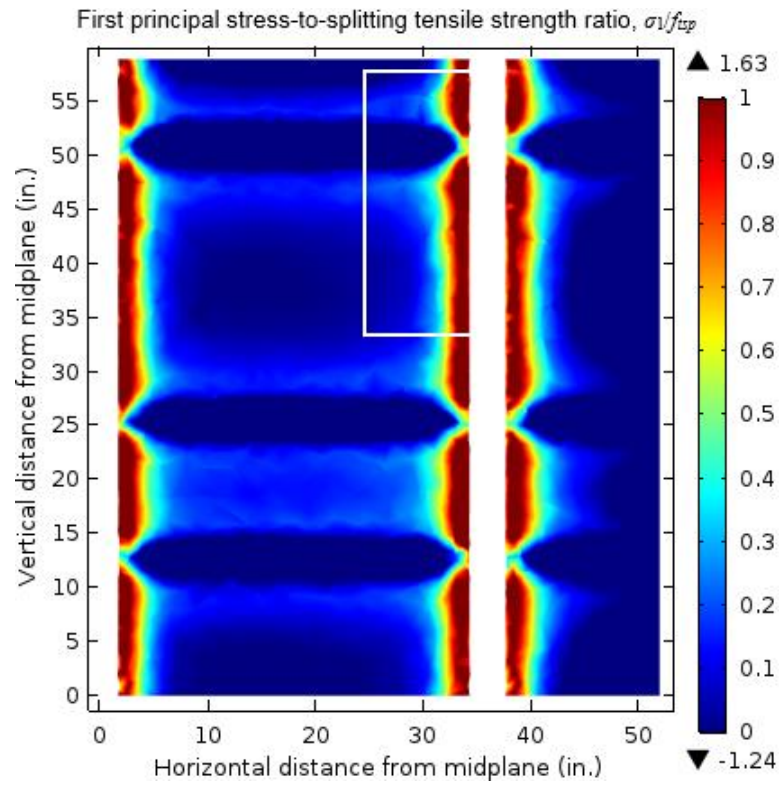
Note: Respective detail contours are shown in Figure 5.23

Figure 5.22: Longitudinal section views of modeled stress-to-splitting tensile strength ratio in post-tensioned mock-up concrete in (a) plane of horizontal ducts, (b) plane of contact between horizontal and vertical ducts, and (c) plane of the vertical ducts



(b)

(Figure 5.22 continued)



(c)
(Figure 5.22 continued)

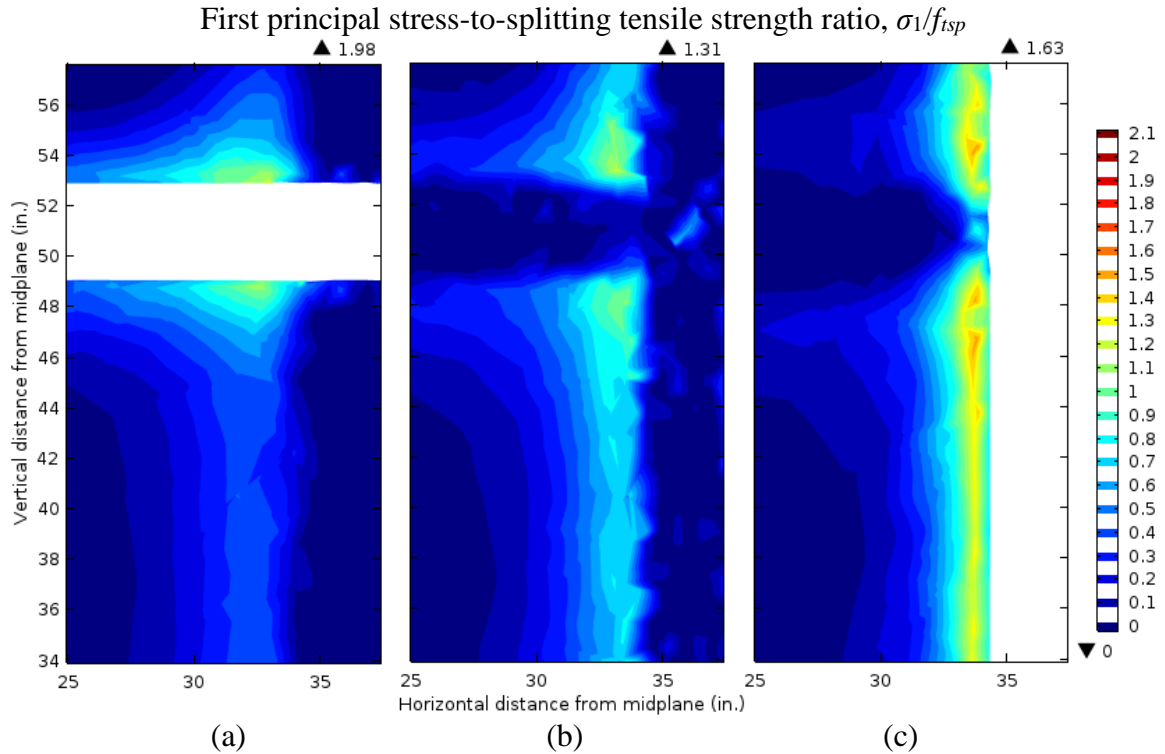


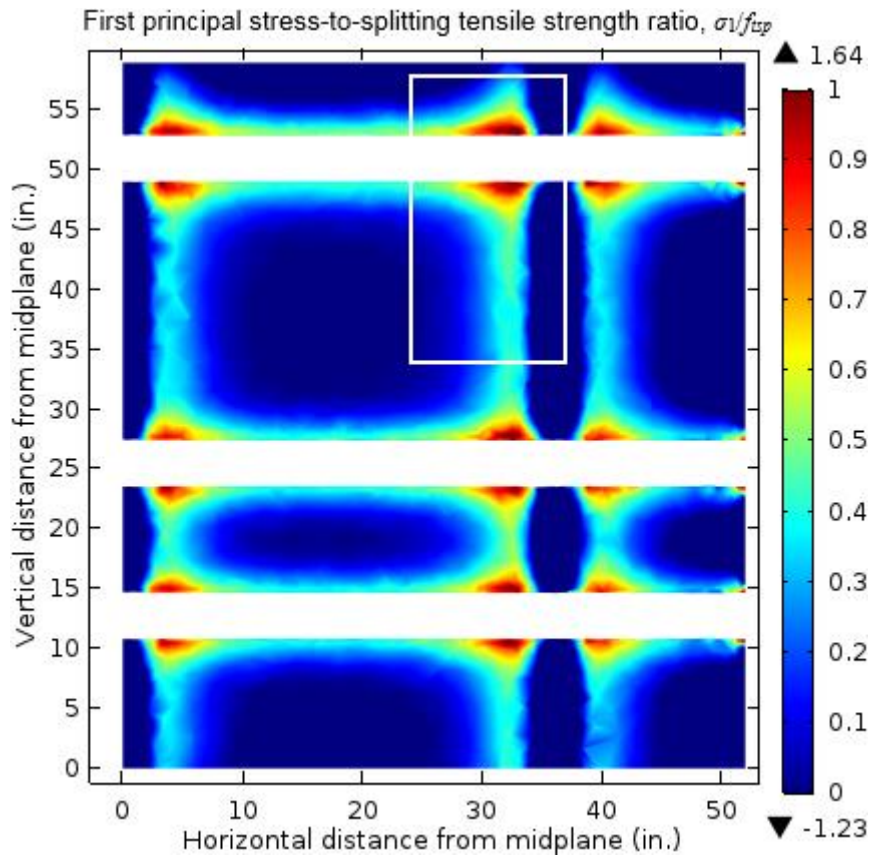
Figure 5.23: Longitudinal section details of modeled stress-to-splitting tensile strength ratio in post-tensioned mock-up concrete in (a) plane of horizontal ducts, (b) plane of contact between horizontal and vertical ducts, and (c) plane of the vertical ducts

Figure 5.24 is analogous to Figure 5.22a but for the case where the curing history was not accounted for. Whereas the prior results included residual thermal stresses and accounted for the influence of the high early-age concrete temperatures on the development of the concrete properties, the results in Figure 5.24 are based solely on tests of fog-cured specimens and the post-tensioning loads and are indicative of the results that would typically be obtained for analysis of such a structure without accounting for the curing history.

The profile of σ_1/f_{tsp} values in Figure 5.24 is comparable to that in Figure 5.22a, but the magnitudes of the ratios are reduced. The maximum σ_1/f_{tsp} value decreases by approximately 17% from 1.98 to 1.64 when the curing history is not accounted for. The decrease is due to the lack of residual stresses and the higher splitting tensile strength and modulus of elasticity of the concrete for the fog-cured condition.

Figure 5.25a shows the detail view of the results in Figure 5.24 for comparison with the results in Figure 5.25b (reproduced from Figure 5.23a) accounting for the curing history. When accounting for the curing history (Figure 5.25b), the general σ_1/f_{tsp} values are slightly higher, resulting in slightly larger contours than when the curing history is not accounted for (Figure 5.25a).

The lower σ_1/f_{tsp} values determined when not accounting for the curing history suggest a lower propensity for cracking in the plane of the post-tensioning ducts than is actually expected based on the curing history. However, aside from the maximum σ_1/f_{tsp} value, the difference between the two cases is not significant, indicating that the stress profiles and cracking risk are governed more by the post-tensioning loads than the curing history of the mock-up concrete.



Note: Detail contour is shown in Figure 5.25a
 Figure 5.24: Ratio of modeled stress to splitting tensile strength in plane of horizontal ducts without accounting for curing history

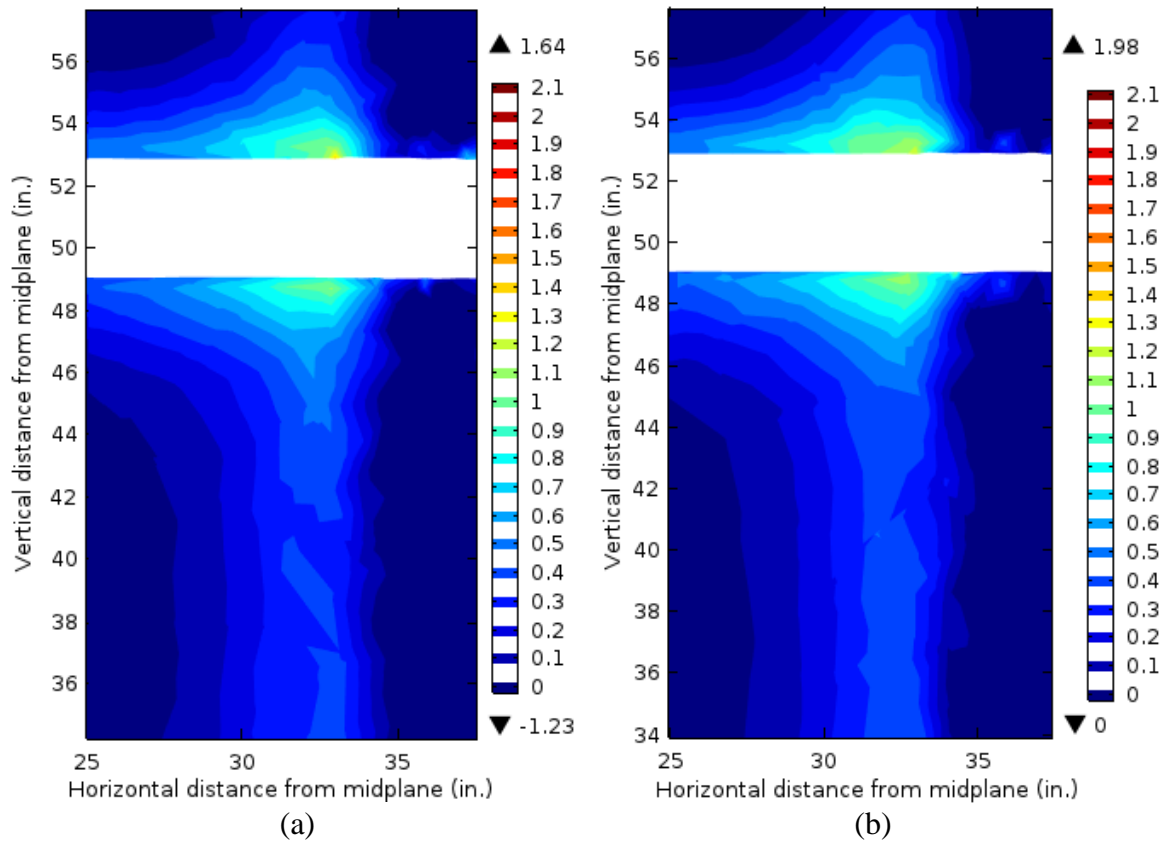


Figure 5.25: Longitudinal section details of modeled stress-to-splitting tensile strength ratio in plane of horizontal ducts (a) without accounting for curing history and (b) accounting for curing history

5.4.3.3 CR3 PCC Post-Tensioning Stresses

As discussed in Section 3.3.2, the mock-up was not loaded to the full 7228-kN (1625-kip) post-tensioning of the CR3 PCC for each tendon. As an extension of the previous results, analysis was conducted with the full CR3 PCC post-tensioning force applied, resulting in Figure 5.26 and Figure 5.27 accounting for the curing history of the mock-up. The maximum tensile stress in Figure 5.26 is 8.89 MPa (1290 psi), a 7% increase from the maximum stress of 8.34 MPa (1210 psi) in the same plane for the mock-up loading (Figure 5.21). Notably greater tensile stresses are seen along the top and bottom of the horizontal post-tensioning ducts in Figure 5.26 due to the greater vertical load applied.

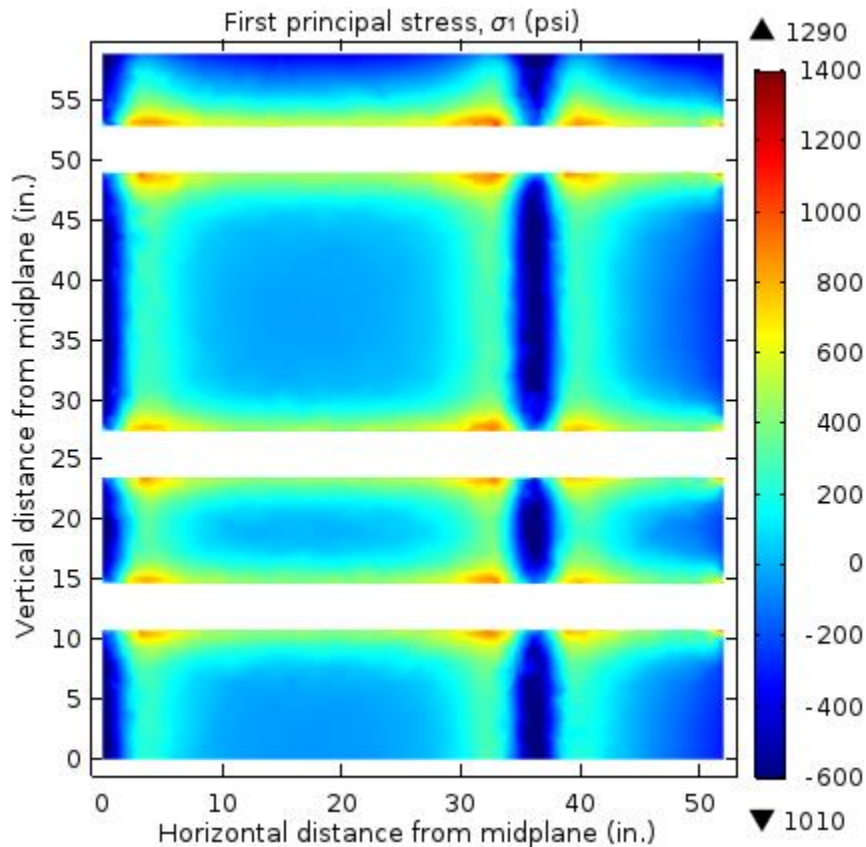
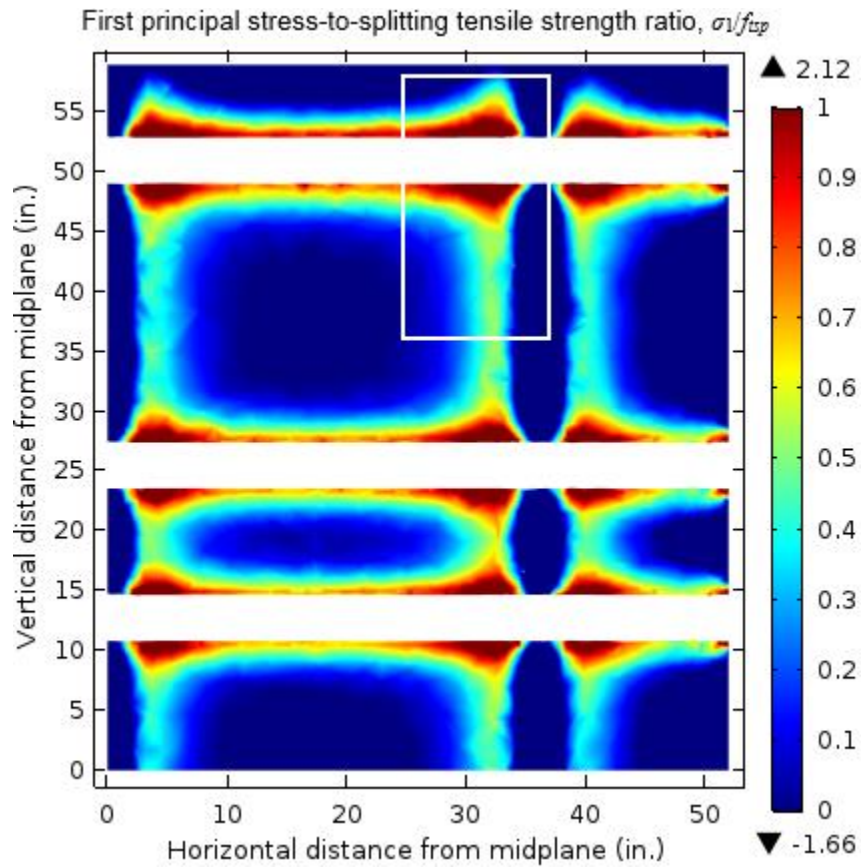


Figure 5.26: Modeled stresses in plane of horizontal ducts with CR3 PCC post-tensioning loads

In Figure 5.27, σ_1/f_{tsp} values approaching and exceeding unity are clearly visible along the top and bottom of the horizontal ducts between the vertical ducts, whereas such ratios in the mock-up loading (Figure 5.22a) were limited to the corners where the ducts overlapped. This suggests that cracking would be expected along nearly the entire length of the horizontal post-tensioning ducts in the CR3 PCC without accounting for the additional radial tensile stresses from the circumferential tendons.

Figure 5.28a shows the detail view of the results in Figure 5.27 for comparison with the results in Figure 5.28b (reproduced from Figure 5.23a) with the mock-up post-tensioning loads. The higher σ_1/f_{tsp} values extending a greater distance from the corner of the ducts in Figure 5.28a indicates that applying full CR3 PCC post-tensioning loads would result in greater cracking risk and more extensive cracking.



Note: Detail contour is shown in Figure 5.28a

Figure 5.27: Ratio of modeled stress to splitting tensile strength in plane of horizontal ducts with CR3 PCC post-tensioning loads

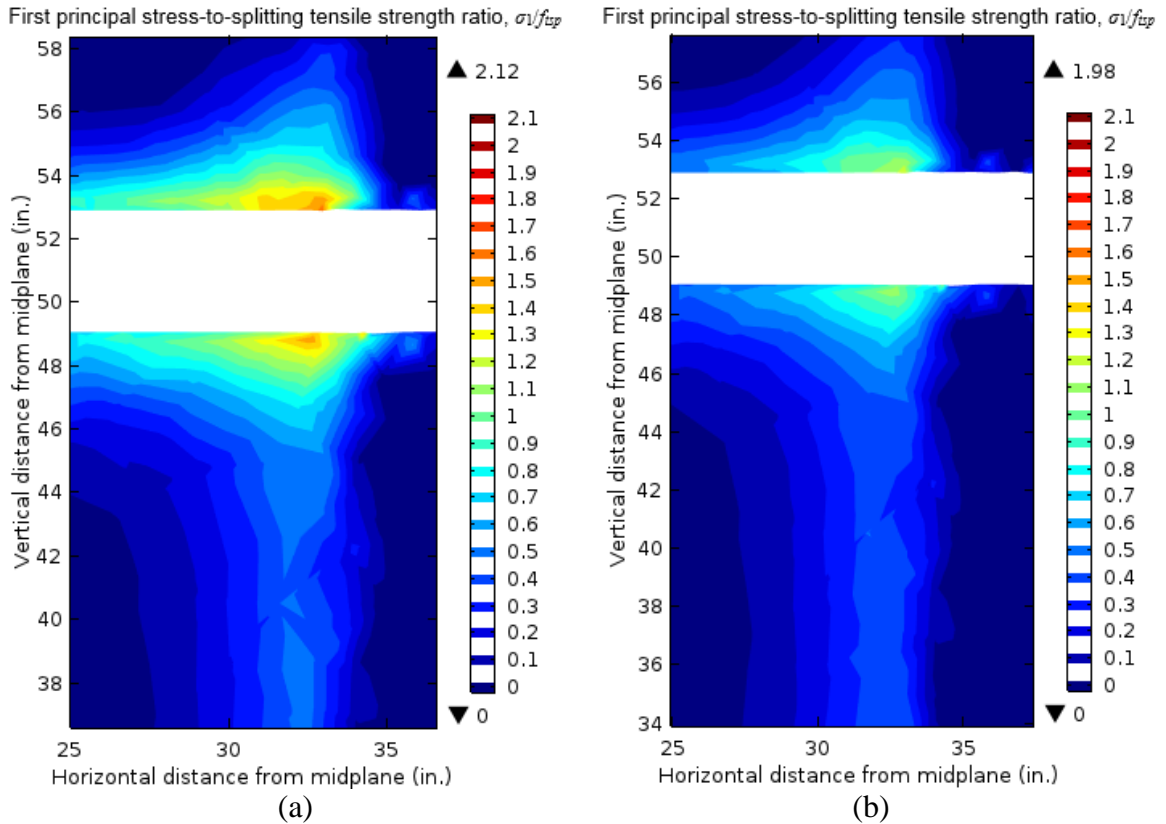


Figure 5.28: Detail contours of modeled stress-to-splitting tensile strength ratio in plane of horizontal ducts with (a) CR3 PCC post-tensioning loads and (b) mock-up post-tensioning loads

Analogous to Figure 5.24 for the mock-up loads, Figure 5.29 shows the σ_1/f_{tsp} values of the concrete with the full CR3 PCC loading without accounting for the curing history. Like the results for the mock-up loading, the profile of σ_1/f_{tsp} values in Figure 5.29 is comparable to that in Figure 5.27, but the maximum predicted σ_1/f_{tsp} value decreases by approximately 17% from 2.12 to 1.76 when the influence of the curing history is not accounted for. Therefore, analyzing the CR3 PCC based on fog-cured specimens predicts a lower propensity for cracking than when accounting for the curing history. Though the difference in general stress profiles was not significant for the investigated cases, the decreased σ_1/f_{tsp} values for fog-cured analysis indicate that failing to account for the curing history could result in overestimations of the capacity of a PCC

for scenarios where additional tensile stresses are developed, such as when accounting for the radial tensile stress generated by the circumferential tendons.

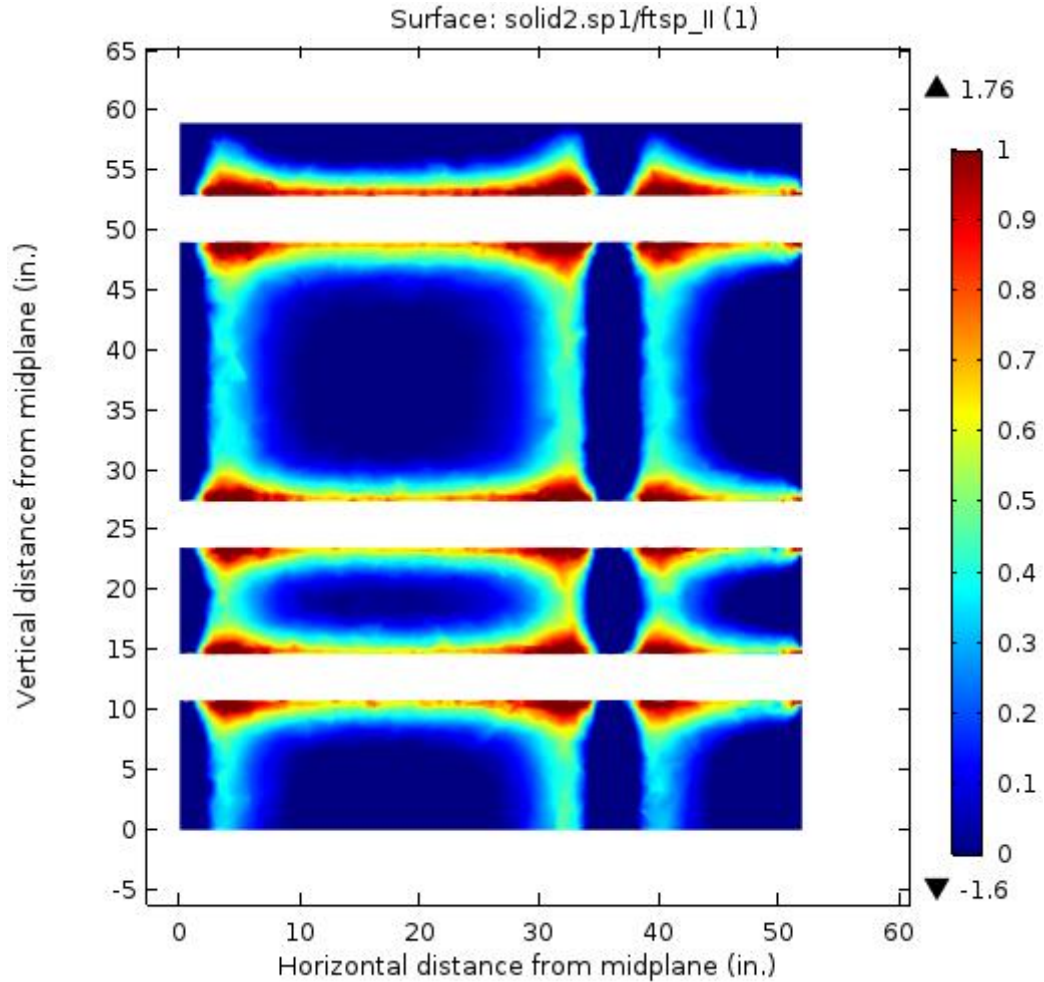


Figure 5.29: Ratio of modeled stress to splitting tensile strength in plane of circumferential ducts in CR3 PCC when post-tensioned without accounting for curing history

5.4.3.4 Discussion of Crack Propagation

Though fracture mechanics analysis was not conducted to model cracking in the mock-up, the qualitative behavior of concrete cracking can be predicted based on the modeled tensile stresses.

Typically, the highest tensile stresses in post-tensioning applications occur in the anchorage zone. However, in the case of the CR3 PCC delaminations, the extent of cracking was limited to individual bays during each occurrence (see Figure 2.7), failing to pass through the heavily reinforced buttresses where the post-tensioning anchorages were located. Similarly, sufficient reinforcement was provided in the anchorage zones of the mock-ups, but the lack of transverse reinforcement away from the anchorage zones leaves the region susceptible to cracking.

Since the coarse aggregate is typically the strongest component of concrete, cracks in concrete tend to propagate around the aggregate rather than through the aggregate (Bazant, 1985). Anderson (2005) notes that aggregates can bridge cracks, increase the toughness of the concrete and reducing crack propagation. However, as was shown in Figure 3.26 and discussed in Section 3.4.5.2, 70 to 80% of the limerock coarse aggregate in the mock-up concrete fractured along the plane of failure during 1-day splitting tensile strength testing. This indicates that the aggregate does not effectively arrest crack propagation through the concrete. The lack of transverse reinforcement and coarse aggregate with sufficient resistance to cracking suggests that crack propagation is likely once cracking has initiated in the plane of the horizontal ducts.

Based on the tensile stress-to-strength ratio contours, continuous cracks are expected to develop in the plane of the post-tensioning ducts along the edges of the vertical and horizontal ducts, encircling regions of low tensile stresses and compressive stresses. Accounting for potential tensile creep failure at 50% of the splitting tensile strength, these cracks are generally expected to propagate about 25 mm (1 in.) from the edge of the ducts. For the CR3 PCC loads, stresses exceeding 50% of the splitting tensile strength indicate cracks extending 51 to 76 mm (2 to 3 in.) from the edge of the ducts. Fracture mechanics analysis would be needed to determine the extent to which the cracks propagate further into the regions of low tensile and compressive stresses between the ducts.

Finally, the stresses modeled for the mock-up and CR3 PCC loads were based on biaxial post-tensioning alone. Adding the influence of radial tensile stress from the circumferential tendons of the CR3 PCC would result in greater tensile stresses in the plane of the circumferential ducts and a greater extent of crack propagation. Assuming continuous 51-mm (2-in.) cracks along the edges of the ducts, the nominal concrete area in the larger spaces between ducts would be reduced by 30%, resulting in higher tensile stresses when the radial stresses were applied. The lack of transverse reinforcement, the low strength of the limerock aggregate used in the concrete, and the high stresses developed in the concrete suggest that the CR3 PCC was susceptible to laminar cracking prior to the operations related to preparing the SGR opening in 2009.

5.5 Conclusions

Compared to ConcreteWorks, COMSOL Multiphysics is a more accurate and thorough modeling system for unique concrete members such as the experimental mock-up of the CR3 PCC. COMSOL is capable of reproducing ConcreteWorks results while also allowing full customization of the model components and parameters so that the influence of post-tensioning ducts, rebar, and steel plates can be modeled. Additionally, COMSOL allows mechanical analysis of the response to externally applied loads such as post-tensioning loads. The accuracy of the thermal models, however, is conditional upon accurate determination or selection of hydration parameters and thermal properties, and values determined for cement pastes may not be representative for concretes containing the cement paste.

Finite element analysis in COMSOL that accounted for the curing history of the mock-up showed that tensile stresses that exceed the splitting tensile strength by up to 98% develop in the plane of the horizontal ducts when the mock-up post-tensioning loads are applied. Contours of the tensile stress-to-splitting tensile strength ratio σ_1/f_{tsp} indicated that cracks would initiate along the edges of the ducts and extend at least 25 mm (1 in.)

from the ducts. When extended to the full post-tensioning loads of the CR3 PCC, the tensile stresses exceeding the splitting tensile strength continued along nearly the entire length of the horizontal post-tensioning ducts, and cracks would be expected to extend as much as 76 mm (3 in.) from the ducts.

Therefore, the analysis predicts tensile cracking in the plane of the horizontal ducts prior to the detensioning of the CR3 PCC for the steam generator replacement (SGR) opening in 2009. Though the tensile stresses decrease rapidly with increasing distance from the ducts, the results did not account for the radial tensile stress generated by the circumferential tendons of the CR3 PCC, suggesting that the stresses identified in this chapter would be exacerbated in a cylindrical structure. Nonlinear fracture mechanics analysis is needed to predict the extent of crack propagation in the mock-up and the CR3 PCC.

Comparing the analysis cases accounting for the concrete curing history with those that did not account for the curing history shows that the general stress behavior is largely governed by the post-tensioning loads rather than the thermal stresses. When not accounting for the curing history, the maximum σ_1/f_{tsp} values decreased by approximately 17%, indicating that such analysis could underestimate the cracking risk of a structure. However, the influence was limited to the maximum stress concentrations since the stress profiles in the corresponding cases were otherwise comparable. The primary source of the tensile stresses under the biaxial post-tensioning loads was the deformation at the duct openings, which warrants further investigation of the compatibility between post-tensioning ducts and mass concrete.

CHAPTER 6

PARAMETER STUDY

6.1 Introduction

In the previous chapter, regions of high tensile stresses indicative of concrete cracking were identified in the plane of the post-tensioning ducts in a model of the mock-up. Though residual tensile stresses from the curing history of the mock-up concrete contributed to the results, the behavior was largely governed by stresses due to the post-tensioning loads. In order to better understand the factors influencing the stresses in the mock-up, a parametric study of the concrete material properties and duct geometry was conducted. Nine points were selected in the plane of the horizontal post-tensioning ducts for evaluation of the stress-to-splitting tensile strength ratio σ_1/f_{tsp} as the parameters were individually varied. Since the stresses from post-tensioning are of primary interest, the COMSOL Multiphysics model utilized in the parametric study was based on the assumption of fog-cured conditions and did not account for the curing history of the mock-up concrete.

6.1.1 Objectives

The objectives of this chapter are to determine the influence of material and geometry parameters on the tensile cracking risk of the CR3 PCC concrete and to identify design approaches that could reduce the risk of cracking.

6.2 Description

The following parameters were investigated in this study: the concrete splitting tensile strength f_{tsp} , modulus of elasticity E_c , and Poisson's ratio ν ; the duct outer

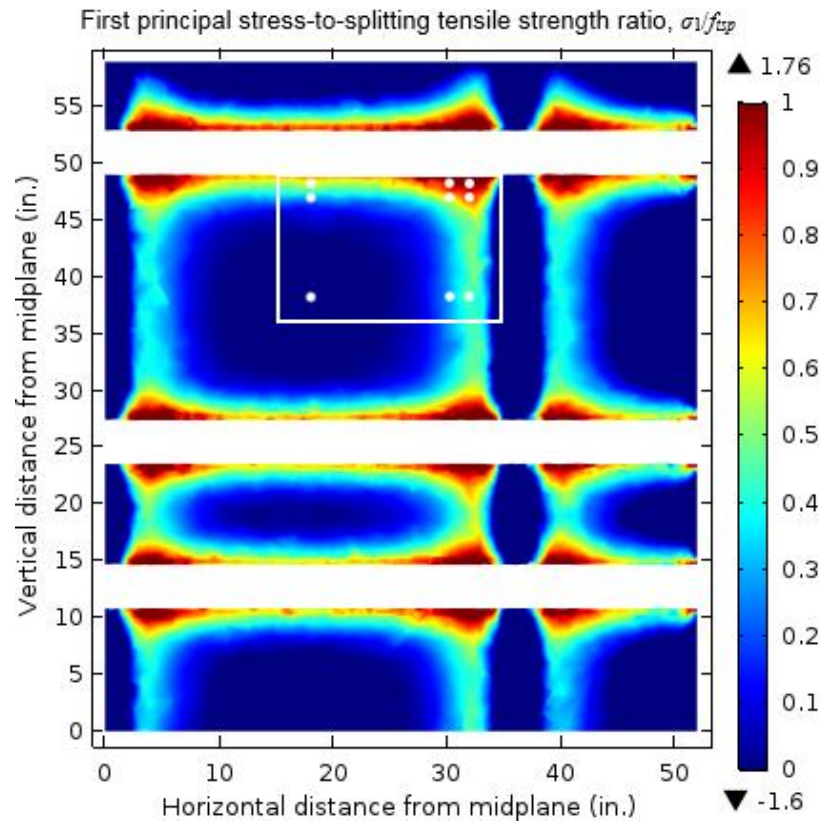
diameter D_{duct} , wall thickness t_{duct} , and modulus of elasticity E_{duct} ; and the vertical, horizontal, and biaxial post-tensioning forces P_v , P_h , and P_b . These parameters and the corresponding values are listed in Table 6.1. With all other parameters held constant at the respective baseline values, each parameter was implemented at 50, 75, 133, and 200% of the baseline value in the mock-up assuming fog-cured conditions for the concrete. Due to limitations of the mock-up geometry, the duct diameter was not implemented at 200% of the original 127-mm (5-in.) value. The baseline results of the parameter study were determined with the CR3 PCC post-tensioning load of 7228-kN (1625-kip) for each tendon.

Table 6.1: Values of investigated parameters

Parameter	Parameter Value				
	50%	75%	100%	133%	200%
Splitting tensile strength, f_{isp} (psi)	327	490	653	871	1,306
Concrete modulus of elasticity, E_c (ksi)	2,262	3,393	4,525	6,033	9,049
Concrete Poisson's ratio, ν	0.10	0.15	0.20	0.27	0.40
Duct diameter, D_{duct} (in.)	2.50	3.75	5.00	6.67	-
Duct wall thickness, t_{duct} (in.)	0.06	0.09	0.12	0.16	0.24
Duct modulus of elasticity, E_{duct} (ksi)	14,863	22,294	29,725	39,633	59,450
Post-tensioning force, P_v, P_h, P_b (kip)	812	1,219	1,625	2,167	3,250

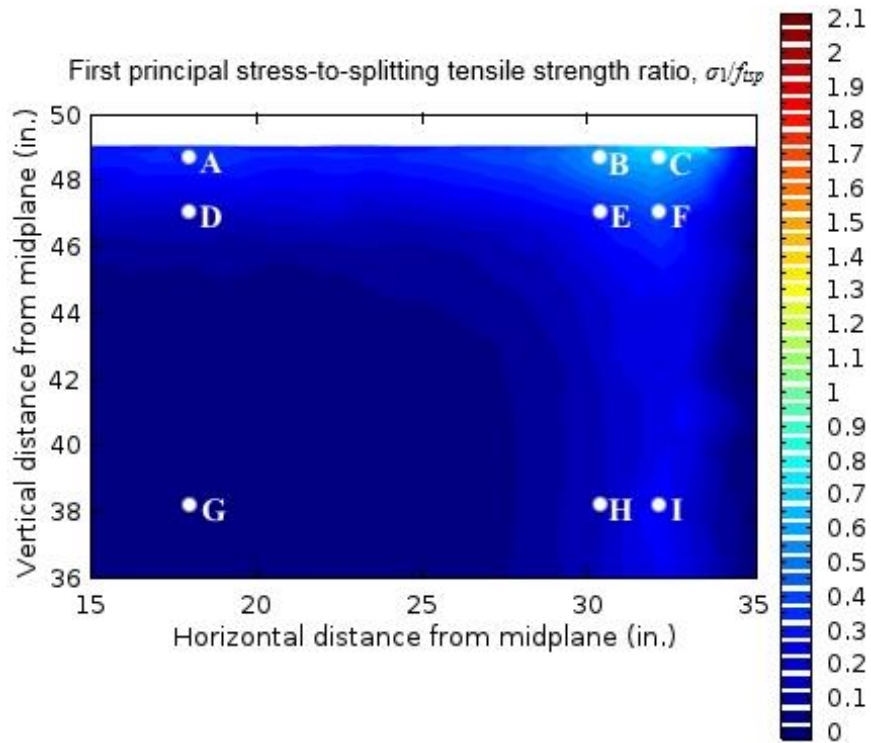
Figure 6.1 shows the baseline σ_1/f_{isp} results and the location of the nine points selected in the plane of the horizontal post-tensioning ducts for evaluation of the σ_1/f_{isp} values as the parameters were varied. Points A, B, and C were located along the lower edge of the top horizontal duct, points D, E, and F were located 38 mm (1.5 in.) below the previous row, and points G, H, and I were located halfway between the horizontal

ducts spaced at 648 mm (25.5 in.) on center. Similarly, points C, F, and I were located 13 mm (0.5 in.) from the edge of the vertical duct, points B, E, and H were located 38 mm (1.5 in.) to the left of the previous column, and points A, D, and G were located halfway between the vertical ducts spaced at 914 mm (36 in.). When the diameter of the ducts was varied, all points except for point G were shifted accordingly to maintain the same distance from the nearest duct surfaces. As shown in Figure 6.1, the σ_1/f_{tsp} values in the area of study decreased the with increasing distance from the ducts, with point C having the highest σ_1/f_{tsp} value and point G having the lowest σ_1/f_{tsp} value.



(a)

Figure 6.1: Longitudinal section view of modeled stress-to-splitting tensile strength ratio with points of evaluation identified, (a) full section and (b) detail



(b)
Figure 6.1 (continued)

6.3 Results and Discussion

The results of the parameter study are presented and discussed in the following sections. For each figure, the legend is arranged to represent the relative orientation of the points in Figure 6.1, and the colors transition from red to purple as the distance from the corner of the ducts increased, corresponding to decreasing baseline σ_1/f_{tsp} values. For a diagonal line between points C and G, the points on either side can be approximated as being symmetric, so the results at points B, A, and D were colored to match the results at Points F, I, and H, respectively. This allows easy identification of parameters that influence the σ_1/f_{tsp} values differently depending on proximity to either duct.

6.3.1 Concrete Material Properties

The results of the parameter study for the concrete splitting tensile strength f_{tsp} , modulus of elasticity E_c , and Poisson's ratio ν are presented in Figure 6.2, Figure 6.3, and Figure 6.4, respectively. Since the σ_1/f_{tsp} value is determined by dividing the stress σ_1 at each point by the tensile splitting strength f_{tsp} , the inverse relationship exhibited in Figure 6.2 is expected. The increasing values at point G with increasing splitting tensile strength are due to the negative (compressive) stresses at that point, for which the magnitude of the σ_1/f_{tsp} value decreases with increasing tensile strength. As shown in Figure 6.2a, the influence of the splitting tensile strength is proportional to the magnitude of the σ_1/f_{tsp} value, resulting in greatest variation at point C and least variation at point G.

Figure 6.2b shows the values presented in Figure 6.2a normalized by corresponding baseline value at each point, resulting in a relative σ_1/f_{tsp} value of 1.0 at each point for a splitting tensile strength of 4.5 MPa (653 psi). Since the influence of the tensile strength is proportional to the magnitude of the σ_1/f_{tsp} value, the relative σ_1/f_{tsp} values in Figure 6.2b were equivalent at each point. As expected, decreasing the splitting tensile strength by 50% to 2.25 MPa (327 psi) results in the σ_1/f_{tsp} value doubling at each point, whereas doubling the splitting tensile strength to 9.0 MPa (1,306 psi) results in the σ_1/f_{tsp} value decreasing by half.

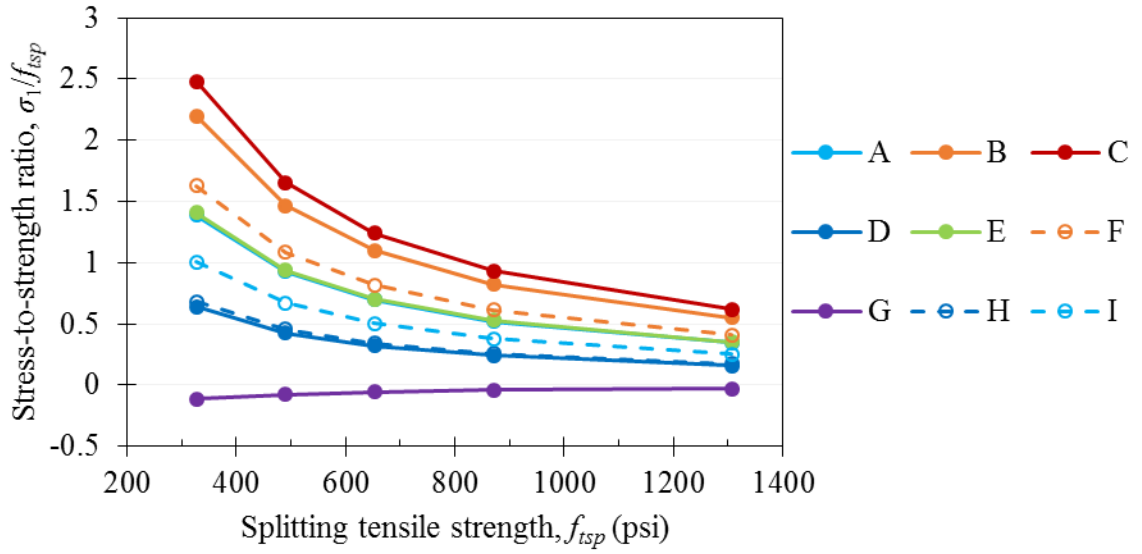
As shown in Figure 6.2, the nonlinear relationship between σ_1/f_{tsp} and the splitting tensile strength results in increasingly higher σ_1/f_{tsp} values for lower tensile strengths. Therefore, reductions in tensile strength would greatly increase the tensile cracking risk of the concrete. On the other hand, increasing the tensile strength decreases the σ_1/f_{tsp} values but at a decreasing rate.

As shown in Figure 6.3, increasing the concrete modulus of elasticity resulted in a slight decrease in the σ_1/f_{tsp} values at points B and C, where the σ_1/f_{tsp} values were greatest. The σ_1/f_{tsp} value also decreased at points A, D, and G, all located halfway between vertical ducts. In contrast, the σ_1/f_{tsp} value increased at points E, F, H, and I,

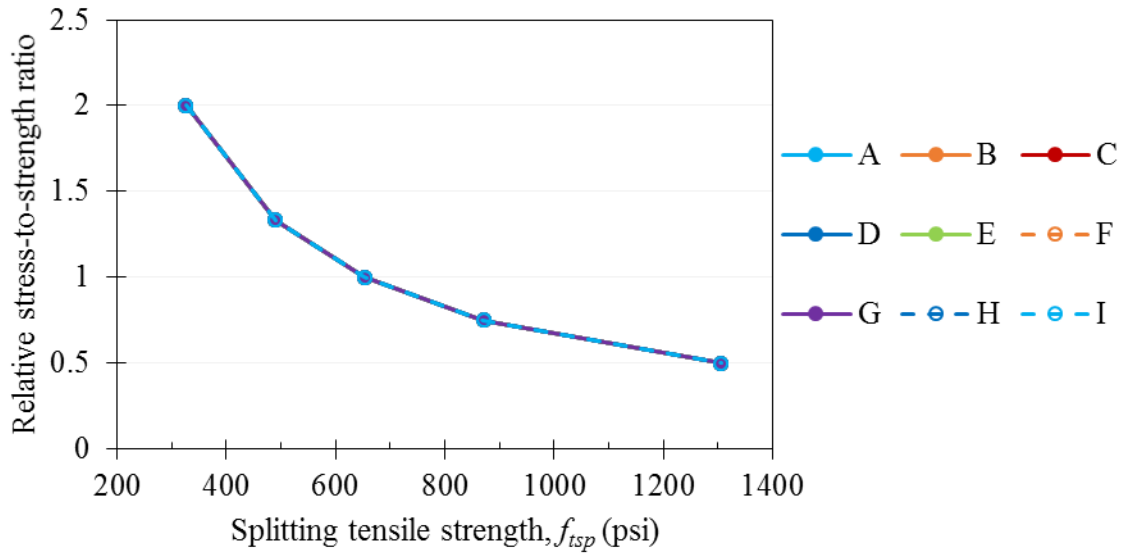
which are in the lower right corner of the grid. As shown in Figure 6.3b, the relative influence of the concrete modulus of elasticity varies by point. The relatively wide variation at point G was due to the low σ_1/f_{tsp} magnitudes at that point; since the stresses are compressive at point G, the vertical axis in Figure 6.3b was scaled without consideration for the values at point G. The relative variation at all other points was generally within 10% of the baseline value for modulus of elasticity values ranging from 15.6 to 62.4 GPa (2,262 to 9,049 ksi).

Though the σ_1/f_{tsp} values at points B and C were still greater than unity when the concrete modulus of elasticity was doubled, increasing the modulus may be an effective means of reducing the cracking risk at the points most susceptible to cracking and could be coupled with other improvements to decrease the overall cracking risk.

As shown in Figure 6.4, the influence of the concrete Poisson's ratio at each point was slight, similar to the influence of the concrete modulus of elasticity. As Poisson's ratio increased, the σ_1/f_{tsp} values decreased at points D, G, H, and I. In contrast, the points closer to the corner of the ducts exhibited slight increases in the σ_1/f_{tsp} values as Poisson's ratio increased. The relative variation at all points except for point G was generally within 5% of the baseline value for Poisson's ratio values ranging from 0.10 to 0.40. However, the Poisson's ratio for concrete typically ranges from 0.15 to 0.20 (Mehta and Monteiro, 2006), so the Poisson's ratio has negligible influence on the σ_1/f_{tsp} values for practical applications.

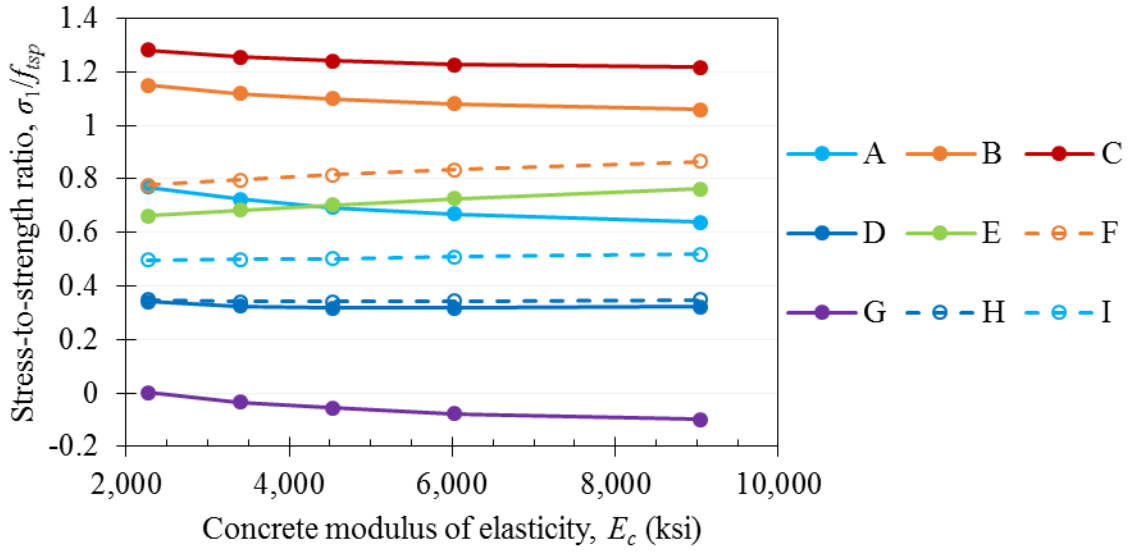


(a)

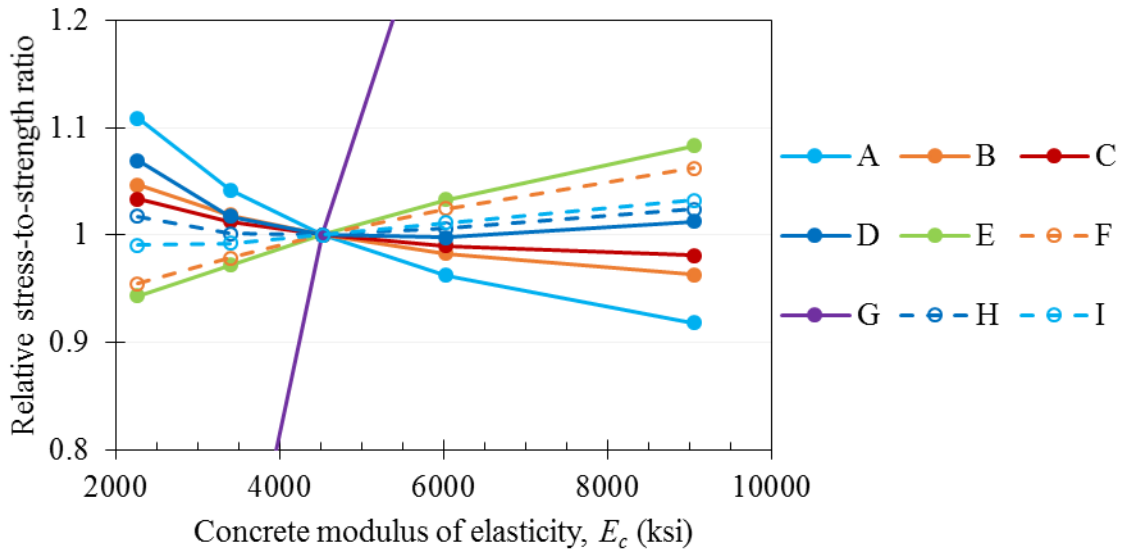


(b)

Figure 6.2: Influence of concrete splitting tensile strength on the (a) σ_1/f_{isp} values at each point and (b) relative σ_1/f_{isp} values at each point

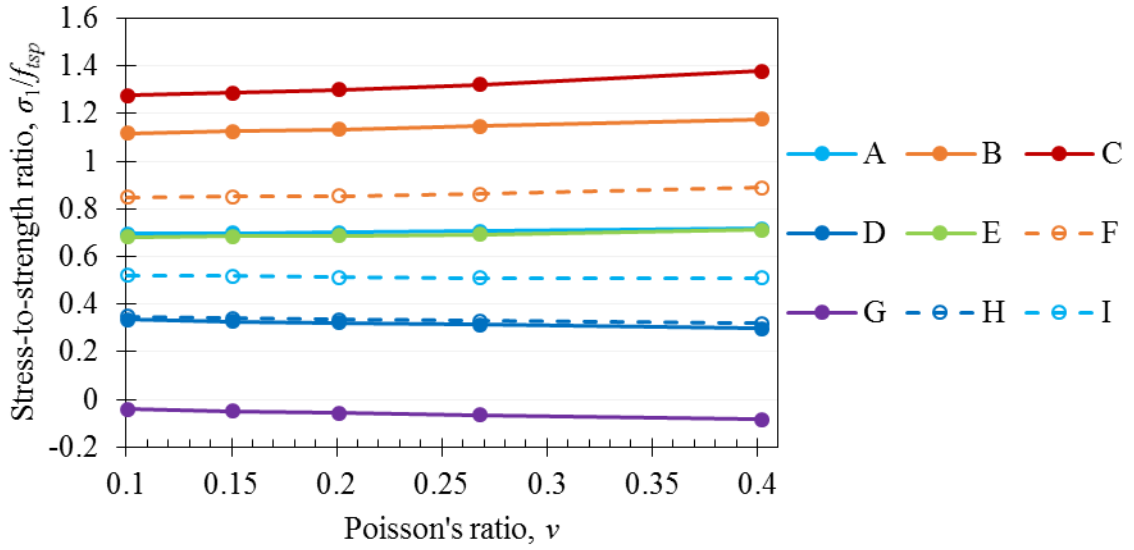


(a)

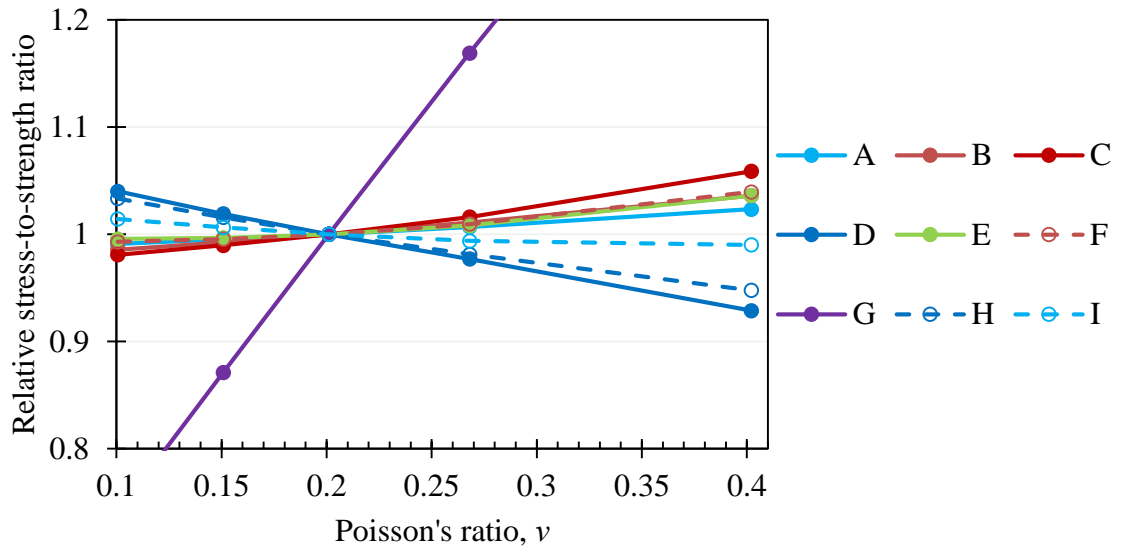


(b)

Figure 6.3: Influence of concrete modulus of elasticity on the (a) σ_1/f_{isp} values at each point and (b) relative σ_1/f_{isp} values at each point



(a)



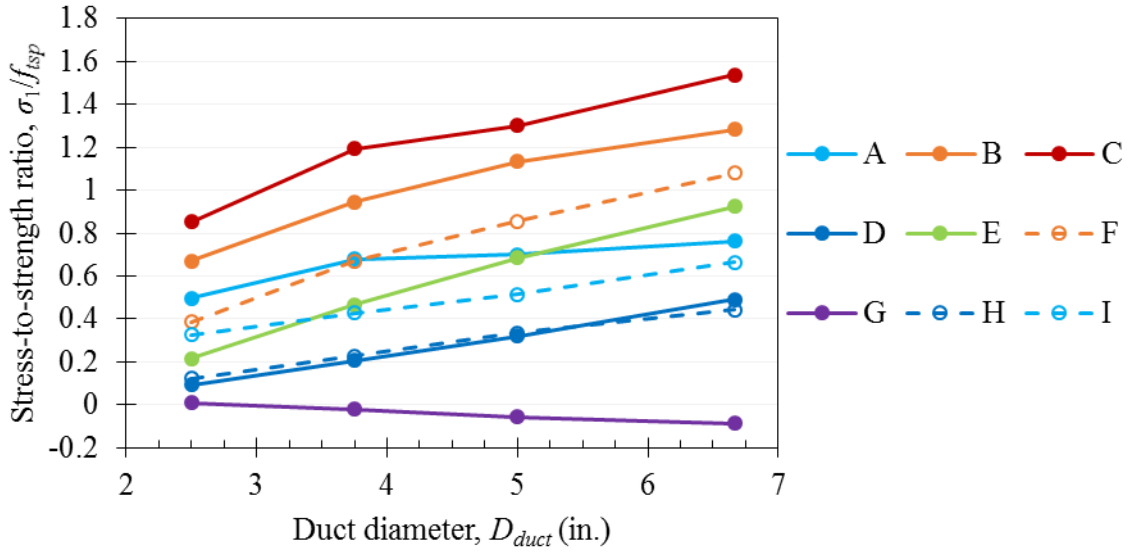
(b)

Figure 6.4: Influence of concrete Poisson's ratio on the (a) σ_1/f_{tsp} values at each point and (b) relative σ_1/f_{tsp} values at each point

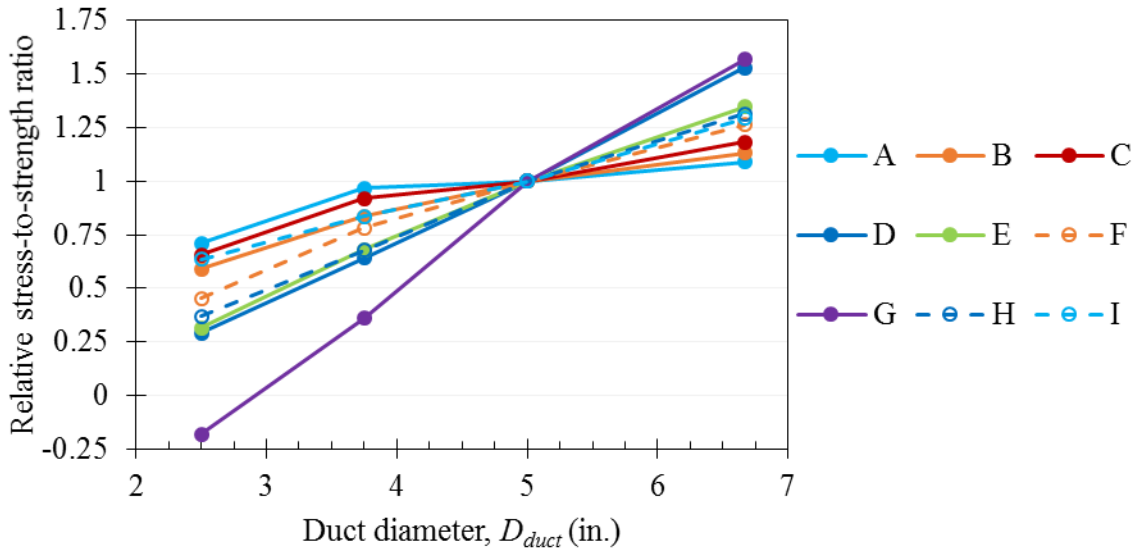
6.3.2 Duct Geometry and Modulus of Elasticity

The results of the parameter study for the duct diameter D_{duct} , duct wall thickness t_{duct} , and duct modulus of elasticity E_{duct} are presented in Figure 6.5, Figure 6.6, and Figure 6.7, respectively. As shown in Figure 6.5, increasing the duct diameter increases the tensile stresses in the concrete at each point except for point G, where the stresses become more compressive. A contributing factor to this behavior is the decreasing area of concrete in the plane of the ducts as the duct diameter is increased. Compared to the influence of the concrete modulus of elasticity and Poisson's ratio, the influence of the duct diameter is significant. As shown in Figure 6.5b, the σ_1/f_{isp} values at all points except for point G decrease to approximately 25 to 75% of the baseline value when the duct diameter is halved to 64 mm (2.5 in.). Conversely the σ_1/f_{isp} values increase to approximately 110 to 150% of the baseline value when the duct diameter is increased by 33% to 169 mm (6.7 in.).

As shown in Figure 6.6 and Figure 6.7, the influence of the duct wall thickness and modulus of elasticity is identical. The parameters have negligible influence on the σ_1/f_{isp} value at point C, where the maximum stresses occur. However, as the duct wall thickness or modulus of elasticity was increased, the σ_1/f_{isp} value increased at points A and B, which are near the horizontal duct, and decreased at points E, F, H, and I, which are near the vertical duct. The relative variation at all points except for point G was generally within 10% of the baseline value for wall thicknesses ranging from 1.5 to 6.0 mm (0.06 to 0.24 in.) and duct modulus of elasticity values ranging from 102.5 to 409.9 GPa (14,863 to 59,450 ksi).

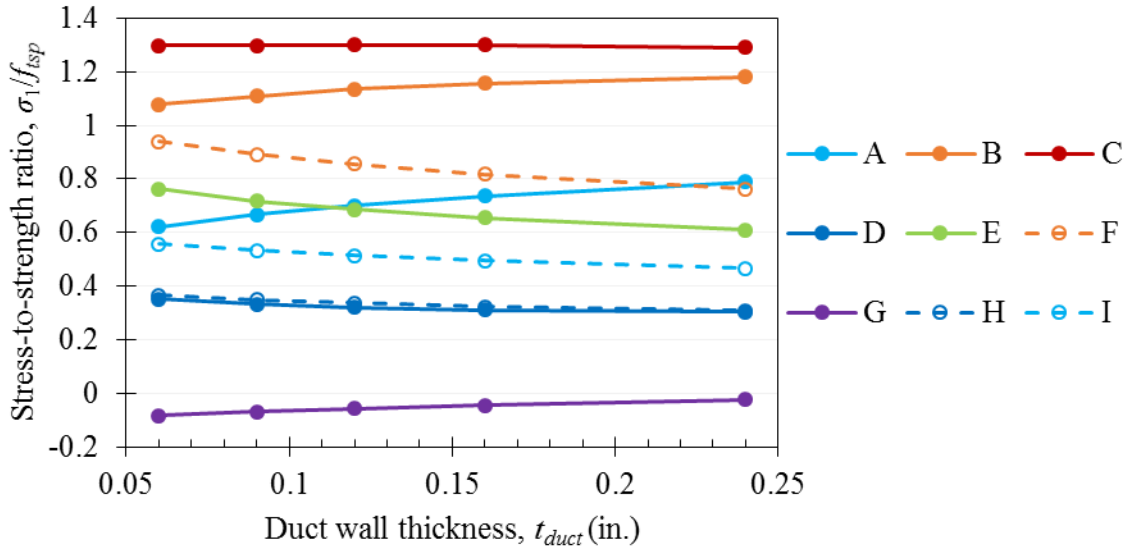


(a)

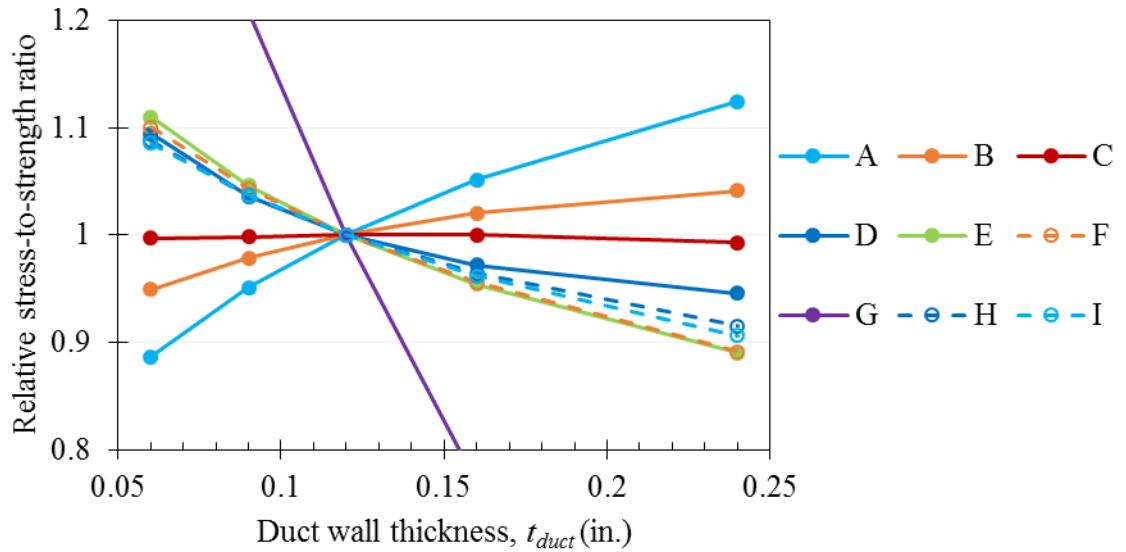


(b)

Figure 6.5: Influence of duct diameter on the (a) σ_1/f_{isp} values at each point and (b) relative σ_1/f_{isp} values at each point

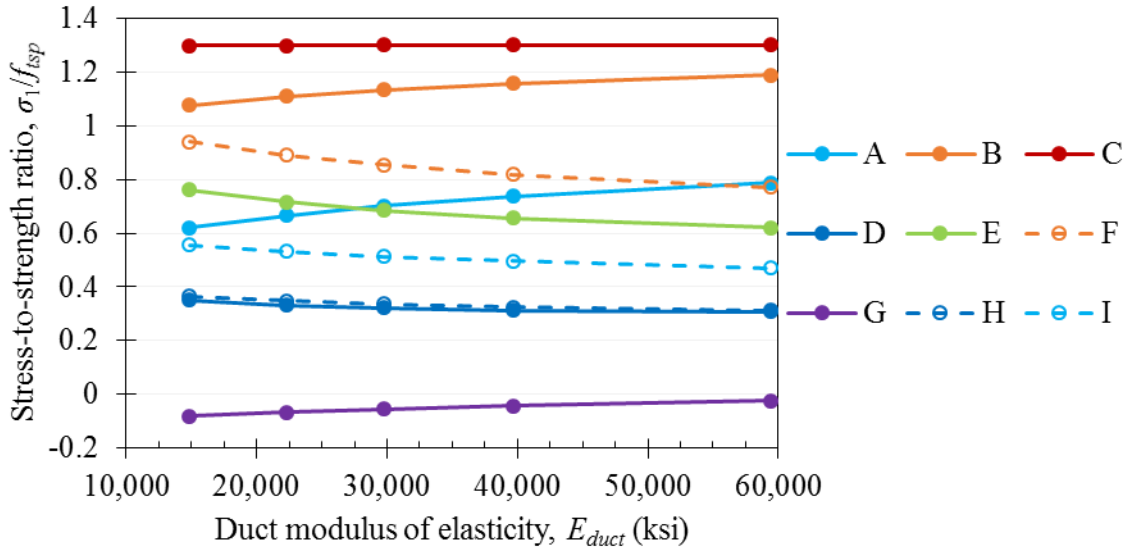


(a)

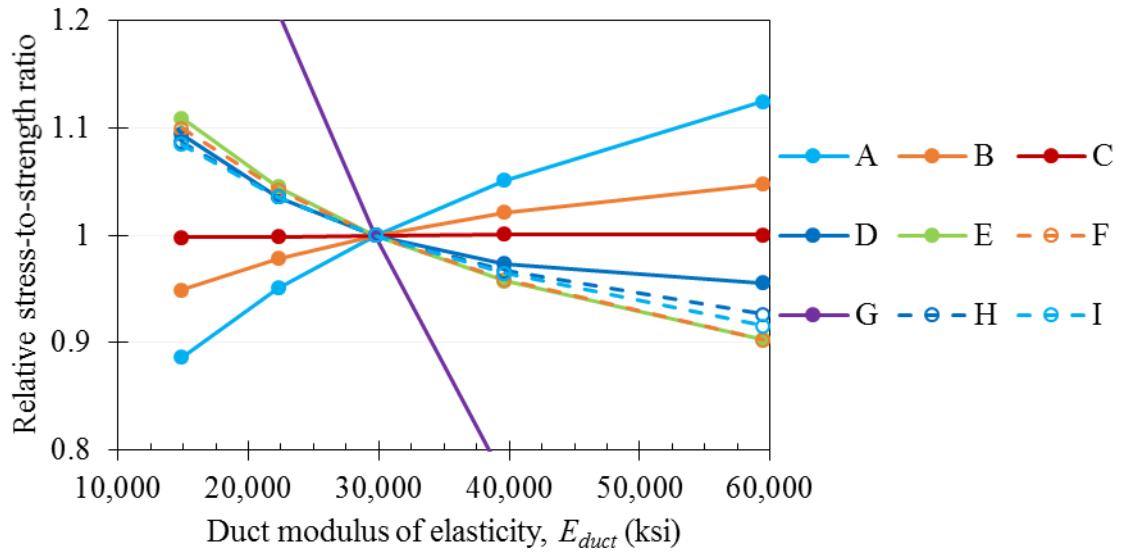


(b)

Figure 6.6: Influence of duct wall thickness on the (a) σ_1/f_{isp} values at each point and (b) relative σ_1/f_{isp} values at each point



(a)



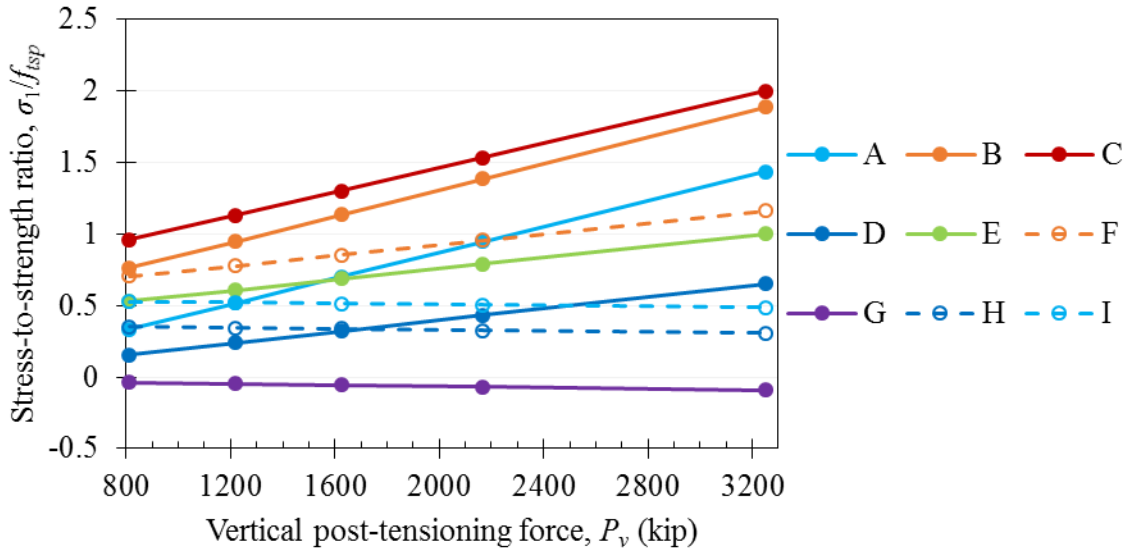
(b)

Figure 6.7: Influence of duct modulus of elasticity on the (a) σ_1/f_{isp} values at each point and (b) relative σ_1/f_{isp} values at each point

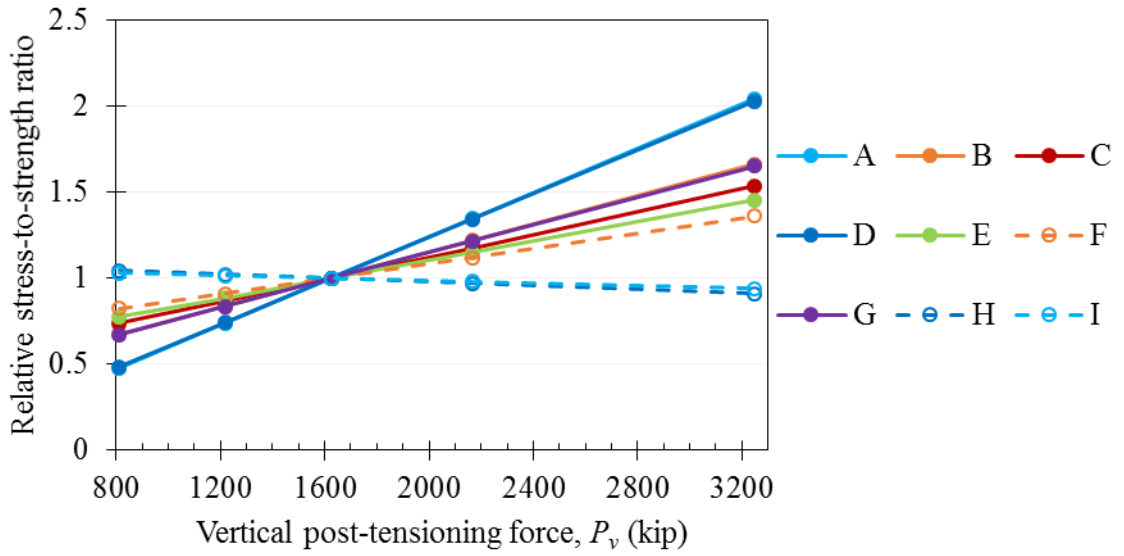
6.3.3 Post-Tensioning Forces

The results of the parameter study for the vertical post-tensioning force P_v , horizontal post-tensioning force P_h , and biaxial post-tensioning force P_b are presented in Figure 6.8, Figure 6.9, and Figure 6.10, respectively. The influence of the vertical and horizontal post tensioning depends on the location of the points of evaluation. Increasing the vertical post-tensioning force increases the tensile stresses at each point except for points G, H, and I, which are located halfway between the horizontal ducts. The greatest increase in tensile stresses occurs at points A, B, and C, which are at the edge of the horizontal duct. Similarly, increasing the horizontal post-tensioning force increases the tensile stresses at each point except for points A, D, and G, which are located halfway between the vertical ducts, and the greatest increase in tensile stresses occurs at points C, F, and I, which are in line with the edge of the vertical duct. The separate influences of the vertical and horizontal post-tensioning forces are informative for understanding the response of the mock-up and CR3 PCC during post-tensioning and detensioning operations. In both cases, the full vertical post-tensioning load was applied to all tendons before horizontal post-tensioning began.

Due to the linear elastic analysis, the influences of the vertical and horizontal post-tensioning forces are additive and can be used to determine the influence of the biaxial post-tensioning forces. Since varying the biaxial post-tensioning force simply scales the loading applied in the baseline case, the resulting σ_1/f_{tsp} curves in Figure 6.10 are lines passing through the origin. Accordingly, the relative influence of the biaxial post-tensioning force in Figure 6.10b is collinear for each point of evaluation, with the relative variation in σ_1/f_{tsp} corresponding to the relative variation of the biaxial force.

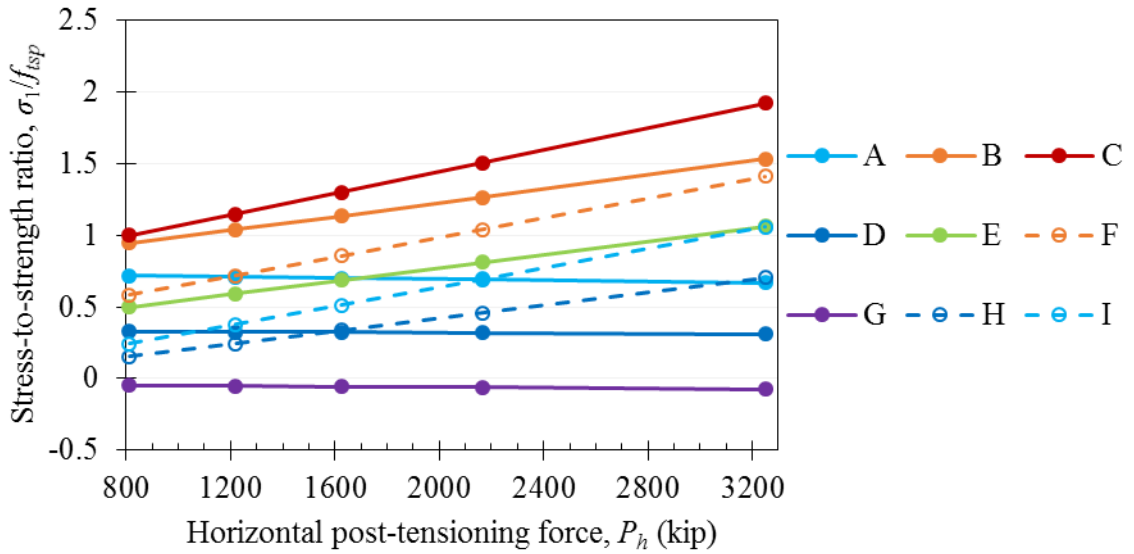


(a)

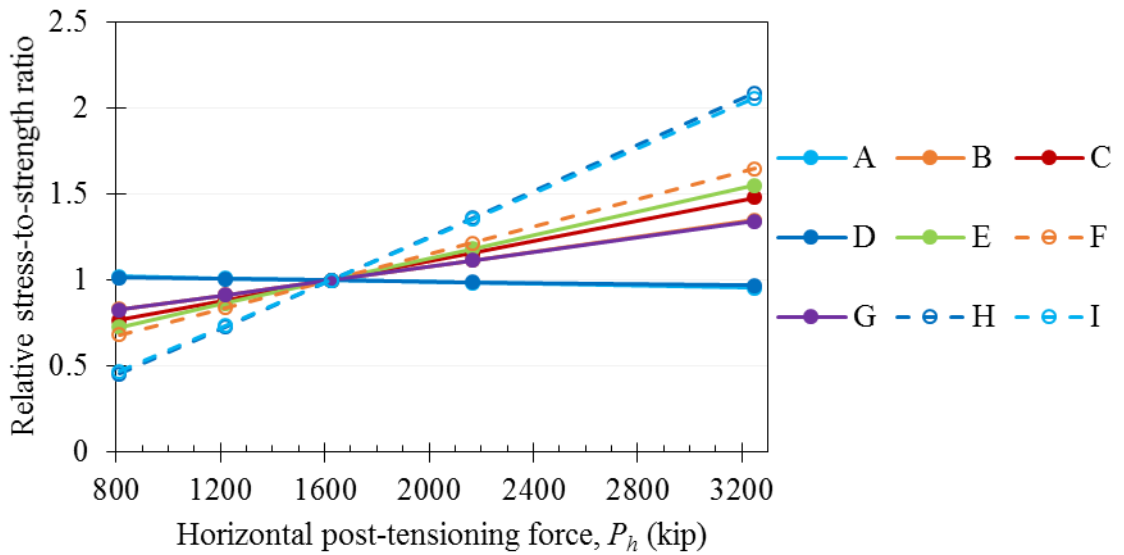


(b)

Figure 6.8: Influence of vertical post-tensioning force on the (a) σ_1/f_{isp} values at each point and (b) relative σ_1/f_{isp} values at each point

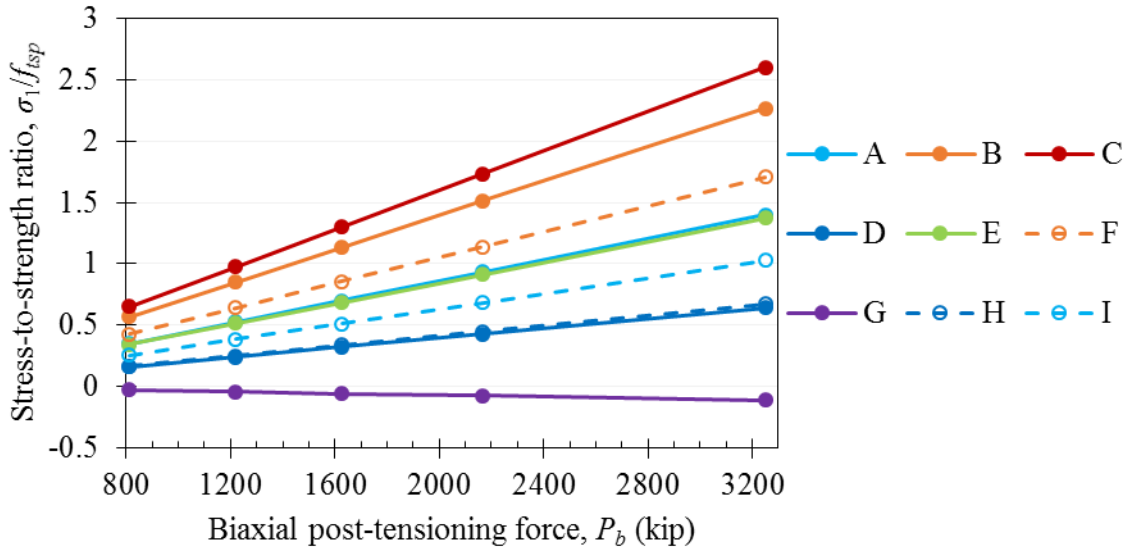


(a)

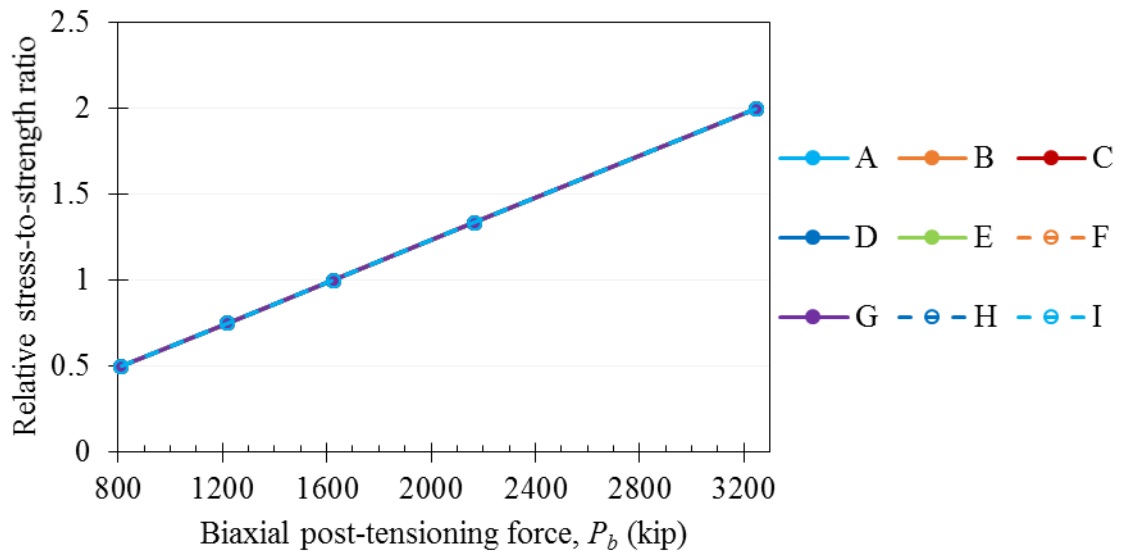


(b)

Figure 6.9: Influence of horizontal post-tensioning force on the (a) σ_1/f_{isp} values at each point and (b) relative σ_1/f_{isp} values at each point



(a)



(b)

Figure 6.10: Influence of biaxial tensioning force on the (a) σ_1/f_{isp} values at each point and (b) relative σ_1/f_{isp} values at each point

6.3.4 Comparison of Parameters

Figure 6.11 shows the influence of each parameter on the σ_1/f_{tsp} value at point C, which has the highest σ_1/f_{tsp} value for each case and would therefore likely be in the area of crack initiation. The duct modulus of elasticity is not shown since the results are coincident with the results for the duct thickness. Aside from the biaxial post-tensioning force, the most notable variation in the σ_1/f_{tsp} value is due to the splitting tensile strength. Increasing the splitting tensile strength by 33% to 6 MPa (871 psi) would decrease σ_1/f_{tsp} by 25% to 0.93 at point C, and the tensile strength would exceed the tensile stress at each of the evaluated points.

As discussed in Chapter 4, the development of tensile strength and modulus of elasticity of concrete can often be related to the development of compressive strength, so increases in splitting tensile strength are likely to be accompanied by increases in modulus of elasticity. Figure 6.11 shows that increasing the modulus of elasticity results in a slight decrease of the σ_1/f_{tsp} value at point C, so the influences of the splitting tensile strength and modulus of elasticity are cooperative.

Another method of effectively managing the σ_1/f_{tsp} value is varying the duct diameter. Decreasing the duct diameter by 25% decreases σ_1/f_{tsp} by 8% to 1.19, and decreasing the duct diameter by 50% decreases σ_1/f_{tsp} by 34% to 0.85. The duct diameter is governed by the size of the tendons used for post-tensioning, so the extent to which the diameter can be reduced may be limited by the tendons.

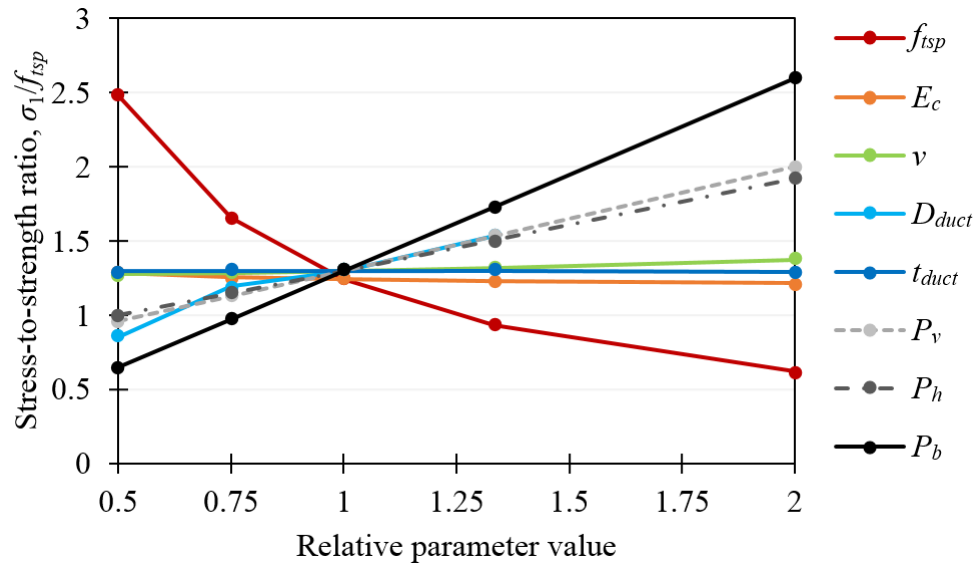


Figure 6.11: Influence of parameters evaluated at point C

6.4 Conclusions

Compared to the modulus of elasticity and Poisson's ratio, the splitting tensile strength of the concrete has a significant influence on the tensile cracking risk of the concrete. Whereas reducing the post-tensioning force would influence the overall design approach of a PCC, adjusting the concrete mix design in order to achieve greater tensile strengths is a relatively simple means of reducing the cracking risk. As was shown in Figure 3.26 and discussed in Section 3.4.5.2, 70 to 80% of the limerock coarse aggregate in the mock-up concrete fractured along the plane of failure during 1-day splitting tensile strength testing, indicating that the limerock aggregate does not contribute significantly to the tensile strength of the concrete. Utilizing a stronger aggregate, such as crushed granite, would be an effective means of increasing the tensile strength of the concrete and therefore reducing the cracking risk in the plane of the horizontal ducts.

For each investigated parameter, the magnitude of variation of σ_1/f_{isp} at point G was minimal and the value was consistently near 0. As shown in a, a significant percentage of the concrete in the plane of the horizontal ducts has σ_1/f_{isp} values either comparable to or more compressive than point G. As discussed in

Sections 2.2.3 and 2.2.4, radial reinforcement was used in the repair of the CR3 PCC delaminations to reinforce the plane of the post-tensioning ducts. If a similar approach were taken for the initial design of PCCs, optimal placement of the radial or transverse reinforcement would be near the corners where the ducts overlap and then along the edges of the ducts as needed. Any reinforcement near point G, away from the ducts, would not be engaged in tension until significant deformation occurred near the ducts.

CHAPTER 7

NONDESTRUCTIVE EVALUATION

7.1 Introduction

In order to investigate the extent to which cracking may have occurred in the mock-ups, nondestructive evaluation (NDE) methods were considered rather than coring so that the mock-ups could be used for future long-term studies. NDE methods are frequently used to rapidly assess the condition of structures without requiring alteration of the structure. Various ultrasonic techniques are used to determine the thickness of members or the location of potential flaws based on signal transit times (ACI 228.R2-13), and post-processing techniques have allowed the production of tomograms from surface readings (Mayer et al., 1990; Schickert et al., 2003). Due to the heterogeneity of concrete, however, relatively large wavelengths and corresponding low frequencies are typically needed to achieve sufficient penetration into the material for useful evaluation; ACI 228.R2-13 notes that 200-kHz waves are typically needed for concrete, whereas the frequencies used for testing metals are often on the order of 1 MHz. The larger wavelengths and lower frequencies limit the precision of the concrete investigations compared to investigations of homogeneous materials like steel (Popovics et al., 2000). Additionally, the typically rough surface of concrete can reduce the transmission of ultrasonic waves into the material (Zhu and Popovics, 2007), and embedded components such as rebar and post-tensioning ducts can interfere with or shadow the desired signals further from the test surface (Schickert, 2005).

Despite the complications of ultrasonic testing of concrete, progress in technology has enabled increasingly robust NDE of concrete structures and members. One recent development is the MIRA ultrasonic shear-wave tomograph (Figure 7.1), which utilizes

an array of 40 shear wave transducers arranged in ten rows of four transducers to generate tomograms of the test object. The ten rows of transducers are spaced at 40 mm (1.57 in.) on center, and the four transducers in each row are spaced at 30 mm (1.18 in.) on center. The dry point contact transducers are spring loaded and have a nominal center frequency of 50 kHz (De La Haza et al., 2013). Each reading generates a collection of 180 pulse-echo transit time measurements, and the synthetic aperture focusing technique (SAFT) is used to generate a 2D B-scan image along the length of the device and through the depth of the test object. Similarly, a series of equally spaced readings can be taken along a linear path, and the collected B-scans can be used to generate D-scans along the path of the readings and through the depth of the test object and C-scans of planes parallel to the surface of the test object.



Figure 7.1: MIRA antenna

7.1.1 Objectives

The first objective of this chapter were to investigate the capability of the MIRA ultrasonic shear-wave tomograph to produce tomograms with sufficient resolution to identify the post-tensioning ducts embedded 248 and 375 mm (9.75 and 14.75 in.) beneath the front surface of the mock-ups. The second objective was to evaluate the tomograms for indications of cracking or delamination in the plane of the horizontal post-tensioning ducts that would be representative of the delaminations in the CR3 PPC.

7.2 Methodology

The front faces of the mock-ups were marked with a 305-by-305-mm (12-by-12-in.) grid consistent with the spacing of the rebar cage shown in Figure 7.2. The paths marked in red in Figure 7.2 were selected for investigation of the capability of the MIRA tomograph to identify members continuous along the path of readings and members crossing the path of readings. Readings were taken at 102-mm (4-in.) intervals along each path. Figure 7.3 shows the orientation of the generated tomograms relative to the MIRA antenna and scan path.

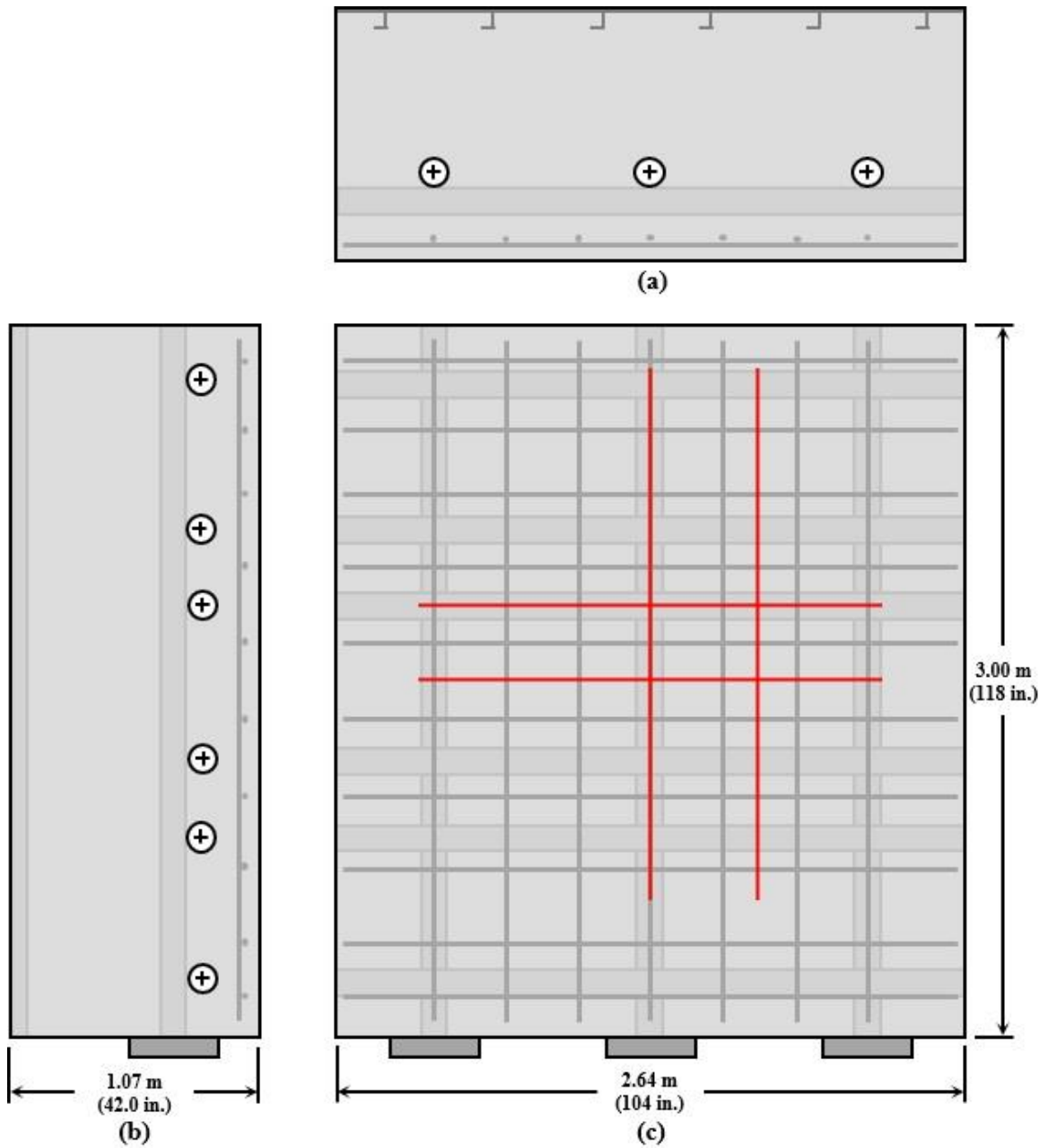


Figure 7.2: Orientation of MIRA scan paths for second mock-up; (a) plan view, (b) side elevation, and (c) front elevation

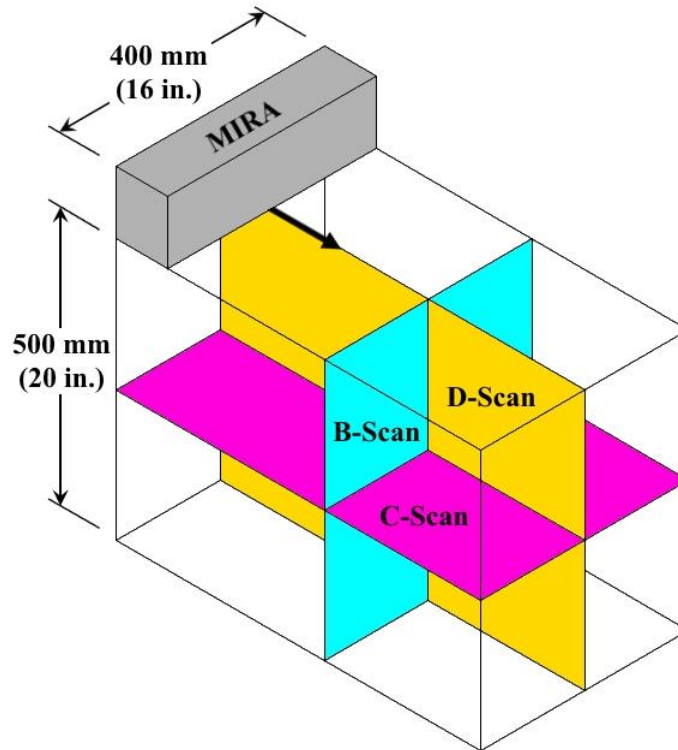


Figure 7.3: Orientation of B-, C-, and D- scan tomograms relative to MIRA antenna and scan path

7.3 Results and Discussion

Figure 7.4 and Figure 7.5 show tomograms obtained along the vertical path between the vertical post-tensioning ducts. The scans are colored so that red areas correspond to regions of high-amplitude reflections indicative of discontinuities in the mock-up and blue areas correspond to regions of low-amplitude reflections indicative of continuous concrete. Figure 7.4a shows clear indications for the location of two vertical rebars as well as an indication for the horizontal post-tensioning duct. Figure 7.4b shows a mostly continuous indication for the plane of the rebar cage as well as distinct indications for the four horizontal ducts completely within the path of the scan. An individual vertical rebar is clearly identifiable in Figure 7.4c, which shows a tomogram of results at depths of 50 to 125 mm (2 to 5 in.), encompassing the rebar cage but not to the depth of the horizontal ducts. The indications in line with the third horizontal duct from

the bottom of the mock-up may be due to a horizontal rebar, though none of the other horizontal rebars crossing the path were identified. The indications may also be from the horizontal duct.

Figure 7.5a and Figure 7.5b are the same as Figure 7.4a and Figure 7.4b, respectively, but Figure 7.5c shows a tomogram of results at depths of 150 to 300 mm (6 to 12 in.), encompassing the horizontal ducts. In contrast to Figure 7.4c, the vertical rebar is no longer indicated, but distinct indications for the four horizontal ducts are present. These results indicate that the MIRA tomograph is capable of producing tomograms with adequate resolution to identify the horizontal ducts. The blue spaces above and below each horizontal duct indication suggest that a full delamination did not occur in the plane of the ducts along this path. However, as shown in Figure 7.5, the shapes of the duct indications are insufficiently defined to conclusively state that no cracking has occurred.

Though the cylindrical shape of the ducts influences the way that the signals are reflected and processed, the faint indications extending above and below each duct could also be due to cracking at the tops and bottoms of the ducts due to the high tensile stresses identified in Chapter 5.

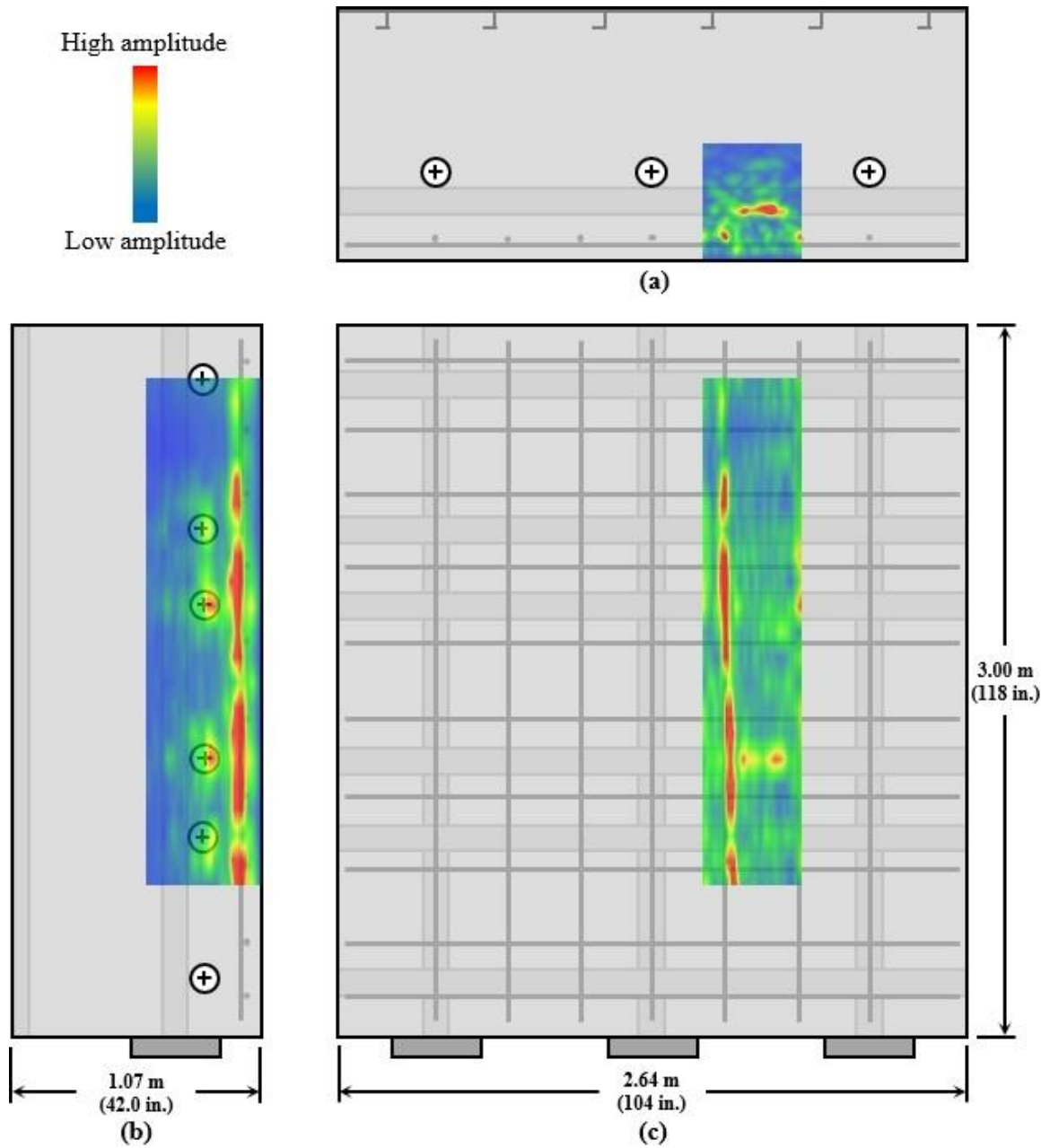


Figure 7.4: MIRA tomograms along path between vertical ducts; (a) plan view with B-scan, (b) side elevation with D-scan, and (c) front elevation with C-scan at depth of rebar cage

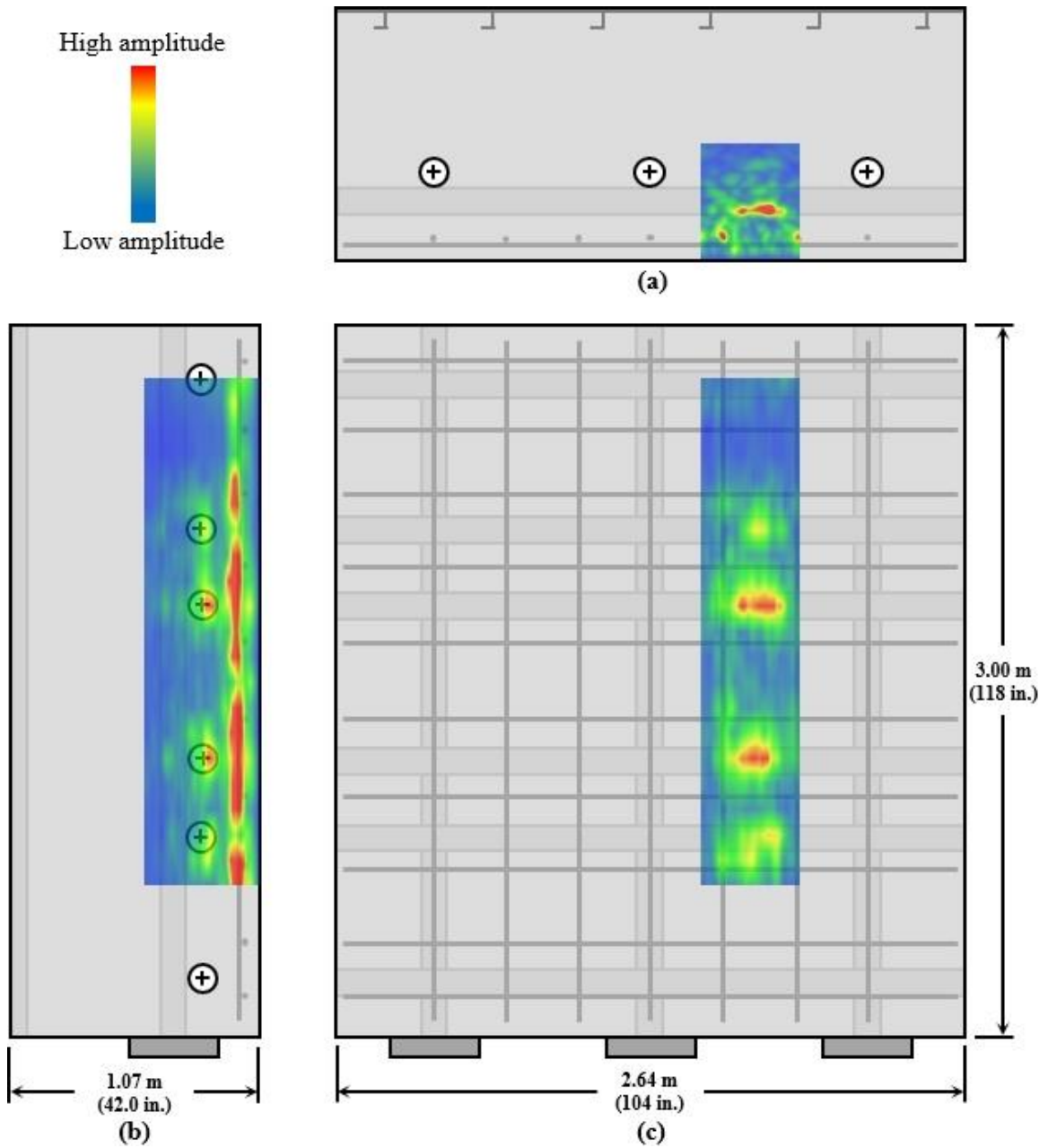


Figure 7.5: MIRA tomograms along path between vertical ducts; (a) plan view with B-scan, (b) side elevation with D-scan, and (c) front elevation with C-scan at depth of horizontal ducts

Figure 7.6 and Figure 7.7 show C-scan tomograms obtained along the middle vertical post-tensioning duct. Figure 7.6 shows the C-scan at the depth of the horizontal post-tensioning ducts, and indications can be seen for all five horizontal ducts along the path of readings, though the indication for the top horizontal duct is understandably faint since the readings did not continue past it. The apparent separations in the indications, particularly visible for the fourth duct from the bottom, may be due to the vertical rebar centered along the path of the readings near the front face of the mock-up.

Figure 7.7 shows the C-scan at the depth of the vertical ducts, and distinct indications along the line of the vertical duct can be seen. The gaps along the length of the vertical duct coincide with the locations where the horizontal ducts pass in front of the vertical duct. Since the MIRA tomograph was oriented horizontally for these scans, no signals would be able to pass around the horizontal ducts to reflect from the vertical duct and return to the antenna.

The clear indications for the horizontal ducts and the vertical duct indicate that the MIRA tomograph is capable of resolving the major embedded components in the mock-up. In particular, the vertical duct is relatively clearly resolved, with little scatter in the indications. This may be due to the orientation of the duct relative to the tomograph; when the tomograph is horizontal, each row of transducers is parallel to the axes of the vertical ducts, and each of the four signals are reflected the same direction. In contrast, each row of transducers is perpendicular to the axes of the horizontal ducts, so the four signals are reflected in different directions by the curvature of the duct.

The clarity of the vertical duct in Figure 7.7 suggests that extensive cracking did not occur in the plane of the horizontal post-tensioning ducts. However, in addition to the curvature of the horizontal ducts, cracking near the edges of the horizontal ducts may have contributed to the scatter in Figure 7.6.

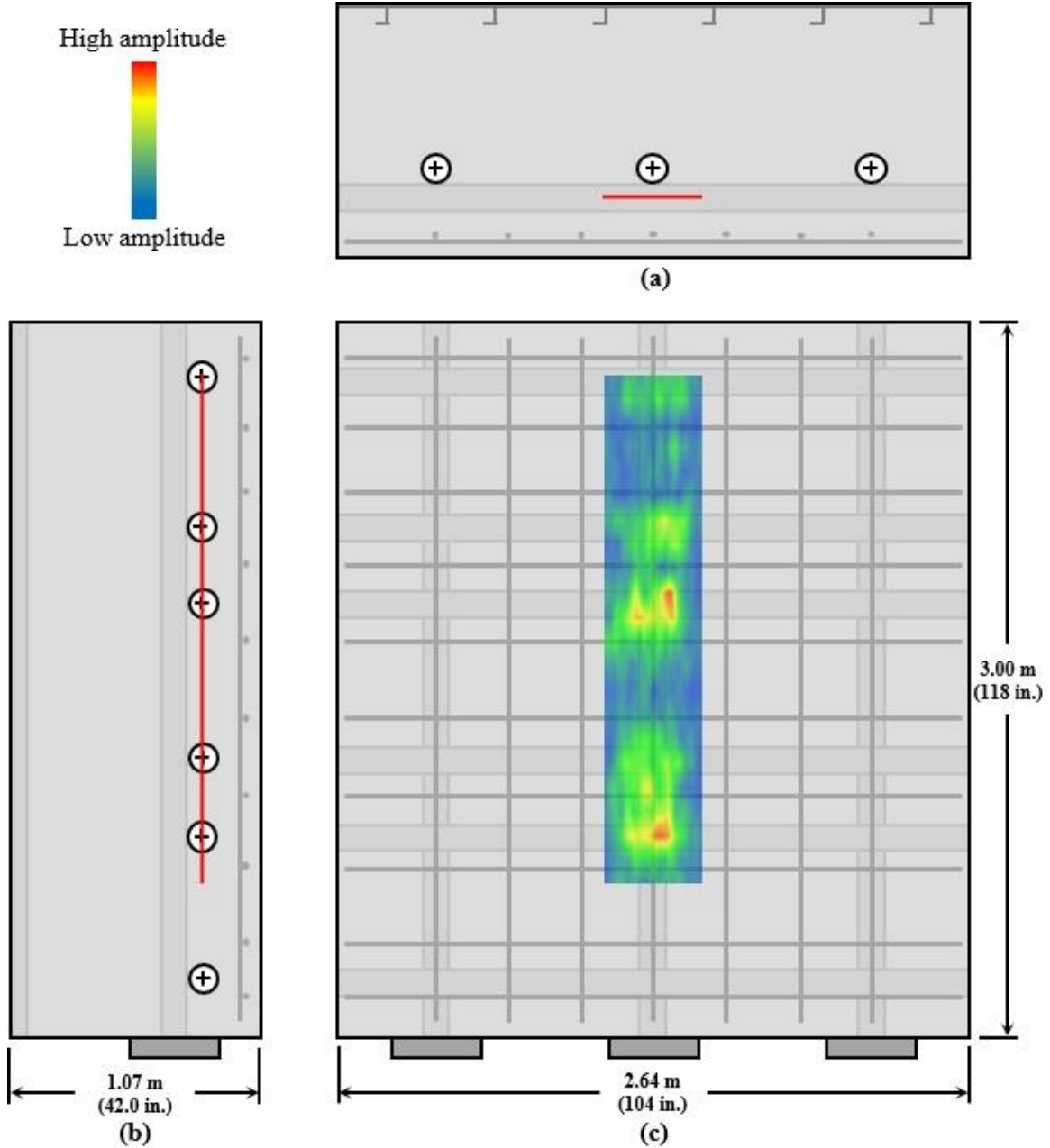


Figure 7.6: MIRA tomogram along middle vertical duct; (a) plan view, (b) side elevation, and (c) front elevation with C-scan at depth of horizontal ducts

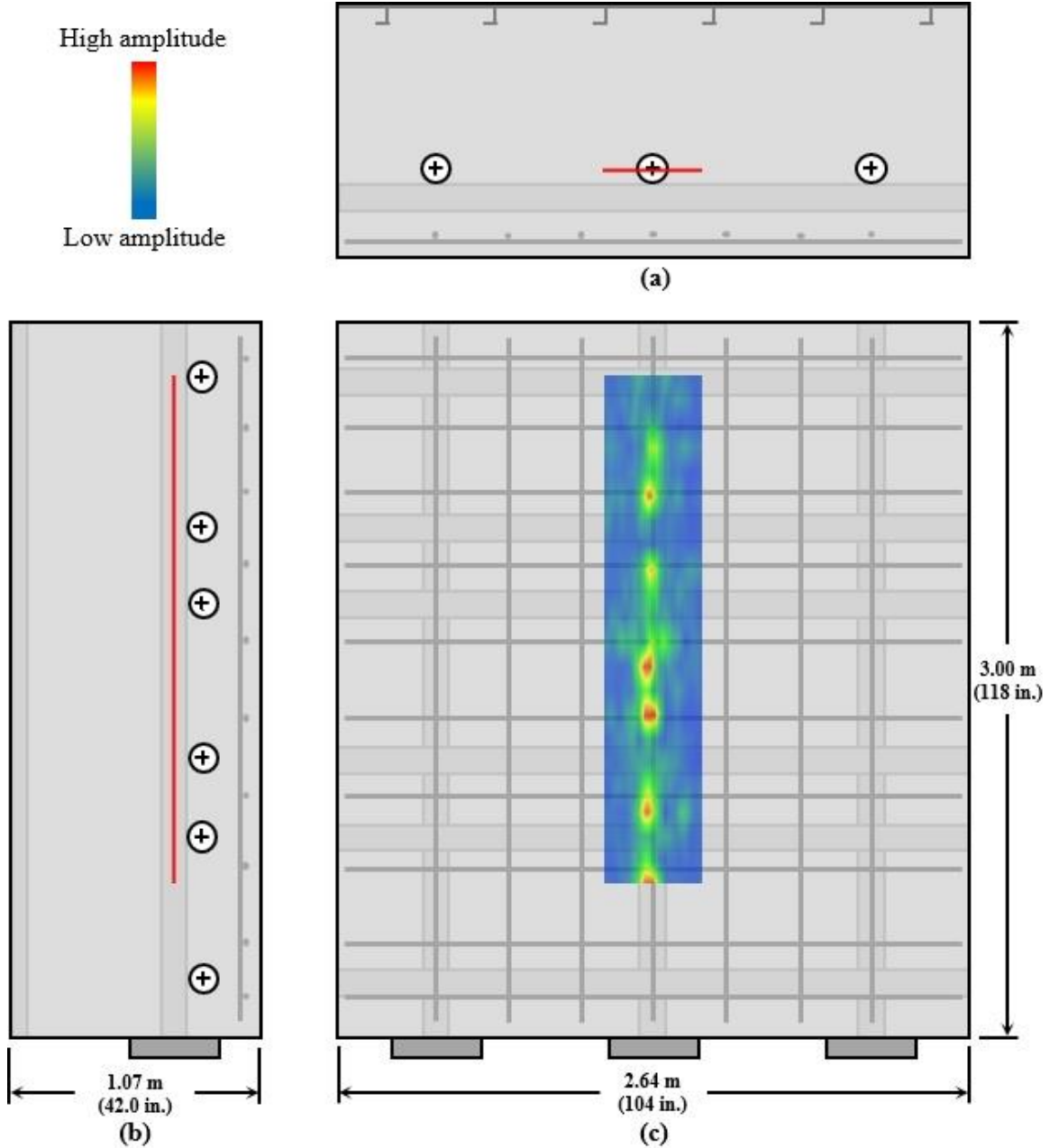


Figure 7.7: MIRA tomogram along middle vertical duct; (a) plan view, (b) side elevation, and (c) front elevation with C-scan at depth of vertical ducts

Figure 7.8 shows tomograms obtained between the middle horizontal post-tensioning ducts. Both the D-scan in Figure 7.8a and the C-scan in Figure 7.8c show clear indications for the vertical post-tensioning ducts. However, the D-scan also shows a very strong indication near the front surface of the mock-up, presumably due to one or two horizontal rebars along the scanning path. As noted for the horizontal ducts in Figure 7.5 and Figure 7.6, the orientation of the vertical ducts relative to the tomograph for the horizontal scanning path results in scatter of the signals and reduced resolution of the indications. Since the middle vertical duct was clearly identified in Figure 7.7c, it is unlikely that cracks along the edge of the duct contributed to the scatter in the same indication in Figure 7.8c.

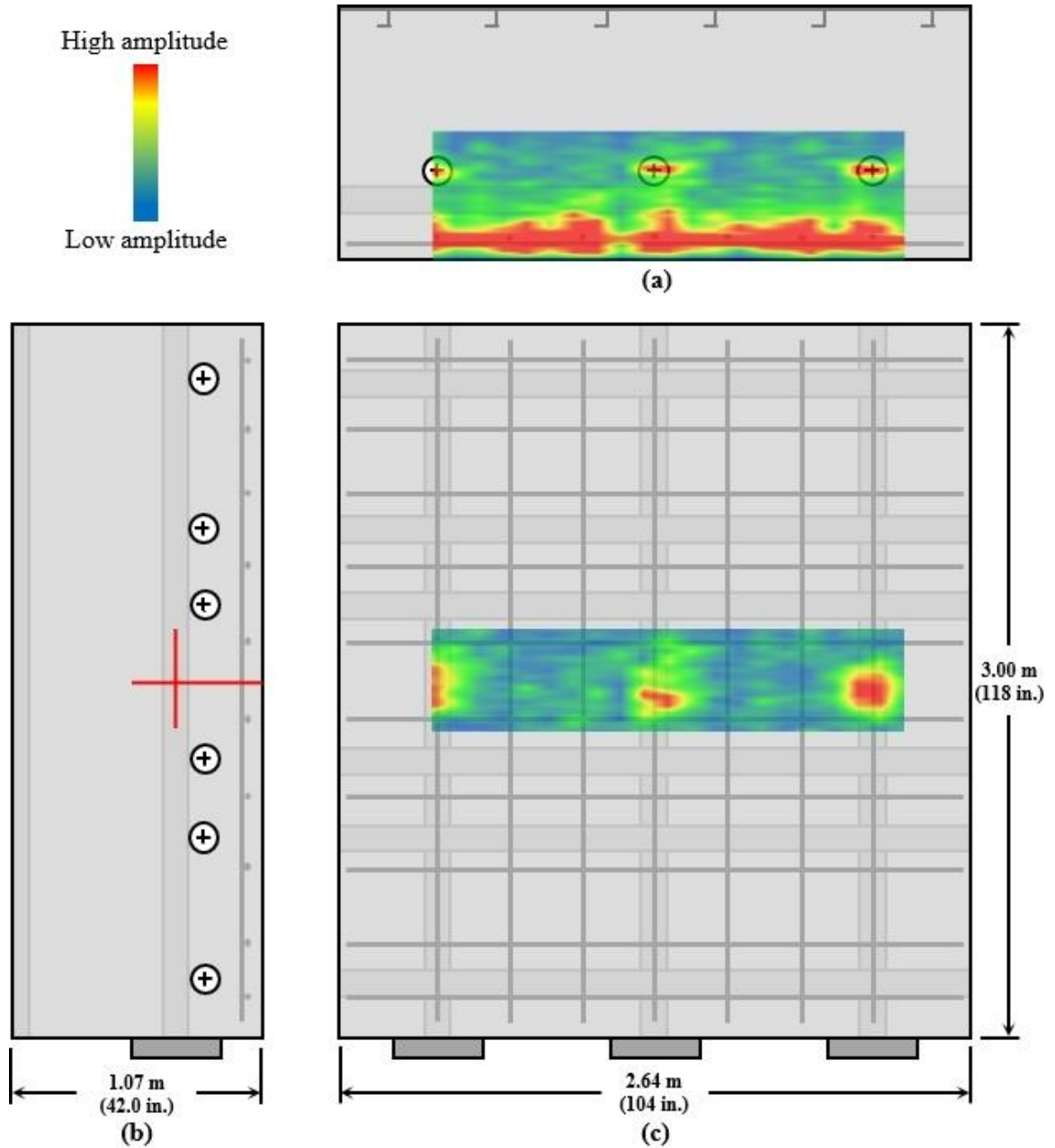


Figure 7.8: MIRA tomograms along path between middle horizontal ducts; (a) plan view with D-scan, (b) side elevation, and (c) front elevation with C-scan at depth of vertical ducts

Figure 7.9 and Figure 7.10 show tomograms obtained along the fourth horizontal post-tensioning duct from the bottom of the mock-up. The D-scan in Figure 7.9a and the C-scan in Figure 7.9c show indications for the rebar cage and the horizontal post-tensioning duct, and the B-scan in Figure 7.9b shows a very distinct indication of the horizontal duct in the section. The high resolution can be attributed to the orientation of the duct relative to the tomograph and the shallower depth of the horizontal ducts relative to the vertical ducts. However, as shown the C-scan at the depth of the horizontal duct in Figure 7.10c, the clarity of the duct is not continuous along the scanning path, and there are regions of scatter and regions of little indication along the length of the duct.

Comparing the C-scans of the vertical duct in Figure 7.7c and horizontal duct in Figure 7.10c, the greater intensity of the horizontal duct is apparent and is likely due to the shallower depth of the duct. However, there are also more noticeable indications around the horizontal duct than there are around the vertical duct. This may also be due to the shallower depth of the C-scan for the horizontal duct, for which signals reflected from nearby components will have greater amplitude than signals reflected from the depth of the vertical ducts.

The results in Figure 7.9 and Figure 7.10 again indicate that the MIRA tomograph is capable of resolving the components embedded in the mock-up concrete. Furthermore, no indication of extensive laminar cracking was identified, though minor cracking near the edge of the ducts may be present in areas of scattered indications.

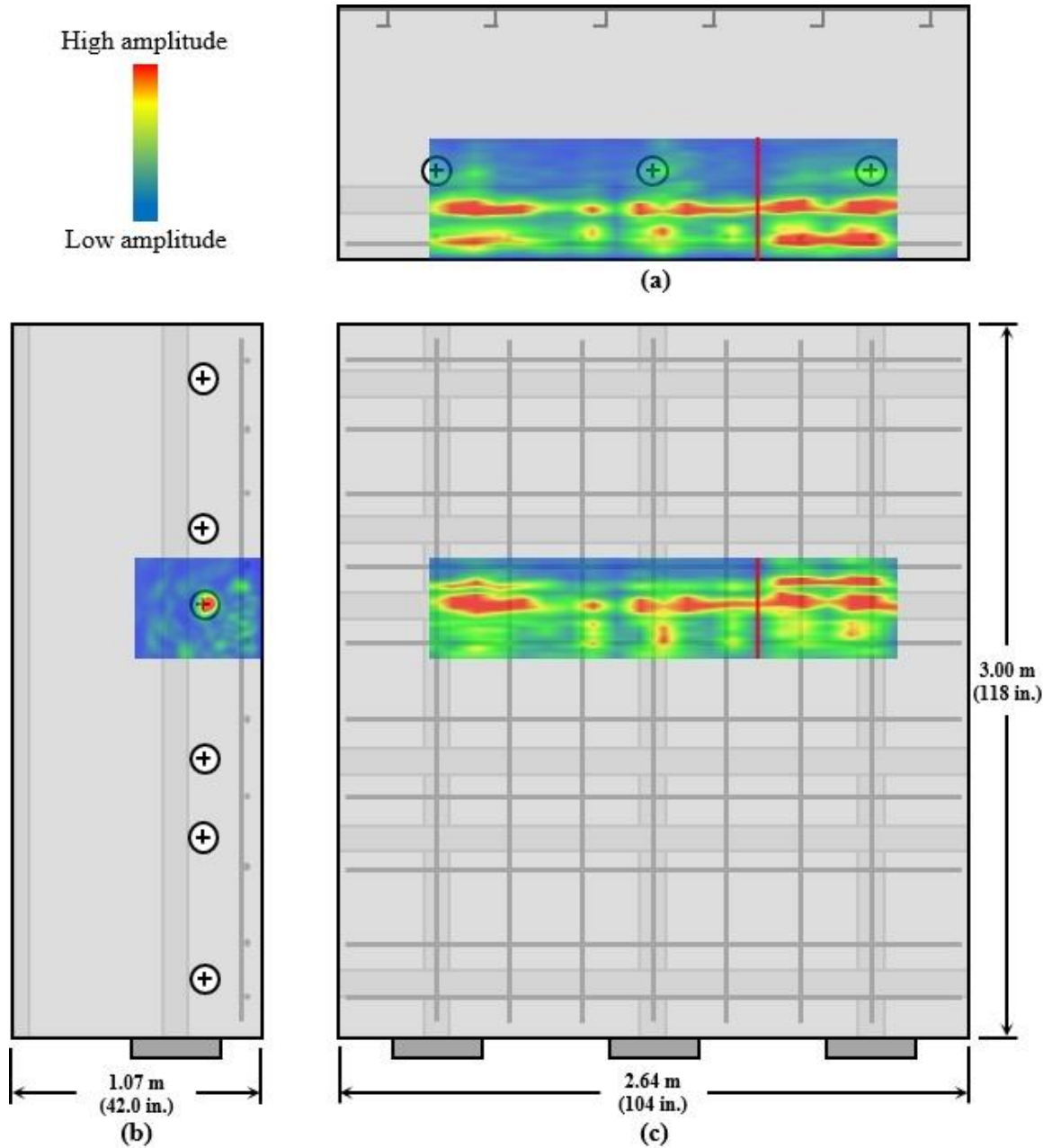


Figure 7.9: MIRA tomograms along horizontal duct; (a) plan view with D-scan, (b) side elevation with B-scan, and (c) front elevation with full-depth C-scan

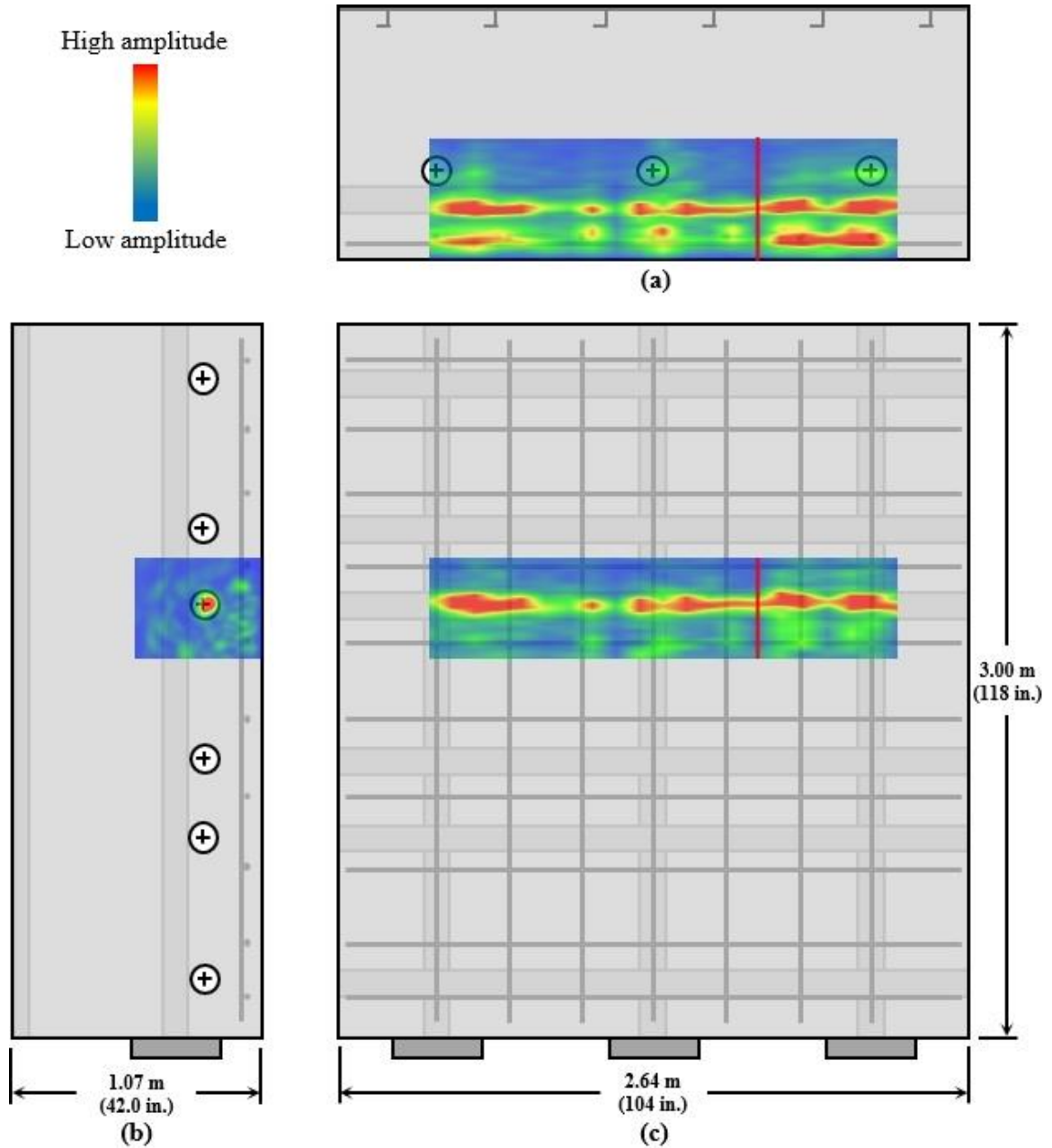


Figure 7.10: MIRA tomograms along horizontal duct; (a) plan view with D-scan, (b) side elevation with B-scan, and (c) front elevation with C-scan at depth of horizontal ducts

7.4 Conclusions

The appreciable correlation between the tomograms presented in this chapter and the mock-up geometry indicate that the MIRA ultrasonic shear-wave tomograph is an effective means of obtaining NDE data for mass concrete structures, even when multiple layers of rebar and ducts are present within 380 mm (15 in.) of the surface. Clear indications for rebar and post-tensioning ducts were identified in each case, with the diameters of the objects ranging from 25 to 127 mm (1 to 5 in.) and the depths of the objects ranging from 51 to 381 mm (2 to 15 in.).

The clear indications for the vertical post-tensioning ducts signify the lack of extensive laminar cracking in the plane of the horizontal ducts. However, greater scatter around the indications for the horizontal ducts than for the deeper vertical ducts suggests that there may be cracking or some other degradation along the horizontal ducts.

CHAPTER 8

CONCLUSIONS AND RECOMMENDATIONS

8.1 Conclusions

A review of mass concrete definitions and classifications in the literature established that the CR3 PCC met many of the criteria for consideration of mass concrete effects with regard to the influence of high temperatures in the behavior of the concrete. The results of thermal stress analysis of the mock-ups indicated that early-age thermal cracking did not occur due to limited temperature differences between the interior and surface of the concrete. However, concrete temperatures exceeding 70 °C (158 °F) in the first mock-up make the concrete susceptible to delayed ettringite formation and accompanied durability issues in the future that could limit long-term structural integrity.

Furthermore, the high concrete temperatures during the first several days of curing were shown result in decreased values of mechanical properties after 7 to 10 days. In particular, the reduction in splitting tensile strength due to high concrete curing temperatures increases the tensile cracking risk of the concrete. Therefore, the influence of mass concrete thermal effects on PCCs should be accounted for in the design and analysis of the structures to ensure that representative mechanical property values are utilized.

The compressive strength of match-cured specimens was found to be approximately 90% of the compressive strength of the fog-cured specimens at the same equivalent age. This suggests that the compressive strength of the in-place concrete can be estimated without match-cured specimens by using compressive strength tests of fog-cured specimens and the equivalent age of the in-place concrete, which can be

determined with the temperature history of the in-place concrete and the activation energy of the cement paste.

The relationship between the splitting tensile strength and the compressive strength of the concrete was found to be consistent between the fog-cured and match-cured specimens. Therefore, the splitting tensile strength of match-cured concrete can be estimated using the relationship between splitting tensile strength and compressive strength of fog-cured specimens of the same concrete. Furthermore, if the 90% relationship is utilized to estimate the compressive strength of the match-cured concrete, the tensile strength of the match-cured concrete can be estimated without conducting any tests on match-cured specimens.

Finite element analysis of the mock-up under post-tensioning loads showed that tensile stresses exceeded the splitting tensile strength by up to 98% in the plane of the horizontal ducts. As a result, cracks are expected in the mock-ups near the corners where the horizontal and vertical ducts overlap, and tensile creep under sustained post-tensioning loads may contribute to propagation of the cracks farther along the ducts. However, low tensile and compressive stresses in the regions away from the ducts in the mock-up limited the potential for tensile cracking to extend through the entire plane of the ducts.

When increased post-tensioning loads representative of the CR3 PCC were analyzed, the regions of anticipated cracking extended farther from the ducts, but the remote areas still had low tensile and compressive stresses that would likely limit crack propagation. However, the contribution of radial tensile stresses due to the circumferential tendons in the CR3 PCC would exacerbate the tensile stresses due to the biaxial loading and potentially lead to cracking throughout the plane of the ducts.

The general stress behavior of the mock-up was largely governed by the post-tensioning loads rather than the thermal stresses and curing history. Though the cracking risk is higher when accounting for the curing history, the influence of thermal stresses

was limited to the maximum stress concentrations since the stress profiles in the corresponding cured and non-cured cases were otherwise comparable. The primary source of the tensile stresses under the biaxial post-tensioning loads was the flattening of the circular ducts.

Adjusting the concrete mix design to develop greater splitting tensile strength would be an effective means of reducing the cracking risk in PCCs. For applications using limerock aggregate, a simple approach would be the use of a stronger aggregate, such as crushed granite, to improve the tensile strength and, thereby, reduce the cracking risk in the plane of the horizontal ducts.

If adding radial reinforcement is selected as a design or rehabilitation approach for PCCs, the optimal placement of the radial or transverse reinforcement would be along the ducts, particularly near the overlapping of the vertical and horizontal ducts, where tensile stresses are greatest. Any reinforcement away from the ducts would not be engaged in tension until significant deformation occurred near the ducts.

The MIRA ultrasonic shear-wave tomograph is an effective means of obtaining NDE data for mass concrete structures, even when multiple layers of rebar and ducts are present near the surface. No indications of extensive laminar cracking in the plane of the horizontal ducts were identified, consistent with the strains measured in the mock-up and the stresses determined by finite element analysis. However, scatter around the indications for the horizontal ducts suggests that cracking may have initiated along the ducts, consistent with the stresses determined along the ducts in the finite element models.

Based on the findings in this work, cracking is expected to have been initiated in the plane of the circumferential ducts prior to detensioning of the CR3 PCC for the steam generator replacement opening in 2009, and the detensioning process may have exacerbated the pre-existing condition.

8.2 Recommendations

Though the 90% relationship between the compressive strength of match-cured and fog-cured specimens at matching equivalent ages likely varies based on the temperature history of the concrete, structures comparable to the CR3 CPC would likely have similar concrete temperature histories, and the relationship may be valid. In the absence of other data, this relationship is recommended for predicting match-cured and in-place compressive strength values based on fog-cured results. The determination of the equivalent age requires the temperature history of the concrete and the apparent activation energy of the cement paste. Rather than experimentally testing for the apparent activation energy, the literature models (Schindler, 2004; Riding et al., 2011) based on the cement composition and fineness are recommended for estimation of the apparent activation energy.

Since the measured tensile strengths of the mock-up concrete were greater than those predicted by the power law relationships recommended in the literature, using the ACI 318 model or other comparable power law models is recommended for obtaining a conservative estimate of the tensile strength in the absence of experimental data for concrete similar to that used in the CR3 PCC. Since the ACI 318 equation for modulus of elasticity provided reasonable predictions of the experimental results with respect to equivalent age, the ACI 318 relationship was recommended for use, particularly in the absence of modulus of elasticity data. Additionally, since most thermal properties of concrete are heavily influenced by the coarse aggregate, identifying thermal property values for concretes containing the same or similar aggregates may be the most effective means of predicting the thermal properties.

If utilizing transverse or radial reinforcement for biaxially or circumferentially post-tensioned structures similar to PCCs, reinforcing the corners where the ducts overlap is the most important consideration, followed by providing reinforcement along the ducts. Aside from the addition of transverse reinforcement, increasing the tensile strength of the

concrete provides the optimum increase in cracking resistance. The selection of an appropriate aggregate with sufficient strength is recommended. Weak, highly porous, or friable aggregate may not be capable of arresting crack propagation and may result in the concrete being susceptible to extensive cracking. Aggregates comparable to crushed granite are recommended for use.

8.3 Future Research

The relationship between the compressive strength of match-cured and fog-cured specimens at matching equivalent ages should be investigated with different curing histories to determine if a consistent relationship can be identified. Additionally, the relationship should be investigated for other concrete mixes with the same curing history to determine the influence of the materials on the development of the mechanical properties.

Nonlinear fracture mechanics analysis should be conducted on the models of the mock-up in order to more accurately predict the cracking behavior of the concrete under biaxial post-tensioning loads. The creep parameters of the CR3 PCC concrete should also be determined so that the influence of tensile creep can be accounted for. These factors may indicate greater potential for cracking than determined by the present analysis. The parameter study should also be extended to account for coupled scenarios of multiple parameters, such as decreasing duct diameter and increasing duct spacing.

Once a model with nonlinear fracture mechanics analysis has been developed, the geometry of the model should be adjusted to a curved form representative of the cylindrical CR3 PCC. This will allow incorporation of the significant radial tensile stresses that are generated by the circumferential tendons and that contribute to delaminations in PCCs.

Finally, subsequent scans of the mock-ups should be conducted during extended loadings in order to see if any of the indications vary over time, which could be indicative of crack propagation or creep. This monitoring will also provide useful information about the reproducibility of the tomograms and the ability to monitor mass concrete structures over time.

APPENDIX A

CALCULATIONS AND DERIVATIONS

The following sections provide detailed calculations or derivations of values and models used in the previous chapters.

A.1 Volume-to-Surface Area Ratio of Typical CR3 PCC Pour

This section provides the calculations for the volume-to-surface area ratio (V/SA) of a typical CR3 PCC bay concrete pour, the majority of which were 3 m (10 ft) high and nominally 6 m (20 ft) long (Progress Energy, 2009).

Dimensions of CR3 PCC bays

wall thickness,

$$t := 42\text{in} = 3.5\text{-ft}$$

inner radius (to concrete-liner interface),

$$r_i := 65\text{ft} + 0.375\text{in} = 65.031\text{-ft}$$

exterior radius,

$$r_o := r_i + t = 68.531\text{-ft}$$

radius to center of wall,

$$r_{\text{center}} := \frac{(r_i + r_o)}{2} = 66.781\text{-ft}$$

circumference at center of wall

$$C_{\text{center}} := 2 \cdot \pi \cdot r_{\text{center}} = 419.599\text{-ft}$$

Dimensions of typical concrete lifts

nominal arc length

(used as arc length at center of wall),

$$L_{\text{lift}} := 20\text{ft}$$

height,

$$h_{\text{lift}} := 10\text{ft}$$

Calculations

volume of lift,

$$V_{\text{lift}} := \pi \cdot (r_o^2 - r_i^2) \cdot h_{\text{lift}} \cdot \left(\frac{L_{\text{lift}}}{2 \cdot \pi \cdot r_{\text{center}}} \right) = 700 \cdot \text{ft}^3 \quad V_{\text{lift}} = 700 \cdot \text{ft}^3$$

combined area of inner and outer faces,

$$SA_{\text{faces}} := 2 \cdot (L_{\text{lift}} \cdot h_{\text{lift}}) = 400 \cdot \text{ft}^2$$

combined area of narrow side faces,

$$SA_{\text{sides}} := 2(h_{\text{lift}} \cdot t) = 70 \cdot \text{ft}^2$$

combined area of top and bottom faces,

$$SA_{\text{topbot}} := 2 \cdot L_{\text{lift}} \cdot t = 140 \cdot \text{ft}^2$$

total surface area of lift,

$$SA_{\text{lift}} := SA_{\text{faces}} + SA_{\text{sides}} + SA_{\text{topbot}} = 610 \cdot \text{ft}^2 \quad SA_{\text{lift}} = 610 \cdot \text{ft}^2$$

volume-to-surface-area ratio,

$$V/SA := \frac{V_{\text{lift}}}{SA_{\text{lift}}} = 13.77 \text{ in} \quad \boxed{V/SA = 13.77 \text{ in}}$$

A.2 Datum Temperature for Nurse-Saul Maturity Function

As discussed in Section 2.6.4, various datum temperature values have been proposed for use in the Nurse-Saul maturity function, and ASTM C1074 provides a method of experimentally determining the appropriate datum temperature of a mortar. The influence of the selected datum temperature on the resulting temperature-time factor is discussed in this section. For concrete with temperature history $T_c(t)$, the Nurse-Saul temperature-time factor can be expressed as follows for constant datum temperature T_0 .

$$M(t) = \int_0^t (T_c - T_0) dt = \int_0^t T_c dt - t \cdot T_0$$

For the same temperature history $T_c(t)$, the temperature-time factor can be expressed as follows for any other constant datum temperature $T_0 + T_\Delta$.

$$M_\Delta(t) = \int_0^t [T_c - (T_0 + T_\Delta)]dt = \int_0^t T_c dt - t(T_0 + T_\Delta)$$

The difference in maturity determined by using the two datum temperatures is as follows.

$$M_\Delta(t) - M(t) = -t \cdot T_\Delta$$

Since the maturity functions begin at time $t = 0$ with maturity $M(0) = 0$, changing the datum temperature T_0 by a value of T_Δ results in a constant change in slope of the maturity index of negative T_Δ . The Arrhenius equivalent age maturity function was also used to model the maturity of the mock-up concrete, and normalizing the Nurse-Saul temperature-time factors so that the maturity indices for the Fog specimens are collinear results in the elimination of the T_Δ influence on the slope. Therefore, the selection of the datum temperature is insignificant as used in the present work for comparison of isothermally cured and match-cured maturities alongside the Arrhenius equivalent age maturity function.

A.3 Model for Specific Heat Capacity of Mock-Up Concrete

In this section, a model is developed for the specific heat capacity of the mock-up concrete as a function of degree of hydration and temperature based on the model developed by van Breugel (1980) and the temperature-dependent specific heat capacity results for the mock-up cement and aggregates as determined in Section 4.4.7.

Masses per m³ of concrete
cement,

$$m_c := 405\text{kg}$$

fine aggregate,

$$m_{fa} := 653\text{kg}$$

coarse aggregate,

$$m_{ca} := 1068\text{kg}$$

water,

$$m_w := 164\text{kg}$$

concrete,

$$m_{\text{concrete}} := m_c + m_{fa} + m_{ca} + m_w = 2290\text{-kg}$$

Specific heat capacity as function of temperature
cement,

$$c_{p,c} := 1.76 \frac{\text{J}}{\text{kg}\cdot\text{K}} \cdot \frac{\text{Temp}}{^\circ\text{C}} + 626 \frac{\text{J}}{\text{kg}\cdot\text{K}}$$

fine aggregate,

$$c_{p,fa} := 1.30 \frac{\text{J}}{\text{kg}\cdot\text{K}} \cdot \frac{\text{Temp}}{^\circ\text{C}} + 659 \frac{\text{J}}{\text{kg}\cdot\text{K}}$$

coarse aggregate,

$$c_{p,ca} := 1.58 \frac{\text{J}}{\text{kg}\cdot\text{K}} \cdot \frac{\text{Temp}}{^\circ\text{C}} + 715 \frac{\text{J}}{\text{kg}\cdot\text{K}}$$

water,

$$c_{p,w} := 4186.8 \frac{\text{J}}{\text{kg}\cdot\text{K}}$$

hydrated cement (van Breusel, 1980),

$$c_{p,cef} := 8.4 \frac{\text{J}}{\text{kg}\cdot\text{K}} \cdot \frac{\text{Temp}}{^\circ\text{C}} + 339 \frac{\text{J}}{\text{kg}\cdot\text{K}}$$

Specific heat capacity of concrete as function of degree of hydration (van Breusel, 1980),

$$c_p := \frac{1}{m} \left[m_c \cdot \alpha_H \cdot c_{p,cef} + m_c \cdot (1 - \alpha_H) \cdot c_{p,c} + m_{fa} \cdot c_{p,fa} + m_{ca} \cdot c_{p,ca} + m_w \cdot c_{p,w} \right]$$

$$c_p \text{ simplify } \rightarrow \frac{1.42\text{-J}\cdot\text{Temp} + 931.93\text{-J}\cdot^\circ\text{C} + 1.17\text{-J}\cdot\text{Temp}\cdot\alpha_H - 50.76\text{-J}\cdot^\circ\text{C}\cdot\alpha_H}{\text{K}\cdot\text{kg}\cdot^\circ\text{C}}$$

A.4 Balance Line and Depth of Thermal Stress Block

In this section, the temperature corresponding to the balance line for thermal stresses and the depth of the thermal stress block are calculated for the temperature profile shown in Figure 23 in Section 3.4.4.

Quadratic best-fit curve of temperatures through section,

$$T(x) := -0.0271 \cdot x^2 + 1.1433 \cdot x + 52.827$$

Vertical offset needed for the integral of $T(x)$ to equal zero (balanced stresses),

$$b := -\left(\frac{\int_0^{42} T(x) \, dx}{42}\right) = -60.902$$

Note: the additive inverse of b is the T value of the balance line

$$b = -60.902$$

Shifted temperature curve,

$$T_{\text{bal}}(x) := T(x) + b \rightarrow 1.1433 \cdot x - 0.0271 \cdot x^2 - 8.0745$$

Check summation of temperatures

$$\text{Check} := \int_0^{42} T_{\text{bal}}(x) \, dx = -0 \qquad \text{Check} = -0$$

Guesses for roots of T_{bal}

$$g_1 := 9$$

Roots of T_{bal}

$$r_1 := \text{root}(T_{\text{bal}}(g_1), g_1) = 8.969$$

$$g_2 := 33$$

$$r_2 := \text{root}(T_{\text{bal}}(g_2), g_2) = 33.219$$

First derivative of T_{bal}

$$t_{\text{bal}}(x) := \frac{d}{dx} T_{\text{bal}}(x) \rightarrow -0.0542 \cdot x + 1.1433$$

Guess for x -value corresponding to maximum value of T_{bal}

$$g_3 := 21$$

x -value corresponding to maximum value of T_{bal}

$$r_{\text{max}} := \text{root}(t_{\text{bal}}(g_3), g_3) = 21.094 \qquad r_{\text{max}} = 21.094$$

Areas of segments of T_{bal}

$$A_1 := \int_0^{r_1} T_{\text{bal}}(x) \, dx = -32.952 \quad A_3 := \int_{r_{\text{max}}}^{r_2} T_{\text{bal}}(x) \, dx = 32.203$$

$$A_2 := \int_{r_1}^{r_{\text{max}}} T_{\text{bal}}(x) \, dx = 32.203 \quad A_4 := \int_{r_2}^{42} T_{\text{bal}}(x) \, dx = -31.453$$

Check summation of areas

$$A_{\text{tot}} := A_1 + A_2 + A_3 + A_4 = -0 \qquad A_{\text{tot}} = -0$$

APPENDIX B

PROPERTIES OF HARDENED CONCRETE, COMPLETE

RESULTS

Whereas results were summarized for presentation in previous chapters, the complete results are provided in the following sections. Additionally, one-way analysis of variance (ANOVA) of the mechanical property results is discussed.

B.1 Percent Absorption, Density, and Percent Permeable Voids

Error! Reference source not found. presents the percent absorption, density, and percent permeable voids results for the second mock-up concrete as determined in accordance with ASTM C642-13 (2013).

Table B.1: Percent absorption, density, and percent permeable voids of hardened concrete for second mock-up

Truck	Measure	Absorption (%)		Bulk Density			Apparent Density		Perm. Voids (%)
		Immersed	Immersed & Boiled	Dry	SSD	SSD, Boiled	(kg/m ³)	(lb/ft ³)	
1	Average	7.5	8.1	2122	2281	2294	2562	159.9	17.2
	Std. Dev.	0.2	0.3	9	9	9	18	1.1	0.6
2	Average	7.2	7.8	2132	2286	2297	2554	159.4	16.5
	Std. Dev.	0.2	0.2	12	9	8	4	0.2	0.4
Both	Average	7.4	7.9	2127	2283	2295	2558	159.7	16.9
	Std. Dev.	0.2	0.3	11	8	8	12	0.8	0.6
	p-value*	0.237	0.197	0.338	0.529	0.666	0.497		0.2

B.2 Mechanical Properties

Results of the tests for compressive strength, splitting tensile strength, modulus of elasticity, and Poisson's ratio are presented in this section. Four series of ANOVA were conducted on the experimental results for each of the four tested mechanical properties of the mock-up concrete. A significance level of $\alpha = 0.05$ was used for all analysis. The null hypotheses were tested in the order listed below, and if a given null hypothesis could not be rejected according to the significance level, the tested sets of data were combined for subsequent analyses.

1. For each mock-up and curing condition and at each age, the mean value of the given property of the concrete from the two trucks was the same.
2. For each mock-up and at each age, the mean value of the given property for the Ext and Int curing conditions was the same.
3. For each curing condition and at each age, the mean value of the given property for the two mock-ups was the same.
4. For the Ext and Int curing conditions, the mean value of the given property was the same at all ages.

If a p-value was less than $\alpha = 0.05$, the result was considered statistically significant and the corresponding null hypothesis was rejected. If a p-value was greater than $\alpha = 0.05$, the result was not considered statistically significant and the corresponding null hypothesis was not rejected.

Compressive strength results for the first mock-up are shown in **Error! Reference source not found.**, **Error! Reference source not found.**, and Figure B.1, and results for the second mock-up are shown in Table B.1, Table B.2, and Figure B.2. Results of ANOVA between the two mock-ups are presented in Table B.3. The first null hypothesis could not be rejected at any age or curing condition for the first mock-up but

was rejected at all three ages for the Fog curing condition for the second mock-up. Therefore, the results from each truck for the first mock-up were combined for further analysis, but the Fog results from the two trucks for the second mock-up were not combined. The second null hypothesis could not be rejected at any age for the second mock-up and could only be rejected at two of the seven testing ages for the first mock-up. These results suggest that the compressive strength values for the Ext and Int concrete were generally not statistically distinct, so the sets of data for the Ext and Int concrete were combined for further analysis. The third null hypothesis was rejected at all five testing ages, indicating that the compressive strength values for the two mock-ups were statistically distinct. Therefore, the results for the two mock-ups were analyzed separately. With a p-value of 0.000 for both mock-ups, the fourth null hypothesis was rejected, indicating that the compressive strength was not constant with respect to time for either mock-up. Therefore, the compressive strength development of the concrete for the two mock-ups was modeled based on the combined Ext and Int results.

Splitting tensile strength results for the first mock-up are shown in **Error! Reference source not found.**, **Error! Reference source not found.**, and Figure B.3, and results for the second mock-up are shown in Table B.4, Table B.5, and Figure B.4. Results of ANOVA between the two mock-ups are presented in Table B.6. The first null hypothesis could not be rejected at any age for any curing condition for either mock-up, so the sets of data from the two trucks were combined for further analysis. The second null hypothesis could only be rejected at two of the six testing ages for the first mock-up and one of the five testing ages for the second mock-up. These results suggest that the splitting tensile strength values for the Ext and Int concrete were generally not statistically distinct, so the sets of data for the Ext and Int concrete were combined for further analysis. The third null hypothesis was rejected at all five testing ages, indicating that the splitting tensile strength values for the two mock-ups were statistically distinct.

Therefore, the results for the two mock-ups were analyzed separately. With a p-value of 0.000 for both mock-ups, the fourth null hypothesis was rejected, indicating that the splitting tensile strength was not constant with respect to time for either mock-up. Therefore, the splitting tensile strength of the concrete for the two mock-ups was modelled based on the combined Ext and Int results.

Modulus of elasticity results for the first mock-up are shown in **Error! Reference source not found.**, **Error! Reference source not found.**, and Figure B.5, and results for the second mock-up are shown in Table B.7, Table B.8, and Figure B.6. Results of ANOVA between the two mock-ups are presented in Table B.9. The first null hypothesis could not be rejected at any age for any curing condition for either mock-up, so the sets of data from the two trucks were combined for further analysis. The second null hypothesis could not be rejected at any age for the second mock-up and could only be rejected for two of the seven testing ages for the first mock-up. These results suggest that the modulus of elasticity values for the Ext and Int concrete were generally not statistically distinct, so the sets of data for the Ext and Int concrete were combined for further analysis. The third null hypothesis was rejected for four of the five testing ages, indicating that the modulus of elasticity values for the two mock-ups were generally statistically distinct. Therefore, the results for the two mock-ups were analyzed separately. With a p-value of 0.250 for the first mock-up, the fourth null hypothesis could not be rejected, indicating that the modulus of elasticity was not statistically unique at any age for the first mock-up. Therefore, the modulus of elasticity for the first mock-up concrete was taken to be a constant value equal to the average value measured for Ext and Int specimens at all tested ages: 24.5 GPa (3,555 ksi). In contrast, with a p-value of 0.002 for the second mock-up, the fourth null hypothesis was rejected, indicating that the modulus of elasticity was not constant with respect to time for the second mock-up.

Therefore, the modulus of elasticity of the concrete for the second mock-up modelled based on the combined Ext and Int results.

Poisson's ratio results for the first mock-up are shown in **Error! Reference source not found.**, **Error! Reference source not found.**, and Figure B.7, and results for the second mock-up are shown in Table B.10, Table B.11, and Figure B.8. Results of ANOVA between the two mock-ups are presented in Table B.12. The first null hypothesis could not be rejected at any age for any curing condition for either mock-up, so the sets of data from the two trucks were combined for further analysis. The second null hypothesis could not be rejected at any age for the first mock-up and could only be rejected for one of the five testing ages for the second mock-up. These results suggest that the Poisson's ratio values for the Ext and Int concrete were generally not statistically distinct, so the sets of data for the Ext and Int concrete were combined for further analysis. The third null hypothesis could not be rejected at any age, indicating that the Poisson's ratio values for the two mock-ups were not statistically distinct, so the sets of data for the two mock-ups were combined for further analysis. With a p-value of 0.126, the fourth null hypothesis could not be rejected, indicating that the Poisson's ratio was not statistically unique at any age. Therefore, the Poisson's ratio for all concrete was taken to be a constant value equal to the average value measured for all concrete at all tested ages: 0.20.

Table B.2: Compressive strength and associated ANOVA results for concrete from the two trucks for the first mock-up

Batch ID	Truck	Specimen	Compressive Strength (psi)											
			1-day	2-day	3-day	7-day	10-day	14-day	28-day	56-day	90-day	180-day		
I-Fog	1	1	2,162	2,519	3,955	3,428	-	5,153	5,118	5,396	5,150	5,484		
		2	1,872	2,970	3,512	4,461	-	5,105	5,438	5,427	6,329	5,619		
		3	2,091	2,639	3,613	4,202	-	3,826	5,254	-	6,266	6,192		
		4	1,986	3,179	3,666	3,673	-	4,549	5,189	-	5,650	6,492		
	Average	2,028	2,827	3,686	3,941	-	4,658	5,250	5,412	5,849	5,947			
	Std. Dev.	127	303	190	474	-	619	137	22	557	476			
	2	1	-	2,948	3,867	3,983	3,915	4,030	5,325	-	5,488	6,658		
		2	-	2,211	3,222	4,272	3,960	3,981	5,139	-	5,770	6,139		
3		-	2,950	3,298	4,853	4,707	4,351	5,010	-	3,026**	5,874			
4		-	2,773	3,426	4,338	4,639	4,634	5,149	-	5,838	-			
Average	-	2,721	3,453	4,361	4,305	4,249	5,156	-	5,699	6,224				
Std. Dev.	-	349	288	362	426	304	129	-	186	399				
Total	Average	2,028	2,774	3,570	4,151	4,305	4,454	5,203	5,412	5,784	6,066			
	Std. Dev.	127	308	258	450	426	502	133	22	416	434			
	p-value*	-	0.663	0.225	0.208	-	0.280	0.359	-	0.679	0.453			

* p-value for one-way ANOVA with significance level $\alpha = 0.05$ and the null hypothesis that, for each mock-up and curing condition and at each age, the mean value of the compressive strength of the concrete from the two trucks was the same

** This value was discarded in accordance with ASTM E178-08 using the upper 1% significance level

Table B.2 (continued)

Batch ID	Truck	Specimen	Compressive Strength (psi)									
			1-day	2-day	3-day	7-day	10-day	14-day	28-day	56-day	90-day	180-day
I-Ext	1	1	2,822	-	3,467	3,627	-	-	4,900	-	5,300	6,268
		2	2,707	-	3,552	4,352	-	-	4,679	-	5,255	5,803
		3	3,063	-	4,100	4,010	-	-	5,222	-	4,635	-
		4	2,882	-	4,248	4,796	-	-	5,345	-	5,029	-
	Average		2,868	-	3,842	4,196	-	-	5,037	-	5,055	6,036
	Std. Dev.		149	-	390	498	-	-	303	-	304	329
	2	1	-	3,957	4,958	4,778	-	-	5,058	-	5,184	5,850
		2	-	3,749	3,478	4,284	-	-	4,685	-	5,543	5,733
3		-	3,475	4,200	4,456	-	-	4,786	-	4,825	5,608	
4		-	3,815	4,128	4,386	-	-	4,742	-	4,807	-	
Average		-	3,749	4,191	4,476	-	-	4,818	-	5,090	5,730	
Std. Dev.		-	202	606	213	-	-	165	-	348	121	
Total	Average		2,868	3,749	4,016	4,336	-	-	4,927	-	5,072	5,852
	Std. Dev.		149	202	507	385	-	-	255	-	303	250
	p-value*		-	-	0.370	0.342	-	-	0.252	-	0.885	0.216

* p-value for one-way ANOVA with significance level $\alpha = 0.05$ and the null hypothesis that, for each mock-up and curing condition and at each age, the mean value of the compressive strength of the concrete from the two trucks was the same

Table B.2 (continued)

Batch ID	Truck	Specimen	Compressive Strength (psi)										
			1-day	2-day	3-day	7-day	10-day	14-day	28-day	56-day	90-day	180-day	
I-Int	1	1	3,190	-	4,280	4,066	-	-	-	4,358	-	4,653	5,542
		2	3,151	-	3,681	4,070	-	-	-	4,266	-	4,573	5,114
		3	3,461	-	3,887	4,319	-	-	-	4,276	-	5,021	-
		4	2,907	-	4,472	3,357	-	-	-	4,449	-	4,054	-
	Average	3,177	-	4,080	3,953	-	-	-	4,337	-	4,575	5,328	
	Std. Dev.	227	-	361	414	-	-	-	85	-	398	303	
	2	1	-	3,154	4,105	4,218	-	-	-	4,320	-	4,395	5,084
		2	-	4,086	3,812	3,709	-	-	-	3,982	-	5,368	5,389
3		-	3,865	3,653	4,771	-	-	-	4,982	-	5,181	5,414	
4		-	4,261	3,536	4,845	-	-	-	5,213	-	4,792	-	
Average	-	3,841	3,776	4,386	-	-	-	4,624	-	4,934	5,296		
Std. Dev.	-	486	246	531	-	-	-	571	-	432	184		
Total	Average	3,177	3,841	3,928	4,169	-	-	-	4,481	-	4,755	5,308	
	Std. Dev.	227	486	329	498	-	-	-	408	-	430	200	
	p-value*	-	-	0.214	0.246	-	-	-	0.359	-	0.268	0.888	

* p-value for one-way ANOVA with significance level $\alpha = 0.05$ and the null hypothesis that, for each mock-up and curing condition and at each age, the mean value of the compressive strength of the concrete from the two trucks was the same

Table B.3: ANOVA results at each age for compressive strength of Ext and Int specimens from first mock-up

Truck	Specimen	1-Day		2-Day		3-Day		7-Day		28-Day		90-Day		180-Day	
		I-Ext	I-Int	I-Ext	I-Int	I-Ext	I-Int	I-Ext	I-Int	I-Ext	I-Int	I-Ext	I-Int	I-Ext	I-Int
1	1	2822	3190			3467	4280	3627	4066	4900	4358	5300	4653	6268	5542
	2	2707	3151			3552	3681	4352	4070	4679	4266	5255	4573	5803	5114
	3	3063	3461			4100	3887	4010	4319	5222	4276	4635	5021		
	4	2882	2907			4248	4472	4796	3357	5345	4449	5029	4054		
2	1			3957	3154	4958	4105	4778	4218	5058	4320	5184	4395	5850	5084
	2			3749	4086	3478	3812	4284	3709	4685	3982	5543	5368	5733	5389
	3			3475	3865	4200	3653	4456	4771	4786	4982	4825	5181	5608	5414
	4			3815	4261	4128	3536	4386	4845	4742	5213	4807	4792		
	p-value*	0.063		0.738		0.687		0.466		0.020		0.110		0.005	

* p-value for one-way ANOVA with significance level $\alpha = 0.05$ and the null hypothesis that, for each mock-up and at each age, the mean value of compressive strength for the Ext and Int curing conditions was the same

Table B.1: Compressive strength and ANOVA results for concrete from the second mock-up

Batch ID	Truck	Specimen	Compressive Strength (MPa)					
			1-day	3-day	7-day	28-day	90-day	
II-Fog	1	1	14.9	23.9	36.2	45.0	48.6	
		2	18.1	22.9	37.5	47.6	47.2	
		3	18.2	27.8	36.5	45.8	48.4	
		4	17.4	27.8	39.2	47.7	47.6	
		Average Std. Dev.	17.1 1.5	25.6 2.6	37.4 1.4	46.5 1.4	47.9 0.7	
	2	1	-	-	30.7	41.4	43.6	
		2	-	-	28.8	42.2	45.9	
		3	-	-	31.3	42.0	43.0	
		4	-	-	30.1	41.8	46.7	
		Average Std. Dev.	- -	- -	30.2 1.1	41.9 0.3	44.8 1.8	
	Total	Average Std. Dev. p-value*	17.1 1.5 -	25.6 2.6 -	33.8 4.0 0.000	44.2 2.7 0.001	46.9 1.7 0.017	
	II-Ext	1	1	26.1	26.9	40.5	42.2	43.0
			2	20.2	32.8	41.2	41.7	41.6
3			21.3	29.4	41.3	40.1	41.4	
4			29.5	30.9	42.5	41.2	39.9	
Average Std. Dev.			24.3 4.3	30.0 2.5	41.4 0.8	41.3 0.9	41.5 1.2	
II-Int	1	1	28.0	34.5	40.3	42.2	41.4	
		2	27.0	26.6	40.6	40.3	45.4	
		3	26.4	35.4	40.7	38.7	44.6	
		4	27.6	28.2	39.3	36.8	43.9	
		Average Std. Dev.	27.2 0.7	31.2 4.4	40.2 0.6	39.5 2.3	43.8 1.7	

* p-value for one-way ANOVA with significance level $\alpha = 0.05$ and the null hypothesis that, for each mock-up and curing condition and at each age, the mean value of the compressive strength of the concrete from the two trucks was the same

Table B.2: ANOVA results at each age for compressive strength of Ext and Int specimens from second mock-up

Specimen	1-Day		3-Day		7-Day		28-Day		90-Day	
	II-Ext	II-Int								
1	3782	4062	3907	5005	5877	5845	6127	6127	6231	6008
2	2934	3915	4759	3852	5976	5889	6048	5849	6040	6581
3	3094	3826	4257	5129	5992	5901	5809	5610	6008	6470
4	4278	3998	4480	4090	6167	5698	5968	5332	5793	6362
p-value*	0.224		0.664		0.067		0.207		0.070	

* p-value for one-way ANOVA with significance level $\alpha = 0.05$ and the null hypothesis that, for each mock-up and at each age, the mean value of compressive strength for the Ext and Int curing conditions was the same

Table B.3: ANOVA results for compressive strength of specimens from both mock-ups

Curing	p-value*				
	2-Day	3-Day	7-Day	28-Day	90-Day
Fog	0.012	0.444	0.011	0.000	0.005
Ext/Int	0.002	0.024	0.000	0.000	0.000

* p-value for one-way ANOVA with significance level $\alpha = 0.05$ and the null hypothesis that, for each curing condition and at each age, the mean value of compressive strength for the two mock-ups was the same

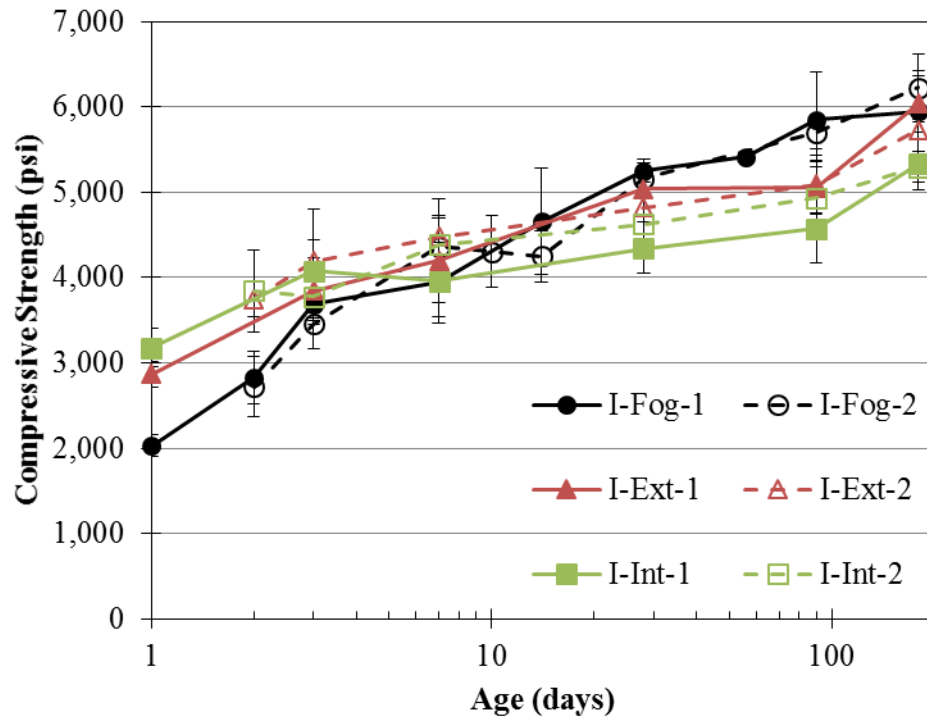


Figure B.1: Compressive strength results for first mock-up sorted by truck and curing condition

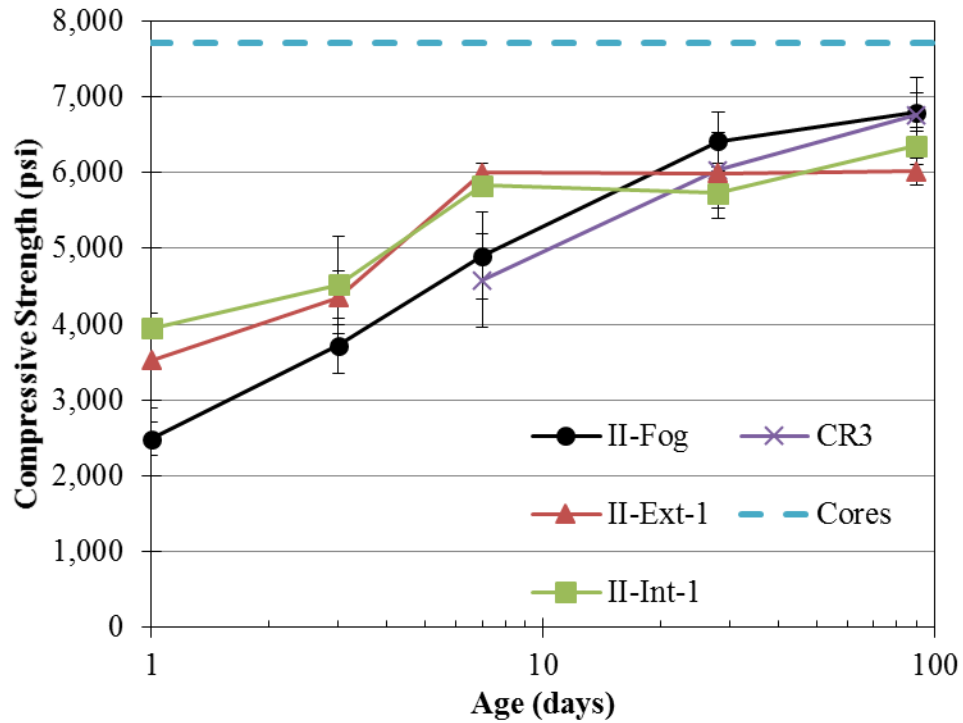


Figure B.2: Compressive strength results for second mock-up

Table B.7: Splitting tensile strength and associated ANOVA results for concrete from the two trucks for the first mock-up

Batch ID	Truck	Specimen	Splitting Tensile Strength (psi)										
			1-day	2-day	3-day	7-day	10-day	14-day	28-day	90-day	180-day		
I-Fog	1	1	419	450	506	488	-	522	537	705	671		
		2	387	464	467	510	-	566	577	773	647		
		3	385	454	484	524	-	520	526	714	768		
		4	361	439	504	560	-	514	595	721	723		
		Average	388	452	490	520	-	530	559	728	702		
	Std. Dev.	24	10	18	30	-	24	33	31	54			
	2	1	-	446	472	515	519	509	593	680	728		
		2	-	469	510	549	586	548	582	768	642		
		3	-	420	480	421	454	524	481	696	727		
		4	-	439	476	562	545	578	642	-			
Average		-	444	484	495	530	532	559	697	699			
Std. Dev.	-	20	17	67	58	18	52	53	49				
Total	Average	388	448	487	510	530	531	559	713	701			
	Std. Dev.	24	16	17	46	58	20	40	43	48			
		p-value*	0.503	0.660	0.523	-	0.932	0.991	0.339	0.935			

* p-value for one-way ANOVA with significance level $\alpha = 0.05$ and the null hypothesis that, for each mock-up and curing condition and at each age, the mean value of the splitting tensile strength of the concrete from the two trucks was the same

Table B.7 (continued)

Batch ID	Truck	Specimen	Splitting Tensile Strength (psi)											
			1-day	2-day	3-day	7-day	10-day	14-day	28-day	90-day	180-day			
I-Ext	1	1	477	-	493	566	-	-	-	-	491	577	535	
		2	530	-	578	599	-	-	-	-	554	612	610	
		3	446	-	609	526	-	-	-	-	504	584	563	
		4	476	-	517	478	-	-	-	-	483	581	-	
	Average	482	-	549	542	-	-	-	-	508	589	569		
	Std. Dev.	35	-	53	52	-	-	-	-	32	16	38		
	2	1	-	495	591	528	-	-	-	-	441	598	667	
		2	-	502	476	535	-	-	-	-	516	552	586	
3		-	470	502	518	-	-	-	-	473	589	577		
4		-	489	589	491	-	-	-	-	541	593	-		
Average	-	489	540	518	-	-	-	-	493	583	610			
Std. Dev.	-	14	59	19	-	-	-	-	44	21	50			
Total	Average	482	489	544	530	-	-	-	-	500	586	590		
	Std. Dev.	35	14	52	39	-	-	-	-	37	18	46		
	p-value*	-	-	0.820	0.416	-	-	-	-	0.599	0.339	0.322		

* p-value for one-way ANOVA with significance level $\alpha = 0.05$ and the null hypothesis that, for each mock-up and curing condition and at each age, the mean value of the splitting tensile strength of the concrete from the two trucks was the same

Table B.7 (continued)

Batch ID	Truck	Specimen	Splitting Tensile Strength (psi)											
			1-day	2-day	3-day	7-day	10-day	14-day	28-day	90-day	180-day			
I-Int	1	1	442	-	482	461	-	-	-	-	506	597	637	
		2	404	-	533	488	-	-	-	-	501	563	525	
		3	401	-	485	489	-	-	-	-	524	552	665	
		4	416	-	467	526	-	-	-	-	505	608	-	
	Average	416	-	492	491	-	-	-	-	509	580	609		
	Std. Dev.	19	-	29	27	-	-	-	-	10	27	74		
	2	1	-	497	390	501	-	-	-	-	466	556	508	
		2	-	494	507	495	-	-	-	-	459	599	557	
		3	-	492	455	473	-	-	-	-	492	448	639	
		4	-	507	501	494	-	-	-	-	527	527	-	
Average	-	498	463	491	-	-	-	-	486	532	568			
Std. Dev.	-	6	54	12	-	-	-	-	31	64	66			
Total	Average	416	498	477	491	-	-	-	-	498	556	588		
	Std. Dev.	19	6	43	19	-	-	-	-	25	52	67		
	p-value*	-	-	0.388	1.000	-	-	-	-	0.207	0.216	0.509		

* p-value for one-way ANOVA with significance level $\alpha = 0.05$ and the null hypothesis that, for each mock-up and curing condition and at each age, the mean value of the splitting tensile strength of the concrete from the two trucks was the same

Table B.8: ANOVA results at each age for splitting tensile strength of Ext and Int specimens from first mock-up

Truck	Specimen	2-day		3-day		7-day		28-day		90-day		180-day	
		I-Ext	I-Int	I-Ext	I-Int	I-Ext	I-Int	I-Ext	I-Int	I-Ext	I-Int	I-Ext	I-Int
1	1	495	497	493	482	566	461	491	506	577	597	535	637
	2	502	494	578	533	599	488	554	501	612	563	610	525
	3	470	492	609	485	526	489	504	524	584	552	563	665
	4	489	507	517	467	478	526	483	505	581	608		
2	1			591	390	528	501	441	466	598	556	667	508
	2			476	507	535	495	516	459	552	599	586	557
	3			502	455	518	473	473	492	589	448	577	639
	4			589	501	491	494	541	527	593	527		
	p-value*	0.295		0.014		0.022		0.853		0.148		0.971	

* p-value for one-way ANOVA with significance level $\alpha = 0.05$ and the null hypothesis that, for each mock-up and at each age, the mean value of splitting tensile strength for the Ext and Int curing conditions was the same

Table B.4: Splitting tensile strength and ANOVA results for concrete from the second mock-up

Batch ID	Truck	Specimen	Splitting Tensile Strength (psi)					
			1-day	3-day	7-day	28-day	90-day	
II-Fog	1	1	448	583	603	509	584	
		2	466	591	504	541	625	
		3	456	539	505	623	610	
		4	454	505	621	573	582	
		Average Std. Dev.	456 7	555 40	558 62	562 48	600 21	
	2	1	-	-	592	463	625	
		2	-	-	501	513	559	
		3	-	-	515	583	649	
		4	-	-	498	531	543	
		Average Std. Dev.	- -	- -	527 44	522 50	594 51	
	Total	Average Std. Dev.	456 7	555 40	542 53	542 50	597 36	
		p-value*	-	-	0.439	0.303	0.828	
	II-Ext	1	1	512	577	642	687	581
			2	537	609	586	635	550
3			525	588	643	631	583	
4			507	561	596	619	590	
Average Std. Dev.			520 13	584 20	616 30	643 30	576 18	
II-Int	1	1	519	690	669	702	611	
		2	508	621	649	684	584	
		3	535	639	545	597	621	
		4	529	613	591	575	517	
		Average Std. Dev.	523 12	641 35	613 56	640 63	583 47	

* p-value for one-way ANOVA with significance level $\alpha = 0.05$ and the null hypothesis that, for each mock-up and curing condition and at each age, the mean value of the splitting tensile strength of the concrete from the two trucks was the same

Table B.5: ANOVA results at each age for splitting tensile strength of Ext and Int specimens from second mock-up

Specimen	1-Day		3-Day		7-Day		28-Day		90-Day	
	II-Ext	II-Int								
1	512	519	577	690	642	669	687	702	581	611
2	537	508	609	621	586	649	635	684	550	584
3	525	535	588	639	643	545	631	597	583	621
4	507	529	561	613	596	591	619	575	590	517
p-value*	0.790		0.030		0.929		0.929		0.782	

* p-value for one-way ANOVA with significance level $\alpha = 0.05$ and the null hypothesis that, for each mock-up and at each age, the mean value of splitting tensile strength for the Ext and Int curing conditions was the same

Table B.6: ANOVA results for splitting tensile strength of specimens from both mock-ups

Curing	p-value*				
	1-Day	3-Day	7-Day	28-Day	90-Day
Fog	0.002	0.002	0.224	0.470	0.000
Ext/Int	0.000	0.000	0.000	0.000	0.614

* p-value for one-way ANOVA with significance level $\alpha = 0.05$ and the null hypothesis that, for each curing condition and at each age, the mean value of splitting tensile strength for the two mock-ups was the same

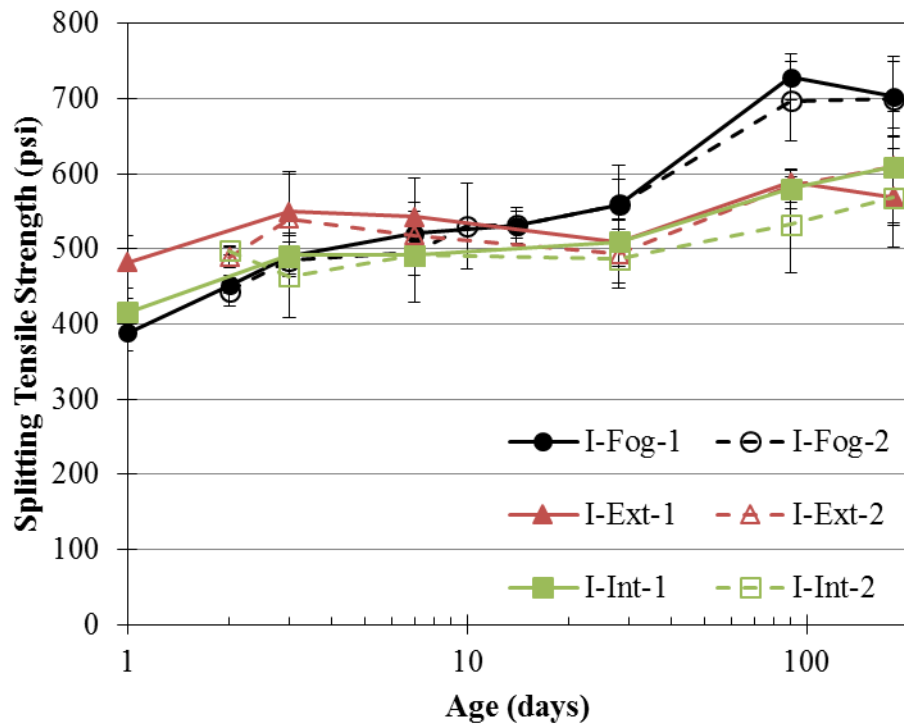


Figure B.3: Splitting tensile strength results for first mock-up sorted by truck and curing condition

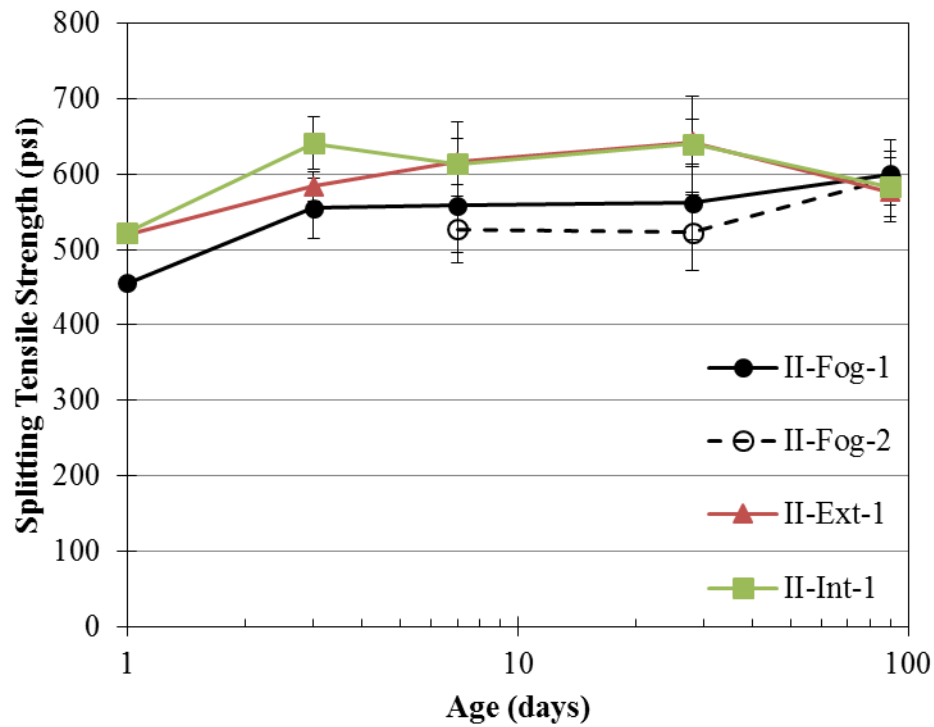


Figure B.4: Splitting tensile strength results for second mock-up sorted by truck and curing condition

Table B.12: Modulus of elasticity and associated ANOVA results for concrete from the two trucks for the first mock-up

Batch ID	Truck	Specimen	Modulus of Elasticity (ksi)											
			1-day	2-day	3-day	7-day	10-day	14-day	28-day	56-day	90-day	180-day		
I-Fog	1	1	3,601	2,856	3,629	3,612	-	4,121	-	4,290	4,181	4,421		
		2	3,131	3,136	-	3,421	-	3,830	3,912	4,350	5,013	3,989		
		3	2,792	3,435	3,341	3,717	-	4,185	4,388	5,254	4,214	4,672		
		Average	3,175	3,142	3,485	3,583	-	4,045	4,150	4,631	4,469	4,361		
		Std. Dev.	407	289	203	150	-	189	337	540	471	345		
			-	3,399	-	4,164	3,944	4,461	3,689	4,293	4,608	3,907		
	2	1	-	3,173	-	3,192	4,726	4,013	4,258	4,365	3,849	3,887		
		2	-	2,778	-	3,657	3,759	3,818	3,700	4,142	4,483	4,681		
		3	-	3,117	-	3,671	4,143	4,097	3,882	4,267	4,313	4,158		
		Average	-	314	-	486	513	330	325	114	407	453		
Total		3,175	3,129	3,485	3,627	4,143	4,071	3,989	4,449	4,391	4,260			
	Std. Dev.	407	270	203	325	513	242	321	402	403	377			
	p-value*	-	0.923	-	0.781	-	0.824	0.439	0.317	0.687	0.571			

* p-value for one-way ANOVA with significance level $\alpha = 0.05$ and the null hypothesis that, for each mock-up and curing condition and at each age, the mean value of the modulus of elasticity of the concrete from the two trucks was the same

Table B.12 (continued)

Batch ID	Truck	Specimen	Modulus of Elasticity (ksi)											
			1-day	2-day	3-day	7-day	10-day	14-day	28-day	56-day	90-day	180-day		
1		1	3,459	-	3,401	3,787	-	-	3,768	3,533	3,487	4,011		
		2	3,374	-	3,574	3,744	-	-	3,555	3,836	3,404	3,645		
		3	3,295	-	3,670	3,771	-	-	3,814	3,162	4,132	4,118		
		Average	3,376	-	3,548	3,768	-	-	3,712	3,510	3,674	3,925		
		Std. Dev.	82	-	136	22	-	-	138	338	398	248		
I-Ext	2	1	-	3,619	-	3,904	-	-	3,032	3,907	3,782	3,775		
		2	-	3,802	-	3,644	-	-	4,084	3,830	3,292	3,615		
		3	-	3,658	-	3,536	-	-	3,474	3,262	3,879	3,803		
		Average	-	3,693	-	3,695	-	-	3,530	3,667	3,651	3,731		
		Std. Dev.	-	97	-	189	-	-	528	352	314	101		
Total		Average	3,376	3,693	3,548	3,731	-	-	3,621	3,589	3,663	3,828		
		SD	82	97	136	127	-	-	359	320	321	200		
		p-value*	-	-	-	0.545	-	-	0.594	0.609	0.939	0.278		

* p-value for one-way ANOVA with significance level $\alpha = 0.05$ and the null hypothesis that, for each mock-up and curing condition and at each age, the mean value of the modulus of elasticity of the concrete from the two trucks was the same

Table B.12 (continued)

Batch ID	Truck	Specimen	Modulus of Elasticity (ksi)										
			1-day	2-day	3-day	7-day	10-day	14-day	28-day	56-day	90-day	180-day	
I-Int	1	1	3,603	-	3,564	3,613	-	-	3,079	2,930	3,334	3,740	
		2	3,578	-	3,382	3,475	-	-	3,640	3,457	4,633	3,165	
		3	3,308	-	3,463	3,417	-	-	3,190	3,737	3,596	3,371	
	Average	3,496	-	3,469	3,501	-	-	3,303	3,375	3,854	3,425		
	Std. Dev.	164	-	91	100	-	-	297	410	687	291		
2	2	1	-	3,615	-	3,457	-	-	2,877	3,338	3,191	3,421	
		2	-	3,541	-	3,512	-	-	3,293	3,261	3,763	3,683	
		3	-	3,365	-	3,379	-	-	3,549	2,966	3,510	3,553	
Average	-	3,507	-	3,449	-	-	3,239	3,188	3,488	3,553			
Std. Dev.	-	128	-	67	-	-	339	196	287	131			
Total	Total	Average	3,496	3,507	3,469	3,475	-	-	3,271	3,281	3,671	3,489	
		SD	164	128	91	81	-	-	287	305	512	214	
		p-value*	-	-	-	0.496	-	-	0.819	0.516	0.442	0.527	

* p-value for one-way ANOVA with significance level $\alpha = 0.05$ and the null hypothesis that, for each mock-up and curing condition and at each age, the mean value of the modulus of elasticity of the concrete from the two trucks was the same

Table B.13: ANOVA results at each age for modulus of elasticity of Ext and Int specimens from first mock-up

Truck	Specimen	1-Day		2-Day		7-Day		28-Day		56-Day		90-Day		180-Day	
		Ext	Int	Ext	Int	Ext	Int	Ext	Int	Ext	Int	Ext	Int	Ext	Int
1	1	3,459	3,603			3,787	3,613	3,768	3,079	3,533	2,930	3,487	3,334	4,011	3,740
	2	3,374	3,578			3,744	3,475	3,555	3,640	3,836	3,457	3,404	4,633	3,645	3,165
	3	3,295	3,308			3,771	3,417	3,814	3,190	3,162	3,737	4,132	3,596	4,118	3,371
2	1			3,619	3,615	3,904	3,457	3,032	2,877	3,907	3,338	3,782	3,191	3,775	3,421
	2			3,802	3,541	3,644	3,512	4,084	3,293	3,830	3,261	3,292	3,763	3,615	3,683
	3			3,658	3,365	3,536	3,379	3,474	3,549	3,262	2,966	3,879	3,510	3,803	3,553
	p-value*	0.318		0.115		0.002		0.092		0.120		0.973		0.018	

* p-value for one-way ANOVA with significance level $\alpha = 0.05$ and the null hypothesis that, for each mock-up and at each age, the mean value of modulus of elasticity for the Ext and Int curing conditions was the same

Table B.7: Modulus of elasticity and ANOVA results for concrete from the second mock-up

Batch ID	Truck	Specimen	Modulus of Elasticity (ksi)				
			2-day	3-day	7-day	28-day	90-day
II-Fog	1	1	3,806	4,186	4,869	3,993	4,675
		2	3,700	4,384	3,578	4,924	5,075
		3	4,282	3,634	4,242	4,733	4,764
		Average Std. Dev.	3,929 310	4,068 389	4,229 646	4,550 492	4,838 210
	2	1	-	-	4,015	4,913	4,326
		2	-	-	3,637	4,232	4,732
		3	-	-	3,471	4,939	4,277
		Average Std. Dev.	- -	- -	3,707 279	4,695 401	4,445 250
	Total	Average Std. Dev. p-value*	3,929 310 -	4,068 389 -	3,968 529 0.268	4,622 409 0.714	4,641 298 0.105
II-Ext	1	1	4,065	3,955	4,106	4,612	4,380
		2	3,729	4,290	3,480	4,582	4,568
		3	4,224	4,473	3,540	4,443	4,515
		Average Std. Dev.	4,006 253	4,240 263	3,709 345	4,546 90	4,488 97
II-Int	1	1	4,014	4,063	3,719	4,384	4,362
		2	3,822	4,374	4,333	3,808	4,384
		3	4,238	4,537	3,624	3,922	4,364
		Average Std. Dev.	4,025 208	4,325 241	3,892 385	4,038 305	4,370 12

* p-value for one-way ANOVA with significance level $\alpha = 0.05$ and the null hypothesis that, for each mock-up and curing condition and at each age, the mean value of the modulus of elasticity of the concrete from the two trucks was the same

Table B.8: ANOVA results at each age for modulus of elasticity of Ext and Int specimens from second mock-up

Specimen	2-Day		3-Day		7-Day		28-Day		90-Day	
	II-Ext	II-Int								
1	4,065	4,014	3,955	4,063	4,106	3,719	4,612	4,384	4,380	4,362
2	3,729	3,822	4,290	4,374	3,480	4,333	4,582	3,808	4,568	4,384
3	4,224	4,238	4,473	4,537	3,540	3,624	4,443	3,922	4,515	4,364
p-value*	0.924		0.700		0.573		0.051		0.106	

* p-value for one-way ANOVA with significance level $\alpha = 0.05$ and the null hypothesis that, for each mock-up and at each age, the mean value of modulus of elasticity for the Ext and Int curing conditions was the same

Table B.9: ANOVA results for modulus of elasticity of specimens from both mock-ups

Curing	p-value*				
	2-Day	3-Day	7-Day	28-Day	90-Day
Fog	0.005	0.156	0.208	0.020	0.250
Ext/Int	0.002	0.000	0.115	0.000	0.000

* p-value for one-way ANOVA with significance level $\alpha = 0.05$ and the null hypothesis that, for each curing condition and at each age, the mean value of modulus of elasticity for the two mock-ups was the same

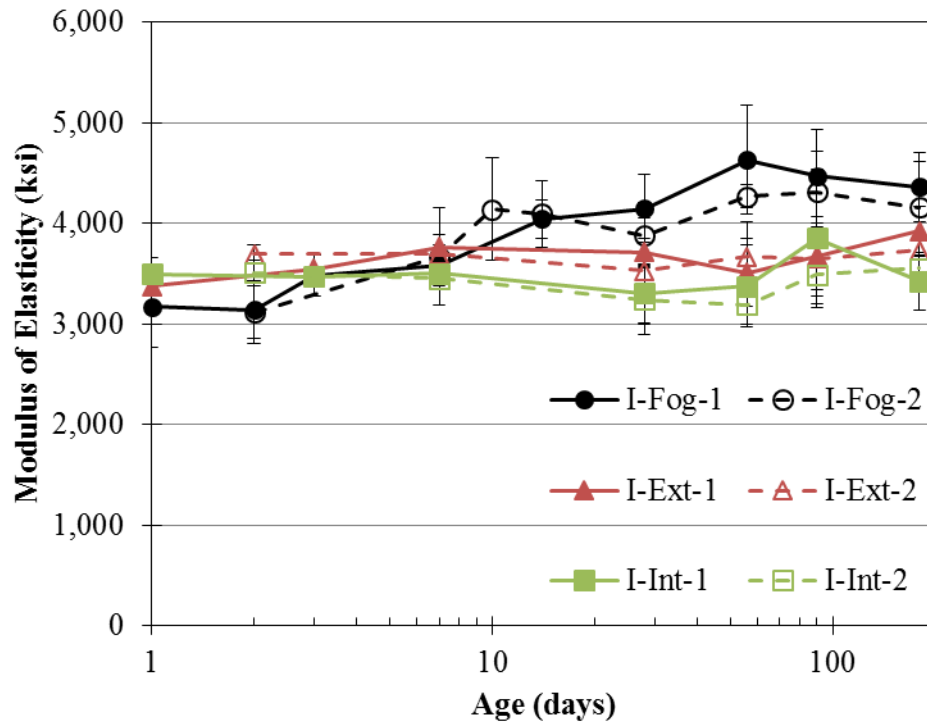


Figure B.5: Modulus of elasticity results for first mock-up sorted by truck and curing condition

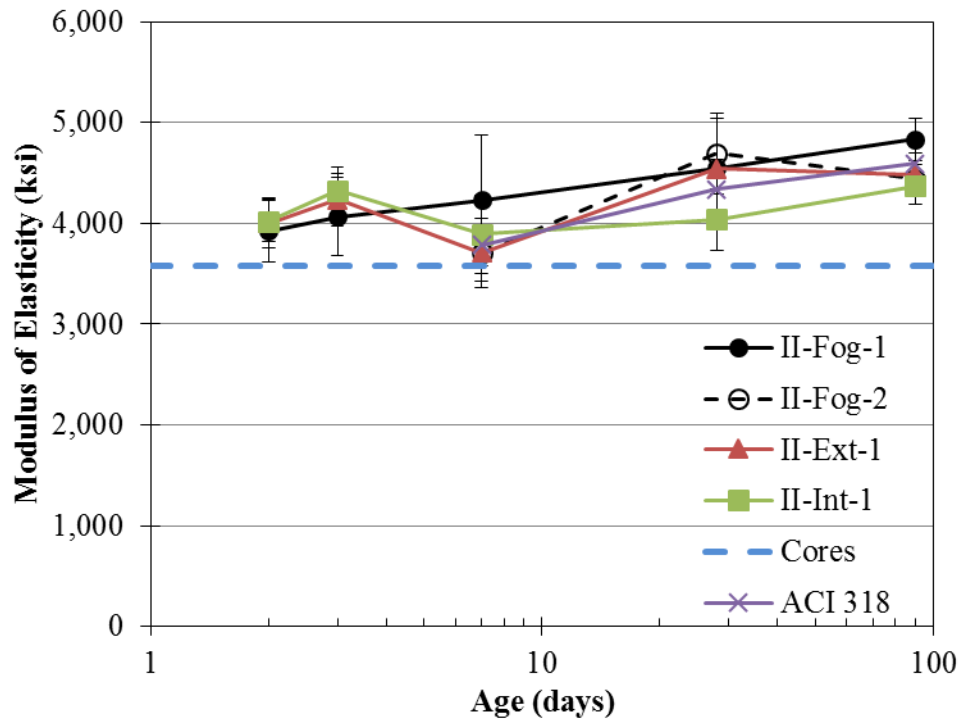


Figure B.6: Modulus of elasticity results for second mock-up sorted by truck and curing condition

Table B.17: Poisson's ratio and associated ANOVA results for concrete from the two trucks for the first mock-up

Batch ID	Truck	Specimen	Poisson's Ratio											
			1-day	2-day	3-day	7-day	10-day	14-day	28-day	56-day	90-day	180-day		
I-Fog	1	1	0.13	0.15	0.19	0.20	-	0.23	-	0.22	0.22	0.22	0.22	0.23
		2	0.15	0.13	-	0.18	-	0.23	0.23	0.22	0.22	0.22	0.22	0.22
		3	-	0.14	0.19	0.20	-	0.21	0.22	0.26	0.23	0.23	0.23	0.24
		Average	0.14	0.14	0.19	0.19	-	0.22	0.22	0.23	0.23	0.22	0.22	0.23
		Std. Dev.	0.009	0.011	0.003	0.013	-	0.014	0.002	0.025	0.003	0.003	0.003	0.010
I-Fog	2	1	-	0.13	-	0.23	0.23	0.22	0.17	0.23	0.25	0.25	0.20	
		2	-	0.16	-	0.18	0.26	0.20	0.20	0.19	0.17	0.17	0.20	
		3	-	0.15	-	0.17	0.20	0.21	0.22	0.22	0.22	0.22	0.23	
		Average	-	0.15	-	0.19	0.23	0.21	0.20	0.21	0.21	0.21	0.21	
		Std. Dev.	-	0.011	-	0.033	0.028	0.011	0.025	0.022	0.041	0.041	0.020	
Total		Average	0.14	0.14	0.19	0.19	0.23	0.22	0.21	0.22	0.22	0.22	0.22	
		Std. Dev.	0.009	0.010	0.003	0.022	0.028	0.014	0.023	0.025	0.027	0.027	0.018	
		p-value*	-	0.580	-	0.977	-	0.234	0.264	0.298	0.690	0.690	0.204	

* p-value for one-way ANOVA with significance level $\alpha = 0.05$ and the null hypothesis that, for each mock-up and curing condition and at each age, the mean value of the Poisson's ratio of the concrete from the two trucks was the same

Table B.17 (continued)

Batch ID	Truck	Specimen	Poisson's Ratio									
			1-day	2-day	3-day	7-day	10-day	14-day	28-day	56-day	90-day	180-day
1		1	0.17	-	0.21	0.17	-	-	0.21	0.19	0.20	0.22
		2	-	-	0.20	0.17	-	-	0.17	0.20	0.21	0.24
		3	0.19	-	0.21	0.22	-	-	0.19	0.18	0.23	0.23
		Average	0.18	-	0.20	0.18	-	-	0.19	0.19	0.22	0.23
		Std. Dev.	0.014	-	0.003	0.029	-	-	0.018	0.013	0.014	0.013
I-Ext	2	1	-	0.17	-	0.23	-	-	0.16	0.20	0.22	0.21
		2	-	0.17	-	0.21	-	-	0.18	0.21	0.18	0.21
		3	-	0.19	-	0.19	-	-	0.18	0.21	0.26	0.23
		Average	-	0.17	-	0.21	-	-	0.18	0.20	0.22	0.22
		Std. Dev.	-	0.012	-	0.021	-	-	0.012	0.007	0.041	0.014
Total		Average	0.18	0.17	0.20	0.20	-	-	0.18	0.20	0.22	0.22
		SD	0.014	0.012	0.003	0.028	-	-	0.016	0.012	0.028	0.014
		p-value*	-	-	-	0.223	-	-	0.238	0.221	0.868	0.319

* p-value for one-way ANOVA with significance level $\alpha = 0.05$ and the null hypothesis that, for each mock-up and curing condition and at each age, the mean value of the Poisson's ratio of the concrete from the two trucks was the same

Table B.17 (continued)

Batch ID	Truck	Specimen	Poisson's Ratio											
			1-day	2-day	3-day	7-day	10-day	14-day	28-day	56-day	90-day	180-day		
1		1	0.20	-	0.21	0.22	-	-	0.16	0.22	0.18	0.22	0.18	0.22
		2	0.20	-	0.21	0.22	-	-	0.20	0.20	0.26	0.19	0.19	0.19
		3	0.19	-	0.21	0.20	-	-	0.18	0.23	0.18	0.19	0.18	0.19
		Average	0.20	-	0.21	0.21	-	-	0.18	0.21	0.21	0.21	0.20	0.20
		Std. Dev.	0.009	-	0.005	0.010	-	-	0.022	0.014	0.048	0.019	0.019	0.019
I-Int	2	1	-	0.16	-	0.22	-	-	0.17	0.20	0.23	0.23	0.23	
		2	-	0.19	-	0.21	-	-	0.21	0.20	0.25	0.20	0.20	
		3	-	0.17	-	0.21	-	-	0.20	0.17	0.17	0.22	0.22	
		Average	-	0.17	-	0.22	-	-	0.20	0.19	0.22	0.22	0.22	
		Std. Dev.	-	0.017	-	0.006	-	-	0.019	0.017	0.040	0.016	0.016	
Total		Average	0.20	0.17	0.21	0.21	-	-	0.19	0.20	0.21	0.20	0.21	
		SD	0.009	0.017	0.005	0.008	-	-	0.021	0.018	0.040	0.017	0.017	
		p-value*	-	-	-	0.438	-	-	0.389	0.173	0.815	0.374	0.374	

* p-value for one-way ANOVA with significance level $\alpha = 0.05$ and the null hypothesis that, for each mock-up and curing condition and at each age, the mean value of Poisson's ratio of the concrete from the two trucks was the same

Table B.18: ANOVA results at each age for Poisson's ratio of Ext and Int specimens from first mock-up

Specimen	1-Day		2-Day		7-Day		28-Day		56-Day		90-Day		180-Day	
	I-Ext	I-Int	I-Ext	I-Int	I-Ext	I-Int	I-Ext	I-Int	I-Ext	I-Int	I-Ext	I-Int	I-Ext	I-Int
1	0.17	0.20			0.17	0.22	0.21	0.16	0.19	0.22	0.20	0.18	0.22	0.22
2		0.20			0.17	0.22	0.17	0.20	0.20	0.20	0.21	0.26	0.24	0.19
3	0.19	0.19			0.22	0.20	0.19	0.18	0.18	0.23	0.23	0.18	0.23	0.19
1			0.17	0.16	0.23	0.22	0.16	0.17	0.20	0.20	0.22	0.23	0.21	0.23
2			0.17	0.19	0.21	0.21	0.18	0.21	0.21	0.20	0.18	0.25	0.21	0.20
3			0.19	0.17	0.19	0.21	0.18	0.20	0.21	0.17	0.26	0.17	0.23	0.22
p-value*	0.179		0.956		0.228		0.709		0.453		0.744		0.157	

* p-value for one-way ANOVA with significance level $\alpha = 0.05$ and the null hypothesis that, for each mock-up and at each age, the mean value of Poisson's ratio for the Ext and Int curing conditions was the same

Table B.10: Poisson's ratio and ANOVA results for concrete from the second mock-up

Batch ID	Truck	Specimen	Poisson's Ratio					
			2-day	3-day	7-day	28-day	90-day	
II-Fog	1	1	0.17	0.21	0.24	0.19	0.18	
		2	0.22	0.23	0.17	0.24	0.24	
		3	0.21	0.18	0.23	0.19	0.23	
		Average Std. Dev.	0.20 0.03	0.21 0.03	0.21 0.04	0.21 0.03	0.22 0.03	
	2	1	-	-	0.23	0.25	0.22	
		2	-	-	0.19	0.18	0.25	
		3	-	-	0.19	0.23	0.21	
		Average Std. Dev.	- -	- -	0.20 0.02	0.22 0.03	0.23 0.02	
	Total	Average Std. Dev.	0.20 0.03	0.21 0.03	0.21 0.03	0.21 0.03	0.22 0.02	
		p-value*	-	-	0.740	0.595	0.64	
	II-Ext-1	1	1	0.18	0.17	0.23	0.21	0.21
			2	0.17	0.22	0.16	0.23	0.21
3			0.22	0.20	0.18	0.23	0.21	
Average Std. Dev.			0.19 0.03	0.20 0.03	0.19 0.03	0.23 0.01	0.21 0.00	
II-Int-1	1	1	0.19	0.18	0.20	0.19	0.19	
		2	0.17	0.21	0.20	0.20	0.21	
		3	0.20	0.24	0.18	0.17	0.21	
		Average Std. Dev.	0.19 0.01	0.21 0.03	0.19 0.01	0.18 0.02	0.20 0.01	

* p-value for one-way ANOVA with significance level $\alpha = 0.05$ and the null hypothesis that, for each mock-up and curing condition and at each age, the mean value of the Poisson's ratio of the concrete from the two trucks was the same

Table B.11: ANOVA results at each age for Poisson's ratio of Ext and Int specimens from second mock-up

Specimen	2-Day		3-Day		7-Day		28-Day		90-Day	
	II-Ext	II-Int								
1	0.18	0.19	0.17	0.18	0.23	0.20	0.21	0.19	0.21	0.19
2	0.17	0.17	0.22	0.21	0.16	0.20	0.23	0.20	0.21	0.21
3	0.22	0.20	0.20	0.24	0.18	0.18	0.23	0.17	0.21	0.21
p-value*	0.941		0.662		0.987		0.020		0.241	

* p-value for one-way ANOVA with significance level $\alpha = 0.05$ and the null hypothesis that, for each mock-up and at each age, the mean value of Poisson's ratio for the Ext and Int curing conditions was the same

Table B.12: ANOVA results for Poisson's ratio of specimens from both mock-ups

Curing	p-value*				
	2-Day	3-Day	7-Day	28-Day	90-Day
Fog	0.003	0.493	0.302	0.690	0.737
Ext/Int	0.155	0.763	0.180	0.072	0.617

* p-value for one-way ANOVA with significance level $\alpha = 0.05$ and the null hypothesis that, for each curing condition and at each age, the mean value of Poisson's ratio for the two mock-ups was the same

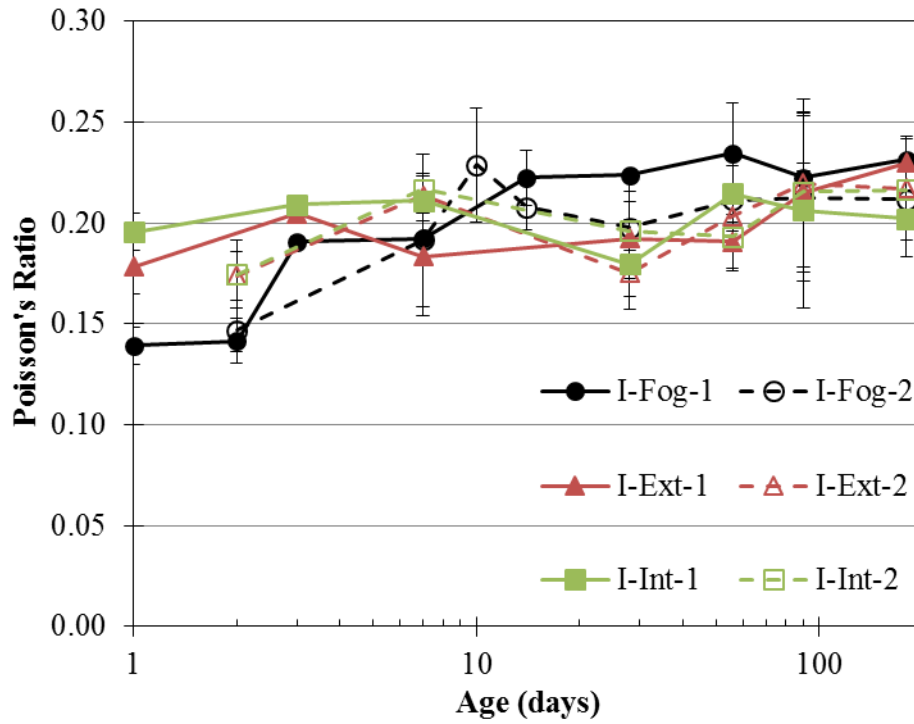


Figure B.7: Poisson's ratio results for first mock-up sorted by truck and curing condition

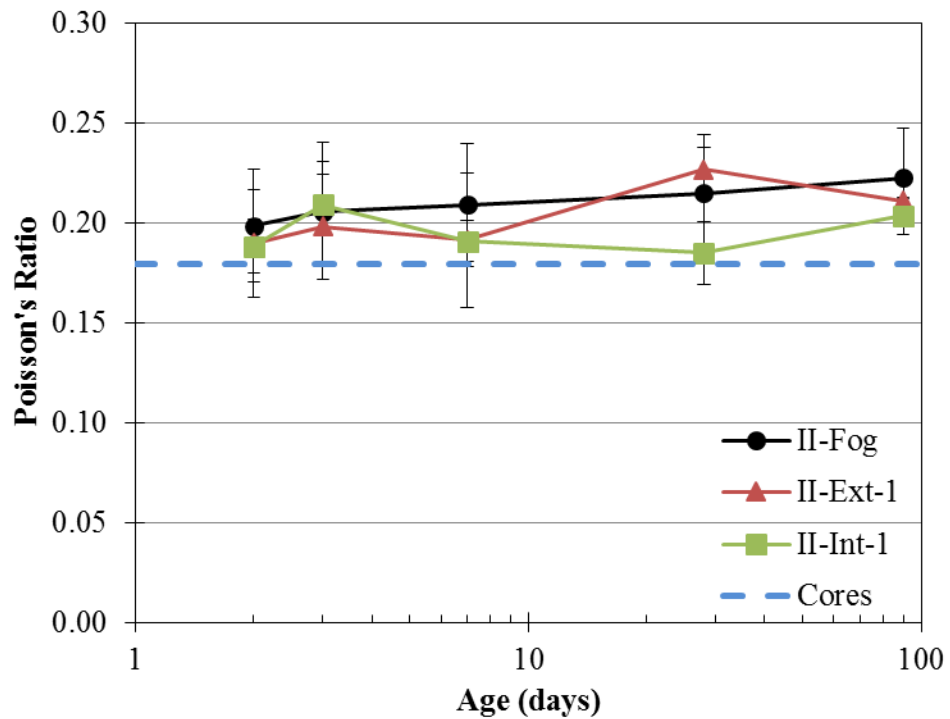


Figure B.8: Poisson's ratio results for second mock-up sorted by truck and curing condition

B.3 Thermal Properties

Results of the tests for thermal diffusivity and CTE for the first mock-up concrete are presented in this section. Thermal diffusivity results are shown in Table B.13, and CTE results are shown in **Error! Reference source not found.** as determined according to CRD-C 29-81 (Army Corps of Engineers, 1981).

Table B.13: Thermal diffusivity results ($1 \text{ m}^2/\text{s} = 38,750 \text{ ft}^2/\text{hr}$)

Truck	Specimen	Thermal Diffusivity, κ ($\text{m}^2/\text{s} \times 10^{-6}$)								
		1-day	2-day	3-day	7-day	10-day	14-day	28-day	56-day	90-day
1	1	0.738	-	0.721	-	0.760	0.728	0.754	0.705	-
	2	0.737	-	0.717	-	0.753	0.747	0.771	0.773	-
	3	0.734	-	0.753	-	0.740	0.736	0.769	0.766	-
	Average Std. Dev.	0.736 0.002	- -	0.730 0.020	- -	0.751 0.010	0.737 0.010	0.764 0.009	0.748 0.037	- -
2	1	-	0.712	-	0.696	0.751	0.783	0.783	-	0.788
	2	-	0.736	-	0.726	0.764	0.710	0.796	0.778	0.773
	3	-	0.688	-	0.740	-	0.734	0.752	0.751	-
	Average Std. Dev.	- -	0.712 0.024	- -	0.721 0.022	0.758 0.009	0.742 0.037	0.777 0.022	0.765 0.019	0.780 0.010
Total	Average	0.736	0.712	0.730	0.721	0.754	0.740	0.771	0.755	0.780
	Std. Dev.	0.002	0.024	0.020	0.022	0.009	0.024	0.017	0.029	0.010
	p-value*	-	-	-	-	0.507	0.817	0.420	0.608	-

* p-value for one-way ANOVA with significance level $\alpha = 0.05$ and the null hypothesis that the concrete from the two trucks is the same

Table B.23: Coefficient of linear thermal expansion results as tested in accordance with CRD-C 29-81 (Army Corps of Engineers, 1981).

ID	Specimen or Measure	Coefficient of Thermal Expansion ($\mu\epsilon/^\circ\text{C}$)										
		1-day	2-day	3-day	7-day	10-day	14-day	28-day	56-day	90-day	All	
I-Fog-1	1	8.11	-	-	6.36	-	5.00	5.79	8.41	12.02	-	-
	2	-	-	-	8.48	-	9.27	7.79	6.05	6.26	-	-
	3	8.91	-	-	10.03	-	10.01	10.46	4.26	7.57	-	-
I-Fog-2	Average	8.51	-	-	8.29	-	8.09	8.01	6.24	8.62	7.93	-
	Std. Dev.	0.57	-	-	1.84	-	2.70	2.34	2.08	3.02	2.10	-
	1	-	7.92	5.68	7.79	8.53	8.04	10.06	6.42	7.17	-	-
Total	2	-	6.80	8.45	11.06	10.62	6.71	10.61	5.20	8.52	-	-
	3	-	8.26	4.79	10.01	6.87	7.78	7.35	8.24	7.18	-	-
	Average	-	7.66	6.30	9.62	8.67	7.51	9.34	6.62	7.62	7.92	-
Total	Std. Dev.	-	0.77	1.91	1.67	1.88	0.71	1.74	1.53	0.78	1.67	-
	Average	8.51	7.66	6.30	8.96	8.67	7.80	8.68	6.43	8.12	7.92	-
	Std. Dev.	0.57	0.77	1.91	1.73	1.88	1.80	1.98	1.65	2.05	1.84	-
	p-value*	-	-	-	0.407	-	0.736	0.475	0.812	0.609	0.259	-

* p-value for one-way ANOVA with significance level $\alpha = 0.05$ and the null hypothesis that the concrete from the two trucks is the same

APPENDIX C

POST-TENSIONING SEQUENCE

This section details the post-tensioning sequence of the two mock-ups. Table C.1 provides the dates and ages of each mock-up at each stage of post-tensioning, and Figure C.1 shows the tensioning and detensioning sequences. Table C.2 and Table C.3 detail the timing of the post-tensioning operations for the first and second mock-ups, respectively.

Table C.1: Dates and ages of mock-up construction and testing

1st Mock-Up			2nd Mock-Up		
Task	Date	Age (days)	Task	Date	Age (days)
Main Block	5/13/2014	0	Main Block	3/11/2015	0
SCC Repair	10/10/2014	150	-	-	-
Top Block	10/31/2014	171	Secondary	4/15/2015	35
PT-Vertical	1/7/2015	239	PT-Vertical	5/19/2015	69
PT-Horizontal	1/9/2015	241	PT-Horizontal	5/21/2015	71
Detension	1/10/2015	242	Detension	5/29/2015	79

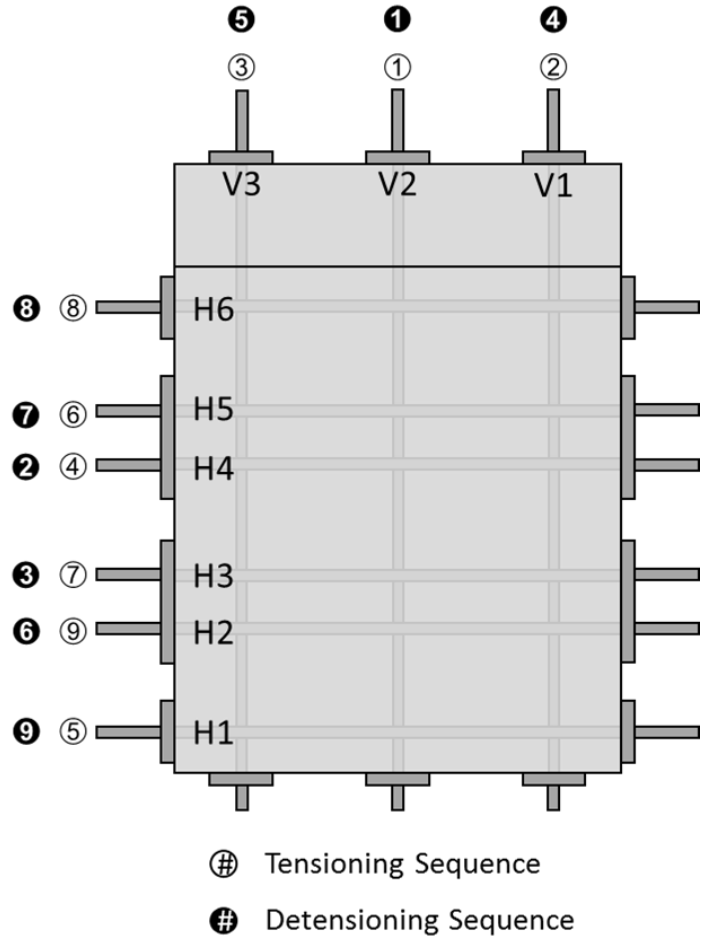


Figure C.1: Identification of post-tensioning rods and post-tensioning and detensioning sequences

Table C.2: Post-tensioning sequence for first mock-up

Step	Description	Time	Date	Step	Description	Time	Date
①	V2 – Begin Jacking	13:34:30	1/7	①	V2 – Lift-Off	8:07:00	1/10
	V2 – Transfer	14:07:30			V2 – Detensioned	8:17:00	
②	V1 – Begin Jacking	14:58:00		②	H4 – Lift-Off	8:47:56	
	V1 – Transfer	15:16:30			H4 – Detensioned	8:54:56	
③	V3 – Begin Jacking	15:57:00		③	H3 – Lift-Off	9:04:46	
	V3 – Transfer	16:14:00			H3 – Detensioned	9:11:56	
	H4 – Begin Jacking	9:32:00	1/8	④	V1 – Lift-Off	9:40:30	
	H4 @ 405 kips	9:38:30			Cycling V1		
	H4 – Detensioned	9:42:30			V1 – Detensioned	10:55:00	
	H4 – Begin Jacking	9:46:00		⑤	V3 – Lift-Off	11:12:30	
	H4 @ 540 kips	9:57:00			V3 – Detensioned	11:17:00	
	H4 – Detensioned	10:07:00		⑥	H2 – Lift-Off	11:37:56	
	H3 – Begin Jacking	10:49:00			H2 – Detensioned	11:43:36	
	H3 @ 270 kips	10:52:30		⑦	H5 – Lift-Off	11:52:36	
	H3 – Detensioned	10:55:30			H5 – Detensioned	11:55:26	
④	H4 – Begin Jacking	17:08:10	⑧	H6 – Lift-Off	12:03:46		
	H4 – Transfer	17:25:00		H6 – Detensioned	12:06:06		
⑤	H1 – Begin Jacking	17:49:30	⑨	H1 – Lift-Off	12:15:56		
	H1 – Transfer	18:03:50		H1 – Detensioned	12:19:16		
⑥	H5 – Begin Jacking	18:22:30	⑦				
	H5 – Transfer	18:37:40					
⑦	H3 – Begin Jacking	18:54:00	⑧	H6 – Begin Jacking	19:21:10		
	H3 – Transfer	19:07:30		H6 – Transfer	19:36:00		
⑧	H6 – Begin Jacking	19:21:10	⑨	H2 – Begin Jacking	19:49:00		
	H6 – Transfer	19:36:00		H2 – Transfer	20:00:40		
⑨	H2 – Begin Jacking	19:49:00					
	H2 – Transfer	20:00:40					

Table C.3: Post-tensioning sequence for second mock-up

Step	Description	Time	Date	Step	Description	Time	Date
①	V2 – Begin Jacking	10:15:00	5/19	①	V2 – Lift-Off	9:54:00	5/29
	V2 – Transfer	10:38:00			V2 – Detensioned	10:06:30	
②	V1 – Begin Jacking	10:55:30		②	H4 – Lift-Off	10:43:30	
	V1 – Transfer	11:13:00			H4 – Detensioned	10:49:30	
③	V3 – Begin Jacking	11:30:30		③	H3 – Lift-Off	11:12:30	
	V3 – Transfer	11:47:30			H3 – Detensioned	11:16:00	
④	H4 – Begin Jacking	15:37:30	④	V1 – Lift-Off	12:18:30		
	H4 – Transfer	15:54:30		V1 – Detensioned	12:24:00		
⑤	H1 – Begin Jacking	16:43:00	⑤	V3 – Lift-Off	12:54:30		
	H1 – Transfer	16:56:30		V3 – Detensioned	12:56:30		
⑥	H5 – Begin Jacking	17:06:30	⑥	H2 – Lift-Off	14:01:30		
	H5 – Transfer	17:17:00		H2 – Detensioned	14:05:30		
⑦	H3 – Begin Jacking	17:28:00	⑦	H5 – Lift-Off	14:14:30		
	H3 – Transfer	17:39:30		H5 – Detensioned	14:20:00		
⑧	H6 – Begin Jacking	17:50:00	⑧	H6 – Lift-Off	14:31:00		
	H6 – Transfer	18:02:00		H6 – Detensioned	14:36:00		
⑨	H2 – Begin Jacking	18:14:30	⑨	H1 – Lift-Off	14:49:00		
	H2 – Transfer	18:26:30		H1 – Detensioned	14:52:30		

REFERENCES

- AASHTO (2007). Standard Method of Test for Coefficient of Thermal Expansion of Hydraulic Cement Concrete (AASHTO TP 60-00). Washington, D.C., American Association of State Highway and Transportation Officials.
- AASHTO (2009). Standard Method of Test for Coefficient of Thermal Expansion of Hydraulic Cement Concrete (AASHTO T 336-09). Washington, D.C., American Association of State Highway and Transportation Officials.
- AASHTO (2011). Standard Method of Test for Coefficient of Thermal Expansion of Hydraulic Cement Concrete (AASHTO T 336-11). Washington, D.C., American Association of State Highway and Transportation Officials.
- Abbott, J. G. and F. L. Thurstone (1979). "Acoustic speckle: Theory and experimental analysis." *Ultrasonic Imaging* 1(4): 303-324.
- ACI Committee 116 (2005). *Cement and Concrete Terminology* (ACI 116R-00). Farmington Hills, MI, American Concrete Institute.
- ACI Committee 207 (1998). *Cooling and Insulating Systems for Mass Concrete* (ACI 207.4R-93). Farmington Hills, MI, American Concrete Institute.
- ACI Committee 207 (2007). *Report on Thermal and Volume Change Effects on Cracking of Mass Concrete* (ACI 207.2R-07). Farmington Hills, MI, American Concrete Institute.
- ACI Committee 207 (2012). *Guide to Mass Concrete* (ACI 207.1R-05). Farmington Hills, MI, American Concrete Institute.
- ACI Committee 209 (2008). *Prediction of creep, shrinkage, and temperature effects in concrete structures* (ACI 209R-92). Farmington Hills, MI, American Concrete Institute.
- ACI Committee 211 (2002). *Standard Practice for Selecting Proportions for Normal, Heavyweight, and Mass Concrete* (ACI 211.1-91). Farmington Hills, MI, American Concrete Institute.
- ACI Committee 214 (2003). *Guide for Obtaining Cores and Interpreting Compressive Strength Results* (ACI 214.4R-03). Farmington Hills, MI, American Concrete Institute.
- ACI Committee 214 (2011). *Guide to Evaluation of Strength Test Results of Concrete* (ACI 214R-11). Farmington Hills, MI, American Concrete Institute.
- ACI Committee 222 (2001). *Protection of metals in concrete against corrosion* (ACI 222R-01). Farmington Hills, MI, American Concrete Institute.

ACI Committee 224 (1997). Cracking of Concrete Members in Direct Tension (ACI 224.2R-92). Farmington Hills, MI, American Concrete Institute.

ACI Committee 228 (2013). Report on Nondestructive Test Methods for Evaluation of Concrete in Structures (ACI 228.2R-13). Farmington Hills, MI, American Concrete Institute.

ACI Committee 301 (2010). Specifications for Structural Concrete (ACI 301-10). Farmington Hills, MI, American Concrete Institute.

ACI Committee 306 (2002). Cold Weather Concreting (ACI 306R-88). Farmington Hills, MI, American Concrete Institute.

ACI Committee 318 (2008). Building Code Requirements for Structural Concrete (ACI 318-08) and Commentary. Farmington Hills, MI, American Concrete Institute.

ACI Committee 347 (2004). Guide to Formwork for Concrete (ACI 347-04). Farmington Hills, MI, American Concrete Institute.

ACI Committee 349 (2007). Code Requirements for Nuclear Safety-Related Concrete Structures (ACI 349-06) and Commentary. Farmington Hills, MI, American Concrete Institute.

ACI Committee 349 (2007). Reinforced concrete design for thermal effects on nuclear power plant structures (ACI 349.1R-07). Farmington Hills, MI, American Concrete Institute.

ACI Committee 517 (1980). Accelerated Curing of Concrete at Atmospheric Pressure - State of the Art. ACI Journal, American Concrete Institute: 429-448.

Adams, W. M., G. Watts and G. Mason (1976). "Estimation of thermal diffusivity from field observations of temperature as a function of time and depth." American Mineralogist 61: 560-568.

Al-Kubaisy, M. A. and A. G. Young (1975). "Failure of concrete under sustained tension." Magazine of Concrete Research 27(92): 171-178.

Alungbe, G. D., M. Tia and D. G. Bloomquist (1992). Effects of Aggregate, Water/Cement Ratio, and Curing on the Coefficient of Linear Thermal Expansion of Concrete. Transportation Record No. 1335, Concrete Technology. Washington, DC, Transportation Research Board: 44-51.

AmerGen Energy Company (2005). License Renewal Application: Oyster Creek Generating Station. Kennett Square, PA.

Anderson, P. (2007). Evaluation of the prestress level in Swedish reactor containments. Transactions of the 19th International Conference on Structural Mechanics in Reactor Technology, Toronto, Ontario.

Anderson, T. L. (2005). Fracture Mechanics: Fundamentals and Applications. Boca Raton, FL, Taylor and Francis Group, LLC.

Artoglu, N., Z. C. Girgin and E. Artoglu (2006). "Evaluation of Ratio between Splitting Tensile Strength and Compressive Strength for Concretes up to 120 MPa and its Application in Strength Criterion." ACI Materials Journal 103(1): 18-24.

Ashar, H. and D. J. Naus (1983). "Overview of the use of prestressed concrete in U.S. nuclear power plants." Nuclear Engineering and Design 75(3): 425-437.

Ashar, H., D. J. Naus and C. P. Tan (1994a). "Prestressed concrete in U.S. nuclear power plants (part 1)." Concrete International 16(5): 30-34.

Ashar, H., C. P. Tan and D. J. Naus (1994b). "Prestressed concrete in U.S. nuclear power plants (part 2)." Concrete International 16(6): 58-61.

ASHRAE (1993). 1993 ASHRAE Handbook—Fundamentals. Atlanta, Georgia, American Society of Heating, Refrigerating, and Air-Conditioning Engineers.

ASME (1995). ASME Boiler & Pressure Vessel Code, Section III, "Rules for construction of nuclear plant components," Division 2. Subsection CC - Code for concrete reactor vessels and containments (ACI standard 359-95). New York, New York, American Society of Mechanical Engineers.

ASTM C31-69 (1969). Standard Method of Making and Curing Concrete Compressive and Flexural Strength Test Specimens in the Field. West Conshohocken, PA, ASTM International.

ASTM C33-13 (2013). Standard Specification for Concrete Aggregates. West Conshohocken, PA, ASTM International.

ASTM C39-12 (2012). Standard Test Method for Compressive Strength of Cylindrical Concrete Specimens. West Conshohocken, PA, ASTM International.

ASTM C42-04 (2004). Standard Test Method for Obtaining and Testing Drilled Cores and Sawed Beams of Concrete. West Conshohocken, PA, ASTM International.

ASTM C42-13 (2013). Standard Test Method for Obtaining and Testing Drilled Cores and Sawed Beams of Concrete. West Conshohocken, PA, ASTM International.

ASTM C109-13 (2013). Standard Test Method for Compressive Strength of Hydraulic Cement Mortars (Using 2-in. or [50-mm] Cube Specimens). West Conshohocken, PA, ASTM International.

ASTM C127-12 (2012). Standard Test Method for Density, Relative Density (Specific Gravity), and Absorption of Coarse Aggregate. West Conshohocken, PA, ASTM International.

ASTM C128-12 (2012). Standard Test Method for Density, Relative Density (Specific Gravity), and Absorption of Fine Aggregate. West Conshohocken, PA, ASTM International.

ASTM C136-06 (2006). Standard Test Method for Sieve Analysis of Fine and Coarse Aggregates. West Conshohocken, PA, ASTM International.

ASTM C138-12 (2012). Standard Test Method for Density (Unit Weight), Yield, and Air Content (Gravimetric) of Concrete. West Conshohocken, PA, ASTM International.

ASTM C143-12 (2012). Standard Test Method for Slump of Hydraulic-Cement Concrete. West Conshohocken, PA, ASTM International.

ASTM C150-11 (2011). Standard Specification for Portland Cement. West Conshohocken, PA, ASTM International.

ASTM C150-67 (1967). Standard Specification for Portland Cement. West Conshohocken, PA, ASTM International.

ASTM C173-12 (2012). Standard Test Method for Air Content of Freshly Mixed Concrete by the Volumetric Method. West Conshohocken, PA, ASTM International.

ASTM C177-13 (2013). Standard Test Method for Steady-State Heat Flux Measurements and Thermal Transmission Properties by Means of the Guarded-Hot-Plate Apparatus. West Conshohocken, PA, ASTM International.

ASTM C186-05 (2005). Standard Test Method for Heat of Hydration of Hydraulic Cement. West Conshohocken, PA, ASTM International.

ASTM C192-13a (2013). Standard Practice for Making and Curing Concrete Test Specimens in the Laboratory. West Conshohocken, PA, ASTM International.

ASTM C227-10 (2010). Standard Test Method for Potential Alkali Reactivity of Cement-Aggregate Combinations (Mortar-Bar Method). West Conshohocken, PA, ASTM International.

ASTM C231-10 (2010). Standard Test Method for Air Content of Freshly Mixed Concrete by the Pressure Method. West Conshohocken, PA, ASTM International.

ASTM C260-10a (2011). Standard Specification for Air-Entraining Admixtures for Concrete. West Conshohocken, PA, ASTM International.

ASTM C289-07 (2007). Standard Test Method for Potential Alkali-Silica Reactivity of Aggregates (Chemical Method). West Conshohocken, PA, ASTM International.

ASTM C295-12 (2012). Standard Test Method for Petrographic Examination of Aggregates for Concrete. West Conshohocken, PA, ASTM International.

ASTM C403-08 (2008). Standard Test Method for Time of Setting of Concrete Mixtures by Penetration Resistance. West Conshohocken, PA, ASTM International.

ASTM C457-08d (2008). Standard Test Method for Microscopical Determination of Parameters of the Air-Void System in Hardened Concrete. West Conshohocken, PA, ASTM International.

ASTM C469-10 (2010). Standard Test Method for Static Modulus of Elasticity and Poisson's Ratio of Concrete in Compression. West Conshohocken, PA, ASTM International.

ASTM C469-14 (2014). Standard Test Method for Static Modulus of Elasticity and Poisson's Ratio of Concrete in Compression. West Conshohocken, PA, ASTM International.

ASTM C490-11 (2011). Standard Practice for Use of Apparatus for the Determination of Length Change of Hardened Cement Paste, Mortar, and Concrete. West Conshohocken, PA, ASTM International.

ASTM C494-13 (2013). Standard Specification for Chemical Admixtures for Concrete. West Conshohocken, PA, ASTM International.

ASTM C496-11 (2011). Standard Test Method for Splitting Tensile Strength of Cylindrical Concrete Specimens. West Conshohocken, PA, ASTM International.

ASTM C511-13 (2013). Standard Specification for Mixing Rooms, Moist Cabinets, Moist Rooms, and Water Storage Tanks Used in the Testing of Hydraulic Cements and Concretes. West Conshohocken, PA, ASTM International.

ASTM C518-10 (2010). Standard Test Method for Steady-State Thermal Transmission Properties by Means of the Heat Flow Meter Apparatus. West Conshohocken, PA, ASTM International.

ASTM C597-09 (2010). Standard Test Method for Pulse Velocity Through Concrete. West Conshohocken, PA, ASTM International.

ASTM C680-14 (2014). Standard Practice for Estimate of the Heat Gain or Loss and the Surface Temperatures of Insulated Flat, Cylindrical, and Spherical Systems by Use of Computer Programs. West Conshohocken, PA, ASTM International.

ASTM C856-04 (2004). Standard Practice for Petrographic Examination of Hardened Concrete. West Conshohocken, PA, ASTM International.

ASTM C1074-11 (2011). Standard Practice for Estimating Concrete Strength by the Maturity Method. West Conshohocken, PA, ASTM International.

ASTM C1107-14 (2014). Standard Specification for Packaged Dry, Hydraulic-Cement Grout (Nonshrink). West Conshohocken, PA, ASTM International.

ASTM C1365-06 (2012). Standard Test Method for Determination of the Proportion of Phases in Portland Cement and Portland-Cement Clinker Using X-Ray Power Diffraction Analysis. West Conshohocken, PA, ASTM International.

ASTM C1383-15 (2015). Standard Test Method for Measuring the P-Wave Speed and the Thickness of Concrete Plates Using the Impact-Echo Method. West Conshohocken, PA, ASTM International.

ASTM C1437-13 (2013). Standard Test Method for Flow of Hydraulic Cement Mortar. West Conshohocken, PA, ASTM International.

ASTM C1542-02 (2010). Standard Test Method for Measuring Length of Concrete Cores. West Conshohocken, PA, ASTM International.

ASTM D2766-95 (2009). Standard Test Method for Specific Heat of Liquids and Solids. West Conshohocken, PA, ASTM International.

ASTM D4748-10 (2011). Standard Test Method for Determining the Thickness of Bound Pavement Layers Using Short-Pulse Radar. West Conshohocken, PA, ASTM International.

ASTM D6432-11 (2011). Standard Guide for Using the Surface Ground Penetrating Radar Method for Subsurface Investigation. West Conshohocken, PA, ASTM International.

ASTM E114-10 (2010). Standard Practice for Ultrasonic Pulse-Echo Straight-Beam Contact Testing. West Conshohocken, PA, ASTM International.

ASTM E178-08 (2008). Standard Practice for Dealing with Outlying Observations. West Conshohocken, PA, ASTM International.

ASTM E228-11 (2011). Standard Test Method for Linear Thermal Expansion of Solid Materials with a Push-Rod Dilatometer. West Conshohocken, PA, ASTM International.

ASTM E289-04 (2010). Standard Test Method for Linear Thermal Expansion of Rigid Solids with Interferometry. West Conshohocken, PA, ASTM International.

ASTM E797-10 (2010). Standard Practice for Measuring Thickness by Manual Ultrasonic Pulse-Echo Contact Method. West Conshohocken, PA, ASTM International.

ASTM E1142-14b (2014). Standard Terminology Relating to Thermophysical Properties. West Conshohocken, PA, ASTM International.

ASTM E1269-11 (2011). Standard Test Method for Determining Specific Heat Capacity by Differential Scanning Calorimetry. West Conshohocken, PA, ASTM International.

ASTM E1461-13 (2013). Standard Test Method for Thermal Diffusivity by the Flash Method. West Conshohocken, PA, ASTM International.

ASTM E1901-08 (2008). Standard Guide for Detection and Evaluation of Discontinuities by Contact Pulse-Echo Straight-Beam Ultrasonic Methods. West Conshohocken, PA, ASTM International.

Bairi, A., J. M. García de María and N. Laraqi (2007). "Thermal diffusivity measurements of building materials based on 2D models." *Computational Materials Science* 38(4): 838-846.

Basu, P. C., V. N. Gupchup and L. R. Bishnoi (2001). *Containment Dome Delamination*. SMiRT 16, Washington, DC.

Bazant, Z. P. (1985). *Mechanics of fracture and progressive cracking in concrete structures*. *Fracture mechanics of concrete: Structural application and numerical calculation*. G. C. Sih and A. DiTommaso. Dordrecht, Netherlands, Springer Netherlands. 4: 1-94.

Bekowich, R. S. (1968). "Instrumentation in prestressed concrete containment structures." *Nuclear Engineering and Design* 8(4): 500-512.

Bentz, D. P. (2007). "Transient plane source measurements of the thermal properties of hydrating cement pastes." *Materials and Structures* 40(10): 1073-1080.

Bilgutay, N. M., J. Saniie, E. S. Furgason and V. L. Newhouse (1979). *Flaw-to-Grain Echo Enhancement*. Ultrasonics International, Graz, Austria, IPC Science and Technology Press, Ltd.

Bishko, A. V., A. A. Samokrutov and V. G. Shevaldykin (2008). *Ultrasonic Echo-Pulse Tomography of Concrete Using Shear Waves Low-Frequency Phased Antenna Arrays*. 17th World Conference on Nondestructive Testing. Shanghai, China.

Bissonnette, B., M. Pigeon and A. M. Vaysburd (2007). "Tensile Creep of Concrete: Study of Its Sensitivity to Basic Parameters." *ACI Materials Journal* 104(4): 360-368.

Book, N. L. and R. M. Barnoff (1973). *Time-Temperature Study of Accelerated Curing of Concrete*. University Park, PA, The Pennsylvania State University.

Braverman, J. (1992). *Turkey Point trip Report: Assessment of Structures and CE (Civil Engineering) Features at Operating Plants, US Nuclear Regulatory Commission*.

Brown, D. (2009). *Petrographic Examination of Concrete Half Core from Delaminated Containment Wall, Crystal River, Florida*. Skokie, Illinois, CTLGroup.

Brown, P. (2003). "First nuclear power plant to close." *The Guardian* Retrieved June 29, 2011, from <http://www.guardian.co.uk/uk/2003/mar/21/nuclear.world>.

Brown, T. D. and M. Y. Javaid (1970). "The thermal conductivity of fresh concrete." *Materials and Structures* 3(18): 411-416.

Burckhardt, C. B. (1978). "Speckle in Ultrasound B-Mode Scans." *IEEE Transactions on Sonics and Ultrasonics* 25(1): 1-6.

Busby, J. and G. Carpenter (2012). *Extended Proactive Materials Degradation Analysis. Regulatory Information Conference 2012, Bethesda, Maryland*.

Carino, N. J. (1984). "The Maturity Method: Theory and Application." *Cement, Concrete, and Aggregates, CCAGDP* 6(2): 61-73.

Carino, N. J. (2004). *The Maturity Method. Handbook on Nondestructive Testing of Concrete*. V. M. Malhotra and N. J. Carino. Boca Raton, Florida, CRC Press.

Carino, N. J. and M. Sansalone (1984). *Pulse-Echo Method for Flaw Detection in Concrete*. Washington, D.C., National Bureau of Standards.

Carino, N. J. and R. C. Tank (1992). "Maturity Function for Concretes Made With Various Cements and Admixtures." *ACI Materials Journal* 89(2).

Carman, A. P. and R. A. Nelson (1921). *The thermal conductivity and diffusivity of concrete*. Engineering Experiment Station. Urbana, University of Illinois. 122: 39.

Carr, H. (2012). *Duke Study: Crystal River Nuke Repairs Could Hit \$3.4B*. ENR Southeast.

CEB-FIP Model Code for Concrete Structures 1990 (1991). *Evaluation of the Time Dependent Behaviour of Concrete*. Bulletin d'Information No. 199. Lausanne, Comité Euro-International du Béton.

- Chang, C. F. and J. W. Chen (2005). "Strength and elastic modulus of carbonated concrete." *ACI Materials Journal* 102(5): 315-321.
- Chirdon, W. M., W. Aquino and K. C. Hover (2007). "A method for measuring transient thermal diffusivity in hydrating Portland cement mortars using an oscillating boundary temperature." *Cement and Concrete Research* 37(5): 680-690.
- Christensen, B. J. (2006). *Time of Setting*. ASTM Special Technical Publication 169D-EB: Significance of Tests and Properties of Concrete and Concrete-Making Materials. J. F. Lamond and J. H. Pielert. West Conshohocken, Pennsylvania: 86-98.
- Clear, R. D., L. Gartland and F. C. Winkelmann (2003). "An empirical correlation for the outside convective air-film coefficient for horizontal roofs." *Energy and Buildings* 35(8): 797-811.
- Clifton, J. R. (1991). *Predicting the Remaining Service Life of Concrete*. Gaithersburg, Maryland, U.S. Department of Commerce, National Institute of Standards and Technology.
- Clifton, J. R. and R. G. Mathey (1971). *Compilation of Data from Laboratory Studies. Interrelations Between Cement and Concrete Properties: Part 6, Compilation of Data from Laboratory Studies*. Washington, D.C., National Bureau of Standards: 1-115.
- Cohen, M. D. and B. Mather (1991). "Sulfate Attack on Concrete - Research Needs." *ACI Materials Journal* 88(1): 62-69.
- COMSOL Group. (2015). "COMSOL Multiphysics." Retrieved November 26, 2015, from <https://www.comsol.com/comsol-multiphysics>.
- Crawford, G. L., J. M. Gudimettla and J. Tanesi (2010). "Interlaboratory Study on Measuring Coefficient of Thermal Expansion of Concrete." *Transportation Research Record: Journal of the Transportation Research Board*(2164): 58-65.
- Cusson, D. and T. Hoogeveen (2006). *Measuring early-age coefficient of thermal expansion in high-performance concrete*. International RILEM Conference on Volume Changes of Hardening Concrete: Testing and Mitigation, Lyngby, Denmark, RILEM Publications SARL.
- D'Aloia, L. and G. Chanvillard (2002). "Determining the "apparent" activation energy of concrete: E_a —numerical simulations of the heat of hydration of cement." *Cement and Concrete Research* 32(8): 1277-1289.
- Davis, R. E., R. W. Carlson, G. E. Troxell and J. W. Kelly (1933). "Cement Investigations for the Hoover Dam." *Journal of the American Concrete Institute* 29: 413-431.

- Davis, R. E., R. W. Carlson, G. E. Troxell and J. W. Kelly (1934). "Cement Investigations for Boulder Dam with Results up to the Age of One Year." *Journal of the American Concrete Institute* 30(5): 485-497.
- Day, R. L. (1994). "Strength Measurement of Concrete Using Different Cylinder Sizes: A Statistical Analysis." *Cement, Concrete and Aggregates* 16(1): 21-30.
- De La Haza, A. O., A. A. Samokrutov and P. A. Samokrutov (2013). "Assessment of concrete structures using the Mira and Eyecon ultrasonic shear wave devices and the SAFT-C image reconstruction technique." *Construction and Building Materials* 38: 1276-1291.
- De Schutter, G. and L. Taerwe (1995). "Specific Heat and Thermal Diffusivity of Hardening Concrete." *Magazine of Concrete Research* 47(172): 203-208.
- De Schutter, G. and L. Taerwe (1996). "Degree of hydration-based description of mechanical properties of early age concrete." *Materials and Structures* 29(6): 335-344.
- Dobreff, S. N. (1973). *Concrete Acceptance Criteria: Crystal River Unit 3*. W. S. O'Brien.
- Dodson, V. H. (1994). *Time of Setting*. ASTM Special Technical Publication 169C-EB: *Significance of Tests and Properties of Concrete and Concrete-Making Materials*. P. Klieger and J. F. Lamond. West Conshohocken, Pennsylvania: 77-87.
- Domone, P. L. (1974). "Uniaxial tensile creep and failure of concrete." *Magazine of Concrete Research* 26(88): 144-152.
- Dunn, D. S., A. L. Pulvirenti and M. A. Hiser (2011). *Containment Liner Corrosion Operating Experience Summary Technical Letter Report – Revision 1*, U.S. Nuclear Regulatory Commission, Office of Nuclear Regulatory Research.
- Erlin, B. (1976). *Petrographic Studies of Concrete for Construction Engineering Consultants*. Northbrook, Illinois, Erlin, Hime Associates, Inc.
- Federal Highway Administration (2011). *Coefficient of Thermal Expansion in Concrete Pavement Design*. Techbrief, Federal Highway Administration.
- Ferraro, C. (2009). *Determination of Test Methods for the Prediction of the Behavior of Mass Concrete*. Doctor of Philosophy, University of Florida.
- Florida Department of Transportation (2015). *FDOT Structures Manual*. Tallahassee, Florida.
- Florida Power and Light Company (1970). *Turkey Point Unit 3 Containment Dome Report*. Miami, Florida, Florida Power and Light, Co.

Frohnsdorff, G., J. R. Clifton and P. W. Brown (1978). History and Status of Standards Relating to Alkalies in Hydraulic Cements. Cement Standards - Evolution and Trends, ASTM STP 663. P. K. Mehta, American Society for Testing and Materials: 16-34.

Gajda, J. (2007). Mass Concrete for Buildings and Bridges. Skokie, Illinois, Portland Cement Association.

Gajda, J. and M. VanGeem (2002). "Controlling Temperatures in Mass Concrete." Concrete International 24(1): 58-62.

Garas Yanni, V. Y. (2009). Multi-scale investigation of tensile creep of ultra-high performance concrete for bridge applications Doctor of Philosophy, Georgia Institute of Technology.

Gardner, R. E. (1974). Tests of Cement. Tampa, Florida, Pittsburgh Testing Laboratory.

Ge, Z. (2005). Predicting temperature and strength development of the field concrete. Doctor of Philosophy, Iowa State University.

Gebhardt, R. F. (1995). "Survey of North American Portland Cements: 1994." Cement, Concrete, and Aggregates, CCAGDP 17(2): 145-189.

Gilbert Associates (1968). Specification for furnishing and delivering of structural concrete: Crystal River Unit No. 3, Florida Power Corporation. Reading, Pennsylvania.

Gilbert Associates (1970). Requirement Outline: Prestressing System Tendon Conduit: Crystal River Unit No. 3, Florida Power Corporation. Reading, Pennsylvania.

Gilbert Associates (1971). Addendum D to Specification for furnishing and delivering of structural concrete: Crystal River Unit No. 3, Florida Power Corporation. Reading, Pennsylvania.

Glasstone, S., K. J. Laidler and H. Eyring (1941). The theory of rate processes: The kinetics of chemical reactions, viscosity, diffusion and electrochemical phenomena. McGraw-Hill, New York.

Glisic, B. (2000). Fiber Optic Sensors and Behavior in Concrete at Early Age. Ph.D., Swiss Federal Institute of Technology in Lausanne.

Goller, B., R. Krieg, G. Messemer and E. Wolf (1987). "On the failure of spherical steel containments under excessive internal pressure." Nuclear Engineering and Design 100(2): 205-219.

Granger, L., F. Fleury and J.-P. Touret (2001a). "Mechanical and leakrate predictions for nuclear power plant containments in accidental conditions." Nuclear Engineering and Design 203(1): 39-55.

Granger, L., C. Y. Rieg, J. P. Touret, F. Fleury, G. Nahas, R. Danisch, L. Brusa, A. Millard, C. Laborderie, F. Ulm, P. Contri, K. Schimmelpfennig, F. Barré, M. Firnhaber, J. Gauvain, N. Coulon, L. M. C. Dutton and A. Tuson (2001b). "Containment Evaluation under Severe Accidents (CESA): synthesis of the predictive calculations and analysis of the first experimental results obtained on the Civaux mock-up." *Nuclear Engineering and Design* 209(1-3): 155-163.

Gray, A. and G. B. Mathews (1895). *A Treatise on Bessel Functions and Their Applications to Physics*. London, Macmillan and Co.

Gray, A., G. B. Mathews and T. M. MacRobert (1922). *A Treatise on Bessel Functions and Their Applications to Physics*. London, Macmillan and Co.

Gregor, F. E. and C. J. Hookham (1993). *Remnant Life Preservation of LWR Plant Structures*. SMiRT-12, Stuttgart, Germany.

Halligan, D. W. (1976). "Prestressed concrete nuclear plant containment structures." *PCI Journal* 21(5): 158-175.

Hansen, P. F., J. H. Hansen, V. Kjaer and E. J. Pedersen (1982). *Thermal Properties of Hardening Cement Paste*. Proceedings of RILEM International Conference on Concrete at Early Ages, Paris, France.

Hansen, P. F. and E. J. Pedersen (1977). "Maturity Computer for controlled curing and hardening of concrete [Maleinstrument til kontrol af betons haerdning]." *Nordisk Betong*(1): 21-25.

Hansen, P. F. and E. J. Pedersen (1985). *Curing of Concrete Structures*. Draft CEB Guide to Durable Concrete Structures. Lausanne, Switzerland, Comité Euro-International du Béton.

Hanson, J. W. (1961). "Tensile Strength and Diagonal Tension Resistance of Structural Lightweight Concrete." *Journal of the American Concrete Institute* 58(7): 1-40.

Hanson, N. W., J. J. Roller, D. M. Schultz, J. T. Julien and T. L. Weinman (1987). *Concrete Containment Tests, Phase 2: Structural Elements with Liner Plates - Interim Report*. Palo Alto, Electric Power Research Institute.

Heinz, D., M. Kalde, U. Ludwig and I. Ruediger (1999). "Present State of Investigation on Damaging Late Ettringite Formation (DLEF) in Mortars and Concretes." *ACI Special Publication* 177.

Heisler, M. P. (1947). "Temperature charts for induction and constant-temperature heating." *Transactions of the A.S.M.E.* 69(3): 227-235.

Hernandez-Bautista, E., D. P. Bentz, S. Sandoval-Torres and P. Cano-Barrita (2014). Modeling Heat and Moisture Transport During Hydration of Cement-Based Materials in Semi-Adiabatic Conditions. COMSOL Conference Boston 2014, Boston, MA.

Herrmann, N., L. Gerlach, H. S. Muller, Y. Le Pape, C. Bento, C. Niklasch and D. Kiefer (2009). PACE-1450 - Experimental investigation of the crack behaviour of prestressed concrete containment walls considering the prestressing loss due to aging. International Conference on Structural Mechanics in Reactor Technology (SMiRT 20), Espoo, Finland.

Herrmann, N., C. Niklasch, D. Kiefer, L. Gerlach, Y. Le Pape and S. Fortier (2008). PACE-1450 - An experimental test setup for the investigation of the crack behaviour of prestressed concrete containment walls. International Conference on Nuclear Engineering (ICONE16), Orlando, Florida.

Hessheimer, M. F. and R. A. Dameron (2006). Containment integrity research at Sandia National Laboratories - an overview. NUREG/CR-6906 SAND2006-2274P, Sandia National Laboratories.

Hessheimer, M. F., E. W. Klamerus, L. D. Lambert, G. S. Rightley and R. A. Dameron (2003). Overpressurization test of a 1:4-scale prestressed concrete containment vessel model. Albuquerque, New Mexico, Sandia National Laboratories.

Higginson, E. C. (1961). "Effect of Steam Curing on the Important Properties of Concrete." ACI Journal 58(9): 281-298.

Hill, H. T. (2012a). Email communication regarding Crystal River 3 bay 56 delamination. B. Dolphyn.

Hill, H. T. (2012b). Email communication regarding Crystal River 3 bay 12 delamination. B. Dolphyn.

Hill, H. T. (2013). Email communication regarding Crystal River 3 liner painting. B. Dolphyn.

Horschel, D. S. (1992). Experimental Results from Pressure Testing a 1:6-Scale Nuclear Power Plant Containment. Albuquerque, NM, Sandia National Laboratories.

Horschel, D. S. and T. E. Blejwas (1983). An Analytical Investigation of the Response of Steel Containment Models to Internal Pressurization. 7th International Conference on Structural Mechanics in Reactor Technology, Chicago.

Horschel, D. S. and D. B. Clauss (1984). The Response of Steel Containment Models to Internal Pressurization. Structural Engineering in Nuclear Facilities. J. J. Ucciferro. Raleigh, North Carolina. 1: 534-553.

IAEA (1998). Assessment and management of ageing of major nuclear power plant components important to safety: Concrete containment buildings. Vienna, International Atomic Energy Agency (IAEA).

Illston, J. M. (1965). "The creep of concrete under uniaxial tension." Magazine of Concrete Research 17(51): 77-84.

Incropera, F. P., D. P. Dewitt, T. L. Bergman and A. S. Lavine (2007). Fundamentals of Heat and Mass Transfer, 6th Edition. Hoboken, New Jersey, John Wiley & Sons, Inc.

Ingersoll, L. R., O. J. Zobel and A. C. Ingersoll (1948). Heat Conduction - With Engineering and Geological Applications. New York, McGraw-Hill Book Company.

Institute, A. C. (2013). ACI Concrete Terminology (ACI CT-13). Farmington Hills, MI, American Concrete Institute.

Jahangirnejad, S., N. Buch and A. Kravchenko (2009). "Evaluation of Coefficient of Thermal Expansion Test Protocol and Its Impact on Jointed Concrete Pavement Performance." ACI Materials Journal 106(1): 64-71.

Janna, W. S. (2000). Engineering Heat Transfer. Boca Raton, Florida, CRC Press.

Jason, L., M. Choinska, G. Pijaudier-Cabot, S. Ghavamian and A. Huerta (2005). Validation of a Damage Plasticity Model for Concrete in Tension and in Compression. VIII International Conference on Computational Plasticity. Barcelona.

Jason, L., S. Ghavamian and A. Courtois (2010). "Truss vs solid modeling of tendons in prestressed concrete structures: Consequences on mechanical capacity of a Representative Structural Volume." Engineering Structures 32(6): 1779-1790.

Jason, L., G. Pijaudier-Cabot, S. Ghavamian and A. Huerta (2007). "Hydraulic behaviour of a representative structural volume for containment buildings." Nuclear Engineering and Design 237(12-13): 1259-1274.

Jayapalan, A. R., M. L. Jue and K. E. Kurtis (2014). "Nanoparticles and Apparent Activation Energy of Portland Cement." Journal of the American Ceramic Society 97(5): 1534-1542.

Jonasson, J.-E., P. Groth and H. Hedlund (1995). Modelling of Temperature and Moisture Field in Concrete to Study Early Age Movements as a Basis for Stress Analysis. International RILEM Symposium on Thermal Cracking in Concrete at Early Ages, London, E & FN Spon.

Kada, H., M. Lachemi, N. Petrov, O. Bonneau and P. C. Aitcin (2002). "Determination of the coefficient of thermal expansion of high performance concrete from initial setting." Materials and Structures 35(1): 35-41.

Kada-Benameur, H., E. Wirquin and B. Duthoit (2000). "Determination of apparent activation energy of concrete by isothermal calorimetry." *Cement and Concrete Research* 30(2): 301-305.

Khan, A. A., W. D. Cook and D. Mitchell (1998). "Thermal Properties and Transient Analysis of Structural Members during Hydration." *ACI Materials Journal* 95(3): 293-303.

Kim, K.-H., S.-E. Jeon, J.-K. Kim and S. Yang (2003). "An experimental study on thermal conductivity of concrete." *Cement and Concrete Research* 33(3): 363-371.

Kim, S.-H. (2012). *Determination of Coefficient of Thermal Expansion for Portland Cement Concrete Pavements for MEPDG Implementation*. Atlanta, GA, Georgia Department of Transportation.

Klamerus, E. W., M. P. Bohn, D. A. Wesley and C. N. Krishnaswamy (1996). *Containment Performance of Prototypical Reactor Containments Subjected to Severe Accident Conditions*. Albuquerque, NM, Sandia National Laboratories.

Krauss, P. D. (1994). *Repair materials and techniques for concrete structures in nuclear power plants*. Oak Ridge, TN, Oak Ridge National Laboratory.

Krautkrämer, J. and H. Krautkrämer (1990). *Ultrasonic Testing of Materials*. Berlin, Germany, Springer-Verlag Berlin Heidelberg.

Krieg, R., F. Eberle, B. Goller, W. Gulden, J. Kadlec, G. Messemer and E. Wolf (1984). "Spherical steel containments of pressurized water reactors under accident conditions - Investigation program and first results." *Nuclear Engineering and Design* 82(1): 77-87.

Kupfer, H., H. K. Hilsdorf and H. Rusch (1969). "Behavior of Concrete Under Biaxial Stresses." *ACI Journal* 66(8): 656-666.

Lambert, L. D. (1993). *Posttest Destructive Examination of the Steel Liner in a 1:6-Scale Reactor Containment Model*, Sandia National Laboratories.

Larson, M. and J.-E. Jonasson (2003). "Linear logarithmic model for concrete creep: I. Formulation and evaluation." *Journal of Advanced Concrete Technology* 1(2): 172-187.

Lea, F. M. (1935). "The relation between the composition and properties of portland cement. A review of some recent chapters in cement research." *Journal of the Society of Chemical Industry* 54(22): 522-527.

Leal da Silva, W. R. and V. Šmilauer "Nomogram for Maximum Temperature of Mass Concrete." *Concrete International* 37(5).

- Lerch, W. and R. H. Bogue (1934). "Heat of Hydration of Portland Cement Pastes." Bureau of Standards Journal of Research 12(5): 645-664.
- Levinson, R. and H. Akbari (2002). "Effects of composition and exposure on the solar reflectance of portland cement concrete." Cement and Concrete Research 32(11): 1679-1698.
- Low, B.-H., S.-A. Tan and T.-F. Fwa (1991). "Determination of Thermal Diffusivity of Construction Materials." Journal of Testing and Evaluation 19(6): 440-449.
- Luk, V. K. (2000). Pretest Round Robin Analysis of a Prestressed Concrete Containment Vessel Model. Albuquerque, NM, Sandia National Laboratories.
- Lura, P., O. M. Jensen and K. van Breugel (2003). "Autogenous shrinkage in high-performance cement paste: An evaluation of basic mechanisms." Cement and Concrete Research 33(2): 223-232.
- Lydon, F. D. and R. V. Balendran (1986). "Some observations on elastic properties of plain concrete." Cement and Concrete Research 16(3): 314-324.
- Ma, W., D. Sample, R. Martin and P. W. Brown (1994). "Calorimetric Study of Cement Blends Containing Fly Ash, Silica Fume, and Slag at Elevated Temperatures." Cement, Concrete, and Aggregates, CCAGDP 16(2): 93-99.
- Magnin, P. A., O. T. von Ramm and F. L. Thurstone (1982). "Frequency Compounding for Speckle Contrast Reduction in Phased Array Images." Ultrasonic Imaging 4(3): 267-281.
- Malhotra, V. M. and P. K. Mehta (1996). Pozzolanic and Cementitious Materials. Amsterdam, The Netherlands, Gordon and Breach Science Publishers.
- Mather, B. (1979). "Concrete Need Not Deteriorate." Concrete International 1(9): 32-37.
- Mayer, K., R. Marklein, K. J. Langenberg and T. Kreutter (1990). "Three-dimensional imaging system based on Fourier transform synthetic aperture focusing technique." Ultrasonics 28(4): 241-255.
- McGillivray, R. T. (1973). Daily Concrete Curing & Form Removal Record, Crystal River Plant Unit No. 3, Pour 743 RB. P. T. Laboratory. Pittsburgh, PA.
- McIntosh, J. D. (1949). "Electrical Curing of Concrete." Magazine of Concrete Research 1(1): 21-28.
- Mehta, D. S., H. W. Osgood, A. J. Bingaman and K. P. Buchert (1977). "Trends in the Design of Pressurized-Water-Reactor Containment Structures and Systems." Nuclear Safety 18(2): 189-202.

Mehta, P. K. and P. J. M. Monteiro (2006). *Concrete: Microstructure, Properties, and Materials*. New York, NY, The McGraw-Hill Companies, Inc.

Meyers, S. L. (1940). "Thermal Coefficient of Expansion of Portland Cement—Long-Time Tests." *Industrial and Engineering Chemistry* 32(8): 1107-1112.

Mills, R. H. (1966). *Factors Influencing Cessation of Hydration in Water Cured Cement Pastes*. Symposium on Structure of Portland Cement Paste and Concrete, Washington, DC, Highway Research Board.

Mindess, S., J. F. Young and D. Darwin (2003). *Concrete*. Upper Saddle River, New Jersey, Prentice Hall.

Moreadith, F. L. and R. E. Pages (1983). "Delaminated Prestressed Concrete Dome: Investigation and Repair." *Journal of Structural Engineering* 109(5): 1235-1249.

Nakamura, S., Y. Sasaki, T. Kitani, K. Hayashi, K. Satoh, H. Eto, K. Nagahara, K. Takigushi and H. Akiyama (1997). Seismic proving test of concrete containment vessels - The evaluation of the test results on curved shear walls with liner for the PCCV test model. 14th International Conference on Structural Mechanics in Reactor Technology (SMiRT 14), Lyon, France.

Nakamura, S., K. Terada, T. Suzuki, M. Soejima, Y. Yamaura, H. Eto, K. Tsuda, K. Takiguchi and H. Akiyama (1996). Seismic Proving Test of Concrete Containment Vessels Part 1: Model Tests of a Curved Shear Wall for the PCCV. Eleventh World Conference on Earthquake Engineering, Mexico.

Naus, D. J. (1986). *Concrete component aging and its significance relative to life extension of nuclear power plants*. Oak Ridge, TN, Oak Ridge National Laboratory.

Naus, D. J. (2007). *Primer on durability of nuclear power plant reinforced concrete structures - A review of pertinent factors*. Oak Ridge, TN, Oak Ridge National Laboratory.

Naus, D. J. (2009). *Information related to visit to Crystal River 3*.

Naus, D. J., C. B. Oland, B. Ellingwood, W. E. Norris and H. L. Graves, III (1998). *Management of aging of nuclear power plant containment structures: Medium: ED; Size: 9 p.*

Naus, D. J., C. B. Oland and B. R. Ellingwood (1996). *Report on aging of nuclear power plant reinforced concrete structures*. Oak Ridge, TN, Oak Ridge National Laboratory.

Neville, A. (2001). "Core Tests: Easy to Perform, Not So Easy to Interpret." *Concrete International* 23(11): 59-68.

- Neville, A. M. (2011). *Properties of Concrete*. England, Pearson Education Limited.
- Newhouse, V. L., N. M. Bilgutay, J. Saniie and E. S. Furgason (1982). "Flaw-to-grain echo enhancement by split-spectrum processing." *Ultrasonics* 20(2): 59-68.
- Newman, A. B. (1936). "Heating and Cooling Rectangular and Cylindrical Solids." *Industrial & Engineering Chemistry* 28(5): 545-548.
- Nucleonics Week (1991). *Containment Liners Found Corroded at Some EDF 900-MW Reactors*. Nucleonics Week. New York, McGraw-Hill: 5-6.
- Nurse, W. R. (1949). "Steam curing of concrete." *Magazine of Concrete Research* 1(2): 79-88.
- Okamoto, K., S. Hayakawa and R. Kamimura (1995). "Experimental study of air leakage from cracks in reinforced concrete walls." *Nuclear Engineering and Design* 156(1-2): 159-165.
- Olson, F. C. W. and J. M. Jackson (1942). "Heating Curves: Theory and Practical Application." *Industrial & Engineering Chemistry* 34(3): 337-341.
- Olson, F. C. W. and O. T. Schultz (1942). "Temperatures in Solids during Heating or Cooling." *Industrial & Engineering Chemistry* 34(7): 874-877.
- Oluokun, F. A. (1991). "Prediction of Concrete Tensile Strength from its Compressive Strength: an Evaluation of Existing Relations for Normal Weight Concrete." *ACI Materials Journal* 88(3): 302-309.
- Oluokun, F. A., E. G. Burdette and J. H. Deatherage (1991). "Elastic Modulus, Poisson's Ratio, and Compressive Strength Relationships at Early Ages." *ACI Materials Journal* 88(1): 3-10.
- O'Neill, M. J. (1966). "Measurement of Specific Heat Functions by Differential Scanning Calorimetry." *Analytical Chemistry* 38(10): 1331-1336.
- Osborne, N. S., H. F. Stimson and D. C. Ginnings (1939). "Measurements of Heat Capacity and Heat of Vaporization of Water in the Range 0° to 100° C." *Journal of Research of the National Bureau of Standards* 23(2): 197-260.
- Owens Corning (2001). *Foamular 150 Rigid Foam Insulation Product Data Sheet*. Toledo, Ohio.
- Pane, I. and W. Hansen (2002). "Concrete Hydration and Mechanical Properties under Nonisothermal Conditions." *ACI Materials Journal* 99(6): 534-542.

Parrott, L. J., M. Geiker, W. A. Gutteridge and D. Killoh (1990). "Monitoring Portland cement hydration: Comparison of methods." *Cement and Concrete Research* 20(6): 919-926.

Penn, I. (2011). Cleaning up a DIY repair on Crystal River nuclear plant could cost \$2.5 billion. *St. Petersburg Times*. St. Petersburg.

Penn, I. (2013). Duke Energy announces closing of Crystal River nuclear power plant. *Tampa Bay Times*. St. Petersburg, Florida.

Performance Improvement International (2010). Root Cause Analysis Assessment - Crystal River Unit 3 Containment Concrete Delamination, Non-Proprietary Version. Oceanside, California.

Persson, B. (1999). "Poisson's ratio of high-performance concrete." *Cement and Concrete Research* 29(10): 1647-1653.

Perumal, V. (2008). Early-age thermal stress analysis of concrete. Master of Engineering, National University of Singapore.

Petti, J. P., D. Naus, A. Sagüés, R. E. Weyers, B. A. Erler and N. S. Berke (2011). Nuclear Containment Steel Liner Corrosion Workshop: Final Summary and Recommendation Report. Albuquerque, New Mexico, Sandia National Laboratories.

Pine Instrument Company (2011). Coefficient of Thermal Expansion of Hydraulic Cement Concrete Measurement System Operation Manual. Grove City, PA, Pine Instrument Company: 84.

Poole, J. L., K. A. Riding, K. J. Folliard, M. C. G. Juenger and A. K. Schindler (2007). "Methods for Calculating Activation Energy for Portland Cement." *ACI Materials Journal* 104(1): 303-311.

Poole, J. L., K. A. Riding, M. C. G. Juenger, K. J. Folliard and A. K. Schindler (2011). "Effect of Chemical Admixtures on Apparent Activation Energy of Cementitious Systems." *Journal of Materials in Civil Engineering* 23(12): 1654-1661.

Popovics, S., N. M. Bilgutay, M. Caraoguz and T. Akgul (2000). "High-Frequency Ultrasound Technique for Testing Concrete." *ACI Materials Journal* 97(1): 58-65.

Progress Energy (2009). Crystal River Unit #3 Containment Delamination Update.

Raphael, J. M. (1984). "Tensile Strength of Concrete." *ACI Journal* 81(2): 158-165.

Riding, K. A. (2007). Early Age Concrete Thermal Stress Measurement and Modeling. Doctor of Philosophy, The University of Texas at Austin.

Riding, K. A., J. L. Poole, K. J. Folliard, M. C. G. Juenger and A. K. Schindler (2011). "New Model for Estimating Apparent Activation Energy of Cementitious Systems." *ACI Materials Journal* 108(5): 550-557.

Riding, K. A., J. L. Poole, K. J. Folliard, M. C. G. Juenger and A. K. Schindler (2012). "Modeling Hydration of Cementitious Systems." *Materials Journal* 109(2): 225-234.

RILEM TC 42-CEA (1981). "Properties of set concrete at early ages: State-of-the-art report." *Materials and Structures* 14(84): 399-450.

Roberts, D. J. (2011). Request for Technical Assistance - Seabrook Station Alkali-Silica Reaction. R. A. Nelson.

Rochester Gas & Electric Corporation (2002). Application for Renewed Operating License: R.E. Ginna Nuclear Power Plant. Rochester, NY.

Rubbers, P. and C. J. Pritchard (2003). "An Overview of Split Spectrum Processing." *NDE.net* 8(8).

Saetta, A. V., B. A. Schrefler and R. V. Vitaliani (1993). "The carbonation of concrete and the mechanism of moisture, heat and carbon dioxide flow through porous materials." *Cement and Concrete Research* 23(4): 761-772.

Sasaki, Y., K. Hattori, M. Goto, T. Hasegawa, T. Hirama, K. Shiba and R. Tanaka (2001a). Seismic Proving Test of a Reinforced Concrete Containment Vessel (RCCV) Part 4 - Results of Shaking Table Tests up to Ultimate Strength. SMiRT 16, Washington, DC.

Sasaki, Y., K. Hattori, M. Nakajima, T. Kobayashi and A. Suzuki (2001b). Seismic Proving Test of a Reinforced Concrete Containment Vessel (RCCV) Part 5 - Simulation Analysis of the Safety Margin Test. SMiRT 16, Washington, DC.

Sasaki, Y., S. Tsurumaki, K. Satoh, H. Fuyama, T. Kitani, H. Eto, K. Tsuda, K. Takiguchi and H. Akiyama (1999). Seismic Proving Test of a Prestressed Concrete Containment Vessel Shaking Test and Analytical Results. 7th International Conference on Nuclear Engineering, Tokyo, Japan.

Saul, A. G. A. (1951). "Principles underlying the steam curing of concrete at atmospheric pressure." *Magazine of Concrete Research* 2(6): 127-140.

Schickert, M. (2005). "Progress in ultrasonic imaging of concrete." *Materials and Structures* 38(9): 807-815.

Schickert, M., M. Krause and W. Müller (2003). "Ultrasonic Imaging of Concrete Elements Using Reconstruction by Synthetic Aperture Focusing Technique." *Journal of Materials in Civil Engineering* 15(3): 235-246.

- Schindler, A. K. (2002). Concrete Hydration, Temperature Development, and Setting at Early-Ages. Doctor of Philosophy, The University of Texas at Austin.
- Schindler, A. K. (2004). "Effect of Temperature on Hydration of Cementitious Materials." *ACI Materials Journal* 101(1): 72-81.
- Schindler, A. K. and K. J. Folliard (2005). "Heat of Hydration Models for Cementitious Materials." *ACI Materials Journal* 102(1): 24-33.
- Serafim, J. L. and M. Guerreiro (1969). "Autogenous and Hygrometric Expansion of Mass Concrete." *ACI Journal* 66(9): 716-719.
- Serhan, S. J. and R. W. Adler (1997). Design Analysis/Calculation: Crystal River 3. Reading, PA, Parsons Power Group Inc.
- Shah, V. N. and C. J. Hookham (1998). "Long-term aging of light water reactor concrete containments." *Nuclear Engineering and Design* 185(1): 51-81.
- Shankar, P. M. and V. L. Newhouse (1985). "Speckle Reduction with Improved Resolution in Ultrasound Images." *IEEE Transactions on Sonics and Ultrasonics* 32(4): 537-543.
- Smith, J. A. (2001). Capacity of prestressed concrete containment vessels with prestressing loss. Albuquerque, New Mexico, Sandia National Laboratories.
- Spletzer, B. L., L. D. Lambert, V. L. Bergman and J. R. Weatherby (1995). Separate Effects Testing and Analyses to Investigate Liner Tearing of the 1:6-Scale Reinforced Concrete Containment Building, Sandia National Laboratories.
- Stark, D. (1980). "Alkali-Silica Reactivity: Some Reconsideration." *Cement, Concrete, and Aggregates, CCAGDP* 2(2): 92-94.
- Steigelmann, W. H. and C. P. Tan (1969). "Containment-System Design and Construction Practices in the United States." *Reactor and Fuel-Processing Technology* 12(2): 151-172.
- Tanesi, J., G. L. Crawford, J. M. Gudimettla and A. Ardani (2012). "Coefficient of Thermal Expansion of Concrete." *Concrete International* 34(4): 55-60.
- Tanesi, J., G. L. Crawford, M. Nicolaescu, R. Meininger and J. M. Gudimettla (2010). "New AASHTO T336-09 Coefficient of Thermal Expansion Test Method: How Will It Affect You?" *Transportation Research Record: Journal of the Transportation Research Board*(2164): 52-57.
- Tank, R. C. and N. J. Carino (1991). "Rate Constant Functions for Strength Development of Concrete." *ACI Materials Journal* 88(1): 74-83.

Tatro, S. B. (2006). Thermal Properties. ASTM Special Technical Publication 169D-EB: Significance of Tests and Properties of Concrete and Concrete-Making Materials. J. F. Lamond and J. H. Pielert. West Conshohocken, Pennsylvania: 226-237.

Taylor, H. F. W., C. Famy and K. L. Scrivener (2001). "Delayed ettringite formation." Cement and Concrete Research 31(5): 683-693.

Tennis, P. D. and J. I. Bhatti (2006). Characteristics of portland and blended cements: results of a survey of manufacturers. Cement Industry Technical Conference, 2006. Conference Record. IEEE.

Texas Department of Transportation. (2010). "Engineering Software - ConcreteWorks." Retrieved May 12, 2013, from <http://www.txdot.gov/inside-txdot/division/information-technology/engineering-software.external.html>.

Texas Department of Transportation (2011). Test Procedure for Determining the Coefficient of Thermal Expansion of Concrete (Tex-428-A). Tex-428-A.

Tia, M., C. Ferraro, A. Lawrence, S. Smith and E. Ochiai (2010). Development of Design Parameters for Mass Concrete Using Finite Element Analysis. Gainesville, Florida, University of Florida: 194.

Twidale, D. and R. Crowder (1991). "Sizewell 'B' - A one tenth scale containment model test for the UK PWR programme." Nuclear Engineering and Design 125(1): 85-93.

U.S. Army Corps of Engineers (1963). Method for Calculation of Thermal Conductivity of Concrete (CRD-C 44-63).

U.S. Army Corps of Engineers (1965). Method of Test for Thermal Conductivity of Lightweight Insulating Concrete (CRD-C 45-65).

U.S. Army Corps of Engineers (1973a). Method of Test for Specific Heat of Aggregates, Concrete, and Other Materials (Method of Mixtures) (CRD-C 124-73).

U.S. Army Corps of Engineers (1973b). Method of Test for Thermal Diffusivity of Concrete (CRD-C 36-73).

U.S. Army Corps of Engineers (1981). Test Method for Coefficient of Linear Thermal Expansion of Concrete (CRD-C 39-81).

U.S. Bureau of Reclamation (1940). Thermal Properties of Concrete. Boulder Canyon Project: Final Reports. Denver, Colorado.

U.S. Bureau of Reclamation (1981). Concrete Manual. Denver, Colorado.

- U.S. Energy Information Administration (2010). Annual Energy Review 2009, U.S. Department of Energy: 273-280.
- U.S. Nuclear Regulatory Commission (1976). Regulatory Guide 1.35, Revision 2. Inservice inspection of ungrouted tendons in prestressed concrete containment structures.
- U.S. Nuclear Regulatory Commission (1990a). Regulatory Guide 1.35.1 Determining prestressing forces for inspection of prestressed concrete containments. Washington, DC, Government Printing Office.
- U.S. Nuclear Regulatory Commission (1990b). Regulatory Guide 1.35, Revision 3. Inservice inspection of ungrouted tendons in prestressed concrete containments. Washington, DC, Government Printing Office.
- U.S. Nuclear Regulatory Commission (2010). Section 3: Nuclear Reactors. Information Digest 2010-2011. 22.
- U.S. Nuclear Regulatory Commission (2011a). U.S. Code of Federal Regulations. Title 10, Energy, Part 50: Domestic licensing of production and utilization facilities. Washington, D.C., Office of the Federal Register.
- U.S. Nuclear Regulatory Commission (2011b) "Crystal River Concrete Containment Separation."
- U.S. Nuclear Regulatory Commission (2012a). Appendix A: U.S. Nuclear Power Reactors. Information Digest 2012-2013. 24.
- U.S. Nuclear Regulatory Commission (2012b). Information Digest 2012-2013. 24.
- U.S. Nuclear Regulatory Commission (2012c). Regulatory Guide 1.90, Revision 2. Inservice inspection of prestressed concrete containment structures with grouted tendons.
- U.S. Nuclear Regulatory Commission (2015). Information Digest 2015-2016. Washington, DC. 27.
- U.S. Nuclear Regulatory Commission. (2016). "Status of License Renewal and Applications and Industry Activities." Retrieved March 4, 2016, 2016, from <http://www.nrc.gov/reactors/operating/licensing/renewal/applications.html>.
- Ukrainczyk, N. (2009). "Thermal diffusivity estimation using numerical inverse solution for 1D heat conduction." International Journal of Heat and Mass Transfer 52(25–26): 5675-5681.
- van Breugel, K. (1980). Artificial Cooling of Hardening Concrete. Delft, Netherlands, Delft University of Technology.

van Breugel, K. (1997). Simulation of Hydration and Formation of Structure in Hardening Cement-Based Materials. Doctor of Philosophy, 2nd Edition, Delft University of Technology.

van Breugel, K. (1998). Prediction of Temperature Development in Hardening Concrete. Prevention of Thermal Cracking in Concrete at Early Ages, RILEM Report 15. R. Springenschmid. London, E&FN Spon: 51-75.

von Rieseemann, W. A. and M. B. Parks (1995). "Current state of knowledge on the behavior of steel liners in concrete containments subjected to overpressurization loads." Nuclear Engineering and Design 157(3): 481-487.

Wahl, H. W. (1968). "Typical design problems and solutions for prestressed concrete containment structures." Nuclear Engineering and Design 8(4): 471-486.

Waller, V., L. d'Aloia, F. Cussigh and S. Lecrux (2004). "Using the maturity method in concrete cracking control at early ages." Cement and Concrete Composites 26(5): 589-599.

Walton, G. N. (1983). Thermal Analysis Research Program Reference Manual. Washington, D.C., National Bureau of Standards.

Weatherby, J. R. and D. B. Clauss (1989). Investigation of Liner Tearing Near Penetrations in a Reinforced Concrete Containment under Severe Accident Loads. 10th International Conference on Structural Mechanics in Reactor Technology, Anaheim, California.

Wheeler, B. (2011) "Evaluating an Unexpected Crack in Containment." Power Engineering 115.

Wilson, D. (2009a). Crystal River Concrete Core Observations: Report of Petrographic Observations. San Diego, California, MACTEC Engineering and Consulting.

Wilson, D. (2009b). Crystal River Steam Generator Replacement Project: Report of Petrographic Observations. San Diego, California, MACTEC Engineering and Consulting.

Won, M. (2005). "Improvements of Testing Procedures for Concrete Coefficient of Thermal Expansion." Transportation Research Record: Journal of the Transportation Research Board 1919: 23-28.

Woods, H., H. H. Steinour and H. R. Starke (1932). "Effect of Composition of Portland Cement on Heat Evolved during Hardening." Industrial and Engineering Chemistry 24(11): 1207-1214.

Zain, M. F. M., H. B. Mahmud, A. Ilham and M. Faizal (2002). "Prediction of splitting tensile strength of high-performance concrete." *Cement and Concrete Research* 32(8): 1251-1258.

Zhu, J. and J. Popovics (2007). "Imaging Concrete Structures Using Air-Coupled Impact-Echo." *Journal of Engineering Mechanics* 133(6): 628-640.

Zoldners, N. G. (1971). "Thermal Properties of Concrete under Sustained Elevated Temperatures." *ACI Special Publication* 25: 1-31.